

Future Prospects in Gravitational Waves: From Testing Fundamental Physics to Instruments beyond LIGO

Thesis by
Brian Christopher Seymour

In Partial Fulfillment of the Requirements for the
Degree of
Doctor of Philosophy

The logo for the California Institute of Technology (Caltech), featuring the word "Caltech" in a bold, orange, sans-serif font.

CALIFORNIA INSTITUTE OF TECHNOLOGY
Pasadena, California

2025
Defended May 05, 2025

© 2025

Brian Christopher Seymour
ORCID: 0000-0002-7865-1052

All rights reserved

ACKNOWLEDGEMENTS

I would like to thank my thesis advisor, Yanbei Chen, for his inspiring support and mentorship throughout my PhD. I am always impressed with his ability to reason through difficult problems and distill it down to its most important pieces, and then make the answer appear it was obvious all along. His exceptional expertise and creative approach to solving physics problems have not only advanced my research but also rubbed off on the entire research group.

I would like to thank Hang Yu for mentoring me during my first two years as a postdoc; I owe much of my subsequent success and understanding to his dedicated guidance and the knowledge he generously shared. I really appreciate his time going into the weeds with me to solve various technical issues over Zoom for those years.

I would also like to thank Alan Weinstein and Katerina Chatziioannou for letting me join in the group meeting for LIGO Lab. Our discussions, along with those with their colleagues, have significantly deepened my understanding of real LIGO data analysis and improved my skills as a physicist. In particular, Alan is brimming with enthusiasm for all sorts of science and was excellent at helping me to practice answering hard questions. Whenever I shared my work with Katerina, I was always impressed with her encyclopedic knowledge of the literature and her associated suggestions for ways to improve the project. I would also like to thank them and Kathryn Zurek for their time serving as committee members.

I would like to thank my undergraduate advisors: Klebert Feitosa, who graciously mentored me when I was just starting out in coding; Adam Mullavey, Arnaud Pele, and Marie Kasprzack for giving me my first exposure to gravitational waves during the LIGO SURF; and Kent Yagi for his invaluable guidance in testing GR, which greatly contributed to my development as a scientist.

Thanks to my colleagues in the TAPIR and LIGO groups including Sizheng Ma, Dongjun Li, Ron Tso, Colin Weller, Andrew Laequer, Su Direkci, James Gardiner, Isaac Legred, Alvin K.Y. Li, Rico K.L. Lo, Jonathan Thompson, Ethan Payne, Jacob Golomb, Sophie Hourihane, Simona Miller, Nicolas Rui, Sarah Habib, Kyle Nelli, Guido Da Re, Rhiannon Udall, Ryan Magee, Lucy Thomas, Kwinten Fransen and Jordan Wilson-Gerow. I would also like to thank Adrian Ka-Wai Chung and Max Isi for their insightful discussions. I also had the privilege of working with a number

of undergraduates in the SURF program including Agla Þórarinsdóttir and Chris Jungkind.

I would also like to thank the friends I have made along the way at Caltech. Thanks to Arun Chakravorty, Hristos Courellis, and Sean Devey for living with me in Harkness through the years with our interesting Wednesday night conversations. My friends have made this experience enjoyable Jacob Golomb, Andrew Lu, Josh Olick-Gibson, Victoria Tobin, Ethan Payne, Samuel Solomon, Roey Lazarovits, Julius Wanner, Severin Schumacher, Tim Rogenmoser, and Pietro Toniolo. Finally to my two friends Matt and Eli, I have learned a lot from them.

Finally, I would like to thank my family for supporting me throughout my life. I would also like to thank my Aunt Beth and Uncle Victor who introduced me to proof based math one night in middle school to show that there are infinite prime numbers. My brother, Mark Seymour, has been an incredible friend and a constant source of inspiration. I cherish all the hiking, skiing, and surfing adventures we have had. I would like to thank my parents, Mary and John Seymour, for their unwavering love and support throughout my life. As I have grown older I have only come to recognize how much work it takes to provide scientific opportunities at crucial age windows. My mother in particular chose to homeschool me because she wanted to make sure that I was exposed to limitless opportunities in academics, and I think my choice to do a research career is due in a large part to this because I self studied science and math up through high school. I am deeply grateful to have been raised in such a caring and supportive family.

ABSTRACT

In this thesis, we study the prospects for gravitational wave astronomy in the future. We focus on a couple of areas for gravitation waves beyond LIGO: improving measurement techniques of cosmological parameters, developing new waveforms for environmental effects, probing fundamental physics in waveforms, and high frequency gravitational wave detectors.

In the first part of this thesis, we develop two methods to constrain cosmological parameters using gravitational-wave observations. The first approach employs the statistical dark siren method, where the observed distribution of binary black hole events—whose luminosity distances are directly measured—is matched against astrophysical population models. By analyzing the Fisher information in the event distribution, we derive the Cramér-Rao bounds to quantify both statistical uncertainties and potential biases arising from unmodeled features in the merger rate and mass distribution. The second approach leverages the benefits of multiband observations with decihertz detectors, which dramatically improve host galaxy identification by refining source localization. This enhanced capability benefits reduces systematic errors in the measurement of the Hubble constant and other cosmological parameters. Together, these methods pave new pathways for precision cosmography using gravitational waves.

In the second part of the thesis, we investigate gravitational-wave signatures arising from binary black holes merging in the vicinity of supermassive black holes (SMBHs). One study focuses on hierarchical triple systems where the orbital motion around an SMBH imprints striking modulations on the gravitational waveforms. In our work, gravitational lensing is highlighted as a pivotal effect—alongside Doppler shifts and de Sitter precession—that is crucial for breaking parameter degeneracies. A complementary analysis considers eccentric orbits, incorporating orbital pericenter precession alongside Doppler and precession effects to further refine parameter estimation. Together, these investigations demonstrate that dynamic lensing and orbital modulations can be leveraged to probe SMBH properties and their environments with unprecedented precision, underscoring the importance of incorporating these environmental effects into waveform models.

In the third work, we explore inspiral tests of general relativity by examining the phase evolution of gravitational-wave signals from coalescing binary systems. First,

we test Giddings’ non-violent non-locality proposal, which posits that quantum information is transferred via a non-local interaction that generates metric perturbations around black holes by creating an effective-one-body waveform. We show that this can be captured by parameterized tests of general relativity waveforms. In the second half, we assess the robustness of post-Newtonian coefficients against unmodeled deviations by introducing parameterized tests that exploit the inherent geometry of the waveform. We show that the tests of general relativity are intimately related to the geometry of the signal manifold and propose a new singular value decomposition method to search for deviations for testing the predictions of general relativity and probing potential modifications to gravitational dynamics.

In the fourth part of this thesis, we explore optimizing the GEO600 detector for high-frequency gravitational wave detection. Although GEO600 is less sensitive than LIGO in the conventional 50–400 Hz band, we demonstrate that by detuning the signal-recycling mirror its sensitivity can be enhanced at tens of kHz. Using simulations with Finesse 3.0, we show that the sensitive point can be effectively scanned across various frequencies by adjusting the detuning angle. This tuning enables GEO600 to better target monochromatic sources, such as boson clouds arising from superradiance, thereby opening a promising new window for high-frequency gravitational wave astronomy.

PUBLISHED CONTENT AND CONTRIBUTIONS

- [1] C. M. Jungkind, B. C. Seymour, L. Laeuger, et al. “Prospects for High-Frequency Gravitational-Wave Detection with GEO600.” In preparation for submission.
B.S. participated in the conception of the project and co-mentored the lead author to complete and write the manuscript.
- [2] B. C. Seymour, J. Golomb, and Y. Chen. “Inspirational tests of general relativity and waveform geometry.” In preparation for submission.
B.S. conceived of the project, did all the calculations, and wrote the manuscript.
- [3] A. Laeuger, B. Seymour, Y. Chen, et al. “Measuring supermassive black hole properties via gravitational radiation from eccentrically orbiting stellar mass black hole binaries.” In: *Phys. Rev. D* 109.6 (2024), p. 064086. DOI: [10.1103/PhysRevD.109.064086](https://doi.org/10.1103/PhysRevD.109.064086). arXiv: [2310.16799](https://arxiv.org/abs/2310.16799) [gr-qc].
B.S. participated in the conception of the project and co-mentored the lead author to complete and write the manuscript.
- [4] B. C. Seymour and Y. Chen. “Gravitational-wave signatures of non-violent non-locality.” Submitted to Physical Review Letters. Nov. 2024. arXiv: [2411.13714](https://arxiv.org/abs/2411.13714) [gr-qc].
B.S. conceived of the project, did all the calculations, and wrote the manuscript.
- [5] B. C. Seymour, H. Yu, and Y. Chen. “Multiband gravitational wave cosmography with dark sirens.” In: *Phys. Rev. D* 108.4 (2023), p. 044038. DOI: [10.1103/PhysRevD.108.044038](https://doi.org/10.1103/PhysRevD.108.044038). arXiv: [2208.01668](https://arxiv.org/abs/2208.01668) [gr-qc].
B.S. conceived of the project, did all the calculations, and wrote the manuscript.
- [6] H. Yu, B. Seymour, Y. Wang, et al. “Uncertainty and Bias of Cosmology and Astrophysical Population Model from Statistical Dark Sirens.” In: *Astrophys. J.* 941.2 (2022), p. 174. DOI: [10.3847/1538-4357/ac9da0](https://doi.org/10.3847/1538-4357/ac9da0). arXiv: [2206.09984](https://arxiv.org/abs/2206.09984) [astro-ph.CO].
B.S. participated in the conception of the project and edited the manuscript.
- [7] H. Yu, Y. Wang, B. Seymour, et al. “Detecting gravitational lensing in hierarchical triples in galactic nuclei with space-borne gravitational-wave observatories.” In: *Phys. Rev. D* 104.10 (2021), p. 103011. DOI: [10.1103/PhysRevD.104.103011](https://doi.org/10.1103/PhysRevD.104.103011). arXiv: [2107.14318](https://arxiv.org/abs/2107.14318) [gr-qc].
B.S. participated in the conception of the project and edited the manuscript.

TABLE OF CONTENTS

Acknowledgements	iii
Abstract	v
Published Content and Contributions	vii
Table of Contents	vii
List of Illustrations	xi
List of Tables	xxvi
Chapter I: Introduction	1
1.1 Hubble Tension with Gravitational Wave Observations	4
1.2 Introduction to Tests of Gravity	6
1.3 Extraction of Environmental Effects in Space-Based Observations	8
1.4 High Frequency Gravitational Wave Detection	9
1.5 Organization of Thesis	11
I Cosmography with Gravitational Waves	30
Chapter II: Uncertainty and bias of cosmology and astrophysical population model from statistical dark sirens	31
2.1 Introduction	31
2.2 Basic framework	34
2.3 Combined astrophysical and cosmological model	38
2.4 Applications to GWTC-3	40
2.5 Bias induced by substructures in the population model	45
2.6 Conclusion and Discussion	48
2.7 Appendix: Validation of the methodology	51
Chapter III: Multiband Gravitational Wave Cosmography with Dark Sirens	61
3.1 Introduction	61
3.2 Measurement of a Binary Black Hole	66
3.3 Cosmological Constraints	74
3.4 Conclusion	77
3.5 Appendix: Antenna Patterns of TianGO	79
3.6 Appendix: Consistency of Statistical Method	80
II Measuring Hierarchical Triples around Active Galactic Nuclei with Decihertz Detectors	95
Chapter IV: Detecting gravitational lensing in hierarchical triples in galactic nuclei with space-borne gravitational-wave observatories	96
4.1 Introduction	96
4.2 GW waveforms including gravitational lensing	99

4.3	Detectability of lensing signatures	113
4.4	PE accuracy including lensing effects	116
4.5	Conclusion and Discussions	119
4.6	Appendix: SPA for waveforms with fast modulation	121
4.7	Appendix: Geometrical derivation of the lensing equation	123
4.8	Appendix: Understanding the improvement in $\Delta \log M_3$ due to repeated lensing	124
Chapter V: Measuring Supermassive Black Hole Properties via Gravitational Radiation from Eccentrically Orbiting Stellar Mass Black Hole Binaries		137
5.1	Introduction	137
5.2	Mathematical Description of the SMBH+BBH Triple System	140
5.3	Parameter Estimation with the Fisher Information Matrix	148
5.4	Results and Discussion	149
5.5	Conclusion and Future Directions	160
5.6	Appendix: Validity of Waveform Approximations	163
5.7	Appendix: Description of Measurement Accuracy	167
III Testing General Relativity with Gravitational Waves		177
Chapter VI: Gravitational-wave signatures of non-violent non-locality		178
6.1	Introduction	178
6.2	Setup	179
6.3	NVNL Waveforms	181
6.4	Extraction of NVNL from data	184
6.5	Conclusion	187
6.6	Appendix: Waveform Details	190
Chapter VII: Inspiral tests of general relativity and waveform geometry		206
7.1	Introduction	206
7.2	Background and Methods	208
7.3	PPE Parameters Capture Generic Phase Deviations	214
7.4	SVD Approach	217
7.5	Conclusion	222
7.6	Appendix: Bias Formula for Multiple μ^a Parameters	224
7.7	Appendix: Derivation of Bayes Factor	224
7.8	Appendix: Multidetector Geometry	227
IV High-Frequency Gravitational Wave Detection		235
Chapter VIII: Prospects for High-Frequency Gravitational-Wave Detection with GEO600		236
8.1	Introduction	236
8.2	Detector Sensitivity	238
8.3	High Frequency Sources	245
8.4	Conclusion	251
8.5	Appendix: Antenna Response Patterns	252

8.6 Appendix: Noise Spectral Densities 257

LIST OF ILLUSTRATIONS

<i>Number</i>	<i>Page</i>
1.1 This image is taken from [10]. It shows the astrophysical horizon of current and future detectors. On the right it shows the GW detections for typical BBH systems. One can see that every BBH merger is observed with third generation detectors (CE [9, 10]/ET[11, 12, 13]) and nearly all are found with LIGO Voyager which is a cryogenic upgrade of LIGO [32]. Additionally, one can see that we are only scraping the surface of detecting a large number of the BNS detections due to them being quieter but much more numerous.	2
1.2 Image taken from [46] and based upon [47]. A schematic diagram of various prominent tests of gravity. On the x-axis the characteristic gravitational potential Φ is shown while the y-axis contains shows the characteristic gravitational curvature R . One can see the regimes of solar system measurements (Lunar laser ranging, LAGEOS, Mercury perihelion precession). The S2 gravity measurements is the tracking of S2 star's orbit about the SgA* [50]. The pulsar measurements probe stronger gravity than solar system tests. Finally the light blue regions are the potentials for gravitational wave detections which show it is probing both high potential and highly curved region of spacetime.	4
1.3 Image taken from [91]. This demonstrates how a ppE dephasing can cause the waveform to deviate from the GR one in the time domain.	7
1.4 Image taken from [156]. This shows the fundamental noises that exist in the design sensitivity of advanced LIGO. One can see that quantum shot noises dominates the noise spectrum at high frequencies.	10

- 2.1 Top: expected number of detection as a function of the redshift z at different values of $h \equiv H_0/(100 \text{ km/s/Mpc})$. From GW events, we can construct such an distribution as a function of D_L first and then convert it to a function of z based on assumed cosmological parameters. Meanwhile, our astrophysical knowledge allows us to construct an expected distribution as a function of z from, e.g., galaxy catalogs. By comparing the two histograms, we can then constrain the value of cosmological parameters. Bottom: the distribution is also affected by astrophysical models (e.g., the location of a peak in the BBH's mass distribution μ_g ; see Sec. 2.3) which could mimic the effect of changing cosmological model. This indicates the significance of jointly analyzing astrophysical and cosmological parameters. 34
- 2.2 Similar to Fig. 2.1 but now we plot the distribution as a function of the detector-frame mass of the primary BH, m_1^d . Combining it with Fig. 2.1 can thus be used to break the degeneracy between astrophysical and cosmological parameters. 35
- 2.3 Uncertainties on cosmological parameters (h, Ω_m) from the redshift histogram (cf. Fig. 2.1) assuming we know exactly the astrophysical model. Throughout this work, we will use red crosses to denote the true values of the parameters (i.e., values at which we evaluate the Fisher information matrix). The error ellipses indicate the 68% credible intervals. We predict an uncertainty on h of ± 0.11 , which agrees well with the gray-dotted curve in fig. 9 in LIGO Scientific Collaboration et al. [1] obtained under the same assumptions. 42
- 2.4 Correlation between astrophysical and cosmological parameters by inverting a 3×3 Fisher matrix including (h, μ_g, R) (top panel) or (h, γ, R) (bottom panel). The cyan ellipses correspond to constraints from the redshift distribution alone (cf. Fig. 2.1). As μ_g and/or γ decreases, h will increase to a greater value. It captures the key features shown in Fig. 10 in [41]. If one further incorporates the information from the mass distribution (orange ellipses; cf. Fig. 2.2), the combined uncertainties can be reduced to the gray ellipses. 43
- 2.5 Error ellipses for a sample of 40 BBH events similar to the GWTC3 catalog. The gray ellipses are obtained by summing the Fisher information from the marginalized redshift and primary mass distribution together, and the olive ones are from the 3D $r(m_1, m_2, z)$ distribution. 44

2.6	Bias on h due to an error in the astrophysical rate Δr given by Eqs. (2.25)-(2.27). An error in m_1 but constant in redshift can then be obtained by summing over all the pixels along a specific $\mu_{m, err}$ (i.e., a vertical line) with appropriate normalization. Likewise, other generic Δr can be obtained by summing over the corresponding pixels. Also shown in the dotted-brown line is an approximation of the detection threshold with $[\mathcal{M}_c(1+z)]^{5/6}/z \simeq constant$	49
2.7	Error ellipses from the 3D $r(m_1, m_2, z)$ distribution assuming 500 BBH events using the model in [46]. Our results show good agreement with those obtained in Fishbach, Holz, and Farr [46] and Farr et al. [39]. It thus validates our approach when n_{obs} is large.	52
3.1	Comparison of detectors with a sample waveform. We plot the instrumental sensitivities for TianGO (orange), LIGO Voyager (blue), LISA (purple), aLIGO design sensitivity (red), Cosmic Explorer 2 (brown), Einstein Telescope D (pink), TianQin (gray), and B-DECIGO (yellow). We also show a sample TianGO waveform for a typical BBH merger (black) at $z = 0.3$, $\mathcal{M}_c = 25M_\odot$, $q = 1.05$, and $T_{obs} = 5$ yr assuming observed by a TianGO-like detector. On the top axis, we give the time until merger.	65
3.2	Measurement accuracy for luminosity distance, angular resolution and comoving volume localization versus redshift. We plot these measurement uncertainties for TianGO + HLI Voyager (red), HLI Voyager (blue), and TianGO (orange). Because we randomize over the angular extrinsic parameters $(\bar{\phi}_S, \bar{\theta}_S, \bar{\phi}_L, \bar{\theta}_L)$, we plot both the median measurement with the line and the shaded region where 80% of binaries lie. We use $\mathcal{M} = 25M_\odot$, $q = 1.05$, $t_a = 5^\circ$ and $T_{obs} = 5$ yr. We use a galaxy number density per comoving volume of $n_{gal} = 0.01$ gal/Mpc ³ to convert comoving volume localization to estimate our ability to identify the GW source.	71

- 3.3 On the top, we plot the probability of an event being localized as a function of redshift for HLI Voyager (green) and TianGO + HLI Voyager (blue). We see that adding TianGO to the HLI Voyager network would nearly double the range at which we can localize a dark siren event. On the bottom, we plot the expected number of localizations in the comoving volume sphere. We use the merger rate equal to the star formation rate (red dashed) from Eq. (3.19). We find that the number of yearly localizations will increase by a factor of 10 by adding TianGO. This figure assumes the same binary parameters as Fig. 3.2, but also uniformly samples the observation time $T_{\text{obs}} \in [0, 5]$ yr. . . . 73
- 3.4 The confidence intervals for Hubble constant H_0 and matter density parameter Ω_m from HLI Voyager (blue), TianGO + HLI Voyager (red), Planck 2018 (yellow) [1], 2 CE 2's + ET-D (cyan), and B-DECIGO + 2 CE 2's + ET-D (pink). GW constraints come from Eq. (3.21) using only fully localized BBH events during a five year observation. We use chirp mass $\mathcal{M}_c = 25M_\odot$ and merger rate density at the star formation rate. One can see that adding TianGO to the Voyager network would improve error in the measurement of the Hubble constant and the matter density parameter. Moreover, the 3G ground network sees a similar improvement with the addition of B-DECIGO assuming it is in a heliocentric orbit. We include the forecasted cosmology constraints for other detector configurations in Tab. 3.1. . . . 74
- 3.5 Constraints on the expansion rate as a function of redshift for various forecasted and current measurements at the 68% CL. We plot the forecasted constraints on HLI Voyager (blue) and TianGO + HLI Voyager (red). We also plot current expansion rate constraints from Planck 2018 (yellow) [1] and from GW170817 (pink) [48]. We produce this plot assuming the Planck parameters as the true values when computing the Fisher matrix, and incorporate only uncertainty on (H_0, Ω_m) for the shaded regions. Notice that three Voyagers can measure the expansion rate relatively accurately below $z \sim 0.1$. Furthermore, adding the decihertz detector TianGO enhances the ability for the expansion rate to be measured. 75

- 3.6 We plot the negative log likelihood of the posterior distribution on the Hubble constant $p(h|\{d_{\text{GW}}\})$ in the 2D simulation. Each curve with n labeled is the median number of *extra* galaxies in the localization region while the Fisher matrix constraint approximation from Eq. (3.21) is also plotted (dashed red). Each curve in the plot corresponds to picking a different angular resolution for the events. This shows that measurement of sources with poor angular resolution will result in weaker Hubble constant constraints due to the increased number of galaxies in the localization region. We also see that with a higher number of events, the likelihood distribution for h tightens. Finally, we see that the Bayesian approach reduces to the Fisher information estimate when there is a uniquely identified galaxy. This is still a conservative estimation on how well we can measure the cosmology as the information from $n > 0$ systems is discarded. 82
- 4.1 Cartoon illustrating the lensing geometry. The top part corresponds to the standard lensing scenario (i.e., the strong lensing) where the source is behind the lens and the deflection angle $\alpha \ll \pi$ (and here we specifically draw the instance when $z_o = \phi_o = 0$). The bottom illustrates the geometry of retro-lensing (also known as the glory). Note in the repeated lensing scenario, we have $D_{OL} \simeq D_{OS} \simeq D \sim 1 \text{ Gpc}$ and $D_{LS} \lesssim 100 \text{ AU} \ll D_{OL}, D_{OS}$ 102
- 4.2 Top panel: magnification $|\mu|$ as a function of the inclination angle ι_J of the outer orbit. Bottom panel: upper and lower envelopes of the amplification factor. Here we assume $M_3 = 10^8 M_\odot$ and $a_o = 100 \text{ AU}$. The outer orbital phase is either $\phi_o = 0$ (for standard lensing) or $\phi_o = \pi$ (for retro-lensing). For such $M_3 = 10^8 M_\odot$, $2\pi f M_3 = 100$ correspond to a GW frequency of $f \simeq 0.03 \text{ Hz}$ 105

- 4.3 Sample waveforms including the lensing effects. Also shown in the grey traces are the proposed instrumental sensitivity of LISA [65] and TianGO [13]. Here we assume $M_3 = 10^8 M_\odot$, $a_o = 100 \text{ AU} \simeq 101 M_3$, and $\iota_J = 87^\circ$. The outer orbit has a period of $P_o = 0.10 \text{ yr}$ and the inner orbit precesses with a period $P_{dS} = 6.8 \text{ yr}$. Each time $\phi_o[t(f)] \simeq 0$ (source behind the lens), the standard lensing happens and is characterized by a sharp a cyan peak in the waveform. When $\phi_o[t(f)] \simeq \pi$ (source in front of the lens), we then have retro-lensing (glory), which is calculated including wave interference and polarization effects [Eq. (4.26)]. Note that the starting frequency of each waveform is chosen so that the inner binary will merge in 5 yr, which is also the fiducial duration of observation assumed in this study. . . . 110
- 4.4 Similar to Fig. 4.3 but for $M_3 = 10^7 M_\odot$, $a_o = 50 \text{ AU} \simeq 507 M_3$, corresponding to an outer orbital period of $P_o = 0.11 \text{ yr}$ and a dS precession period of $P_{dS} = 38 \text{ yr}$. In this scenario only the standard lensing has a significant effect on the waveform. 111
- 4.5 Threshold value of $(90^\circ - \iota_J)$ such that the secondary image in the standard-lensing case has a magnification of $|\mu_2| \geq 0.1$ [which corresponds to $\eta \leq 1.27$; Eq. (4.14)]. Also shown in the grey-dashed and brown-solid traces are lines corresponding to an outer orbital period of $P_o = 0.1 \text{ yr}$ and a dS precession period of $P_{dS} = 10 \text{ yr}$ 112
- 4.6 Threshold value of $(90^\circ - \iota_J)$ such that the magnification of the first retro-lensing image has $|\mu_\pi| \geq 0.1$. Note that in this case the color bar has a logarithm scale. 113

- 4.7 Mismatch ϵ of the waveform as a function of the inclination ι_J for three different outer orbital configurations, assuming a TianGO-like decihertz detector. In each panel, we use the grey trace to indicate the mismatch between a waveform without any lensing signatures with the one including the standard lensing (source behind the lens). The mismatches between waveforms with standard lensing only and those further including retro-lensing effects are illustrated in the olive traces. The purple traces shows the mismatches between the lensing signatures calculated under the classical/geometrical limit (for both standard and retro lensing) and those incorporating wave effects. The top and middle panels both have out orbital periods of $P_o \simeq 0.1 \text{ yr}$ and the bottom panel has $P_o = 0.06 \text{ yr}$. For a relatively light lens with $M_3 \lesssim 10^7 M_\odot$, there is a decent chance of detecting the standard lensing. For more massive lenses $M_3 \simeq 10^8 M_\odot$, we might further detect the glory (retro-lensing). Recall that we have $w = 8\pi M_3 f = 12 (M_3/10^7 M_\odot) (f/0.01 \text{ Hz}) \gg 1$ and therefore the geometrical limit is typically a good approximation as indicated by the purple traces. 125
- 4.8 Similar to Fig. 4.7 but for LISA. We also moved the source's luminosity distance from 1 Gpc to 200 Mpc so that the source's the SNR in LISA is greater than 8. For LISA, the standard lensing could have a decent detectability (a few to ten percent) while the retro-lensing are typically too weak to be detectable. 126
- 4.9 PE accuracy for systems with (solid traces) and without (dotted traces) the (standard) gravitational lensing, assuming detection by a single, TianGO-like detector. Here we fix $\iota_J = 87^\circ$ and vary the mass of the central SMBH. The semi-major axis is chosen such that the outer orbital period is $P_o = 0.1 \text{ yr}$. For this ι_J , we have $\epsilon > 1/2\rho^2$ when $M_3 \gtrsim 1.7 \times 10^6$ or $\eta_{min} \lesssim 1$. Both $\log M_3$ and $\bar{\theta}_J$ can be determined better by orders of magnitude. The determination of the opening angle $\Delta\lambda_L$ is also improved, especially when P_{dS} in the range of 10-45 years. 127
- 4.10 PE accuracy for κ where $\kappa = M_l/M_3$ [Eq. (4.36)]. The source's orientation and sky location are the same as in Fig. 4.9. The error in κ decreases roughly linearly with M_3 and it can be constrained to a 1% accuracy for $M_3 \gtrsim 10^7 M_\odot$ 128

4.11	Error ellipses for the simple static lensing (i.e., $\eta = \beta/\theta_{\text{Ein}} = \text{constant}$ for the entire waveform). At each given η , the PE error $\Delta \log M_3$ is highly correlated with $\Delta\eta$, and thus the PE error obtained by inverting the Fisher matrix is much greater than the inverse of the diagonal elements. On the other hand, the orientation of the error ellipse varies as η varies [Eq. (4.47)]. Therefore, in the case of repeated lensing where $\eta = \eta(t)$ due to the outer orbit's motion, different values of η are sampled and thus breaks the degeneracy between $\log M_3$ and η , allowing a PE much better than the static lensing case [cf. eq. (32) in Ref. [57].]	128
5.1	Top: Geometry of the SMBH+BBH triple system. Bottom, inset: View of the triple system normal to the plane of the outer orbit. The outer orbit angular momentum \hat{L}_o points out of the page. See the discussion below and Table 5.1 for definition of all parameters. Figure dimensions are not an indication of true scale.	140
5.2	An example waveform $\tilde{h}(f)$ with $M_3 = 10^8 M_\odot$, $a_o = 100M_3$, and $e_o = 0.3$, along with approximate sensitivity curves for B-DECIGO, TianGO, and LISA used in the Fisher matrix calculations done in this work. The red dashed curve gives the same waveform but with the effects of de Sitter precession removed.	150
5.3	Fractional uncertainty in M_3 as measured by B-DECIGO for three different eccentricities $e_o = \{0.001, 0.3, 0.6\}$. At each point in the contour plot, we take the median uncertainty over a set of combinations of $(\gamma_o, \alpha_o, \phi_o)$. The purple region corresponds to where the outer binary merges in less time than the observation duration. We lightly shade out the region with an outer orbital period greater than 10 years, where the cumulative effect of the Doppler shift becomes small.	152
5.4	Same as Fig. 5.3, but measured by LISA instead.	153
5.5	Uncertainty in a_o as measured by B-DECIGO for three different eccentricities $e_o = \{0.001, 0.3, 0.6\}$. The same sampling procedure as used in Fig. 5.3 is applied here.	154
5.6	Same as Fig. 5.5, but measured by LISA instead.	155

5.7	Contour plot for the fractional uncertainty in M_3 as measured by B-DECIGO, taken from Fig. 5.3. Plotted on top of the contours are lines of constant $a_o^{5/2}/M_3^{3/2}$ and $M_3^{1/2}/a_o^{1/2}$ to indicate the structure of the contours.	156
5.8	Uncertainty in e_o as measured by B-DECIGO for three different eccentricities $e_o = \{0.001, 0.3, 0.6\}$. The same sampling procedure as used in Fig. 5.3 is applied here.	158
5.9	Same as Fig. 5.8, but measured by LISA instead.	159
5.10	The fractional uncertainties in M_3 obtainable by B-DECIGO (blue), TianGO (orange), and LISA (green) as the eccentricity is varied. The solid, dashed, and dotted lines correspond to different choices of $(M_3, a_o/M_3)$	161
5.11	Same as Fig. 5.10, but estimating the outer eccentricity variance Δe_o	162
6.1	The real part of the dimensionless $h_{22}(t)$ strain for $A_{22} = 5 \times 10^{-2}$. This is the <i>full waveform</i> before the principal component analysis is done, so it contains all perturbations. These signals are aligned at very early times so that their signals overlap at low frequencies but they stochastically diverge as they reach the plunge. The apparent ringdown difference is primarily due to the phenomenological ringdown attachment, but we only do the testing GR analyses with the inspiral piece.	182
6.2	Frequency domain phase deviation realizations for $A_{22} = 1$. Using time domain waveform realizations shown in Fig. 6.1, we plot the amount of dephasing from GR that they will have. We also plot the frequency at which the binary crosses the inner most stable circular orbit (dashed blue) and the frequency at which the inspiral portion of the waveform is matched to the ringdown (dashed black). Note that $A_{22} = 1$ is not a small deviation from GR, so we calculated this at $A_{22} \ll 1$ and scaled it appropriately. One can see that the secular effect of NVNL is nearly zero while the theory predicts random dephasing from GR.	182
6.3	The largest principal component modes of the covariance matrix. All modes with odd $l + m$ are zero since we are confined to the orbital plane with $\theta = \pi/2$. The largest eigenvector accounts for $\sim 97\%$ of the phase variance for each of the modes. One can see that similar deviations happen for all (ℓ, m) modes.	184

- 6.4 The log Bayes factor projected constraint for Hanford-Livingston-Virgo network operating at O3 Livingston sensitivity (positive favors GR). We plot this for various values of A and for increasing numbers of events. The line corresponding to $-10 \log$ Bayes factor is shown for the optimal PCA model (black) and PN coefficients (other colors) where GR is disfavored. Using an event list, we perform parameter estimation for five years of detectable events and then compute the Bayes factor for the hierarchical test of GR. Note that the PCA model is best able to constrain the effects of NVNL most stringently, but the PN coefficients are able to detect a violation of $A \neq 0$ nearly as well. We also see that the largest PN orders perform the best. For a five year observation, the bound for the PCA model is $A < 6.2 \times 10^{-3}$ 188
- 6.5 The log Bayes factor for the Hanford-Livingston-Virgo network operating at CE sensitivity (positive favors GR). This plot shows the same scaling as Fig. 6.4, but contains more events since CE detects more in a five year period. For a five year observation, the bound for the PCA model is $A < 4.2 \times 10^{-4}$ 189
- 6.6 Comparison of how much variance is captured by the PCA estimator. We see that the full $\Delta\Psi$ is well described by this. While some of the variance is not captured at low frequencies, at high frequencies there is a nearly perfect match, especially at larger frequencies. The other PCA terms contain about 3% of the variance that is not accounted for in the primary one here as discussed in the main text. 194
- 6.7 The log Bayes factor for the Hanford-Livingston-Virgo network at O3 Livingston sensitivity (positive favors GR). One can see that the red curve favors NVNL at large events, while blue favors GR. The whiskers correspond to the upper and lower bounds are $\pm 1\sigma$ percentile values due to randomness associated with the order of events. If one sees a loud clear event early, then it is easier to favor/disfavor GR. 194
- 6.8 We show the running estimate of A for an O3 network. In blue, we show the 1σ and 2σ confidence region when we inject $A_t = 0$. We can see that the error shrinks as events are observed. In blue, we inject $A_t = 6 \times 10^{-3}$, and one can see that as events are observed the probability density narrows and detects a violation. 195

- 6.9 We show the running estimate of A for the CE network in an analogous manner of Fig. 6.8. In red, we inject $A_t = 0$, and in blue $A_t = 3 \times 10^{-4}$. One can see that as more observations are made, the confidence region begins to exclude $A = 0$ 196
- 7.1 Illustration of degeneracy when testing GR. We show the injected signal (blue) which depends on the true GR parameters θ_t and the beyond GR parameters λ_t . The model signal at the true GR parameters θ_t (red) is shown and the best fit signal is at the maximum likelihood point θ_{ML} (black). The GR waveform is modified by Δh which causes biases to the GR waveform, thus residual signal to measure beyond GR deviations is given by the perpendicular signal Δh^\perp . Note that this is a high dimensional manifold where (d_1, d_2, d_3) are the values of the signal at particular frequency bins. 208
- 7.2 In this plot, we visually show how the ppE tests of GR can capture generic bGR deviations. The GR manifold (black) is a line that is at the intersection between the true bGR manifold (red) and the ppE manifold (blue). One can see that the perpendicular part of the signal from GR is $\rho_\perp = \|\Delta h_\perp\|$ which is the residual SNR after allowing the GR parameters to be biased $h_{\text{GR}}^{\text{ML}} = h_{\text{GR}}(\theta_t + \Delta\theta_{\text{bias}})$. One can see that the best fit ppE parameter is located at the blue mark and has residual SNR $\rho_\perp^{\text{ppE}} = \mathcal{O}\rho_\perp$ as given in Eq. (7.28). Finally, the brown line is the missed signal from our TGR model. With this picture in mind, we can explore how well tests of GR capture generic deviations. 213
- 7.3 Residual amplitude for PN injected deviations from GR for a GW150914 like detection. On the left is the GR waveform (black) and O3 Livingston ASD (cyan). We show the waveform residuals that would be caused by injection what we show in Fig. 7.4 from parameterized tests. On the right, we show what the residual deviation is after the stealth biases in the GR parameters are accounted for. While the original total bias to the SNR is $\|\Delta h\| = 5$, the perpendicular waveforms have much less signal $\|\Delta h_\perp\| \sim 0.5$ 215

- 7.4 Visualization of how the frequency domain representations of the parameterized tests. On the left, we show the dephasing for a GW150914 like detection and scale the parameter normalizations such that $\|\Delta h\| = 5$. On the right, we show the residual (perpendicular) phase deviation in the injection after the GR deviations are marginalized over. One can see that the total dephasing of the perpendicular waveforms is noticeably smaller, and the function has multiple roots that correspond to what the residual deviation looks like after removing the GR uncertainties. 216
- 7.5 The overlap between deviations injected (y-axis) and the recovery model (x-axis). We use GW150914 event parameters with three detectors at O3 Livingston sensitivity, all extrinsic parameters measured and intrinsic parameters $(\mathcal{M}_c, q, \chi_{\text{eff}}, \chi_p)$. One can see that injecting a deviation at $k/2$ -th PN order fractionally from GR is perfectly captured on the diagonal but has less overlap as the injection and recovery order grow. This means that if there is a true deviation, the significance drops slowly as you search for the wrong PN order $k_{\text{rec}} \neq k_{\text{inj}}$ because the intrinsic parameters will capture the difference. Note that we do not include $k = 5$ in either of these plots because it is nearly completely degenerate with phase of coalescence. 218
- 7.6 The overlap between deviations injected (y-axis) and the recovery model (x-axis). We use GW150914 event parameters with three detectors at O3 Livingston sensitivity, all extrinsic parameters measured and intrinsic parameters (\mathcal{M}_c, q) . This can be directly compared to Fig. 7.5 which measures the parameters $(\chi_{\text{eff}}, \chi_p)$ additionally. One can see that ignoring the parameter uncertainty of the spin parameters means that the overlap is higher for these waveforms since the spins cannot bias the waveforms. 218
- 7.7 We show the visualization of the SVD operation. For our choice of the SVD, we use $H_{ik} = \Delta h_k^\perp(f_i)w(f_i)$ as given in Eq. (7.49). The matrix \mathbf{U} is a square matrix that represents linear redefinitions of $\delta\varphi_k$ while the matrix \mathbf{V} is linear combinations of $\Delta h_k^\perp(f_i)w(f_i)$ which diagonalize \mathbf{H} . Finally, the matrix $\mathbf{\Sigma}$ is ordered by singular value that ranks the importance of each principal mode. 220

- 7.8 Demonstration of the SVD on different PN waveform deviations. In transparent solid, different $\Delta\Psi_k^\perp$ are shown and the dashed lines are the SVD modes for GW150914 like event. Note that we normalize each $\Delta\Psi_k^\perp$ so that $\|\Delta h_k^\perp\| = 1$ so each signal is equally weighted in the SVD. One can see that the dashed black line is the dominant SVD term that best fits each waveform. Additionally the red and blue curves represent subdominant SVD dephasing that are orthogonal to each other. One can see that each of these PN waveform deviations is captured by only a few SVD modes, which explains how degeneracies would form when using the original parameter space. 222
- 7.9 Construction of SVD multiparameter tests. We start by orthogonalizing the ppE deviations from GR. One can see that each of these three ppE waveforms had approximately the same but they have different perpendicular length of the GR manifold at the point. Next, we construct the SVD basis by choosing the directions that are best fit by looking at the perpendicular ppE components. One can see that the SVD 1 in the third step is perpendicular to SVD 2. 223
- 8.1 GEO600 optical layout used in Finesse model. FI: Faraday isolator, MPR: power-recycling mirror, MSR: signal-recycling mirror, BS: beam splitter, PD: photodiode for DC readout. MFE and MCE are the far east mirror and central east mirror. ϕ is the detuning angle of the MSR in degrees of a wavelength. The notation for the north arm is analogous. 238
- 8.2 Strain sensitivity $A_h(f)$ of GEO600 at different detuning angles of the MSR, as well as a scanned sensitivity curve (black), which is a summation of all possible MSR detuning angles. All sensitivities assume normal incidence of the GWs. As the detuning angle of the MSR is increased from $\phi = 0^\circ$ (tuned configuration for GEO600), the detection region becomes increasingly narrow-band, in that the frequency bandwidth stays constant while the SRC resonant frequency increases. The scanned sensitivity curve is plotted to show the possible values that can be achieved across the kHz frequency range by shifting the MSR. 243

- 8.3 Strain sensitivity $A_h(f)$ of the aLIGO design at different detuning angles of the MSR, assuming normal incidence of the GWs. When the angle of the MSR is decreased from $\phi = 90^\circ$ (tuned configuration for aLIGO that corresponds to ‘signal extraction’ [111, 103]), the frequency of peak sensitivity gradually decreases in the neighborhood of $f \sim \mathcal{O}(100 \text{ Hz})$, while its bandwidth simultaneously narrows. Note that we use $\phi = 1^\circ$ to represent the ‘signal recycling’ limit, as setting $\phi = 0$ exactly corresponds to a configuration completely dominated by classical noise. There is no enhancement in sensitivity at frequencies in the kHz from aLIGO detuning the MSR. The peaks in sensitivity occurring at integer multiples of 37.5 kHz (FSR) are created by the Fabry-Perot cavities and are independent of the MSR detuning angle. 244
- 8.4 Strain sensitivity $A_h(f)$ of GEO600 tuned (purple), anti-tuned (gray), and scanned (dashed), which is a summation of all possible MSR detuning angles. The aLIGO design sensitivity (red) [112] and Cosmic Explorer’s design sensitivity (light blue) [112] are also shown. All sensitivities assume normal incidence of the GWs. GEO600’s scanned sensitivity curve shows the possible frequencies in the kHz range where it would have an advantageous narrow band detection to that of Cosmic Explorer and aLIGO. 245
- 8.5 Left: contour lines corresponding to a SNR of eight for GWs sourced from both vector (solid) and scalar (dashed) boson clouds. The contour lines correspond to the strain sensitivities of aLIGO (blue), tuned GEO600 (orange), and GEO600 with different MSR detuning angles. The shaded gray region corresponds to the parameter space where the superradiance condition fails. Right: SNR of GWs sourced from both vector (solid) and scalar (dashed) boson clouds across a range of boson rest energies for a $0.3 M_\odot$ BH. The SNR curves are calculated with the same strain sensitivities as the left plot and have the same corresponding colors. The dotted black line represents where the SNR is eight. All GWs are sourced from within the galaxy, being simulated from a distance of 30 kPc. 247

- 8.6 Strain sensitivity $A_h(f)$ of the aLIGO design (light blue) and scanned GEO600 (light gray), assuming normal incidence of the GWs. Three different GW waveforms are plotted as $2|\tilde{h}_+(f)|\sqrt{f}$. The GW amplitudes are from compact binary mergers of three different sub-solar masses, observed from a distance of 30 kPc. 250
- 8.7 Left: sky-averaged antenna patterns $\mathcal{R}(f)$ for aLIGO (light blue), folded GEO600 (purple), a 600m Michelson interferometer (brown), and a 1200m Michelson interferometer (gray). The folding factor given in Eq. (8.31) relates the angular response of an unfolded Michelson interferometer (brown) to its folded counterpart (purple); one can see that the folding factor sharply reduces the angular response at frequencies where it was previously strong. Right: antenna patterns $F(\theta_{\hat{n}}, \phi_{\hat{n}})$ of folded GEO600 for the following incident-angled GWs: overhead (light blue), completely along one detector arm (gray), and two in-between angles (purple and brown). Here, $F(\theta_{\hat{n}}, \phi_{\hat{n}}) = \sqrt{|F_+(f; \phi_{\hat{n}}, \theta_{\hat{n}})|^2 + |F_\times(f; \phi_{\hat{n}}, \theta_{\hat{n}})|^2}$ since we assume an inclination angle of zero. One can see that the angular behavior of antenna patterns is very frequency dependent at high frequencies. 256
- 8.8 Strain sensitivity $A_h(f)$ of GEO600 with a tuned MSR (left) and an anti-tuned MSR (right), including all modeled noise sources and the total sensitivity, both with and without sky-averaging (though individual sources are only shown for normal incidence). BM: Brownian motion, TE: thermo-elastic, TR: thermo-refractive. 262

LIST OF TABLES

<i>Number</i>	<i>Page</i>
2.1 Values of (θ^A, θ^C) used in our study to construct the Fisher information matrix (Eq. (2.3)) and estimate the bias due to Δr (Eq. (2.11)). .	40
3.1 Dark siren constraints on the Hubble constant and matter density parameter for various detector configurations. We use the same methodology as for this table as in the rest of this paper. We find the Fisher matrix confidence interval on the cosmological parameters by using only dark sirens which are completely localized.	77
5.1 Relevant parameters in BBH+SMBH triple system for GW observed by detectors. Bars over angles indicate the Solar System coordinate frame.	141
8.1 Mirror parameters used in the GEO600 Finesse model [107, 108, 109, 110]. Ppm: parts per million, kg: kilogram.	242

Chapter 1

INTRODUCTION

The detection of gravitational waves (GWs) from compact binary coalescences [1, 2, 3, 4, 5] provides us a new window from which to observe the universe. Since the first event, GW150914, in 2015 [1], detections have grown rapidly as detector sensitivities have improved and additional instruments have come online. The network currently consists of two Laser Interferometer Gravitational-Wave Observatory (LIGO) detectors in the United States [6], Virgo in Italy [7], and the Kamioka Gravitational Wave Detector (KAGRA) interferometer in Japan [8]. Third-generation ground-based facilities—Cosmic Explorer [9, 10] and the Einstein Telescope [11, 12, 13]—are in the planning stages. In space, future observatories span multiple frequency bands. LISA (launch 2035) [14, 15], TianQin [16], and Taiji [17, 18] are proposed millihertz space based detectors which focus on the $\sim 10^{-3} - 10^{-1}$ Hz bands. Additionally, decihertz concepts are B-DECIGO [19, 20] and TianGO [21, 22] which have optimized sensitivity in the 0.01 – 1 Hz band. On the low-frequency end, pulsar timing arrays have delivered the first evidence of a stochastic GW background in the nanohertz regime [23, 24, 25] and are poised to resolve individual supermassive-black-hole binaries in upcoming data releases [26]. At the opposite extreme, dedicated high-frequency experiments aim to probe GWs in the kilohertz–gigahertz bands—well above LIGO’s range—using resonant bars, microwave cavities, and novel interferometric techniques [27, 28].

Beyond mere detection, GW observations enable rich secondary science via both individual–event follow-ups and statistical population studies. The LVK collaboration reports merger rates and distributions of source masses, spins and redshifts/distances [29, 30], which constrain compact-binary formation channels—isolated versus dynamical—and ongoing analyses seek multiple BBH subpopulations as the catalog grows. Because the cosmic star-formation rate peaked at $z \sim 2$ [31], it is expected that the merger rate density should evolve with the redshift. Indeed, results from GWTC-3 have found evidence of higher merger rates in the past [30]. The potential of next generation detectors is shown in Fig. 1.1 which shows the observational horizon of future GW detectors [10]. One can see that third generation detectors will be able to detect most BBH in the universe while the rate at which we resolve the BNS will be much larger [10].

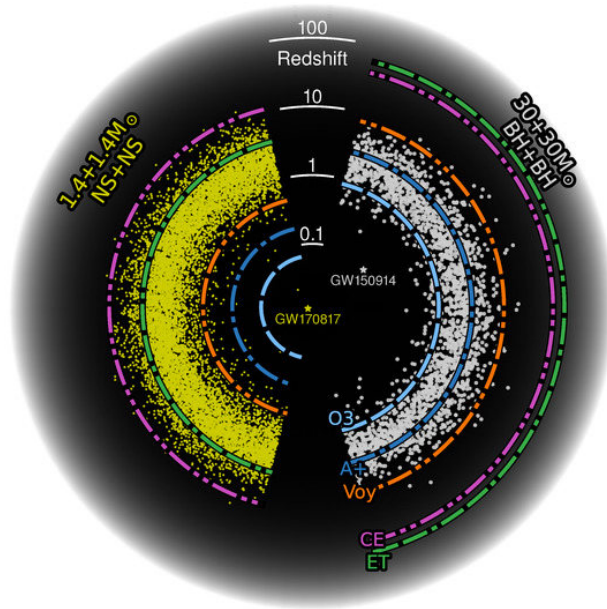


Figure 1.1: This image is taken from [10]. It shows the astrophysical horizon of current and future detectors. On the right it shows the GW detections for typical BBH systems. One can see that every BBH merger is observed with third generation detectors (CE [9, 10]/ET [11, 12, 13]) and nearly all are found with LIGO Voyager which is a cryogenic upgrade of LIGO [32]. Additionally, one can see that we are only scraping the surface of detecting a large number of the BNS detections due to them being quieter but much more numerous.

One of the most promising areas for GW astronomy is to provide a third independent measurement of the local expansion rate of the universe. The Hubble constant H_0 describes the current expansion rate of the local universe, and there is considerable discrepancy between the two leading measurements using the cosmic microwave background with Planck [33] and the distance ladder measurements of Type 1a supernova of SH0ES [34, 35]. Currently these early and late universe measurements disagree with a statistical significance of around 4σ [36, 37]. While electromagnetic (EM) measurements such as Planck/SH0ES measure the redshift and infer the luminosity distance indirectly, the GW approach to measuring the Hubble constant uses measurements of the luminosity distance from the detectors. The best candidates for this approach are binary neutron star (BNS) mergers with EM counterparts since this directly measures the luminosity distance and redshift with multimessenger astronomical measurements [38]. Because this method is independent of the standard candles used in the EM observations, it is viewed as a clean way to break the Hubble

tension, this depends on which GW method is used, but so far only a single event, GW170817 [2], has been observed as a multimessenger event.

Meanwhile, large-scale structure surveys—most recently DESI—have measured baryon acoustic oscillations and redshift-space distortions that are consistent with Planck’s Λ CDM parameters [39, 40, 33]. Intriguingly, DESI has also reported hints of evolution in the dark-energy equation of state $w(z)$ [40], underscoring how GW-based cosmology will play a crucial role in cross-checking and extending late-time probes of cosmic acceleration.

Measurement of GWs also allows us to study the nature of the strong, dynamical behavior of general relativity directly. Tests of GR are generally classified into three categories, solar system, binary pulsar and GW tests [41]. Solar system tests very precisely measure the motion of objects in the solar system where gravity is weak the system is moving nonrelativistically. Binary pulsars were the first evidence of GW [42], and are strongly gravitating systems which are moving slowly compared to the speed of light [43, 44, 45]. Finally, GW allow us to study the behavior of GR when objects strongly warp spacetime and are dynamically evolving nearly at the speed of light. The layout of this is schematically shown in Fig. 1.2, which shows the characteristic gravitational potential Φ on the x-axis and the characteristic gravitational curvature R [46, 47]. Additionally, the radiation reaction timescale of gravitational waves is very fast compared to the bound energy in the signal. As a consequence, these systems chirp up in frequency and radiate a large amount of energy in the final moments of the merger ($E_{\text{GW}}/M_{\text{tot}} \sim 5\%$) [48, 49].

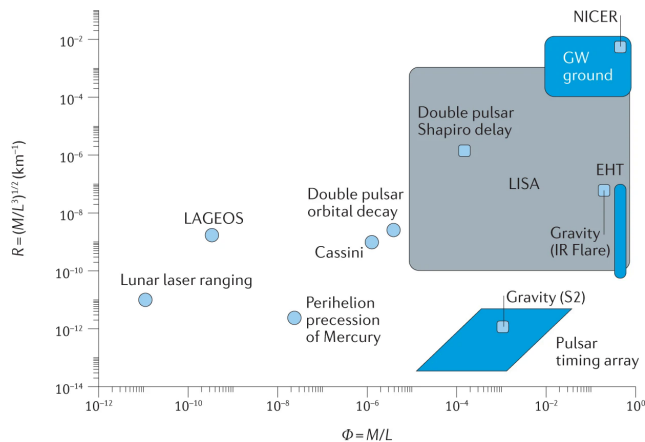


Figure 1.2: Image taken from [46] and based upon [47]. A schematic diagram of various prominent tests of gravity. On the x-axis the characteristic gravitational potential Φ is shown while the y-axis contains shows the characteristic gravitational curvature R . One can see the regimes of solar system measurements (Lunar laser ranging, LAGEOS, Mercury perihelion precession). The S2 gravity measurements is the tracking of S2 star's orbit about the SgA* [50]. The pulsar measurements probe stronger gravity than solar system tests. Finally the light blue regions are the potentials for gravitational wave detections which show it is probing both high potential and highly curved region of spacetime.

1.1 Hubble Tension with Gravitational Wave Observations

In this section, I will briefly summarize the literature about the method for measuring the cosmological parameters in gravitational wave data are done. There are three major methods for this, termed the *bright siren*, *dark siren*, and *spectral siren* methods.

Due to the limited angular and distance resolution of current GW detectors, it is challenging to uniquely identify individual galaxies using GW data alone. The angular resolution for a BBH signal is $\Delta\Omega \sim 100 - 3000 \text{ deg}^2$ for two detector triggers and $\Delta\Omega \sim 30 - 100 \text{ deg}^2$ for three detector observations. An order of magnitude estimation for the number of galaxies in the localization region shows that even in the best case there are tens of thousands of galaxies in the localization region

$$N_{\text{gal}} \sim 3 \times 10^4 \left(\frac{\Delta\Omega}{50 \text{ deg}^2} \right) \left(\frac{\Delta D_L/D_L}{0.2} \right) \left(\frac{D_L}{1000 \text{ Mpc}} \right)^3 \quad (1.1)$$

where I used the fact that the comoving galaxy density is around $n_g \sim 0.01 \text{ gal/Mpc}^3$ [51] and I chose parameters for a pretty well localized BBH event, GW200311 [4, 5].

The bright siren method is the first one to be proposed in which one identifies a coincident EM counterpart during a merger that has a NS in it [38]. This is most likely to happen for BNS mergers, but could happen for a NSBH merger with tidal disruption event [52, 53, 54]. If it is possible, such a method is very good since it does not suffer from astrophysical systematics and is very simple. In practice, the observation of EM counterparts has only definitively happened for the GW170817 BNS merger [2] with its corresponding EM counterpart [55, 56, 2]. While GW170817 did allow for the measurement of the Hubble constant [57], its uncertainty was too wide compared to the errors in the Hubble tension measurements [57, 33, 35, 34, 36, 37]. As a matter of fact, we may have been lucky to observe a bright-siren BNS merger so early in the LIGO observational window [58, 59].

The dark-siren method extends the bright-siren concept to mergers without electromagnetic counterparts by statistically associating the GW-inferred luminosity distance posterior with large-scale galaxy redshift catalogs [60, 61, 62, 63, 64, 65, 66]. In this framework, each galaxy within the three-dimensional localization volume is weighted by its probability of hosting the event, yielding an H_0 posterior that tightens as detector sky localization and catalog completeness improve. These statistical techniques gain further leverage by incorporating realistic galaxy clustering, which exploits density correlations to sharpen redshift estimates [67, 68, 69, 70]. In GWTC-3, applying the catalog method to well-localized GW190814 produced a modest but measurable reduction in the H_0 uncertainty [71, 72, 73]. Looking ahead, next-generation network sensitivities may shrink the comoving volume enough to allow unique host identification from GW data alone [74].

Finally, although gravitational waves provide a direct measurement of the luminosity distance but not the redshift, we can infer the redshift by adopting an astrophysical model for the mass distribution of merging BBHs. This method is called the spectral siren method [75, 76, 77]. Rather than relying on a fixed example, the spectral siren method assumes (or actively fits for) a source frame mass distribution for black holes. By comparing the distribution implied by the detector-frame measurements with the assumed source frame distribution through an assumed cosmology, one can infer the redshift and, consequently, the cosmological parameters that best relate the two [76]. By stacking together and measuring both astrophysical model and cosmological parameters across many events, this allows these the cosmological parameters to be measured.

Chapter 2 will examine the spectral siren method and quantify how well the cosmology + astrophysical distribution can be jointly measured. It will also provide a framework for how much the Hubble constant is biased if an incorrect mass distribution model is used. Chapter 3 will focus on how a space-based Decihertz detector could enable ground-based detectors to improve their angular resolution so that the dark siren method can localize events tight enough to identify a single galaxy.

1.2 Introduction to Tests of Gravity

The waveform emitted by two compact objects closely encodes the strong and dynamical regime of GR. The first indirect evidence of GW came from observations of the orbital decay rate in the Hulse-Taylor pulsar [42, 41]. In 2015, LIGO directly measured GW and confirmed its consistency with GR [78, 79]. Thus far, the tests of GR have passed with flying colors [80, 41, 81], however searching for deviations to GR at relativistic and highly curvature spacetimes would allow us to test its behavior at the most extreme regimes. I will describe the most important techniques for testing GR in GW observations.

The most prominent way to look for deviations in the inspiral is to search for terms that deviate in power laws in frequency that are motivated by Eq. (1.2) [78, 82, 83, 84, 79]. The framework was originally derived by Yunes and Pretorius who called it the parameterized post-Einsteinian (ppE) formalism [85]. Other PN tests such as the TIGER [86, 87] and FTI [88, 89] are also done which differ by normalizations and tapering assumptions. The complex strain of a GR waveform is

$$h(f) = h_+ - ih_\times = A_{\text{gr}}(f)e^{i\Psi_{\text{gr}}(f)} \quad (1.2)$$

where the amplitude $A_{\text{gr}}(f)$ and phase $\Psi_{\text{gr}}(f)$ are computed for a particular choice of parameters through the stationary phase approximation. The GR frequency domain phase is

$$\Delta\Psi_{\text{gr}}(f) = 2\pi ft_c - \varphi_c - \frac{\pi}{4} + \frac{3}{128\eta}(\pi\tilde{f})^{-5/3} \sum_{i=0}^7 [\varphi_i + \varphi_{il} \log(\pi\tilde{f})] (\pi\tilde{f})^{i/3}, \quad (1.3)$$

where $\tilde{f} = M(1+z)f$ is the dimensionless frequency, $M(1+z)$ detector frame total mass, η symmetric mass ratio, and φ_c, t_c being phase and time of coalescence [79]. Throughout my thesis, I will take the form of the tests that is equivalent to what LIGO releases in their testing GR in GWTC3 paper [79]. They present the results as fractional deviations to the nonspinning 3.5PN TaylorF2 phase [90]. The LVK looks for evidence of

$$\{\delta\hat{\varphi}_{-2}, \delta\hat{\varphi}_0, \delta\hat{\varphi}_1, \delta\hat{\varphi}_2, \delta\hat{\varphi}_3, \delta\hat{\varphi}_4, \delta\hat{\varphi}_{5l}, \delta\hat{\varphi}_6, \delta\hat{\varphi}_{6l}, \delta\hat{\varphi}_7\} \quad (1.4)$$

where $\delta\hat{\varphi}_k$ are fractional deviation coefficients from GR at the $k/2$ th PN order [83, 84, 79].

Searching for power law deviations to the frequency domain dephasing can be directly related to the intrinsic features of the frequency chirp rate. Since $\Psi_{\text{gr}}(f)$ is intrinsically related to the time frequency relation $t(f)$, it can be directly related to the *luminosity* and *binding energy* of the binary. This can be seen in the frequency evolution equation

$$\frac{df}{dt} = \underbrace{\frac{dE}{dt}}_{\text{diss.}} \underbrace{\frac{\partial f}{\partial E}}_{\text{cons.}}, \quad (1.5)$$

where I denote the *dissipative* term and *conservative* term. The dissipative term corresponds to how quickly energy is leaving the system do to GW while the conservative term is the relationship between binding energy and GW frequency. If there were an additional scalar field that was radiating energy in addition to GR, this would be a dissipative modification while modifications to the binding energy and conservative dynamics would modify the latter term. Thus, we can conclude that PN order analysis *relates deviations of the binary's orbit* \leftrightarrow *terms in the frequency domain phase*. In Fig. 1.3, a time domain example of what this dephasing looks like is shown.

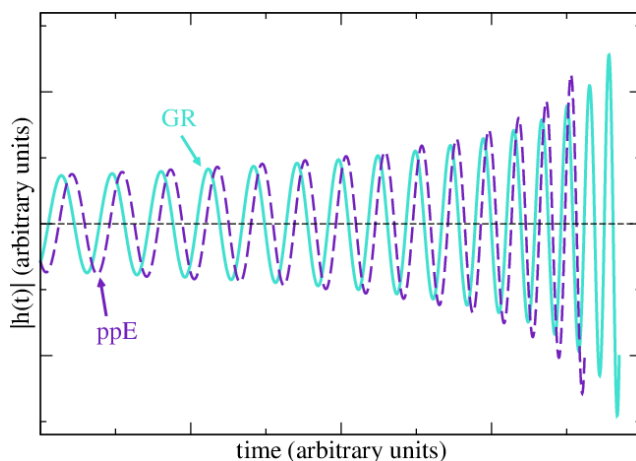


Figure 1.3: Image taken from [91]. This demonstrates how a ppE dephasing can cause the waveform to deviate from the GR one in the time domain.

There are a number of other tests of GR with GW that can be now done. After a binary mergers, the ringdown can be used to test the no-hair theorem [92, 93, 94]. Since the quasi-normal modes (QNM) only depend on the mass and spin of the final

BH, measurement of multiple QNM can check consistency of the Kerr BH solution [95, 96]. Using GW170817, the relative difference between the propagation of GW and EM can be measured which improved the bound on the mass of the graviton [82, 97, 98, 99]. Finally, as more detectors are included to the network, searches for alternative polarizations can be done [100, 101, 102, 103, 104, 105, 106, 107, 108].

In Chapter 6, I modeled the effects of non-violent nonlocality on the waveforms for BBH that would exist in LIGO. I simulate BBH mergers using an effective-one-body formalism to compute the modification to the orbit due to the conservative effects. In Chapter 7, I demonstrate that the PN deformation coefficients have an intrinsic geometric meaning in their capacity to test GR. I explain geometrically why they can capture generic deviations to GR, and propose a new singular value decomposition approach for performing multiparameter tests of GR.

1.3 Extraction of Environmental Effects in Space-Based Observations

GW binaries have multiple formation channels – typically characterized by isolated binary evolution and dynamical formation channels [109, 110]. The isolated binary evolution is more characterized by binaries formed in the field as normal stars which then supernova and common envelope evolution brings them together. Alternatively, BH and NS could form binaries in dense gravitational potentials such as globular clusters or active galactic nucleus (AGN) disks. The dynamical formation channel is facilitated by chaotic many body encounters near active galactic nuclei or globular clusters [111, 112] and Lidov-Kozai oscillations [113].

Results from LIGO have shown there are systems which constituents masses that exceed the predictions of isolated binary evolution [114, 115, 116, 117]. It is possible that these binaries could be a subpopulation of the BBH that LVK measures due to hierarchical mergers [118, 119, 120, 121]. Hierarchical mergers are normally difficult to achieve in the galactic field because kicks can eject the remnants from the galaxies but the deep potential well of the AGN could trap these remnants [120, 121, 122]. Mergers near AGN could occur due to gaseous effects [123, 124, 125, 126, 127, 128, 129] which add friction for BBH before radiation reaction can kick in. Gas can also cause the BBH to migrate its orbit to be closer to the supermassive black hole (SMBH) [130, 131]. Additionally, even in vacuum, dynamical encounters near the SMBH can cause mergers nearby [132, 133, 134, 135, 136, 137, 138, 139, 140].

If a BBH is closely orbiting a SMBH, space-based detectors can infer its orbit due to modulations from the orbit. These terms include the Doppler shift from the center of mass of the BBH moving, de Sitter precession of the inner spin about the orbital spin and pericenter precession [141, 142, 143, 144, 145, 146, 147, 148]. Additionally, there can be repeated gravitational lensing due to the SMBH [149, 150] if the outer orbit is nearly aligned with the line of sight. Note that space-based detectors are needed for such a detection because there are only seconds for a LVK observation to have any triple GW modification [148, 147]. The dominant effect on the frequency domain waveform is the Doppler shift Φ_D

$$\Phi_D = 2\pi i f r(t(f)) \quad (1.6)$$

where $r(t(f))$ is the location of the particle at time $t(f)$ along the line of sight. For a circular outer orbit, another modulation is needed (typically de Sitter precession [146]). An eccentric outer orbit actually is much easier to measure since the periastron precession allows the Doppler shift to break the degeneracy between semimajor axis and inclination alone [151].

Chapter 4 discusses our work about strong lensing signatures for a BBH+SMBH system for measurement with space based detector such as LISA or TianGO. We show that there is a 3 – 10% chance for these signatures to be detected, and if present would significantly improve the detection of the mass and orbit of the SMBH in conjunction with Doppler shift and de Sitter precession effects. In Chapter 5, we extend previous results that assumed circular outer orbits [146] by allowing eccentricity of the outer orbit. Despite this adding additional parameters to measure, this allows degeneracies to be broken and more accurate extraction of the SMBH mass and orbit.

1.4 High Frequency Gravitational Wave Detection

The sensitivity of GW detectors is limited by a couple of different fundamental noise sources. In this section, I will briefly discuss how the power spectral density (PSD) of GW detector is calculated. The PSD is related to the expectation value of noise n [152, 153, 154, 155]

$$\langle n(f)n^*(f') \rangle = \frac{1}{2}\delta(f - f')S(f) \quad (1.7)$$

where $S(f)$ is the PSD of the GW detector. It is useful to define the noise weighted inner product

$$(h_1|h_2) = 4\Re \int_0^\infty \frac{h_1(f)h_2^*(f)}{S(f)} df, \quad (1.8)$$

which is related to the signal to noise ratio via $\rho = \sqrt{\langle h|h \rangle}$.

Let us now describe typical noises for a ground-based interferometer and how they are related to the PSD. As you can see in Fig. 1.4 from the LIGO white paper [156], there are a number of fundamental noises in LIGO when operating at design sensitivity. One can see that the quantum noise (purple) is the main noise source at high frequencies which is due to shot noise [157, 158]. At low frequencies, quantum noise creates radiation pressure that limit the GW detector. Additionally at low frequencies there is seismic noise from vibrations of the earth (brown) and gravity gradient noise from time varying Newtonian gravity at the detector (green). Additionally, there are other fundamental noise sources from the coating Brownian noise (red), coating Thermo-optic noise (dash cyan), and substrate Brownian noise (dash orange) and excess gas (dash yellow).

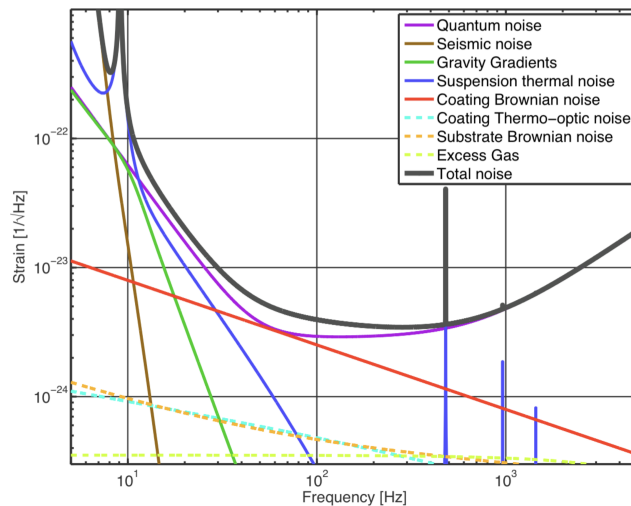


Figure 1.4: Image taken from [156]. This shows the fundamental noises that exist in the design sensitivity of advanced LIGO. One can see that quantum shot noises dominates the noise spectrum at high frequencies.

The noise sources are related to the GW strain noise via transfer functions. The photon flux in the output port is

$$i(f) = T_h(f)h(f) + \sum_j T_j(f)n_j(f), \quad (1.9)$$

where $T_h(f)$ is the transfer function for the response of GW, $h(f)$ is a GW pointed that is head on in the detector, $T_j(f)$ is the noise transfer function for noise source

$n_j(f)$. Since we assume n_j has a PSD S_j , the PSD of the detector is equal to

$$S_h(f) = \frac{1}{|T_h(f)|^2} \sum_j |T_j(f)|^2 S_j(f). \quad (1.10)$$

To improve the sensitivity of the detector, one typically tries to reduce both the amount of noise $S_j(f)$ and the degree to which it couple into the GW readout channel $T_j(f)$. However note that $T_h(f)$ can be modified by detector design choices so that the detector maximally responds to GW.

In Chapter 8, we will discuss how we can improve the sensitivity of GEO600 [159], a dual-recycled, folded-arm, Michelson interferometer (MI) [160, 161, 162]. We study how it can be made sensitive to GW in the tens of kHz frequency range. We do this by modifying the transfer function $T_h(f)$ through detuning the location of the signal recycling mirror.

1.5 Organization of Thesis

Here is a list of the abstracts for each chapter in this thesis.

Chapter 2: Uncertainty and bias of cosmology and astrophysical population model from statistical dark sirens

Gravitational-wave (GW) radiation from a coalescing compact binary is a standard siren as the luminosity distance of each event can be directly measured from the amplitude of the signal. One possibility to constrain cosmology using the GW siren is to perform statistical inference on a population of binary black hole (BBH) events. In essence, this statistical method can be viewed as follows. We can modify the shape of the distribution of observed BBH events by changing cosmological parameters until it eventually matches the distribution constructed from an astrophysical population model, thereby allowing us to determine the cosmological parameters. In this work, we derive the Cramér-Rao bound for both cosmological parameters and those governing the astrophysical population model from this statistical dark siren method by examining the Fisher information contained in the event distribution. Our study provides analytical insights and enables fast yet accurate estimations of the statistical accuracy of dark siren cosmology. Furthermore, we consider the bias in cosmology due to unmodeled substructures in the merger rate and the mass distribution. We find a 1% deviation in the astrophysical model can lead to a more than 1% error in the Hubble constant. This could limit the accuracy of dark siren cosmology when there are more than 10^4 BBH events detected.

Chapter 3: Multiband Gravitational Wave Cosmography with Dark Sirens

Gravitational waves might help resolve the tension between early and late Universe measurements of the Hubble constant, and this possibility can be enhanced with a gravitational wave detector in the decihertz band as we will demonstrate in this study. Such a detector is particularly suitable for the multiband observation of stellar-mass black hole binaries between space and ground, which would significantly improve the source localization accuracy thanks to a long baseline for timing triangulation, hence promoting the "dark siren" cosmology. Proposed decihertz concepts include DECIGO/B-DECIGO, TianGO, and others. We consider here the prospects of multiband observation of dark siren binaries with a variety of network configurations. We find that a multiband observation can uniquely identify a black hole binary to a single galaxy to a cosmological distance, and thus a dark siren behaves as if it had an electromagnetic counterpart. Considering only fully localized dark sirens, we use a Fisher matrix approach to estimate the error in the Hubble constant and matter density parameter. We find that a decihertz detector substantially improves our ability to measure cosmological parameters because it enables host galaxies to be identified out to a larger distance without the systematics from statistical techniques based on comparing the population distribution.

Chapter 4: Detecting gravitational lensing in hierarchical triples in galactic nuclei with space-borne gravitational-wave observatories

Stellar-mass binary black holes (BBHs) may merge in the vicinity of a supermassive black hole (SMBH). It is suggested that the gravitational-wave (GW) emitted by a BBH has a high probability to be lensed by the SMBH if the BBH's orbit around the SMBH (i.e., the outer orbit) has a period of less than a year and is less than the duration of observation of the BBH by a space-borne GW observatory. For such a "BBH + SMBH" triple system, the de Sitter precession of the BBH's orbital plane is also significant. In this work, we thus study GW waveforms emitted by the BBH and then modulated by the SMBH due to effects including Doppler shift, de Sitter precession, and gravitational lensing. We show specifically that for an outer orbital period of 0.1 yr and an SMBH mass of $10^7 M_\odot$, there is a 3% – 10% chance for the standard, strong lensing signatures to be detectable by space-borne GW detectors such as LISA and/or TianGO. For more massive lenses ($\gtrsim 10^8 M_\odot$) and more compact outer orbits with periods $\lesssim 0.1$ yr, retro-lensing of the SMBH (which is closely related to the glory-scattering) might also have a 1%-level chance of detection. Furthermore, by combining the lensing effects and the dynamics of

the outer orbit, we find the mass of the central SMBH can be accurately determined with a fraction error of $\sim 10^{-4}$. This is much better than the case of static lensing because the degeneracy between the lens' mass and the source's angular position is lifted by the outer orbital motion. Including lensing effects also allows the de Sitter precession to be detectable at a precession period 3 times longer than the case without lensing. Lastly, we demonstrate that one can check the consistency between the SMBH's mass determined from the orbital dynamics and the one inferred from gravitational lensing, which serves as a test on theories behind both phenomena. The statistical error on the deviation between two masses can be constrained to a 1% level.

Chapter 5: Measuring Supermassive Black Hole Properties via Gravitational Radiation from Eccentrically Orbiting Stellar Mass Black Hole Binaries

There may exist stellar-mass binary black holes (BBH) which merge while orbiting nearby a supermassive black hole (SMBH). In such a triple system, the SMBH will modulate the gravitational waveform of the BBH through orbital Doppler shift and de Sitter precession of the angular momentum. Future space-based GW observatories focused on the millihertz and decihertz band will be uniquely poised to observe these waveform modulations, as the GW frequency from stellar-mass BBHs varies slowly in this band while modulation effects accumulate. In this work, we apply the Fisher information matrix formalism to estimate how well space-borne GW detectors can measure properties of BBH+SMBH hierarchical triples using the GW from orbiting BBH. We extend previous work by considering the more realistic case of an eccentric orbit around the SMBH, and notably include the effects of orbital pericenter precession. We find that for detector concepts such as LISA, B-DECIGO, and TianGO, we can extract the SMBH mass and semimajor axis of the orbit with a fractional uncertainty below the 0.1% level over a wide range of triple system parameters. Furthermore, we find that the effects of pericenter precession and orbital eccentricity significantly improve our ability to measure this system. We also find that while LISA could measure these systems, the decihertz detector concepts B-DECIGO and TianGO would enable better sensitivity to the triple's parameters.

Chapter 6: Gravitational-wave signatures of non-violent non-locality

Measurement of gravitational waves can provide precision tests of the nature of black holes and compact objects. In this work, we test Giddings' non-violent non-locality proposal, which posits that quantum information is transferred via a nonlocal inter-

action that generates metric perturbations around black holes. In contrast to firewalls, these quantum fluctuations would be spread out over a larger distance range — up to a Schwarzschild radius away. In this letter, we model the modification to the gravitational waveform from non-violent non-locality. We modify the nonspinning EOBNRv2 effective one body waveform to include metric perturbations that are due to a random Gaussian process. We find that the waveform exhibits random deviations which are particularly important in the late inspiral-plunge phase. We find an optimal dephasing parameter for detecting this effect with a principal component analysis. This is particularly intriguing because it predicts random phase deviations across different gravitational wave events, providing theoretical support for hierarchical tests of general relativity. We estimate the constraint on the perturbations in non-violent non-locality with events for the LIGO-Virgo network and for a third-generation network.

Chapter 7: Inspiral tests of general relativity and waveform geometry

The phase evolution of gravitational waves encodes critical information about the orbital dynamics of binary systems. In this work, we test the robustness of post-Newtonian coefficients against unmodeled deviations from general relativity. We demonstrate that these parameterized tests are flexible and sensitive in detecting generic deviations in the waveform. This universality arises from examining the inherent geometry of the waveform signal and understanding how biases manifest. We use the singular value decomposition to propose templates that are orthogonal to parameterized tests, avoiding degeneracies and enhancing the detection of potential deviations.

Chapter 8: Prospects for High-Frequency Gravitational-Wave Detection with GEO600

Current ground-based interferometers are optimized for sensitivity around 200 Hz. While they are not currently utilized for GW detection, interferometric detectors also feature narrow bands of strong sensitivity where the sideband fields created by a GW are resonant in the optical system. For certain interferometer configurations, small changes to system parameters allow the narrow band of high sensitivity to be scanned over a much larger range of frequencies, potentially enabling broadband detection at high frequencies. In this paper, we investigate whether simply modifying the detuning angle of the signal-recycling mirror of the GEO600 interferometer can make this experiment sensitive to GWs in the kilohertz frequency range. Using

Finesse 3.0, we compute the strain sensitivity for GEO600 across a frequency range from several kHz to tens of kHz for various detuning angles. We then calculate the sensitivity of GEO600 to various proposed high-frequency GW sources and compare its ability to detect such sources to that of other ground-based interferometers.

References

- [1] B. P. Abbott et al. “Observation of Gravitational Waves from a Binary Black Hole Merger.” In: *Phys. Rev. Lett.* 116.6 (2016), p. 061102. DOI: [10.1103/PhysRevLett.116.061102](https://doi.org/10.1103/PhysRevLett.116.061102). arXiv: [1602.03837](https://arxiv.org/abs/1602.03837) [gr-qc].
- [2] B. P. Abbott et al. “GW170817: Observation of Gravitational Waves from a Binary Neutron Star Inspiral.” In: *Phys. Rev. Lett.* 119.16 (2017), p. 161101. DOI: [10.1103/PhysRevLett.119.161101](https://doi.org/10.1103/PhysRevLett.119.161101). arXiv: [1710.05832](https://arxiv.org/abs/1710.05832) [gr-qc].
- [3] B. P. Abbott et al. “GWTC-1: A Gravitational-Wave Transient Catalog of Compact Binary Mergers Observed by LIGO and Virgo during the First and Second Observing Runs.” In: *Phys. Rev. X* 9.3 (2019), p. 031040. DOI: [10.1103/PhysRevX.9.031040](https://doi.org/10.1103/PhysRevX.9.031040). arXiv: [1811.12907](https://arxiv.org/abs/1811.12907) [astro-ph.HE].
- [4] R. Abbott et al. “GWTC-2: Compact Binary Coalescences Observed by LIGO and Virgo During the First Half of the Third Observing Run.” In: *Phys. Rev. X* 11 (2021), p. 021053. DOI: [10.1103/PhysRevX.11.021053](https://doi.org/10.1103/PhysRevX.11.021053). arXiv: [2010.14527](https://arxiv.org/abs/2010.14527) [gr-qc].
- [5] R. Abbott et al. “GWTC-3: Compact Binary Coalescences Observed by LIGO and Virgo During the Second Part of the Third Observing Run.” In: (Nov. 2021). arXiv: [2111.03606](https://arxiv.org/abs/2111.03606) [gr-qc].
- [6] J. Aasi et al. “Advanced LIGO.” In: *Class. Quant. Grav.* 32 (2015), p. 074001. DOI: [10.1088/0264-9381/32/7/074001](https://doi.org/10.1088/0264-9381/32/7/074001). arXiv: [1411.4547](https://arxiv.org/abs/1411.4547) [gr-qc].
- [7] F. Acernese et al. “Advanced Virgo: a second-generation interferometric gravitational wave detector.” In: *Class. Quant. Grav.* 32.2 (2015), p. 024001. DOI: [10.1088/0264-9381/32/2/024001](https://doi.org/10.1088/0264-9381/32/2/024001). arXiv: [1408.3978](https://arxiv.org/abs/1408.3978) [gr-qc].
- [8] T. Akutsu et al. “Overview of KAGRA: Detector design and construction history.” In: *PTEP* 2021.5 (2021), 05A101. DOI: [10.1093/ptep/ptaa125](https://doi.org/10.1093/ptep/ptaa125). arXiv: [2005.05574](https://arxiv.org/abs/2005.05574) [physics.ins-det].
- [9] D. Reitze et al. “Cosmic Explorer: The U.S. Contribution to Gravitational-Wave Astronomy beyond LIGO.” In: *Bull. Am. Astron. Soc.* 51.7 (2019), p. 035. arXiv: [1907.04833](https://arxiv.org/abs/1907.04833) [astro-ph.IM].
- [10] M. Evans et al. “A Horizon Study for Cosmic Explorer: Science, Observatories, and Community.” In: (Sept. 2021). arXiv: [2109.09882](https://arxiv.org/abs/2109.09882) [astro-ph.IM].

- [11] M. Punturo et al. “The Einstein Telescope: A third-generation gravitational wave observatory.” In: *Class. Quant. Grav.* 27 (2010). Ed. by F. Ricci, p. 194002. DOI: [10.1088/0264-9381/27/19/194002](https://doi.org/10.1088/0264-9381/27/19/194002).
- [12] M. Maggiore et al. “Science Case for the Einstein Telescope.” In: *JCAP* 03 (2020), p. 050. DOI: [10.1088/1475-7516/2020/03/050](https://doi.org/10.1088/1475-7516/2020/03/050). arXiv: [1912.02622](https://arxiv.org/abs/1912.02622) [[astro-ph.CO](#)].
- [13] M. Branchesi et al. “Science with the Einstein Telescope: a comparison of different designs.” In: *JCAP* 07 (2023), p. 068. DOI: [10.1088/1475-7516/2023/07/068](https://doi.org/10.1088/1475-7516/2023/07/068). arXiv: [2303.15923](https://arxiv.org/abs/2303.15923) [[gr-qc](#)].
- [14] P. Amaro-Seoane et al. “Laser Interferometer Space Antenna.” In: (Feb. 2017). arXiv: [1702.00786](https://arxiv.org/abs/1702.00786) [[astro-ph.IM](#)].
- [15] P. Auclair et al. “Cosmology with the Laser Interferometer Space Antenna.” In: (Apr. 2022). arXiv: [2204.05434](https://arxiv.org/abs/2204.05434) [[astro-ph.CO](#)].
- [16] J. Luo et al. “TianQin: a space-borne gravitational wave detector.” In: *Class. Quant. Grav.* 33.3 (2016), p. 035010. DOI: [10.1088/0264-9381/33/3/035010](https://doi.org/10.1088/0264-9381/33/3/035010). arXiv: [1512.02076](https://arxiv.org/abs/1512.02076) [[astro-ph.IM](#)].
- [17] W.-R. Hu and Y.-L. Wu. “The Taiji Program in Space for gravitational wave physics and the nature of gravity.” In: *Natl. Sci. Rev.* 4.5 (2017), pp. 685–686. DOI: [10.1093/nsr/nwx116](https://doi.org/10.1093/nsr/nwx116).
- [18] W.-H. Ruan, Z.-K. Guo, R.-G. Cai, et al. “Taiji program: Gravitational-wave sources.” In: *Int. J. Mod. Phys. A* 35.17 (2020), p. 2050075. DOI: [10.1142/S0217751X2050075X](https://doi.org/10.1142/S0217751X2050075X). arXiv: [1807.09495](https://arxiv.org/abs/1807.09495) [[gr-qc](#)].
- [19] S. Sato et al. “The status of DECIGO.” In: *J. Phys. Conf. Ser.* 840.1 (2017). Ed. by D. Giardini and P. Jetzer, p. 012010. DOI: [10.1088/1742-6596/840/1/012010](https://doi.org/10.1088/1742-6596/840/1/012010).
- [20] S. Kawamura et al. “Current status of space gravitational wave antenna DECIGO and BDECIGO.” In: (June 2020). arXiv: [2006.13545](https://arxiv.org/abs/2006.13545) [[gr-qc](#)].
- [21] K. A. Kuns, H. Yu, Y. Chen, et al. “Astrophysics and cosmology with a decihertz gravitational-wave detector: TianGO.” In: *Phys. Rev. D* 102.4 (2020), p. 043001. DOI: [10.1103/PhysRevD.102.043001](https://doi.org/10.1103/PhysRevD.102.043001). arXiv: [1908.06004](https://arxiv.org/abs/1908.06004) [[gr-qc](#)].
- [22] K. A. Kuns. “Future Networks of Gravitational Wave Detectors: Quantum Noise and Space Detectors.” PhD thesis. University of California, Santa Barbara, Mar. 2019.
- [23] Z. Arzoumanian et al. “The NANOGrav 12.5 yr Data Set: Search for an Isotropic Stochastic Gravitational-wave Background.” In: *Astrophys. J. Lett.* 905.2 (2020), p. L34. DOI: [10.3847/2041-8213/abd401](https://doi.org/10.3847/2041-8213/abd401). arXiv: [2009.04496](https://arxiv.org/abs/2009.04496) [[astro-ph.HE](#)].

- [24] A. Afzal et al. “The NANOGrav 15 yr Data Set: Search for Signals from New Physics.” In: *Astrophys. J. Lett.* 951.1 (2023). [Erratum: *Astrophys.J.Lett.* 971, L27 (2024), Erratum: *Astrophys.J.* 971, L27 (2024)], p. L11. doi: [10.3847/2041-8213/acdc91](https://doi.org/10.3847/2041-8213/acdc91). arXiv: [2306.16219](https://arxiv.org/abs/2306.16219) [[astro-ph.HE](#)].
- [25] G. Agazie et al. “The NANOGrav 15 yr Data Set: Evidence for a Gravitational-wave Background.” In: *Astrophys. J. Lett.* 951.1 (2023), p. L8. doi: [10.3847/2041-8213/acdac6](https://doi.org/10.3847/2041-8213/acdac6). arXiv: [2306.16213](https://arxiv.org/abs/2306.16213) [[astro-ph.HE](#)].
- [26] Z. Arzoumanian et al. “The NANOGrav 12.5 yr Data Set: Bayesian Limits on Gravitational Waves from Individual Supermassive Black Hole Binaries.” In: *Astrophys. J. Lett.* 951.2 (2023), p. L28. doi: [10.3847/2041-8213/acdbc7](https://doi.org/10.3847/2041-8213/acdbc7). arXiv: [2301.03608](https://arxiv.org/abs/2301.03608) [[astro-ph.GA](#)].
- [27] A. M. Cruise. “The potential for very high-frequency gravitational wave detection.” In: *Class. Quant. Grav.* 29 (2012), p. 095003. doi: [10.1088/0264-9381/29/9/095003](https://doi.org/10.1088/0264-9381/29/9/095003).
- [28] N. Aggarwal et al. “Challenges and opportunities of gravitational-wave searches at MHz to GHz frequencies.” In: *Living Rev. Rel.* 24.1 (2021), p. 4. doi: [10.1007/s41114-021-00032-5](https://doi.org/10.1007/s41114-021-00032-5). arXiv: [2011.12414](https://arxiv.org/abs/2011.12414) [[gr-qc](#)].
- [29] R. Abbott et al. “Population Properties of Compact Objects from the Second LIGO-Virgo Gravitational-Wave Transient Catalog.” In: *Astrophys. J. Lett.* 913.1 (2021), p. L7. doi: [10.3847/2041-8213/abe949](https://doi.org/10.3847/2041-8213/abe949). arXiv: [2010.14533](https://arxiv.org/abs/2010.14533) [[astro-ph.HE](#)].
- [30] R. Abbott et al. “Population of Merging Compact Binaries Inferred Using Gravitational Waves through GWTC-3.” In: *Phys. Rev. X* 13.1 (2023), p. 011048. doi: [10.1103/PhysRevX.13.011048](https://doi.org/10.1103/PhysRevX.13.011048). arXiv: [2111.03634](https://arxiv.org/abs/2111.03634) [[astro-ph.HE](#)].
- [31] P. Madau and M. Dickinson. “Cosmic Star Formation History.” In: *Ann. Rev. Astron. Astrophys.* 52 (2014), pp. 415–486. doi: [10.1146/annurev-astro-081811-125615](https://doi.org/10.1146/annurev-astro-081811-125615). arXiv: [1403.0007](https://arxiv.org/abs/1403.0007) [[astro-ph.CO](#)].
- [32] R. Adhikari, N. Smith, A. Brooks, et al. “LIGO Voyager Upgrade Concept.” In: (2017). LIGO Document T1400226. URL: <https://dcc.ligo.org/LIGO-T1400226>.
- [33] N. Aghanim et al. “Planck 2018 results. VI. Cosmological parameters.” In: *Astron. Astrophys.* 641 (2020). [Erratum: *Astron.Astrophys.* 652, C4 (2021)], A6. doi: [10.1051/0004-6361/201833910](https://doi.org/10.1051/0004-6361/201833910). arXiv: [1807.06209](https://arxiv.org/abs/1807.06209) [[astro-ph.CO](#)].
- [34] A. G. Riess et al. “A 2.4% Determination of the Local Value of the Hubble Constant.” In: *Astrophys. J.* 826.1 (2016), p. 56. doi: [10.3847/0004-637X/826/1/56](https://doi.org/10.3847/0004-637X/826/1/56). arXiv: [1604.01424](https://arxiv.org/abs/1604.01424) [[astro-ph.CO](#)].

- [35] A. G. Riess, S. Casertano, W. Yuan, et al. “Cosmic Distances Calibrated to 1% Precision with Gaia EDR3 Parallaxes and Hubble Space Telescope Photometry of 75 Milky Way Cepheids Confirm Tension with Λ CDM.” In: *Astrophys. J. Lett.* 908.1 (2021), p. L6. DOI: [10.3847/2041-8213/abdbaf](https://doi.org/10.3847/2041-8213/abdbaf). arXiv: [2012.08534](https://arxiv.org/abs/2012.08534) [astro-ph.CO].
- [36] L. Verde, T. Treu, and A. G. Riess. “Tensions between the Early and the Late Universe.” In: *Nature Astron.* 3 (July 2019), p. 891. DOI: [10.1038/s41550-019-0902-0](https://doi.org/10.1038/s41550-019-0902-0). arXiv: [1907.10625](https://arxiv.org/abs/1907.10625) [astro-ph.CO].
- [37] D. Camarena and V. Marra. “On the use of the local prior on the absolute magnitude of Type Ia supernovae in cosmological inference.” In: *Mon. Not. Roy. Astron. Soc.* 504 (2021), pp. 5164–5171. DOI: [10.1093/mnras/stab1200](https://doi.org/10.1093/mnras/stab1200). arXiv: [2101.08641](https://arxiv.org/abs/2101.08641) [astro-ph.CO].
- [38] B. F. Schutz. “Determining the Hubble Constant from Gravitational Wave Observations.” In: *Nature* 323 (1986), pp. 310–311. DOI: [10.1038/323310a0](https://doi.org/10.1038/323310a0).
- [39] A. Dey et al. “Overview of the DESI Legacy Imaging Surveys.” In: *Astron. J.* 157.5 (2019), p. 168. DOI: [10.3847/1538-3881/ab089d](https://doi.org/10.3847/1538-3881/ab089d). arXiv: [1804.08657](https://arxiv.org/abs/1804.08657) [astro-ph.IM].
- [40] A. G. Adame et al. “DESI 2024 VI: cosmological constraints from the measurements of baryon acoustic oscillations.” In: *JCAP* 02 (2025), p. 021. DOI: [10.1088/1475-7516/2025/02/021](https://doi.org/10.1088/1475-7516/2025/02/021). arXiv: [2404.03002](https://arxiv.org/abs/2404.03002) [astro-ph.CO].
- [41] C. M. Will. “The Confrontation between General Relativity and Experiment.” In: *Living Rev. Rel.* 17 (2014), p. 4. DOI: [10.12942/lrr-2014-4](https://doi.org/10.12942/lrr-2014-4). arXiv: [1403.7377](https://arxiv.org/abs/1403.7377) [gr-qc].
- [42] R. A. Hulse and J. H. Taylor. “Discovery of a pulsar in a binary system.” In: *Astrophys. J. Lett.* 195 (1975), pp. L51–L53. DOI: [10.1086/181708](https://doi.org/10.1086/181708).
- [43] I. H. Stairs. “Testing general relativity with pulsar timing.” In: *Living Rev. Rel.* 6 (2003), p. 5. DOI: [10.12942/lrr-2003-5](https://doi.org/10.12942/lrr-2003-5). arXiv: [astro-ph/0307536](https://arxiv.org/abs/astro-ph/0307536).
- [44] M. Kramer et al. “Tests of general relativity from timing the double pulsar.” In: *Science* 314 (2006), pp. 97–102. DOI: [10.1126/science.1132305](https://doi.org/10.1126/science.1132305). arXiv: [astro-ph/0609417](https://arxiv.org/abs/astro-ph/0609417).
- [45] N. Wex. “Testing Relativistic Gravity with Radio Pulsars.” In: (Feb. 2014). arXiv: [1402.5594](https://arxiv.org/abs/1402.5594) [gr-qc].
- [46] M. Bailes et al. “Gravitational-wave physics and astronomy in the 2020s and 2030s.” In: *Nature Rev. Phys.* 3.5 (2021), pp. 344–366. DOI: [10.1038/s42254-021-00303-8](https://doi.org/10.1038/s42254-021-00303-8).

- [47] N. Yunes, K. Yagi, and F. Pretorius. “Theoretical Physics Implications of the Binary Black-Hole Mergers GW150914 and GW151226.” In: *Phys. Rev. D* 94.8 (2016), p. 084002. doi: [10.1103/PhysRevD.94.084002](https://doi.org/10.1103/PhysRevD.94.084002). arXiv: [1603.08955](https://arxiv.org/abs/1603.08955) [gr-qc].
- [48] J. Healy, C. O. Lousto, and Y. Zlochower. “Remnant mass, spin, and recoil from spin aligned black-hole binaries.” In: *Phys. Rev. D* 90.10 (2014), p. 104004. doi: [10.1103/PhysRevD.90.104004](https://doi.org/10.1103/PhysRevD.90.104004). arXiv: [1406.7295](https://arxiv.org/abs/1406.7295) [gr-qc].
- [49] B. P. Abbott et al. “Properties of the Binary Black Hole Merger GW150914.” In: *Phys. Rev. Lett.* 116.24 (2016), p. 241102. doi: [10.1103/PhysRevLett.116.241102](https://doi.org/10.1103/PhysRevLett.116.241102). arXiv: [1602.03840](https://arxiv.org/abs/1602.03840) [gr-qc].
- [50] R. Abuter et al. “Detection of the gravitational redshift in the orbit of the star S2 near the Galactic centre massive black hole.” In: *Astron. Astrophys.* 615 (2018), p. L15. doi: [10.1051/0004-6361/201833718](https://doi.org/10.1051/0004-6361/201833718). arXiv: [1807.09409](https://arxiv.org/abs/1807.09409) [astro-ph.GA].
- [51] H.-Y. Chen and D. E. Holz. “Finding the One: Identifying the Host Galaxies of Gravitational-Wave Sources.” In: (Dec. 2016). arXiv: [1612.01471](https://arxiv.org/abs/1612.01471) [astro-ph.HE].
- [52] M. Vallisneri. “Prospects for gravitational wave observations of neutron star tidal disruption in neutron star / black hole binaries.” In: *Phys. Rev. Lett.* 84 (2000), p. 3519. doi: [10.1103/PhysRevLett.84.3519](https://doi.org/10.1103/PhysRevLett.84.3519). arXiv: [gr-qc/9912026](https://arxiv.org/abs/gr-qc/9912026).
- [53] M. Shibata and K. Taniguchi. “Merger of black hole and neutron star in general relativity: Tidal disruption, torus mass, and gravitational waves.” In: *Phys. Rev. D* 77 (2008), p. 084015. doi: [10.1103/PhysRevD.77.084015](https://doi.org/10.1103/PhysRevD.77.084015). arXiv: [0711.1410](https://arxiv.org/abs/0711.1410) [gr-qc].
- [54] B. Shiralilou, G. Raaijmakers, B. Duboef, et al. “Measuring the Hubble Constant with Dark Neutron Star–Black Hole Mergers.” In: *Astrophys. J.* 955.2 (2023), p. 149. doi: [10.3847/1538-4357/acf3dc](https://doi.org/10.3847/1538-4357/acf3dc). arXiv: [2207.11792](https://arxiv.org/abs/2207.11792) [astro-ph.CO].
- [55] M. Nicholl et al. “The Electromagnetic Counterpart of the Binary Neutron Star Merger LIGO/VIRGO GW170817. III. Optical and UV Spectra of a Blue Kilonova From Fast Polar Ejecta.” In: *Astrophys. J. Lett.* 848.2 (2017), p. L18. doi: [10.3847/2041-8213/aa9029](https://doi.org/10.3847/2041-8213/aa9029). arXiv: [1710.05456](https://arxiv.org/abs/1710.05456) [astro-ph.HE].
- [56] D. A. Coulter et al. “Swope Supernova Survey 2017a (SSS17a), the Optical Counterpart to a Gravitational Wave Source.” In: *Science* 358 (2017), p. 1556. doi: [10.1126/science.aap9811](https://doi.org/10.1126/science.aap9811). arXiv: [1710.05452](https://arxiv.org/abs/1710.05452) [astro-ph.HE].

- [57] B. P. Abbott et al. “A gravitational-wave standard siren measurement of the Hubble constant.” In: *Nature* 551.7678 (2017), pp. 85–88. DOI: [10.1038/nature24471](https://doi.org/10.1038/nature24471). arXiv: [1710.05835](https://arxiv.org/abs/1710.05835) [[astro-ph.CO](#)].
- [58] S. Mastroianni, R. Duque, E. Chassande-Mottin, et al. “The potential role of binary neutron star merger afterglows in multimessenger cosmology.” In: *Astron. Astrophys.* 652 (2021), A1. DOI: [10.1051/0004-6361/202040229](https://doi.org/10.1051/0004-6361/202040229). arXiv: [2012.12836](https://arxiv.org/abs/2012.12836) [[astro-ph.HE](#)].
- [59] R. Mochkovitch, F. Daigne, R. Duque, et al. “Prospects for kilonova signals in the gravitational-wave era.” In: *Astron. Astrophys.* 651 (2021), A83. DOI: [10.1051/0004-6361/202140689](https://doi.org/10.1051/0004-6361/202140689). arXiv: [2103.00943](https://arxiv.org/abs/2103.00943) [[astro-ph.HE](#)].
- [60] W. Del Pozzo. “Inference of the cosmological parameters from gravitational waves: application to second generation interferometers.” In: *Phys. Rev. D* 86 (2012), p. 043011. DOI: [10.1103/PhysRevD.86.043011](https://doi.org/10.1103/PhysRevD.86.043011). arXiv: [1108.1317](https://arxiv.org/abs/1108.1317) [[astro-ph.CO](#)].
- [61] H.-Y. Chen, M. Fishbach, and D. E. Holz. “A two per cent Hubble constant measurement from standard sirens within five years.” In: *Nature* 562.7728 (2018), pp. 545–547. DOI: [10.1038/s41586-018-0606-0](https://doi.org/10.1038/s41586-018-0606-0). arXiv: [1712.06531](https://arxiv.org/abs/1712.06531) [[astro-ph.CO](#)].
- [62] M. Fishbach, R. Gray, I. Magaña Hernandez, et al. “A Standard Siren Measurement of the Hubble Constant from GW170817 without the Electromagnetic Counterpart.” In: *ApJ* 871.1, L13 (Jan. 2019), p. L13. DOI: [10.3847/2041-8213/aaf96e](https://doi.org/10.3847/2041-8213/aaf96e). arXiv: [1807.05667](https://arxiv.org/abs/1807.05667) [[astro-ph.CO](#)].
- [63] G. Scelfo, L. Boco, A. Lapi, et al. “Exploring galaxies-gravitational waves cross-correlations as an astrophysical probe.” In: *J. Cosmology Astropart. Phys.* 2020.10, 045 (Oct. 2020), p. 045. DOI: [10.1088/1475-7516/2020/10/045](https://doi.org/10.1088/1475-7516/2020/10/045). arXiv: [2007.08534](https://arxiv.org/abs/2007.08534) [[astro-ph.CO](#)].
- [64] A. Finke, S. Foffa, F. Iacovelli, et al. “Cosmology with LIGO/Virgo dark sirens: Hubble parameter and modified gravitational wave propagation.” In: *J. Cosmology Astropart. Phys.* 2021.8, 026 (Aug. 2021), p. 026. DOI: [10.1088/1475-7516/2021/08/026](https://doi.org/10.1088/1475-7516/2021/08/026). arXiv: [2101.12660](https://arxiv.org/abs/2101.12660) [[astro-ph.CO](#)].
- [65] C. Cigarrán Díaz and S. Mukherjee. “Mapping the cosmic expansion history from LIGO-Virgo-KAGRA in synergy with DESI and SPHEREx.” In: *MNRAS* 511.2 (Apr. 2022), pp. 2782–2795. DOI: [10.1093/mnras/stac208](https://doi.org/10.1093/mnras/stac208). arXiv: [2107.12787](https://arxiv.org/abs/2107.12787) [[astro-ph.CO](#)].
- [66] S. Mukherjee, A. Krolewski, B. D. Wandelt, et al. “Cross-correlating dark sirens and galaxies: measurement of H_0 from GWTC-3 of LIGO-Virgo-KAGRA.” In: *arXiv e-prints*, arXiv:2203.03643 (Mar. 2022), arXiv:2203.03643. arXiv: [2203.03643](https://arxiv.org/abs/2203.03643) [[astro-ph.CO](#)].

- [67] C. L. MacLeod and C. J. Hogan. “Precision of Hubble constant derived using black hole binary absolute distances and statistical redshift information.” In: *Phys. Rev. D* 77 (2008), p. 043512. DOI: [10.1103/PhysRevD.77.043512](https://doi.org/10.1103/PhysRevD.77.043512). arXiv: [0712.0618](https://arxiv.org/abs/0712.0618) [astro-ph].
- [68] R. Nair, S. Bose, and T. D. Saini. “Measuring the Hubble constant: Gravitational wave observations meet galaxy clustering.” In: *Phys. Rev. D* 98.2 (2018), p. 023502. DOI: [10.1103/PhysRevD.98.023502](https://doi.org/10.1103/PhysRevD.98.023502). arXiv: [1804.06085](https://arxiv.org/abs/1804.06085) [astro-ph.CO].
- [69] R. Gray et al. “Cosmological inference using gravitational wave standard sirens: A mock data analysis.” In: *Phys. Rev. D* 101.12 (2020), p. 122001. DOI: [10.1103/PhysRevD.101.122001](https://doi.org/10.1103/PhysRevD.101.122001). arXiv: [1908.06050](https://arxiv.org/abs/1908.06050) [gr-qc].
- [70] S. Mukherjee, B. D. Wandelt, S. M. Nissanke, et al. “Accurate precision cosmology with redshift unknown gravitational wave sources.” In: *Phys. Rev. D* 103.4, 043520 (Feb. 2021), p. 043520. DOI: [10.1103/PhysRevD.103.043520](https://doi.org/10.1103/PhysRevD.103.043520). arXiv: [2007.02943](https://arxiv.org/abs/2007.02943) [astro-ph.CO].
- [71] M. Soares-Santos et al. “First Measurement of the Hubble Constant from a Dark Standard Siren using the Dark Energy Survey Galaxies and the LIGO/Virgo Binary–Black-hole Merger GW170814.” In: *Astrophys. J. Lett.* 876.1 (2019), p. L7. DOI: [10.3847/2041-8213/ab14f1](https://doi.org/10.3847/2041-8213/ab14f1). arXiv: [1901.01540](https://arxiv.org/abs/1901.01540) [astro-ph.CO].
- [72] B. P. Abbott et al. “A Gravitational-wave Measurement of the Hubble Constant Following the Second Observing Run of Advanced LIGO and Virgo.” In: *Astrophys. J.* 909.2 (2021), p. 218. DOI: [10.3847/1538-4357/abdcb7](https://doi.org/10.3847/1538-4357/abdcb7). arXiv: [1908.06060](https://arxiv.org/abs/1908.06060) [astro-ph.CO].
- [73] R. Abbott et al. “Constraints on the cosmic expansion history from GWTC-3.” In: (Nov. 2021). arXiv: [2111.03604](https://arxiv.org/abs/2111.03604) [astro-ph.CO].
- [74] B. C. Seymour, H. Yu, and Y. Chen. “Multiband gravitational wave cosmography with dark sirens.” In: *Phys. Rev. D* 108.4 (2023), p. 044038. DOI: [10.1103/PhysRevD.108.044038](https://doi.org/10.1103/PhysRevD.108.044038). arXiv: [2208.01668](https://arxiv.org/abs/2208.01668) [gr-qc].
- [75] W. M. Farr, M. Fishbach, J. Ye, et al. “A Future Percent-Level Measurement of the Hubble Expansion at Redshift 0.8 With Advanced LIGO.” In: *Astrophys. J. Lett.* 883.2 (2019), p. L42. DOI: [10.3847/2041-8213/ab4284](https://doi.org/10.3847/2041-8213/ab4284). arXiv: [1908.09084](https://arxiv.org/abs/1908.09084) [astro-ph.CO].
- [76] J. M. Ezquiaga and D. E. Holz. “Spectral Sirens: Cosmology from the Full Mass Distribution of Compact Binaries.” In: *Phys. Rev. Lett.* 129.6 (2022), p. 061102. DOI: [10.1103/PhysRevLett.129.061102](https://doi.org/10.1103/PhysRevLett.129.061102). arXiv: [2202.08240](https://arxiv.org/abs/2202.08240) [astro-ph.CO].
- [77] H. Yu, B. Seymour, Y. Wang, et al. “Uncertainty and Bias of Cosmology and Astrophysical Population Model from Statistical Dark Sirens.” In: *Astrophys. J.* 941.2 (2022), p. 174. DOI: [10.3847/1538-4357/ac9da0](https://doi.org/10.3847/1538-4357/ac9da0). arXiv: [2206.09984](https://arxiv.org/abs/2206.09984) [astro-ph.CO].

- [78] B. P. Abbott et al. “Tests of general relativity with GW150914.” In: *Phys. Rev. Lett.* 116.22 (2016). [Erratum: *Phys.Rev.Lett.* 121, 129902 (2018)], p. 221101. DOI: [10.1103/PhysRevLett.116.221101](https://doi.org/10.1103/PhysRevLett.116.221101). arXiv: [1602.03841](https://arxiv.org/abs/1602.03841) [gr-qc].
- [79] R. Abbott et al. “Tests of General Relativity with GWTC-3.” Dec. 2021. arXiv: [2112.06861](https://arxiv.org/abs/2112.06861) [gr-qc].
- [80] N. Yunes and X. Siemens. “Gravitational-Wave Tests of General Relativity with Ground-Based Detectors and Pulsar Timing-Arrays.” In: *Living Rev. Rel.* 16 (2013), p. 9. DOI: [10.12942/lrr-2013-9](https://doi.org/10.12942/lrr-2013-9). arXiv: [1304.3473](https://arxiv.org/abs/1304.3473) [gr-qc].
- [81] E. Berti et al. “Testing General Relativity with Present and Future Astrophysical Observations.” In: *Class. Quant. Grav.* 32 (2015), p. 243001. DOI: [10.1088/0264-9381/32/24/243001](https://doi.org/10.1088/0264-9381/32/24/243001). arXiv: [1501.07274](https://arxiv.org/abs/1501.07274) [gr-qc].
- [82] B. P. Abbott et al. “Tests of General Relativity with GW170817.” In: *Phys. Rev. Lett.* 123.1 (2019), p. 011102. DOI: [10.1103/PhysRevLett.123.011102](https://doi.org/10.1103/PhysRevLett.123.011102). arXiv: [1811.00364](https://arxiv.org/abs/1811.00364) [gr-qc].
- [83] B. P. Abbott et al. “Tests of General Relativity with the Binary Black Hole Signals from the LIGO-Virgo Catalog GWTC-1.” In: *Phys. Rev. D* 100.10 (2019), p. 104036. DOI: [10.1103/PhysRevD.100.104036](https://doi.org/10.1103/PhysRevD.100.104036). arXiv: [1903.04467](https://arxiv.org/abs/1903.04467) [gr-qc].
- [84] R. Abbott et al. “Tests of general relativity with binary black holes from the second LIGO-Virgo gravitational-wave transient catalog.” In: *Phys. Rev. D* 103.12 (2021), p. 122002. DOI: [10.1103/PhysRevD.103.122002](https://doi.org/10.1103/PhysRevD.103.122002). arXiv: [2010.14529](https://arxiv.org/abs/2010.14529) [gr-qc].
- [85] N. Yunes and F. Pretorius. “Fundamental Theoretical Bias in Gravitational Wave Astrophysics and the Parameterized Post-Einsteinian Framework.” In: *Phys. Rev. D* 80 (2009), p. 122003. DOI: [10.1103/PhysRevD.80.122003](https://doi.org/10.1103/PhysRevD.80.122003). arXiv: [0909.3328](https://arxiv.org/abs/0909.3328) [gr-qc].
- [86] T. G. F. Li, W. Del Pozzo, S. Vitale, et al. “Towards a generic test of the strong field dynamics of general relativity using compact binary coalescence.” In: *Phys. Rev. D* 85 (2012), p. 082003. DOI: [10.1103/PhysRevD.85.082003](https://doi.org/10.1103/PhysRevD.85.082003). arXiv: [1110.0530](https://arxiv.org/abs/1110.0530) [gr-qc].
- [87] M. Agathos, W. Del Pozzo, T. G. F. Li, et al. “TIGER: A data analysis pipeline for testing the strong-field dynamics of general relativity with gravitational wave signals from coalescing compact binaries.” In: *Phys. Rev. D* 89.8 (2014), p. 082001. DOI: [10.1103/PhysRevD.89.082001](https://doi.org/10.1103/PhysRevD.89.082001). arXiv: [1311.0420](https://arxiv.org/abs/1311.0420) [gr-qc].
- [88] J. Meidam et al. “Parametrized tests of the strong-field dynamics of general relativity using gravitational wave signals from coalescing binary black holes: Fast likelihood calculations and sensitivity of the method.” In: *Phys.*

- Rev. D* 97.4 (2018), p. 044033. doi: [10.1103/PhysRevD.97.044033](https://doi.org/10.1103/PhysRevD.97.044033). arXiv: [1712.08772](https://arxiv.org/abs/1712.08772) [gr-qc].
- [89] A. K. Mehta, A. Buonanno, R. Cotesta, et al. “Tests of general relativity with gravitational-wave observations using a flexible theory-independent method.” In: *Phys. Rev. D* 107.4 (2023), p. 044020. doi: [10.1103/PhysRevD.107.044020](https://doi.org/10.1103/PhysRevD.107.044020). arXiv: [2203.13937](https://arxiv.org/abs/2203.13937) [gr-qc].
- [90] A. Buonanno, B. Iyer, E. Ochsner, et al. “Comparison of post-Newtonian templates for compact binary inspiral signals in gravitational-wave detectors.” In: *Phys. Rev. D* 80 (2009), p. 084043. doi: [10.1103/PhysRevD.80.084043](https://doi.org/10.1103/PhysRevD.80.084043). arXiv: [0907.0700](https://arxiv.org/abs/0907.0700) [gr-qc].
- [91] Z. Carson and K. Yagi. “Testing General Relativity with Gravitational Waves.” In: (Nov. 2020). doi: [10.1007/978-981-15-4702-7_41-1](https://doi.org/10.1007/978-981-15-4702-7_41-1). arXiv: [2011.02938](https://arxiv.org/abs/2011.02938) [gr-qc].
- [92] S. Gossan, J. Veitch, and B. S. Sathyaprakash. “Bayesian model selection for testing the no-hair theorem with black hole ringdowns.” In: *Phys. Rev. D* 85 (2012), p. 124056. doi: [10.1103/PhysRevD.85.124056](https://doi.org/10.1103/PhysRevD.85.124056). arXiv: [1111.5819](https://arxiv.org/abs/1111.5819) [gr-qc].
- [93] J. Meidam, M. Agathos, C. Van Den Broeck, et al. “Testing the no-hair theorem with black hole ringdowns using TIGER.” In: *Phys. Rev. D* 90.6 (2014), p. 064009. doi: [10.1103/PhysRevD.90.064009](https://doi.org/10.1103/PhysRevD.90.064009). arXiv: [1406.3201](https://arxiv.org/abs/1406.3201) [gr-qc].
- [94] S. Bhagwat, X. J. Forteza, P. Pani, et al. “Ringdown overtones, black hole spectroscopy, and no-hair theorem tests.” In: *Phys. Rev. D* 101.4 (2020), p. 044033. doi: [10.1103/PhysRevD.101.044033](https://doi.org/10.1103/PhysRevD.101.044033). arXiv: [1910.08708](https://arxiv.org/abs/1910.08708) [gr-qc].
- [95] R. A. Konoplya and A. Zhidenko. “Quasinormal modes of black holes: From astrophysics to string theory.” In: *Rev. Mod. Phys.* 83 (2011), pp. 793–836. doi: [10.1103/RevModPhys.83.793](https://doi.org/10.1103/RevModPhys.83.793). arXiv: [1102.4014](https://arxiv.org/abs/1102.4014) [gr-qc].
- [96] E. Berti, V. Cardoso, and A. O. Starinets. “Quasinormal modes of black holes and black branes.” In: *Class. Quant. Grav.* 26 (2009), p. 163001. doi: [10.1088/0264-9381/26/16/163001](https://doi.org/10.1088/0264-9381/26/16/163001). arXiv: [0905.2975](https://arxiv.org/abs/0905.2975) [gr-qc].
- [97] T. Baker, E. Bellini, P. G. Ferreira, et al. “Strong constraints on cosmological gravity from GW170817 and GRB 170817A.” In: *Phys. Rev. Lett.* 119.25 (2017), p. 251301. doi: [10.1103/PhysRevLett.119.251301](https://doi.org/10.1103/PhysRevLett.119.251301). arXiv: [1710.06394](https://arxiv.org/abs/1710.06394) [astro-ph.CO].
- [98] S. Boran, S. Desai, E. O. Kahya, et al. “GW170817 Falsifies Dark Matter Emulators.” In: *Phys. Rev. D* 97.4 (2018), p. 041501. doi: [10.1103/PhysRevD.97.041501](https://doi.org/10.1103/PhysRevD.97.041501). arXiv: [1710.06168](https://arxiv.org/abs/1710.06168) [astro-ph.HE].

- [99] J. Sakstein and B. Jain. “Implications of the Neutron Star Merger GW170817 for Cosmological Scalar-Tensor Theories.” In: *Phys. Rev. Lett.* 119.25 (2017), p. 251303. doi: [10.1103/PhysRevLett.119.251303](https://doi.org/10.1103/PhysRevLett.119.251303). arXiv: [1710.05893](https://arxiv.org/abs/1710.05893) [astro-ph.CO].
- [100] A. Nishizawa, A. Taruya, K. Hayama, et al. “Probing non-tensorial polarizations of stochastic gravitational-wave backgrounds with ground-based laser interferometers.” In: *Phys. Rev. D* 79 (2009), p. 082002. doi: [10.1103/PhysRevD.79.082002](https://doi.org/10.1103/PhysRevD.79.082002). arXiv: [0903.0528](https://arxiv.org/abs/0903.0528) [astro-ph.CO].
- [101] A. Nishizawa. “Generalized framework for testing gravity with gravitational-wave propagation. I. Formulation.” In: *Phys. Rev. D* 97.10 (2018), p. 104037. doi: [10.1103/PhysRevD.97.104037](https://doi.org/10.1103/PhysRevD.97.104037). arXiv: [1710.04825](https://arxiv.org/abs/1710.04825) [gr-qc].
- [102] S. Hou, Y. Gong, and Y. Liu. “Polarizations of Gravitational Waves in Horndeski Theory.” In: *Eur. Phys. J. C* 78.5 (2018), p. 378. doi: [10.1140/epjc/s10052-018-5869-y](https://doi.org/10.1140/epjc/s10052-018-5869-y). arXiv: [1704.01899](https://arxiv.org/abs/1704.01899) [gr-qc].
- [103] Y. Gong and S. Hou. “The Polarizations of Gravitational Waves.” In: *Universe* 4.8 (2018). Ed. by G. Calcagni, p. 85. doi: [10.3390/universe4080085](https://doi.org/10.3390/universe4080085). arXiv: [1806.04027](https://arxiv.org/abs/1806.04027) [gr-qc].
- [104] H. Takeda, A. Nishizawa, Y. Michimura, et al. “Polarization test of gravitational waves from compact binary coalescences.” In: *Phys. Rev. D* 98.2 (2018), p. 022008. doi: [10.1103/PhysRevD.98.022008](https://doi.org/10.1103/PhysRevD.98.022008). arXiv: [1806.02182](https://arxiv.org/abs/1806.02182) [gr-qc].
- [105] Y. Hagihara, N. Era, D. Iikawa, et al. “Constraining extra gravitational wave polarizations with Advanced LIGO, Advanced Virgo and KAGRA and upper bounds from GW170817.” In: *Phys. Rev. D* 100.6 (2019), p. 064010. doi: [10.1103/PhysRevD.100.064010](https://doi.org/10.1103/PhysRevD.100.064010). arXiv: [1904.02300](https://arxiv.org/abs/1904.02300) [gr-qc].
- [106] P. T. H. Pang, R. K. L. Lo, I. C. F. Wong, et al. “Generic searches for alternative gravitational wave polarizations with networks of interferometric detectors.” In: *Phys. Rev. D* 101.10 (2020), p. 104055. doi: [10.1103/PhysRevD.101.104055](https://doi.org/10.1103/PhysRevD.101.104055). arXiv: [2003.07375](https://arxiv.org/abs/2003.07375) [gr-qc].
- [107] K. Schumacher, N. Yunes, and K. Yagi. “Gravitational wave polarizations with different propagation speeds.” In: *Phys. Rev. D* 108.10 (2023), p. 104038. doi: [10.1103/PhysRevD.108.104038](https://doi.org/10.1103/PhysRevD.108.104038). arXiv: [2308.05589](https://arxiv.org/abs/2308.05589) [gr-qc].
- [108] K. Schumacher, C. Talbot, D. E. Holz, et al. “Better early than never: A new test for superluminal gravitational wave polarizations.” In: (Jan. 2025). arXiv: [2501.18125](https://arxiv.org/abs/2501.18125) [gr-qc].
- [109] K. A. Postnov and L. R. Yungelson. “The Evolution of Compact Binary Star Systems.” In: *Living Rev. Rel.* 17 (2014), p. 3. doi: [10.12942/lrr-2014-3](https://doi.org/10.12942/lrr-2014-3). arXiv: [1403.4754](https://arxiv.org/abs/1403.4754) [astro-ph.HE].

- [110] I. Mandel and A. Farmer. “Merging stellar-mass binary black holes.” In: *Phys. Rept.* 955 (2022), pp. 1–24. doi: [10.1016/j.physrep.2022.01.003](https://doi.org/10.1016/j.physrep.2022.01.003). arXiv: [1806.05820](https://arxiv.org/abs/1806.05820) [[astro-ph.HE](#)].
- [111] S. Sigurdsson and E. S. Phinney. “Binary–Single Star Interactions in Globular Clusters.” In: *Astrophys. J.* 415 (1993), p. 631. doi: [10.1086/173190](https://doi.org/10.1086/173190).
- [112] M. Dall’Amico, M. Mapelli, S. Torniamenti, et al. “Eccentric black hole mergers via three-body interactions in young, globular, and nuclear star clusters.” In: *Astron. Astrophys.* 683 (2024), A186. doi: [10.1051/0004-6361/202348745](https://doi.org/10.1051/0004-6361/202348745). arXiv: [2303.07421](https://arxiv.org/abs/2303.07421) [[astro-ph.HE](#)].
- [113] J. H. VanLandingham, M. C. Miller, D. P. Hamilton, et al. “The Role of the Kozai–lidov Mechanism in Black Hole Binary Mergers in Galactic Centers.” In: *Astrophys. J.* 828.2 (2016), p. 77. doi: [10.3847/0004-637X/828/2/77](https://doi.org/10.3847/0004-637X/828/2/77). arXiv: [1604.04948](https://arxiv.org/abs/1604.04948) [[astro-ph.HE](#)].
- [114] R. Abbott et al. “GW190521: A Binary Black Hole Merger with a Total Mass of $150M_{\odot}$.” In: *Phys. Rev. Lett.* 125.10 (2020), p. 101102. doi: [10.1103/PhysRevLett.125.101102](https://doi.org/10.1103/PhysRevLett.125.101102). arXiv: [2009.01075](https://arxiv.org/abs/2009.01075) [[gr-qc](#)].
- [115] S. E. Woosley. “Pulsational Pair-Instability Supernovae.” In: *Astrophys. J.* 836.2 (2017), p. 244. doi: [10.3847/1538-4357/836/2/244](https://doi.org/10.3847/1538-4357/836/2/244). arXiv: [1608.08939](https://arxiv.org/abs/1608.08939) [[astro-ph.HE](#)].
- [116] K. Belczynski et al. “The Effect of Pair-Instability Mass Loss on Black Hole Mergers.” In: *Astron. Astrophys.* 594 (2016), A97. doi: [10.1051/0004-6361/201628980](https://doi.org/10.1051/0004-6361/201628980). arXiv: [1607.03116](https://arxiv.org/abs/1607.03116) [[astro-ph.HE](#)].
- [117] M. Spera and M. Mapelli. “Very massive stars, pair-instability supernovae and intermediate-mass black holes with the SEVN code.” In: *Mon. Not. Roy. Astron. Soc.* 470.4 (2017), pp. 4739–4749. doi: [10.1093/mnras/stx1576](https://doi.org/10.1093/mnras/stx1576). arXiv: [1706.06109](https://arxiv.org/abs/1706.06109) [[astro-ph.SR](#)].
- [118] R. Abbott et al. “Properties and Astrophysical Implications of the $150 M_{\odot}$ Binary Black Hole Merger GW190521.” In: *Astrophys. J. Lett.* 900.1 (2020), p. L13. doi: [10.3847/2041-8213/aba493](https://doi.org/10.3847/2041-8213/aba493). arXiv: [2009.01190](https://arxiv.org/abs/2009.01190) [[astro-ph.HE](#)].
- [119] D. Gerosa and M. Fishbach. “Hierarchical mergers of stellar-mass black holes and their gravitational-wave signatures.” In: *Nature Astron.* 5.8 (2021), pp. 749–760. doi: [10.1038/s41550-021-01398-w](https://doi.org/10.1038/s41550-021-01398-w). arXiv: [2105.03439](https://arxiv.org/abs/2105.03439) [[astro-ph.HE](#)].
- [120] F. Antonini, M. Gieles, and A. Gualandris. “Black hole growth through hierarchical black hole mergers in dense star clusters: implications for gravitational wave detections.” In: *Mon. Not. Roy. Astron. Soc.* 486.4 (2019), pp. 5008–5021. doi: [10.1093/mnras/stz1149](https://doi.org/10.1093/mnras/stz1149). arXiv: [1811.03640](https://arxiv.org/abs/1811.03640) [[astro-ph.HE](#)].

- [121] M. A. S. Martinez, G. Fragione, K. Kremer, et al. “Black Hole Mergers from Hierarchical Triples in Dense Star Clusters.” In: *ApJ* 903.1, 67 (Nov. 2020), p. 67. doi: [10.3847/1538-4357/abba25](https://doi.org/10.3847/1538-4357/abba25). arXiv: [2009.08468](https://arxiv.org/abs/2009.08468) [astro-ph.GA].
- [122] Y. Yang, I. Bartos, V. Gayathri, et al. “Hierarchical Black Hole Mergers in Active Galactic Nuclei.” In: *Phys. Rev. Lett.* 123 (18 Nov. 2019), p. 181101. doi: [10.1103/PhysRevLett.123.181101](https://doi.org/10.1103/PhysRevLett.123.181101). URL: <https://link.aps.org/doi/10.1103/PhysRevLett.123.181101>.
- [123] B. McKernan, K. E. S. Ford, W. Lyra, et al. “Intermediate mass black holes in AGN discs - I. Production and growth.” In: *MNRAS* 425.1 (Sept. 2012), pp. 460–469. doi: [10.1111/j.1365-2966.2012.21486.x](https://doi.org/10.1111/j.1365-2966.2012.21486.x). arXiv: [1206.2309](https://arxiv.org/abs/1206.2309) [astro-ph.GA].
- [124] I. Bartos, B. Kocsis, Z. Haiman, et al. “Rapid and Bright Stellar-mass Binary Black Hole Mergers in Active Galactic Nuclei.” In: *ApJ* 835.2, 165 (Feb. 2017), p. 165. doi: [10.3847/1538-4357/835/2/165](https://doi.org/10.3847/1538-4357/835/2/165). arXiv: [1602.03831](https://arxiv.org/abs/1602.03831) [astro-ph.HE].
- [125] N. C. Stone, B. D. Metzger, and Z. Haiman. “Assisted inspirals of stellar mass black holes embedded in AGN discs: solving the ‘final au problem’.” In: *MNRAS* 464.1 (Jan. 2017), pp. 946–954. doi: [10.1093/mnras/stw2260](https://doi.org/10.1093/mnras/stw2260). arXiv: [1602.04226](https://arxiv.org/abs/1602.04226) [astro-ph.GA].
- [126] B. McKernan, K. E. S. Ford, J. Bellovary, et al. “Constraining Stellar-mass Black Hole Mergers in AGN Disks Detectable with LIGO.” In: *ApJ* 866.1, 66 (Oct. 2018), p. 66. doi: [10.3847/1538-4357/aadae5](https://doi.org/10.3847/1538-4357/aadae5). arXiv: [1702.07818](https://arxiv.org/abs/1702.07818) [astro-ph.HE].
- [127] H. Tagawa, Z. Haiman, and B. Kocsis. “Formation and Evolution of Compact Object Binaries in AGN Disks.” In: *arXiv e-prints*, arXiv:1912.08218 (Dec. 2019), arXiv:1912.08218. arXiv: [1912.08218](https://arxiv.org/abs/1912.08218) [astro-ph.GA].
- [128] B. McKernan, K. E. S. Ford, I. Bartos, et al. “Ram-pressure Stripping of a Kicked Hill Sphere: Prompt Electromagnetic Emission from the Merger of Stellar Mass Black Holes in an AGN Accretion Disk.” In: *ApJ* 884.2, L50 (Oct. 2019), p. L50. doi: [10.3847/2041-8213/ab4886](https://doi.org/10.3847/2041-8213/ab4886). arXiv: [1907.03746](https://arxiv.org/abs/1907.03746) [astro-ph.HE].
- [129] Y. Yang, I. Bartos, V. Gayathri, et al. “Hierarchical Black Hole Mergers in Active Galactic Nuclei.” In: *Phys. Rev. Lett.* 123.18, 181101 (Nov. 2019), p. 181101. doi: [10.1103/PhysRevLett.123.181101](https://doi.org/10.1103/PhysRevLett.123.181101). arXiv: [1906.09281](https://arxiv.org/abs/1906.09281) [astro-ph.HE].
- [130] J. M. Bellovary, M.-M. Mac Low, B. McKernan, et al. “Migration Traps in Disks around Supermassive Black Holes.” In: *ApJ* 819.2, L17 (Mar. 2016), p. L17. doi: [10.3847/2041-8205/819/2/L17](https://doi.org/10.3847/2041-8205/819/2/L17). arXiv: [1511.00005](https://arxiv.org/abs/1511.00005) [astro-ph.GA].

- [131] A. Secunda, J. Bellovary, M.-M. Mac Low, et al. “Orbital Migration of Interacting Stellar Mass Black Holes in Disks around Supermassive Black Holes.” In: *ApJ* 878.2, 85 (June 2019), p. 85. doi: [10.3847/1538-4357/ab20ca](https://doi.org/10.3847/1538-4357/ab20ca). arXiv: [1807.02859](https://arxiv.org/abs/1807.02859) [astro-ph.HE].
- [132] R. M. O’Leary, B. Kocsis, and A. Loeb. “Gravitational waves from scattering of stellar-mass black holes in galactic nuclei.” In: *Mon. Not. Roy. Astron. Soc.* 395.4 (2009), pp. 2127–2146. doi: [10.1111/j.1365-2966.2009.14653.x](https://doi.org/10.1111/j.1365-2966.2009.14653.x). arXiv: [0807.2638](https://arxiv.org/abs/0807.2638) [astro-ph].
- [133] F. Antonini and H. B. Perets. “Secular Evolution of Compact Binaries near Massive Black Holes: Gravitational Wave Sources and Other Exotica.” In: *ApJ* 757.1, 27 (Sept. 2012), p. 27. doi: [10.1088/0004-637X/757/1/27](https://doi.org/10.1088/0004-637X/757/1/27). arXiv: [1203.2938](https://arxiv.org/abs/1203.2938) [astro-ph.GA].
- [134] F. Antonini and F. A. Rasio. “Merging Black Hole Binaries in Galactic Nuclei: Implications for Advanced-LIGO Detections.” In: *ApJ* 831.2, 187 (Nov. 2016), p. 187. doi: [10.3847/0004-637X/831/2/187](https://doi.org/10.3847/0004-637X/831/2/187). arXiv: [1606.04889](https://arxiv.org/abs/1606.04889) [astro-ph.HE].
- [135] J. H. VanLandingham, M. C. Miller, D. P. Hamilton, et al. “The Role of the Kozai–Lidov Mechanism in Black Hole Binary Mergers in Galactic Centers.” In: *ApJ* 828.2, 77 (Sept. 2016), p. 77. doi: [10.3847/0004-637X/828/2/77](https://doi.org/10.3847/0004-637X/828/2/77). arXiv: [1604.04948](https://arxiv.org/abs/1604.04948) [astro-ph.HE].
- [136] C. Petrovich and F. Antonini. “Greatly Enhanced Merger Rates of Compact-object Binaries in Non-spherical Nuclear Star Clusters.” In: *ApJ* 846.2, 146 (Sept. 2017), p. 146. doi: [10.3847/1538-4357/aa8628](https://doi.org/10.3847/1538-4357/aa8628). arXiv: [1705.05848](https://arxiv.org/abs/1705.05848) [astro-ph.HE].
- [137] N. W. C. Leigh, A. M. Geller, B. McKernan, et al. “On the rate of black hole binary mergers in galactic nuclei due to dynamical hardening.” In: *MNRAS* 474.4 (Mar. 2018), pp. 5672–5683. doi: [10.1093/mnras/stx3134](https://doi.org/10.1093/mnras/stx3134). arXiv: [1711.10494](https://arxiv.org/abs/1711.10494) [astro-ph.GA].
- [138] X. Chen and W.-B. Han. “Extreme-mass-ratio inspirals produced by tidal capture of binary black holes.” In: *Communications Physics* 1.1, 53 (Sept. 2018), p. 53. doi: [10.1038/s42005-018-0053-0](https://doi.org/10.1038/s42005-018-0053-0). arXiv: [1801.05780](https://arxiv.org/abs/1801.05780) [astro-ph.HE].
- [139] G. Fragione, N. W. C. Leigh, and R. Perna. “Black hole and neutron star mergers in galactic nuclei: the role of triples.” In: *MNRAS* 488.2 (Sept. 2019), pp. 2825–2835. doi: [10.1093/mnras/stz1803](https://doi.org/10.1093/mnras/stz1803). arXiv: [1903.09160](https://arxiv.org/abs/1903.09160) [astro-ph.GA].
- [140] J. Samsing, I. Bartos, D. J. D’Orazio, et al. “Active Galactic Nuclei as Factories for Eccentric Black Hole Mergers.” In: *arXiv e-prints*, arXiv:2010.09765 (Oct. 2020), arXiv:2010.09765. arXiv: [2010.09765](https://arxiv.org/abs/2010.09765) [astro-ph.HE].

- [141] L. Randall and Z.-Z. Xianyu. “A Direct Probe of Mass Density Near Inspiring Binary Black Holes.” In: *Astrophys. J.* 878.2 (2019), p. 75. DOI: [10.3847/1538-4357/ab20c6](https://doi.org/10.3847/1538-4357/ab20c6). arXiv: [1805.05335](https://arxiv.org/abs/1805.05335) [gr-qc].
- [142] K. Inayoshi, N. Tamanini, C. Caprini, et al. “Probing stellar binary black hole formation in galactic nuclei via the imprint of their center of mass acceleration on their gravitational wave signal.” In: *Phys. Rev. D* 96.6 (2017), p. 063014. DOI: [10.1103/PhysRevD.96.063014](https://doi.org/10.1103/PhysRevD.96.063014). arXiv: [1702.06529](https://arxiv.org/abs/1702.06529) [astro-ph.HE].
- [143] V. Cardoso, F. Duque, and G. Khanna. “Gravitational tuning forks and hierarchical triple systems.” In: *Phys. Rev. D* 103.8 (2021), p. L081501. DOI: [10.1103/PhysRevD.103.L081501](https://doi.org/10.1103/PhysRevD.103.L081501). arXiv: [2101.01186](https://arxiv.org/abs/2101.01186) [gr-qc].
- [144] B. Liu, D. Lai, and Y.-H. Wang. “Binary Mergers near a Supermassive Black Hole: Relativistic Effects in Triples.” In: *Astrophys. J. Lett.* 883.1 (2019), p. L7. DOI: [10.3847/2041-8213/ab40c0](https://doi.org/10.3847/2041-8213/ab40c0). arXiv: [1906.07726](https://arxiv.org/abs/1906.07726) [astro-ph.HE].
- [145] B. Liu and D. Lai. “Probing the Spins of Supermassive Black Holes with Gravitational Waves from Surrounding Compact Binaries.” In: *Astrophys. J.* 924.2 (2022), p. 127. DOI: [10.3847/1538-4357/ac3aef](https://doi.org/10.3847/1538-4357/ac3aef). arXiv: [2105.02230](https://arxiv.org/abs/2105.02230) [astro-ph.HE].
- [146] H. Yu and Y. Chen. “Direct determination of supermassive black hole properties with gravitational-wave radiation from surrounding stellar-mass black hole binaries.” In: *Phys. Rev. Lett.* 126.2 (2021), p. 021101. DOI: [10.1103/PhysRevLett.126.021101](https://doi.org/10.1103/PhysRevLett.126.021101). arXiv: [2009.02579](https://arxiv.org/abs/2009.02579) [gr-qc].
- [147] I. M. Romero-Shaw, N. Loutrel, and M. Zevin. “Inferring interference: Identifying a perturbing tertiary with eccentric gravitational wave burst timing.” In: *Phys. Rev. D* 107.12 (2023), p. 122001. DOI: [10.1103/PhysRevD.107.122001](https://doi.org/10.1103/PhysRevD.107.122001). arXiv: [2211.07278](https://arxiv.org/abs/2211.07278) [gr-qc].
- [148] Y. Meiron, B. Kocsis, and A. Loeb. “Detecting triple systems with gravitational wave observations.” In: *Astrophys. J.* 834.2 (2017), p. 200. DOI: [10.3847/1538-4357/834/2/200](https://doi.org/10.3847/1538-4357/834/2/200). arXiv: [1604.02148](https://arxiv.org/abs/1604.02148) [astro-ph.HE].
- [149] D. J. D’Orazio and A. Loeb. “Repeated gravitational lensing of gravitational waves in hierarchical black hole triples.” In: *Phys. Rev. D* 101.8 (2020), p. 083031. DOI: [10.1103/PhysRevD.101.083031](https://doi.org/10.1103/PhysRevD.101.083031). arXiv: [1910.02966](https://arxiv.org/abs/1910.02966) [astro-ph.HE].
- [150] H. Yu, Y. Wang, B. Seymour, et al. “Detecting gravitational lensing in hierarchical triples in galactic nuclei with space-borne gravitational-wave observatories.” In: (July 2021). arXiv: [2107.14318](https://arxiv.org/abs/2107.14318) [gr-qc].
- [151] A. Laeuger, B. Seymour, Y. Chen, et al. “Measuring supermassive black hole properties via gravitational radiation from eccentrically orbiting stellar mass black hole binaries.” In: *Phys. Rev. D* 109.6 (2024), p. 064086. DOI: [10.1103/PhysRevD.109.064086](https://doi.org/10.1103/PhysRevD.109.064086). arXiv: [2310.16799](https://arxiv.org/abs/2310.16799) [gr-qc].

- [152] L. S. Finn. “Detection, measurement and gravitational radiation.” In: *Phys. Rev. D* 46 (1992), pp. 5236–5249. DOI: [10.1103/PhysRevD.46.5236](https://doi.org/10.1103/PhysRevD.46.5236). arXiv: [gr-qc/9209010](https://arxiv.org/abs/gr-qc/9209010).
- [153] C. Cutler and E. E. Flanagan. “Gravitational waves from merging compact binaries: How accurately can one extract the binary’s parameters from the inspiral wave form?.” In: *Phys. Rev. D* 49 (1994), pp. 2658–2697. DOI: [10.1103/PhysRevD.49.2658](https://doi.org/10.1103/PhysRevD.49.2658). arXiv: [gr-qc/9402014](https://arxiv.org/abs/gr-qc/9402014).
- [154] E. E. Flanagan and S. A. Hughes. “Measuring gravitational waves from binary black hole coalescences: 1. Signal-to-noise for inspiral, merger, and ringdown.” In: *Phys. Rev. D* 57 (1998), pp. 4535–4565. DOI: [10.1103/PhysRevD.57.4535](https://doi.org/10.1103/PhysRevD.57.4535). arXiv: [gr-qc/9701039](https://arxiv.org/abs/gr-qc/9701039).
- [155] E. E. Flanagan and S. A. Hughes. “Measuring gravitational waves from binary black hole coalescences: 2. The Waves’ information and its extraction, with and without templates.” In: *Phys. Rev. D* 57 (1998), pp. 4566–4587. DOI: [10.1103/PhysRevD.57.4566](https://doi.org/10.1103/PhysRevD.57.4566). arXiv: [gr-qc/9710129](https://arxiv.org/abs/gr-qc/9710129).
- [156] L. S. Collaboration. “Instrument science white paper.” 2015. URL: <https://dcc.ligo.org/LIGO-T1400316/public>.
- [157] M. Maggiore. “Gravitational Waves. Vol. 1: Theory and Experiments.” Oxford Master Series in Physics. Oxford University Press, 2007. ISBN: 978-0-19-857074-5, 978-0-19-852074-0.
- [158] P. R. Saulson. “Fundamentals of Interferometric Gravitational Wave Detectors.” 2nd. ed. World Scientific, 2017. ISBN: 978-981-314-307-4, 978-981-314-620-4. DOI: [10.1142/10116](https://doi.org/10.1142/10116).
- [159] K. L. Dooley et al. “GEO 600 and the GEO-HF upgrade program: successes and challenges.” In: *Class. Quant. Grav.* 33 (2016), p. 075009. DOI: [10.1088/0264-9381/33/7/075009](https://doi.org/10.1088/0264-9381/33/7/075009). arXiv: [1510.00317 \[physics.ins-det\]](https://arxiv.org/abs/1510.00317).
- [160] B. Willke et al. “The GEO 600 gravitational wave detector.” In: *Class. Quant. Grav.* 19 (2002). Ed. by D. G. Blair, pp. 1377–1387. DOI: [10.1088/0264-9381/19/7/321](https://doi.org/10.1088/0264-9381/19/7/321).
- [161] S. Hild. “Beyond the First Generation: Extending the Science Range of the Gravitational Wave Detector GEO600..” PhD thesis. Gottfried Wilhelm Leibniz Universität Hannover, Hannover, 2007.
- [162] A. Freise. “The next generation of interferometry: Multi frequency modelling, control concepts and implementation.” PhD thesis. Hannover U., 2003.

Part I

**Cosmography with Gravitational
Waves**

*Chapter 2*UNCERTAINTY AND BIAS OF COSMOLOGY AND
ASTROPHYSICAL POPULATION MODEL FROM
STATISTICAL DARK SIRENS

- [1] H. Yu, B. Seymour, Y. Wang, et al. “Uncertainty and Bias of Cosmology and Astrophysical Population Model from Statistical Dark Sirens.” In: *Astrophys. J.* 941.2 (2022), p. 174. DOI: [10.3847/1538-4357/ac9da0](https://doi.org/10.3847/1538-4357/ac9da0). arXiv: [2206.09984](https://arxiv.org/abs/2206.09984) [[astro-ph.CO](https://arxiv.org/archive/astro)].

2.1 Introduction

The key to study modern cosmology is to measure a relation between distance and redshift. In electromagnetic (EM) observations, the redshift to the source can be directly measured (e.g., by comparing the measured spectra to the ones obtained in terrestrial laboratories), and the challenge is to constrain the distance. To do so, it relies on utilizing some forms of standard references. One possibility is to use “standard candles” with known intrinsic luminosity, and the best-known example is a type-Ia supernovae [1, 2]. Another possibility is to use a “standard ruler” with a known size, and the imprint of sound waves in the Cosmic Microwave Background is such an example [3, 4, 5]. However, a tension on the value of the Hubble Constant, conventionally denoted by H_0 , emerges between the latest results of the two sets of measurements [6]. It thus calls for a third method to either reconcile or confirm the tension.

This brings observations using gravitational waves (GWs) to people’s attention, a new possibility opened up by Advanced LIGO (aLIGO; [7]), Advanced Virgo [8], and KAGRA [9, 10]. GW events are “standard sirens” in cosmology [11, 12] as the amplitude of an event encodes directly the luminosity distance to the source. If the redshift information can be further constrained, we can then determine the values of cosmological parameters.

One way to obtain the redshift information is through multi-messenger observation of an event. If we can simultaneously observe a GW event and its EM counterpart, corresponding to a “bright siren,” we can then identify the host galaxy of the event, from which we can further extract the redshift [12, 13]. A GW event involving

neutron stars (either a binary neutron star, or BNS, or a neutron star-black hole event) is an ideal candidate here. Indeed, the first BNS event, GW170817, is a highly successful example [14, 15]. From this event alone, we were able to constrain the Hubble constant to $H_0 = 70_{-8}^{+12} \text{ km s}^{-1} \text{ Mpc}^{-1}$ within the 68% credible interval. With future detectors like LIGO-Voyager [16] or third-generation (3G) GW detectors including the Einstein Telescope [17] and the Cosmic Explorer [18, 19, 20], it is potentially possible to constrain H_0 with percent level accuracy and the normalized matter density Ω_m to an accuracy of $O(10\%)$ [21]. However, such bright sirens are rare and GW170817 is the only joint observation to date. Even with 3G detectors, Califano et al. [22] estimates that only 0.1% of detectable BNSs will have observable EM counterparts. Besides a direct EM counterpart, it is also possible to constrain cosmology from matter effects in coalescing BNSs [23].

Alternatively, we may further utilize information in binary black hole (BBH) events, which consists of the majority of event catalogs [24, 25, 26, 27, 28, 29, 30, 31, 32, 33]. An EM counterpart is typically not expected for a BBH event, and therefore a BBH corresponds to a dark siren (though a counterpart might be possible if the BBH resides in a gaseous environment; see, e.g., [34]). While for a single event, it is challenging to obtain the redshift due to the perfect degeneracy between redshift and mass (unless the source can be accurately localized to only a few potential host galaxies, a point we will get back to at Sec. 2.6), we can nonetheless infer the redshift distribution of a collection of BBH events statistically.

Initially, the statistical inference was done by comparing a BBH event catalog with galaxy catalogs (e.g., [11, 13, 35, 36]). Later, people realized that features in the mass distribution of BBH events could also be used to constrain the cosmological parameters (e.g., [37, 38, 39, 40, 41, 42, 43]). In both cases, one computes the likelihood of each event to happen given a set of cosmological parameters as well as an assumed astrophysical population model. The likelihood for all the events are then multiplied together to get the likelihood of the observed population given the assumed cosmological and astrophysical parameters. This is further converted to a posterior distribution of parameters with an assumed prior distribution [44, 45].

In essence, the statistical approach corresponds to a comparison between two histograms, or distributions. One distribution is obtained from the observed BBH events with respect to either the luminosity distance or detector-frame masses (or both as a high-dimensional distribution). The other distribution is constructed from our astrophysical model with respect to either redshift or source-frame masses (or

both). By varying the values of cosmological parameters, as well as those governing the astrophysical population, we can eventually match up the two distributions, thereby constraining cosmology and population model simultaneously.

With this view, we propose an especially convenient way to assess the statistical power of dark siren cosmology. In particular, we can analytically construct the Fisher information encoded in the distributions. From that, we can both estimate the uncertainties on the parameters governing the distributions and understand correlations among the parameters. As we will show later, even with a few simplifying assumptions, this approach predicts a similar level of uncertainty on the Hubble constant when applied to the GWTC-3 catalog [28], as well as many other key features obtained in LIGO Scientific Collaboration et al. [41]. It also reproduces the results of previous studies (e.g., [46, 39]) when forecasting the future constraints on both the population model and cosmology with hundreds to thousands of BBH events. Therefore, our approach serves as a simple and analytical way to study the statistical dark siren method, which can be especially useful when making quick but decently accurate predictions for the future when a large number of events are expected. It thus complements the more accurate yet also more complicated hierarchical inference approach [44].

Furthermore, our approach can be used to study the bias on cosmological and/or astrophysical parameters due to errors in the assumed population models. We will first provide a general framework to study the bias due to any form of errors, and then as a case study, we will examine in detail how unmodeled substructures in the mass and/or redshift model would affect the inference of the Hubble constant. This is motivated by the latest population model by LIGO Scientific Collaboration, Virgo Collaboration, and al. [47] where signs of substructures are suggested.

The rest of the paper is organized as follows. In Sec. 2.2, we provide the mathematical framework to construct the Fisher information matrix of a distribution, which estimates the covariance matrix when jointly fitting cosmological parameters and population properties. We will also consider the bias induced on the cosmological parameters due to structures not captured by a parameterized population model with a specific functional form. We then describe the astrophysical model adopted in our study in Sec. 2.3. The application to the GWTC-3 catalog is presented in Sec. 2.4. To further validate our method, we also present the reproduction of previous studies' results using our method in App. 2.7. In Sec. 2.5, we consider the bias on cosmological inference induced by unmodeled substructures in both the mass distribution

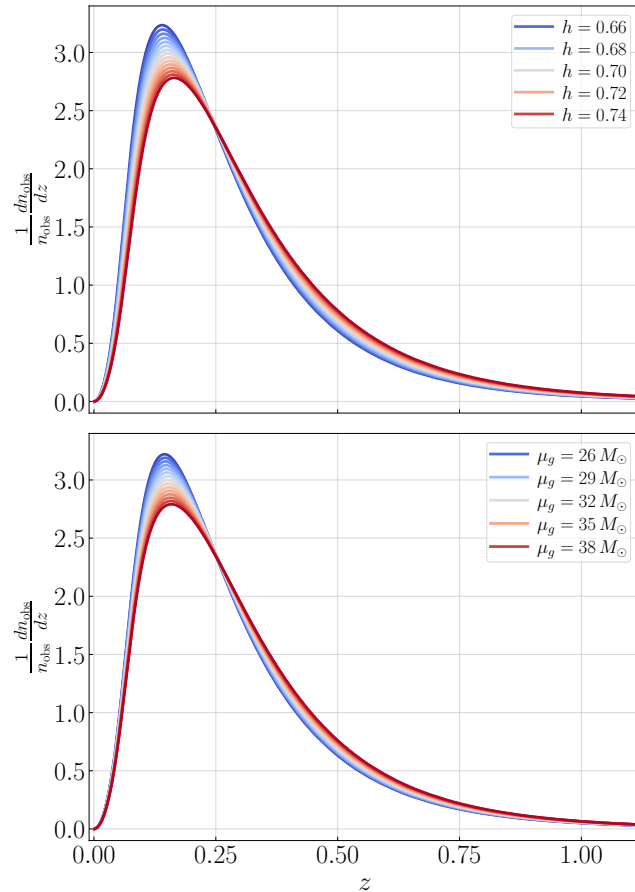


Figure 2.1: Top: expected number of detection as a function of the redshift z at different values of $h \equiv H_0/(100 \text{ km/s/Mpc})$. From GW events, we can construct such an distribution as a function of D_L first and then convert it to a function of z based on assumed cosmological parameters. Meanwhile, our astrophysical knowledge allows us to construct an expected distribution as a function of z from, e.g., galaxy catalogs. By comparing the two histograms, we can then constrain the value of cosmological parameters. Bottom: the distribution is also affected by astrophysical models (e.g., the location of a peak in the BBH's mass distribution μ_g ; see Sec. 2.3) which could mimic the effect of changing cosmological model. This indicates the significance of jointly analyzing astrophysical and cosmological parameters.

and merger rate function, and we set requirements on the accuracy of the population in order for the bias to be below the statistical error. Lastly, we conclude and discuss in Sec. 2.6.

2.2 Basic framework

We demonstrate in this work that in essence, the statistical dark siren approach corresponds to a comparison between a measured distribution of GW events and the

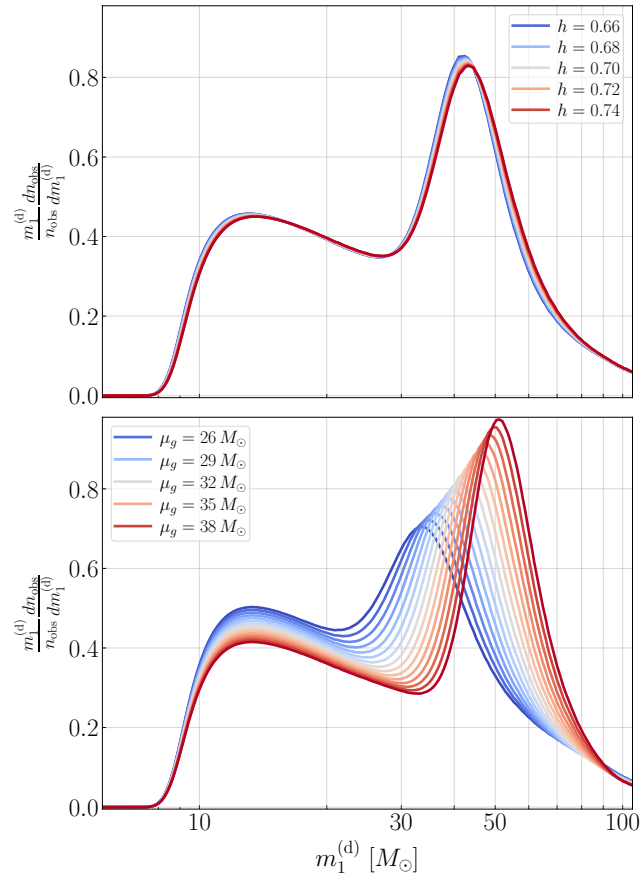


Figure 2.2: Similar to Fig. 2.1 but now we plot the distribution as a function of the detector-frame mass of the primary BH, $m_1^{(d)}$. Combining it with Fig. 2.1 can thus be used to break the degeneracy between astrophysical and cosmological parameters.

one we construct based on our knowledge (or assumption) of the cosmology and the astrophysical source population.

Examples are illustrated in Figs. 2.1 and 2.2. Here the y-axis is the normalized detection probability density of GW events (the parameters are consistent with those inferred from GWTC-3; Sec. 2.4). The x-axis can be the redshift z or the mass of the primary (either the detector-frame one $m_1^{(d)}$ or the source-frame one m_1). While for illustration purpose we focus on marginalized one-dimensional distributions, the analysis in this section can be straightforwardly extended to high-dimensional distributions as well.

Without loss of generality, we can construct a histogram of observed BBHs events with respect to a general coordinate x (which can be the redshift z , the mass of the primary black hole m_1 , or other quantities). The expected number of observations in the i 'th bin at $[x_i, x_i + \Delta x)$ can be written as $r_i(\theta^C, \theta^A)\Delta x$, where r is the event

density. We use $\boldsymbol{\theta}^C = (H_0, \Omega_m, \dots)$ to denote the cosmological parameters and $\boldsymbol{\theta}^A$ the other astrophysical parameters. The number of observations in the i 'th bin, n_i , follows a Poisson distribution ¹

$$p [n_i | r_i(\boldsymbol{\theta}^C, \boldsymbol{\theta}^A)] = \frac{(r_i \Delta x)^{n_i} \exp(-r_i \Delta x)}{n_i!}. \quad (2.1)$$

The Fisher information of $\boldsymbol{\theta} = (\boldsymbol{\theta}^C, \boldsymbol{\theta}^A)$ at a given bin i is given by

$$\begin{aligned} I_{i,ab} &= \sum_{n_i=0}^{\infty} p[n_i | r_i(\boldsymbol{\theta})] \left[\frac{\partial \log p(n_i | r_i)}{\partial r_i} \right]^2 \left[\frac{\partial r_i(\boldsymbol{\theta})}{\partial \theta_a} \right] \left[\frac{\partial r_i(\boldsymbol{\theta})}{\partial \theta_b} \right], \\ &= \left[\frac{\partial r_i(\boldsymbol{\theta})}{\partial \theta_a} \right] \left[\frac{\partial r_i(\boldsymbol{\theta})}{\partial \theta_b} \right] \sum_{n_i=0}^{\infty} p[n_i | r_i(\boldsymbol{\theta})] \left[\frac{\partial \log p(n_i | r_i)}{\partial r_i} \right]^2, \\ &= \frac{\Delta x}{r_i} \left[\frac{\partial r_i(\boldsymbol{\theta})}{\partial \theta_a} \right] \left[\frac{\partial r_i(\boldsymbol{\theta})}{\partial \theta_b} \right], \\ &= r_i \left[\frac{\partial \log r_i(\boldsymbol{\theta})}{\partial \theta_a} \right] \left[\frac{\partial \log r_i(\boldsymbol{\theta})}{\partial \theta_b} \right] \Delta x, \end{aligned} \quad (2.2)$$

where we have used the subscripts a, b to denote the (a, b) 'th element in the Fisher information matrix and the derivatives are evaluated at the true values of $\boldsymbol{\theta}$ (or in practice, our best estimation of $\boldsymbol{\theta}$). Summing over all the bins and convert the discrete sum into an integral over dx , we thus arrive at the Fisher information matrix

$$I_{ab}(\boldsymbol{\theta}) = \int r(x|\boldsymbol{\theta}) \left[\frac{\partial \log r(x|\boldsymbol{\theta})}{\partial \theta_a} \right] \left[\frac{\partial \log r(x|\boldsymbol{\theta})}{\partial \theta_b} \right] dx. \quad (2.3)$$

From the distribution, the covariance matrix of $\boldsymbol{\theta}$, $\text{Cov}(\boldsymbol{\theta})$, can be estimated by the Cramér-Rao bound as

$$\text{Cov}(\boldsymbol{\theta}) = [\mathbf{I}(\boldsymbol{\theta})]^{-1}. \quad (2.4)$$

For future convenience, we also define \mathbf{I}^C where the differentiation in Eq. (2.3) is done only with respect to $\boldsymbol{\theta}^C$, or $\theta_{a,b} \in \{\boldsymbol{\theta}^C\}$. Effectively, \mathbf{I}^C corresponds to the case where we have perfect knowledge on the astrophysical event rate, while \mathbf{I} considers further the covariance between astrophysical population models and cosmological parameters.

¹Here for simplicity, we ignore the inference uncertainty of each individual event's parameters (e.g., redshift and mass, etc.). As we will see in later sections, the results we obtain under this simplification is decently accurate. The uncertainty on individual event's parameters smears out fine details but keeps the broad, coarse-grained features in the population distribution. Current analysis focuses on the coarse-grained part (see, e.g., [41]), though for high-precision cosmology, it would be critical to also capture substructures in the model (see later in Sec. 2.5). A more general treatment incorporating the uncertainty (and potentially systematic bias) on individual events is deferred to a future study.

Note that in the analysis above, we have assumed that the astrophysical model has the correct functional form and only has unknown parameter values. It might also be possible that the astrophysical model is formally inaccurate (e.g., due to substructures in the model and/or evolution in the population). In this case, the estimation of cosmological parameters can be systematically biased.

To calculate the bias, we suppose the true rate (denoted by a superscript ‘‘ t ’’) in the i 'th bin can be written as

$$r_i^t = r_i(\theta^C, \theta^A) + \Delta r_i. \quad (2.5)$$

We can expand the log-likelihood around the true θ^C and $\Delta r_i = 0$ (the expansion around θ^A can be straightforwardly included; yet the covariance between θ^A and θ^C has been accounted for the Fisher matrix in Eq. (2.3) and therefore we ignore it here),

$$\begin{aligned} \Delta \log p &= \frac{\partial^2 \log p}{\partial \theta_a^C \partial \theta_b^C} \Delta \theta_a^C \Delta \theta_b^C + \frac{\partial^2 \log p}{\partial \theta_a^C \partial r_i^t} \Delta \theta_a^C \Delta r_i \\ &+ \frac{\partial^2 \log p}{\partial (r_i^t)^2} \Delta r_i^2, \end{aligned} \quad (2.6)$$

where the first derivative vanishes because at true values the probability is maximized.

The bias in the cosmological parameter induced by Δr_i is then given by setting

$$0 = \frac{\Delta \log p}{\Delta \theta_a^C}, \quad (2.7)$$

or

$$\frac{\partial^2 \log p}{\partial \theta_a^C \partial \theta_b^C} \Delta \theta_b^C = - \frac{\partial^2 \log p}{\partial \theta_a^C \partial r_i^t} \Delta r_i. \quad (2.8)$$

Computing the expectation with respect to n_i at each bin and then summing over bins, we arrive at

$$\begin{aligned} &\Delta \theta_b^C \sum_i \sum_{n_i} p(n_i | \theta) \frac{\partial^2 \log p}{\partial \theta_a^C \partial \theta_b^C} \\ &= - \sum_i \Delta r_i \sum_{n_i} p(n_i | \theta) \frac{\partial^2 \log p}{\partial \theta_a^C \partial r_i^t}. \end{aligned} \quad (2.9)$$

If we further notice

$$\sum_{n_i} p(n_i | \theta) \frac{\partial^2 \log p}{\partial \theta_a \partial \theta_b} = - \sum_{n_i} p(n_i | \theta) \frac{\partial \log p}{\partial \theta_a} \frac{\partial \log p}{\partial \theta_b}, \quad (2.10)$$

we arrive at

$$\Delta\theta^C = - [\mathbf{I}^C]^{-1} \int \left[\frac{\partial \log r(x|\theta)}{\partial \theta^C} \right] \Delta r(x) dx. \quad (2.11)$$

We can thus use Eq. (2.11) to study how an error in the astrophysical rate model, $\Delta r(x)$, propagates to the cosmological parameters, θ^C . Note that while we focus on $\Delta\theta^C$ in this study, our framework can also be straightforwardly extended to study the bias on astrophysical parameters.

2.3 Combined astrophysical and cosmological model

In this section, we derive the expected event rate $r(m_1, m_2, z|\theta)$ which can then be used to construct the Fisher information [Eq. (2.3)] and/or estimate the bias on θ^C [Eq. (2.11)].

Suppose the intrinsic distribution of GW events is [46, 41]

$$\frac{dn}{dm_1 dm_2 dz}(m_1, m_2, z|\theta) = R p(m_1, m_2, z|\theta), \quad (2.12)$$

where R is total number of BBHs and we normalize the probabilities such that

$$\int dm_1 dm_2 dz p(m_1, m_2, z|\theta) = 1. \quad (2.13)$$

The expectation of the observed event density is

$$\begin{aligned} r(m_1, m_2, z|\theta) &= \frac{dn_{obs}}{dm_1 dm_2 dz}(m_1, m_2, z|\theta) \\ &= R P_{det}[m_1, m_2, D_L(z|\theta^C)] p(m_1, m_2, z|\theta), \end{aligned} \quad (2.14)$$

where D_L is the luminosity distance and $P_{det} \in [0, 1]$ is the fraction of GW events with (m_1, m_2, z) that are detectable.

The above expression is generic. To proceed, we further make simplifying assumptions following Fishbach, Holz, and Farr [46] and consistent with LIGO Scientific Collaboration et al. [41]. In particular, we assume

$$p(m_1, m_2, z|\theta) = p(m_1, m_2|\theta^A) p(z|\theta^A, \theta^C), \quad (2.15)$$

where $p(m_1, m_2|\theta^A)$ describes the mass distribution and we assume that it is independent of the redshift. The redshift distribution is then captured by $p(z|\theta^A, \theta^C)$. We separately normalize the two distributions as $\int p(m_1, m_2|\theta^A) dm_1 dm_2 = 1$ and $\int p(z|\theta^A, \theta^C) dz = 1$.

For the rest of our study, we will focus on the case where $p(m_1, m_2|\theta^A)$ is described by the Power Law + Peak model [48, 49] and we use the same notation as used in LIGO Scientific Collaboration et al. [41]. In this case, the distribution of the mass of the primary BH, m_1 , (with $m_1 \geq m_2$) contains two components: a truncated power-law component defined between (M_{\min}, M_{\max}) with $p(m_1) \propto m_1^{-\alpha}$, and a Gaussian peak centered at μ_g and with a width of σ_g . The overall height of the Gaussian peak is governed by a parameter λ_g . For a given m_1 , the secondary mass then follows a truncated power-law between (M_{\min}, m_1) with a slope $p(m_2) \propto m_2^\beta$. Additionally, we smooth the lower end of both m_1 and m_2 with a sigmoid function defined in eq. (B7) in LIGO Scientific Collaboration, Virgo Collaboration, and al. [47] and with a parameter δ_m .

For the redshift model, we further write

$$p(z|\theta^A, \theta^C) \propto \frac{dV_c}{dz} (z|\theta^C) \frac{\psi(z|\theta^A)}{1+z}, \quad (2.16)$$

where $V_c(z|\theta^C)$ is the comoving volume and the $1/(1+z)$ term converts from detector-frame to source-frame time. A general parameterization of the $\psi(z)$ piece can be written as [50]

$$\psi(z) = \left[1 + (1+z_p)^{-\gamma-k}\right] \frac{(1+z)^\gamma}{1 + [(1+z)/(1+z_p)]^{\gamma+k}}, \quad (2.17)$$

where γ and k respectively describe the low- and high-redshift power-law slopes and z_p corresponds to a peak in $\psi(z)$. For GWTC-3 where most events are detected at low redshifts, $\psi(z)$ simplifies to (see, e.g., [46])

$$\psi(z) = (1+z)^\gamma. \quad (2.18)$$

We will adopt Eq. (2.18) for our analysis and drop (z_p, k) .

Under the model described above, there are 9 astrophysical parameters $\theta^A = (M_{\min}, M_{\max}, \delta_m, \alpha, \beta, \lambda_g, \mu_g, \sigma_g, \gamma)^\top$. For the cosmological part, we assumed a flat universe described by $\theta^C = (H_0, \Omega_m)^\top$ with H_0 the Hubble constant and Ω_m the mass density normalized by the critical density. For future convenience, we will define $h = H_0/(100 \text{ km s}^{-1} \text{ Mpc}^{-1})$.

To estimate P_{det} , we follow Fishbach, Holz, and Farr [46] and approximate the observed signal-to-noise ratio (SNR) of an event as

$$\rho[m_1, m_2, D_L(z|\theta^C)] = \rho_0 \Theta, \quad (2.19)$$

Table 2.1: Values of (θ^A, θ^C) used in our study to construct the Fisher information matrix (Eq. (2.3)) and estimate the bias due to Δr (Eq. (2.11)).

M_{min}	M_{max}	δ_m	α	β	λ_g	μ_g	σ_g	γ	h	Ω_m
$6.5 M_\odot$	$112.5 M_\odot$	$2.5 M_\odot$	3.78	-0.81	0.03	$32.27 M_\odot$	$3.88 M_\odot$	4.59	0.7	0.3

where ρ_0 is a characteristic SNR of the source and Θ accounts for the change in the SNR due to angular projection, with

$$\log \Theta \sim \mathcal{N}\left(0, \sigma_{\log \Theta}^2\right), \quad (2.20)$$

$$\sigma_{\log \Theta}^2 = \frac{\sigma_{\log \Theta, 0}^2}{1 + \rho_0 / \rho_{th}}, \quad (2.21)$$

where $\sigma_{\log \Theta, 0}^2$ and ρ_{th} are further parameters controlling the shape of Θ .

Suppose sources with $\rho > \rho_{th}$ are detectable, we have

$$\begin{aligned} P_{det} &= \int_{\log \Theta_{th}}^{\infty} p(\log \Theta) d \log \Theta \\ &= \frac{1}{2} \text{Erfc} \left(\frac{\log \Theta_{th}}{\sqrt{2} \sigma_{\log \Theta}} \right), \end{aligned} \quad (2.22)$$

where $\Theta_{th} = \rho_{th} / \rho_0$ and Erfc is the complementary error function.

2.4 Applications to GWTC-3

In this section, we apply our method to GWTC-3 [28] and estimate the uncertainties on (θ^A, θ^C) when jointly fitting the astrophysical population distribution and cosmology together. Despite the simplicity of our method, it successfully captures many qualitative features and gives accurate predictions on different parameters' uncertainties as reported in LIGO Scientific Collaboration et al. [41]. Further validation of our method can be found in Appx. 2.7 where we also apply our method to reproduce results in [46, 39].

Note that to evaluate the Fisher information matrix (Eq. (2.3)), we need to take derivatives around the ‘‘true’’ model parameters. These values are mostly approximated by the ones inferred in LIGO Scientific Collaboration et al. [41] and we summarize them in Table 2.1. Figs. 2.1 and 2.2 are also generated with the same set of parameters (except for the one listed in the legend). Note that we slightly modified the values of $M_{min} = 6.5 M_\odot$ and $\delta_m = 2.5 M_\odot$ to make our Fig. 2.2 more similar

to fig. 1 in LIGO Scientific Collaboration et al. [41].² The overall scale R is set so that the total number of BBH detection is $n_{obs} = \int r(m_1, m_2, z|\theta) dm_1 dm_2 dz = 40$, consistent with the number of BBH events used in [41].

To approximate P_{det} , we compute the characteristic ρ_0 using a single detector with LIGO Hanford's sensitivity in the third observing run [51] for each $[m_1, m_2, D_L(z|\theta^C)]$. The waveform is generated with the IMRPhenomD approximation ([52]; the waveform is computed using PYCBC [53]) and the source is placed at an effective distance of $2.3D_L$ [54]. We further use $\rho_{th} = 8$ and $\sigma_{\log \Theta, 0}^2 = 0.25$ when computing Eq. (2.22).

Using redshift distribution while holding population model fixed

Firstly, we consider the case where we constrain the cosmological parameters using the redshift distribution of BBH events while treating the underlying astrophysical population as known and fixed. An astrophysical expectation can be constructed using the coarse-grained distribution of galaxies. Indeed, when each BBH event is localized with limited accuracy and thousands of galaxies or more lie within the uncertainty volume, a galaxy catalog mainly serves as an estimation of the overall, smoothed shape of $\psi(z)$, which we model as a simple power law as in Eq. (2.18). In this case, cosmological parameters are constrained by requesting consistency between the distribution of observed BBH events and our astrophysical expectation, as demonstrated in the upper panel of Fig. 2.1. (We will return to this later in Sec. 2.6 to discuss how an improved localization accuracy together with a complete galaxy catalog could help.)

In Fig. 2.3, we present the constraints on (h, Ω_m) from the marginalized redshift distribution $r(z|\theta) = \int r(m_1, m_2, z|\theta) dm_1 dm_2$ (cf. Fig. 2.1). The result is obtained by inverting a 3×3 Fisher matrix involving (h, Ω_m, R) and treating θ^A as known (Eq. (2.3) with x replaced by z). Our approach predicts an uncertainty in h to be 0.11, nicely agreeing with the results shown in Fig. 9 in LIGO Scientific Collaboration et al. [41]. Ω_m , on the other hand, is not well constrained (in fact, its error is greater than its true value and thus it exceeds the capability of Fisher matrix) because of both the relatively small sample size ($n_{obs} = 40$) and the fact that most events are detected at low redshift with $z < 0.5$.

²There are likely two peaks in the mass distribution as suggested in LIGO Scientific Collaboration, Virgo Collaboration, and al. [47] and the lower one (around $m_1 = 10 M_\odot$) is not captured by the Power Law + Peak model adopted by LIGO Scientific Collaboration et al. [41].

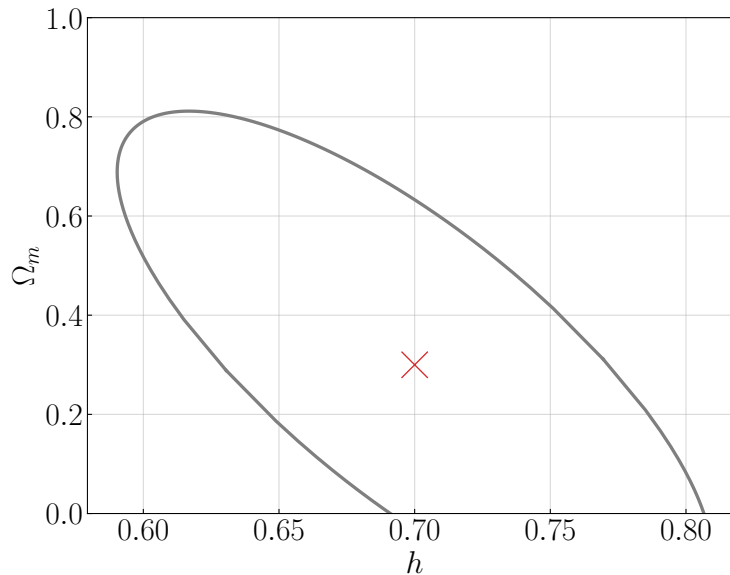


Figure 2.3: Uncertainties on cosmological parameters (h , Ω_m) from the redshift histogram (cf. Fig. 2.1) assuming we know exactly the astrophysical model. Throughout this work, we will use red crosses to denote the true values of the parameters (i.e., values at which we evaluate the Fisher information matrix). The error ellipses indicate the 68% credible intervals. We predict an uncertainty on h of ± 0.11 , which agrees well with the gray-dotted curve in fig. 9 in LIGO Scientific Collaboration et al. [41] obtained under the same assumptions.

However, as pointed out in, e.g., Mastrogiovanni et al. [40] and LIGO Scientific Collaboration et al. [41], and illustrated in Fig. 2.1, the constraints on the cosmological parameters rely critically on the assumptions of the astrophysical model. We elaborate on this point further in Fig. 2.4 in the cyan error ellipses. We obtained these ellipses by inverting a 3×3 Fisher matrix involving (h, μ_g, R) in the top panel and one involving (h, γ, R) in the bottom panel. We notice strong anti-correlations between h and μ_g and between h and γ , consistent with the results shown in LIGO Scientific Collaboration et al. [41]. This demonstrates that with the redshift distribution of BBH events alone, measuring cosmological parameters can be challenging unless we have a highly precise knowledge of the intrinsic population model.

Jointly fitting astrophysical population model and cosmology

Fortunately, besides the redshift distribution itself, we also have information on other properties of BBH events such as the mass distribution. As demonstrated in Fig. 2.2, the partial degeneracy between h and μ_g shown in redshift distribution (Fig. 2.1)

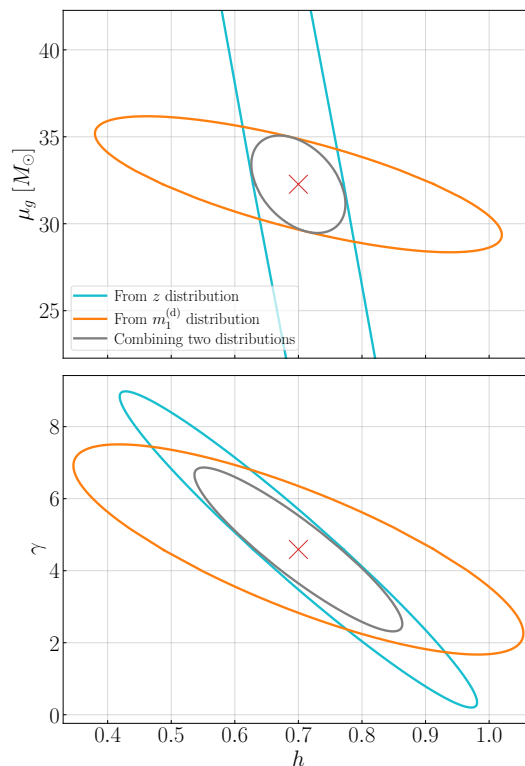


Figure 2.4: Correlation between astrophysical and cosmological parameters by inverting a 3×3 Fisher matrix including (h, μ_g, R) (top panel) or (h, γ, R) (bottom panel). The cyan ellipses correspond to constraints from the redshift distribution alone (cf. Fig. 2.1). As μ_g and/or γ decreases, h will increase to a greater value. It captures the key features shown in Fig. 10 in [41]. If one further incorporates the information from the mass distribution (orange ellipses; cf. Fig. 2.2), the combined uncertainties can be reduced to the gray ellipses.

can be largely broken once we include the distribution of the detector-frame mass distribution of the primary, $r[m_1^{(d)}|\boldsymbol{\theta}] = \int [r(m_1, m_2, z)/(1+z)] dm_2 dz$.

Similar to how we obtain the cyan ellipses in Fig. 2.4, we also construct Fisher matrices for (h, μ_g, R) in the top panel (or (h, γ, R) in the bottom panel) from the $m_1^{(d)}$ distribution. The results are shown in the orange ellipses. Since distributions of both z and $m_1^{(d)}$ are available in a GW catalog, we can combine them together, leading to the gray ellipses in Fig. 2.4. This allows us to individually constrain h and μ_g to good accuracy (assuming other parameters in $\boldsymbol{\theta}$ are known), and the covariance between h and γ can also be significantly reduced.

Combining the Fisher information from the redshift and mass distributions together is largely similar to the hierarchical inference performed in LIGO Scientific Collaboration et al. [41]. To illustrate this point, we now invert the full Fisher matrix

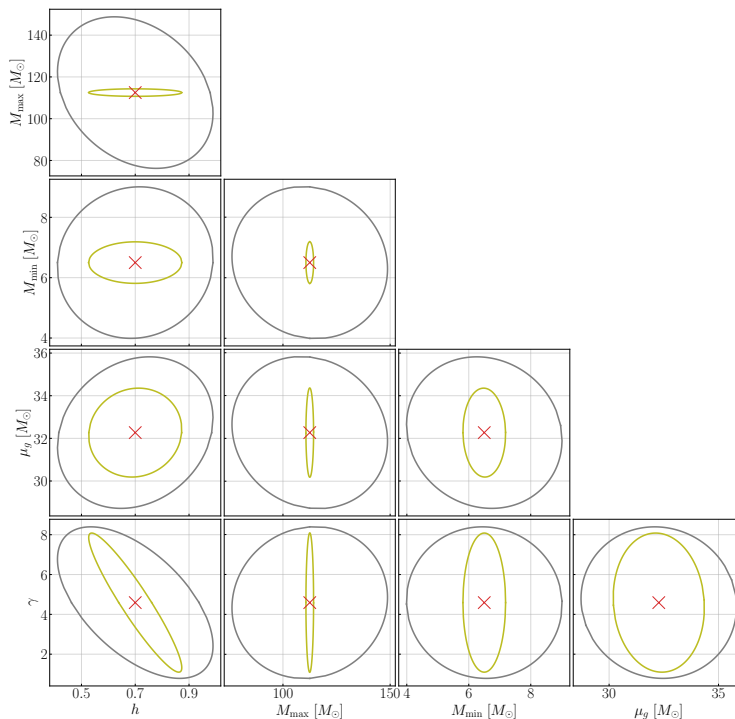


Figure 2.5: Error ellipses for a sample of 40 BBH events similar to the GWTC3 catalog. The gray ellipses are obtained by summing the Fisher information from the marginalized redshift and primary mass distribution together, and the olive ones are from the 3D $r(m_1, m_2, z)$ distribution.

(note that in Fig. 2.4 we considered only submatrices) and the results are shown in Fig. 2.5. More specifically, we construct two Fisher matrices using Eq. (2.3) with x respectively substituted by z and $m_1^{(d)}$. The two matrices are summed together and then inverted to give us the gray error ellipses.

Overall, our result shows nice agreement with the one reported in LIGO Scientific Collaboration et al. [41]. In particular, the 68% credible interval for h is $h = 0.70 \pm 0.29$ and it exhibits a strong anti-correlation with γ and M_{max} whose uncertainties are also consistent with fig. 5 in LIGO Scientific Collaboration et al. [41]. Because we used a simple approximation of P_{det} [Eqs. (2.19)-(2.22)] and we ignored the statistical error on each individual event, we do not expect an exact reproduction of the results in LIGO Scientific Collaboration et al. [41]. Due to our simplifying treatments, μ_g is better constrained than in LIGO Scientific Collaboration et al. [41] and its correlation with h as well as with other parameters is lifted (see also Fig. 2.4 and note the gray error ellipse in the upper panel is much smaller than the one in the bottom panel).

In fact, we can directly construct a Fisher matrix from a 3-dimensional (3D) distribution $r(m_1, m_2, z|\theta)$. This leads to the olive ellipses in Fig. 2.5. This contains more information and thus leads to tighter constraints on parameters compared to combining two marginalized distributions (gray ellipses). For GWTC-3 with only slightly more than 40 BBH events, however, we do not have a high ‘‘SNR’’ in the 3D histogram $r(m_1, m_2, z|\theta)$.³ Therefore, summing marginalized distribution in z and in $m_1^{(d)}$ (gray ellipses) provides a better agreement of GWTC-3 results [41] than the 3D distribution (olive ellipses). Nonetheless, as the sample size increases, we would expect that the 3D distribution becomes a more accurate prediction (which we validate in Appendix 2.7 by reproducing the results in [46, 39]). Therefore, in addition to the $1/\sqrt{n_{obs}}$ reduction in the uncertainties (as obviously seen in Eqs. (2.3) and (2.14)), we would expect the results reported in LIGO Scientific Collaboration et al. [41] to improve further from the gray ellipses to the olive ones as the SNR of each bin in the 3D distribution increases (with the expectation of the bin becomes greater than its Poissonian error; see Footnote 3). This can be especially valuable for constraining M_{max} as changing it can significantly alter P_{det} at large redshift, a point we will illustrate further when discussing the bias on cosmological parameters.

2.5 Bias induced by substructures in the population model

Having discussed in the previous section the parameter estimation uncertainties when jointly fitting the cosmological and astrophysical models, we now consider the bias in the cosmological parameters (especially H_0) induced by inaccuracies in our astrophysical model, which is naturally expected if our parameterized model is insufficient to capture all the details in the true population model. Indeed, we note that the specific functional form assumed in our study (the Power Law+ Peak model) is not significantly preferred over, e.g., a Broken Power Law model [41]. More possibilities with different parametrizations are also considered in, e.g., LIGO Scientific Collaboration, Virgo Collaboration, and al. [47] and Roulet et al. [55]. Furthermore, the mass distribution could contain more complicated features [56] and/or be redshift dependent [57, 58, 59, 60], introducing more features beyond what is captured

³Consider a discrete example. We would need at least 8 different bins to constrain $(M_{min}, M_{max}, \delta_m, \alpha, \lambda_g, \mu_g, \sigma_g)$ in the histogram of m_1 or $m_1^{(d)}$. For the secondary mass m_2 , we would additionally need 2 more bins to determine the power-law slope β . The redshift distribution requires at least 3 bins to constrain (γ, h) . Thus a full 3D histogram would require more than 48 bins. This is greater than the sample size used by LIGO Scientific Collaboration et al. [41]. Nonetheless, there will be enough events to populate the 3D histogram when aLIGO reaches its designed sensitivity and detects $\mathcal{O}(1,000)$ events per year (as assumed in, e.g., [39]).

by the model described in Sec. 2.3. Similarly, an error in the redshift model $\psi(z)$ could also bias the inferred cosmology [61].

Suppose the true event density can be written as

$$r^t(m_1, m_2, z) = RP_{\text{det}} \times [(1 - \Delta r_0)p(m_1, m_2, z|\boldsymbol{\theta}) + \Delta r_0 p_{\text{err}}(m_1, m_2, z)], \quad (2.23)$$

and our parameterized model captures the $r = RP_{\text{det}}p(m_1, m_2, z|\boldsymbol{\theta})$ part. This leads to an error of

$$\Delta r(m_1, m_2, z) = \Delta r_0 [RP_{\text{det}}p_{\text{err}}(m_1, m_2, z) - r(m_1, m_2, z)], \quad (2.24)$$

where p_{err} specifies the shape of the deviation and it is normalized to $\int p_{\text{err}}(m_1, m_2, z) dm_1 dm_2 dz = 1$, and Δr_0 is an overall factor governing the magnitude of the deviation. We note further that the $-r$ term only affects the overall number of GW events when plugged into Eq. (2.11) and therefore can be absorbed by a rescaling of R ; when $\Delta r_0 > 0$, it decreases the value of R . For the rest of the section we will focus on the effect induced by p_{err} .

In particular, we focus on bias induced by unmodeled local substructures. For this, we write

$$p_{\text{err}}(m_1, m_2, z) = p_{\text{err}}(m_1, m_2)p_{\text{err}}(z), \quad (2.25)$$

with

$$p_{\text{err}}(m_1, m_2) \propto \frac{1}{m_1 - M_{\text{min}}} \exp\left[\frac{-(m_1 - \mu_{m,\text{err}})^2}{2\sigma_{m,\text{err}}^2}\right], \quad (2.26)$$

$$p_{\text{err}}(z) \propto \frac{1}{1+z} \frac{dV_c}{dz} \exp\left[\frac{-(z - \mu_{z,\text{err}})^2}{2\sigma_{z,\text{err}}^2}\right], \quad (2.27)$$

where the location of the substructure is governed by $\mu_{m,\text{err}}$ and $\mu_{z,\text{err}}$ and width by $\sigma_{m,\text{err}}$ and $\sigma_{z,\text{err}}$. In our study, we vary $(\mu_{m,\text{err}}, \mu_{z,\text{err}})$ and fix $\sigma_{m,\text{err}} = 1 M_\odot$ and $\sigma_{z,\text{err}} = 0.025$. As a brief aside, we note that the local error considered here can serve as the building block for considering more extended errors, as a generic Δr can be viewed as the superposition of many such local substructures.

To set the overall factor Δr_0 , we request

$$\frac{\Delta r_0 \int P_{\text{det}} p_{\text{err}} dm_1 dm_2 dz}{\int P_{\text{det}} dm_1 dm_2 dz} = 0.01. \quad (2.28)$$

In other words, we assume the unmodeled substructure contains 1% of the BBH events. Note that we choose $\Delta r_0 > 0$ for the simplicity of our discussion, Δr_0 can be either positive (a local peak) or negative (a local trough).

In this section, we follow Fishbach, Holz, and Farr [46] and approximate P_{det} according to the aLIGO design sensitivity. In particular, we approximate the characteristic SNR as

$$\rho_0 = 8 \left[\frac{\mathcal{M}_c(1+z)}{10 M_\odot} \right]^{5/6} \left(\frac{1 \text{ Gpc}}{D_L} \right), \quad (2.29)$$

where $\mathcal{M}_c = m_1^{3/5} m_2^{3/5} / (m_1 + m_2)^{1/5}$ is the chirp mass of the BBH. Following Fishbach, Holz, and Farr [46], we further set $\rho_{th} = 8$ and $\sigma_{\log \Theta, 0}^2 = 0.3$ in Eq. (2.21).

We are now ready to evaluate the bias due to Δr (Eq. (2.24)) on cosmological parameters according to Eq. (2.11). Here we focus on the bias on h and we consider $\theta^C = (h, R)^T$ in Eq. (2.11). The result is shown in Fig. 2.6.

Firstly, we note that the bias is independent of n_{obs} . This is because in Eq. (2.11) we have $[\mathbf{I}^C]^{-1} \propto n_{obs}^{-1}$ whereas $\Delta r \propto n_{obs}$. This is in contrast to the statistical uncertainty discussed in Sec. 2.4 which reduces as $n_{obs}^{-1/2}$. Therefore, while we expect a significant reduction in the statistical uncertainty as current detects become increasingly more sensitive, and as the 3G GW detectors like Cosmic Explorer [19] and Einstein Telescope [17] come online in 2030s, the systematic bias would persist unless we incorporate more sophisticated models. In particular, we would expect to detect 15,000 BBH events every month with 3G detector [62]. This means we would reduce the statistical error on h to sub-percent level within a month of observation according to Fig. 2.5. This is below the bias shown in Fig. 2.6 and therefore the dark siren cosmology would be limited by uncertainties in our astrophysical population model.

We further note that for large $\mu_{m,err}$ and small $\mu_{z,err}$ (the bottom-right part of Fig. 2.6), the bias is nearly a constant. The bias then gradually decreases and then becomes negative as $\mu_{m,err}$ decreases and the $\mu_{z,err}$ increases, or as we go to the top left part of Fig. 2.6. The transition is characterized by the line of $\rho_0 = 8$ (the brown-dotted line in Fig. 2.6), where we have used $m_1 = m_2 = \mu_{m,err}$ to evaluate \mathcal{M}_c and $\mu_{z,err}$ to evaluate D_L in Eq. (2.29).

These features can be understood as the following. Because we assume p_{err} is caused by local substructures and model it as a multivariate Gaussian in m_1 and

z (and uniform in m_2), from Eq. (2.11) the bias is approximately given by⁴

$$\begin{aligned} \Delta h &\propto \frac{\partial \log r(\mu_{m,err}, \mu_{m,err}, \mu_{z,err} | \theta)}{\partial h}, \\ &\sim \frac{\partial \log P_{det}}{\partial h} + \frac{\partial \log (dV_c/dz)}{\partial h}, \end{aligned} \quad (2.30)$$

where in the second line we have selected out the terms that have non vanishing derivatives with respect to h and those values are approximately evaluated at $(m_1, m_2, z) = (\mu_{m,err}, \mu_{m,err}, \mu_{z,err})$.

In the bottom-right part of Fig. 2.6, $P_{det} \simeq 1$. Thus the only contribution to Δh comes from $\partial \log (dV_c/dz) / \partial h = 3/h$, which is a constant. This is why the bias is nearly constant in this region. Physically, the excess events contained in a Δr reduces the smooth component in $(dn_{obs}/dz)/n_{obs}$ so that the curve integrates to 1. According to Fig. 2.1, a decrease in the $(dn_{obs}/dz)/n_{obs}$ curve at small z means h is biased towards a greater value.

As we move towards the top-left part of Fig. 2.6, P_{det} changes from 1 to 0. Numerically, the slope is the steepest when $\Theta_{th} = \rho_{th}/\rho_0$ is around 1. Because changing h changes the value of ρ_0 at a given redshift $\mu_{z,err}$, the $\partial \log P_{det}/\partial h$ term in Eq. (2.30) now starts to contribute. This drives changes the bias Δh to a more negative value. Depending on the location, a local substructure containing 1% of BBH events could bias the estimation of h by about 1% in either the positive or the negative direction. As we mentioned above, the statistical error on h will drop below 1% with about 10^4 events. This is likely beyond aLIGO's expected detection number, yet it can be easily achieved with 3G detectors. Our study thus sets requirements of the accuracy of our astrophysical population model in the 3G era.

2.6 Conclusion and Discussion

In this study, we derived the Cramér-Rao bound of both astrophysical and cosmological parameters from the distributions (both marginalized and high-dimensional) of BBH events. Our approach complements the hierarchical inference currently employed by, e.g., LIGO Scientific Collaboration et al. [41]. Its analytical simplicity makes it especially useful in predicting the performance of future detectors and providing insights in the statistics.

⁴Here we treat $p(z)$ as an un-normalized function and use R to absorb the normalization to simplify the discussion. Note that h and R are not completely degenerate because of P_{det} , and it can be seen from Fig. 2.1. In the real calculation, we include both h and R in θ^C and hence I^C when evaluating Eq. (2.11) to account for the correlation between them arising from this freedom in the definition of $p(z)$ and R .

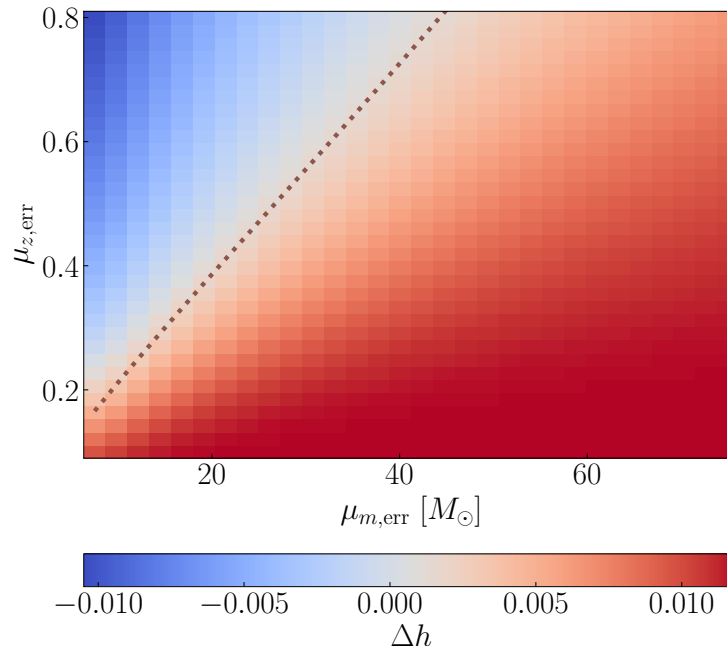


Figure 2.6: Bias on h due to an error in the astrophysical rate Δr given by Eqs. (2.25)-(2.27). An error in m_1 but constant in redshift can then be obtained by summing over all the pixels along a specific $\mu_{m,err}$ (i.e., a vertical line) with appropriate normalization. Likewise, other generic Δr can be obtained by summing over the corresponding pixels. Also shown in the dotted-brown line is an approximation of the detection threshold with $[\mathcal{M}_c(1+z)]^{5/6}/z \simeq \text{constant}$.

The basic framework to both perform joint astrophysical and cosmological parameter estimations and compute bias in parameters due to errors in the assumed model was presented in Sec. 2.2. The specific population model in our analysis was introduced in Sec. 2.3, which we then applied to place constraints on a BBH sample similar to GWTC3 in Sec. 2.4. In particular, we found that the GWTC3 results can be well reproduced if we combine the Fisher information of both the BBHs' redshift distribution and the mass distribution together. In the future, tighter constraints (in addition to the $\sqrt{n_{obs}}$ reduction in the errors) would be expected as more events would allow us to construct an accurate 3D distribution of BBH events in the (m_1, m_2, z) space. Then in Sec. 2.5, we further considered the bias induced by unmodeled substructures in the population model. The bias due to other forms of Δr can be readily obtained by summing over relevant pixels in Fig. 2.6 with proper reweighting. For instance, a substructure in m_1 but constant in z can be obtained by summing along a vertical line in Fig. 2.6. If the error Δr contains 1% of the observed population, it could easily bias the estimation in the Hubble constant by more than

1%. Therefore, to achieve a high-precision cosmology from statistical dark siren, it would require a high level of accuracy in the astrophysical model with fine details captured.

Note further that our Eq. (2.11) applies not only to cosmological parameters but also astrophysical ones as we can simply replace θ^C to θ^A , or any other subset of θ . This could be of astrophysical significance. For example, the location of the mass gap due to pair instability supernovae could be biased by substructures produced by dynamical formation channels or the redshift-dependence in the mass function [57, 63, 60]. Our Eq. (2.11) thus provides a simple and analytical way to quantify the bias.

As a first step, our current model does not include the statistical error on each individual event's component mass and luminosity distance. This may be a subdominant effect for events that are well above the detection threshold, which are typically the ones selected for population studies (see, e.g., [47, 41, 55]). Intuitively, the uncertainty on each event's parameters slightly blurs the measured distribution and smears out sharp features. Yet since both $p(m_1, m_2)$ and $p(z)$ are smooth functions in our study (and in [41]), such a blurring should not be significant(, but see the discussion below on galaxy catalogs). However, information of the population is also contained in sources that are marginally detectable (or undetectable; see the discussion in [64]). These events could happen at locations where P_{det} has large derivatives with respect to θ and thus may potentially contribute to the Fisher information. To utilize them properly, incorporating their parameter estimation errors would be critical, and we plan to investigate this in a follow-up study.

We also assumed the galaxy catalog provides only the smoothed shape of the redshift model $p(z)$. This is the case because the GW event localization accuracy is currently limited. In the other limit where a BBH could be localized to a single host galaxy (which can be achieved with a decihertz space-borne detector; [65]), a dark siren would behave effectively like a bright BNS event with EM counterpart identified, because the host galaxy in this case can be identified from the sky localization [66, 67, 68]. This could lead to a strong constraint in cosmology [13] without needing assumptions in the underlying population model. In the intermediate case, an accurate localization plus a complete galaxy catalog could mean sharp spikes in $p(z)$ and therefore $r(z)$. Whereas h can be nearly degenerate with an overall power-law slope γ in $\psi(z)$ (which is also the limiting factor on how well we can measure h ; Fig. 2.5), it could hardly be confused with sharp spikes. Therefore the constraints on h could

thus be improved. Besides using the location of each individual event, the spatial clustering of BBH events is yet another possibility to enhance our constrain on cosmology and reduce its systematic errors [69, 70, 71, 72]. A more quantitative study incorporating these effects coherently is to be carried out in future investigations.

ACKNOWLEDGMENTS

We thank Katerina Chatziioannou, Hsin-Yu Chen, and the LVC colleagues for helpful discussions and comments during the preparation of the manuscript. This material is based upon work supported by NSF’s LIGO Laboratory which is a major facility fully funded by the National Science Foundation. H.Y. acknowledges the support of the Sherman Fairchild Foundation. Y.C. and B.S. acknowledge support from the Brinson Foundation, the Simons Foundation (Award Number 568762), and by NSF Grants PHY-2011961, PHY-2011968, PHY-1836809.

Software: Python3 [73], NumPy [74], SciPy [75], Matplotlib [76], PYCBC [53].

2.7 Appendix: Validation of the methodology

In this Appendix, we further validate our approach by reproducing some results from [46] and [39].

Following Fishbach, Holz, and Farr [46], here we consider a Truncated Power Law mass model given by

$$p(m_1, m_2 | \alpha, M_{\max}) \propto \frac{m_1^{-\alpha}}{m_1 - 5 M_{\odot}} \mathcal{H}(M_{\max} - m_1), \quad (2.31)$$

where \mathcal{H} is the Heaviside function, and the existence of an upper mass gap M_{\max} is motivated by the pair-instability supernovae [77]. Since our focus here is to reproduce the results of Fishbach, Holz, and Farr [46], we use this mass model despite the fact that it is currently disfavored by the latest data [49, 41, 55]. The $\psi(z)$ part in the redshift model (Eq. 2.16) given by Eq. (2.18). We particularly adopt $(\alpha, M_{\max}, \lambda) = (1, 40 M_{\odot}, 3)$ in our calculation. The P_{det} is computed following Sec. 2.5 (see Eqs. (2.22) and (2.29)).

In Fig. 2.7, we present the 68% credible interval for the key parameters based on the Fisher information matrix, Eq. (2.3), with $n_{\text{obs}} = 500$. In particular, we highlight the bottom-right corner of Fig. 2.7 where we show the error ellipse for (λ, α) . We notice a positive correlation between the two quantities and their uncertainties are, respectively, $\Delta\lambda = 0.68$ and $\Delta\alpha = 0.21$. Both results show nice agreement with the top-left panel in fig. 5 in Fishbach, Holz, and Farr [46]. Moreover, because in

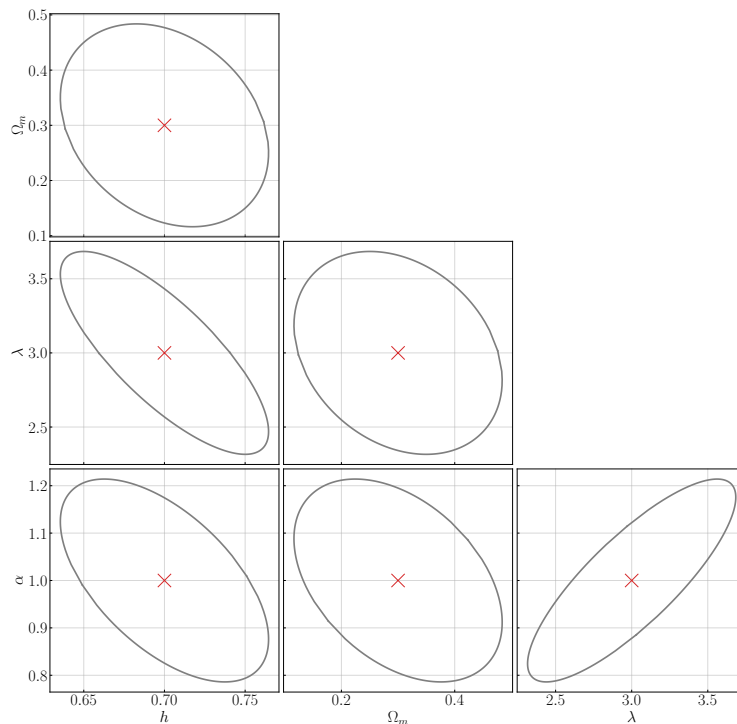


Figure 2.7: Error ellipses from the 3D $r(m_1, m_2, z)$ distribution assuming 500 BBH events using the model in [46]. Our results show good agreement with those obtained in Fishbach, Holz, and Farr [46] and Farr et al. [39]. It thus validates our approach when n_{obs} is large.

the mass model, Eq. (2.31) there is a clear feature set by M_{max} , it thus allows the determination of h as proposed in, e.g., Farr et al. [39] and demonstrated in the left-most column of Fig. 2.7. Consistent with Farr et al. [39], we note the uncertainty on h from 500 events is $\Delta h = 0.065$. The consistency between our Fig. 2.7 and previous studies thus validates our approach in constraining both the astrophysical and cosmological parameters.

References

- [1] A. G. Riess, W. H. Press, and R. P. Kirshner. “A Precise Distance Indicator: Type IA Supernova Multicolor Light-Curve Shapes.” In: *ApJ* 473 (Dec. 1996), p. 88. doi: [10.1086/178129](https://doi.org/10.1086/178129). arXiv: [astro-ph/9604143](https://arxiv.org/abs/astro-ph/9604143) [astro-ph].
- [2] A. G. Riess, S. Casertano, W. Yuan, et al. “Cosmic Distances Calibrated to 1% Precision with Gaia EDR3 Parallaxes and Hubble Space Telescope Photometry of 75 Milky Way Cepheids Confirm Tension with Λ CDM.” In: *ApJ* 908.1, L6 (Feb. 2021), p. L6. doi: [10.3847/2041-8213/abdabf](https://doi.org/10.3847/2041-8213/abdabf). arXiv: [2012.08534](https://arxiv.org/abs/2012.08534) [astro-ph.CO].

- [3] D. N. Spergel, L. Verde, H. V. Peiris, et al. “First-Year Wilkinson Microwave Anisotropy Probe (WMAP) Observations: Determination of Cosmological Parameters.” In: *ApJS* 148.1 (Sept. 2003), pp. 175–194. DOI: [10.1086/377226](https://doi.org/10.1086/377226). arXiv: [astro-ph/0302209](https://arxiv.org/abs/astro-ph/0302209) [[astro-ph](#)].
- [4] Planck Collaboration and et al. “Planck 2013 results. XVI. Cosmological parameters.” In: *A&A* 571, A16 (Nov. 2014), A16. DOI: [10.1051/0004-6361/201321591](https://doi.org/10.1051/0004-6361/201321591). arXiv: [1303.5076](https://arxiv.org/abs/1303.5076) [[astro-ph.CO](#)].
- [5] Planck Collaboration and et al. “Planck 2018 results. VI. Cosmological parameters.” In: *A&A* 641, A6 (Sept. 2020), A6. DOI: [10.1051/0004-6361/201833910](https://doi.org/10.1051/0004-6361/201833910). arXiv: [1807.06209](https://arxiv.org/abs/1807.06209) [[astro-ph.CO](#)].
- [6] L. Verde, T. Treu, and A. G. Riess. “Tensions between the early and late Universe.” In: *Nature Astronomy* 3 (Sept. 2019), pp. 891–895. DOI: [10.1038/s41550-019-0902-0](https://doi.org/10.1038/s41550-019-0902-0). arXiv: [1907.10625](https://arxiv.org/abs/1907.10625) [[astro-ph.CO](#)].
- [7] LIGO Scientific Collaboration. “Advanced LIGO.” In: *Classical and Quantum Gravity* 32.7, 074001 (Apr. 2015), p. 074001. DOI: [10.1088/0264-9381/32/7/074001](https://doi.org/10.1088/0264-9381/32/7/074001). arXiv: [1411.4547](https://arxiv.org/abs/1411.4547) [[gr-qc](#)].
- [8] Virgo Collaboration and et al. “Advanced Virgo: a second-generation interferometric gravitational wave detector.” In: *Classical and Quantum Gravity* 32.2, 024001 (Jan. 2015), p. 024001. DOI: [10.1088/0264-9381/32/2/024001](https://doi.org/10.1088/0264-9381/32/2/024001). arXiv: [1408.3978](https://arxiv.org/abs/1408.3978) [[gr-qc](#)].
- [9] Kagra Collaboration and et al. “KAGRA: 2.5 generation interferometric gravitational wave detector.” In: *Nature Astronomy* 3 (Jan. 2019), pp. 35–40. DOI: [10.1038/s41550-018-0658-y](https://doi.org/10.1038/s41550-018-0658-y). arXiv: [1811.08079](https://arxiv.org/abs/1811.08079) [[gr-qc](#)].
- [10] Kagra Collaboration and et al. “Overview of KAGRA: Detector design and construction history.” In: *Progress of Theoretical and Experimental Physics* 2021.5, 05A101 (May 2021), 05A101. DOI: [10.1093/ptep/ptaa125](https://doi.org/10.1093/ptep/ptaa125). arXiv: [2005.05574](https://arxiv.org/abs/2005.05574) [[physics.ins-det](#)].
- [11] B. F. Schutz. “Determining the Hubble constant from gravitational wave observations.” In: *Nature* 323.6086 (Sept. 1986), pp. 310–311. DOI: [10.1038/323310a0](https://doi.org/10.1038/323310a0).
- [12] D. E. Holz and S. A. Hughes. “Using Gravitational-Wave Standard Sirens.” In: *ApJ* 629.1 (Aug. 2005), pp. 15–22. DOI: [10.1086/431341](https://doi.org/10.1086/431341). arXiv: [astro-ph/0504616](https://arxiv.org/abs/astro-ph/0504616) [[astro-ph](#)].
- [13] X. Chen and W.-B. Han. “Extreme-mass-ratio inspirals produced by tidal capture of binary black holes.” In: *Communications Physics* 1.1, 53 (Sept. 2018), p. 53. DOI: [10.1038/s42005-018-0053-0](https://doi.org/10.1038/s42005-018-0053-0). arXiv: [1801.05780](https://arxiv.org/abs/1801.05780) [[astro-ph.HE](#)].
- [14] B. P. Abbott, R. Abbott, T. D. Abbott, et al. “Multi-messenger Observations of a Binary Neutron Star Merger.” In: *ApJ* 848.2, L12 (Oct. 2017), p. L12. DOI: [10.3847/2041-8213/aa91c9](https://doi.org/10.3847/2041-8213/aa91c9). arXiv: [1710.05833](https://arxiv.org/abs/1710.05833) [[astro-ph.HE](#)].

- [15] B. P. Abbott, R. Abbott, T. D. Abbott, et al. “A gravitational-wave standard siren measurement of the Hubble constant.” In: *Nature* 551.7678 (Nov. 2017), pp. 85–88. doi: [10.1038/nature24471](https://doi.org/10.1038/nature24471). arXiv: [1710.05835](https://arxiv.org/abs/1710.05835) [[astro-ph.CO](#)].
- [16] R. X. Adhikari, K. Arai, A. F. Brooks, et al. “A cryogenic silicon interferometer for gravitational-wave detection.” In: *Classical and Quantum Gravity* 37.16, 165003 (Aug. 2020), p. 165003. doi: [10.1088/1361-6382/ab9143](https://doi.org/10.1088/1361-6382/ab9143). arXiv: [2001.11173](https://arxiv.org/abs/2001.11173) [[astro-ph.IM](#)].
- [17] B. Sathyaprakash, M. Abernathy, F. Acernese, et al. “Scientific Potential of Einstein Telescope.” In: *arXiv e-prints*, arXiv:1108.1423 (Aug. 2011), arXiv:1108.1423. arXiv: [1108.1423](https://arxiv.org/abs/1108.1423) [[gr-qc](#)].
- [18] B. P. Abbott, R. Abbott, T. D. Abbott, et al. “Exploring the sensitivity of next generation gravitational wave detectors.” In: *Classical and Quantum Gravity* 34.4, 044001 (Feb. 2017), p. 044001. doi: [10.1088/1361-6382/aa51f4](https://doi.org/10.1088/1361-6382/aa51f4). arXiv: [1607.08697](https://arxiv.org/abs/1607.08697) [[astro-ph.IM](#)].
- [19] D. Reitze, R. X. Adhikari, S. Ballmer, et al. “Cosmic Explorer: The U.S. Contribution to Gravitational-Wave Astronomy beyond LIGO.” In: *Bulletin of the American Astronomical Society*. Vol. 51. Sept. 2019, 35, p. 35. arXiv: [1907.04833](https://arxiv.org/abs/1907.04833) [[astro-ph.IM](#)].
- [20] M. Evans, R. X. Adhikari, C. Afle, et al. “A Horizon Study for Cosmic Explorer: Science, Observatories, and Community.” In: *arXiv e-prints*, arXiv:2109.09882 (Sept. 2021), arXiv:2109.09882. arXiv: [2109.09882](https://arxiv.org/abs/2109.09882) [[astro-ph.IM](#)].
- [21] H.-Y. Chen, P. S. Cowperthwaite, B. D. Metzger, et al. “A Program for Multimessenger Standard Siren Cosmology in the Era of LIGO A+, Rubin Observatory, and Beyond.” In: *ApJ* 908.1, L4 (Feb. 2021), p. L4. doi: [10.3847/2041-8213/abdab0](https://doi.org/10.3847/2041-8213/abdab0). arXiv: [2011.01211](https://arxiv.org/abs/2011.01211) [[astro-ph.CO](#)].
- [22] M. Califano, I. de Martino, D. Vernieri, et al. “Constraining Λ CDM cosmological parameters with Einstein Telescope mock data.” In: *arXiv e-prints*, arXiv:2205.11221 (May 2022), arXiv:2205.11221. arXiv: [2205.11221](https://arxiv.org/abs/2205.11221) [[astro-ph.CO](#)].
- [23] C. Messenger and J. Read. “Measuring a Cosmological Distance-Redshift Relationship Using Only Gravitational Wave Observations of Binary Neutron Star Coalescences.” In: *Phys. Rev. Lett.* 108.9, 091101 (Mar. 2012), p. 091101. doi: [10.1103/PhysRevLett.108.091101](https://doi.org/10.1103/PhysRevLett.108.091101). arXiv: [1107.5725](https://arxiv.org/abs/1107.5725) [[gr-qc](#)].
- [24] LIGO Scientific Collaboration, Virgo Collaboration, and et al. “Binary Black Hole Mergers in the First Advanced LIGO Observing Run.” In: *Physical Review X* 6.4, 041015 (Oct. 2016), p. 041015. doi: [10.1103/PhysRevX.6.041015](https://doi.org/10.1103/PhysRevX.6.041015). arXiv: [1606.04856](https://arxiv.org/abs/1606.04856) [[gr-qc](#)].

- [25] LIGO Scientific Collaboration, Virgo Collaboration, and et al. “GWTC-1: A Gravitational-Wave Transient Catalog of Compact Binary Mergers Observed by LIGO and Virgo during the First and Second Observing Runs.” In: *Physical Review X* 9.3, 031040 (July 2019), p. 031040. DOI: [10.1103/PhysRevX.9.031040](https://doi.org/10.1103/PhysRevX.9.031040). arXiv: [1811.12907](https://arxiv.org/abs/1811.12907) [[astro-ph.HE](#)].
- [26] LIGO Scientific Collaboration, Virgo Collaboration, and et al. “GWTC-2: Compact Binary Coalescences Observed by LIGO and Virgo during the First Half of the Third Observing Run.” In: *Physical Review X* 11.2, 021053 (Apr. 2021), p. 021053. DOI: [10.1103/PhysRevX.11.021053](https://doi.org/10.1103/PhysRevX.11.021053). arXiv: [2010.14527](https://arxiv.org/abs/2010.14527) [[gr-qc](#)].
- [27] LIGO Scientific Collaboration, Virgo Collaboration, and et al. “GWTC-2.1: Deep Extended Catalog of Compact Binary Coalescences Observed by LIGO and Virgo During the First Half of the Third Observing Run.” In: *arXiv e-prints*, arXiv:2108.01045 (Aug. 2021), arXiv:2108.01045. arXiv: [2108.01045](https://arxiv.org/abs/2108.01045) [[gr-qc](#)].
- [28] LIGO Scientific Collaboration, Virgo Collaboration, KAGRA Collaboration, et al. “GWTC-3: Compact Binary Coalescences Observed by LIGO and Virgo During the Second Part of the Third Observing Run.” In: *arXiv e-prints*, arXiv:2111.03606 (Nov. 2021), arXiv:2111.03606. arXiv: [2111.03606](https://arxiv.org/abs/2111.03606) [[gr-qc](#)].
- [29] A. H. Nitz, C. Capano, A. B. Nielsen, et al. “1-OGC: The First Open Gravitational-wave Catalog of Binary Mergers from Analysis of Public Advanced LIGO Data.” In: *ApJ* 872.2, 195 (Feb. 2019), p. 195. DOI: [10.3847/1538-4357/ab0108](https://doi.org/10.3847/1538-4357/ab0108). arXiv: [1811.01921](https://arxiv.org/abs/1811.01921) [[gr-qc](#)].
- [30] A. H. Nitz, T. Dent, G. S. Davies, et al. “2-OGC: Open Gravitational-wave Catalog of Binary Mergers from Analysis of Public Advanced LIGO and Virgo Data.” In: *ApJ* 891.2, 123 (Mar. 2020), p. 123. DOI: [10.3847/1538-4357/ab733f](https://doi.org/10.3847/1538-4357/ab733f). arXiv: [1910.05331](https://arxiv.org/abs/1910.05331) [[astro-ph.HE](#)].
- [31] R. Gray et al. “Cosmological inference using gravitational wave standard sirens: A mock data analysis.” In: *Phys. Rev. D* 101.12 (2020), p. 122001. DOI: [10.1103/PhysRevD.101.122001](https://doi.org/10.1103/PhysRevD.101.122001). arXiv: [1908.06050](https://arxiv.org/abs/1908.06050) [[gr-qc](#)].
- [32] T. Venumadhav, B. Zackay, J. Roulet, et al. “New binary black hole mergers in the second observing run of Advanced LIGO and Advanced Virgo.” In: *Phys. Rev. D* 101.8, 083030 (Apr. 2020), p. 083030. DOI: [10.1103/PhysRevD.101.083030](https://doi.org/10.1103/PhysRevD.101.083030). arXiv: [1904.07214](https://arxiv.org/abs/1904.07214) [[astro-ph.HE](#)].
- [33] S. Olsen, T. Venumadhav, J. Mushkin, et al. “New binary black hole mergers in the LIGO–Virgo O3a data.” In: *arXiv e-prints*, arXiv:2201.02252 (Jan. 2022), arXiv:2201.02252. arXiv: [2201.02252](https://arxiv.org/abs/2201.02252) [[astro-ph.HE](#)].
- [34] B. McKernan, K. E. S. Ford, I. Bartos, et al. “Ram-pressure Stripping of a Kicked Hill Sphere: Prompt Electromagnetic Emission from the Merger of Stellar Mass Black Holes in an AGN Accretion Disk.” In: *ApJ* 884.2, L50

- (Oct. 2019), p. L50. DOI: [10.3847/2041-8213/ab4886](https://doi.org/10.3847/2041-8213/ab4886). arXiv: [1907.03746](https://arxiv.org/abs/1907.03746) [[astro-ph.HE](#)].
- [35] M. Fishbach, R. Gray, I. Magaña Hernandez, et al. “A Standard Siren Measurement of the Hubble Constant from GW170817 without the Electromagnetic Counterpart.” In: *ApJ* 871.1, L13 (Jan. 2019), p. L13. DOI: [10.3847/2041-8213/aaf96e](https://doi.org/10.3847/2041-8213/aaf96e). arXiv: [1807.05667](https://arxiv.org/abs/1807.05667) [[astro-ph.CO](#)].
- [36] A. Finke, S. Foffa, F. Iacovelli, et al. “Cosmology with LIGO/Virgo dark sirens: Hubble parameter and modified gravitational wave propagation.” In: *J. Cosmology Astropart. Phys.* 2021.8, 026 (Aug. 2021), p. 026. DOI: [10.1088/1475-7516/2021/08/026](https://doi.org/10.1088/1475-7516/2021/08/026). arXiv: [2101.12660](https://arxiv.org/abs/2101.12660) [[astro-ph.CO](#)].
- [37] D. F. Chernoff and L. S. Finn. “Gravitational Radiation, Inspiring Binaries, and Cosmology.” In: *ApJ* 411 (July 1993), p. L5. DOI: [10.1086/186898](https://doi.org/10.1086/186898). arXiv: [gr-qc/9304020](https://arxiv.org/abs/gr-qc/9304020) [[gr-qc](#)].
- [38] S. R. Taylor, J. R. Gair, and I. Mandel. “Cosmology using advanced gravitational-wave detectors alone.” In: *Phys. Rev. D* 85.2, 023535 (Jan. 2012), p. 023535. DOI: [10.1103/PhysRevD.85.023535](https://doi.org/10.1103/PhysRevD.85.023535). arXiv: [1108.5161](https://arxiv.org/abs/1108.5161) [[gr-qc](#)].
- [39] W. M. Farr, M. Fishbach, J. Ye, et al. “A Future Percent-level Measurement of the Hubble Expansion at Redshift 0.8 with Advanced LIGO.” In: *ApJ* 883.2, L42 (Oct. 2019), p. L42. DOI: [10.3847/2041-8213/ab4284](https://doi.org/10.3847/2041-8213/ab4284). arXiv: [1908.09084](https://arxiv.org/abs/1908.09084) [[astro-ph.CO](#)].
- [40] S. Mastrogiovanni, K. Leyde, C. Karathanasis, et al. “On the importance of source population models for gravitational-wave cosmology.” In: *Phys. Rev. D* 104.6, 062009 (Sept. 2021), p. 062009. DOI: [10.1103/PhysRevD.104.062009](https://doi.org/10.1103/PhysRevD.104.062009). arXiv: [2103.14663](https://arxiv.org/abs/2103.14663) [[gr-qc](#)].
- [41] LIGO Scientific Collaboration, Virgo Collaboration, KAGRA Collaboration, et al. “Constraints on the cosmic expansion history from GWTC-3.” In: *arXiv e-prints*, arXiv:2111.03604 (Nov. 2021), arXiv:2111.03604. arXiv: [2111.03604](https://arxiv.org/abs/2111.03604) [[astro-ph.CO](#)].
- [42] J. M. Ezquiaga and D. E. Holz. “Jumping the gap: searching for LIGO’s biggest black holes.” In: *arXiv e-prints*, arXiv:2006.02211 (May 2020), arXiv:2006.02211. arXiv: [2006.02211](https://arxiv.org/abs/2006.02211) [[astro-ph.HE](#)].
- [43] J. M. Ezquiaga and D. E. Holz. “Spectral Sirens: Cosmology from the Full Mass Distribution of Compact Binaries.” In: *Phys. Rev. Lett.* 129.6, 061102 (Aug. 2022), p. 061102. DOI: [10.1103/PhysRevLett.129.061102](https://doi.org/10.1103/PhysRevLett.129.061102). arXiv: [2202.08240](https://arxiv.org/abs/2202.08240) [[astro-ph.CO](#)].
- [44] I. Mandel, W. M. Farr, and J. R. Gair. “Extracting distribution parameters from multiple uncertain observations with selection biases.” In: *MNRAS* 486.1 (June 2019), pp. 1086–1093. DOI: [10.1093/mnras/stz896](https://doi.org/10.1093/mnras/stz896). arXiv: [1809.02063](https://arxiv.org/abs/1809.02063) [[physics.data-an](#)].

- [45] E. Thrane and C. Talbot. “An introduction to Bayesian inference in gravitational-wave astronomy: Parameter estimation, model selection, and hierarchical models.” In: *PASA* 36, e010 (Mar. 2019), e010. DOI: [10.1017/pasa.2019.2](https://doi.org/10.1017/pasa.2019.2). arXiv: [1809.02293](https://arxiv.org/abs/1809.02293) [astro-ph.IM].
- [46] M. Fishbach, D. E. Holz, and W. M. Farr. “Does the Black Hole Merger Rate Evolve with Redshift?.” In: *ApJ* 863.2, L41 (Aug. 2018), p. L41. DOI: [10.3847/2041-8213/aad800](https://doi.org/10.3847/2041-8213/aad800). arXiv: [1805.10270](https://arxiv.org/abs/1805.10270) [astro-ph.HE].
- [47] LIGO Scientific Collaboration, Virgo Collaboration, and et al. “Population Properties of Compact Objects from the Second LIGO-Virgo Gravitational-Wave Transient Catalog.” In: *ApJ* 913.1, L7 (May 2021), p. L7. DOI: [10.3847/2041-8213/abe949](https://doi.org/10.3847/2041-8213/abe949). arXiv: [2010.14533](https://arxiv.org/abs/2010.14533) [astro-ph.HE].
- [48] C. Talbot and E. Thrane. “Measuring the Binary Black Hole Mass Spectrum with an Astrophysically Motivated Parameterization.” In: *ApJ* 856.2, 173 (Apr. 2018), p. 173. DOI: [10.3847/1538-4357/aab34c](https://doi.org/10.3847/1538-4357/aab34c). arXiv: [1801.02699](https://arxiv.org/abs/1801.02699) [astro-ph.HE].
- [49] LIGO Scientific Collaboration and Virgo Collaboration. “Population Properties of Compact Objects from the Second LIGO-Virgo Gravitational-Wave Transient Catalog.” In: *ApJ* 913.1, L7 (May 2021), p. L7. DOI: [10.3847/2041-8213/abe949](https://doi.org/10.3847/2041-8213/abe949). arXiv: [2010.14533](https://arxiv.org/abs/2010.14533) [astro-ph.HE].
- [50] P. Madau and M. Dickinson. “Cosmic Star-Formation History.” In: *ARA&A* 52 (Aug. 2014), pp. 415–486. DOI: [10.1146/annurev-astro-081811-125615](https://doi.org/10.1146/annurev-astro-081811-125615). arXiv: [1403.0007](https://arxiv.org/abs/1403.0007) [astro-ph.CO].
- [51] A. Buikema, C. Cahillane, G. L. Mansell, et al. “Sensitivity and performance of the Advanced LIGO detectors in the third observing run.” In: *Phys. Rev. D* 102.6, 062003 (Sept. 2020), p. 062003. DOI: [10.1103/PhysRevD.102.062003](https://doi.org/10.1103/PhysRevD.102.062003). arXiv: [2008.01301](https://arxiv.org/abs/2008.01301) [astro-ph.IM].
- [52] S. Khan, S. Husa, M. Hannam, et al. “Frequency-domain gravitational waves from nonprecessing black-hole binaries. II. A phenomenological model for the advanced detector era.” In: *Phys. Rev. D* 93.4, 044007 (Feb. 2016), p. 044007. DOI: [10.1103/PhysRevD.93.044007](https://doi.org/10.1103/PhysRevD.93.044007). arXiv: [1508.07253](https://arxiv.org/abs/1508.07253) [gr-qc].
- [53] A. Nitz, I. Harry, D. Brown, et al. *gwastro/pycbc: v2.0.4 release of PyCBC*. Version v2.0.4. June 2022. DOI: [10.5281/zenodo.6646669](https://doi.org/10.5281/zenodo.6646669). URL: <https://doi.org/10.5281/zenodo.6646669>.
- [54] B. Allen, W. G. Anderson, P. R. Brady, et al. “FINDCHIRP: An algorithm for detection of gravitational waves from inspiraling compact binaries.” In: *Phys. Rev. D* 85.12, 122006 (June 2012), p. 122006. DOI: [10.1103/PhysRevD.85.122006](https://doi.org/10.1103/PhysRevD.85.122006). arXiv: [gr-qc/0509116](https://arxiv.org/abs/gr-qc/0509116) [gr-qc].

- [55] J. Roulet, H. S. Chia, S. Olsen, et al. “Distribution of effective spins and masses of binary black holes from the LIGO and Virgo O1-O3a observing runs.” In: *Phys. Rev. D* 104.8, 083010 (Oct. 2021), p. 083010. doi: [10.1103/PhysRevD.104.083010](https://doi.org/10.1103/PhysRevD.104.083010). arXiv: [2105.10580](https://arxiv.org/abs/2105.10580) [astro-ph.HE].
- [56] V. Tiwari and S. Fairhurst. “The Emergence of Structure in the Binary Black Hole Mass Distribution.” In: *ApJ* 913.2, L19 (June 2021), p. L19. doi: [10.3847/2041-8213/abfbc7](https://doi.org/10.3847/2041-8213/abfbc7). arXiv: [2011.04502](https://arxiv.org/abs/2011.04502) [astro-ph.HE].
- [57] S. Mukherjee. “The redshift dependence of black hole mass distribution: Is it reliable for standard sirens cosmology?.” In: *arXiv e-prints*, arXiv:2112.10256 (Dec. 2021), arXiv:2112.10256. arXiv: [2112.10256](https://arxiv.org/abs/2112.10256) [astro-ph.CO].
- [58] M. Mapelli, Y. Bouffanais, F. Santoliquido, et al. “The cosmic evolution of binary black holes in young, globular, and nuclear star clusters: rates, masses, spins, and mixing fractions.” In: *MNRAS* 511.4 (Apr. 2022), pp. 5797–5816. doi: [10.1093/mnras/stac422](https://doi.org/10.1093/mnras/stac422). arXiv: [2109.06222](https://arxiv.org/abs/2109.06222) [astro-ph.HE].
- [59] L. A. C. van Son, S. E. de Mink, T. Callister, et al. “The Redshift Evolution of the Binary Black Hole Merger Rate: A Weighty Matter.” In: *ApJ* 931.1, 17 (May 2022), p. 17. doi: [10.3847/1538-4357/ac64a3](https://doi.org/10.3847/1538-4357/ac64a3). arXiv: [2110.01634](https://arxiv.org/abs/2110.01634) [astro-ph.HE].
- [60] C. Karathanasis, S. Mukherjee, and S. Mastrogiovanni. “Binary black holes population and cosmology in new lights: Signature of PISN mass and formation channel in GWTC-3.” In: *arXiv e-prints*, arXiv:2204.13495 (Apr. 2022), arXiv:2204.13495. arXiv: [2204.13495](https://arxiv.org/abs/2204.13495) [astro-ph.CO].
- [61] Z.-Q. You, X.-J. Zhu, G. Ashton, et al. “Standard-siren Cosmology Using Gravitational Waves from Binary Black Holes.” In: *ApJ* 908.2, 215 (Feb. 2021), p. 215. doi: [10.3847/1538-4357/abd4d4](https://doi.org/10.3847/1538-4357/abd4d4). arXiv: [2004.00036](https://arxiv.org/abs/2004.00036) [astro-ph.CO].
- [62] S. Vitale, W. M. Farr, K. K. Y. Ng, et al. “Measuring the Star Formation Rate with Gravitational Waves from Binary Black Holes.” In: *ApJ* 886.1, L1 (Nov. 2019), p. L1. doi: [10.3847/2041-8213/ab50c0](https://doi.org/10.3847/2041-8213/ab50c0). arXiv: [1808.00901](https://arxiv.org/abs/1808.00901) [astro-ph.HE].
- [63] J. María Ezquiaga and D. E. Holz. “Spectral sirens: cosmology from the full mass distribution of compact binaries.” In: *arXiv e-prints*, arXiv:2202.08240 (Feb. 2022), arXiv:2202.08240. arXiv: [2202.08240](https://arxiv.org/abs/2202.08240) [astro-ph.CO].
- [64] J. Roulet, T. Venumadhav, B. Zackay, et al. “Binary black hole mergers from LIGO/Virgo O1 and O2: Population inference combining confident and marginal events.” In: *Phys. Rev. D* 102.12, 123022 (Dec. 2020), p. 123022. doi: [10.1103/PhysRevD.102.123022](https://doi.org/10.1103/PhysRevD.102.123022). arXiv: [2008.07014](https://arxiv.org/abs/2008.07014) [astro-ph.HE].

- [65] K. A. Kuns, H. Yu, Y. Chen, et al. “Astrophysics and cosmology with a decihertz gravitational-wave detector: TianGO.” In: *Phys. Rev. D* 102.4, 043001 (Aug. 2020), p. 043001. doi: [10.1103/PhysRevD.102.043001](https://doi.org/10.1103/PhysRevD.102.043001). arXiv: [1908.06004](https://arxiv.org/abs/1908.06004) [gr-qc].
- [66] H.-Y. Chen and D. E. Holz. “Finding the One: Identifying the Host Galaxies of Gravitational-Wave Sources.” In: *arXiv e-prints*, arXiv:1612.01471 (Dec. 2016), arXiv:1612.01471. arXiv: [1612.01471](https://arxiv.org/abs/1612.01471) [astro-ph.HE].
- [67] S. Borhanian, A. Dhani, A. Gupta, et al. “Dark Sirens to Resolve the Hubble-Lemaître Tension.” In: *arXiv e-prints*, arXiv:2007.02883 (July 2020), arXiv:2007.02883. arXiv: [2007.02883](https://arxiv.org/abs/2007.02883) [astro-ph.CO].
- [68] B. C. Seymour, H. Yu, and Y. Chen. “Multiband Gravitational Wave Cosmography with Dark Sirens.” In: *arXiv e-prints*, arXiv:2208.01668 (Aug. 2022), arXiv:2208.01668. arXiv: [2208.01668](https://arxiv.org/abs/2208.01668) [gr-qc].
- [69] S. Mukherjee, B. D. Wandelt, S. M. Nissanke, et al. “Accurate precision cosmology with redshift unknown gravitational wave sources.” In: *Phys. Rev. D* 103.4, 043520 (Feb. 2021), p. 043520. doi: [10.1103/PhysRevD.103.043520](https://doi.org/10.1103/PhysRevD.103.043520). arXiv: [2007.02943](https://arxiv.org/abs/2007.02943) [astro-ph.CO].
- [70] G. Scelfo, L. Boco, A. Lapi, et al. “Exploring galaxies-gravitational waves cross-correlations as an astrophysical probe.” In: *J. Cosmology Astropart. Phys.* 2020.10, 045 (Oct. 2020), p. 045. doi: [10.1088/1475-7516/2020/10/045](https://doi.org/10.1088/1475-7516/2020/10/045). arXiv: [2007.08534](https://arxiv.org/abs/2007.08534) [astro-ph.CO].
- [71] C. Cigarrán Díaz and S. Mukherjee. “Mapping the cosmic expansion history from LIGO-Virgo-KAGRA in synergy with DESI and SPHEREx.” In: *MNRAS* 511.2 (Apr. 2022), pp. 2782–2795. doi: [10.1093/mnras/stac208](https://doi.org/10.1093/mnras/stac208). arXiv: [2107.12787](https://arxiv.org/abs/2107.12787) [astro-ph.CO].
- [72] S. Mukherjee, A. Krolewski, B. D. Wandelt, et al. “Cross-correlating dark sirens and galaxies: measurement of H_0 from GWTC-3 of LIGO-Virgo-KAGRA.” In: *arXiv e-prints*, arXiv:2203.03643 (Mar. 2022), arXiv:2203.03643. arXiv: [2203.03643](https://arxiv.org/abs/2203.03643) [astro-ph.CO].
- [73] G. Van Rossum and F. L. Drake. “Python 3 Reference Manual.” Scotts Valley, CA: CreateSpace, 2009. ISBN: 1441412697.
- [74] C. R. Harris, K. J. Millman, S. J. van der Walt, et al. “Array programming with NumPy.” In: *Nature* 585.7825 (Sept. 2020), pp. 357–362. doi: [10.1038/s41586-020-2649-2](https://doi.org/10.1038/s41586-020-2649-2). URL: <https://doi.org/10.1038/s41586-020-2649-2>.
- [75] P. Virtanen, R. Gommers, T. E. Oliphant, et al. “SciPy 1.0: Fundamental Algorithms for Scientific Computing in Python.” In: *Nature Methods* 17 (2020), pp. 261–272. doi: [10.1038/s41592-019-0686-2](https://doi.org/10.1038/s41592-019-0686-2).

- [76] J. D. Hunter. “Matplotlib: A 2D graphics environment.” In: *Computing in Science & Engineering* 9.3 (2007), pp. 90–95. doi: [10.1109/MCSE.2007.55](https://doi.org/10.1109/MCSE.2007.55).
- [77] W. A. Fowler and F. Hoyle. “Neutrino Processes and Pair Formation in Massive Stars and Supernovae..” In: *ApJS* 9 (Dec. 1964), p. 201. doi: [10.1086/190103](https://doi.org/10.1086/190103).

MULTIBAND GRAVITATIONAL WAVE COSMOGRAPHY WITH DARK SIRENS

- [1] B. C. Seymour, H. Yu, and Y. Chen. “Multiband gravitational wave cosmography with dark sirens.” In: *Phys. Rev. D* 108.4 (2023), p. 044038. DOI: [10.1103/PhysRevD.108.044038](https://doi.org/10.1103/PhysRevD.108.044038). arXiv: [2208.01668](https://arxiv.org/abs/2208.01668) [gr-qc].

3.1 Introduction

The Hubble-Lemaître constant H_0 describes the current expansion rate of the universe. Currently, there is substantial deviation between Planck measurements of the cosmic microwave background fluctuations [1] and SH0ES measurements of Type Ia supernova with the distance ladder [2, 3]. Notably, the Hubble tension between these early and late universe measurements differs by at least 4σ [4, 5]. Moreover, the tension has occurred since the first Planck results [6] and strengthened with time. It is important to validate whether such Hubble tension truly exists or whether it is due to astrophysical systematics because it could signify violation from the Λ CDM concordance model [5, 7, 8]. One signature for departure from the concordance model would be apparent redshift evolution H_0 [9].

If the Hubble tension is proven robust with further measurements, there are a number of possible explanations with new physics. An extensive discussion of these possibilities is given in a recent review [10], and a comparison between many of such theories is given in [11]. These proposals can be classified generally either as *early-time* modification of the sound horizon or *late-time* modification of the Hubble expansion.

Let us first discuss new physics before recombination which would lower the value of Hubble constant as measured by Planck. Early dark energy adds an additional scalar field which acts like a cosmological constant and ends after recombination [12, 13]. The time of matter-radiation equality can be shifted by adding additional relativistic degrees of freedom with dark radiation [14, 15, 16] or neutrino self-interactions [17, 18]. Finally, there are proposals that the photon mass cannot be perfectly measured due to the lifetime of the universe from Heisenberg’s uncertainty principle, and this translates to uncertainty on the Hubble constant [19, 20].

There are also a number of ways to create a smooth late time deformation in $H(z)$ with unchanged CMB physics. These include phantom dark energy [21, 22], running vacuum model [23, 24], phenomenologically emergent dark energy [25], vacuum phase transition [26, 27], and a phase transition in dark energy [28, 29, 30]. Many of these modify the equation of state parameter of the dark energy or change how $\Omega_\Lambda(z)$ evolves with redshift. Another way to change the evolution of $H(z)$ is by introducing additional interactions. These class includes well-known beyond GR theories such as Brans-Dicke gravity [31], $f(R)$ gravity [32], and Galileon gravity [33]. Additionally, this includes interacting dark energy [34, 35, 36, 37] where dark energy and dark matter interact, and decaying dark matter [38, 39, 40] where dark matter decays into an unknown dark radiation. Finally, the homogeneous and isotropic assumption of Λ CDM can be broken with chameleon dark energy [41, 42, 43], cosmic voids [44], and inhomogeneous causal horizons [45].

The detection of gravitational waves (GW) can provide an independent *late* universe measurement of the Hubble constant. By measuring the expansion rate in the late universe, GW could be used as an independent measurement of the Hubble constant from SH0ES. Furthermore, with a distribution of GW events at low redshifts ($z \sim 0.0 - 0.5$), an anomalous evolution of the expansion rate could be observed. In particular, the luminosity distance of the source can be obtained from the measured gravitational waveform [46]. A Hubble constant measurement can be readily attained from a standard siren: a binary neutron star (BNS) merger with a coincident EM counterpart [46, 47]. With the optical measurement of the redshift from EM followup and luminosity distance measurement from the GW detector, one can directly measure the Hubble constant. Indeed, the Hubble constant was measured with the BNS GW170817 [48] and its corresponding EM counterpart [49, 50, 51].

However, only a small number of GW events are expected to be bright BNS mergers with EM counterparts. The majority of observed GW events are binary black hole (BBH) events without EM counterparts, which are thus known as *dark sirens*. Notably, many BBH events have already been detected and cataloged [52, 53, 54, 55, 56, 57]. Dark sirens can measure the Hubble constant by statistical techniques using galaxy catalogues [46, 58, 59, 60, 61, 62, 63, 64] and features in the mass distribution [65, 66, 67, 68, 69, 70]. These statistical techniques can be further extended with realistic galaxy clustering which provide improvements in identifying the redshift due to galaxy density correlations [71, 72, 73, 74]. These statistical techniques have been applied to the GWTC-3 catalog, and the Hubble constant is measured as

$H_0 = 68_{-12}^{+13}$ km s⁻¹Mpc⁻¹ using only dark sirens [75] at 68% credible level. By combining the statistical method with the only standard siren GW170817, the Hubble constant is measured as $H_0 = 68_{-6}^{+8}$ km s⁻¹Mpc⁻¹. For reference, GW170817 alone gives a Hubble constant value of $H_0 = 69_{-8}^{+17}$ km s⁻¹Mpc⁻¹ [48]. We need to bear in mind that the statistical dark siren approach relies fundamentally on population models so there is additional systematic uncertainties [75, 70]. In contrast, the Planck Hubble constant measurement was $H_0 = 67.4_{-0.5}^{+0.5}$ km s⁻¹Mpc⁻¹ [1] and the SHOES measurement was $H_0 = 72.5_{-1.0}^{+1.0}$ km s⁻¹Mpc⁻¹ [76] which corresponds to the 4 σ tension [4].

One new potential class of detector is one in the decihertz range (0.01 - 1 Hz), and such a detector may aid in measuring the Hubble constant. This detector would lie in between the millihertz LISA band [77] and the 10 - 1000 Hz ground band. A decihertz detector has many advantages for measuring the Hubble constant. First, it would provide early warning for BNS mergers which would help guarantee EM identification [78, 79]. Second, a joint decihertz detection would improve the parameter estimation for stellar mass BBH by measuring their waves several years before they enter into the ground band [78, 80]. Since statistical approaches to dark sirens are degraded by having too many galaxies inside of the localization volume, having a better angular localization will significantly help measure the cosmological parameters. Furthermore, the fascinating possibility of a multiband detection exists where a decihertz detector observes a BBH inspiral and then the ground based detectors measure the merger and ringdown. A decihertz multiband detection has been found to substantially improve parameter estimation accuracy [78]. By combining decihertz and ground detectors, the detector network can uniquely localize a BBH to a its host galaxy without any EM counterpart. While a ground network can do this on its own [81], the addition of a decihertz detector will significantly increase the range at which the BBH can be localized. In this way, a multiband detection of a BBH can behave like a standard siren.

Right now, there are a number of existing and proposed gravitational wave detectors. Advanced LIGO [82], Advanced Virgo [83], and KAGRA [84] are operating ground based gravitational wave detectors and are second-generation (2G) detectors. Following the 2G detectors, LIGO Voyager aims to maximize the reach of existing LIGO observatory facilities by adding cryogenic operation, heavier silicon test masses, and improved quantum squeezing [85, 86]. Einstein Telescope [87] and Cosmic Explorer [88] are the 3rd generation of ground-based detectors with

planned arm lengths of 10 km and 40 km, respectively, which aim to begin observation in the mid 2030s. 3G detectors can break the distance-inclination degeneracy using higher order spherical harmonic modes which would improve Hubble constant measurement [89].

At frequencies below ~ 1 Hz, detecting gravitational waves may best be carried out in space due to technical challenges [90, 91]. LISA [77, 92], TianQin [93], and Taiji [94, 95], are proposed space based detectors which focus on the $\sim 10^{-3} - 10^{-1}$ Hz bands. LISA can measure the Hubble constant with dark sirens [96] with accuracy of 5% and may be able to measure it with EMRIs [97] to an accuracy of 1% to 3%, though it is likely that ground detectors will surpass this by the time it is operational. Ref. [98] studied measuring the Hubble constant measurement with TianQin and LISA/Einstein Telescope. In the far future, there are proposals for a microhertz GW detector [99]. At very low frequencies, it may be possible for a pulsar timing array to measure the effect of a super massive black hole binary [100]. Furthermore, there are a number of space based plans for a decihertz detector in the 0.01 – 1 Hz band. The Japanese detector DECIGO is an ambitious prospect that consists of three clusters of interferometers with a 1000km arm length [101, 102, 103]. Big Bang Observer is concept like DECIGO by the European Space Agency [104]. Previous work found that Big Bang Observer alone would provide precision cosmological tests by measuring and localizing nearly every GW event in the universe [105]. Recently, Ref. [106] studied the capabilities of DECIGO and other decihertz detectors to measure the Hubble constant. B-DECIGO is a planned pathfinder mission of DECIGO with a single interferometer and a 100 km arm length [101, 102]. Finally, TianGO is a space based decihertz concept which is designed with nearer-term technology [78, 107].

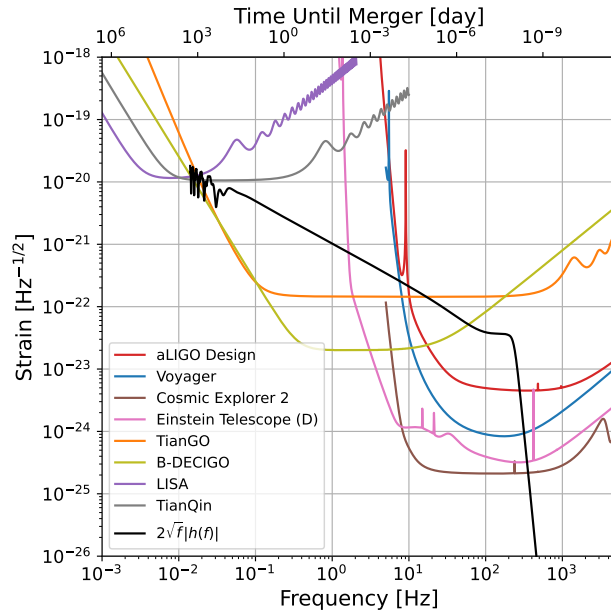


Figure 3.1: Comparison of detectors with a sample waveform. We plot the instrumental sensitivities for TianGO (orange), LIGO Voyager (blue), LISA (purple), aLIGO design sensitivity (red), Cosmic Explorer 2 (brown), Einstein Telescope D (pink), TianQin (gray), and B-DECIGO (yellow). We also show a sample TianGO waveform for a typical BBH merger (black) at $z = 0.3$, $\mathcal{M}_c = 25M_\odot$, $q = 1.05$, and $T_{\text{obs}} = 5$ yr assuming observed by a TianGO-like detector. On the top axis, we give the time until merger.

For this analysis, we study how well we can measure the expansion rate of the universe by measuring BBH with future ground detectors and decihertz concepts. We consider two representative decihertz detectors: (i) TianGO in the LIGO Voyager era, and (ii) B-DECIGO in the ET/CE era. TianGO is chosen because it represents a possible near term decihertz detector. In such a timescale, it would be operational in late 2020s/early 2030s and be working with the LIGO Voyager network. B-DECIGO is a longer term prospect, which would be operational in the late 2030s.

We forecast how well a dark siren can be localized with the Fisher matrix formalism [108, 109] with both detector setups. If such a comoving volume contains only one galaxy, we consider the dark siren to be *localized*. We consider the case where localized events will have measured redshift due to either spectroscopic follow-up or from a complete galaxy catalog. We find that adding a decihertz detector to the network improves the range at which a dark siren can be localized. We then constrain the Hubble constant and matter density parameter by stacking the localized dark siren events together with the BBH merger rate inferred

by LIGO/Virgo/KAGRA [110]. We assume that the Hubble constant and matter density are the Planck values and fix all other cosmological parameters. Our study motivates how a decihertz detector can complement the cosmological measurement capabilities of ground based detectors.

The rest of the paper is organized as follows. In Sec. 3.2, we describe the observed strain in a space based detector, and we use the Fisher matrix formalism to forecast the measurement uncertainties with a multiband detection. In Sec. 3.3, we describe how we stack localized events together and the forecast dark siren constraints on the Hubble constant and matter density parameter for various detector setups. We then conclude this work in Sec. 3.4. Finally, App. 3.5 delves into the space-based waveform specifics, and App. 3.6 justifies the conservative approach of considering only localized dark sirens. Throughout the work, we use $G = c = 1$.

3.2 Measurement of a Binary Black Hole

TianGO Waveform

Let us first model the waveform in a space detector. TianGO is orbiting the sun at an inclination of 60° , similar to the orbit of LISA [111]. Thus, there are two coordinate frames for the geometry of TianGO. We denote the ecliptic frame to have basis $(\hat{x}, \hat{y}, \hat{z})$ where \hat{z} is normal to the orbit of the earth. The frame with $(\hat{x}, \hat{y}, \hat{z})$ is fixed on the center of TianGO with (\hat{x}, \hat{y}) oriented along its two arms. We denote \hat{N} as the line of sight vector and \hat{L} is the direction of binary angular momentum. We can write the waveform as [80]

$$\tilde{h}(f) = \Lambda(f)e^{-i[\Phi_P(f)+\Phi_D(f)]}\tilde{h}_c(f), \quad (3.1)$$

where $\tilde{h}_c(f)$ is the carrier waveform, $\Lambda(f)$ is the amplitude in Eq. (3.2), $\Phi_P(f)$ is the polarization phase in Eq. (3.3), and $\Phi_D(f)$ is the phase modulation due to Doppler effect in Eq. (3.4). The carrier waveform is independent of the antenna patterns and only depends on the intrinsic parameters $(\mathcal{M}_z, q, D_L, t_c, \phi_c)$ where $\mathcal{M}_z = (1+z)\mathcal{M}_c$ is the detector frame chirp mass, q is the mass ratio, D_L is the luminosity distance, and t_c, ϕ_c are the time and phase of coalescence. Because we wish to model the gravitational waveform over the frequencies in both TianGO and Voyager, the carrier waveform is modeled with a phenomenological waveform that combines inspiral, merger and ringdown. Specifically, we use a IMRPhenomD waveform [112, 113].

The notable difference for a space-based detector compared to a ground one is that the orientation and location change with time. Thus, the amplitude and polarization

phase which characterize the antenna patterns acquire a frequency dependence and are derived in [114, 115] for a space based detector. We write them as

$$\Lambda(f) = [A_+^2 F_+^2(f) + A_\times^2 F_\times^2(f)]^{1/2}, \quad (3.2)$$

$$\Phi_P = \arctan \left[\frac{-A_\times F_\times(f)}{A_+ F_+(f)} \right]. \quad (3.3)$$

$F_{+,\times}(\phi_S, \theta_S, \psi_S)$ are the detector beam pattern coefficient where (ϕ_S, θ_S) are the direction of $\hat{\mathbf{N}}$ in the TianGO corotating frame and the barred ones denote quantities in the ecliptic frame, and ψ_S is the polarization phase. The polarization amplitudes are $A_+ = 1 + (\hat{\mathbf{L}} \cdot \hat{\mathbf{N}})^2$ and $A_\times = 2\hat{\mathbf{L}} \cdot \hat{\mathbf{N}}$. Additionally, there is a phase modulation due to the Doppler effect induced by the orbital motion of the detector (which we have assumed to be a heliocentric one),

$$\Phi_D(f) = 2\pi f \tau, \quad (3.4)$$

$$= 2\pi f R_{\text{AU}} \sin \bar{\theta}_S \cos (\bar{\phi}_t(f) - \bar{\phi}_S), \quad (3.5)$$

where $\tau = -\mathbf{d} \cdot \hat{\mathbf{N}}$, \mathbf{d} is the vector from barycenter to detector, R_{AU} is one AU, and $\bar{\phi}_t(f)$ is the azimuthal location of the solar orbit of the detector. The explicit expressions for $F_{+,\times}$, $\hat{\mathbf{L}} \cdot \hat{\mathbf{N}}$, $\bar{\phi}_t(f)$ are given in App. 3.5. The ground waveforms are the same as Eq. (3.1), but they are approximated as $f \rightarrow \infty$ for $\Lambda(f)$, $\Phi_P(f)$, $\Phi_D(f)$ since the antenna patterns are nearly constant while it is in band.

In Fig. 3.1, we plot a sample TianGO BBH waveform, along with the sensitivity of some gravitational wave detectors. This waveform terminates on the left side because of the 5 year observation time. It exhibits amplitude modulation around $f \sim 2 \cdot 10^{-2}$ Hz because TianGO's orientation $\hat{\mathbf{N}}$ is changing with a period of a year.

Parameter Estimation Background

Let us now describe how we use the Fisher analysis to estimate parameter uncertainties. The Fisher matrix formalism provides a useful approximation to parameter estimation in the high SNR limit [108, 109, 116]. We consider a binary with parameters θ^a and

$$\theta^a = (\ln \mathcal{M}_z, q, \ln D_L, t_c, \phi_c, \bar{\phi}_S, \bar{\theta}_S, \bar{\phi}_L, \bar{\theta}_L). \quad (3.6)$$

The variance for a specific parameter θ^a is found on the diagonal of the inverse of the Fisher matrix

$$\Delta \theta^a = \sqrt{(\Gamma^{-1})_{aa}}, \quad (3.7)$$

where the Fisher information matrix is defined as

$$\Gamma_{ab} \equiv \left(\frac{\partial \tilde{h}}{\partial \theta_a} \middle| \frac{\partial \tilde{h}}{\partial \theta_b} \right), \quad (3.8)$$

and the waveform template $\tilde{h}(f, \theta)$ is a function of frequency f and parameters θ . The inner product between two signals $\tilde{h}(f), \tilde{g}(f)$ is defined as

$$(\tilde{g}|\tilde{h}) = 4 \operatorname{Re} \int_0^\infty \frac{\tilde{g}^*(f)\tilde{h}(f)}{S_n(f)} df \quad (3.9)$$

where $S_n(f)$ is the detector noise spectral density. In the case of a network of detectors, we sum the individual Fisher matrix for each detector d

$$(\Gamma_{ab})^{\text{net}} = \sum_d \Gamma_{ab}^d. \quad (3.10)$$

Results from Parameter Estimation

To understand how a decihertz detector can enhance the parameter estimation of a BBH, we examine the results obtained using TianGO with the HLI Voyager network. The luminosity distance is defined by

$$D_L(z) = \frac{1+z}{H_0} \int_0^z \frac{dz'}{E(z')} \quad (3.11)$$

where

$$E(z) \equiv \sqrt{\Omega_m (1+z)^3 + \Omega_\Lambda}. \quad (3.12)$$

For precision tests of cosmology, we are mostly interested in the luminosity distance accuracy and volume localization. The size of the solid angle ellipse $\Delta\Omega$ can be expressed by [114]

$$\Delta\Omega = 2\pi \sin \bar{\theta}_S \sqrt{\Sigma_{\bar{\phi}_S \bar{\phi}_S} \Sigma_{\bar{\theta}_S \bar{\theta}_S} - \left(\Sigma_{\bar{\theta}_S \bar{\phi}_S}\right)^2}. \quad (3.13)$$

The uncertainty in comoving volume can be related to the angular uncertainty by Eq. (28) of Ref. [117]

$$\Delta V_C = \frac{D_L^2}{(1+z)^2} \Delta\Omega \Delta D_C, \quad (3.14)$$

where the comoving distance equals $D_C = D_L/(1+z)$. Using a change of variables, the comoving volume uncertainty can be rewritten as

$$\Delta V_C = \frac{D_L^2}{(1+z)^3 + D_L H(z) (1+z)} \Delta\Omega \Delta D_L, \quad (3.15)$$

where $H(z) = H_0 E(z)$.

Systematic errors beyond the detector sensitivity can degrade the accuracy of the luminosity distance. The first of which is the gravitational lensing which changes the luminosity distance. We use the fit from [118]

$$\frac{(\Delta D_L)_{\text{lens}}}{D_L} = 0.066 \left[\frac{1 - (1+z)^{-0.25}}{0.25} \right]^{1.8}. \quad (3.16)$$

Once a particular galaxy is identified, the peculiar velocity adds uncertainty to the amount of cosmological redshift. The measured redshift is the sum of the cosmological and Doppler redshift. We can express the peculiar velocity systematic error as [119]

$$\frac{(\Delta D_L)_{pv}}{D_L} = \left| 1 - \frac{(1+z)^2}{D_L H(z)} \right| \sigma_v, \quad (3.17)$$

where we have assumed $\sigma_v = 200 \text{ km s}^{-1}/c$. The relative magnitude of this effect decreases rapidly with distance since the cosmological redshift increases while the RMS peculiar velocity is approximately constant.

Figure 3.2 gives the measurement accuracy for luminosity distance, angular resolution, and spatial localization. We considered a binary of $\mathcal{M}_c = 25M_\odot$, $q = 1.05$, a trailing angle between earth and TianGO of $t_a = 5^\circ$, and a 5 year observation. The measurement accuracy strongly depends upon inclination ι of the binary, in addition to orientation of the detector network at merger. Therefore, we randomize over $(\bar{\phi}_S, \bar{\theta}_S, \bar{\phi}_L, \bar{\theta}_L)$ in the figure. The line represents the median measurement accuracy while the shaded region contains 80% of possible systems. While we use a 5 year observing time for TianGO, the TianGO's parameter estimation is not particularly sensitive to the observing time as long as it is above ~ 1 week as most of the SNR comes from frequencies above 0.1 Hz (see Fig. 3.1).

In the top part of Fig. 3.2, we show the fractional uncertainty in the luminosity distance $\Delta D_L/D_L$ versus redshift. One can see that the addition of TianGO does not significantly improve the ability to measure the luminosity distance compared with the HLI network. Most of the SNR from the event comes from the ground network, so the addition of TianGO improves the luminosity distance measurement by a factor of only 1.5¹. We also plot the lensing and peculiar velocity systematic errors here. We see that the systematic error due to peculiar velocity is only large enough to affect our measurement for very close events. Meanwhile, the effect of lensing is negligible and can be ignored in the future sections about cosmology.

In the middle panel of Fig. 3.2, we give the angular resolution $\Delta\Omega$ versus redshift. We see an angular resolution improvement by a factor of 20 for the addition of TianGO to the HLI Voyager network. The long baseline between earth and TianGO is responsible for this upgraded sky localization sensitivity.

¹Note that we have published a previous paper where we found that TianGO improved the luminosity distance measurement of the HLI Voyager network (Fig. 3 and Fig. 13 of [78]). There was an error in the space waveform code.

Finally, let us describe the comoving volume localization in the bottom panel of Fig. 3.2. We plot the comoving volume localization from Eq. (3.15), and find that adding TianGO improves the comoving volume localization by a factor 30. We use a comoving galaxy density of $n_{\text{gal}} = 0.01 \text{ gal/Mpc}^3$ [81]. This corresponds to the number density which are about 25% as bright as the Milky Way. This is because the majority of the GW are expected to come from galaxies at least this luminous [59]. If $n_{\text{gal}}\Delta V_C < 1$, we say the galaxy was localized. Using this criterion, we find that HLI Voyager can localize galaxies up to $z \sim 0.15$, while TianGO + HLI Voyager can localize them up to $z \sim 0.30$. Note that error bands are large and asymmetric because the line-of-sight direction and detector configuration greatly affect the measurement accuracy. For example, a gravitational wave that is face-on to the ecliptic plane would be poorly localized by TianGO since the Doppler term does not give any information, while a GW coming edge-on will measure $\Delta\Omega$ well (and correspondingly $\Delta V_C \sim D_L^2 \Delta D_L \Delta\Omega$).

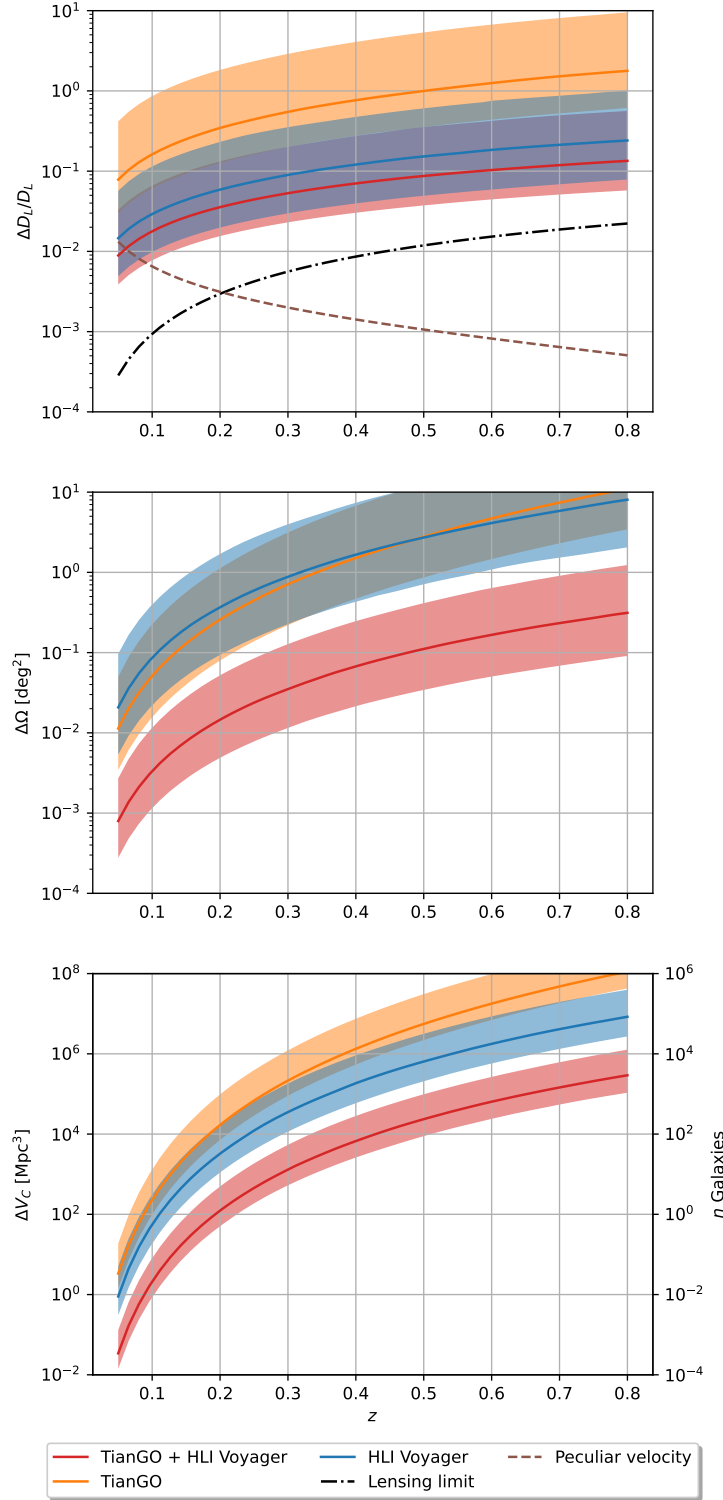


Figure 3.2: Measurement accuracy for luminosity distance, angular resolution and comoving volume localization versus redshift. We plot these measurement uncertainties for TianGO + HLI Voyager (red), HLI Voyager (blue), and TianGO (orange). Because we randomize over the angular extrinsic parameters ($\bar{\phi}_S, \bar{\theta}_S, \bar{\phi}_L, \bar{\theta}_L$), we plot both the median measurement with the line and the shaded region where 80% of binaries lie. We use $\mathcal{M} = 25M_\odot$, $q = 1.05$, $t_a = 5^\circ$ and $T_{\text{obs}} = 5$ yr. We use a galaxy number density per comoving volume of $n_{\text{gal}} = 0.01$ gal/ Mpc^3 to convert comoving volume localization to estimate our ability to identify the GW source.

Event Rate

To infer cosmological parameters, we stack all dark siren events that the network can localize. Let us now estimate how many dark sirens can be localized. First, the merger rate density $\mathcal{R}(z)$ describes the number of mergers in a comoving volume per year. We model it with a power law model and choose with $\kappa = 2.7$ so that it corresponds to the Madau-Dickinson star formation rate [120]

$$\mathcal{R}(z) = \mathcal{R}_0 (1 + z)^\kappa . \quad (3.18)$$

Since this is the source frame merger rate density, an additional factor of $1/(1 + z)$ is needed to convert time from the source frame to the detector frame. Therefore, we write the detector-frame merger rate of sources with $z < z_m$ as

$$R_{\text{obs}}(z_m) = \int_0^{z_m} \mathcal{R}(z') \frac{1}{1 + z'} \frac{dV_c}{dz'} dz' , \quad (3.19)$$

where

$$\frac{dV_c}{dz} = \frac{4\pi d_c^2(z)}{H_0 E(z)} . \quad (3.20)$$

We use the BBH merger rate $\mathcal{R}_0 = 20 \text{ Gpc}^{-3} \text{ yr}^{-1}$ and $\kappa = 2.7$ which consistent with GWTC-3 [110].

In Fig. 3.3, we give the number of detections per year which can be fully localized for HLI Voyager with and without TianGO. We see that TianGO will nearly double the range at which a BBH can be localized to a single host. This corresponds to an order of magnitude increase in localization rate. Furthermore, since the localizations occur at higher redshift, we can probe cosmological parameters beyond just the Hubble constant.

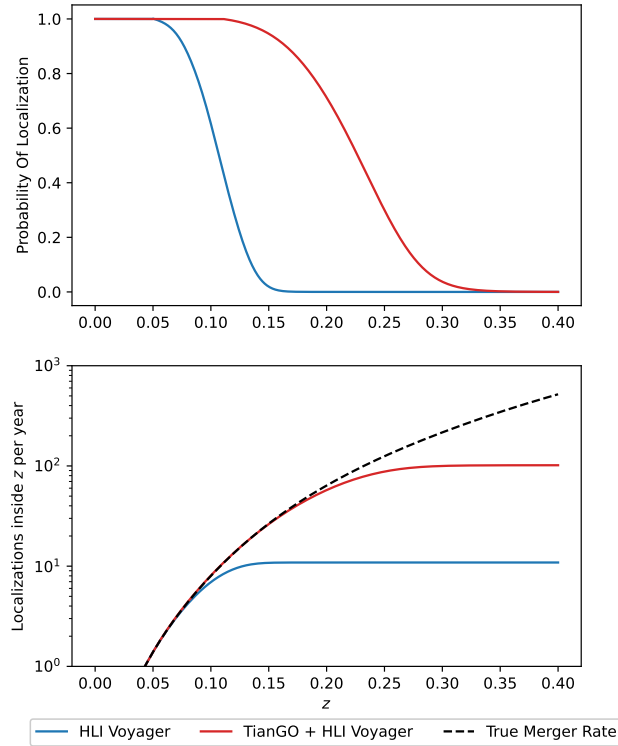


Figure 3.3: On the top, we plot the probability of an event being localized as a function of redshift for HLI Voyager (green) and TianGO + HLI Voyager (blue). We see that adding TianGO to the HLI Voyager network would nearly double the range at which we can localize a dark siren event. On the bottom, we plot the expected number of localizations in the comoving volume sphere. We use the merger rate equal to the star formation rate (red dashed) from Eq. (3.19). We find that the number of yearly localizations will increase by a factor of 10 by adding TianGO. This figure assumes the same binary parameters as Fig. 3.2, but also uniformly samples the observation time $T_{\text{obs}} \in [0, 5]$ yr.

3.3 Cosmological Constraints

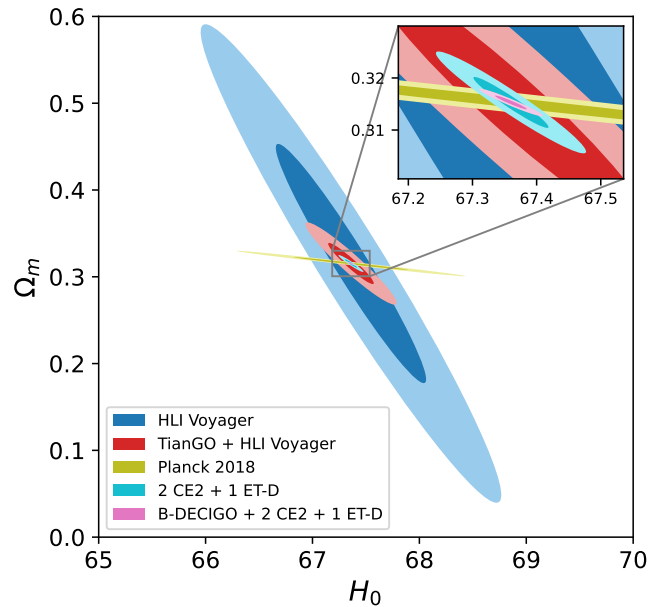


Figure 3.4: The confidence intervals for Hubble constant H_0 and matter density parameter Ω_m from HLI Voyager (blue), TianGO + HLI Voyager (red), Planck 2018 (yellow) [1], 2 CE 2's + ET-D (cyan), and B-DECIGO + 2 CE 2's + ET-D (pink). GW constraints come from Eq. (3.21) using only fully localized BBH events during a five year observation. We use chirp mass $\mathcal{M}_c = 25M_\odot$ and merger rate density at the star formation rate. One can see that adding TianGO to the Voyager network would improve error in the measurement of the Hubble constant and the matter density parameter. Moreover, the 3G ground network sees a similar improvement with the addition of B-DECIGO assuming it is in a heliocentric orbit. We include the forecasted cosmology constraints for other detector configurations in Tab. 3.1.

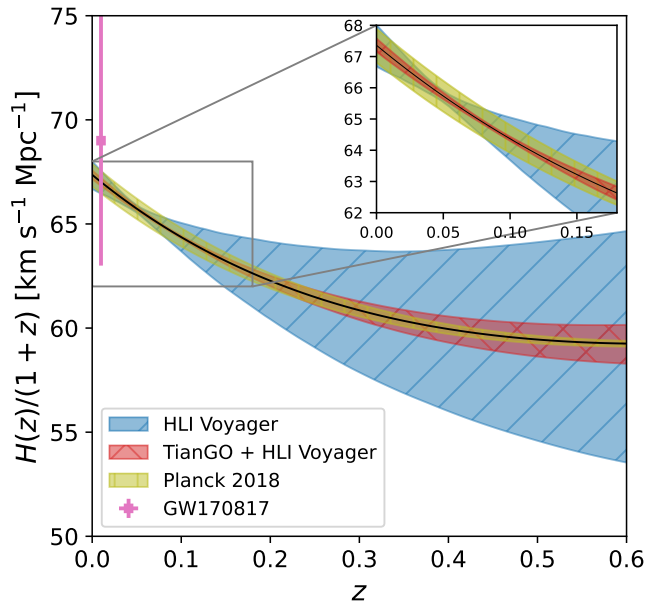


Figure 3.5: Constraints on the expansion rate as a function of redshift for various forecasted and current measurements at the 68% CL. We plot the forecasted constraints on HLI Voyager (blue) and TianGO + HLI Voyager (red). We also plot current expansion rate constraints from Planck 2018 (yellow) [1] and from GW170817 (pink) [48]. We produce this plot assuming the Planck parameters as the true values when computing the Fisher matrix, and incorporate only uncertainty on (H_0, Ω_m) for the shaded regions. Notice that three Voyagers can measure the expansion rate relatively accurately below $z \sim 0.1$. Furthermore, adding the decihertz detector TianGO enhances the ability for the expansion rate to be measured.

Given a set of gravitational wave observations, we wish to compute the consistent values of the cosmology. Others have studied how to measure the Hubble constant with dark sirens using statistical inference [59, 121, 70]. Currently, statistical methods are used because the LVK’s best localized BBHs have comoving volume resolution of $\Delta V_c \sim 10^5 \text{Mpc}^3$ [75] which has thousands of galaxies inside. Since our sources are well localized, we can directly measure the redshift of each dark siren event from the uniquely identified host galaxy. We demonstrate this in 2D with a mock simulation in App. 3.6 that the likelihood function breaks down to the particularly simple answer for well localized sources. We stress that our approach of using the localization condition of $n_{\text{gal}} \Delta V_c < 1$ is a conservative approach. This does not require a catalogue since optical telescopes can measure the redshift of the galaxy after the event. Furthermore, galaxy clustering can improve the cosmology constraints [71]. Additionally, more massive galaxies are statistically more likely to be the source of the GW, so this would further improve the ability to localize a GW

in the Bayesian approach. Under the localization assumption, a dark siren (BBH) will behave like a bright one (i.e., BNS) for cosmology.

Let us now describe how to compute confidence intervals on the cosmology with a set of dark siren observations. For a set of cosmological parameters $\mathbf{H} = (H_0, \Omega_m, \dots)$, we can compute their confidence intervals with a Fisher matrix

$$\tilde{\Gamma}_{ij} = \sum_{\text{event } k} \frac{1}{(\Delta D_L(z_k))^2} \frac{\partial D_L(z_k, \mathbf{H})}{\partial H_i} \frac{\partial D_L(z_k, \mathbf{H})}{\partial H_j}, \quad (3.21)$$

where we use the tilde $\tilde{\Gamma}$ to distinguish from the waveform parameter estimation matrix used in the last section. Then the error in a cosmological parameter is

$$\Delta H_i = \sqrt{(\tilde{\Gamma}^{-1})_{ii}}. \quad (3.22)$$

In the nearby universe, the Fisher matrix result reduces to $(\Delta H_0/H_0)^2 = (\Delta D_L/D_L)^2$

In Fig. 3.4, we plot the two sigma confidence intervals on the Hubble constant and matter density parameter using only uniquely localized BBH events. We use a five year observation period, and randomly pick $(\bar{\phi}_S, \bar{\theta}_S, \bar{\phi}_L, \bar{\theta}_L)$. We use $\mathcal{M}_c = 25M_\odot$, $q = 1.05$, a trailing angle of 5° , and uniformly randomize the time until merger. The luminosity distance of the events was sampled accordingly by Eq. (3.19). This corresponds to 2515 events with $z < 0.4$. There were 43 events localized by HLI Voyager alone and 476 events localized by HLI Voyager + TianGO.

The addition of TianGO substantially improves our ability to measure the cosmology. Fig. 3.4 shows the improvement of using TianGO for measuring the Hubble constant and matter density parameter. Because a multiband measurement increases the distance we can uniquely localize a galaxy, we can measure the matter density parameter much more accurately. HLI Voyager measures H_0 to 1% and Ω_m to 40%, and TianGO upgrades H_0 to 0.3% and Ω_m to 8%, while Planck measured H_0 to 0.8% and Ω_m to 2%. We also give the uncertainty ellipse for a possible 3G network consisting of 2 CE2's and 1 ET-D, and also we combine B-DECIGO with the 3G network. We can see an improvement in both near-term and long-term networks by adding a decihertz detector, particularly in the matter density parameter since its effect is most pronounced at larger redshifts. Using the covariance matrix containing (H_0, Ω_m) , we can see how well the expansion rate is measured as a function of redshift. In Fig. 3.5, we plot the expansion rate $H(z)/(1+z)$ versus redshift where we shade the 68% CL regions. We can see that gravitational wave detectors are measuring the redshift region $z \sim 0.2$ well because the localizations are occurring

	$\Delta H_0/H_0$	$\Delta\Omega_m$	Localizations / 5 yr	Notes
3 V (+ T)	1×10^{-2} (2×10^{-3})	1×10^{-1} (2×10^{-2})	43 (476)	Voyager at Hanford, Livingston, India sites.
1 CE2 + 1 ET-D (+ T)	2×10^{-3} (6×10^{-4})	1×10^{-2} (3×10^{-3})	382 (1930)	CE2 at Hanford, ET-D at GEO-600 sites.
2 CE2 + 1 ET-D (+ T)	1×10^{-3} (5×10^{-4})	6×10^{-3} (2×10^{-3})	843 (2410)	CE2 at Hanford, Livingston. ET-D at GEO-600 sites.
2 CE2 + 2V (+ T)	1×10^{-3} (6×10^{-4})	9×10^{-3} (3×10^{-3})	556 (2211)	CE2 at Virgo, India sites. Voyager at Hanford, Livingston sites.
1 CE2 + 1 ET-D (+ B-Decigo)	2×10^{-3} (5×10^{-4})	1×10^{-2} (2×10^{-3})	380 (4758)	CE2 at Hanford, ET-D at GEO-600 sites. B-Decigo placed in 5° trailing Heliocentric orbit
2 CE2 + 1 ET-D (+ B-Decigo)	1×10^{-3} (3×10^{-4})	6×10^{-3} (1×10^{-3})	835 (5770)	CE2 at Hanford, Livingston, ET-D at GEO-600 sites. B-Decigo placed in 5° trailing Heliocentric orbit

Table 3.1: Dark siren constraints on the Hubble constant and matter density parameter for various detector configurations. We use the same methodology as for this table as in the rest of this paper. We find the Fisher matrix confidence interval on the cosmological parameters by using only dark sirens which are completely localized.

here because most of localized events are at this redshift. At large redshifts, the cosmic expansion rate uncertainty grows because the matter density parameter is more poorly measured. For reference, we also plot the constraints from GW170817 and Planck 2018. Note that we only show Fig. 3.5 up to $z = 0.6$ since we cannot measure Ω_Λ, Ω_k well enough with localized BBH sources.

Finally, we estimate the constraints on the Hubble constant and matter density parameter for various 2G to 3G detector networks in Tab. 3.1. Specifically, we compare the cosmological constraints from localized dark sirens during a 5 year observation period. For the 3G detectors, we consider Cosmic Explorer 2 (CE2), and Einstein Telescope D (ET-D). We see that even with 2 CE2’s and ET-D, TianGO improves the ability to measure the Hubble constant by a factor of 2, and the matter density parameter by a factor of 3. This is because we see a sizable improvement in the number of localized events.

For the long-term multiband case, we use a network consisting of B-DECIGO, CE2, and ET-D. Because the orbit of B-DECIGO is still under discussion [122], we placed it in a trailing 5° orbit like TianGO. We performed the same analysis as in Section 3.3. We find that the addition of B-DECIGO can improve the cosmological measurement capabilities of the 3G detectors.

3.4 Conclusion

In this paper, we studied how a space-based decihertz detector can enhance the sensitivity of a ground network for dark siren cosmological measurement. We construct the case that these detectors will measure a significant number of ‘bright’ dark siren

BBH — GW from which we can uniquely localize and uniquely identify the host galaxy. We then use a Fisher matrix formalism to place constraints on the cosmological parameters. We estimated how well the Hubble constant and matter density parameter could be measured by BBH dark sirens with a five year observation of TianGO plus three LIGO Voyagers. The result is the multiband detection of dark sirens improves the measurement of the Hubble constant by about a factor of 3. The larger redshift localized events allows the matter density parameter to be resolved in the multiband case.

In the future, it would be interesting to extend our analysis to include dark sirens which are non-uniquely identified, but are still well localized. Since the fully localized criterion leaves out events with just a small number of galaxies, information about the cosmology can still be extracted from these events. Moreover, there are other effects which can improve the sensitivity further, such as exploiting the clustering of galaxies to improve localization [71] and weighting the galaxies by luminosity [73].

Measuring the cosmology with gravitational waves is easier when the host galaxy is uniquely identified. The statistical dark siren approach is degenerate with parameters such the merger rate evolution with redshift and the BBH population model (as discussed in the GWTC-3 cosmology paper [75]). Simultaneously measuring the cosmology and these population parameters can be done by looking at the distribution of BBH events [123, 74, 70], but would result in a less sensitive measurement of the cosmological parameters. Otherwise, if these factors are not jointly measured, this would bias the measurement of the Hubble constant [124, 70]. Consequently, a multiband detection of dark sirens with uniquely identified hosts has the potential to isolate the measurement of cosmological parameters from these population parameters.

ACKNOWLEDGMENTS

B.S. acknowledges support by the National Science Foundation Graduate Research Fellowship under Grant No. DGE-1745301. H.Y. acknowledges the support of the Sherman Fairchild Foundation. Y.C. and B.S. acknowledge support from the Brinson Foundation, the Simons Foundation (Award Number 568762), and by NSF Grants PHY-2011961, PHY-2011968, PHY-1836809.

3.5 Appendix: Antenna Patterns of TianGO

The standard formula for the plus and cross antenna patterns of a detector is

$$F_+ = \left(\frac{1 + \cos^2 \theta_S}{2} \right) \cos 2\phi_S \cos 2\psi_S - \cos \theta_S \sin 2\phi_S \sin 2\psi_S, \quad (3.23)$$

$$F_\times = \left(\frac{1 + \cos^2 \theta_S}{2} \right) \cos 2\phi_S \cos 2\psi_S + \cos \theta_S \sin 2\phi_S \sin 2\psi_S, \quad (3.24)$$

where (ϕ_S, θ_S) are in the detector frame. We use the `pycbc` detector class to get the ground based antenna patterns [125]. The antenna patterns of a space detector are more complicated however, because the detector has changing orientation. This means that the antenna patterns have time dependence $F_{+,\times}(t)$, which we will use the time frequency relation to find their frequency dependence.

To find the detector beam pattern coefficients, let us first describe the geometry of the system. We have two coordinate systems: unbarred coordinates $(\hat{x}, \hat{y}, \hat{z})$ which correspond to the individual detector and barred coordinates $(\bar{\hat{x}}, \bar{\hat{y}}, \bar{\hat{z}})$ in the ecliptic frame. The relationship between the orientation of the detector frame and the ecliptic is

$$\begin{aligned} \hat{x}(t) &= -\frac{\sin 2\bar{\phi}_t}{4} \bar{\hat{x}} + \frac{3 + \cos 2\bar{\phi}_t}{4} \bar{\hat{y}} + \frac{\sqrt{3}}{2} \sin \bar{\phi}_t \bar{\hat{z}}, \\ \hat{y}(t) &= \hat{z}(t) \times \hat{x}(t), \\ \hat{z}(t) &= -\frac{\sqrt{3}}{2} (\cos \bar{\phi}_t \bar{\hat{x}} + \sin \bar{\phi}_t \bar{\hat{y}}) + \frac{1}{2} \bar{\hat{z}}, \end{aligned} \quad (3.25)$$

where the phase of TianGO in the ecliptic frame is equal to

$$\bar{\phi}_t(f) = \frac{2\pi t(f)}{1 \text{ yr}} - t_a, \quad (3.26)$$

where t_a is the trailing angle, and equal to 5° for TianGO. The time as a function of frequency is [78]

$$t(f) = t_c - 5 (8\pi f)^{-8/3} \mathcal{M}_z^{-5/3} \left[1 + \frac{4}{3} \left(\frac{743}{336} + \frac{\mu}{M} x - \frac{32\pi}{5} x^{3/2} \right) \right], \quad (3.27)$$

where μ is the reduced mass and

$$x = (\pi M_z f)^{2/3}. \quad (3.28)$$

We can now write $(\phi_S(f), \theta_S(f), \psi_S(f))$ for the TianGO detector using Eq. (3.25),

$$\cos \theta_S(f) = \frac{1}{2} \cos \bar{\theta}_S - \frac{\sqrt{3}}{2} \sin \bar{\theta}_S \cos (\bar{\phi}_t(f) - \bar{\phi}_S), \quad (3.29)$$

$$\phi_S(f) = \bar{\phi}_t(f) + \arctan \left[\frac{\sqrt{3} \cos \bar{\theta}_S + \sin \bar{\theta}_S \cos (\bar{\phi}_t(f) - \bar{\phi}_S)}{2 \sin \bar{\theta}_S \sin (\bar{\phi}_t(f) - \bar{\phi}_S)} \right]. \quad (3.30)$$

The polarization phase of TianGO is

$$\tan \psi_S(f) = \frac{\hat{\mathbf{L}} \cdot \hat{\mathbf{z}} - (\hat{\mathbf{L}} \cdot \hat{\mathbf{N}}) (\hat{\mathbf{z}} \cdot \hat{\mathbf{N}})}{\hat{\mathbf{N}} \cdot (\hat{\mathbf{L}} \times \hat{\mathbf{z}})} \quad (3.31)$$

where

$$\hat{\mathbf{N}} \cdot \hat{\mathbf{z}} = \cos \theta_S(f), \quad (3.32)$$

$$\hat{\mathbf{L}} \cdot \hat{\mathbf{z}} = \frac{1}{2} \cos \bar{\theta}_L - \frac{\sqrt{3}}{2} \sin \bar{\theta}_L \cos [\bar{\phi}_t(f) - \bar{\phi}_L], \quad (3.33)$$

$$\hat{\mathbf{L}} \cdot \hat{\mathbf{N}} = \cos \bar{\theta}_L \cos \bar{\phi}_S + \sin \bar{\theta}_L \sin \bar{\theta}_S \cos (\bar{\phi}_L - \bar{\phi}_S), \quad (3.34)$$

$$\begin{aligned} \hat{\mathbf{N}} \cdot (\hat{\mathbf{L}} \times \hat{\mathbf{z}}) &= \frac{1}{2} \sin \bar{\theta}_L \sin \bar{\theta}_S \sin (\bar{\phi}_L - \bar{\phi}_S) \\ &\quad - \frac{\sqrt{3}}{2} \cos \bar{\phi}_t(f) (\cos \bar{\theta}_L \sin \bar{\theta}_S \sin \bar{\phi}_S - \cos \bar{\theta}_S \sin \bar{\theta}_L \sin \bar{\phi}_L) \\ &\quad - \frac{\sqrt{3}}{2} \sin \bar{\phi}_t(f) (\cos \bar{\theta}_S \sin \bar{\theta}_L \cos \bar{\phi}_L - \cos \bar{\theta}_L \sin \bar{\theta}_S \cos \bar{\phi}_S). \end{aligned} \quad (3.35)$$

3.6 Appendix: Consistency of Statistical Method

In the statistical method, we wish to break the $z - D_L$ degeneracy by using a galaxy catalog with the gravitational wave observation. We will use the method described in a variety of sources [59, 73]. If we wish to constrain the cosmological parameters \mathbf{H} and have gravitational wave data d_{GW} , then with Bayes theorem, we have

$$p(\mathbf{H}|d_{\text{GW}}) \propto p(H_0)p(d_{\text{GW}}|\mathbf{H}) \quad (3.36)$$

where

$$p(d_{\text{GW}}|\mathbf{H}) = \frac{1}{\beta(\mathbf{H})} \int p(d_{\text{GW}}, D_L, \phi_S, \theta_S, z|\mathbf{H}) dD_L d\phi_S d\theta_S dz, \quad (3.37)$$

$$= \frac{1}{\beta(\mathbf{H})} \int p(d_{\text{GW}}|D_L(z, \mathbf{H}), \phi_S, \theta_S) p_0(z, \phi_S, \theta_S) d\phi_S d\theta_S dz. \quad (3.38)$$

The first term in the integral is approximated with a multivariate Gaussian distribution

$$p(d_{\text{GW}}|D_L(z, \mathbf{H}), \phi_S, \theta_S) = N(D_L(z, \mathbf{H}) - \hat{D}_L, \sigma_{D_L}^2) N(\phi_S - \hat{\phi}_S, \sigma_{\phi_S}^2) N(\theta_S - \hat{\theta}_S, \sigma_{\theta_S}^2), \quad (3.39)$$

where $N(x - \mu, \sigma^2)$ is the probability density function of the normal distribution, $(\hat{D}_L, \hat{\phi}_S, \hat{\theta}_S)$ are the true event parameters, and $(\sigma_{D_L}, \sigma_{\phi_S}, \sigma_{\theta_S})$ is given by the Fisher matrix analysis in Eq. (10). The second term in the integral is the galaxy catalog

$$p_0(z, \phi_S, \theta_S|\mathbf{H}) = \frac{1}{N_{\text{gal}}} \sum_i^{N_{\text{gal}}} N(z - z^i, \sigma_{z_i}^2) \delta(\phi_S - \phi_S^i) \delta(\theta_S - \theta_S^i), \quad (3.40)$$

where σ_{z_i} is the variance due to the peculiar velocity. The variables (z^i, ϕ^i, θ^i) are the mean redshift and angular location of the i th galaxy, while unbarred variables are parameters.

The angular uncertainty is negligible and the distribution is replaced with a Dirac delta function $\delta(\phi_S - \bar{\phi}_S^i)$ and similarly for θ_S . Finally, the normalization $\beta(\mathbf{H})$ is

$$\beta(\mathbf{H}) = \int_{d_{\text{GW}} > d_{\text{GW}}^{\text{th}}} p(d_{\text{GW}}, D_L, \phi_S, \theta_S, z | \mathbf{H}) dD_L d\phi_S d\theta_S dz dd_{\text{GW}}, \quad (3.41)$$

where

$$p(d_{\text{GW}}, D_L, \phi_S, \theta_S, z | \mathbf{H}) = p(d_{\text{GW}} | D_L(z, \mathbf{H}), \phi_S, \theta_S) p_0(z, \phi_S, \theta_S), \quad (3.42)$$

and where $d_{\text{GW}}^{\text{th}}$ is the detection threshold. Note that Eq. (3.37) reduces to the Fisher matrix confidence interval Eq. (3.21) on \mathbf{H} if only one galaxy has nonvanishing likelihood. This reduction can be derived by examining (3.38) in the case that there is only one galaxy inside the volume. This happens when all other galaxies in the sum in $p_0(z, \phi_S, \theta_S | \mathbf{H})$ do not contribute to the integral in Eq. (3.38).

Now, let us demonstrate the statistical method in 2D and examine its convergence as a function of the number of galaxies inside the localization region. We assume that $D_L = z/H_0$ and that the peculiar velocity uncertainty is subdominant. Thus, we assume the peculiar velocity is a very sharp Gaussian and absorb it into σ_{D_L} . If we call $h = (H_0)/(H_0)_{\text{true}}$, the likelihood function is

$$p(d_{\text{GW}} | h) = \frac{1}{\beta(h)} \frac{1}{N_{\text{gal}}} \sum_i N(\hat{D}_L - D_L^i(h), \sigma_{D_L}^2) N(\hat{\phi}_S - \phi_S^i, \sigma_{\phi_S}^2) N(\hat{\theta}_S - \theta_S^i, \sigma_{\theta_S}^2) \quad (3.43)$$

where $D_L^i(h) = z^i/H_0 = z^i/[h(H_0)_{\text{true}}]$ and $\sigma_z = \sigma_{D_L}(H_0)_{\text{true}}$. In this 2D case, $\beta(h) \propto h^2$.

If we need to stack events, we generalize Eq. (3.43) to be the product of the likelihood function of each event²,

$$p(\{d_{\text{GW}}\} | h) = \prod_{\text{event } e}^N p((d_{\text{GW}})_e | h). \quad (3.44)$$

If we assume a uniform prior on h , then $p(h | \{d_{\text{GW}}\}) \propto p(\{d_{\text{GW}}\} | h)$. In Fig. 3.6, we plot the posterior on h for 30 and 300 events. In this figure, we vary the angular

²Technically, there is another factor $p(N|h)$ in front of the product which depends on the intrinsic astrophysical merger rate and comoving volume surveyed. It is discussed after Eq. (7) in Ref. [73].

resolution of the events for each curve. We plot the median number of potential host galaxies for the events. One can see that as events are nearly perfectly localized ($n \rightarrow 0$), the posterior on h approaches the Fisher likelihood in Eq. (3.21).

Due to the potential systematics possible in such an experiment, we list the precise choices we used to make the plot. Our distance resolution was $\Delta D_L/D_L = 0.15z + 10^{-2}$ and our angular resolutions varied between $\Delta\phi_S = \frac{z}{1000}$ deg to $\Delta\phi_S = 100z$ deg. These scaled with redshift linearly due to the SNR scaling of parameter measurement, while the 10^{-2} is the same order as the peculiar velocity error (so a few close events do not dominate). We uniformly placed 3×10^6 galaxies throughout the disc in the $z \in [0, 2)$ 'redshift window.' For each event, we randomly picked a galaxy with $z \in [0, 1)$. The particular redshift window can have a systematic effect on the statistical method [124], and we chose our galaxy disc to be much bigger than the redshift window to avoid artificial boundary effects.

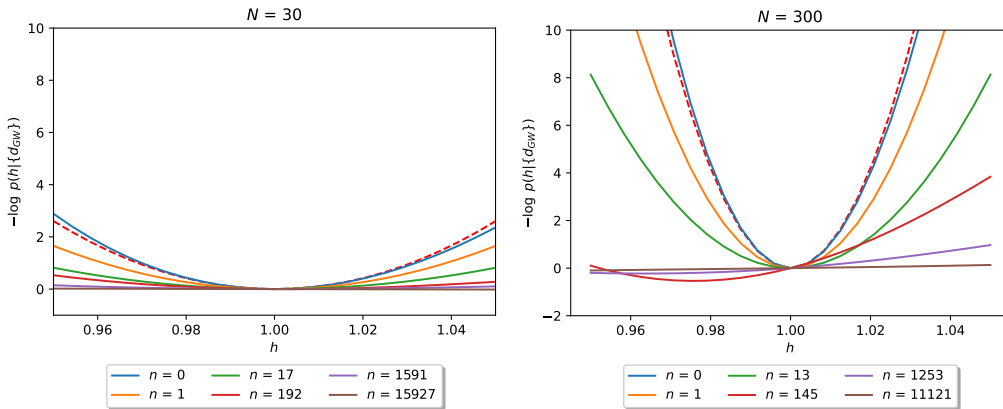


Figure 3.6: We plot the negative log likelihood of the posterior distribution on the Hubble constant $p(h | \{d_{\text{GW}}\})$ in the 2D simulation. Each curve with n labeled is the median number of *extra* galaxies in the localization region while the Fisher matrix constraint approximation from Eq. (3.21) is also plotted (dashed red). Each curve in the plot corresponds to picking a different angular resolution for the events. This shows that measurement of sources with poor angular resolution will result in weaker Hubble constant constraints due to the increased number of galaxies in the localization region. We also see that with a higher number of events, the likelihood distribution for h tightens. Finally, we see that the Bayesian approach reduces to the Fisher information estimate when there is a uniquely identified galaxy. This is still a conservative estimation on how well we can measure the cosmology as the information from $n > 0$ systems is discarded.

References

- [1] N. Aghanim et al. “Planck 2018 results. VI. Cosmological parameters.” In: *Astron. Astrophys.* 641 (2020). [Erratum: *Astron. Astrophys.* 652, C4 (2021)], A6. DOI: [10.1051/0004-6361/201833910](https://doi.org/10.1051/0004-6361/201833910). arXiv: [1807.06209](https://arxiv.org/abs/1807.06209) [[astro-ph.CO](#)].
- [2] A. G. Riess, S. Casertano, W. Yuan, et al. “Cosmic Distances Calibrated to 1% Precision with Gaia EDR3 Parallaxes and Hubble Space Telescope Photometry of 75 Milky Way Cepheids Confirm Tension with Λ CDM.” In: *Astrophys. J. Lett.* 908.1 (2021), p. L6. DOI: [10.3847/2041-8213/abdbaf](https://doi.org/10.3847/2041-8213/abdbaf). arXiv: [2012.08534](https://arxiv.org/abs/2012.08534) [[astro-ph.CO](#)].
- [3] A. G. Riess et al. “A 2.4% Determination of the Local Value of the Hubble Constant.” In: *Astrophys. J.* 826.1 (2016), p. 56. DOI: [10.3847/0004-637X/826/1/56](https://doi.org/10.3847/0004-637X/826/1/56). arXiv: [1604.01424](https://arxiv.org/abs/1604.01424) [[astro-ph.CO](#)].
- [4] L. Verde, T. Treu, and A. G. Riess. “Tensions between the Early and the Late Universe.” In: *Nature Astron.* 3 (July 2019), p. 891. DOI: [10.1038/s41550-019-0902-0](https://doi.org/10.1038/s41550-019-0902-0). arXiv: [1907.10625](https://arxiv.org/abs/1907.10625) [[astro-ph.CO](#)].
- [5] D. Camarena and V. Marra. “On the use of the local prior on the absolute magnitude of Type Ia supernovae in cosmological inference.” In: *Mon. Not. Roy. Astron. Soc.* 504 (2021), pp. 5164–5171. DOI: [10.1093/mnras/stab1200](https://doi.org/10.1093/mnras/stab1200). arXiv: [2101.08641](https://arxiv.org/abs/2101.08641) [[astro-ph.CO](#)].
- [6] P. A. R. Ade et al. “Planck 2013 results. XVI. Cosmological parameters.” In: *Astron. Astrophys.* 571 (2014), A16. DOI: [10.1051/0004-6361/201321591](https://doi.org/10.1051/0004-6361/201321591). arXiv: [1303.5076](https://arxiv.org/abs/1303.5076) [[astro-ph.CO](#)].
- [7] S. Vagnozzi. “New physics in light of the H_0 tension: An alternative view.” In: *Phys. Rev. D* 102.2 (2020), p. 023518. DOI: [10.1103/PhysRevD.102.023518](https://doi.org/10.1103/PhysRevD.102.023518). arXiv: [1907.07569](https://arxiv.org/abs/1907.07569) [[astro-ph.CO](#)].
- [8] N. Jackson. “The Hubble Constant.” In: *Living Rev. Rel.* 10 (2007), p. 4. DOI: [10.12942/lrr-2007-4](https://doi.org/10.12942/lrr-2007-4). arXiv: [0709.3924](https://arxiv.org/abs/0709.3924) [[astro-ph](#)].
- [9] C. Krishnan, E. Ó. Colgáin, M. M. Sheikh-Jabbari, et al. “Running Hubble Tension and a H_0 Diagnostic.” In: *Phys. Rev. D* 103.10 (2021), p. 103509. DOI: [10.1103/PhysRevD.103.103509](https://doi.org/10.1103/PhysRevD.103.103509). arXiv: [2011.02858](https://arxiv.org/abs/2011.02858) [[astro-ph.CO](#)].
- [10] L. Perivolaropoulos and F. Skara. “Challenges for Λ CDM: An update.” In: *New Astron. Rev.* 95 (2022), p. 101659. DOI: [10.1016/j.newar.2022.101659](https://doi.org/10.1016/j.newar.2022.101659). arXiv: [2105.05208](https://arxiv.org/abs/2105.05208) [[astro-ph.CO](#)].
- [11] N. Schöneberg, G. Franco Abellán, A. Pérez Sánchez, et al. “The H_0 Olympics: A fair ranking of proposed models.” In: *Phys. Rept.* 984 (2022), pp. 1–55. DOI: [10.1016/j.physrep.2022.07.001](https://doi.org/10.1016/j.physrep.2022.07.001). arXiv: [2107.10291](https://arxiv.org/abs/2107.10291) [[astro-ph.CO](#)].

- [12] V. Poulin, T. L. Smith, T. Karwal, et al. “Early Dark Energy Can Resolve The Hubble Tension.” In: *Phys. Rev. Lett.* 122.22 (2019), p. 221301. DOI: [10.1103/PhysRevLett.122.221301](https://doi.org/10.1103/PhysRevLett.122.221301). arXiv: [1811.04083](https://arxiv.org/abs/1811.04083) [astro-ph.CO].
- [13] P. Agrawal, F.-Y. Cyr-Racine, D. Pinner, et al. “Rock ’n’ Roll Solutions to the Hubble Tension.” In: (Apr. 2019). arXiv: [1904.01016](https://arxiv.org/abs/1904.01016) [astro-ph.CO].
- [14] M. A. Buen-Abad, M. Schmaltz, J. Lesgourgues, et al. “Interacting Dark Sector and Precision Cosmology.” In: *JCAP* 01 (2018), p. 008. DOI: [10.1088/1475-7516/2018/01/008](https://doi.org/10.1088/1475-7516/2018/01/008). arXiv: [1708.09406](https://arxiv.org/abs/1708.09406) [astro-ph.CO].
- [15] L. Lancaster, F.-Y. Cyr-Racine, L. Knox, et al. “A tale of two modes: Neutrino free-streaming in the early universe.” In: *JCAP* 07 (2017), p. 033. DOI: [10.1088/1475-7516/2017/07/033](https://doi.org/10.1088/1475-7516/2017/07/033). arXiv: [1704.06657](https://arxiv.org/abs/1704.06657) [astro-ph.CO].
- [16] D. Green et al. “Messengers from the Early Universe: Cosmic Neutrinos and Other Light Relics.” In: *Bull. Am. Astron. Soc.* 51.7 (2019), p. 159. arXiv: [1903.04763](https://arxiv.org/abs/1903.04763) [astro-ph.CO].
- [17] F.-Y. Cyr-Racine and K. Sigurdson. “Limits on Neutrino-Neutrino Scattering in the Early Universe.” In: *Phys. Rev. D* 90.12 (2014), p. 123533. DOI: [10.1103/PhysRevD.90.123533](https://doi.org/10.1103/PhysRevD.90.123533). arXiv: [1306.1536](https://arxiv.org/abs/1306.1536) [astro-ph.CO].
- [18] C. D. Kreisch, F.-Y. Cyr-Racine, and O. Doré. “Neutrino puzzle: Anomalies, interactions, and cosmological tensions.” In: *Phys. Rev. D* 101.12 (2020), p. 123505. DOI: [10.1103/PhysRevD.101.123505](https://doi.org/10.1103/PhysRevD.101.123505). arXiv: [1902.00534](https://arxiv.org/abs/1902.00534) [astro-ph.CO].
- [19] S. Capozziello, M. Benetti, and A. D. A. M. Spallicci. “Addressing the cosmological H_0 tension by the Heisenberg uncertainty.” In: *Found. Phys.* 50.9 (2020), pp. 893–899. DOI: [10.1007/s10701-020-00356-2](https://doi.org/10.1007/s10701-020-00356-2). arXiv: [2007.00462](https://arxiv.org/abs/2007.00462) [gr-qc].
- [20] A. D. A. M. Spallicci, M. Benetti, and S. Capozziello. “The Heisenberg Limit at Cosmological Scales.” In: *Found. Phys.* 52.1 (2022), p. 23. DOI: [10.1007/s10701-021-00531-z](https://doi.org/10.1007/s10701-021-00531-z). arXiv: [2112.07359](https://arxiv.org/abs/2112.07359) [physics.gen-ph].
- [21] G. Alestas, L. Kazantzidis, and L. Perivolaropoulos. “ H_0 tension, phantom dark energy, and cosmological parameter degeneracies.” In: *Phys. Rev. D* 101.12 (2020), p. 123516. DOI: [10.1103/PhysRevD.101.123516](https://doi.org/10.1103/PhysRevD.101.123516). arXiv: [2004.08363](https://arxiv.org/abs/2004.08363) [astro-ph.CO].
- [22] E. Di Valentino, A. Melchiorri, and J. Silk. “Reconciling Planck with the local value of H_0 in extended parameter space.” In: *Phys. Lett. B* 761 (2016), pp. 242–246. DOI: [10.1016/j.physletb.2016.08.043](https://doi.org/10.1016/j.physletb.2016.08.043). arXiv: [1606.00634](https://arxiv.org/abs/1606.00634) [astro-ph.CO].

- [23] S. Banerjee, D. Benisty, and E. I. Guendelman. “Running Dark Energy and Dark Matter from Dynamical Spacetime.” In: *Bulg. J. Phys.* 48.2 (2021), pp. 117–137. arXiv: [1910.03933 \[gr-qc\]](#).
- [24] S. Basilakos, N. E. Mavromatos, and J. Solà. “Starobinsky-like inflation and running vacuum in the context of Supergravity.” In: *Universe* 2.3 (2016), p. 14. doi: [10.3390/universe2030014](#). arXiv: [1505.04434 \[gr-qc\]](#).
- [25] X. Li and A. Shafieloo. “A Simple Phenomenological Emergent Dark Energy Model can Resolve the Hubble Tension.” In: *Astrophys. J. Lett.* 883.1 (2019), p. L3. doi: [10.3847/2041-8213/ab3e09](#). arXiv: [1906.08275 \[astro-ph.CO\]](#).
- [26] E. Di Valentino, O. Mena, S. Pan, et al. “In the realm of the Hubble tension—a review of solutions.” In: *Class. Quant. Grav.* 38.15 (2021), p. 153001. doi: [10.1088/1361-6382/ac086d](#). arXiv: [2103.01183 \[astro-ph.CO\]](#).
- [27] R. R. Caldwell, W. Komp, L. Parker, et al. “A Sudden gravitational transition.” In: *Phys. Rev. D* 73 (2006), p. 023513. doi: [10.1103/PhysRevD.73.023513](#). arXiv: [astro-ph/0507622](#).
- [28] A. Banihashemi, N. Khosravi, and A. H. Shirazi. “Ginzburg-Landau Theory of Dark Energy: A Framework to Study Both Temporal and Spatial Cosmological Tensions Simultaneously.” In: *Phys. Rev. D* 99.8 (2019), p. 083509. doi: [10.1103/PhysRevD.99.083509](#). arXiv: [1810.11007 \[astro-ph.CO\]](#).
- [29] A. Banihashemi, N. Khosravi, and A. H. Shirazi. “Phase transition in the dark sector as a proposal to lessen cosmological tensions.” In: *Phys. Rev. D* 101.12 (2020), p. 123521. doi: [10.1103/PhysRevD.101.123521](#). arXiv: [1808.02472 \[astro-ph.CO\]](#).
- [30] G. Benevento, W. Hu, and M. Raveri. “Can Late Dark Energy Transitions Raise the Hubble constant?.” In: *Phys. Rev. D* 101.10 (2020), p. 103517. doi: [10.1103/PhysRevD.101.103517](#). arXiv: [2002.11707 \[astro-ph.CO\]](#).
- [31] J. Solà Peracaula, A. Gomez-Valent, J. de Cruz Pérez, et al. “Brans–Dicke Gravity with a Cosmological Constant Smooths Out Λ CDM Tensions.” In: *Astrophys. J. Lett.* 886.1 (2019), p. L6. doi: [10.3847/2041-8213/ab53e9](#). arXiv: [1909.02554 \[astro-ph.CO\]](#).
- [32] R. D’Agostino and R. C. Nunes. “Measurements of H_0 in modified gravity theories: The role of lensed quasars in the late-time Universe.” In: *Phys. Rev. D* 101.10 (2020), p. 103505. doi: [10.1103/PhysRevD.101.103505](#). arXiv: [2002.06381 \[astro-ph.CO\]](#).
- [33] N. Frusciante, S. Peirone, L. Atayde, et al. “Phenomenology of the generalized cubic covariant Galileon model and cosmological bounds.” In: *Phys. Rev. D* 101.6 (2020), p. 064001. doi: [10.1103/PhysRevD.101.064001](#). arXiv: [1912.07586 \[astro-ph.CO\]](#).

- [34] P. Wang and X.-H. Meng. “Can vacuum decay in our universe?.” In: *Class. Quant. Grav.* 22 (2005), pp. 283–294. DOI: [10.1088/0264-9381/22/2/003](https://doi.org/10.1088/0264-9381/22/2/003). arXiv: [astro-ph/0408495](https://arxiv.org/abs/astro-ph/0408495).
- [35] E. Di Valentino, A. Melchiorri, and O. Mena. “Can interacting dark energy solve the H_0 tension?.” In: *Phys. Rev. D* 96.4 (2017), p. 043503. DOI: [10.1103/PhysRevD.96.043503](https://doi.org/10.1103/PhysRevD.96.043503). arXiv: [1704.08342](https://arxiv.org/abs/1704.08342) [[astro-ph.CO](https://arxiv.org/abs/astro-ph)].
- [36] W. Yang, S. Pan, R. C. Nunes, et al. “Dark calling Dark: Interaction in the dark sector in presence of neutrino properties after Planck CMB final release.” In: *JCAP* 04 (2020), p. 008. DOI: [10.1088/1475-7516/2020/04/008](https://doi.org/10.1088/1475-7516/2020/04/008). arXiv: [1910.08821](https://arxiv.org/abs/1910.08821) [[astro-ph.CO](https://arxiv.org/abs/astro-ph)].
- [37] M. Aljaf, D. Gregoris, and M. Khurshudyan. “Constraints on interacting dark energy models through cosmic chronometers and Gaussian process.” In: *Eur. Phys. J. C* 81.6 (2021), p. 544. DOI: [10.1140/epjc/s10052-021-09306-2](https://doi.org/10.1140/epjc/s10052-021-09306-2). arXiv: [2005.01891](https://arxiv.org/abs/2005.01891) [[astro-ph.CO](https://arxiv.org/abs/astro-ph)].
- [38] K. Ichiki, M. Oguri, and K. Takahashi. “WMAP constraints on decaying cold dark matter.” In: *Phys. Rev. Lett.* 93 (2004), p. 071302. DOI: [10.1103/PhysRevLett.93.071302](https://doi.org/10.1103/PhysRevLett.93.071302). arXiv: [astro-ph/0403164](https://arxiv.org/abs/astro-ph/0403164).
- [39] O. E. Bjaelde, S. Das, and A. Moss. “Origin of ΔN_{eff} as a Result of an Interaction between Dark Radiation and Dark Matter.” In: *JCAP* 10 (2012), p. 017. DOI: [10.1088/1475-7516/2012/10/017](https://doi.org/10.1088/1475-7516/2012/10/017). arXiv: [1205.0553](https://arxiv.org/abs/1205.0553) [[astro-ph.CO](https://arxiv.org/abs/astro-ph)].
- [40] Z. Berezhiani, A. D. Dolgov, and I. I. Tkachev. “Reconciling Planck results with low redshift astronomical measurements.” In: *Phys. Rev. D* 92.6 (2015), p. 061303. DOI: [10.1103/PhysRevD.92.061303](https://doi.org/10.1103/PhysRevD.92.061303). arXiv: [1505.03644](https://arxiv.org/abs/1505.03644) [[astro-ph.CO](https://arxiv.org/abs/astro-ph)].
- [41] J. Khoury and A. Weltman. “Chameleon cosmology.” In: *Phys. Rev. D* 69 (2004), p. 044026. DOI: [10.1103/PhysRevD.69.044026](https://doi.org/10.1103/PhysRevD.69.044026). arXiv: [astro-ph/0309411](https://arxiv.org/abs/astro-ph/0309411).
- [42] J. Khoury and A. Weltman. “Chameleon fields: Awaiting surprises for tests of gravity in space.” In: *Phys. Rev. Lett.* 93 (2004), p. 171104. DOI: [10.1103/PhysRevLett.93.171104](https://doi.org/10.1103/PhysRevLett.93.171104). arXiv: [astro-ph/0309300](https://arxiv.org/abs/astro-ph/0309300).
- [43] R.-G. Cai, Z.-K. Guo, L. Li, et al. “Chameleon dark energy can resolve the Hubble tension.” In: *Phys. Rev. D* 103.12 (2021), p. 121302. DOI: [10.1103/PhysRevD.103.L121302](https://doi.org/10.1103/PhysRevD.103.L121302). arXiv: [2102.02020](https://arxiv.org/abs/2102.02020) [[astro-ph.CO](https://arxiv.org/abs/astro-ph)].
- [44] L. Lombriser. “Consistency of the local Hubble constant with the cosmic microwave background.” In: *Phys. Lett. B* 803 (2020), p. 135303. DOI: [10.1016/j.physletb.2020.135303](https://doi.org/10.1016/j.physletb.2020.135303). arXiv: [1906.12347](https://arxiv.org/abs/1906.12347) [[astro-ph.CO](https://arxiv.org/abs/astro-ph)].
- [45] P. Fosalba and E. Gaztanaga. “Explaining Cosmological Anisotropy: Evidence for Causal Horizons from CMB data.” In: (Nov. 2020). DOI: [10.1093/mnras/stab1193](https://doi.org/10.1093/mnras/stab1193). arXiv: [2011.00910](https://arxiv.org/abs/2011.00910) [[astro-ph.CO](https://arxiv.org/abs/astro-ph)].

- [46] B. F. Schutz. “Determining the Hubble Constant from Gravitational Wave Observations.” In: *Nature* 323 (1986), pp. 310–311. doi: [10.1038/323310a0](https://doi.org/10.1038/323310a0).
- [47] D. E. Holz and S. A. Hughes. “Using gravitational-wave standard sirens.” In: *Astrophys. J.* 629 (2005), pp. 15–22. doi: [10.1086/431341](https://doi.org/10.1086/431341). arXiv: [astro-ph/0504616](https://arxiv.org/abs/astro-ph/0504616).
- [48] B. P. Abbott et al. “A gravitational-wave standard siren measurement of the Hubble constant.” In: *Nature* 551.7678 (2017), pp. 85–88. doi: [10.1038/nature24471](https://doi.org/10.1038/nature24471). arXiv: [1710.05835](https://arxiv.org/abs/1710.05835) [[astro-ph.CO](#)].
- [49] M. Nicholl et al. “The Electromagnetic Counterpart of the Binary Neutron Star Merger LIGO/VIRGO GW170817. III. Optical and UV Spectra of a Blue Kilonova From Fast Polar Ejecta.” In: *Astrophys. J. Lett.* 848.2 (2017), p. L18. doi: [10.3847/2041-8213/aa9029](https://doi.org/10.3847/2041-8213/aa9029). arXiv: [1710.05456](https://arxiv.org/abs/1710.05456) [[astro-ph.HE](#)].
- [50] D. A. Coulter et al. “Swope Supernova Survey 2017a (SSS17a), the Optical Counterpart to a Gravitational Wave Source.” In: *Science* 358 (2017), p. 1556. doi: [10.1126/science.aap9811](https://doi.org/10.1126/science.aap9811). arXiv: [1710.05452](https://arxiv.org/abs/1710.05452) [[astro-ph.HE](#)].
- [51] B. P. Abbott et al. “GW170817: Observation of Gravitational Waves from a Binary Neutron Star Inspiral.” In: *Phys. Rev. Lett.* 119.16 (2017), p. 161101. doi: [10.1103/PhysRevLett.119.161101](https://doi.org/10.1103/PhysRevLett.119.161101). arXiv: [1710.05832](https://arxiv.org/abs/1710.05832) [[gr-qc](#)].
- [52] R. Abbott et al. “GWTC-2: Compact Binary Coalescences Observed by LIGO and Virgo During the First Half of the Third Observing Run.” In: *Phys. Rev. X* 11 (2021), p. 021053. doi: [10.1103/PhysRevX.11.021053](https://doi.org/10.1103/PhysRevX.11.021053). arXiv: [2010.14527](https://arxiv.org/abs/2010.14527) [[gr-qc](#)].
- [53] R. Abbott et al. “GWTC-3: Compact Binary Coalescences Observed by LIGO and Virgo During the Second Part of the Third Observing Run.” In: (Nov. 2021). arXiv: [2111.03606](https://arxiv.org/abs/2111.03606) [[gr-qc](#)].
- [54] T. Venumadhav, B. Zackay, J. Roulet, et al. “New binary black hole mergers in the second observing run of Advanced LIGO and Advanced Virgo.” In: *Phys. Rev. D* 101.8 (2020), p. 083030. doi: [10.1103/PhysRevD.101.083030](https://doi.org/10.1103/PhysRevD.101.083030). arXiv: [1904.07214](https://arxiv.org/abs/1904.07214) [[astro-ph.HE](#)].
- [55] S. Olsen, T. Venumadhav, J. Mushkin, et al. “New binary black hole mergers in the LIGO–Virgo O3a data.” In: (Jan. 2022). arXiv: [2201.02252](https://arxiv.org/abs/2201.02252) [[astro-ph.HE](#)].
- [56] A. H. Nitz, C. Capano, A. B. Nielsen, et al. “1-OGC: The First Open Gravitational-wave Catalog of Binary Mergers from Analysis of Public Advanced LIGO Data.” In: *ApJ* 872.2, 195 (Feb. 2019), p. 195. doi: [10.3847/1538-4357/ab0108](https://doi.org/10.3847/1538-4357/ab0108). arXiv: [1811.01921](https://arxiv.org/abs/1811.01921) [[gr-qc](#)].

- [57] A. H. Nitz, T. Dent, G. S. Davies, et al. “2-OGC: Open Gravitational-wave Catalog of Binary Mergers from Analysis of Public Advanced LIGO and Virgo Data.” In: *ApJ* 891.2, 123 (Mar. 2020), p. 123. DOI: [10.3847/1538-4357/ab733f](https://doi.org/10.3847/1538-4357/ab733f). arXiv: [1910.05331](https://arxiv.org/abs/1910.05331) [[astro-ph.HE](#)].
- [58] W. Del Pozzo. “Inference of the cosmological parameters from gravitational waves: application to second generation interferometers.” In: *Phys. Rev. D* 86 (2012), p. 043011. DOI: [10.1103/PhysRevD.86.043011](https://doi.org/10.1103/PhysRevD.86.043011). arXiv: [1108.1317](https://arxiv.org/abs/1108.1317) [[astro-ph.CO](#)].
- [59] H.-Y. Chen, M. Fishbach, and D. E. Holz. “A two per cent Hubble constant measurement from standard sirens within five years.” In: *Nature* 562.7728 (2018), pp. 545–547. DOI: [10.1038/s41586-018-0606-0](https://doi.org/10.1038/s41586-018-0606-0). arXiv: [1712.06531](https://arxiv.org/abs/1712.06531) [[astro-ph.CO](#)].
- [60] M. Fishbach, R. Gray, I. Magaña Hernandez, et al. “A Standard Siren Measurement of the Hubble Constant from GW170817 without the Electromagnetic Counterpart.” In: *ApJ* 871.1, L13 (Jan. 2019), p. L13. DOI: [10.3847/2041-8213/aaf96e](https://doi.org/10.3847/2041-8213/aaf96e). arXiv: [1807.05667](https://arxiv.org/abs/1807.05667) [[astro-ph.CO](#)].
- [61] G. Scelfo, L. Boco, A. Lapi, et al. “Exploring galaxies-gravitational waves cross-correlations as an astrophysical probe.” In: *J. Cosmology Astropart. Phys.* 2020.10, 045 (Oct. 2020), p. 045. DOI: [10.1088/1475-7516/2020/10/045](https://doi.org/10.1088/1475-7516/2020/10/045). arXiv: [2007.08534](https://arxiv.org/abs/2007.08534) [[astro-ph.CO](#)].
- [62] A. Finke, S. Foffa, F. Iacovelli, et al. “Cosmology with LIGO/Virgo dark sirens: Hubble parameter and modified gravitational wave propagation.” In: *J. Cosmology Astropart. Phys.* 2021.8, 026 (Aug. 2021), p. 026. DOI: [10.1088/1475-7516/2021/08/026](https://doi.org/10.1088/1475-7516/2021/08/026). arXiv: [2101.12660](https://arxiv.org/abs/2101.12660) [[astro-ph.CO](#)].
- [63] C. Cigarrán Díaz and S. Mukherjee. “Mapping the cosmic expansion history from LIGO-Virgo-KAGRA in synergy with DESI and SPHEREx.” In: *MNRAS* 511.2 (Apr. 2022), pp. 2782–2795. DOI: [10.1093/mnras/stac208](https://doi.org/10.1093/mnras/stac208). arXiv: [2107.12787](https://arxiv.org/abs/2107.12787) [[astro-ph.CO](#)].
- [64] S. Mukherjee, A. Krolewski, B. D. Wandelt, et al. “Cross-correlating dark sirens and galaxies: measurement of H_0 from GWTC-3 of LIGO-Virgo-KAGRA.” In: *arXiv e-prints*, arXiv:2203.03643 (Mar. 2022), arXiv:2203.03643. arXiv: [2203.03643](https://arxiv.org/abs/2203.03643) [[astro-ph.CO](#)].
- [65] S. R. Taylor, J. R. Gair, and I. Mandel. “Cosmology using advanced gravitational-wave detectors alone.” In: *Phys. Rev. D* 85.2, 023535 (Jan. 2012), p. 023535. DOI: [10.1103/PhysRevD.85.023535](https://doi.org/10.1103/PhysRevD.85.023535). arXiv: [1108.5161](https://arxiv.org/abs/1108.5161) [[gr-qc](#)].
- [66] W. M. Farr, M. Fishbach, J. Ye, et al. “A Future Percent-level Measurement of the Hubble Expansion at Redshift 0.8 with Advanced LIGO.” In: *ApJ* 883.2, L42 (Oct. 2019), p. L42. DOI: [10.3847/2041-8213/ab4284](https://doi.org/10.3847/2041-8213/ab4284). arXiv: [1908.09084](https://arxiv.org/abs/1908.09084) [[astro-ph.CO](#)].

- [67] S. Mastrogiovanni, K. Leyde, C. Karathanasis, et al. “On the importance of source population models for gravitational-wave cosmology.” In: *Phys. Rev. D* 104.6, 062009 (Sept. 2021), p. 062009. DOI: [10.1103/PhysRevD.104.062009](https://doi.org/10.1103/PhysRevD.104.062009). arXiv: [2103.14663](https://arxiv.org/abs/2103.14663) [gr-qc].
- [68] J. M. Ezquiaga and D. E. Holz. “Jumping the Gap: Searching for LIGO’s Biggest Black Holes.” In: *Astrophys. J. Lett.* 909.2 (2021), p. L23. DOI: [10.3847/2041-8213/abe638](https://doi.org/10.3847/2041-8213/abe638). arXiv: [2006.02211](https://arxiv.org/abs/2006.02211) [astro-ph.HE].
- [69] J. M. Ezquiaga and D. E. Holz. “Spectral Sirens: Cosmology from the Full Mass Distribution of Compact Binaries.” In: *Phys. Rev. Lett.* 129.6 (2022), p. 061102. DOI: [10.1103/PhysRevLett.129.061102](https://doi.org/10.1103/PhysRevLett.129.061102). arXiv: [2202.08240](https://arxiv.org/abs/2202.08240) [astro-ph.CO].
- [70] H. Yu, B. Seymour, Y. Wang, et al. “Uncertainty and bias of cosmology and astrophysical population model from statistical dark sirens.” In: *arXiv e-prints*, arXiv:2206.09984 (June 2022), arXiv:2206.09984. arXiv: [2206.09984](https://arxiv.org/abs/2206.09984) [astro-ph.CO].
- [71] C. L. MacLeod and C. J. Hogan. “Precision of Hubble constant derived using black hole binary absolute distances and statistical redshift information.” In: *Phys. Rev. D* 77 (2008), p. 043512. DOI: [10.1103/PhysRevD.77.043512](https://doi.org/10.1103/PhysRevD.77.043512). arXiv: [0712.0618](https://arxiv.org/abs/0712.0618) [astro-ph].
- [72] R. Nair, S. Bose, and T. D. Saini. “Measuring the Hubble constant: Gravitational wave observations meet galaxy clustering.” In: *Phys. Rev. D* 98.2 (2018), p. 023502. DOI: [10.1103/PhysRevD.98.023502](https://doi.org/10.1103/PhysRevD.98.023502). arXiv: [1804.06085](https://arxiv.org/abs/1804.06085) [astro-ph.CO].
- [73] R. Gray et al. “Cosmological inference using gravitational wave standard sirens: A mock data analysis.” In: *Phys. Rev. D* 101.12 (2020), p. 122001. DOI: [10.1103/PhysRevD.101.122001](https://doi.org/10.1103/PhysRevD.101.122001). arXiv: [1908.06050](https://arxiv.org/abs/1908.06050) [gr-qc].
- [74] S. Mukherjee, B. D. Wandelt, S. M. Nissanke, et al. “Accurate precision cosmology with redshift unknown gravitational wave sources.” In: *Phys. Rev. D* 103.4, 043520 (Feb. 2021), p. 043520. DOI: [10.1103/PhysRevD.103.043520](https://doi.org/10.1103/PhysRevD.103.043520). arXiv: [2007.02943](https://arxiv.org/abs/2007.02943) [astro-ph.CO].
- [75] R. Abbott et al. “Constraints on the cosmic expansion history from GWTC-3.” In: (Nov. 2021). arXiv: [2111.03604](https://arxiv.org/abs/2111.03604) [astro-ph.CO].
- [76] A. G. Riess et al. “A Comprehensive Measurement of the Local Value of the Hubble Constant with 1 km/s/Mpc Uncertainty from the Hubble Space Telescope and the SH0ES Team.” In: (Dec. 2021). arXiv: [2112.04510](https://arxiv.org/abs/2112.04510) [astro-ph.CO].
- [77] P. Amaro-Seoane et al. “Laser Interferometer Space Antenna.” In: (Feb. 2017). arXiv: [1702.00786](https://arxiv.org/abs/1702.00786) [astro-ph.IM].

- [78] K. A. Kuns, H. Yu, Y. Chen, et al. “Astrophysics and cosmology with a decihertz gravitational-wave detector: TianGO.” In: *Phys. Rev. D* 102.4 (2020), p. 043001. DOI: [10.1103/PhysRevD.102.043001](https://doi.org/10.1103/PhysRevD.102.043001). arXiv: [1908.06004](https://arxiv.org/abs/1908.06004) [gr-qc].
- [79] M. A. Sedda et al. “The missing link in gravitational-wave astronomy: discoveries waiting in the decihertz range.” In: *Class. Quant. Grav.* 37.21 (2020), p. 215011. DOI: [10.1088/1361-6382/abb5c1](https://doi.org/10.1088/1361-6382/abb5c1). arXiv: [1908.11375](https://arxiv.org/abs/1908.11375) [gr-qc].
- [80] H. Yu and Y. Chen. “Direct determination of supermassive black hole properties with gravitational-wave radiation from surrounding stellar-mass black hole binaries.” In: *Phys. Rev. Lett.* 126.2 (2021), p. 021101. DOI: [10.1103/PhysRevLett.126.021101](https://doi.org/10.1103/PhysRevLett.126.021101). arXiv: [2009.02579](https://arxiv.org/abs/2009.02579) [gr-qc].
- [81] H.-Y. Chen and D. E. Holz. “Finding the One: Identifying the Host Galaxies of Gravitational-Wave Sources.” In: (Dec. 2016). arXiv: [1612.01471](https://arxiv.org/abs/1612.01471) [astro-ph.HE].
- [82] J. Aasi et al. “Advanced LIGO.” In: *Class. Quant. Grav.* 32 (2015), p. 074001. DOI: [10.1088/0264-9381/32/7/074001](https://doi.org/10.1088/0264-9381/32/7/074001). arXiv: [1411.4547](https://arxiv.org/abs/1411.4547) [gr-qc].
- [83] F. Acernese et al. “Advanced Virgo: a second-generation interferometric gravitational wave detector.” In: *Class. Quant. Grav.* 32.2 (2015), p. 024001. DOI: [10.1088/0264-9381/32/2/024001](https://doi.org/10.1088/0264-9381/32/2/024001). arXiv: [1408.3978](https://arxiv.org/abs/1408.3978) [gr-qc].
- [84] T. Akutsu et al. “KAGRA: 2.5 Generation Interferometric Gravitational Wave Detector.” In: *Nature Astron.* 3.1 (2019), pp. 35–40. DOI: [10.1038/s41550-018-0658-y](https://doi.org/10.1038/s41550-018-0658-y). arXiv: [1811.08079](https://arxiv.org/abs/1811.08079) [gr-qc].
- [85] R. Adhikari, N. Smith, A. Brooks, et al. “LIGO Voyager Upgrade Concept.” In: (2017). LIGO Document T1400226. URL: <https://dcc.ligo.org/LIGO-T1400226>.
- [86] R. X. Adhikari et al. “A cryogenic silicon interferometer for gravitational-wave detection.” In: *Class. Quant. Grav.* 37.16 (2020), p. 165003. DOI: [10.1088/1361-6382/ab9143](https://doi.org/10.1088/1361-6382/ab9143). arXiv: [2001.11173](https://arxiv.org/abs/2001.11173) [astro-ph.IM].
- [87] M. Punturo et al. “The Einstein Telescope: A third-generation gravitational wave observatory.” In: *Class. Quant. Grav.* 27 (2010). Ed. by F. Ricci, p. 194002. DOI: [10.1088/0264-9381/27/19/194002](https://doi.org/10.1088/0264-9381/27/19/194002).
- [88] D. Reitze et al. “Cosmic Explorer: The U.S. Contribution to Gravitational-Wave Astronomy beyond LIGO.” In: *Bull. Am. Astron. Soc.* 51.7 (2019), p. 035. arXiv: [1907.04833](https://arxiv.org/abs/1907.04833) [astro-ph.IM].
- [89] S. Borhanian, A. Dhani, A. Gupta, et al. “Dark Sirens to Resolve the Hubble–Lemaître Tension.” In: *Astrophys. J. Lett.* 905.2 (2020), p. L28. DOI: [10.3847/2041-8213/abcaf5](https://doi.org/10.3847/2041-8213/abcaf5). arXiv: [2007.02883](https://arxiv.org/abs/2007.02883) [astro-ph.CO].

- [90] E. D. Hall et al. “Gravitational-wave physics with Cosmic Explorer: Limits to low-frequency sensitivity.” In: *Phys. Rev. D* 103.12 (2021), p. 122004. DOI: [10.1103/PhysRevD.103.122004](https://doi.org/10.1103/PhysRevD.103.122004). arXiv: [2012.03608](https://arxiv.org/abs/2012.03608) [gr-qc].
- [91] J. Harms, B. J. J. Slagmolen, R. X. Adhikari, et al. “Low-Frequency Terrestrial Gravitational-Wave Detectors.” In: *Phys. Rev. D* 88.12 (2013), p. 122003. DOI: [10.1103/PhysRevD.88.122003](https://doi.org/10.1103/PhysRevD.88.122003). arXiv: [1308.2074](https://arxiv.org/abs/1308.2074) [gr-qc].
- [92] P. Auclair et al. “Cosmology with the Laser Interferometer Space Antenna.” In: (Apr. 2022). arXiv: [2204.05434](https://arxiv.org/abs/2204.05434) [astro-ph.CO].
- [93] J. Luo et al. “TianQin: a space-borne gravitational wave detector.” In: *Class. Quant. Grav.* 33.3 (2016), p. 035010. DOI: [10.1088/0264-9381/33/3/035010](https://doi.org/10.1088/0264-9381/33/3/035010). arXiv: [1512.02076](https://arxiv.org/abs/1512.02076) [astro-ph.IM].
- [94] W.-R. Hu and Y.-L. Wu. “The Taiji Program in Space for gravitational wave physics and the nature of gravity.” In: *Natl. Sci. Rev.* 4.5 (2017), pp. 685–686. DOI: [10.1093/nsr/nwx116](https://doi.org/10.1093/nsr/nwx116).
- [95] W.-H. Ruan, Z.-K. Guo, R.-G. Cai, et al. “Taiji program: Gravitational-wave sources.” In: *Int. J. Mod. Phys. A* 35.17 (2020), p. 2050075. DOI: [10.1142/S0217751X2050075X](https://doi.org/10.1142/S0217751X2050075X). arXiv: [1807.09495](https://arxiv.org/abs/1807.09495) [gr-qc].
- [96] W. Del Pozzo, A. Sesana, and A. Klein. “Stellar binary black holes in the LISA band: a new class of standard sirens.” In: *Mon. Not. Roy. Astron. Soc.* 475.3 (2018), pp. 3485–3492. DOI: [10.1093/mnras/sty057](https://doi.org/10.1093/mnras/sty057). arXiv: [1703.01300](https://arxiv.org/abs/1703.01300) [astro-ph.CO].
- [97] D. Laghi, N. Tamanini, W. Del Pozzo, et al. “Gravitational-wave cosmology with extreme mass-ratio inspirals.” In: *Mon. Not. Roy. Astron. Soc.* 508.3 (2021), pp. 4512–4531. DOI: [10.1093/mnras/stab2741](https://doi.org/10.1093/mnras/stab2741). arXiv: [2102.01708](https://arxiv.org/abs/2102.01708) [astro-ph.CO].
- [98] L.-G. Zhu, L.-H. Xie, Y.-M. Hu, et al. “Constraining the Hubble constant to a precision of about 1% using multi-band dark standard siren detections.” In: *Sci. China Phys. Mech. Astron.* 65.5 (2022), p. 259811. DOI: [10.1007/s11433-021-1859-9](https://doi.org/10.1007/s11433-021-1859-9). arXiv: [2110.05224](https://arxiv.org/abs/2110.05224) [astro-ph.CO].
- [99] A. Sesana et al. “Unveiling the gravitational universe at μ -Hz frequencies.” In: *Exper. Astron.* 51.3 (2021), pp. 1333–1383. DOI: [10.1007/s10686-021-09709-9](https://doi.org/10.1007/s10686-021-09709-9). arXiv: [1908.11391](https://arxiv.org/abs/1908.11391) [astro-ph.IM].
- [100] A. D. A. M. Spallicci. “On the complementarity of pulsar timing and space laser interferometry for the individual detection of supermassive black hole binaries.” In: *Astrophys. J.* 764 (2013), p. 187. DOI: [10.1088/0004-637X/764/2/187](https://doi.org/10.1088/0004-637X/764/2/187). arXiv: [1107.5984](https://arxiv.org/abs/1107.5984) [gr-qc].
- [101] S. Kawamura et al. “Current status of space gravitational wave antenna DECIGO and BDECIGO.” In: (June 2020). arXiv: [2006.13545](https://arxiv.org/abs/2006.13545) [gr-qc].

- [102] S. Sato et al. “The status of DECIGO.” In: *J. Phys. Conf. Ser.* 840.1 (2017). Ed. by D. Giardini and P. Jetzer, p. 012010. DOI: [10.1088/1742-6596/840/1/012010](https://doi.org/10.1088/1742-6596/840/1/012010).
- [103] N. Seto, S. Kawamura, and T. Nakamura. “Possibility of direct measurement of the acceleration of the universe using 0.1-Hz band laser interferometer gravitational wave antenna in space.” In: *Phys. Rev. Lett.* 87 (2001), p. 221103. DOI: [10.1103/PhysRevLett.87.221103](https://doi.org/10.1103/PhysRevLett.87.221103). arXiv: [astro-ph/0108011](https://arxiv.org/abs/astro-ph/0108011).
- [104] J. Crowder and N. J. Cornish. “Beyond LISA: Exploring future gravitational wave missions.” In: *Phys. Rev. D* 72 (2005), p. 083005. DOI: [10.1103/PhysRevD.72.083005](https://doi.org/10.1103/PhysRevD.72.083005). arXiv: [gr-qc/0506015](https://arxiv.org/abs/gr-qc/0506015).
- [105] C. Cutler and D. E. Holz. “Ultra-high precision cosmology from gravitational waves.” In: *Phys. Rev. D* 80 (2009), p. 104009. DOI: [10.1103/PhysRevD.80.104009](https://doi.org/10.1103/PhysRevD.80.104009). arXiv: [0906.3752 \[astro-ph.CO\]](https://arxiv.org/abs/0906.3752).
- [106] M. Liu, C. Liu, Y.-M. Hu, et al. “Dark-siren Cosmology with Decihertz Gravitational-wave Detectors.” In: (May 2022). arXiv: [2205.06991 \[astro-ph.CO\]](https://arxiv.org/abs/2205.06991).
- [107] K. A. Kuns. “Future Networks of Gravitational Wave Detectors: Quantum Noise and Space Detectors.” PhD thesis. University of California, Santa Barbara, Mar. 2019.
- [108] L. S. Finn. “Detection, measurement and gravitational radiation.” In: *Phys. Rev. D* 46 (1992), pp. 5236–5249. DOI: [10.1103/PhysRevD.46.5236](https://doi.org/10.1103/PhysRevD.46.5236). arXiv: [gr-qc/9209010](https://arxiv.org/abs/gr-qc/9209010).
- [109] C. Cutler and E. E. Flanagan. “Gravitational waves from merging compact binaries: How accurately can one extract the binary’s parameters from the inspiral wave form?.” In: *Phys. Rev. D* 49 (1994), pp. 2658–2697. DOI: [10.1103/PhysRevD.49.2658](https://doi.org/10.1103/PhysRevD.49.2658). arXiv: [gr-qc/9402014](https://arxiv.org/abs/gr-qc/9402014).
- [110] R. Abbott et al. “The population of merging compact binaries inferred using gravitational waves through GWTC-3.” In: (Nov. 2021). arXiv: [2111.03634 \[astro-ph.HE\]](https://arxiv.org/abs/2111.03634).
- [111] S. V. Dhurandhar, K. R. Nayak, S. Koshti, et al. “Fundamentals of the LISA stable flight formation.” In: *Classical and Quantum Gravity* 22.3 (Feb. 2005), pp. 481–487. DOI: [10.1088/0264-9381/22/3/002](https://doi.org/10.1088/0264-9381/22/3/002). arXiv: [gr-qc/0410093 \[astro-ph\]](https://arxiv.org/abs/gr-qc/0410093).
- [112] S. Khan, S. Husa, M. Hannam, et al. “Frequency-domain gravitational waves from nonprecessing black-hole binaries. II. A phenomenological model for the advanced detector era.” In: *Phys. Rev. D* 93.4 (2016), p. 044007. DOI: [10.1103/PhysRevD.93.044007](https://doi.org/10.1103/PhysRevD.93.044007). arXiv: [1508.07253 \[gr-qc\]](https://arxiv.org/abs/1508.07253).

- [113] S. Husa, S. Khan, M. Hannam, et al. “Frequency-domain gravitational waves from nonprecessing black-hole binaries. I. New numerical waveforms and anatomy of the signal.” In: *Phys. Rev. D* 93.4 (2016), p. 044006. doi: [10.1103/PhysRevD.93.044006](https://doi.org/10.1103/PhysRevD.93.044006). arXiv: [1508.07250](https://arxiv.org/abs/1508.07250) [gr-qc].
- [114] C. Cutler. “Angular resolution of the LISA gravitational wave detector.” In: *Phys. Rev. D* 57 (1998), pp. 7089–7102. doi: [10.1103/PhysRevD.57.7089](https://doi.org/10.1103/PhysRevD.57.7089). arXiv: [gr-qc/9703068](https://arxiv.org/abs/gr-qc/9703068).
- [115] T. A. Apostolatos, C. Cutler, G. J. Sussman, et al. “Spin induced orbital precession and its modulation of the gravitational wave forms from merging binaries.” In: *Phys. Rev. D* 49 (1994), pp. 6274–6297. doi: [10.1103/PhysRevD.49.6274](https://doi.org/10.1103/PhysRevD.49.6274).
- [116] M. Vallisneri. “Use and abuse of the Fisher information matrix in the assessment of gravitational-wave parameter-estimation prospects.” In: *Phys. Rev. D* 77 (2008), p. 042001. doi: [10.1103/PhysRevD.77.042001](https://doi.org/10.1103/PhysRevD.77.042001). arXiv: [gr-qc/0703086](https://arxiv.org/abs/gr-qc/0703086).
- [117] D. W. Hogg. “Distance measures in cosmology.” In: (May 1999). arXiv: [astro-ph/9905116](https://arxiv.org/abs/astro-ph/9905116).
- [118] C. M. Hirata, D. E. Holz, and C. Cutler. “Reducing the weak lensing noise for the gravitational wave Hubble diagram using the non-Gaussianity of the magnification distribution.” In: *Phys. Rev. D* 81 (2010), p. 124046. doi: [10.1103/PhysRevD.81.124046](https://doi.org/10.1103/PhysRevD.81.124046). arXiv: [1004.3988](https://arxiv.org/abs/1004.3988) [astro-ph.CO].
- [119] C. Gordon, K. Land, and A. Slosar. “Cosmological Constraints from Type Ia Supernovae Peculiar Velocity Measurements.” In: *Phys. Rev. Lett.* 99 (2007), p. 081301. doi: [10.1103/PhysRevLett.99.081301](https://doi.org/10.1103/PhysRevLett.99.081301). arXiv: [0705.1718](https://arxiv.org/abs/0705.1718) [astro-ph].
- [120] P. Madau and M. Dickinson. “Cosmic Star Formation History.” In: *Ann. Rev. Astron. Astrophys.* 52 (2014), pp. 415–486. doi: [10.1146/annurev-astro-081811-125615](https://doi.org/10.1146/annurev-astro-081811-125615). arXiv: [1403.0007](https://arxiv.org/abs/1403.0007) [astro-ph.CO].
- [121] B. P. Abbott et al. “A Gravitational-wave Measurement of the Hubble Constant Following the Second Observing Run of Advanced LIGO and Virgo.” In: *Astrophys. J.* 909.2 (2021), p. 218. doi: [10.3847/1538-4357/abdcb7](https://doi.org/10.3847/1538-4357/abdcb7). arXiv: [1908.06060](https://arxiv.org/abs/1908.06060) [astro-ph.CO].
- [122] S. Kawamura et al. “Space gravitational-wave antennas DECIGO and B-DECIGO.” In: *Int. J. Mod. Phys. D* 28.12 (2019), p. 1845001. doi: [10.1142/S0218271818450013](https://doi.org/10.1142/S0218271818450013).
- [123] Z.-Q. You, X.-J. Zhu, G. Ashton, et al. “Standard-siren Cosmology Using Gravitational Waves from Binary Black Holes.” In: *ApJ* 908.2, 215 (Feb. 2021), p. 215. doi: [10.3847/1538-4357/abd4d4](https://doi.org/10.3847/1538-4357/abd4d4). arXiv: [2004.00036](https://arxiv.org/abs/2004.00036) [astro-ph.CO].

- [124] E. Trott and D. Huterer. “Challenges for the statistical gravitational-wave method to measure the Hubble constant.” In: (Nov. 2021). arXiv: [2112.00241 \[astro-ph.CO\]](#).
- [125] C. M. Biwer, C. D. Capano, S. De, et al. “PyCBC Inference: A Python-based parameter estimation toolkit for compact binary coalescence signals.” In: *Publ. Astron. Soc. Pac.* 131.996 (2019), p. 024503. doi: [10.1088/1538-3873/aaef0b](#). arXiv: [1807.10312 \[astro-ph.IM\]](#).

Part II

Measuring Hierarchical Triples around Active Galactic Nuclei with Decihertz Detectors

DETECTING GRAVITATIONAL LENSING IN HIERARCHICAL TRIPLES IN GALACTIC NUCLEI WITH SPACE-BORNE GRAVITATIONAL-WAVE OBSERVATORIES

- [1] H. Yu, Y. Wang, B. Seymour, et al. “Detecting gravitational lensing in hierarchical triples in galactic nuclei with space-borne gravitational-wave observatories.” In: *Phys. Rev. D* 104.10 (2021), p. 103011. doi: [10.1103/PhysRevD.104.103011](https://doi.org/10.1103/PhysRevD.104.103011). arXiv: [2107.14318](https://arxiv.org/abs/2107.14318) [gr-qc].

4.1 Introduction

Since September 14, 2015 [1], ground-based gravitational-wave (GW) observatories including LIGO [2], Virgo [3], and KAGRA [4] have achieved great success with tens of GW events detected so far [5, 6]. A new window for human beings to observe the Universe using GW radiation has since been opened up. Looking towards future, more excitements await us as multiple space-borne GW observatories are proposed to be launched in the near future, including LISA [7], TianQin [8], Taiji [9], B-DECIGO [10, 11], Decihertz Observatories [12], and TianGO [13]. Their sensitivity covers the 0.001 to 0.1 Hz band, allowing them to observe typical, stellar-mass binary black hole (BBH) systems for years prior to the final merger. It thus opens the possibility of using the slowly chirping GW radiation from a stellar-mass BBH as a carrier signal to search for external modulations induced by environmental perturbations.

One particularly interesting scenario is if the stellar-mass BBH is in a galactic nucleus where a supermassive black hole (SMBH) resides. Such a hierarchical triple system (“BBH + SMBH”) is expected because there are theories predicting that the environment in a galactic nucleus can facilitate the merger of stellar-mass BBH. One channel that has been studied extensively in the literature is due to gaseous effects [14, 15, 16, 17, 18, 19]. If the BBH lives in a gaseous disk of an active galactic nuclei (AGN), the gas can provide extra frictional force on the BBH in addition to the force induced by GW radiation and thus hardens its orbit (the inner orbit). In addition to shrinking the orbit of the BBH itself, gas can also help the center of mass of the BBH to migrate in the AGN disk and thus alter its orbit around the SMBH [20,

21]. Even without gas, dynamical interactions of a variety of flavors may also help the formation of compact BBHs [22, 23, 24, 25, 26, 27, 28, 29, 30, 31], providing yet another channel for the formation of ‘‘BBH + SMBH’’ triple systems.

Similar to the formation channels, the environmental perturbation on the BBH’s GW waveform in such a triple system can also be divided up into two main classes. One is still due to the gaseous friction, and its main effect is to make the BBH appear to be more massive than its true value [32, 33, 34, 35]. This effect is most prominent when the GW decay timescale of the BBH is a few kilo-years (comparable to the hardening timescale due to the gas), but is subdominant for more compact (i.e., ‘‘harder’’) BBHs that will merge in a few years.

The other type of modulation is directly related to the gravitational field of the SMBH and is the main focus of our discussion here. The leading-order effect arises from the orbital motion of the center of mass of the BBH orbiting around the SMBH (i.e., the outer orbit), leading to a Doppler phase shift in the GW waveform emitted by the BBH. It has been shown that this Doppler phase shift might be detectable for BBHs as far as 1 pc away from the SMBH [36], and when the outer orbital period is less than a few years (set by the duration of the observation), the frequency of the Doppler phase shift can be measured, which further constrains the mass density enclosed by the outer orbit [37]. Beyond the leading-order effect, the Newtonian tidal effect (which typically manifested as the Lidov-Kozai effect) may also play a role for a triple system with an inner orbital separation of $\sim 0.1 AU$ [38, 39, 40]. For more compact BBHs with separation of $\sim 10^{-3} AU$, Ref. [41] showed that the (post-Newtonian) de Sitter-like precession of the BBH’s orbital plane [42, 43, 44] is the more critical correction to the waveform and can be detectable by space-borne GW detectors out to a cosmological distance of $\sim 1 Gpc$. Combining the de Sitter-like precession and the Doppler shift, Ref. [41] further demonstrated that the mass of the central SMBH can be determined, which complements the existing direct methods of measuring the mass of an SMBH [45].

Recently, Ref. [46] further considered the strong gravitational lensing of the BBH’s GW caused by the SMBH and showed that there is a high geometrical probability ($\sim 10\%$) for lensing to happen if the BBH is in an outer orbit with a period of less than a year (shorter than the duration of the observation). Ref. [46] referred to this as ‘‘repeated lensing.’’ Indeed, if the outer period is long (much longer than the observation duration), then in order for the BBH to be lensed, it needs to have both the right azimuthal and polar angles such that the angular separation between the source

and the lens is sufficiently small to be comparable with the Einstein ring. However, the short orbital period in the repeated-lensing regime allows the inner BBH to scan through the azimuthal angle and there will thus always be an instant during the observation when the BBH is behind the SMBH. Therefore, the BBH only needs to have the right polar angle. Furthermore, because the outer orbital radius is smaller, it is also more likely for the BBH to be within the Einstein ring of the SMBH.

Ref. [46] focused on the standard strong lensing, which treats the SMBH as a Newtonian point particle and lensing happens when the source is behind the lens (i.e., the source and the observer are on opposite sides of the lens). Meanwhile, the strong gravity field of the SMBH can further lead to relativistic lensing signatures [47, 48, 49, 50, 51]. One such example is retro-lensing (which is also closely related to the glory-scattering of an SMBH) [52, 53, 54, 55, 56]. Retro-lensing happens when the BBH is in front of the SMBH: the GW emitted by the BBH towards the SMBH gets bent by the strong gravity potential of the SMBH by an angle of approximately π and eventually reaches the observer. For the same reason that repeated strong lensing is likely in BBH + SMBH triples, repeated retro-lensing also has a relatively high probability to happen (as it corresponds to the same geometrical configuration as the standard lensing but just with the outer orbital phase shifted by π). Therefore, retro-lensing should also be incorporated in the waveform modeling.

Furthermore, the parameter space where repeated lensing happens [46] largely overlaps with the parameter space where the de Sitter precession is detectable [41]. It is thus critical to incorporate both effects in the waveform modeling. More importantly, we note that including the lensing effects does not introduce any new parameters compared to the one needed for modeling the orbital dynamics. As shown in Ref. [57], the lensing effect can be parameterized in terms of the mass of the lens (i.e., the SMBH) and the sky projection of the source for point-source lenses. All of them can also be independently inferred from the combination of Doppler shift and de Sitter precession as illustrated in Ref. [41]. Therefore, the two effects can be combined to enhance the overall parameter estimation (PE) accuracy, and checked against each other to test the consistency of theories behind each effect.

Therefore, in this work our goal is to construct GW waveforms of a BBH in the vicinity of an SMBH, including effects of the SMBH on both the orbital dynamics (Doppler shift and de Sitter precession) and lensing (standard lensing and retro-lensing). We will further use the waveform to quantify the detectability of the lensing

signatures. Moreover, we also assess the accuracy of PE of the triple system, in particular the mass of the central SMBH.

Throughout this study, we will refer to the stellar-mass BBH (consists of $M_1, M_2 \sim$ a few $\times 10 M_\odot$) as the inner binary and quantities associated with it will often be denoted with a subscript ‘‘ i .’’ The inner orbit decays via gravitational radiation; the GW it emits serves as the signal carrier in our study. The orbit of the inner binary’s center of mass around the SMBH ($M_3 \sim 10^5 - 10^{10} M_\odot$) is referred to as the outer orbit and is denoted with a subscript ‘‘ o .’’ The GW radiation of the outer binary can be safely ignored for systems of our interest. For simplicity, we ignore the spin of the SMBH and treat it as a Schwarzschild BH. We further restrict our discussion here to the simple case where both the inner and the outer orbits are circular. The general case that allows for orbital eccentricities is deferred to future studies. Moreover, all values in our study are measured in the detector frame. In other words, they are redshifted by the cosmological expansion ($z_{cos} \sim 0.2 - 0.3$ for sources at a luminosity distance on the order of 1 Gpc) and the gravity of the SMBH ($z_{grav} \sim 10^{-3} - 0.01$ for typical outer orbits we consider). We use geometrical units $G = c = 1$.

The paper is organized as follows. In Sec. 4.2 we describe our construction of the GW waveform including effects due to both standard strong lensing (Sec. 4.2) and retro-lensing (Sec. 4.2). We then examine the detectability of lensing effects by space-based GW observatories like LISA [7] and TianGO [13] in Sec. 4.3 by considering the mismatches between waveforms with and without lensing. The PE analysis including both lensing and orbital dynamics (Doppler + de Sitter) is presented in Sec. 4.4. Specifically, we consider the enhancement in the PE accuracy of the SMBH’s mass in Sec. 4.4, followed in Sec. 4.4 by a study on how well we can test the consistency between the SMBH’s mass determined from the lensing signal and that from the orbital dynamics. Lastly, we conclude in Sec. 7.5 together with a discussion on effects to be further incorporated by future studies.

4.2 GW waveforms including gravitational lensing

In this section, we describe our modeling of the GW waveform. We will start by briefly reviewing the waveform construction without lensing effects, which closely follows Ref. [41]. This is followed by Sec. 4.2 in which we consider the standard lensing. In Sec. 4.2, we further incorporate the retro-lensing into the waveform. We conclude our waveform modeling in Sec. 4.2 by examining a few representative

waveforms including lensing effects and sketching out the parameter space for the lensing signatures to be potentially significant.

Following Ref. [57], we write the lensed waveform [denoted by a superscript “ (l) ”] as

$$\tilde{h}^{(l)}(f) = F(f)\tilde{h}(f), \quad (4.1)$$

where $\tilde{h}(f)$ is the frequency-domain waveform without lensing and the quantity $F(f)$ is an amplification factor due to the gravitational lensing.

To model $\tilde{h}(f)$, we follow Ref. [41] and write (see also Refs [58, 59])

$$\begin{aligned} \tilde{h}(f) &= \Lambda(t)\tilde{h}_c(f) \\ &= [A_+^2(t)F_+^2(t) + A_\times^2(t)F_\times^2(t)]^{1/2} \\ &\quad \times \exp\{-i[\Phi_p(t) + 2\Phi_T(t) + \Phi_D(t)]\}\tilde{h}_c(f), \end{aligned} \quad (4.2)$$

where $\tilde{h}_c(f)$ is the antenna-independent carrier waveform, which we further model using the quadrupole formula as

$$\begin{aligned} \tilde{h}_c(f) &= \left(\frac{5}{96}\right)^{1/2} \frac{\mathcal{M}^{5/6}}{\pi^{2/3}D} f^{-7/6} \\ &\quad \times \exp\left\{i\left[2\pi f t_c - \phi_c - \frac{\pi}{4} + \frac{3}{4}(8\pi\mathcal{M}f)^{-5/3}\right]\right\}, \end{aligned} \quad (4.3)$$

where \mathcal{M} , D , t_c , and ϕ_c are the chirp mass (in the detector frame), luminosity distance, time and phase of coalescence, respectively.

The antenna response is incorporated under the leading-order stationary phase approximation (SPA), which first evaluates each quantity as a function of time t , and then express the time as a function of frequency, $t = t(f)$, following

$$t(f) = t_c - 5(8\pi f)^{-8/3}\mathcal{M}^{-5/3}. \quad (4.4)$$

Furthermore, in Eq. (4.2) we have defined $A_+ = 1 + (\hat{\mathbf{L}}_i \cdot \hat{\mathbf{N}})^2$ and $A_\times = -2\hat{\mathbf{L}}_i \cdot \hat{\mathbf{N}}$, where $\hat{\mathbf{L}}_i$ is the orientation of the inner orbital angular momentum and $\hat{\mathbf{N}}$ is the line of sight. The quantities F_+ and F_\times are the “detector beam-pattern”, $\Phi_p = \arctan[-A_\times F_\times / A_+ F_+]$ is the polarization phase, and Φ_T is the Thomas precession phase. Their expressions can be found in, e.g., Refs. [58, 59, 41]. Note that they are time-dependent because of motions of both the detector in the solar frame and the inner binary in the SMBH frame. Specifically, we assume the detector follows an orbit as described in Ref. [60] and the its explicit orientation can be found in, e.g.,

Ref. [41] for a 90°-detector like TianGO [13], and Ref. [59] for a 60°-detector like LISA [7]. For the inner binary's orientation, we include the de Sitter-like precession [42, 43], which can be expressed as [41]

$$\frac{d\hat{\mathbf{L}}_i}{dt} = \Omega_{\text{dS}} \hat{\mathbf{L}}_o \times \hat{\mathbf{L}}_i = \frac{3}{2} \frac{M_3}{a_o} \Omega_o \hat{\mathbf{L}}_o \times \hat{\mathbf{L}}_i, \quad (4.5)$$

for a circular outer orbit. Here $\Omega_o = 2\pi/P_o = \sqrt{M_3/a_o^3}$ is the orbital period with M_3 the mass of the SMBH and a_o the semi-major axis of the outer orbit. We denote the outer orbital angular momentum as \mathbf{L}_o and the total angular momentum of the triple as $\mathbf{J} = \mathbf{L}_o + \mathbf{L}_i \simeq \mathbf{L}_o$. We will further define $\lambda_L \equiv \arccos(\hat{\mathbf{L}}_i \cdot \hat{\mathbf{L}}_o)$ as the opening angle between the inner and outer orbital angular momenta.

Lastly, the center of mass motion of the inner binary around the SMBH and the detector around the Sun are included via a Doppler phase, Φ_D , as [59]

$$\Phi_D = 2\pi f \left[r_{o,\parallel} \cos\left(\Omega_o t + \phi^{(0)}\right) + r_{\oplus,\parallel} \cos\left(\frac{2\pi t}{yr} - \bar{\phi}_S\right) \right], \quad (4.6)$$

where $r_{o,\parallel} = a_o \sin \iota_J$ and $r_{\oplus,\parallel} = AU \sin \bar{\theta}_S$. Here $\iota_J = \arccos(\hat{\mathbf{L}}_o \cdot \hat{\mathbf{N}})$ is the inclination of the outer orbit, $\phi^{(0)}$ is an initial phase, and $\bar{\theta}_S$ and $\bar{\phi}_S$ are the polar and azimuthal angles of $\hat{\mathbf{N}}$ in the solar frame (following the notations used in Ref. [41], we use a bar to denote angular coordinates in the solar frame). Consistent with the treatment in Ref. [59], we include only the phase term of the Doppler shift Φ_D but drop the amplitude boosts like $\sim (1 - \dot{r}_{o,\parallel})$ for simplicity. Indeed, when we consider each term's contribution to parameter estimation by computing $(\partial \tilde{h} / \partial r_{o,\parallel})$, the magnitude of the phase term's contribution is $\propto 2\pi f$ while the amplitude term's contribution is $\propto \Omega_o \sim 10^{-5} \times 2\pi f$. For similar reasons, we ignore the time shifts [due to the propagation of the wave from the inner binary to the SMBH $\sim r_{o,\parallel} \lesssim 0.5$ day and from the Sun to the detector $\sim r_{\oplus,\parallel} \sim 500$ s, as well as the extra time delay induced by the SMBH $\sim M_3 \lesssim 500$ s] in other non-Doppler terms in $\Lambda(t)$ because their variation rate is much smaller compared to the GW frequency f .

Before we proceed to discuss the lensing amplification factor $F(f)$ in Secs. 4.2 (for standard lensing) and 4.2 (for retro-lensing), we would like to emphasize that the various effects entering our waveform modeling are typically computed using the lowest-order approximations. This is because our goal is to examine the detectability of various lensing effects and to estimate their effects on the PE accuracy. The

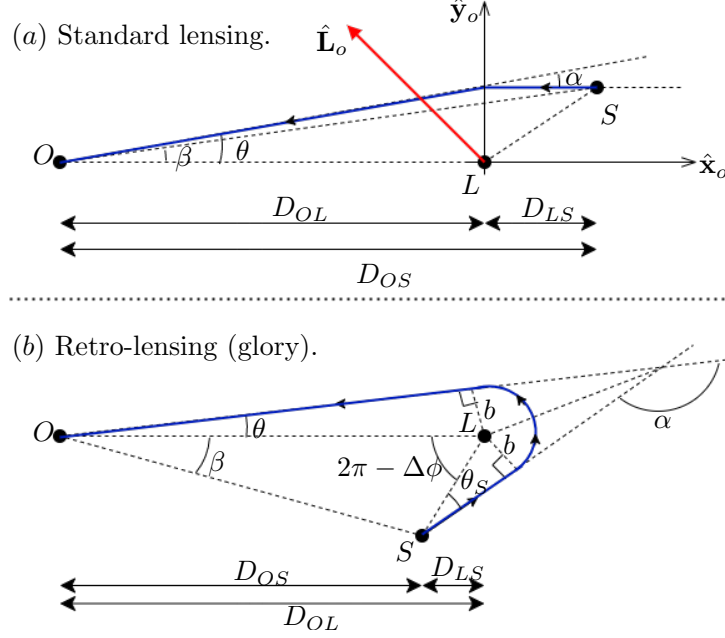


Figure 4.1: Cartoon illustrating the lensing geometry. The top part corresponds to the standard lensing scenario (i.e., the strong lensing) where the source is behind the lens and the deflection angle $\alpha \ll \pi$ (and here we specifically draw the instance when $z_o = \phi_o = 0$). The bottom illustrates the geometry of retro-lensing (also known as the glory). Note in the repeated lensing scenario, we have $D_{OL} \simeq D_{OS} \simeq D \sim 1 \text{ Gpc}$ and $D_{LS} \lesssim 100 \text{ AU} \ll D_{OL}, D_{OS}$.

construction of sufficiently precise templates that can be used for, e.g., signal detection via matched-filtering, are deferred to future studies. Nonetheless, we derive in Appx. 4.6 a general expression that improves the accuracy of the waveform under the SPA when the antenna response has a fast temporal variation. The waveform in Appx. 4.6, while not used in this work for simplicity, can be readily adopted by future studies when more accurate waveforms are desired.

Standard lensing under weak-deflection limit

We start the discussion of lensing effects by considering the standard lensing scenario, illustrated in the top part in Fig. 4.1. This corresponds to the well-known strong lensing by the SMBH. In this scenario, the GW emitted by the source (S , which is the inner binary consisting of M_1 and M_2) is bent by the lens (L , which is the SMBH M_3) and then arrives at the observer O . We use β and θ to indicate the angular location of the source and the image, respectively. The deflection angle is

indicated by α . Geometrically, we have

$$\beta = \theta - \frac{D_{LS}}{D_{OS}}\alpha. \quad (4.7)$$

Note in this case, $\alpha \ll \pi$ and therefore the weak-deflection limit applies (which is to be contrasted with the retro-lensing scenario in Sec. 4.2).

For future convenience, we construct a reference frame (x_o, y_o, z_o) centered on the SMBH M_3 and $\hat{\mathbf{x}}_o$ is aligned with the line of sight $\hat{\mathbf{N}}$ (i.e., along the line OL). The x_o - y_o plane is defined by the plane formed by the line of sight $\hat{\mathbf{N}}$ and the total angular momentum of the system $\hat{\mathbf{J}} \simeq \hat{\mathbf{L}}_o$ (as the spin of the SMBH is ignored). The inclination of the outer orbit is defined as ι_J with $\cos \iota_J = \hat{\mathbf{N}} \cdot \hat{\mathbf{L}}_o$.

In this frame, we can write the source location as

$$\begin{cases} x_o(t) = a_o \sin \iota_J \cos \phi_o(t), \\ y_o(t) = a_o \cos \iota_J \cos \phi_o(t), \\ z_o(t) = -a_o \sin \phi_o(t), \end{cases} \quad (4.8)$$

where $\phi_o(t) = \Omega_o t + \phi_o^{(0)}$ is the orbital phase of the outer orbit with $\Omega_o = \sqrt{M_3/a_o^3}$. Using these coordinates, we further have

$$D_{LS}(t) = x_o(t), \quad (4.9)$$

$$\beta(t) = \frac{\sqrt{y_o^2(t) + z_o^2(t)}}{D_{OL}}. \quad (4.10)$$

Approximating the lens as a point mass (as we typically have $a_o \sim 100$ – $1,000 M_3 \gg M_3$ for systems of interests), we then have a time-dependent $F(t; f)$ as [57] (see also Refs. [61, 46]; note this is applied only when $x_o > 0$ or the source is behind the lens)

$$\begin{aligned} F(t; f) = \exp \left\{ \frac{\pi w}{4} + i \frac{w}{2} \left[\ln \left(\frac{w}{2} \right) - 2\phi_m(\eta) \right] \right\} \\ \times \Gamma \left(1 - i \frac{w}{2} \right) {}_1F_1 \left(i \frac{w}{2}, 1; i \frac{w\eta^2}{2} \right), \end{aligned} \quad (4.11)$$

where $w(f) = 8\pi M_3 f$, $\phi_m[\eta(t)] = [\eta_m(t) - \eta(t)]^2/2 - \ln \eta(t)$, and $\eta_m(t) = \left\{ \eta(t) + [\eta^2(t) + 4]^{1/2} \right\}/2$. The quantity $\eta(t)$ is the angular location of the source normalized by the Einstein radius, $\eta(t) = \beta(t)/\theta_{\text{Ein}}(t)$ with $\theta_{\text{Ein}}(t) = \sqrt{4M_3 D_{LS}(t)/(D_{OS} D_{OL})}$ the Einstein radius. Under the SPA, the time t can be further treated as a function of f via Eq. (4.4). Note that both $\beta(t)$ and $D_{LS}(t)$ vary with the outer orbital phase. When the outer orbital period is shorter than the duration of the observation

$P_{obs} \sim 5 \text{ yr}$, we can see multiple lensing-induced peaks (as we will see shortly in, e.g., Fig. 4.3), and therefore the system is repeatedly lensed [46].

When $w \gg 1$ or $f \gg 1 \text{ mHz} (M_3/10^7 M_\odot)^{-1}$ (, which is a condition typically well-satisfied for systems we are interested in), the full expression Eq. (4.11) reduces to the geometrical limit as a sum over images j [62, 57]

$$F(t; f) = \sum_j |\mu_j|^{1/2} \exp(2\pi i f t_{l,j} - i\pi n_j), \quad (4.12)$$

where μ_j is the magnification of the j 'th image, $t_{l,j}$ is the time delay of each image (we use the subscript ‘ l ’ to indicate it is a quantity associated with lensing effects), and $n_j = 0, 1/2$, or 1 when the image’s traveling time is a minimum, saddle point, or maximum. For the standard-lensing configuration and treating M_3 as a point mass, two images form and

$$F(t; f) = |\mu_1(t)|^{1/2} - i|\mu_2(t)|^{1/2} e^{2\pi i f \Delta t_l(t)}, \quad (4.13)$$

where

$$\mu_{1,2}(t) = \frac{1}{2} \pm \frac{\eta^2(t) + 2}{2\eta(t) [\eta^2(t) + 4]^{1/2}}, \quad (4.14)$$

$$\Delta t_l(t) = 4M_3 \left(\frac{\eta(t) [\eta^2(t) + 4]^{1/2}}{2} + \ln \left\{ \frac{[\eta^2(t) + 4]^{1/2} + \eta(t)}{[\eta^2(t) + 4]^{1/2} - \eta(t)} \right\} \right). \quad (4.15)$$

Retro-lensing

When the BBH is in front of the SMBH, its GW can still experience a retro-lensing with the wave bent by the SMBH by an angle of $\simeq \pi$. This is also known as the ‘‘glory’’ and is caused by the short-range attractive force of the SMBH. The geometry is illustrated in the bottom of Fig. 4.1.

We define $\Delta\phi = \phi_O - \phi_S + 2\pi$ such that $\Delta\phi \in [0, 2\pi)$, with $\phi_{O(S)}$ the azimuthal angle of the observer (source) in the projected plot shown in the bottom of Fig. 4.1. As we prove in Appx. 4.7, we have the following geometrical relations when the observer, source, and lens are nearly aligned,

$$\pi - \Delta\phi \simeq \frac{D_{OL}}{D_{LS}} \theta - \alpha, \quad (4.16)$$

$$\tan \beta = \tan \theta - \frac{D_{LS}}{D_{OS}} \tan \alpha. \quad (4.17)$$

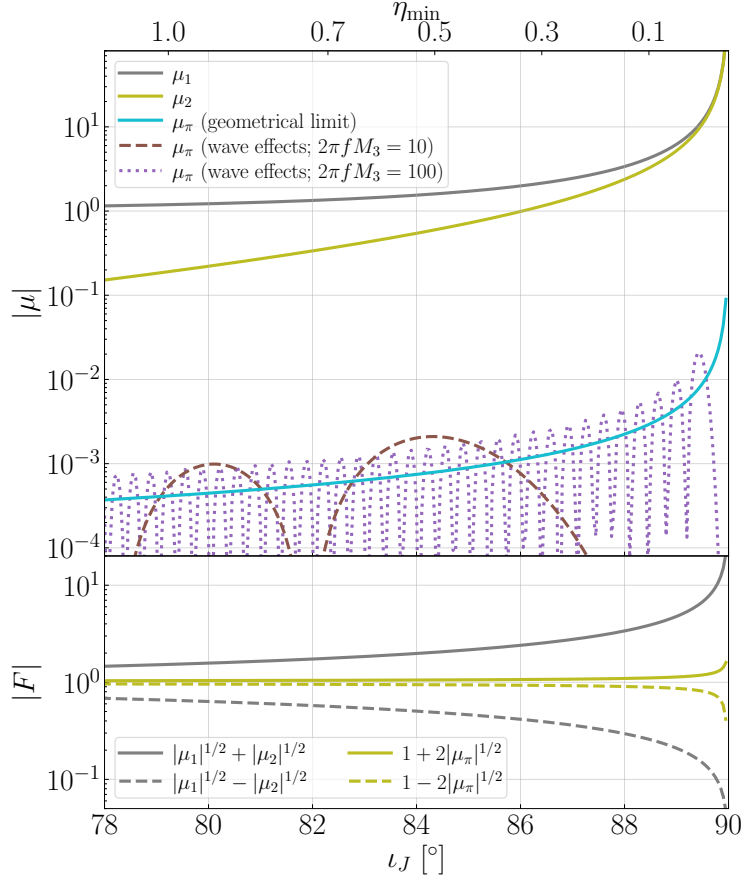


Figure 4.2: Top panel: magnification $|\mu|$ as a function of the inclination angle ι_J of the outer orbit. Bottom panel: upper and lower envelopes of the amplification factor. Here we assume $M_3 = 10^8 M_\odot$ and $a_o = 100 \text{ AU}$. The outer orbital phase is either $\phi_o = 0$ (for standard lensing) or $\phi_o = \pi$ (for retro-lensing). For such $M_3 = 10^8 M_\odot$, $2\pi f M_3 = 100$ correspond to a GW frequency of $f \simeq 0.03 \text{ Hz}$.

For a Schwarzschild lens, the closest impact a photon can make is $b_{ps} = 3\sqrt{3}M_3$ for it to not be absorbed by the lens (see, e.g., Ref. [52]). Light rays having an impact parameter b slightly greater than b_{ps} may eventually reach the observer after making one or more turns around the SMBH. Infinitely many images thus form at [56]

$$\theta_m = \theta_m^0 \mp \zeta_m \Delta\alpha, \quad (4.18)$$

with

$$\alpha = \pm\Delta\alpha \pm m\pi, \quad (4.19)$$

$$\theta_m^0 = \theta_{ps} \left[1 + e^{(c_2 - m\pi)/c_1} \right], \quad (4.20)$$

$$\zeta_m = \frac{\theta_{ps}}{c_1} e^{(c_2 - m\pi)/c_1}, \quad (4.21)$$

where $\theta_{ps} = b_{ps}/D_{OL}$, $m \in \mathbb{N}^+$, and c_1 and c_2 are constants determined by the metric. For the Schwarzschild metric, $c_1 = 1$ and $c_2 = \ln \left[216(7 - 4\sqrt{3}) \right] - \pi \simeq -0.40$, leading to $\theta_{ps} = 5.35M/D_{OL}$ and $\zeta_m = 0.15M/D_{OL} \exp [-(m-1)\pi]$ [56]. For high alignment, the amplification of each image is given by [55, 56]

$$\begin{aligned} \mu_{m\pi}(t) &= \left(\frac{D_{OS}}{D_{LS}} \right)^2 \frac{\theta_m^0 \zeta_m}{\sin \Delta\phi(t)}, \\ &\simeq \frac{0.80}{\sin \Delta\phi(t)} \left(\frac{M_3}{D_{LS}} \right)^2 e^{-(m-1)\pi}, \\ &\simeq \frac{0.80}{\beta(t)} \left(\frac{M_3^2}{D_{LS} D_{OL}} \right) e^{-(m-1)\pi}, \end{aligned} \quad (4.22)$$

where in the second line we have plugged in the values for a Schwarzschild BH and used $D_{OS} \simeq D_{OL}$ in our case; in the third line we have expressed $\sin \Delta\phi$ in terms of β using the geometrical relations Eqs. (4.16) and (4.17). Although there are infinitely many images, the amplification decreases exponentially for large m . Thus, for the rest of the work we will focus only on the pair of $m = 1$ images whose magnifications are denoted by μ_π .

While we derived retrolensing magnification in the geometric approximation, we can find the same result in wave scattering picture. Note that per unit time, the energy received by a detector with area A_{det} from a source with an isotropic luminosity dE/dt is $A_{det}/(4\pi D_{OS}^2) (dE/dt)$. At the same time, the source's emission may first reach the SMBH (lens) and then scatter towards the observer. The detector receives energy at a rate $1/(4\pi r_S^2) (d\sigma/d\Omega) (A_{det}/D_{OL}^2) (dE/dt)$, where r_S is the distance from the source to the lens with $r_S \simeq D_{LS}$ when the relative alignment is high, and $d\sigma/d\Omega$ is the cross section of the SMBH and it is further a function of the $\gamma(t)$, the angle of the outgoing rays with respect to the incoming ones. Geometrically, $\sin \gamma \simeq (D_{OS}/D_{LS})\beta$. The magnification is thus

$$\mu(t) = \left(\frac{D_{OS}}{D_{OL} D_{LS}} \right)^2 \left\{ \frac{d\sigma}{d\Omega} [\gamma(t)] \right\}. \quad (4.23)$$

The classical cross-section of a Schwarzschild SMBH is [63]

$$\left\{ \frac{d\sigma}{d\Omega} [\gamma(t)] \right\}_{geo} = \frac{b [\gamma(t)] [db/d\gamma(t)]}{\sin \gamma(t)}, \quad (4.24)$$

where

$$b(\gamma)/M_3 \simeq 3\sqrt{3} + 3.48 \exp(-\gamma), \quad \text{when } \gamma \simeq \pi. \quad (4.25)$$

We immediately see that magnification calculated using the classical cross section reduces to the one calculated in Eq. (4.22) under the geometrical limit.

However, the classical/geometrical cross section assumes the scattering of a flow of particles and does not include effects of wave interference nor the spin of the wave. Ref. [63] incorporated the wave effects (interference and the polarization) under a semi-classical approach and found that near glory, the cross section for each ray can be written as

$$\begin{aligned} \left\{ \frac{d\sigma}{d\Omega} [\gamma(t)] \right\}_{\text{wave}} &= \frac{2\pi^2}{\lambda} b_g^2 \left(\frac{db}{d\gamma} \right) J_{2s}^2 \left[\frac{2\pi}{\lambda} b_g \sin \gamma(t) \right], \\ &= 84.65 M_3^2 (f M_3) J_{2s}^2 [33.62 f M_3 \sin \gamma(t)] \end{aligned} \quad (4.26)$$

where $\lambda = 1/f = 2\pi/\omega$ is the GW wavelength, s is the spin of the scattered wave ($s = 2$ for GW), b_g is the impact parameter at the glory point ($b_g = 3\sqrt{3}M$ for a Schwarzschild BH), and J_{2s} is the Bessel function of order $2s$. In the second line, we have plugged in numerical values for a Schwarzschild BH. Note further that for sufficiently small x and $s = 2$, the Bessel function can be expanded as $J_4(x) \simeq x^4/384$. This means that the glory will be dark for a polarized wave while it has an infinite magnification under the geometrical limit. On the other hand, the location of the first peak of $J_4(x)$ is at $x \simeq 5.32$, which corresponds to

$$\sin \gamma \simeq \frac{D_{OS}}{D_{LS}} \beta \simeq 9.94 \times 10^{-3} \left(\frac{2\pi f M_3}{100} \right)^{-1}. \quad (4.27)$$

Therefore, for GW at higher frequencies and/or for more massive lenses, the glory is dark for smaller range of alignments. In other words, the wave result [Eq. (4.26)] approach better to the geometrical limit [Eq. (4.24)] at greater values of $(2\pi f M_3)$ (i.e., shorter wavelength; see also Fig. 4.2 which we will discuss shortly).

Once we have the magnification of each retro-lensed image μ_π , we compute the magnification factor of the GW waveform $F(t; f)$ as [cf. Eq. (4.12)]

$$F(t; f) = 1 + 2|\mu_\pi(t)|^{1/2} \exp [2\pi i f t_\pi(t)], \quad (4.28)$$

where we simply approximate the time delay as $t_\pi(t) \simeq 2D_{LS}(t) + \pi b_g$ [64]. We do not further refine the solution because it does not affect the detectability of the glory. Because during the derivation process, we have made the assumption of high-alignment in various places, which would require $\Delta\alpha \simeq |\gamma - \pi| \simeq (D_{OS}/D_{LS})\beta \ll 1$ (see also, sec. 2.3 in Ref. [56]), we adopt here an *ad hoc* cut and only apply the retro-lensing amplification when $(D_{OS}/D_{LS})\beta < \pi/12$. A more rigorous treatment of the

magnification that is valid at arbitrary angles is deferred to future studies. Higher-order images are also ignored because their magnification drops exponentially with respect to the winding number of the SMBH.

Sample waveforms

In the top panel of Fig. 4.2 we compare the magnifications of various images. Here $\mu_{1,2}$ are the magnifications corresponding to the primary and secondary images formed by the standard strong lensing under the weak-deflection limit [Eq. (4.14)]. The cyan curve, denoted by μ_π , is the magnification of the retro-lensing under the geometrical limit [Eq. (4.22); it is also equivalent to the combination of Eqs. (4.23) and (4.24)]. The glory magnification including wave effects [Eq. (4.26)] are shown in the dashed-brown and dotted-purple traces for two different values of $2\pi f M_3 = 10$ and 100, respectively. To generate the plot, we have assumed a lens with mass $M_3 = 10^8 M_\odot$ and inclination $\iota_J = 87^\circ$. We further set $\phi_o = 0$ for the standard lensing under the weak-deflection limit and $\phi_o = \pi$ for the retro-lensing. Whereas the geometrical glory has an infinite magnification as $\iota_J \rightarrow 90^\circ$, the wave calculations lead to a vanishing glory at perfect alignment. On the other hand, at larger values of $2\pi f M_3$ (or effectively, shorter wavelengths), the wave result follows more closely the classical/geometrical value and the central dark spot has a smaller angular size [Eq. (4.27)]. As a result, such systems will be more favorable for the detection of retro-lensing signatures.

We also present the upper and lower envelopes of the amplification factor $|F|$ in the bottom panel in Fig. 4.2. Because we have $2\pi f \Delta t_l \sim w = 8\pi f M_3 \gg 1$, the phase between different images changes rapidly, causing $|F|$ oscillates between the envelopes as the inner binary's frequency f evolves.

Putting different ingredients together, we show a sample waveform including various effects together in Fig. 4.3. Here the dashed-red trace is the waveform for an isolated binary. When the SMBH is present, it induces a de Sitter-like precession of the inner binary's orbital plane [41] and modifies its antenna response as shown in the solid-olive trace. Each time when the inner binary is behind the SMBH ($\phi_o \simeq 0$), it further experiences the standard strong lensing by the SMBH [Eq. (4.11)], leading to the cyan peaks in the plot. The separation between two adjacent cyan peaks corresponds to the period of the outer orbit P_o and the duration of each lensing event

is approximately given by $0.5\mathcal{P}_l P_o$ [46], where

$$\begin{aligned}\mathcal{P}_l &\simeq \frac{2}{\pi} \arcsin \left[\frac{D_{OL}\theta_{Ein}(\phi_o = 0)}{a_o} \right] \\ &\simeq 0.13 \left(\frac{a_o/M_3}{100} \right)^{-1/2},\end{aligned}\quad (4.29)$$

is the geometrical probability of the inner binary to be significantly lensed by the SMBH (i.e., the geometrical probability of $\eta = \beta/\theta_{Ein} \leq 1$). When the inner binary is in front of the SMBH ($\phi_o \simeq \pi$), it is then retro-lensed by the SMBH, leading to the purple peaks in Fig. 4.3. We have used Eq. (4.26) for the retro-lensing calculation to incorporate wave effects.

To generate Fig. 4.3, we assume $M_3 = 10^8 M_\odot$, $a_o = 100 \text{ AU}$, leading to an outer orbit period of $P_o = 0.10 \text{ yr}$ and a de Sitter precession period of $P_{dS} = 6.8 \text{ yr}$. We randomly choose $(\bar{\theta}_S, \bar{\phi}_S) = (33^\circ, 147^\circ)$ for the line of sight in the solar frame. The orientation of the outer orbit \hat{L}_o in the solar frame (following the same notation as in Ref. [41]) is then set to $(\bar{\theta}_J, \bar{\phi}_J) = (120^\circ, 147.5^\circ)$ so that the outer orbit has an inclination $\iota_J = 87^\circ$. We further set the phase of the outer orbit to be $\phi_o = -\pi/2$ at the merger of the inner binary as a conservative demonstration of the lensing effect, which essentially zeros the lensing signatures when the inner binary reaches the more sensitive ground-based GW detectors. The inner binary (signal carrier) has $M_1 = M_2 = 50 M_\odot$ and the initial frequency is set such that the binary merges in 5 yr. The opening angle between \hat{L}_i and \hat{L}_o is $\lambda_L = \pi/4$.

As a comparison, we also consider the case where a less massive SMBH acts as the lens in Fig. 4.4. This time we set $M_3 = 10^7 M_\odot$ and $a_o = 50 \text{ AU}$, leading to a similar outer orbital period of $P_o = 0.11 \text{ yr}$. The rest parameters are the same as in Fig. 4.3. The standard lensing (cyan) still have easily visible features in the waveform, yet the retro-lensing can hardly be detectable. Indeed, for high alignment and at a fixed value of P_o , we have $\mu_{1,2} \propto M_3^{2/3}$ while $\mu_\pi \propto M_3^{5/3}$ [Eqs. (4.14) and (4.22)], and therefore the detection of retro-lensing favors more massive SMBHs.

Parameter space for significant lensing

We can systematically examine the parameter space over which lensing is likely to be significant, as demonstrated in Figs. 4.5 and 4.6. In Fig. 4.5, we consider the threshold ι_J required to make the magnification of the secondary image in the standard lensing scenario be $|\mu_2| \geq 0.1$ [Eq. (4.14)]. The upper envelope of the amplification factor $|F| \simeq 1 + |\mu_2|^{1/2} \simeq 1.3$. Note this corresponds to $\eta \leq 1.27$,

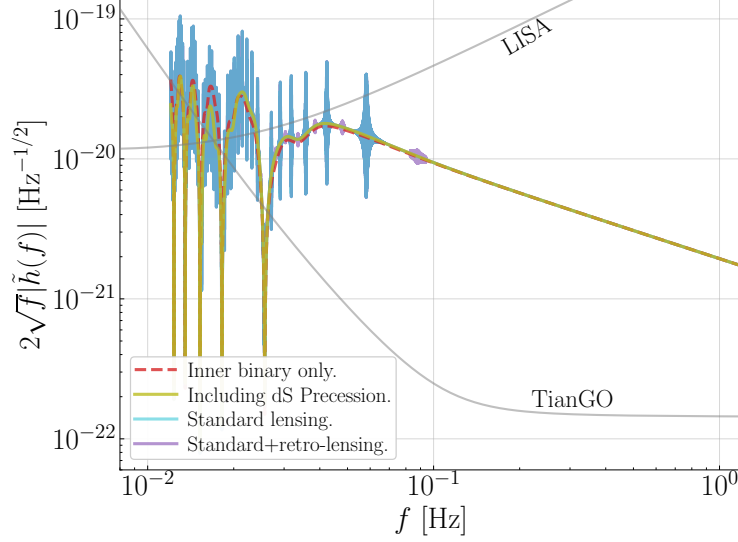


Figure 4.3: Sample waveforms including the lensing effects. Also shown in the grey traces are the proposed instrumental sensitivity of LISA [65] and TianGO [13]. Here we assume $M_3 = 10^8 M_\odot$, $a_o = 100 \text{ AU} \simeq 101 M_3$, and $\iota_J = 87^\circ$. The outer orbit has a period of $P_o = 0.10 \text{ yr}$ and the inner orbit precesses with a period $P_{dS} = 6.8 \text{ yr}$. Each time $\phi_o[t(f)] \simeq 0$ (source behind the lens), the standard lensing happens and is characterized by a sharp cyan peak in the waveform. When $\phi_o[t(f)] \simeq \pi$ (source in front of the lens), we then have retro-lensing (glory), which is calculated including wave interference and polarization effects [Eq. (4.26)]. Note that the starting frequency of each waveform is chosen so that the inner binary will merge in 5 yr, which is also the fiducial duration of observation assumed in this study.

and thus the angle $90^\circ - \iota_J$ indicated by the color bar over 90° is broadly consistent with the (repeated) lensing probability \mathcal{P}_l defined in Eq. (4.29). Also shown in the dashed-grey (or the solid-brown) trace is the line corresponding to the outer orbital period being $P_o = 0.1 \text{ yr}$ (or the period of the de Sitter-like precession of the inner orbital plane being $P_{dS} = 10 \text{ yr}$). We see that along the line of $P_o = 0.1 \text{ yr}$, we might expect to see significant strong lensing over a range of $\sim 10^\circ$ for the outer inclination angle, meaning that the geometrical probability for the significant strong lensing to happen (repeatedly) could be $\sim 10\%$.

To put this parameter space under astrophysical contexts, we also show in the solid-black line locations where the GW decay timescale of the outer orbit to be $a_o/\dot{a}_{o,gw} = 1 \text{ Gyr}$, with $\dot{a}_{o,gw}$ the decay rate of the outer orbit due to GW radiation and we have used $M_1 + M_2 = 100 M_\odot$. Along the line of $P_o = 0.1 \text{ yr}$, the GW decay timescale of the outer orbit is typically between 10 Myr to 1 Gyr. This means that after the formation of inner binary, it needs to be able to merge within 10 Myr in order for us to catch

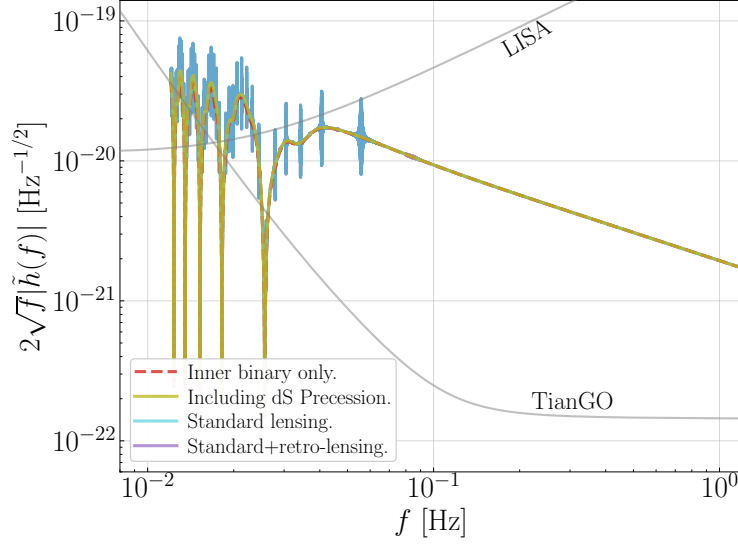


Figure 4.4: Similar to Fig. 4.3 but for $M_3 = 10^7 M_\odot$, $a_o = 50 \text{ AU} \approx 507 M_3$, corresponding to an outer orbital period of $P_o = 0.11 \text{ yr}$ and a dS precession period of $P_{dS} = 38 \text{ yr}$. In this scenario only the standard lensing has a significant effect on the waveform.

such a triple system. We will discuss this point more in Sec. 7.5. Furthermore, the locations of migration traps in AGN disks [20] are shown in the dotted-olive traces as a potential mechanism to form the inner binaries near the SMBH (see also the discussion in Ref. [46]).

Similarly, we show in Fig. 4.6 the threshold inclination for the magnification of the retro-lensing (in the geometrical/classical limit) to be $|\mu_\pi| \geq 0.1$ [Eq. (4.22)]. For a massive lens with $M_3 \gtrsim 10^8$, there is a 1%-level chance for the retro-lensing to be significant (under the geometrical limit). While rare, such effects are produced by the strong gravity field near the light ring of the SMBH and thus serve as valuable probes of gravity at a different regime than that probed by the standard (strong) lensing (see, e.g., [66]).

As a brief summary, we note a waveform including the Doppler shift, the de Sitter-like precession, and the gravitational lensing can be fully constructed with 13 parameters, $(\mathcal{M}, D, t_c, \phi_c, \bar{\theta}_S, \bar{\phi}_S, \bar{\theta}_J, \bar{\phi}_J, M_3, a_o, \lambda_L, \phi^{(0)}, \alpha_0)$. This is the same set of the parameters as used in Ref. [41] because lensing does not introduce new unknown parameters (see the discussion below). Specifically, $(\mathcal{M}, D, t_c, \phi_c)$ are used to calculate the carrier signal [Eq. (4.3)] under the quadrupole formula. One can also include corrections at higher post-Newtonian orders but they are critical near the final merger and are thus beyond the interest of this work focusing on the external

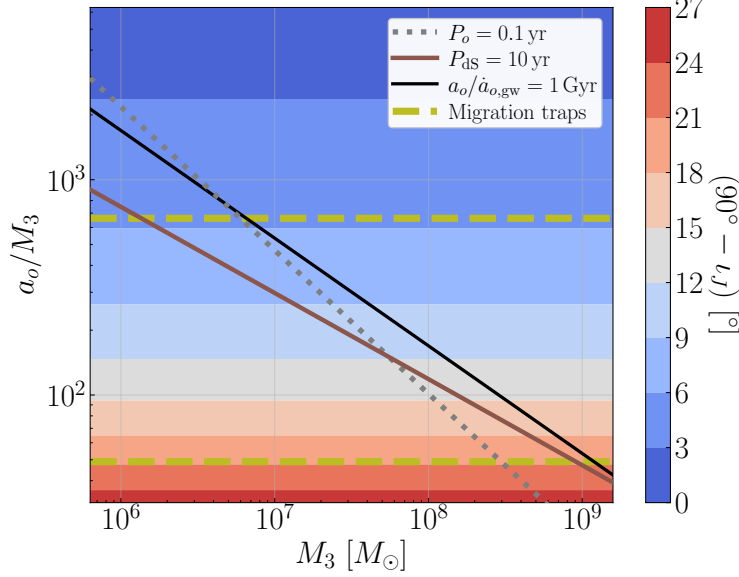


Figure 4.5: Threshold value of $(90^\circ - \iota_J)$ such that the secondary image in the standard-lensing case has a magnification of $|\mu_2| \geq 0.1$ [which corresponds to $\eta \leq 1.27$; Eq. (4.14)]. Also shown in the grey-dashed and brown-solid traces are lines corresponding to an outer orbital period of $P_o = 0.1 \text{ yr}$ and a dS precession period of $P_{\text{dS}} = 10 \text{ yr}$.

modulation in the early inspiral stage. The line of sight direction \hat{N} is specified by the solar-frame coordinates $(\bar{\theta}_S, \bar{\phi}_S)$ and the orientation of the outer orbital angular momentum \hat{L}_o is given by $(\bar{\theta}_J, \bar{\phi}_J)$. To determine the location of the inner binary in the outer orbit, we use $(M_3, a_o, \phi^{(0)})$ with $\phi^{(0)}$ a reference phase at $t = 0$ ¹. The orientation of the inner orbit can be further determined with an opening angle $\lambda_L = \arccos(\hat{L}_i \cdot \hat{L}_o)$ and a reference precession angle α_0 at $t = 0$.

Before we proceed to following sections, we note that it is particularly interesting to combine gravitational lensing with the de Sitter-like precession of the inner orbital plane induced by the SMBH. Not only do the two effects share similar parameter space as shown in Fig. 4.5 (see also Refs. [46, 41]), but more importantly, combining the precession with the Doppler shift also determines *all* the parameters entering the lensing calculation. Indeed, by measuring the frequency of the Doppler shift $\Omega_o = \sqrt{M_3/a_o^3}$ and the frequency of the de Sitter precession $\Omega_{\text{dS}} = (3/2)(M_3/a_o)\Omega_o$ [42, 43]², we can determine the mass of the lens M_3 and the lens-source distance a_o [41].

¹While using (M_3, a_o) is conceptually simple, we nonetheless use (M_3, ω_o) when calculating the Fisher matrices in Sec. 4.4 as it is more numerically accurate.

²This expression assumes a circular outer orbit and $M_3 \gg M_{1,(2)}$. When the outer orbit is elliptical, the eccentricity can be constrained from the Doppler shift [41]. In this case, the instantaneous precession rate (see, e.g., Ref. [67]) should be used.

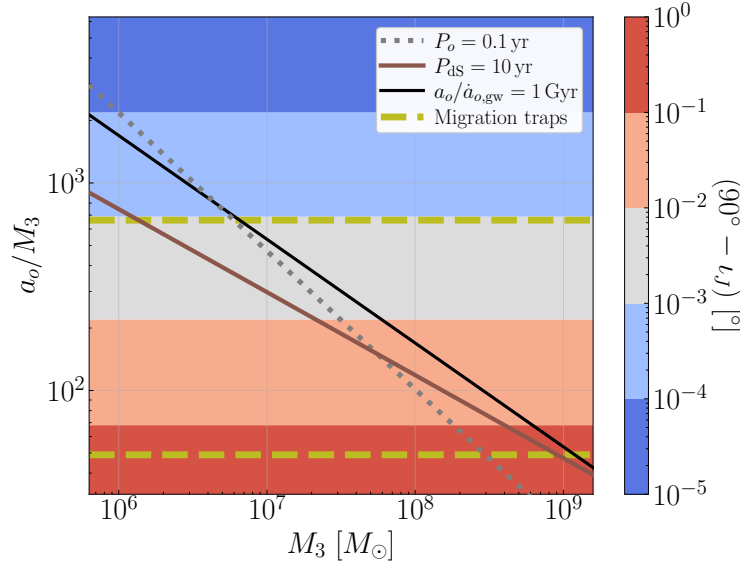


Figure 4.6: Threshold value of $(90^\circ - \iota_J)$ such that the magnification of the first retro-lensing image has $|\mu_\pi| \geq 0.1$. Note that in this case the color bar has a logarithm scale.

The outer orbital phase $\phi_o(t)$ can be measured from the Doppler phase shift. Lastly, as the inner orbital plane precesses around the outer orbit, we can further infer the orientation of the outer orbit and hence ι_J from the time evolution of the inner orbit's orientation. Consequently, lensing is a new effect to be incorporated to the study presented in Ref. [41] without introducing new unknown parameters. It can thus be used to both enhance the PE uncertainty of the outer orbital parameters and test our understanding of the strong field gravity.

4.3 Detectability of lensing signatures

In this Section we examine the detectability of the lensing signatures by considering mismatches (to be defined below) of waveforms with and without the lensing effects.

For this purpose, we first define the fitting factor (FF) between two waveforms as [68, 69],

$$FF(h_1, h_2) = \frac{\langle h_1 | h_2 \rangle}{\sqrt{\langle h_1 | h_1 \rangle \langle h_2 | h_2 \rangle}} \quad (4.30)$$

where

$$\langle h_1 | h_2 \rangle \equiv 2 \int \frac{\tilde{h}_1^*(f) \tilde{h}_2(f) + \tilde{h}_1(f) \tilde{h}_2^*(f)}{S_n(f)} df. \quad (4.31)$$

We can then compute the mismatch ϵ

$$\epsilon = 1 - FF. \quad (4.32)$$

There is a threshold mismatch, ϵ_{th} , given by

$$\epsilon_{th} = \frac{1}{\langle h_1|h_1 \rangle + \langle h_2|h_2 \rangle} \simeq \frac{1}{2\rho^2}, \quad (4.33)$$

where the second equality applies when $h_1 \simeq h_2$ and ρ is the signal-to-noise ratio (SNR) of the GW event. It is *necessary* to have $\epsilon > \epsilon_{th} \simeq 1/2\rho^2$ in order for the two waveforms to be distinguishable [68, 69]. Note that the condition $\epsilon > \epsilon_{th}$ is also equivalent to $\langle h_1 - h_2|h_1 - h_2 \rangle > 1$.

In Fig. 4.7, we compute the mismatch ϵ between different waveforms. The grey traces correspond to the mismatch between a waveform without any lensing signature and one including only the standard (strong) lensing [i.e., the source is only lensed when it is behind the lens or the SMBH and the deflection angle $\alpha \ll \pi$; Eq. (4.11)]. The olive traces compare the waveforms with and without retro-lensing; wave effects are incorporated by computing the scattering cross-section using Eq. (4.26). They exhibit oscillatory features because the cross-section of retro-lensing is oscillatory (Fig. 4.2), yet the varying ϕ_o effectively allows different values of the scattering angle to be probed, which smooths out the oscillation. Lastly, in the purple traces we compare the mismatch between waveforms calculated under the geometrical limit and those include wave effects. More specifically, the geometrical waveforms are calculated using Eq. (4.13) for the standard-lensing part and Eq. (4.24) for the retro-lensing part. The waveforms including wave effects are instead calculated using Eqs. (4.11) and (4.26). We note further that the purple traces are in fact dominated by the contribution from retro-lensing [Eq. (4.24) vs. Eq. (4.26); see also Fig. 4.2]. The geometrical limit of the standard strong lensing typically provides a very good approximation to the full expression including wave effects as $2\pi f M_3 \gg 1$ in our case.

To generate the plot, we have assumed detection of the source with TianGO [13]. The parameters we consider here are similar to the ones used in Fig. 4.3 except that we vary the orientation of \hat{L}_o by changing $\bar{\theta}_J$, which further varies the inclination ι_J between the line of sight and the outer orbit. Also shown in the plot as a comparison is the red-dotted line corresponding to $1/2\rho^2$ (assuming a waveform without lensing effects; though the SNR ρ is generally similar with and without gravitational lensing).

In the three panels of Fig. 4.7, we consider three different combinations of (M_3, a_o) . From top to bottom, we have $(M_3/M_\odot, a_o/AU) = (10^7, 50)$, $(10^8, 100)$, $(10^8, 70)$, corresponding to $(P_o, P_{dS}) = (0.11, 38)$, $(0.10, 6.8)$, $(0.06, 2.8)$ yr. For the standard

lensing, it might be detectable for a lens with $M_3 = 10^7 M_\odot$ if $|\iota_J - 90^\circ| \lesssim 7.5^\circ$, which is nicely consistent with Fig. 4.5. Along the line of fixed P_o , the lensing signature becomes more prominent as the mass of the lens M_3 increases. This is also shown in Fig. 4.7 if we compare the middle panel with the top one. This indicates that for BBHs near massive SMBH with $M_3 \sim 10^8 M_\odot$, repeated strong lensing is indeed a critical component to be included in the waveform modeling.

As for the retro-lensing, there is a small chance for it to be potentially detectable if the lens is sufficiently massive $M_3 \gtrsim 10^8 M_\odot$ and the outer orbit is compact with $P_o \lesssim 0.1 \text{ yr}$. While a dark glory is expected for a polarized wave like GW at high alignment, for M_3 this massive, it is only dark for a very small range of angles [Eq. (4.27)] and is further washed out by varying ϕ_o . Indeed, for $2\pi f M_3 \gtrsim 100$, the wave cross-section approaches the geometrical/classical value well (Fig. 4.2) and thus high alignment favors the detectability as shown in Fig. 4.7. On the other hand, distinguishing the GW diffraction signature from the classical one [Eq. (4.26) vs. Eq. (4.24)] would be challenging given the sensitivity of TianGO, and it would rely on more sensitive detectors such as DECIGO [11] and/or the Big Bang Observer [70].

Note specifically that we have kept the outer orbital phase to be $\phi_o = -\pi/2$ at the merger of the inner binary when we compute the mismatches. The values presented in Fig. 4.7 are thus *conservative* estimates (i.e., small mismatches) because in the frequency band of $f \gtrsim 0.1 \text{ Hz}$ where TianGO is most sensitive (and this band includes the sensitivity band of ground-based GW observatories), the inner binary is far away from being affected by both the standard lensing and the retro-lensing. While the detectability could be enhanced if the inner binary happens to be lensed when $f \gtrsim 0.1 \text{ Hz}$, the inner binary spends only a small amount of time at this frequency band ($< 1 \text{ week}$ for the BBH we consider), therefore the probability is low [lower than the probability of repeated lensing by another factor of \mathcal{P}_l ; Eq. (4.29)]. Consequently, we do not focus on the more optimistic case here.

The lensing effects could also be detected by detectors like LISA [7] (whose sensitivity is given by Ref. [65]) that are more sensitive in the millihertz band. The result is shown in Fig. 4.8. The parameters we assume are the same as in Fig. 4.7 except for that we move the source's luminosity distance to $D = 200 \text{ Mpc}$ so that the SNR is greater than 8. The retro-lensing is too weak to be detectable with the sensitivity of LISA, yet the standard lensing may still have a decent chance to be detectable. For

an outer orbital period of 0.1 yr and a lens mass of $10^7 M_\odot$ ($10^8 M_\odot$), the probability for the standard lensing signature to be measurable is about 3% (10%).

4.4 PE accuracy including lensing effects

Enhancing the PE accuracy of the SMBH properties

As we mentioned briefly at the end of Sec. 4.2, including the lensing effects does not introduce new free parameters to the waveform. Therefore, we naturally expect that including the lensing effects would enhance the PE accuracy of the SMBH properties compared to the results obtained in Ref. [41] using orbital dynamics (Doppler shift and de Sitter precession) alone, as extra constraints are placed on the waveform. We examine this point quantitatively in this Section using the Fisher matrix approach. In particular, we write the waveform including lensing effects $\tilde{h}^{(l)}$ [Eq. (4.1)] in terms of 13 parameters as described in Sec. 4.2. We construct the Fisher matrix $\mathbf{\Gamma}$ whose elements are given by

$$\Gamma_{ij} = \left\langle \frac{\partial \tilde{h}^{(l)}}{\partial \theta_i} \middle| \frac{\partial \tilde{h}^{(l)}}{\partial \theta_j} \right\rangle, \quad (4.34)$$

where θ_i is one of the 13 parameters. The PE error can then be obtained by inverting the Fisher matrix,

$$\mathbf{\Sigma} = (\mathbf{\Gamma})^{-1}. \quad (4.35)$$

The diagonal element Σ_{ii} corresponds to the statistical variance of parameter θ_i , and the off-diagonal element Σ_{ij} corresponds to the covariance between θ_i and θ_j .

In Fig. 4.9, we show the PE uncertainties of various parameters with (solid traces) and without (dotted traces) the lensing effects. Because retro-lensing is weak and the mismatch it induces is only marginally detectable (Sec. 4.3), we thus ignore all the retro-lensing effects in the analysis here (and in Sec. 4.4). The source is assumed to be detected by a TianGO-like decihertz observatory [13]. We vary the mass of the SMBH M_3 and choose the outer orbit's semi-major axis a_o such that the outer orbital period is fixed at $P_o = 0.1$ yr. Other parameters are the same as in Fig. 4.3, leading to $\iota_J = 87^\circ$. Moreover, the outer orbital phase is fixed at $\phi_o = -\pi/2$ at the merger so that the BBH's signal is *not* lensed in TianGO's most sensitive band, $f \gtrsim 0.1$ Hz (corresponding to the last week of the inner BBH's inspiral). In the top x-axis, we also show the minimum value of η_{min} reached during the 5-year observation period. Note that we have restricted our discussion here to systems with $\eta_{min} < 1$, and the mismatches between waveforms with and without lensing satisfy $\epsilon > \epsilon_{th}$.

The top panel in Fig. 4.9 shows the fractional error in mass of the SMBH. Without lensing (dotted trace), it can be constrained to $\Delta \log M_3 = O(10\%)$ from the peri-

ods of the outer orbit and the de Sitter precession, P_o and P_{dS} . If the inner BBH also experiences significant strong lensing by the SMBH (solid trace), then the PE uncertainty can be reduced by almost 3 orders of magnitude to $\Delta \log M_3 = \mathcal{O}(10^{-4})$.

It is worth to note that the error in $\Delta \log M_3$ is much smaller than the value obtained in Ref. [57] for *static* lensing. The reason is detailed in Appx. 4.8. In brief, this is because the time delay between the primary and secondary images, $\Delta t_l \sim 8M_3\eta$ for $\eta \ll 2$ [or $2M_3\eta^2$ for $\eta \gg 2$; Eq. (4.15)], is the best measured quantity when lensing is static (i.e., η stays as a constant during the observation period). As a result, M_3 and η are highly correlated. Nonetheless, as η varies due to the outer orbital motion, the waveform effectively samples different values of Δt_l . This thus breaks the degeneracy between M_3 and η and allows M_3 to be determined to a much better accuracy than in the case of static lensing studied in Ref. [57].

Similarly, because most constraints are from combining information at different values of Δt_l instead of from a single instance (e.g., at $\phi_o = 0$), the results shown in Fig. 4.9 does not depend sensitively on the value of ι_J as long as the lensing is detectable (Fig. 4.7) so that the formalism of Fisher matrix applies.

Once we have the uncertainty in $\log M_3$, the outer orbit's semi-major axis typically has an error $\Delta \log a_o \simeq \Delta \log M_3/3$, as the outer orbital period can be accurately determined by the Doppler shift [41]. Thus, the lensing signatures can also help constraining ι_J from the instantaneous values of η , which further leads to a better determination of the orientation of the outer orbit's angular momentum \hat{L}_o (as \hat{N} can be measured from the motion of the detector around the Sun; see Refs. [59, 13]). This point is illustrated in the middle panel in Fig. 4.9 where the error in $\bar{\theta}_J$ is shown.

As \hat{L}_o is the axis around which the inner orbital plane (i.e., \hat{L}_i) precesses, a better determined \hat{L}_o also enhances the detectability of the precession signature. We demonstrate this in the bottom panel of Fig. 4.9. One may argue that the result of the Fisher matrix is self-contained only if $\Delta \lambda_L < \lambda_L$ [41]. Without lensing, this condition is not satisfied until $M_3 \gtrsim 3 \times 10^7 M_\odot$ or $P_{\text{dS}} \lesssim 15 \text{ yr}$ for the sources we consider here. On the other hand, this condition can be satisfied for less massive SMBHs with $M_3 \gtrsim 6 \times 10^6 M_\odot$ (corresponding to $P_{\text{dS}} \lesssim 44 \text{ yr}$) if the inner binary is also lensed by the SMBH. In other words, lensing effects help enhancing the detectability of the de Sitter precession of the inner binary and allow it to be measurable at a P_{dS} about 3 times greater than the one without lensing.

Consistency tests

In principle, the lensing does not introduce any new free parameter. We can nonetheless introduce an ad hoc parameter κ , defined via

$$M_l = \kappa M_3, \quad (4.36)$$

where M_3 is the mass of the SMBH for evaluating the orbital dynamics (Doppler phase shift and dS precession) and M_l is the SMBH mass determining the lensing. In other words, the parameter κ serves as an indicator of the consistency between the two effects. Nominally $\kappa = 1$ and the mass of the SMBH creating the lensing is the same as that affecting the orbital dynamics. On the other hand, deviation may exist due to theoretical approximations made when constructing the waveform. After more careful waveform modeling, κ can be further used to test the general theory of relativity, as the orbital dynamics and the lensing effects are induced by gravity at different regions around the SMBH. This is similar to how one may constrain deviations from general relativity using the Shapiro time delay [71, 72]. It is thus interesting to ask the question of how well we can measure the deviation of κ from unity.

In Fig. 4.10 we show the statistical uncertainty on κ as a function of M_3 . The source orientation and sky location is the same as in Fig. 4.9. We note the error in κ decreases roughly as $M_3^{-4/3}$ and it can be constrained to a 1% accuracy for $M_3 \gtrsim 10^7 M_\odot$.

One might understand the scaling of $\Delta\kappa$ as the following. How well we can measure $\Delta\kappa$ depends on how well we can measure the mass of the SMBH from the precession frequency Ω_{dS} . Ignoring covariance with different angles, we approximately have $\Delta \log M_3 \propto \Delta \log \Omega_{\text{dS}} \propto \Omega_{\text{dS}}^{-2}$ [58, 41]. If we hold the outer orbital frequency constant, we thus have $\Omega_{\text{dS}} \propto M_3^{2/3}$. Consequently, we approximately have $\Delta\kappa \propto M_3^{-4/3}$ as shown in Fig. 4.10.

Meanwhile, it is interesting to note that the uncertainty in κ is smaller than the numerically obtained uncertainty in M_3 when we include only the Doppler shift and the de Sitter precession in the waveform (the dotted trace in the upper panel in Fig. 4.9). This is because the lensing signature still helps constraining the orientation of the outer orbit ι_l in a way that cannot be mimicked by a rescaling of the mass M_l (this is why we can simultaneously determine M_l and η in the static lensing case; Ref. [57] and Appx. 4.8). A better constrained ι_l means a better determination of parameters such as $\bar{\theta}_l$ and λ_L that are partially degenerate with M_3 in the no-lensing case. As

a result, the PE accuracy on M_3 can still be improved even we do not directly use it to evaluate the lensing.

4.5 Conclusion and Discussions

We studied the GW waveform emitted by a stellar-mass BBH in the vicinity of an SMBH, including effects such as the Doppler phase shift due to the outer orbital motion, the de Sitter-like of \hat{L}_i around \hat{L}_o , and (repeated) gravitational lensing caused by the SMBH.

For lensing, we considered not only the standard strong lensing which happens when the source is behind the lens (Sec. 4.2), but also retro-lensing when the source is in front of the lens (Sec. 4.2).

We then examined the detectability of various lensing effects by considering the mismatches they induce (Sec. 4.3). For a lens with a mass of $M_3 = 10^7 M_\odot$ and an outer orbital period of $P_o = 0.1 \text{ yr}$, there is a $\sim 3\%$ ($\sim 10\%$) chance for the strong lensing to be detectable by LISA [7] (TianGO [13]), and this probability increases with increasing M_3 if P_o is held constant. For massive lens with $M_3 \gtrsim 10^8 M_\odot$ and compact outer orbits with $P_o \lesssim 0.1 \text{ yr}$, there is also a small probability for the retro-lensing to be detectable for TianGO. The retro-lensing calculated with a classical cross-section [Eq. (4.24)] is typically accurate enough for a source at $\approx 1 \text{ Gpc}$ given the sensitivity of TianGO. Effects of wave interference and polarization in the glory scattering [Eq. (4.26)] might be measurable if the source is at a closer distance ($\lesssim 300 \text{ Mpc}$) or the detector is more sensitive (e.g., DECIGO [11] and/or the Big Bang Observer [70]). On the other hand, the geometrical limit of the strong lensing [Eq. (4.13)] typically provides a good approximation to the full expression, Eq. (4.11). This is because we have $w = 8\pi f M_3 \gg 1$, and wave effects would show up only if we have $\eta < 1/w \ll 1$. Such an almost exact alignment is unlikely and therefore is not considered as the main case in our current study (but see, e.g., Ref. [73], for discussions on lensing when an exact alignment happens).

Because including the lensing does not introduce any new free parameters than what have already been used to incorporate the outer orbital dynamics, it greatly reduces the PE uncertainties, especially the statistical errors of the SMBH properties (Sec. 4.4). In fact, the error in M_3 can be better than in the case of static lensing, because the varying outer orbit breaks the degeneracy between M_3 and the source's angular position on the sky η . Furthermore, for strongly lensed BBHs, the de Sitter precession can also be detected at a longer period. Lastly, we indicated in Sec. 4.4

that since the mass of the SMBH can be separately inferred from the outer orbital dynamics and from the lensing effects, comparing the two inferences can thus serve as a way to test the consistency of the theoretical modeling behind each effect, and eventually, a way to test the general theory of relativity.

We note that as our main goal here is to consider the detectability of various lensing effects and estimate their impacts on the PE, we only adopted the lowest-order approximation for each effect in our waveform construction. More careful treatments are needed by future studies if we want to build waveforms that are accurate enough to serve as detection templates.

For example, we assumed that both the inner and the outer orbits are circular in our study for simplicity. However, eccentricities in both orbits may be expected especially if the inner binary is formed via dynamical channels (see, e.g., Refs. [22, 23, 24, 25, 26, 27, 28, 29, 30, 31]). The qualitative effects of eccentricity have been argued in Ref. [41]. An eccentric outer orbit might potentially enhance the PE accuracy as it reduces the period of precession. On the other hand, an eccentric inner orbit decreases the inner binary's merger time, giving the precession less time to accumulate its effect. Furthermore, if the inner binary's merger time is shorter than the outer orbital period, it would decrease the probability for lensing to happen [46]. It would be crucial to properly incorporate them in future waveform studies to quantitatively understand the role of eccentricity.

The spin of the SMBH is also a critical component to be incorporated in future studies. Throughout the analysis, we have assumed that the SMBH is a non-spinning Schwarzschild BH for simplicity, whereas astrophysical SMBHs may have significant spin [74]. While the Lense-Thirring precession has a longer period than the de Sitter precession for sources we consider here [41], it has nonetheless been shown to have potentially significant role in modulating the orientation of the inner BBH [43, 69, 75]. Besides affecting the orbital dynamics, the spin may also modify the lensing signatures [76, 77, 78]. Therefore, similar to testing the consistency in the SMBH's mass (Sec. 4.4), one may further check the consistency in the spin of the SMBH by comparing its value inferred from the Lense-Thirring effect in the orbital dynamics and that from gravitational lensing. This may serve as yet another way of testing general relativity.

Moreover, Ref. [79] recently suggested that fast Doppler motion can further cause aberration in GW rays and is another ingredient to be added in the future. For inner binaries that are even closer to the SMBH than what we considered here, the

quasinormal modes of the SMBH might be further excited [80]. If the inner binary is observed at a lower frequency with a GW decay timescale much longer than the duration of the observation, gaseous effect might also play a role [32, 35] together with Lidov-Kozai oscillations [38, 39].

The astrophysical formation of such a hierarchical triple system is another topic that requires further dedicated studies. Because of complicated environmental effects in galactic nuclei, there are a few potential limiting requirements the triple system needs to satisfy. For example, the inner binary needs to merge efficiently before the outer orbit decays due to GW radiation (black traces in Figs. 4.5 and 4.6). The inner binary also needs to be able to survive evaporation due to dynamical interactions with environmental stars on a timescale of typically a few Myr [23, 81]. These conditions could be satisfied by both the gaseous channel [15] and the dynamical channels [31], though the inner binary produced by some dynamical channels may have too high an eccentricity that it will merge before it orbits the SMBH by a complete cycle, disfavoring the detectability of both lensing and precession. In fact, we note the discussion on the astrophysical population in Ref. [46] applies here as well. This suggests that migration traps in AGN disks [20] would be particularly promising places to produce sources of interest to our study here (as also indicated in Fig. 4.5). Another possibility is the tidal capture of a binary by the SMBH as suggested in Ref. [28]. More careful examination of these channels and other candidates as well as the distributions of the inner and outer orbital parameters they can produce will be of great value.

ACKNOWLEDGMENTS

We thank Kumar Shwetketu Virbhadra, Xilong Fan, and the anonymous referee for useful comments to this work. H.Y. acknowledges the support of the Sherman Fairchild Foundation. B.S. acknowledges support by the National Science Foundation Graduate Research Fellowship under Grant No. DGE-1745301. Research of Y.W. and Y.C. are supported by the Simons Foundation (Award Number 568762), the Brinson Foundation, and the National Science Foundation (Grants PHY-2011968, PHY-2011961 and PHY-1836809).

4.6 Appendix: SPA for waveforms with fast modulation

Suppose we can write the time-domain waveform as

$$h(t) = \Lambda(t)h_C(t) \equiv \Lambda(t)A(t) \cos \Phi(t), \quad (4.37)$$

where $A(t)$ and $\Phi(t)$ are the amplitude and phase of the carrier waveform, and $\Lambda(t)$ is an external modulation factor induced by, e.g., the precession of the source/detector plane and/or the time-variation of the lensing configuration. Here we assume that the external modulation $\Lambda(t)$ may have a fast temporal variation rate compared to the variation rate of intrinsic amplitude of the carrier, $|d \ln \Lambda(t)/dt| > |d \ln A(t)/dt|$, [but $\Lambda(t)$ still varies on a timescale longer than the typical SPA duration t_{SPA} which we define below]. We can thus improve the accuracy of the waveform by including more expansion terms than the lowest-order SPA does.

Specifically, we have (for $f \geq 0$)

$$\begin{aligned}
\tilde{h}(f) &= \int h(t') e^{2\pi i f t'} dt', & (4.38) \\
&\simeq \frac{1}{2} \int \Lambda(t') A(t') e^{-i[\Phi(t') - 2\pi f t']} dt', \\
&\simeq \frac{1}{2} \int \left\{ \Lambda A + \left[\frac{d\Lambda}{dt} A + \Lambda \frac{dA}{dt} \right] (t' - t) \right. \\
&\quad \left. + \left[\frac{1}{2} \frac{d^2\Lambda}{dt^2} A + \frac{d\Lambda}{dt} \frac{dA}{dt} + \frac{1}{2} \Lambda \frac{d^2A}{dt^2} \right] (t' - t)^2 \right\} \\
&\quad \times \exp \left\{ -i \left[\Phi - 2\pi f t + \pi \frac{df}{dt} (t' - t)^2 \right] \right\} dt', & (4.39)
\end{aligned}$$

where in the second line, we have dropped the fast oscillating term and in the third line, we have expanded all the time-dependent quantities around a time t when $(d\Phi/dt)(t) = 2\pi f$. For conciseness, when a time-dependent quantity is evaluated at t , we dropped its argument by writing $\Lambda \equiv \Lambda(t)$ and similarly for other quantities.

If we ignore all the time derivatives on the amplitude terms as $|d \ln A/dt| < |d \ln \Lambda/dt| \ll f$ and $|d^2 \ln A/dt^2| < |d^2 \ln \Lambda(t)/dt^2| < f^2$, then we arrive at the standard (lowest-order) SPA approximation ($f \geq 0$)

$$\begin{aligned}
\tilde{h}^{(0)}(f) &= \frac{1}{2} \frac{\Lambda A}{\sqrt{df/dt}} \exp [i(2\pi f t - \Phi - \pi/4)], \\
&\equiv \frac{1}{2} \Lambda \tilde{h}_C(f). & (4.40)
\end{aligned}$$

Following the convention in Ref. [58], we have defined the terms excluding $\Lambda/2$ as $\tilde{h}_C(f)$.

The lowest-order SPA is an excellent approximation if the amplitudes stay as constants over the duration when the wave oscillates at frequency f . The characteristic

duration is given by

$$\begin{aligned} t_{SPA} &= \int \exp \left[-\pi \frac{df}{dt} (t - t')^2 \right] dt', \\ &= \sqrt{\frac{1}{df/dt}} = \sqrt{\frac{1}{3} P_i t_{gw}}, \end{aligned} \quad (4.41)$$

where P_i is the inner orbital period and $t_{gw} = a_i/|da_i/dt|$ is the instantaneous GW decay timescale. In other words, the wave stays at frequency f for a time given by the duration of the geometrical mean of the orbital period and the GW decay timescale. For inner binary's at $P_i \sim 100$ s and $t_{gw} \sim 3$ yr, we have $t_{SPA} \sim 0.6$ day and it decreases as $f^{-11/6}$ as the inner binary evolves to higher frequencies.

When the amplitude may change by a non-negligible amount during t_{SPA} , we can improve the accuracy of the SPA waveform by including derivatives on the amplitude variations. Note the terms $\propto (t' - t)$ in Eq. (4.39) vanishes because the integrand is odd around t . Including the terms $\propto (t' - t)^2$, we have

$$\begin{aligned} \tilde{h}^{(1)}(f) &= \frac{1}{2} \Lambda \tilde{h}_C(f) \\ &+ \frac{1}{4\pi i} \frac{\tilde{h}_C(f)}{df/dt} \left[\frac{1}{2} \frac{d^2 \Lambda}{dt^2} + \frac{1}{A} \frac{d\Lambda}{dt} \frac{dA}{dt} + \frac{1}{2} \frac{\Lambda}{A} \frac{d^2 A}{dt^2} \right]. \end{aligned} \quad (4.42)$$

If we further note

$$\frac{\tilde{h}_C}{A df/dt} \frac{dA}{dt} = \left(\frac{d\tilde{h}_C}{df} - 2\pi i t \tilde{h}_C \right), \quad (4.43)$$

our expression reduces to eq. (38) in Ref. [58] when we ignore the terms involving second order time derivatives. Nonetheless, the $d^2 \Lambda(t)/dt^2$ and the $d^2 A/dt^2$ terms also come at the $(t' - t)^2$ order and are thus left in the expression. The $d^2 \Lambda(t)/dt^2$ can be particularly important because $\Lambda(t)$ can be fast varying. Indeed, Ref. [46] argued that duration of a strong-lensing event is approximately $0.5 \mathcal{P}_l P_o$, where $\mathcal{P}_l \sim 0.1$ is the geometrical probability for the strong-lensing to happen and $P_o \sim 0.1$ yr is the period of the outer orbit.

4.7 Appendix: Geometrical derivation of the lensing equation

We derive here the geometrical relations shown in Eqs. (4.16) and (4.17) for the retro lensing scenario (lower part of Fig. 4.1).

First, note that all the angles around O sum to 2π , we immediately arrive at the Ohanian lens equation

$$\Delta\phi - \pi = \alpha - \theta - \theta_S. \quad (4.44)$$

We further have

$$\begin{aligned}
D_{OS} \tan \beta &= D_{LS} \tan (2\pi - \Delta\phi), \\
&= D_{LS} \{ \tan [(\pi - \alpha) + \theta + \theta_S] \} \\
&\simeq D_{LS} [-\tan(\alpha) + \tan \theta + \tan \theta_S].
\end{aligned} \tag{4.45}$$

Note further that the impact parameter can be written as

$$b = D_{OS}\theta = D_{LS}\theta_S. \tag{4.46}$$

Therefore, in our case we have $\theta \ll \theta_S \simeq D_{OS}/D_{LS}\theta (\ll 1)$. We thus arrive at Eqs. (4.16) and (4.17) presented in the main text.

4.8 Appendix: Understanding the improvement in $\Delta \log M_3$ due to repeated lensing

In this Appendix we explain why our PE uncertainty in $\Delta \log M_3$ (top panel in Fig. 4.9) is better than the results obtained in eq. (32) in Ref. [57].

The reason is illustrated in Fig. 4.11 where we show the error ellipses between $\log M_3$ and η for the static lensing case at different values of η . For each given η , we note $\log M_3$ and η are highly correlated. This is because the best constrained quantity is the time delay between the primary and the secondary images, $\Delta t_l \sim 8M_3\eta$ for $\eta \ll 2$ [or $2M_3\eta^2$ for $\eta \gg 2$; Eq. (4.15)]. Indeed, we see that in the plot the error ellipses roughly corresponds to lines defined by

$$\begin{aligned}
\Delta\eta &\simeq -\frac{\Delta t_l}{\partial(\Delta t_l)/\partial\eta} \Delta \log M_3, \\
&\simeq \begin{cases} -\eta \Delta \log M_3, & \text{for } \eta \ll 2, \\ -\frac{\eta}{2} \Delta \log M_3, & \text{for } \eta \gg 2. \end{cases}
\end{aligned} \tag{4.47}$$

On the other hand, we note that the orientation of the error ellipse changes as η changes (for a fixed M_3). Thus if the information at two different values of η can be combined, the joint uncertainty will be greatly reduced. This is exactly the situation in the repeated lensing scenario. As the inner binary orbits around the SMBH, we sample the lensing signatures at different values of η , allowing the mass of the SMBH to be determined much better than the static lensing case.

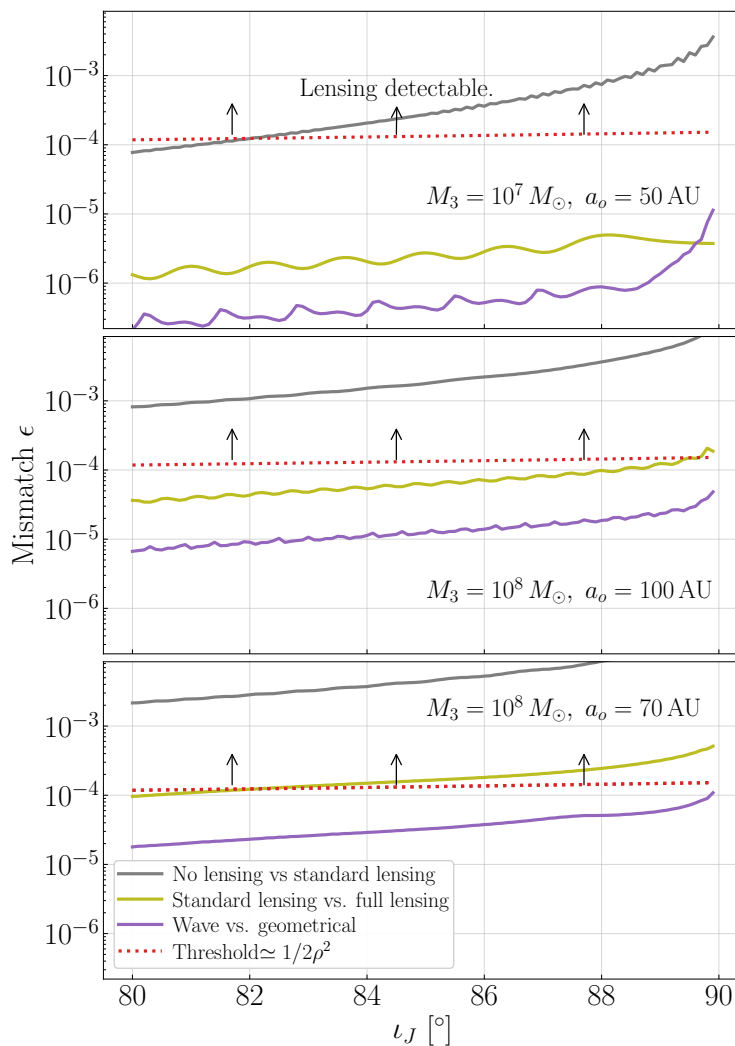


Figure 4.7: Mismatch ϵ of the waveform as a function of the inclination ι_J for three different outer orbital configurations, assuming a TianGO-like decihertz detector. In each panel, we use the grey trace to indicate the mismatch between a waveform without any lensing signatures with the one including the standard lensing (source behind the lens). The mismatches between waveforms with standard lensing only and those further including retro-lensing effects are illustrated in the olive traces. The purple traces shows the mismatches between the lensing signatures calculated under the classical/geometrical limit (for both standard and retro lensing) and those incorporating wave effects. The top and middle panels both have out orbital periods of $P_o \simeq 0.1 \text{ yr}$ and the bottom panel has $P_o = 0.06 \text{ yr}$. For a relatively light lens with $M_3 \lesssim 10^7 M_\odot$, there is a decent chance of detecting the standard lensing. For more massive lenses $M_3 \simeq 10^8 M_\odot$, we might further detect the glory (retro-lensing). Recall that we have $w = 8\pi M_3 f = 12 (M_3/10^7 M_\odot) (f/0.01 \text{ Hz}) \gg 1$ and therefore the geometrical limit is typically a good approximation as indicated by the purple traces.

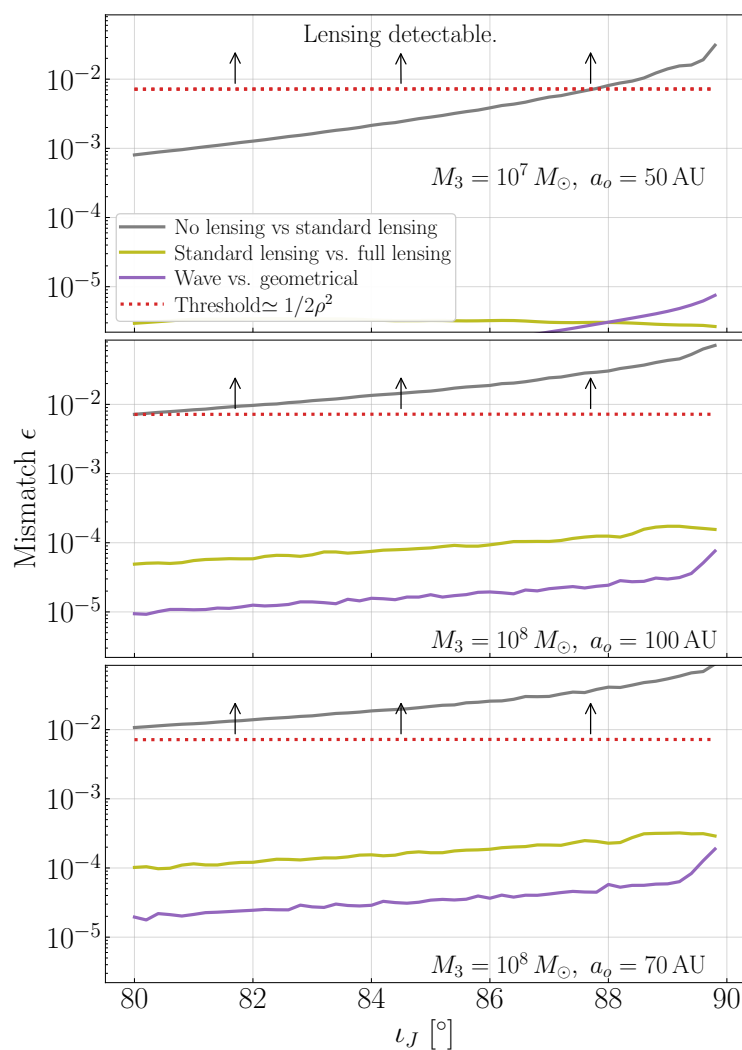


Figure 4.8: Similar to Fig. 4.7 but for LISA. We also moved the source’s luminosity distance from 1 Gpc to 200 Mpc so that the source’s SNR in LISA is greater than 8. For LISA, the standard lensing could have a decent detectability (a few to ten percent) while the retro-lensing are typically too weak to be detectable.

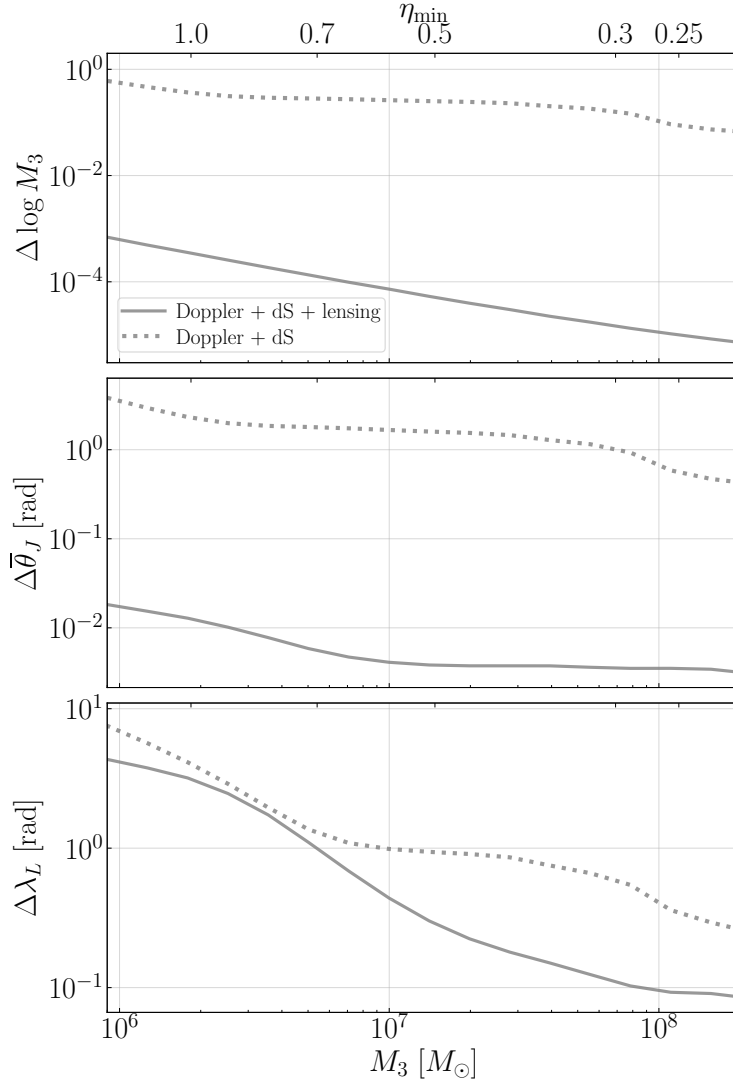


Figure 4.9: PE accuracy for systems with (solid traces) and without (dotted traces) the (standard) gravitational lensing, assuming detection by a single, TianGO-like detector. Here we fix $\iota_J = 87^\circ$ and vary the mass of the central SMBH. The semi-major axis is chosen such that the outer orbital period is $P_o = 0.1 \text{ yr}$. For this ι_J , we have $\epsilon > 1/2\rho^2$ when $M_3 \gtrsim 1.7 \times 10^6$ or $\eta_{\min} \lesssim 1$. Both $\log M_3$ and $\bar{\theta}_J$ can be determined better by orders of magnitude. The determination of the opening angle $\Delta\lambda_L$ is also improved, especially when P_{dS} in the range of 10-45 years.

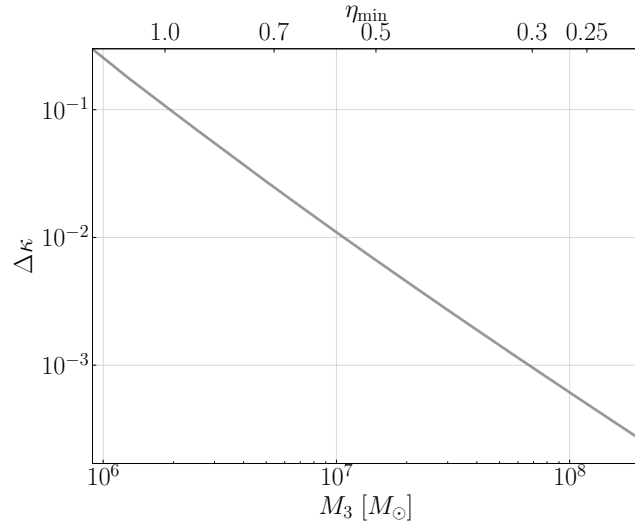


Figure 4.10: PE accuracy for κ where $\kappa = M_l/M_3$ [Eq. (4.36)]. The source’s orientation and sky location are the same as in Fig. 4.9. The error in κ decreases roughly linearly with M_3 and it can be constrained to a 1% accuracy for $M_3 \gtrsim 10^7 M_\odot$.

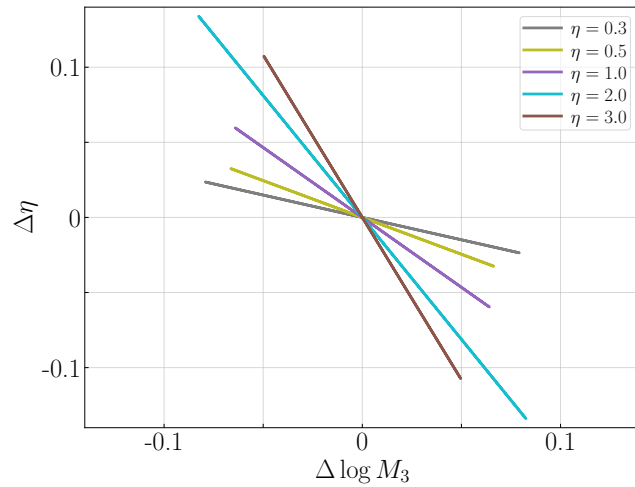


Figure 4.11: Error ellipses for the simple static lensing (i.e., $\eta = \beta/\theta_{Ein} = \text{constant}$ for the entire waveform). At each given η , the PE error $\Delta \log M_3$ is highly correlated with $\Delta \eta$, and thus the PE error obtained by inverting the Fisher matrix is much greater than the inverse of the diagonal elements. On the other hand, the orientation of the error ellipse varies as η varies [Eq. (4.47)]. Therefore, in the case of repeated lensing where $\eta = \eta(t)$ due to the outer orbit’s motion, different values of η are sampled and thus breaks the degeneracy between $\log M_3$ and η , allowing a PE much better than the static lensing case [cf. eq. (32) in Ref. [57].]

References

- [1] LIGO Scientific Collaboration and Virgo Collaboration. “Observation of Gravitational Waves from a Binary Black Hole Merger.” In: *Phys. Rev. Lett.* 116.6, 061102 (Feb. 2016), p. 061102. DOI: [10.1103/PhysRevLett.116.061102](https://doi.org/10.1103/PhysRevLett.116.061102). arXiv: [1602.03837](https://arxiv.org/abs/1602.03837) [gr-qc].
- [2] LIGO Scientific Collaboration. “Advanced LIGO.” In: *Classical and Quantum Gravity* 32.7, 074001 (Apr. 2015), p. 074001. DOI: [10.1088/0264-9381/32/7/074001](https://doi.org/10.1088/0264-9381/32/7/074001). arXiv: [1411.4547](https://arxiv.org/abs/1411.4547) [gr-qc].
- [3] F. Acernese, M. Agathos, K. Agatsuma, et al. “Advanced Virgo: a second-generation interferometric gravitational wave detector.” In: *Classical and Quantum Gravity* 32.2, 024001 (Jan. 2015), p. 024001. DOI: [10.1088/0264-9381/32/2/024001](https://doi.org/10.1088/0264-9381/32/2/024001). arXiv: [1408.3978](https://arxiv.org/abs/1408.3978) [gr-qc].
- [4] Kagra Collaboration and et al. “KAGRA: 2.5 generation interferometric gravitational wave detector.” In: *Nature Astronomy* 3 (Jan. 2019), pp. 35–40. DOI: [10.1038/s41550-018-0658-y](https://doi.org/10.1038/s41550-018-0658-y). arXiv: [1811.08079](https://arxiv.org/abs/1811.08079) [gr-qc].
- [5] LIGO Scientific Collaboration and Virgo Collaboration. “GWTC-1: A Gravitational-Wave Transient Catalog of Compact Binary Mergers Observed by LIGO and Virgo during the First and Second Observing Runs.” In: *Physical Review X* 9.3, 031040 (July 2019), p. 031040. DOI: [10.1103/PhysRevX.9.031040](https://doi.org/10.1103/PhysRevX.9.031040). arXiv: [1811.12907](https://arxiv.org/abs/1811.12907) [astro-ph.HE].
- [6] LIGO Scientific Collaboration and Virgo Collaboration. “GWTC-2: Compact Binary Coalescences Observed by LIGO and Virgo during the First Half of the Third Observing Run.” In: *Physical Review X* 11.2, 021053 (Apr. 2021), p. 021053. DOI: [10.1103/PhysRevX.11.021053](https://doi.org/10.1103/PhysRevX.11.021053). arXiv: [2010.14527](https://arxiv.org/abs/2010.14527) [gr-qc].
- [7] P. Amaro-Seoane, H. Audley, S. Babak, et al. “Laser Interferometer Space Antenna.” In: *arXiv e-prints*, arXiv:1702.00786 (Feb. 2017), arXiv:1702.00786. arXiv: [1702.00786](https://arxiv.org/abs/1702.00786) [astro-ph.IM].
- [8] J. Luo, L.-S. Chen, H.-Z. Duan, et al. “TianQin: a space-borne gravitational wave detector.” In: *Classical and Quantum Gravity* 33.3, 035010 (Feb. 2016), p. 035010. DOI: [10.1088/0264-9381/33/3/035010](https://doi.org/10.1088/0264-9381/33/3/035010). arXiv: [1512.02076](https://arxiv.org/abs/1512.02076) [astro-ph.IM].
- [9] W.-R. Hu and Y.-L. Wu. “The Taiji Program in Space for gravitational wave physics and the nature of gravity.” In: *National Science Review* 4.5 (Oct. 2017), pp. 685–686. ISSN: 2095-5138. DOI: [10.1093/nsr/nwx116](https://doi.org/10.1093/nsr/nwx116). eprint: <https://academic.oup.com/nsr/article-pdf/4/5/685/31566708/nwx116.pdf>. URL: <https://doi.org/10.1093/nsr/nwx116>.
- [10] T. Nakamura, M. Ando, T. Kinugawa, et al. “Pre-DECIGO can get the smoking gun to decide the astrophysical or cosmological origin of GW150914-like binary black holes.” In: *Progress of Theoretical and Experimental Physics*

- 2016.9, 093E01 (Sept. 2016), 093E01. DOI: [10.1093/ptep/ptw127](https://doi.org/10.1093/ptep/ptw127). arXiv: [1607.00897](https://arxiv.org/abs/1607.00897) [astro-ph.HE].
- [11] S. Kawamura, M. Ando, N. Seto, et al. “Current status of space gravitational wave antenna DECIGO and B-DECIGO.” In: *arXiv e-prints*, arXiv:2006.13545 (June 2020), arXiv:2006.13545. arXiv: [2006.13545](https://arxiv.org/abs/2006.13545) [gr-qc].
- [12] M. Arca Sedda, C. P. L. Berry, K. Jani, et al. “The Missing Link in Gravitational-Wave Astronomy: Discoveries waiting in the decihertz range.” In: *arXiv e-prints*, arXiv:1908.11375 (Aug. 2019), arXiv:1908.11375. arXiv: [1908.11375](https://arxiv.org/abs/1908.11375) [gr-qc].
- [13] K. A. Kuns, H. Yu, Y. Chen, et al. “Astrophysics and cosmology with a decihertz gravitational-wave detector: TianGO.” In: *Phys. Rev. D* 102 (4 Aug. 2020), p. 043001. DOI: [10.1103/PhysRevD.102.043001](https://doi.org/10.1103/PhysRevD.102.043001). URL: <https://link.aps.org/doi/10.1103/PhysRevD.102.043001>.
- [14] B. McKernan, K. E. S. Ford, W. Lyra, et al. “Intermediate mass black holes in AGN discs - I. Production and growth.” In: *MNRAS* 425.1 (Sept. 2012), pp. 460–469. DOI: [10.1111/j.1365-2966.2012.21486.x](https://doi.org/10.1111/j.1365-2966.2012.21486.x). arXiv: [1206.2309](https://arxiv.org/abs/1206.2309) [astro-ph.GA].
- [15] I. Bartos, B. Kocsis, Z. Haiman, et al. “Rapid and Bright Stellar-mass Binary Black Hole Mergers in Active Galactic Nuclei.” In: *ApJ* 835.2, 165 (Feb. 2017), p. 165. DOI: [10.3847/1538-4357/835/2/165](https://doi.org/10.3847/1538-4357/835/2/165). arXiv: [1602.03831](https://arxiv.org/abs/1602.03831) [astro-ph.HE].
- [16] N. C. Stone, B. D. Metzger, and Z. Haiman. “Assisted inspirals of stellar mass black holes embedded in AGN discs: solving the ‘final au problem’.” In: *MNRAS* 464.1 (Jan. 2017), pp. 946–954. DOI: [10.1093/mnras/stw2260](https://doi.org/10.1093/mnras/stw2260). arXiv: [1602.04226](https://arxiv.org/abs/1602.04226) [astro-ph.GA].
- [17] B. McKernan, K. E. S. Ford, J. Bellovary, et al. “Constraining Stellar-mass Black Hole Mergers in AGN Disks Detectable with LIGO.” In: *ApJ* 866.1, 66 (Oct. 2018), p. 66. DOI: [10.3847/1538-4357/aadae5](https://doi.org/10.3847/1538-4357/aadae5). arXiv: [1702.07818](https://arxiv.org/abs/1702.07818) [astro-ph.HE].
- [18] H. Tagawa, Z. Haiman, and B. Kocsis. “Formation and Evolution of Compact Object Binaries in AGN Disks.” In: *arXiv e-prints*, arXiv:1912.08218 (Dec. 2019), arXiv:1912.08218. arXiv: [1912.08218](https://arxiv.org/abs/1912.08218) [astro-ph.GA].
- [19] Y. Yang, I. Bartos, V. Gayathri, et al. “Hierarchical Black Hole Mergers in Active Galactic Nuclei.” In: *Phys. Rev. Lett.* 123.18, 181101 (Nov. 2019), p. 181101. DOI: [10.1103/PhysRevLett.123.181101](https://doi.org/10.1103/PhysRevLett.123.181101). arXiv: [1906.09281](https://arxiv.org/abs/1906.09281) [astro-ph.HE].
- [20] J. M. Bellovary, M.-M. Mac Low, B. McKernan, et al. “Migration Traps in Disks around Supermassive Black Holes.” In: *ApJ* 819.2, L17 (Mar. 2016), p. L17. DOI: [10.3847/2041-8205/819/2/L17](https://doi.org/10.3847/2041-8205/819/2/L17). arXiv: [1511.00005](https://arxiv.org/abs/1511.00005) [astro-ph.GA].

- [21] A. Secunda, J. Bellovary, M.-M. Mac Low, et al. “Orbital Migration of Interacting Stellar Mass Black Holes in Disks around Supermassive Black Holes.” In: *ApJ* 878.2, 85 (June 2019), p. 85. doi: [10.3847/1538-4357/ab20ca](https://doi.org/10.3847/1538-4357/ab20ca). arXiv: [1807.02859](https://arxiv.org/abs/1807.02859) [astro-ph.HE].
- [22] R. M. O’Leary, B. Kocsis, and A. Loeb. “Gravitational waves from scattering of stellar-mass black holes in galactic nuclei.” In: *MNRAS* 395.4 (June 2009), pp. 2127–2146. doi: [10.1111/j.1365-2966.2009.14653.x](https://doi.org/10.1111/j.1365-2966.2009.14653.x). arXiv: [0807.2638](https://arxiv.org/abs/0807.2638) [astro-ph].
- [23] F. Antonini and H. B. Perets. “Secular Evolution of Compact Binaries near Massive Black Holes: Gravitational Wave Sources and Other Exotica.” In: *ApJ* 757.1, 27 (Sept. 2012), p. 27. doi: [10.1088/0004-637X/757/1/27](https://doi.org/10.1088/0004-637X/757/1/27). arXiv: [1203.2938](https://arxiv.org/abs/1203.2938) [astro-ph.GA].
- [24] F. Antonini and F. A. Rasio. “Merging Black Hole Binaries in Galactic Nuclei: Implications for Advanced-LIGO Detections.” In: *ApJ* 831.2, 187 (Nov. 2016), p. 187. doi: [10.3847/0004-637X/831/2/187](https://doi.org/10.3847/0004-637X/831/2/187). arXiv: [1606.04889](https://arxiv.org/abs/1606.04889) [astro-ph.HE].
- [25] J. H. VanLandingham, M. C. Miller, D. P. Hamilton, et al. “The Role of the Kozai–Lidov Mechanism in Black Hole Binary Mergers in Galactic Centers.” In: *ApJ* 828.2, 77 (Sept. 2016), p. 77. doi: [10.3847/0004-637X/828/2/77](https://doi.org/10.3847/0004-637X/828/2/77). arXiv: [1604.04948](https://arxiv.org/abs/1604.04948) [astro-ph.HE].
- [26] C. Petrovich and F. Antonini. “Greatly Enhanced Merger Rates of Compact-object Binaries in Non-spherical Nuclear Star Clusters.” In: *ApJ* 846.2, 146 (Sept. 2017), p. 146. doi: [10.3847/1538-4357/aa8628](https://doi.org/10.3847/1538-4357/aa8628). arXiv: [1705.05848](https://arxiv.org/abs/1705.05848) [astro-ph.HE].
- [27] N. W. C. Leigh, A. M. Geller, B. McKernan, et al. “On the rate of black hole binary mergers in galactic nuclei due to dynamical hardening.” In: *MNRAS* 474.4 (Mar. 2018), pp. 5672–5683. doi: [10.1093/mnras/stx3134](https://doi.org/10.1093/mnras/stx3134). arXiv: [1711.10494](https://arxiv.org/abs/1711.10494) [astro-ph.GA].
- [28] X. Chen and W.-B. Han. “Extreme-mass-ratio inspirals produced by tidal capture of binary black holes.” In: *Communications Physics* 1.1, 53 (Sept. 2018), p. 53. doi: [10.1038/s42005-018-0053-0](https://doi.org/10.1038/s42005-018-0053-0). arXiv: [1801.05780](https://arxiv.org/abs/1801.05780) [astro-ph.HE].
- [29] G. Fragione, N. W. C. Leigh, and R. Perna. “Black hole and neutron star mergers in galactic nuclei: the role of triples.” In: *MNRAS* 488.2 (Sept. 2019), pp. 2825–2835. doi: [10.1093/mnras/stz1803](https://doi.org/10.1093/mnras/stz1803). arXiv: [1903.09160](https://arxiv.org/abs/1903.09160) [astro-ph.GA].
- [30] W.-B. Han and X. Chen. “Testing general relativity using binary extreme-mass-ratio inspirals.” In: *MNRAS* 485.1 (May 2019), pp. L29–L33. doi: [10.1093/mnrasl/slz021](https://doi.org/10.1093/mnrasl/slz021). arXiv: [1801.07060](https://arxiv.org/abs/1801.07060) [gr-qc].

- [31] J. Samsing, I. Bartos, D. J. D’Orazio, et al. “Active Galactic Nuclei as Factories for Eccentric Black Hole Mergers.” In: *arXiv e-prints*, arXiv:2010.09765 (Oct. 2020), arXiv:2010.09765. arXiv: [2010.09765 \[astro-ph.HE\]](#).
- [32] X. Chen, Z.-Y. Xuan, and P. Peng. “Fake Massive Black Holes in the Millihertz Gravitational-wave Band.” In: *ApJ* 896.2, 171 (June 2020), p. 171. doi: [10.3847/1538-4357/ab919f](#). arXiv: [2003.08639 \[astro-ph.HE\]](#).
- [33] X. Chen. “Distortion of Gravitational-wave Signals by Astrophysical Environments.” In: *arXiv e-prints*, arXiv:2009.07626 (Sept. 2020), arXiv:2009.07626. arXiv: [2009.07626 \[astro-ph.HE\]](#).
- [34] A. Caputo, L. Sberna, A. Toubiana, et al. “Gravitational-wave Detection and Parameter Estimation for Accreting Black-hole Binaries and Their Electromagnetic Counterpart.” In: *ApJ* 892.2, 90 (Apr. 2020), p. 90. doi: [10.3847/1538-4357/ab7b66](#). arXiv: [2001.03620 \[astro-ph.HE\]](#).
- [35] A. Toubiana, L. Sberna, A. Caputo, et al. “Detectable Environmental Effects in GW190521-like Black-Hole Binaries with LISA.” In: *Phys. Rev. Lett.* 126.10, 101105 (Mar. 2021), p. 101105. doi: [10.1103/PhysRevLett.126.101105](#). arXiv: [2010.06056 \[astro-ph.HE\]](#).
- [36] K. Inayoshi, N. Tamanini, C. Caprini, et al. “Probing stellar binary black hole formation in galactic nuclei via the imprint of their center of mass acceleration on their gravitational wave signal.” In: *Phys. Rev. D* 96.6, 063014 (Sept. 2017), p. 063014. doi: [10.1103/PhysRevD.96.063014](#). arXiv: [1702.06529 \[astro-ph.HE\]](#).
- [37] L. Randall and Z.-Z. Xianyu. “A Direct Probe of Mass Density near Inspiral Binary Black Holes.” In: *ApJ* 878.2, 75 (June 2019), p. 75. doi: [10.3847/1538-4357/ab20c6](#). arXiv: [1805.05335 \[gr-qc\]](#).
- [38] B.-M. Hoang, S. Naoz, B. Kocsis, et al. “Detecting Supermassive Black Hole-induced Binary Eccentricity Oscillations with LISA.” In: *ApJ* 875.2, L31 (Apr. 2019), p. L31. doi: [10.3847/2041-8213/ab14f7](#). arXiv: [1903.00134 \[astro-ph.HE\]](#).
- [39] B. Deme, B.-M. Hoang, S. Naoz, et al. “Detecting Kozai-Lidov Imprints on the Gravitational Waves of Intermediate-mass Black Holes in Galactic Nuclei.” In: *ApJ* 901.2, 125 (Oct. 2020), p. 125. doi: [10.3847/1538-4357/abafa3](#). arXiv: [2005.03677 \[astro-ph.HE\]](#).
- [40] R. S. Chandramouli and N. Yunes. “The Trouble with Triples: Ready-to-use Analytic Model for Gravitational Waves from a Hierarchical Triple with Kozai-Lidov Oscillations.” In: *arXiv e-prints*, arXiv:2107.00741 (July 2021), arXiv:2107.00741. arXiv: [2107.00741 \[gr-qc\]](#).
- [41] H. Yu and Y. Chen. “Direct Determination of Supermassive Black Hole Properties with Gravitational-Wave Radiation from Surrounding Stellar-Mass Black Hole Binaries.” In: *Phys. Rev. Lett.* 126.2, 021101 (Jan. 2021), p. 021101. doi: [10.1103/PhysRevLett.126.021101](#). arXiv: [2009.02579 \[gr-qc\]](#).

- [42] C. M. Will. “New General Relativistic Contribution to Mercury’s Perihelion Advance.” In: *Phys. Rev. Lett.* 120.19, 191101 (May 2018), p. 191101. DOI: [10.1103/PhysRevLett.120.191101](https://doi.org/10.1103/PhysRevLett.120.191101). arXiv: [1802.05304](https://arxiv.org/abs/1802.05304) [gr-qc].
- [43] B. Liu, D. Lai, and Y.-H. Wang. “Binary Mergers near a Supermassive Black Hole: Relativistic Effects in Triples.” In: *ApJ* 883.1, L7 (Sept. 2019), p. L7. DOI: [10.3847/2041-8213/ab40c0](https://doi.org/10.3847/2041-8213/ab40c0). arXiv: [1906.07726](https://arxiv.org/abs/1906.07726) [astro-ph.HE].
- [44] A. Kuntz, F. Serra, and E. Trincherini. “Effective two-body approach to the hierarchical three-body problem.” In: *Phys. Rev. D* 104.2, 024016 (July 2021), p. 024016. DOI: [10.1103/PhysRevD.104.024016](https://doi.org/10.1103/PhysRevD.104.024016). arXiv: [2104.13387](https://arxiv.org/abs/2104.13387) [hep-th].
- [45] B. M. Peterson. “Measuring the Masses of Supermassive Black Holes.” In: *Space Sci. Rev.* 183.1-4 (Sept. 2014), pp. 253–275. DOI: [10.1007/s11214-013-9987-4](https://doi.org/10.1007/s11214-013-9987-4).
- [46] D. J. D’Orazio and A. Loeb. “Repeated gravitational lensing of gravitational waves in hierarchical black hole triples.” In: *Phys. Rev. D* 101.8, 083031 (Apr. 2020), p. 083031. DOI: [10.1103/PhysRevD.101.083031](https://doi.org/10.1103/PhysRevD.101.083031). arXiv: [1910.02966](https://arxiv.org/abs/1910.02966) [astro-ph.HE].
- [47] K. S. Virbhadra and G. F. R. Ellis. “Schwarzschild black hole lensing.” In: *Phys. Rev. D* 62.8, 084003 (Oct. 2000), p. 084003. DOI: [10.1103/PhysRevD.62.084003](https://doi.org/10.1103/PhysRevD.62.084003). arXiv: [astro-ph/9904193](https://arxiv.org/abs/astro-ph/9904193) [astro-ph].
- [48] V. Bozza. “Gravitational lensing in the strong field limit.” In: *Phys. Rev. D* 66.10, 103001 (Nov. 2002), p. 103001. DOI: [10.1103/PhysRevD.66.103001](https://doi.org/10.1103/PhysRevD.66.103001). arXiv: [gr-qc/0208075](https://arxiv.org/abs/gr-qc/0208075) [gr-qc].
- [49] V. Bozza and G. Scarpetta. “Strong deflection limit of black hole gravitational lensing with arbitrary source distances.” In: *Phys. Rev. D* 76.8, 083008 (Oct. 2007), p. 083008. DOI: [10.1103/PhysRevD.76.083008](https://doi.org/10.1103/PhysRevD.76.083008). arXiv: [0705.0246](https://arxiv.org/abs/0705.0246) [gr-qc].
- [50] E. F. Eiroa and C. M. Sendra. “Gravitational lensing by a regular black hole.” In: *Classical and Quantum Gravity* 28.8, 085008 (Apr. 2011), p. 085008. DOI: [10.1088/0264-9381/28/8/085008](https://doi.org/10.1088/0264-9381/28/8/085008). arXiv: [1011.2455](https://arxiv.org/abs/1011.2455) [gr-qc].
- [51] K. S. Virbhadra. “Relativistic images of Schwarzschild black hole lensing.” In: *Phys. Rev. D* 79.8, 083004 (Apr. 2009), p. 083004. DOI: [10.1103/PhysRevD.79.083004](https://doi.org/10.1103/PhysRevD.79.083004). arXiv: [0810.2109](https://arxiv.org/abs/0810.2109) [gr-qc].
- [52] J. -. Luminet. “Image of a spherical black hole with thin accretion disk..” In: *A&A* 75 (May 1979), pp. 228–235.
- [53] D. E. Holz and J. A. Wheeler. “Retro-MACHOs: π in the Sky?.” In: *ApJ* 578.1 (Oct. 2002), pp. 330–334. DOI: [10.1086/342463](https://doi.org/10.1086/342463). arXiv: [astro-ph/0209039](https://arxiv.org/abs/astro-ph/0209039) [astro-ph].

- [54] E. F. Eiroa and D. F. Torres. “Strong field limit analysis of gravitational retrolensing.” In: *Phys. Rev. D* 69.6, 063004 (Mar. 2004), p. 063004. DOI: [10.1103/PhysRevD.69.063004](https://doi.org/10.1103/PhysRevD.69.063004). arXiv: [gr-qc/0311013](https://arxiv.org/abs/gr-qc/0311013) [gr-qc].
- [55] V. Bozza. “Gravitational lensing by black holes.” In: *General Relativity and Gravitation* 42.9 (Sept. 2010), pp. 2269–2300. DOI: [10.1007/s10714-010-0988-2](https://doi.org/10.1007/s10714-010-0988-2). arXiv: [0911.2187](https://arxiv.org/abs/0911.2187) [gr-qc].
- [56] E. F. Eiroa. “Strong deflection gravitational lensing.” In: *arXiv e-prints*, arXiv:1212.4535 (Dec. 2012), arXiv:1212.4535. arXiv: [1212.4535](https://arxiv.org/abs/1212.4535) [gr-qc].
- [57] R. Takahashi and T. Nakamura. “Wave Effects in the Gravitational Lensing of Gravitational Waves from Chirping Binaries.” In: *ApJ* 595.2 (Oct. 2003), pp. 1039–1051. DOI: [10.1086/377430](https://doi.org/10.1086/377430). arXiv: [astro-ph/0305055](https://arxiv.org/abs/astro-ph/0305055) [astro-ph].
- [58] T. A. Apostolatos, C. Cutler, G. J. Sussman, et al. “Spin-induced orbital precession and its modulation of the gravitational waveforms from merging binaries.” In: *Phys. Rev. D* 49.12 (June 1994), pp. 6274–6297. DOI: [10.1103/PhysRevD.49.6274](https://doi.org/10.1103/PhysRevD.49.6274).
- [59] C. Cutler. “Angular resolution of the LISA gravitational wave detector.” In: *Phys. Rev. D* 57.12 (June 1998), pp. 7089–7102. DOI: [10.1103/PhysRevD.57.7089](https://doi.org/10.1103/PhysRevD.57.7089). arXiv: [gr-qc/9703068](https://arxiv.org/abs/gr-qc/9703068) [gr-qc].
- [60] S. V. Dhurandhar, K. R. Nayak, S. Koshti, et al. “Fundamentals of the LISA stable flight formation.” In: *Classical and Quantum Gravity* 22.3 (Feb. 2005), pp. 481–487. DOI: [10.1088/0264-9381/22/3/002](https://doi.org/10.1088/0264-9381/22/3/002). arXiv: [gr-qc/0410093](https://arxiv.org/abs/gr-qc/0410093) [astro-ph].
- [61] D. J. D’Orazio and R. Di Stefano. “Periodic self-lensing from accreting massive black hole binaries.” In: *MNRAS* 474.3 (Mar. 2018), pp. 2975–2986. DOI: [10.1093/mnras/stx2936](https://doi.org/10.1093/mnras/stx2936). arXiv: [1707.02335](https://arxiv.org/abs/1707.02335) [astro-ph.HE].
- [62] T. T. Nakamura and S. Deguchi. “Wave Optics in Gravitational Lensing.” In: *Progress of Theoretical Physics Supplement* 133 (Jan. 1999), pp. 137–153. DOI: [10.1143/PTPS.133.137](https://doi.org/10.1143/PTPS.133.137).
- [63] R. A. Matzner, C. Dewitte-Morette, B. Nelson, et al. “Glory scattering by black holes.” In: *Phys. Rev. D* 31.8 (Apr. 1985), pp. 1869–1878. DOI: [10.1103/PhysRevD.31.1869](https://doi.org/10.1103/PhysRevD.31.1869).
- [64] V. Bozza and L. Mancini. “Time Delay in Black Hole Gravitational Lensing as a Distance Estimator.” In: *General Relativity and Gravitation* 36.2 (Feb. 2004), pp. 435–450. DOI: [10.1023/B:GERG.0000010486.58026.4f](https://doi.org/10.1023/B:GERG.0000010486.58026.4f). arXiv: [gr-qc/0305007](https://arxiv.org/abs/gr-qc/0305007) [gr-qc].

- [65] T. Robson, N. J. Cornish, and C. Liu. “The construction and use of LISA sensitivity curves.” In: *Classical and Quantum Gravity* 36.10, 105011 (May 2019), p. 105011. DOI: [10.1088/1361-6382/ab1101](https://doi.org/10.1088/1361-6382/ab1101). arXiv: [1803.01944](https://arxiv.org/abs/1803.01944) [astro-ph.HE].
- [66] C.-M. Claudel, K. S. Virbhadra, and G. F. R. Ellis. “The geometry of photon surfaces.” In: *Journal of Mathematical Physics* 42.2 (Feb. 2001), pp. 818–838. DOI: [10.1063/1.1308507](https://doi.org/10.1063/1.1308507). arXiv: [gr-qc/0005050](https://arxiv.org/abs/gr-qc/0005050) [gr-qc].
- [67] B. M. Barker and R. F. O’Connell. “Gravitational two-body problem with arbitrary masses, spins, and quadrupole moments.” In: *Phys. Rev. D* 12.2 (July 1975), pp. 329–335. DOI: [10.1103/PhysRevD.12.329](https://doi.org/10.1103/PhysRevD.12.329).
- [68] L. Lindblom, B. J. Owen, and D. A. Brown. “Model waveform accuracy standards for gravitational wave data analysis.” In: *Phys. Rev. D* 78.12, 124020 (Dec. 2008), p. 124020. DOI: [10.1103/PhysRevD.78.124020](https://doi.org/10.1103/PhysRevD.78.124020). arXiv: [0809.3844](https://arxiv.org/abs/0809.3844) [gr-qc].
- [69] Y. Fang, X. Chen, and Q.-G. Huang. “Impact of a Spinning Supermassive Black Hole on the Orbit and Gravitational Waves of a Nearby Compact Binary.” In: *ApJ* 887.2, 210 (Dec. 2019), p. 210. DOI: [10.3847/1538-4357/ab510e](https://doi.org/10.3847/1538-4357/ab510e). arXiv: [1908.01443](https://arxiv.org/abs/1908.01443) [astro-ph.HE].
- [70] G. M. Harry, P. Fritschel, D. A. Shaddock, et al. “Laser interferometry for the Big Bang Observer.” In: *Classical and Quantum Gravity* 23.15 (Aug. 2006), pp. 4887–4894. DOI: [10.1088/0264-9381/23/15/008](https://doi.org/10.1088/0264-9381/23/15/008).
- [71] C. M. Will. “Propagation Speed of Gravity and the Relativistic Time Delay.” In: *ApJ* 590.2 (June 2003), pp. 683–690. DOI: [10.1086/375164](https://doi.org/10.1086/375164). arXiv: [astro-ph/0301145](https://arxiv.org/abs/astro-ph/0301145) [astro-ph].
- [72] C. M. Will. “The Confrontation between General Relativity and Experiment.” In: *Living Reviews in Relativity* 17.1, 4 (Dec. 2014), p. 4. DOI: [10.12942/lrr-2014-4](https://doi.org/10.12942/lrr-2014-4). arXiv: [1403.7377](https://arxiv.org/abs/1403.7377) [gr-qc].
- [73] Z. Hongsheng and F. Xilong. “Poisson-Arago spot for gravitational waves.” In: *arXiv e-prints*, arXiv:1809.06511 (Sept. 2018), arXiv:1809.06511. arXiv: [1809.06511](https://arxiv.org/abs/1809.06511) [gr-qc].
- [74] C. S. Reynolds. “The spin of supermassive black holes.” In: *Classical and Quantum Gravity* 30.24, 244004 (Dec. 2013), p. 244004. DOI: [10.1088/0264-9381/30/24/244004](https://doi.org/10.1088/0264-9381/30/24/244004). arXiv: [1307.3246](https://arxiv.org/abs/1307.3246) [astro-ph.HE].
- [75] B. Liu and D. Lai. “Probing the Spins of Supermassive Black Holes with Gravitational Waves from Surrounding Compact Binaries.” In: *arXiv e-prints*, arXiv:2105.02230 (May 2021), arXiv:2105.02230. arXiv: [2105.02230](https://arxiv.org/abs/2105.02230) [astro-ph.HE].
- [76] V. Bozza. “Quasiequatorial gravitational lensing by spinning black holes in the strong field limit.” In: *Phys. Rev. D* 67.10, 103006 (May 2003), p. 103006. DOI: [10.1103/PhysRevD.67.103006](https://doi.org/10.1103/PhysRevD.67.103006). arXiv: [gr-qc/0210109](https://arxiv.org/abs/gr-qc/0210109) [gr-qc].

- [77] V. Bozza, F. de Luca, G. Scarpetta, et al. “Analytic Kerr black hole lensing for equatorial observers in the strong deflection limit.” In: *Phys. Rev. D* 72.8, 083003 (Oct. 2005), p. 083003. DOI: [10.1103/PhysRevD.72.083003](https://doi.org/10.1103/PhysRevD.72.083003). arXiv: [gr-qc/0507137](https://arxiv.org/abs/gr-qc/0507137) [gr-qc].
- [78] V. Bozza, F. de Luca, and G. Scarpetta. “Kerr black hole lensing for generic observers in the strong deflection limit.” In: *Phys. Rev. D* 74.6, 063001 (Sept. 2006), p. 063001. DOI: [10.1103/PhysRevD.74.063001](https://doi.org/10.1103/PhysRevD.74.063001). arXiv: [gr-qc/0604093](https://arxiv.org/abs/gr-qc/0604093) [gr-qc].
- [79] A. Torres-Orjuela, X. Chen, and P. Amaro-Seoane. “Excitation of gravitational wave modes by a center-of-mass velocity of the source.” In: *arXiv e-prints*, arXiv:2010.15856 (Oct. 2020), arXiv:2010.15856. arXiv: [2010.15856](https://arxiv.org/abs/2010.15856) [astro-ph.CO].
- [80] V. Cardoso, F. Duque, and G. Khanna. “Gravitational tuning forks and hierarchical triple systems.” In: *arXiv e-prints*, arXiv:2101.01186 (Jan. 2021), arXiv:2101.01186. arXiv: [2101.01186](https://arxiv.org/abs/2101.01186) [gr-qc].
- [81] H. Yu, S. Ma, M. Giesler, et al. “Spin and eccentricity evolution in triple systems: From the Lidov-Kozai interaction to the final merger of the inner binary.” In: *Phys. Rev. D* 102.12, 123009 (Dec. 2020), p. 123009. DOI: [10.1103/PhysRevD.102.123009](https://doi.org/10.1103/PhysRevD.102.123009). arXiv: [2007.12978](https://arxiv.org/abs/2007.12978) [gr-qc].

MEASURING SUPERMASSIVE BLACK HOLE PROPERTIES VIA GRAVITATIONAL RADIATION FROM ECCENTRICALLY ORBITING STELLAR MASS BLACK HOLE BINARIES

- [1] A. Laeuger, B. Seymour, Y. Chen, et al. “Measuring supermassive black hole properties via gravitational radiation from eccentrically orbiting stellar mass black hole binaries.” In: *Phys. Rev. D* 109.6 (2024), p. 064086. DOI: [10.1103/PhysRevD.109.064086](https://doi.org/10.1103/PhysRevD.109.064086). arXiv: [2310.16799](https://arxiv.org/abs/2310.16799) [gr-qc].

5.1 Introduction

Since the first detection of gravitational waves (GWs), GW astronomy by ground-based detectors has cemented itself as an advantageous method for studying binary systems of compact objects, the majority of which are binary black holes (BBHs) [1, 2, 3]. Within the population of observed BBHs, there are systems with progenitors whose masses exceed the predictions of stellar evolution [4, 5, 6, 7]. One possible explanation of this detection could be that the progenitors themselves were themselves products of previous mergers [8, 9, 10, 11]. The deep potential wells created by supermassive black holes (SMBHs) and their host galactic nuclei could trap the products of stellar mass BBH mergers, making galactic nuclei ideal locations for generating many repeated compact object mergers [12, 10, 11]. Numerical simulations of BBH formation in galactic nuclei due to gas friction [13, 14] and dynamic capture through gravitational interactions [15] suggest that the cosmological merger rate of BBH near galactic nuclei could be of order \sim a few $\text{Gpc}^{-3}\text{yr}^{-1}$. Studying the properties of these repeated merger systems and of the SMBHs which encourage their formation could open a new window on understanding the dynamics of galactic nuclei and the processes which drive galaxy evolution. The most recent analysis of the BBH population in GWTC-3 is consistent with contributions from both isolated and AGN formations [16], though more observations are needed.

In a hierarchical triple system consisting of a stellar-mass BBH orbiting an SMBH, as depicted in Fig. 5.1, the presence of the SMBH would modulate the BBH GW signal through many effects. For example, the velocity of the BBH in its orbit will produce a Doppler shift in the waveform [17, 18, 19]. Allowing the BBH to take an

eccentric orbit around the SMBH introduces relativistic effects such as pericenter precession as the outer orbital path approaches near the SMBH [20]. Furthermore, the presence of the SMBH will cause the orbital angular momentum of the inner binary \hat{L}_i to experience de Sitter precession about the orbital angular momentum of the outer binary \hat{L}_o [21]. This effect modulates the inclination angle of the BBH angular momentum relative to an observatory in the Solar System. The Lidov-Kozai and Lense-Thirring effects also play a role in the evolution of hierarchical triples [22, 23].

By measuring the effects of Doppler shifts, pericenter precession, and de Sitter precession on the stellar-mass BBH gravitational waveform, one can measure the properties of this triple system, including the SMBH mass, semimajor axis of the outer orbit, and various angles describing the system geometry [24, 23, 19, 17, 18, 20, 22]. In order to substantially modulate the GW signal, these effects must accumulate over time scales on the order of an orbital period, which for typical BBH+SMBH triple systems can range from months to years. But because the current ground detectors in LIGO/Virgo/KAGRA are most sensitive between 10 Hz to a few kHz, which correspond to only the final seconds before merger for a stellar-mass BBH, current GW observatories are not optimal for extracting hierarchical triple system parameters through the influence of the SMBH on the waveform [25, 26].

However, the coming decades could see the construction of a number of proposed space-based detectors which would be sensitive to frequencies below ~ 1 -10 Hz. Building low frequency detectors in space is necessary due to technical challenges from seismic noise [27, 28] and the need to create arms which are large compared to the curvature of the Earth. The LISA [29], TianQin [30], and Taiji [31, 32] detectors will target the millihertz GW band, while detector concepts such as B-DECIGO [33, 34] and TianGO [35, 36] will focus on the decihertz band. Since the instantaneous orbital decay timescale due to GW emission during inspiral scales roughly with $\omega_{orb}^{-8/3}$ [37], space-based low-frequency detectors could observe stellar mass BBH for much longer times than ground detectors, making them more favorable for measurements of SMBH-driven effects in the BBH waveform.

Measuring a SMBH with an orbiting binary's GW would be useful for studying the environment at the center of galaxies. In a recent work by Yu and Chen, it is shown that these proposed low-frequency GW observatories could feasibly measure properties of interest to the few percent level over a wide range of possible BBH+SMBH systems [24]. Current observational methods for measuring proper-

ties of SMBHs and their local environments include tracking the orbital dynamics of nearby test masses, like stars, and reverberation mapping of the emission line fluxes from the accretion disk, if the SMBH is active [38]. Recent advances in observational technology and modeling active galactic nuclei have enabled constraints of the masses of their central SMBHs to roughly 10% precision [39, 40, 41, 42], though the results obtained by each method do not always agree [43]. Adding a GW-based technique to this toolkit could expand the set of observable SMBHs with well-constrained properties to those which may have few electromagnetic radiation sources nearby [24] or foster improvements in established electromagnetic techniques through comparisons of joint measurements. Indeed, there has been significant progress in understanding how space-based GW observatories may be able to measure properties of SMBHs and the objects orbiting them through a variety of triple system phenomena [44, 23, 45, 46, 47].

The initial work of Yu and Chen assumes a circular Newtonian outer orbit in the BBH+SMBH triple system [24]; however, it is expected that formation channels for these systems, especially those which are dynamical in nature, should produce a sizeable population of triples with eccentric outer orbits [48]. In this work, we examine how adding a nonzero eccentricity to the outer orbit affects parameter measurement uncertainties. We demonstrate that a nonzero outer eccentricity can significantly improve these uncertainties compared to the circular case, primarily through the inclusion of outer orbit pericenter precession. In order to estimate parameter uncertainties, we rely on the Fisher information matrix, a method which has been frequently used in the past to gauge the measurability of compact binary parameters by ground-based GW observatories [49]. In short, we find that uncertainties in triple system parameters can consistently fall below the 0.1% level, and that these parameters are measured more precisely with larger e_o and by detectors targeting the decihertz band. We also find that the general trends in parameter measurement are influenced almost entirely by pericenter and de Sitter precession.

In Sec. 5.2, we outline the mathematical description of the gravitational waveform emitted from a BBH in a hierarchical triple and detected by a space-borne observatory. In Sec. 5.3, we outline the Fisher matrix calculation as applied to parameter estimation and explain some simplifications we make to the computation. In Sec. 5.4, we present the results of our Fisher matrix computations, and in Sec. 5.5, we offer conclusions and possible directions for this work to proceed in the future. In this work, we use geometrized units $G = c = 1$.

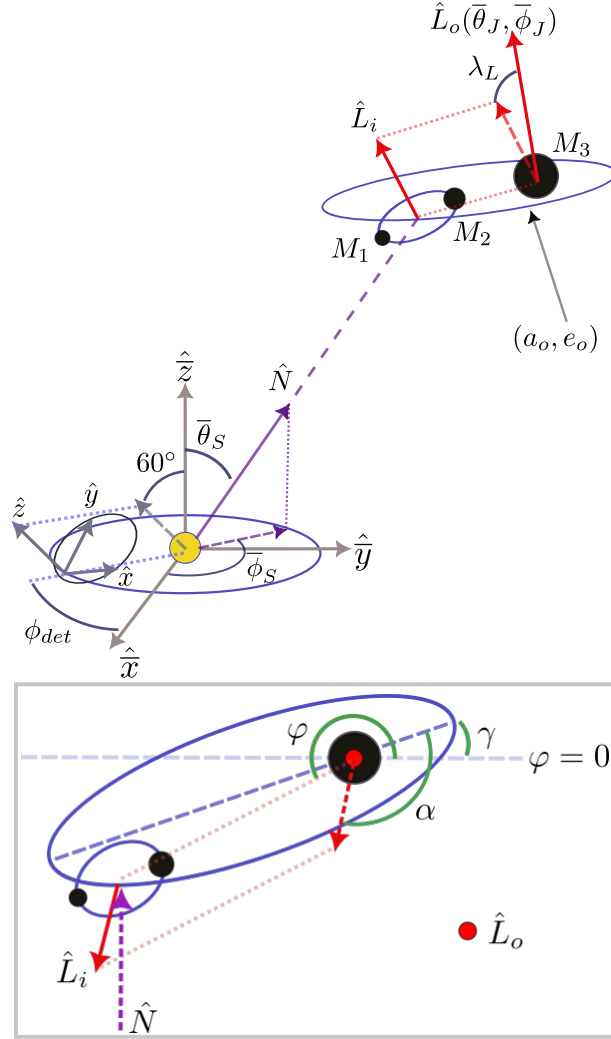


Figure 5.1: Top: Geometry of the SMBH+BBH triple system. Bottom, inset: View of the triple system normal to the plane of the outer orbit. The outer orbit angular momentum \hat{L}_o points out of the page. See the discussion below and Table 5.1 for definition of all parameters. Figure dimensions are not an indication of true scale.

5.2 Mathematical Description of the SMBH+BBH Triple System

Geometry

We first describe the full geometry of the SMBH+BBH triple system with an eccentric outer orbit. Table 5.1 below outlines the set of relevant parameters used in calculating the waveform measured by a space-borne GW observatory. In Fig. 5.1, the barred coordinates demarcate a Solar System centered coordinate system, while the unbarred coordinates demarcate a coordinate system based on the orientation of the observatory.

θ^a	Definition
$\log \mathcal{M}_z$	Detector Frame Chirp Mass: $\mu^{3/5}(m_1 + m_2)^{2/5}$
q	Mass Ratio M_2/M_1
$\log D_L$	Luminosity Distance
t_c	Coalescence Time
ϕ_c	Coalescence Phase
$\bar{\theta}_S, \bar{\phi}_S$	Line of Sight of BBH+SMBH Triple
$\bar{\theta}_J, \bar{\phi}_J$	Orientation of Total Angular Momentum \mathbf{J}
λ_L	Angle Between \mathbf{L}_i and \mathbf{L}_o
α_0	Initial Phase of \mathbf{L}_i Around \mathbf{L}_o
$\log M_3$	SMBH Mass
$\log a_o$	Outer Orbit Semimajor Axis
γ_o	Initial Outer Orbit Argument of Pericenter (See Note 1)
e_o	Outer Orbit Eccentricity
φ_0	Initial BBH Azimuthal Coordinate

Table 5.1: Relevant parameters in BBH+SMBH triple system for GW observed by detectors. Bars over angles indicate the Solar System coordinate frame.

In order to compute the antenna response, we need to be able to convert from the unbarred coordinates to the barred coordinates, which for a constellation-preserving observatory such as LISA, is as follows [50]:

$$\hat{x} = -\frac{1}{4} \sin(2\phi_d) \hat{\hat{x}} + \frac{3 + \cos(2\phi_d)}{4} \hat{\hat{y}} + \frac{\sqrt{3}}{2} \sin(\phi_d) \hat{\hat{z}} \quad (5.1)$$

$$\hat{y} = \frac{-3 + \cos(2\phi_d)}{4} \hat{\hat{x}} + \frac{1}{4} \sin(2\phi_d) \hat{\hat{y}} - \frac{\sqrt{3}}{2} \cos(\phi_d) \hat{\hat{z}} \quad (5.2)$$

$$\hat{z} = -\frac{\sqrt{3}}{2} \cos(\phi_d) \hat{\hat{x}} - \frac{\sqrt{3}}{2} \sin(\phi_d) \hat{\hat{y}} + \frac{1}{2} \hat{\hat{z}}. \quad (5.3)$$

We note that even though B-DECIGO will possess a different detector geometry than LISA during its orbit, we use the same configuration to simplify the analysis. The sky location of the hierarchical triple is $(\bar{\theta}_S, \bar{\phi}_S)$, which points along the vector \hat{N} , and has a luminosity distance of D_L . The triple itself consists of a BBH with black holes of masses M_1 and M_2 , or equivalently, a chirp mass of $\mathcal{M} = \frac{(M_1 M_2)^{3/5}}{(M_1 + M_2)^{1/5}}$ and mass ratio of $q = M_2/M_1$, and an SMBH of mass M_3 . The shape of the BBH's orbit around the SMBH can be determined by the semimajor axis a_o , the eccentricity e_o ,

the angle γ_o , analogous to the initial Keplerian argument of pericenter¹, and the initial BBH azimuthal coordinate φ_o .

The unit vector of the angular momentum of the two lighter black holes in the binary system is \hat{L}_i , and the unit vector of the angular momentum of the binary's orbit about the SMBH is \hat{L}_o . The opening angle λ_L is defined by

$$\cos \lambda_L = \hat{L}_o \cdot \hat{L}_i. \quad (5.4)$$

For $|\vec{L}_o| \gg |\vec{L}_i|$ and neglecting long time scale orbital effects as well as the spin of the SMBH (see Sec. 5.2), the opening angle stays constant in time, but the orientation of \hat{L}_i traces a cone around \hat{L}_o due to de Sitter precession, with

$$\frac{d\hat{L}_i}{dt} = \Omega_{dS} \hat{L}_o \times \hat{L}_i. \quad (5.5)$$

Based on Eq. (9.200) of [52], we use the instantaneous de Sitter precession frequency²

$$\Omega_{dS}(t) = \frac{3}{2} \frac{M_3}{r(t)} \dot{\varphi}(t), \quad (5.6)$$

where r is the distance from the SMBH to the center of the BBH and $\varphi(t)$ is the azimuthal coordinate of the BBH in its orbit (as shown in the inset of Fig. 5.1). The orbit-averaged precession rate is

$$\langle \Omega_{dS} \rangle = \frac{3}{2} \frac{M_3}{a_o(1-e_o^2)} \Omega_o, \quad (5.7)$$

where $\Omega_o \equiv \sqrt{M_3/a_o^3}$ is the Newtonian orbital frequency. The phase of \hat{L}_i in this cone, as shown in the inset of Fig. 5.1, can be found by integrating the time-dependent de Sitter precession rate:

$$\alpha(t) = \alpha_0 + \int_t^{t_c} \Omega_{dS}(t') dt', \quad (5.8)$$

where α_0 is the phase at the time of the binary coalescence t_c .

It is also useful to define the inclination angle ι_J of the outer orbit angular momentum, given by

$$\cos \iota_J = \hat{N} \cdot \hat{L}_o. \quad (5.9)$$

¹Of course, the outer orbit is not strictly Keplerian. A rigorous definition of the instantaneous argument of pericenter is subtle, though the picture of an elliptical orbital path with a pericenter that rotates in space at the 1PN-accurate angular velocity of $\frac{3M_3}{a_o(1-e_o^2)}$ is appropriate as a rough approximation. Within the mathematical framework of [51], γ_o is implemented as a simple arbitrary rotation of the orbital plane, as in Eq. (5.12).

²Eq. (1) of the previous work [24] gave the orbit-averaged de Sitter precession rate, which agrees with Eq. (5.6).

BBH Orbit in Schwarzschild Spacetime

Despite the fact that there does not exist an analytic description of an elliptical orbit in Schwarzschild spacetime, there are well-established methods for computing Schwarzschild geodesics which can be applied to numerically calculate the BBH orbital trajectory [51, 53, 54, 55, 56]. In particular, we follow the procedure of [51]. Defining $p = \frac{a_o}{M_3}(1 - e_o^2)$ for semimajor axis a_o and e_o , we find a minimum and maximum orbital radius

$$r_{\min} = \frac{pM_3}{1 + e_o}, \quad r_{\max} = \frac{pM_3}{1 - e_o}. \quad (5.10)$$

Stable orbits only exist for $p > 6 + 2e_o$ [51], and we will exclude unstable systems from this analysis.

A relativistic anomaly χ , which ranges from 0 to 2π , is defined so that

$$r(\chi) = \frac{pM_3}{1 + e_o \cos \chi}. \quad (5.11)$$

Furthermore, the azimuthal coordinate is given by

$$\varphi(\chi) = 2\left(\frac{p}{p - 6 + 2e_o}\right)^{1/2} \left[F\left(\frac{\chi}{2} + \frac{\pi}{2}, k^2\right) - F\left(\frac{\pi}{2}, k^2\right) \right] + \gamma_o, \quad (5.12)$$

where $k^2 = \frac{4e_o}{p - 6 + 2e_o}$, F is the incomplete elliptic integral of the first kind, and γ_o denotes the initial argument of pericenter for the outer orbit (see Note 1).

The relationship between time and the relativistic anomaly is given by

$$t(\chi) = p^2 M_3 (p - 2 - 2e_o)^{1/2} (p - 2 + 2e_o)^{1/2} \times \int_0^\chi d\chi' \left\{ (p - 2 - 2e_o \cos \chi')^{-1} (1 + e_o \cos \chi')^{-2} \times (p - 6 - 2e_o \cos \chi')^{-1/2} \right\}. \quad (5.13)$$

In the end, the geodesic has a doubly periodic structure, and the radius has a period of $r(\chi)$ has a period of $P_r = t(2\pi)$. During a time of P_r , however, the azimuthal variable travels further than 2π , which is the relativistic pericenter precession. It is useful to define the shift in angle over a radial period. This is equal to

$$\Delta\varphi = 4\left(\frac{p}{p - 6 + 2e_o}\right)^{1/2} F(\pi/2, k^2). \quad (5.14)$$

We note that this matches the 1PN GR result [57] for the amount of precession during a radial period in the limit $p \gg 1$

$$\Delta\varphi \approx 2\pi(1 + 3/p) = 6\pi/p + 2\pi. \quad (5.15)$$

Defining the azimuthal frequency $\Omega_\varphi \equiv \Delta\varphi/P_r$, it is shown that $\varphi(t) - \Omega_\varphi t$ is P_r -periodic [51]. We note that $\varphi(t)$ itself is *not* periodic – since the orbit precesses, it takes $< P_r$ time for φ to move through 2π radians. Even though the precession angle over a full orbit remains constant, the time it takes to move through the precession angle will depend on the BBH distance from the SMBH (conserving angular momentum), so for an eccentric orbit, the time to complete a full 2π in φ will depend on the starting value of φ itself.

To find $r(t)$ and $\varphi(t)$ numerically over many full orbits, we calculate the orbit over $\chi \in [0, 2\pi]$ and utilize the periodicity of $r(\chi)$ and $\varphi(t) - \Omega_\varphi t$. We furthermore choose some $\chi_0 \equiv \chi(t = 0)$ so that $\varphi(\chi_0) = \varphi_0$, where φ_0 is the initial azimuthal coordinate of the BBH in the plane of the outer orbit (see the bottom of Fig. 5.1). Furthermore, $\dot{r}(t)$ and $\dot{\varphi}(t)$ can be calculated by application of the chain rule to the expressions relating r , φ , and t to χ above.

Waveform

We can now proceed to calculate the strain detected by the space-based observatory, using the formalism of [21]. The overall measured signal is

$$\tilde{h}(f) = \tilde{h}_C \sqrt{(A_+ F_+)^2 + (A_\times F_\times)^2} \times \exp\{-i[\Phi_P + 2\Phi_T + \Phi_D]\}, \quad (5.16)$$

where \tilde{h}_C is the carrier waveform of the BBH, $A_{+,\times}$ and $F_{+,\times}$ are the polarization amplitude and antenna response, respectively, and Φ_P , Φ_D , and Φ_T are the polarization, Thomas, and Doppler phases. The carrier waveform in the frequency domain to leading post-Newtonian (PN) order is [58]

$$\tilde{h}_C(f) = \left(\frac{5}{96}\right)^{1/2} \frac{\mathcal{M}^{5/6}}{\pi^{2/3} D_L} f^{-7/6} \times \exp\{i[2\pi f t_c - \phi_c - \frac{\pi}{4} + \frac{3}{4}(8\pi \mathcal{M} f)^{-5/3}]\}, \quad (5.17)$$

where t_c and ϕ_c are the time and phase at coalescence. To the leading PN order, the relationship between GW frequency and time is given by

$$t(f) \approx t_c - \frac{5}{256\pi^{8/3}} \frac{1}{\mathcal{M}^{5/3} f^{8/3}}. \quad (5.18)$$

The two polarizations of the strain, h_+ and h_\times , are modified by the amplitude factors

$$A_+ = 1 + (\hat{L}_i \cdot \hat{N})^2 \quad (5.19)$$

$$A_\times = -2\hat{L}_i \cdot \hat{N}, \quad (5.20)$$

and furthermore, the antenna responses for a 90-degree detector are

$$F_+(\theta_S, \phi_S, \psi_S) = \frac{1}{2}(1 + \cos^2 \theta_S) \cos 2\phi_S \cos 2\psi_S - \cos \theta_S \sin 2\phi_S \sin 2\psi_S, \quad (5.21)$$

$$F_{\times}(\theta_S, \phi_S, \psi_S) = \frac{1}{2}(1 + \cos^2 \theta_S) \cos 2\phi_S \sin 2\psi_S + \cos \theta_S \sin 2\phi_S \cos 2\psi_S, \quad (5.22)$$

where

$$\tan \psi_S(t) = \frac{\hat{L}_i \cdot \hat{z} - (\hat{L}_i \cdot \hat{N})(\hat{z} \cdot \hat{N})}{\hat{N} \cdot (\hat{L}_i \times \hat{z})}. \quad (5.23)$$

Note the use of the detector-frame coordinates in Eqs. (5.21) and (5.22). For a triangular detector such as LISA or B-DECIGO, the antenna pattern acquires a factor of $\sqrt{3}/2$ and there are two effective detectors [59].

Let us now specify the phases in Eq. (5.16). Since the phases are slowly varying functions of time, the stationary phase approximation is used to convert them into frequency-dependent components via Eq. (5.18) — i.e., for some function $g(t)$ appearing in the time-domain waveform $h(t)$, $g(f) \approx g(t(f))$ [60]. The polarization phase is given by

$$\tan \Phi_P(t) = -\frac{A_{\times}(t)F_{\times}(t)}{A_{+}(t)F_{+}(t)}. \quad (5.24)$$

The Thomas phase arises from the evolution of the principle $+$ –polarization axis [21], and thus the inner orbital phase of the two stellar mass BH in the BBH, as the angular momentum \hat{L}_i precesses. It is given by

$$\Phi_T(t) = -\int_t^{t_c} dt \left[\frac{\hat{L}_i \cdot \hat{N}}{1 - (\hat{L}_i \cdot \hat{N})^2} \right] (\hat{L}_i \times \hat{N}) \cdot \frac{d\hat{L}_i}{dt}. \quad (5.25)$$

The final phase term is the Doppler phase shift, the phase shift induced by the changing distance between the detector and the GW source. There are two contributions to this phase. The first is the contribution from the detector, given at a particular time t by

$$\Phi_{D,\text{det}} = 2\pi f \times (1 \text{ AU}) \sin \theta_S \cos(\phi_{\text{det}} - \phi_S). \quad (5.26)$$

The other is from the source, which is modulated by the changing orbital radius as well as the inclination of the outer orbit and the position of the BBH in that orbit:

$$\Phi_{D,\text{src}} = 2\pi f \times r \sin \iota_J \sin \varphi. \quad (5.27)$$

Gravitational lensing from the SMBH and its host galactic nucleus is neglected in this waveform, though its effects on parameter estimation have been studied in [44, 61].

Neglected Orbital Dynamics

A three body system is complicated, and exhibits some interesting phenomenology. We will now discuss several additional well-known behaviors, and why we neglect them. A useful benchmark for comparison is that the characteristic frequency for de Sitter precession scales as

$$\Omega_{\text{dS}} = \frac{1}{1.1 \text{ yr}} \left(\frac{100}{a_o/M_3} \right)^{5/2} \left(\frac{10^8 M_\odot}{M_3} \right) \left(\frac{1 - 0.3^2}{1 - e^2} \right). \quad (5.28)$$

We consider the implications of non-zero BH spins on the orbital dynamics. The precession of \hat{L}_o around the spin of the SMBH \hat{S}_3 with $S_3 = \chi_3 M_3^2$ has characteristic frequency [23]

$$\Omega_{L_o, S_3} = \frac{S_3(4 + 3(M_1 + M_2)/M_3)}{2a_o^3(1 - e_o^2)^{3/2}}. \quad (5.29)$$

If we consider the case $M_3 \gg M_1 + M_2$

$$\frac{1}{t_{L_o, S_3}} = \frac{1}{9.7 \text{ yr}} \left(\frac{\chi_3}{0.7} \right) \left(\frac{100}{a_o/M_3} \right)^3 \left(\frac{1 - 0.3^2}{1 - e^2} \right)^{3/2}. \quad (5.30)$$

Even for rapidly spinning SMBHs, this effect is about one order of magnitude slower than de Sitter precession, so for now, we neglect it. It is worth noting that each successive effect included in the waveform modulation generally increases the amount of Fisher information. As such, we expect that future inclusion of this effect will lead to further improved parameter estimation uncertainties.

Lense-Thirring precession of \hat{L}_i around \hat{S}_3 also contributes to the orbital dynamics, with

$$\Omega_{L_i, S_3} = \frac{S_3}{2a_o^3(1 - e_o^2)^{3/2}}. \quad (5.31)$$

This precession frequency is one-quarter of Ω_{L_o, S_3} , and thus, since we treat Ω_{L_o, S_3} as small in this work, we do the same for Ω_{L_i, S_3} .

As in [24], we also neglect the precession of \hat{L}_i around the spins of the two stellar mass BH. The opening angle of this precession will be of order 1° , much less than a typical value of λ_L [62]. Also, the effects of this spin-induced precession should be easily distinguishable from the Doppler shift or de Sitter precession because the spin-induced precession will occur over just days, rather than years, for GW frequencies in the bands of space-based observatories.

We also consider Lidov-Kozai oscillations, the Newtonian tidal effect which exchanges inner orbit eccentricity with inclination between \hat{L}_o and \hat{L}_i [63]. These

oscillations have a characteristic frequency of [23]

$$\Omega_{\text{LK}} = \Omega_i \frac{M_3}{M_1 + M_2} \left(\frac{a_i}{a_o \sqrt{1 - e_o^2}} \right)^3, \quad (5.32)$$

where $\Omega_i = \sqrt{(M_1 + M_2)/a_i^3}$. The LK timescale is

$$\frac{1}{t_{\text{LK}}} = \frac{1}{67 \text{ yr}} \left(\frac{10^8 M_\odot}{M_3} \right)^2 \left(\frac{100}{a_o/M_3} \right)^3 \times \left(\frac{1 - 0.3^2}{1 - e^2} \right)^{3/2} \left(\frac{10^{-2} \text{ Hz}}{f} \right). \quad (5.33)$$

In our frequency band of interest, this effect occurs over much longer time scales than the de Sitter precession, and since both de Sitter precession and Lidov-Kozai oscillations modulate L_i , we neglect the slower of the two processes. We refer the reader to Fig. 1 of [24] for a depiction of the accumulation timescales of various effects in the outer orbit evolution across the parameter space of SMBH masses and outer orbit semimajor axes that we consider.

We furthermore assume that the eccentricity of the inner binary e_i is zero. As explained in [24], the inner eccentricity does not affect any component of the measured strain outside of the carrier waveform $\tilde{h}_C(f)$, and thus should influence parameter estimation uncertainties primarily through the SNR. Furthermore, the eccentric Kozai-Lidov mechanism can drive periodic modulation of e_i between moderate and very high values. The GW signal frequency from a stellar-mass BBH can be pushed into the sensitivity range of space-based observatories when the inner eccentricity is high, so the eccentric Kozai-Lidov mechanism can produce periodic high SNR bursts in these detectors, driving up the total SNR measured for that particular binary [64, 65]. However, the time scale of this periodic burst behavior scales roughly as [66] $\Omega_o^{-2} f (1 - e_o^2)^{3/2}$. These effects therefore occur much more slowly than de Sitter and pericenter precession, and thus are left for implementation into future analyses.

A higher e_i also leads to faster merger times; however, high eccentricity BBHs can still remain in the millihertz and decihertz frequency bands throughout the entire observation period with just a larger initial separation between the two stellar mass BHs. So, it is expected that even for e_i approaching 1, such BBHs will offer long enough integration times to generate a moderate SNR, and therefore the inner eccentricity should not significantly alter the results of the simplified Fisher matrix analysis (see [24] for a more detailed discussion).

5.3 Parameter Estimation with the Fisher Information Matrix

In this analysis, we implement the Fisher information matrix method (as done in [24]) as a simple estimator for how well properties of a BBH+SMBH triple system can be measured. We make a number of well-supported assumptions to reduce the complexity of the numerical methods used to estimate parameter uncertainties.

Parameter Uncertainties from the Fisher Information Matrix

We first outline how the Fisher information matrix (from now on, Fisher matrix) is used to estimate parameter measurement uncertainties. The elements of the Fisher matrix are defined as

$$\Gamma_{ab} \equiv \left(\frac{\partial \tilde{h}(f)}{\partial \theta_a} \middle| \frac{\partial \tilde{h}(f)}{\partial \theta_b} \right), \quad (5.34)$$

where

$$(\tilde{g}|\tilde{h}) = 4 \operatorname{Re} \int_0^\infty \frac{\tilde{g}^*(f)\tilde{h}(f)}{S_n(f)} df^3, \quad (5.35)$$

\tilde{h} is the frequency-domain waveform, $S_n(f)$ is the PSD of the detector noise, and θ_a are the various parameters of the system. In practice, we limit the frequency bounds of integration to $[f_{min}, f_{max}]$, where f_{max} is at the upper edge of the detector sensitivity range and $t(f_{max}) - t(f_{min}) = 5$ years (via Eq. (5.18)) — see Sec. 5.4.

We note that we use a finite difference method to compute $\partial \tilde{h}/\partial \theta_a$. To choose a finite parameter difference $\Delta \theta_a$ from which to estimate $\partial \tilde{h}/\partial \theta_a$, we minimize the quantity ϵ , analogous to waveform mismatch,

$$\epsilon = 1 - \frac{(\partial_{[\Delta \theta_a]} \tilde{h} | \partial_{[4\Delta \theta_a]} \tilde{h})}{\sqrt{(\partial_{[\Delta \theta_a]} \tilde{h} | \partial_{[\Delta \theta_a]} \tilde{h})(\partial_{[4\Delta \theta_a]} \tilde{h} | \partial_{[4\Delta \theta_a]} \tilde{h})}}, \quad (5.36)$$

where

$$\partial_{[\Delta \theta]} \tilde{h} = \frac{\tilde{h}(\theta + \Delta \theta) - \tilde{h}(\theta - \Delta \theta)}{2\Delta \theta}. \quad (5.37)$$

Empirically choosing $\Delta \theta_a$ to make ϵ small gives us the best accuracy in computing the numerical derivative, as ϵ begins to increase once $\Delta \theta_a$ becomes so small that the changes in \tilde{h} are smaller than computer precision. The choice of $4\Delta \theta_a$ to compare to $\Delta \theta_a$ is arbitrary.

The Fisher information matrix is related to the covariance matrix roughly by

$$\Sigma_{ab} = [\Gamma^{-1}]_{ab} + \mathcal{O}(\rho^{-4}), \quad (5.38)$$

³We make the approximation that the PSD $S_n(f)$ varies slowly enough so that $S_n(f)$ for the GW frequency in the BBH frame and the Doppler-shifted GW frequency in the observer frame are roughly equal. See App. 5.6.

where ρ is the signal-to-noise ratio (SNR). So, in the limit of large SNR, the covariance between two parameters $\Delta\theta_i\Delta\theta_j$ is approximately equal to the corresponding element of the inverse of the Fisher information matrix. As such, the parameter estimation uncertainty is given by $\Delta\theta_i = (\Sigma_{ii})^{0.5}$. If a network of GW detectors were to observe the same system, the Fisher information matrix would scale as the sum of the matrix elements for each detector, or

$$(\Gamma_{ab})^{\text{network}} = \sum_{\text{det}} \Gamma_{ab}^{\text{det}}. \quad (5.39)$$

This also applies to a triangular observatory, wherein three arms compose two interferometric detectors.

Reduced Fisher Matrix Dimensions

We can reduce the dimensions of the Fisher matrix by removing certain physical parameters from the analysis. Doing so reduces the total computation time as well as the condition number, leading to improved numerical accuracy in the Fisher matrix inversion [49]. From the parameters listed in Table 5.1, our Fisher matrices include the following 12 parameters:

$$\theta_a = (\log D_L, \bar{\theta}_S, \bar{\phi}_S, \bar{\theta}_J, \bar{\phi}_J, \lambda_L, \alpha_0, \log M_3, \log \Omega_o, \gamma_o, e_o, \varphi_0). \quad (5.40)$$

We can remove parameters which we expect will have strong priors obtained from other GW measurements, or which contribute only weakly to the gravitational waveform. For example, we assume that space-based detectors like LISA or TianGO will act in conjunction with ground-based observatories, which are far more sensitive to the chirp mass \mathcal{M} , the mass ratio q , and the time and phase of coalescence t_c and ϕ_c [36], and thus treat these four parameters as perfectly known in our analysis. Removing the chirp mass from the Fisher matrix also improves the numerical stability of our analysis. Furthermore, we neglect the spins of the three black holes because the precessional effects they induce accumulate much more slowly than the outer orbital motion and de Sitter precession, as described in Sec. 5.2.

5.4 Results and Discussion

We examine a BBH+SMBH triple system with fixed parameters $M_1 = M_2 = 50M_\odot$, $t_c = 0$, $\phi_c = 0$, $D_L = 1\text{Gpc}$, $(\bar{\theta}_S, \bar{\phi}_S) = (33^\circ, 147^\circ)$, $(\bar{\theta}_J, \bar{\phi}_J) = (75^\circ, 150^\circ)$, and $\lambda_L = 45^\circ$. For B-DECIGO, TianGO, and LISA, we compute the Fisher matrix where the integration is taken over a frequency window corresponding to an observation time of five years and the highest frequency is $f_{\text{max}} = 12\text{ Hz}$ — this roughly

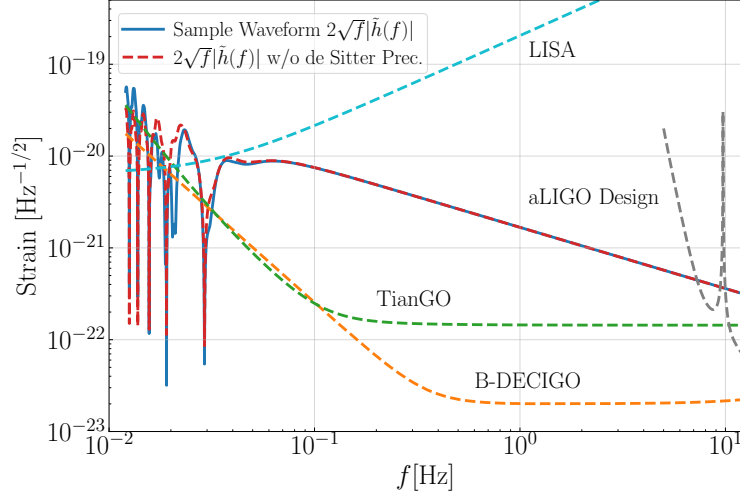


Figure 5.2: An example waveform $\tilde{h}(f)$ with $M_3 = 10^8 M_\odot$, $a_o = 100 M_3$, and $e_o = 0.3$, along with approximate sensitivity curves for B-DECIGO, TianGO, and LISA used in the Fisher matrix calculations done in this work. The red dashed curve gives the same waveform but with the effects of de Sitter precession removed.

corresponds to a lowest frequency of $f_{\min} \sim 12$ mHz. In Fig. 5.2, we plot an example frequency-domain waveform along with the B-DECIGO, TianGO, and LISA sensitivity curves used in computing Fisher matrix elements.

In Fig. 5.3, we plot the fractional uncertainty in the SMBH mass M_3 , measured by B-DECIGO, as we vary M_3 and a_o . The Fisher matrix breaks down if e_o is identically zero, so in order to facilitate comparisons to the circular orbits used in [24], we use $e_o = 0.001$. At each point, we sample the covariance found with the Fisher matrix over combinations of the three geometrical phases — that is, 6 choices of γ_o , φ_o and α_o , or 216 sets of $(\gamma_o, \alpha_o, \varphi_o)$ — and find the median.

The purple regions denote where the outer binary merges in less than the proposed observation length of five years. We expect systems in this region to be exceedingly rare, as there is only a short window for such systems to form in order to be detected by B-DECIGO. We also shade out the region where the outer orbital period P_{outer} exceeds twice the observation duration. In this region, the most dominant source of waveform modulation — namely, the Doppler phase shift — is difficult to measure because the BBH only passes through a small range of angles over the observation period. Furthermore, when the Doppler phase shift varies slowly, remaining roughly constant over the observation run, it becomes degenerate with t_c , which itself can be changed by a simple redefinition of when $t = 0$. So, in this shaded region, our assumption that t_c can be safely removed from the list of parameters in the Fisher

matrix does not hold well. Indeed, we encounter problems with numerical instability when computing the Fisher matrix in this region of the contour plots.

Figure 5.4 gives the same results, but using the LISA detector response and noise curve instead of that of B-DECIGO. The contour plots using the TianGO observatory have a similar structure to those using B-DECIGO, as the two detectors have similar sensitivity curves. Across the majority of the parameter space studied, the two sets of contours differ only in magnitude and not in shape, so for the sake of brevity, they are omitted here.

We note that the fractional uncertainty in the outer orbit semimajor axis $\Delta a_o/a_o$ follows a similar contour structure to that of $\Delta M_3/M_3$. For the outer orbit,

$$3 \frac{a_o^3}{M_3} \frac{\Delta a_o}{a_o} \approx \frac{1}{\Omega_o^2} \frac{\Delta M_3}{M_3} - 2 \frac{1}{\Omega_o^2} \frac{\Delta \Omega_o}{\Omega_o}. \quad (5.41)$$

Our calculations determined that across the $(M_3, a_o/M_3)$ parameters space, $\Delta \Omega_o/\Omega_o$ is much smaller in magnitude than $\Delta M_3/M_3$, so

$$\frac{\Delta a_o}{a_o} \approx \frac{1}{3} \frac{\Delta M_3}{M_3}. \quad (5.42)$$

This result is verified in the structures of Figs. 5.5 and 5.6, and we observe that both B-DECIGO and LISA have the potential to realize fractional uncertainties in M_3 and a_o significantly below the 0.1% level across a wide range of parameters of the triple systems.

To understand the structure of the contour plots, we examine the contour plot in Fig. 5.7. For small M_3 and a_o/M_3 , the shape of the contours are roughly separated by lines of constant a_o^5/M_3^3 . We correlate these trends to evolving components of the waveform. First, the de Sitter precession frequency is proportional to $\Omega_{\text{dS}} \propto \sqrt{M_3^3/a_o^5}$. As discussed in App. 5.7, the Thomas phase and polarization phase scale as $\Phi_T \sim \Omega_{\text{dS}} t$. Thus, measurement accuracy scales with the number of de Sitter cycles within the five-year window. In this region of parameter space, the modulations of de Sitter precession are the dominant effect for how well we can measure M_3, a_o .

For larger M_3 and a wide range of a_o/M_3 , the shape of the contours are roughly separated by lines of constant a_o/M_3 . In this region, the Doppler phase is the dominant term in the frequency domain waveform phase. The Doppler phase magnitude features a degeneracy between a_o and $\sin \iota_J$ (with $\sin \iota_J$ being a function of the angles $\bar{\theta}_S, \bar{\phi}_S, \bar{\theta}_J,$ and $\bar{\phi}_J$), as these quantities appear in the magnitude only as the

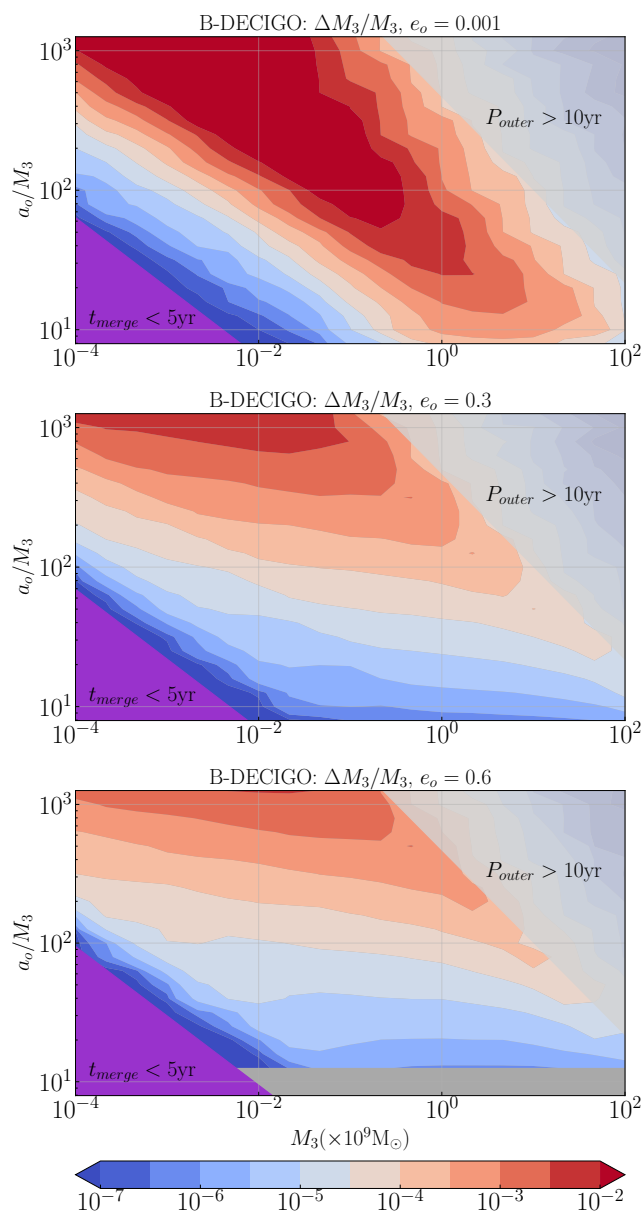


Figure 5.3: Fractional uncertainty in M_3 as measured by B-DECIGO for three different eccentricities $e_o = \{0.001, 0.3, 0.6\}$. At each point in the contour plot, we take the median uncertainty over a set of combinations of $(\gamma_o, \alpha_o, \phi_o)$. The purple region corresponds to where the outer binary merges in less time than the observation duration. We lightly shade out the region with an outer orbital period greater than 10 years, where the cumulative effect of the Doppler shift becomes small.

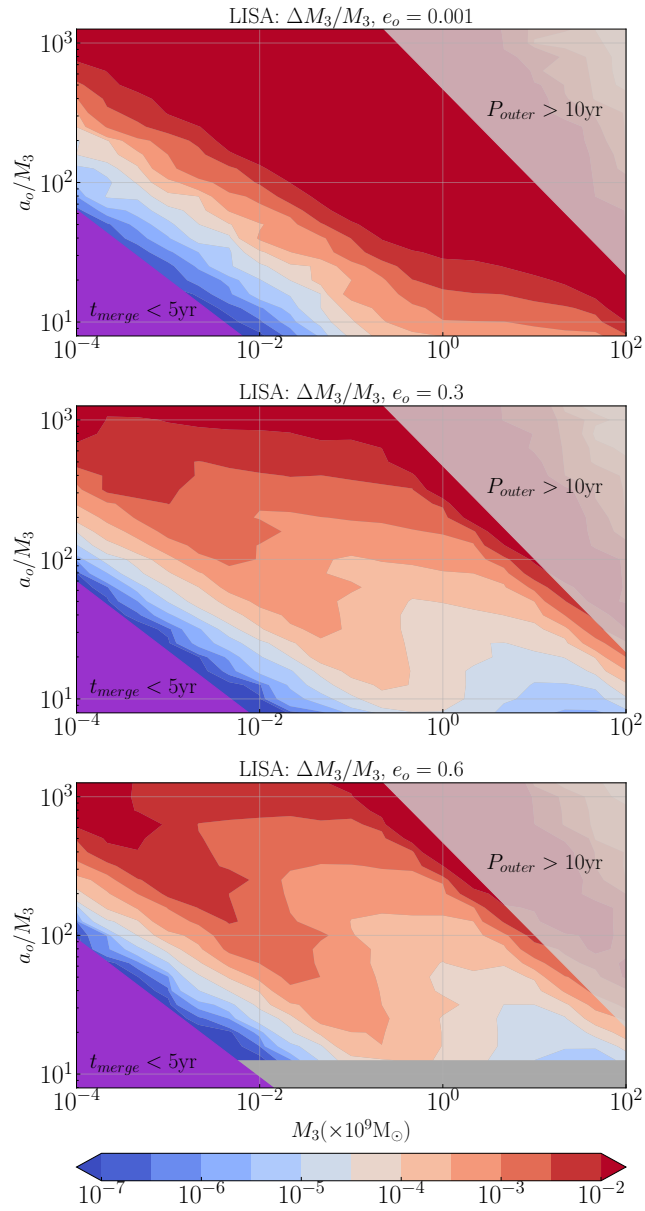


Figure 5.4: Same as Fig. 5.3, but measured by LISA instead.

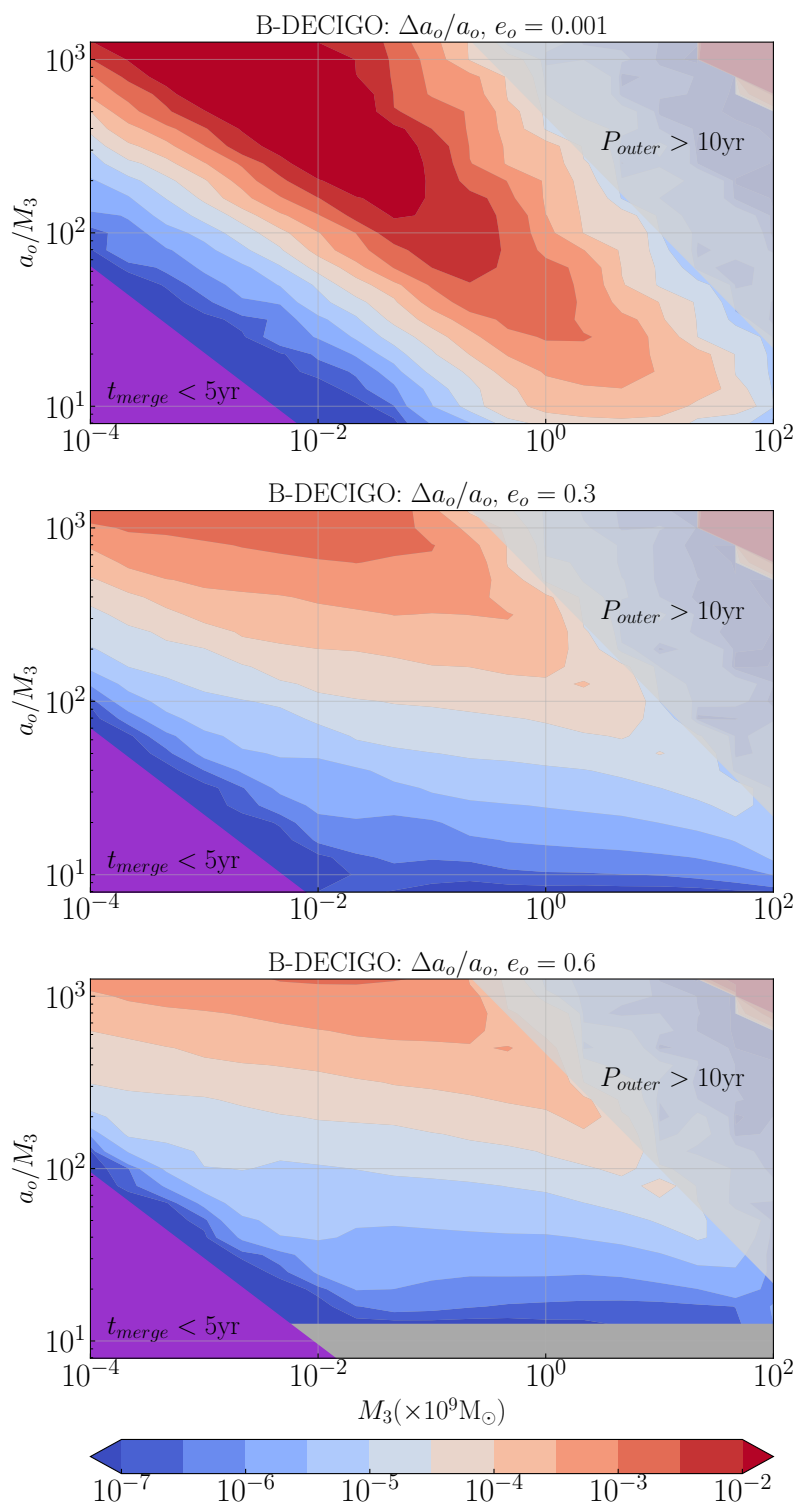


Figure 5.5: Uncertainty in a_o as measured by B-DECIGO for three different eccentricities $e_o = \{0.001, 0.3, 0.6\}$. The same sampling procedure as used in Fig. 5.3 is applied here.

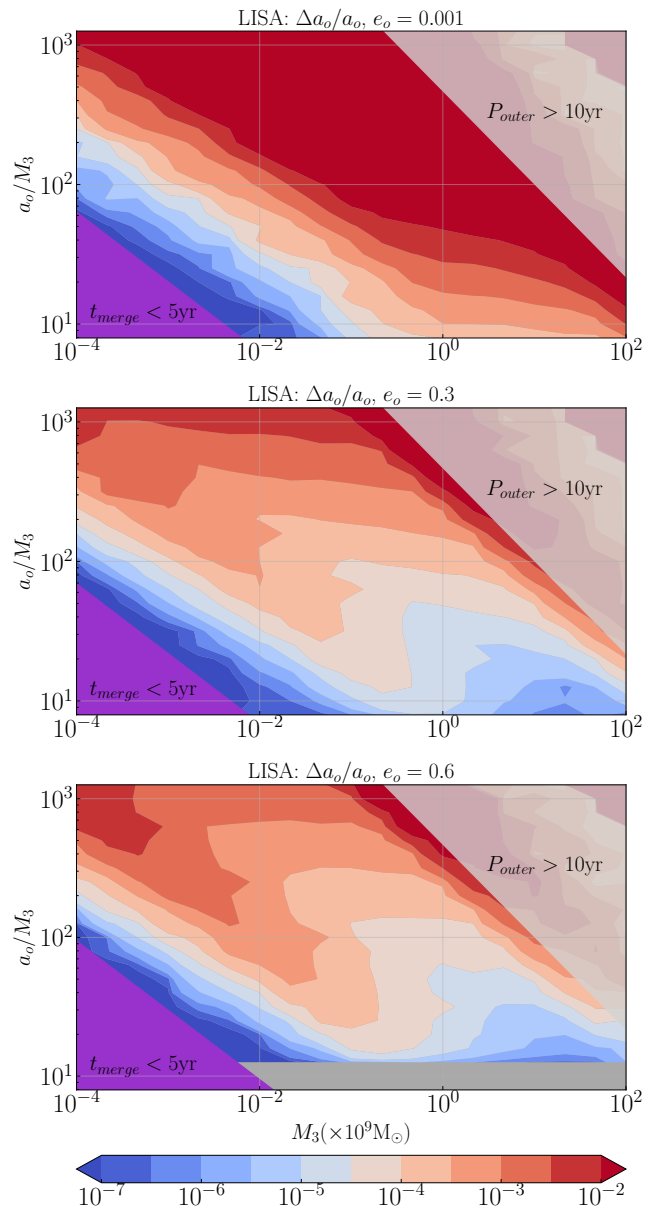


Figure 5.6: Same as Fig. 5.5, but measured by LISA instead.

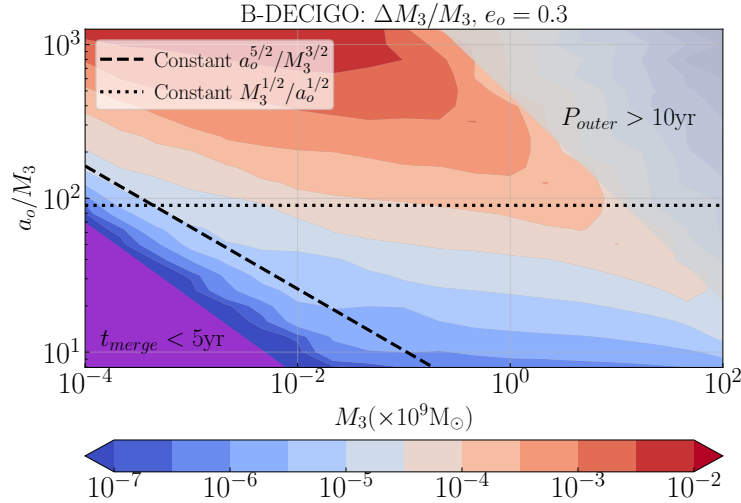


Figure 5.7: Contour plot for the fractional uncertainty in M_3 as measured by B-DECIGO, taken from Fig. 5.3. Plotted on top of the contours are lines of constant $a_o^{5/2}/M_3^{3/2}$ and $M_3^{1/2}/a_o^{1/2}$ to indicate the structure of the contours.

product $a_o \sin \iota_J = M_3^{1/3} \Omega_o^{-2/3} \sin \iota_J$. This degeneracy is broken by the inclusion of relativistic pericenter precession, as this produces different periods in the radial and azimuthal motion of the BBH in the outer orbit (cf. Sec. 5.2). The inclusion of this precession produces lines of constant $\Delta M_3/M_3$ that scale roughly with $(a_o/M_3)^{3/2}$. See App. 5.7 for more detailed discussion.

Studying Fig. 5.3, we see that for $e_o \approx 0$, these flat contours do not appear, as for a circular orbit, pericenter precession is essentially consistent with an increase in Ω_o . The resulting contour plot shape is similar to the results seen in Fig. 5 of [24], where e_o is assumed to be zero – over a wide range of the parameter space, de Sitter precession is the dominant effect in determining $\Delta M_3/M_3$. However, once $e_o > 0$, pericenter precession, rather than de Sitter precession, becomes the leading contribution to $\Delta M_3/M_3$ over a significant portion of the parameter space. The importance of pericenter precession is further emphasized by comparing the magnitudes of $\Delta M_3/M_3$ in our plots to Fig. 5 of [24], which sets $e_o = 0$ and therefore does not include pericenter precession (though it does include all other effects used in this work). With pericenter precession included, the parameter uncertainties across a wide region of the overall parameter space can drop by multiple orders of magnitude.

We also estimate how well the eccentricity can be measured with B-DECIGO and LISA as shown in Fig. 5.8 and Fig. 5.9. These results suggest that the eccentricity can be constrained to high precision, with B-DECIGO able to achieve a lower bound

of $\Delta e_o \sim 10^{-6} - 10^{-5}$ and LISA able to achieve $\Delta e_o \sim 10^{-5} - 10^{-4}$ across a substantial portion of the parameter space where precession is detectable. Once again, we see the importance of de Sitter precession in the measurability of this parameter — in the portion of the parameter space where de Sitter precession is rapid, equivalent estimation uncertainties match contours of equal de Sitter precession period. Unlike the contour plots for $\Delta M_3/M_3$, the shape of these contours is not heavily dictated by power laws related to pericenter precession. Indeed, there are no degeneracies between e_o and other waveform parameters which are broken by pericenter precession.

An important question is the impact of increasing outer orbit eccentricity on the ability to measure parameters like M_3 , a_o , and e_o itself. In Figs. 5.10 and 5.11, we consider B-DECIGO, LISA, and the TianGO concept and three different combinations of $(M_3, a_o/M_3)$ across our chosen parameter space. We study the effect of increasing eccentricity on the estimation uncertainties in M_3 and e_o (still averaging over initial orbital angles) and find that increasing eccentricity can produce marginal improvements in the measurement of M_3 and e_o — a factor of \sim a few — though such improvement is not universal across $(M_3, a_o/M_3)$ parameter space.

Considering the arguments given in App. 5.7, we see that the leading contributions to the Fisher matrix elements come from the derivatives of Φ_D , Φ_P , and Φ_T . Noting that these phases evolve at secular rates of Ω_{dS} (for Φ_P and Φ_T) or $\Omega_{\text{pericenter}} = \Omega_o \frac{3}{p}$ (for Φ_D — specifically, this is the rate at which the degeneracy between a_o and $\sin \iota_J$ is broken), and recalling that these rates scale with $(1 - e_o^2)^{-1}$, it follows that larger eccentricities produce more rapid evolution, larger Fisher matrix entries, and ultimately smaller parameter uncertainties.

The relative sensitivities between the three detectors are responsible for the clear hierarchy in the parameter uncertainties they produce. For example, the rates of precession and orbital velocity are sensitive to both M_3 and e_o but with different dependencies, so there exist degeneracies between these two parameters. These degeneracies can be lifted by observing the system over long periods of time so that these effects can accumulate, enabling tighter constraints on their respective individual rates. Examining Fig. 5.2, we see that LISA effectively measures the BBH signal over a smaller frequency band than the other two detectors in the five years prior to merger. Since the LISA sensitivity is poorer than the other two detectors in the frequencies sampled in the five year observation run, the SNR of the waveform is reduced and it becomes more difficult to extract the waveform modulations driven

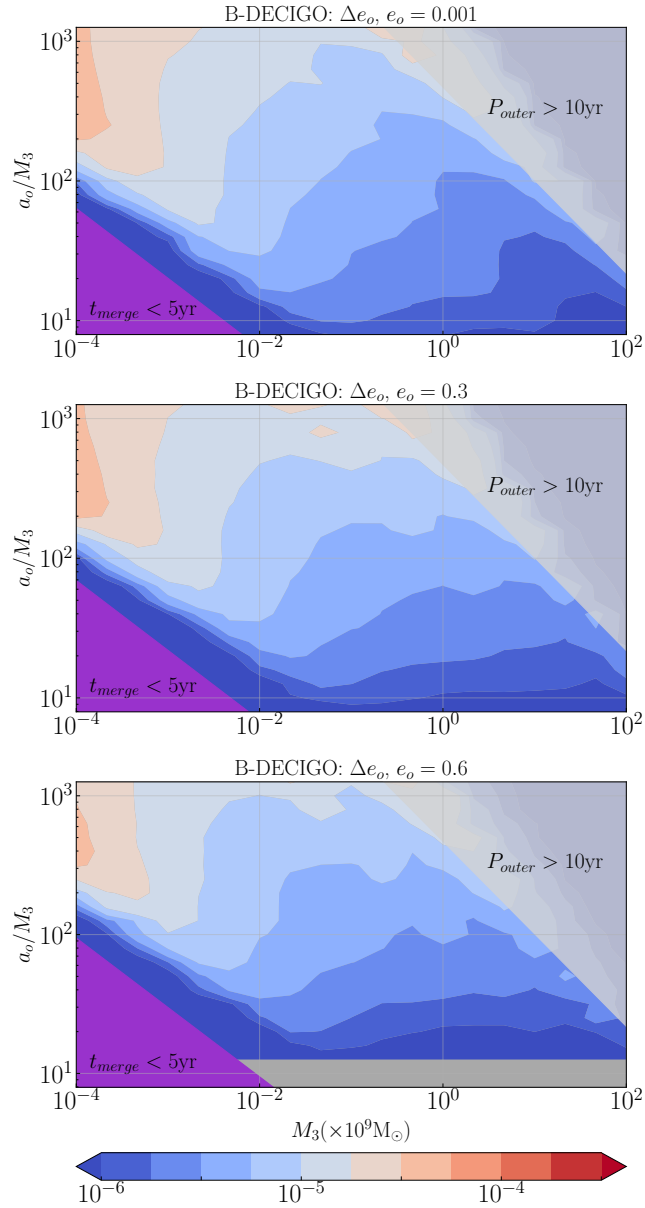


Figure 5.8: Uncertainty in e_o as measured by B-DECIGO for three different eccentricities $e_o = \{0.001, 0.3, 0.6\}$. The same sampling procedure as used in Fig. 5.3 is applied here.

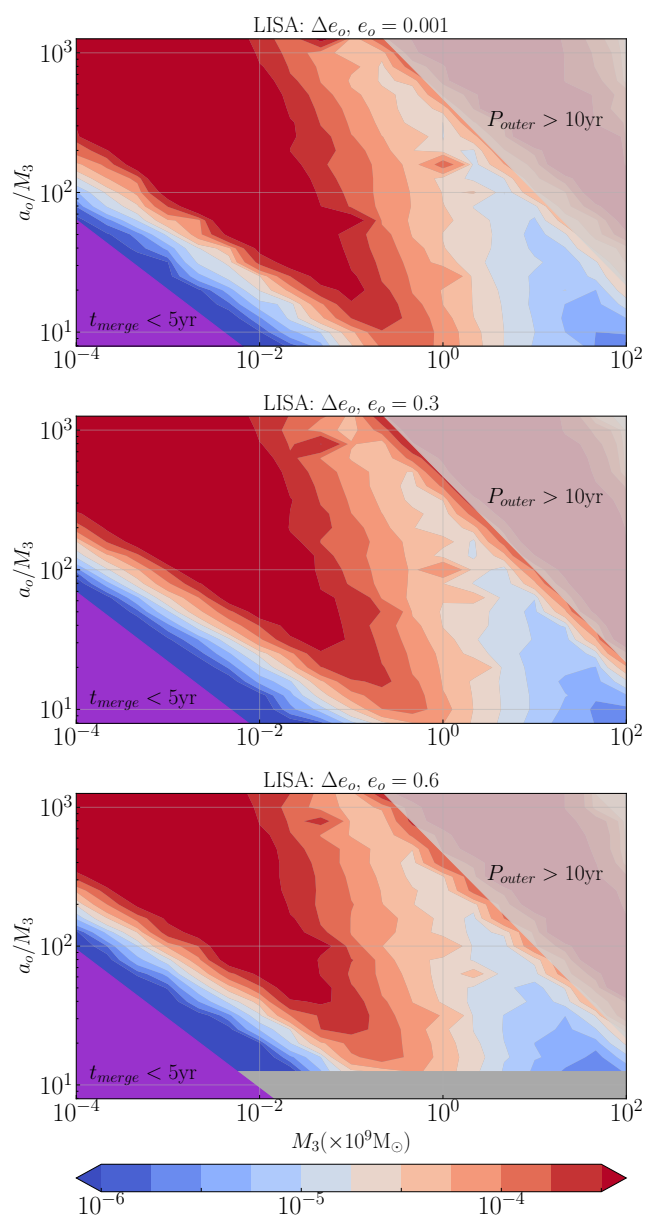


Figure 5.9: Same as Fig. 5.8, but measured by LISA instead.

by orbital and precessional effects over that period of time. Therefore, the degeneracies are not as cleanly lifted in LISA measurements, especially when these rates are slow (i.e., low M_3 , high a_o/M_3), producing less precise parameter estimates.

The primary effect of eccentricity then is to increase the strength of waveform modulations by increasing the magnitude of the precessional effects (pericenter, de Sitter); however, we see that for the LISA observatory, the improvement in parameter estimation uncertainty with rising e_o is not as significant as in B-DECIGO and TianGO, and in some cases, a larger e_o produces larger uncertainties. While increasing the eccentricity boosts the orbit averaged rate of de Sitter and pericenter precession (Cf. Eqs. 5.7 and 5.15), the majority of this evolution occurs when the BBH is near the outer orbit pericenter and the instantaneous precession rate is largest. So, for systems with slow outer orbits (once again, low M_3 and high a_o/M_3), an increasing eccentricity constrains the majority of the waveform modulation effects to a shorter time window, as the BBH passes through the region near the pericenter at a faster rate. The GW radiation from the BBH then evolves through a smaller range of frequencies while the waveform is significantly modulated.

We also note that as long as the stellar-mass BBH is able to complete a few orbits around the SMBH during the observation window, the parameter estimation uncertainties are not highly sensitive to the various geometric angles that appear in the system ($\bar{\theta}_S, \bar{\phi}_S, \bar{\theta}_J, \bar{\phi}_J, \lambda_L, \alpha_0, \gamma_o$, and φ_0), at least for generic choices of these angles (i.e., not taking $\lambda_L = 0$ or π , where de Sitter precession does not occur). These angles primarily appear in basic trigonometric functions present in the detector antenna response function, Doppler phase shift, and evolution of the inner orbit angular momentum, and thus keep the magnitudes of these waveform modulations constant within a factor of a few for the majority of possible angles. The condition on the number of outer orbits completed during the observation window holds in the vast majority of our studied parameter space.

5.5 Conclusion and Future Directions

Using the Fisher information matrix, we have shown that future space-based GW observatories may be able to precisely constrain the properties of BBH+SMBH triple systems, like the SMBH mass and outer orbit semimajor axis and eccentricity, through the GW signal observed from the BBH. We have demonstrated that the rate of change of the Doppler phase shift and the de Sitter precession rate are the dominant factors determining of the measurability of triple system parameters and

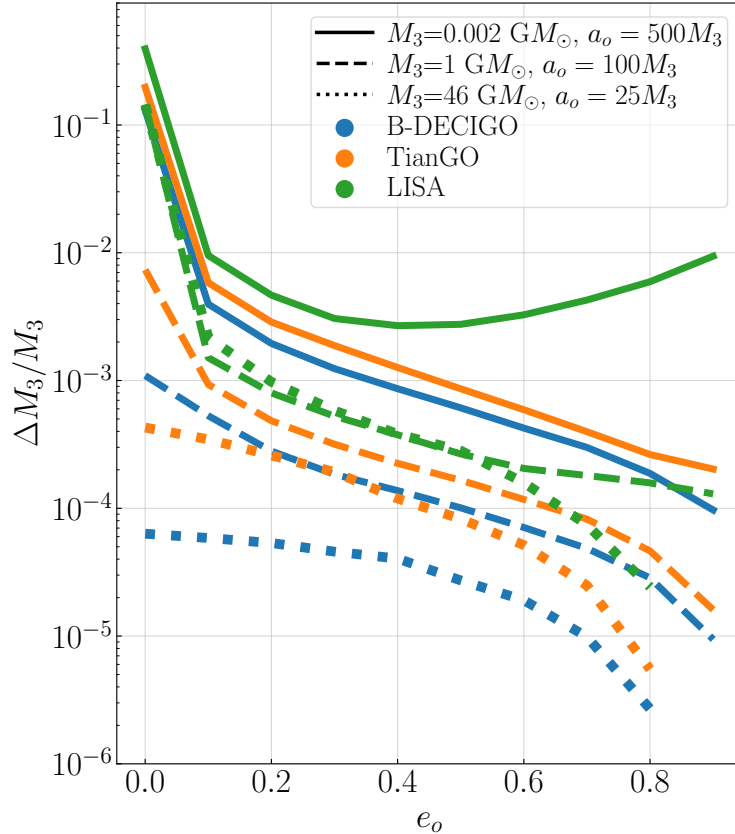


Figure 5.10: The fractional uncertainties in M_3 obtainable by B-DECIGO (blue), TianGO (orange), and LISA (green) as the eccentricity is varied. The solid, dashed, and dotted lines correspond to different choices of $(M_3, a_o/M_3)$.

that an increasing outer orbit eccentricity leads to improved measurement uncertainties through greater Doppler phase shift modulation and faster de Sitter precession. We have also shown that the planned LISA detector is capable of measuring these systems, though decihertz detector concepts such as TianGO or B-DECIGO would possess a competitive advantage over LISA in measuring such quantities.

There are some important limitations of the Fisher information method implemented in this work. As described in [49], a high SNR is required for the inverse Fisher matrix to give the covariance of the posterior probability distribution for the true source parameters $\vec{\theta}_0$. While the SNR we compute for our waveform is generally ~ 40 for TianGO, it is only ~ 4 for LISA, suggesting that the true parameter estimation uncertainties may be significantly different than those calculated here. However, the inverse Fisher matrix is also a *lower bound* for the uncertainty of an unbiased estimator of $\vec{\theta}_0$ [49], so our results essentially offer a best-case scenario for the parameter

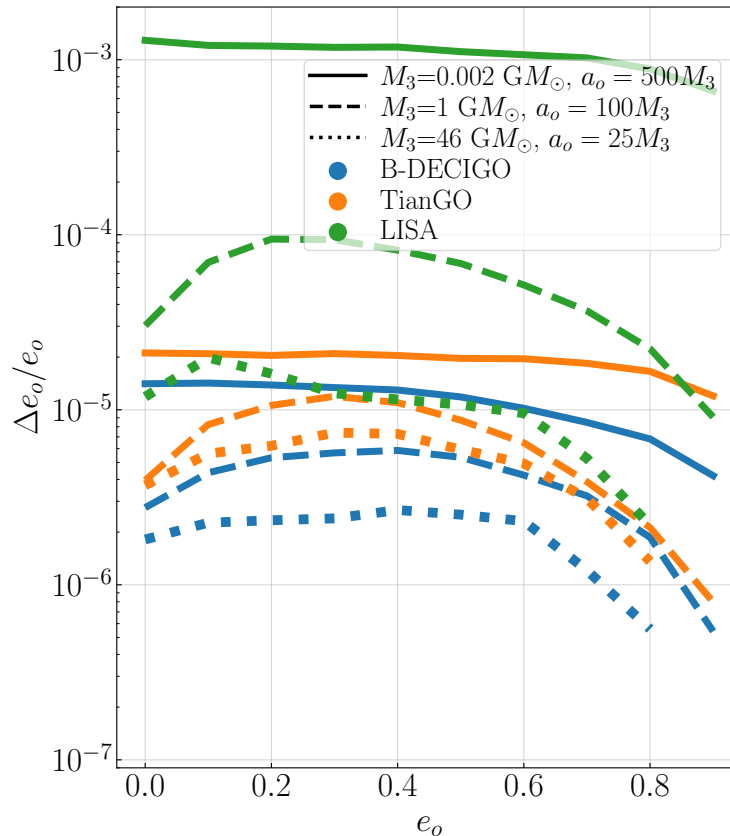


Figure 5.11: Same as Fig. 5.10, but estimating the outer eccentricity variance Δe_o .

estimation precision obtainable by future space-based observatories. A more thorough approach to this analysis will implement a full Bayesian methodology.

We can further develop this work by inclusion of additional effects into the waveform. One can implement the spin-precession effects that we chose to neglect in 5.2 due to their significantly slower time scales. Furthermore, for triple systems with lower outer binary merger times (i.e., with M_3 and a_o/M_3 near the purple regions shown in the contour plots such as Fig. 5.3), the semimajor axis and outer eccentricity can evolve significantly in time due to radiation reaction [37]. Considering the frequency integral that composes the Fisher matrix elements, we can include the effects of gravitational redshift and Doppler frequency shift, which would require the waveform and detector sensitivity to be evaluated at different frequencies in the integrand. Also, the stationary phase approximation used in the frequency domain waveform (outlined in App. 5.6) may not hold well for highly eccentric outer orbits, as the outer orbital angle varies quite rapidly near the pericenter for such orbits.

In Ref. [44], it is discussed how gravitational lensing of GWs by the SMBH combined with the de Sitter precession of \hat{L}_i can further constrain the parameters of a triple system as estimated by a space-based GW observatory, even in the case of a circular outer orbit. It would be interesting to examine the combined effects of an eccentric outer orbit and repeated GW lensing in parameter estimation problems.

Finally, measurements of the motion of a BBH through space through its modulated waveform may prove useful for understanding phenomena besides BBH+SMBH hierarchical triples. For example, measuring the evolving Doppler shift and aberrations induced by the evolving position and velocity of an isolated BBH might enable estimates of BBH kicks that occur shortly before merger or improve the precision of estimates of the Hubble constant by further constraining the redshifts of GW standard sirens [67, 68].

ACKNOWLEDGMENTS

This work was supported in part by the Caltech LIGO Summer Undergraduate Research Fellowship and by the REU program of the NSF. B.S. acknowledges support by the National Science Foundation Graduate Research Fellowship under Grant No. DGE-1745301. H.Y. is supported by NSF PHY-2308415.

5.6 Appendix: Validity of Waveform Approximations

We consider some approximations that are made in the formulation of the frequency domain waveform. For the source frame waveform $h_s(t_s) = A_s(t_s)e^{-i\Phi_s(t_s)}$, we define the connection between time and gravitational wave frequency in the source frame by

$$\dot{\Phi}_s(t_s) = 2\pi f_s. \quad (5.43)$$

The outer orbit of the BBH induces a change in the time at which a GW of a particular frequency reaches a fixed observer, which we denote t_o . Clearly marking the dependencies of various times on one another,

$$t_o(t_s) = t_s + t_{\parallel}(t_s) + D_L/c, \quad (5.44)$$

where $t_{\parallel} = a_o \sin \iota_J \sin \varphi$ is the time it takes for a radiated GW to propagate from the BBH to the SMBH along the direction of \hat{N} , assuming a circular outer orbit.

With h_s and h_o being the strain in the source and observer frames, we then have

$$h_o(t_o) = h_s(t_s) = h_s(t_o - t_{\parallel} - D_L/c), \quad (5.45)$$

which in the Fourier transform (as a function of the observed frequency f_o) becomes

$$\tilde{h}_o(f_o) = \int h_s(t_o - t_{\parallel} - D_L/c) e^{2\pi i f_o t_o} dt_o. \quad (5.46)$$

Inputting the form of $h_s(t_s)$ gives

$$\tilde{h}_o(f_o) = \int A_s(t_o - t_{\parallel} - D_L/c) e^{-i\Phi_s(t_o - t_{\parallel} - D_L/c)} e^{2\pi i f_o t_o} dt_o, \quad (5.47)$$

and assigning $t_o - D_L/c = t$ so that $t_s = t - t_{\parallel}$ produces

$$\tilde{h}_o(f_o) = e^{2\pi i f_o D_L/c} \int A_s(t - t_{\parallel}) e^{-i\Phi_s(t - t_{\parallel})} e^{2\pi i f_o t} dt. \quad (5.48)$$

For a typical system we study (e.g., $M_3 = 10^8 M_{\odot}$, $a_o = 100 M_3$), $t_{\parallel} \sim 10^4 - 10^5$ seconds (depending on the orbital angle) and $i_{\parallel} \sim t_{\parallel} \Omega_o \sim 0.01 - 0.1$.

We can make a number of simplifications to this expression. First, $\Phi_s(t - t_{\parallel}) \approx \Phi_s(t) - 2\pi f_s t_{\parallel}$ as long as $\dot{f}_s t_{\parallel} \ll f_s$. For an inspiral regime BBH with two $50 M_{\odot}$ BH, $f_s/\dot{f}_s \sim 3 \times 10^3 f_s^{-8/3}$ s [37], and with the majority of the time-integration taking place with $f_s \lesssim 0.1$ Hz, the approximation using $\dot{f}_s t_{\parallel} \ll f_s$ holds well.

We apply a similar approximation to $A_s(t - t_{\parallel})$. The time scale for the evolution of the GW amplitude is roughly [58, 37] $A_s/\dot{A}_s \sim \frac{3}{2} \frac{f_s}{\dot{f}_s} \gg t_{\parallel}$, so we can reasonably approximate $A_s(t - t_{\parallel}) \approx A_s(t)$. This simplifies Eq. (5.48) to

$$\tilde{h}_o(f_o) \approx e^{2\pi i f_o D_L/c} \int A_s(t) e^{-i[\Phi_s(t) - 2\pi f_s t_{\parallel}(t)]} e^{2\pi i f_o t} dt. \quad (5.49)$$

Consider an expansion of $F(t) = \Phi_s(t) - 2\pi f_s t_{\parallel}(t)$ around some time t' . Noting that t_{\parallel} is a function of t , we find

$$\begin{aligned} \Phi_s(t) - 2\pi f_s t_{\parallel}(t) &\approx \Phi_s(t') - 2\pi f_s t_{\parallel}(t') \\ &+ 2\pi(f_s - f_s \dot{t}_{\parallel} - \dot{f}_s t_{\parallel})(t - t') + \frac{1}{2} \ddot{F}(t')(t - t')^2 + \dots \end{aligned} \quad (5.50)$$

Since $\dot{f}_s/f_s \ll \dot{t}_{\parallel}/t_{\parallel}$, the linear term approximates to $2\pi f_s(1 - \dot{t}_{\parallel})$. Now, to complete the Fourier transform, we turn to the stationary phase approximation (SPA). Namely, the majority of the integral comes from the region where the argument of the oscillating term is stationary, which occurs at a time τ when $f_o - f_s(\tau)(1 - \dot{t}_{\parallel}(\tau)) = 0$.

Inserting the second order expansion found above into the Fourier transform gives

$$\begin{aligned} \tilde{h}_o(f_o) &\approx e^{2\pi i f_o D_L/c} \int A_s(\tau) \exp \left\{ -i[-2\pi f_o t + \Phi_s(\tau) - 2\pi f_s(\tau) t_{\parallel}(\tau) \right. \\ &\quad \left. + 2\pi f_s(\tau)(1 - \dot{t}_{\parallel}(\tau))(t - \tau) + \frac{1}{2} \ddot{F}(\tau)(t - \tau)^2 + \dots] \right\} dt, \end{aligned} \quad (5.51)$$

which simplifies to

$$\tilde{h}_o(f_o) \approx e^{2\pi i[f_o D_L/c + f_s(\tau)t_{\parallel}(\tau)]} e^{2\pi i f_s(\tau)(1-i_{\parallel}(\tau))\tau} \int A_s(\tau) e^{-i[\Phi_s(\tau) + \frac{1}{2}\ddot{F}(\tau)(t-\tau)^2 + \dots]} dt, \quad (5.52)$$

recalling that $f_s(\tau)(1 - i_{\parallel}(\tau)) = f_o$.

The expression \ddot{F} has terms proportional to \dot{f}_s , $\ddot{f}_s t_{\parallel}$, $\dot{f}_s \dot{t}_{\parallel}$, and $f_s \ddot{t}_{\parallel}$. For our typical system, the three latter terms are generally much smaller than the first, allowing a reasonable approximation of $\ddot{F} \sim \ddot{\Phi}_s$.

Carrying out this integral is a standard exercise as in [69], and we see that Eq. (5.52) evaluates to

$$\tilde{h}_o(f_o) \approx \frac{\sqrt{\pi}}{2} e^{2\pi i f_o D_L/c + i\dot{F}(\tau(f))\tau - iF(\tau(f)) + i\pi/4} \times A_s(\tau(f)) \left(\frac{2}{\ddot{F}_s(\tau(f))} \right)^{1/2}, \quad (5.53)$$

recalling $F = \Phi_s - 2\pi f_s t_{\parallel}$ and noting that Eq. (5.18) can be used to convert time-dependent quantities into frequency dependent ones. It is clear that the Doppler shift is built directly into this definition – the components of the source radiation (e.g., A_s , $\ddot{F} \approx \ddot{\Phi}_s$) which appear in the observed strain are evaluated at a time τ when the source radiation is emitted at frequency $f_s = f/(1 - i_{\parallel})$. The ratio of the observed frequency to source frequency matches the expansion of the exact form of the Doppler shift given in Eq. (5.55) below (in the low i_{\parallel} limit).

This result poses a problem for carrying out Fisher matrix calculations. The Fisher matrix formalism relies on integration over the observed frequencies; while there exists a monotonic relation between the source GW frequency and time, the inclusion of the Doppler frequency shift results in the same observed frequency originating from multiple distinct source frequencies. Furthermore, the PSD term must be evaluated at the observed frequency, while standard results for the GW signal in the frequency domain are parameterized by the source frequency. Without a one-to-one relationship between the observed frequency and source frequency, carrying out the Fisher matrix calculations requires careful attention to these subtleties when evaluating the frequency domain integrand. Future iterations of this analysis will more carefully implement the Doppler shift in comparing the GW signal in the source and observer frames. For example, the analysis in [45] computes the time domain waveform, splits it into segments with $\dot{f}_o > 0$ and $\dot{f}_o < 0$, and transforms each segment separately into the frequency domain using the SPA before recombining. The analysis in [70] resolves the issues in the SPA with a non-monotonic f_o using higher order time derivatives of f_o , and the analysis in [71] offers an alternative method to

computing frequency-domain waveforms that avoids the divergences that appear in the SPA when \dot{f}_o crosses zero.

For the sake of computational simplicity, we choose to carry out the Fisher matrix computations under the approximation that $i_{\parallel} \ll 1$. With this simplification (which holds fairly well across the majority of our parameter space, as we describe below), $f_{obs} \approx f_{src}$ and thus the following simple relation emerges:

$$\tilde{h}_o(f) \approx e^{2\pi i f (D_L/c + t_{\parallel})} \tilde{h}_s(f). \quad (5.54)$$

Let us more completely explain why we can reasonably neglect the change in GW frequency due to the Doppler shift induced by the BBH orbital velocity around the SMBH. The (exact) longitudinal Doppler shifted frequency is given by

$$f_{obs} = f_{src} \frac{\sqrt{1 + \beta_{\parallel}}}{\sqrt{1 - \beta_{\parallel}}}, \quad (5.55)$$

where f_{obs} and f_{src} are the observed and source frequencies, and $\beta_{\parallel} = v_{\parallel}/c = \dot{t}_{\parallel}$ is the source velocity along the line of sight. Using the methods of Sec. 5.2, the maximum orbital velocity occurs at pericenter, with

$$\beta = \frac{p - 2 - 2e_o}{p\sqrt{(p - 2)^2 - 4e_o^2}} (1 + e_o) \sqrt{p - 6 + 2e_o}. \quad (5.56)$$

Depending on the argument of pericenter, the magnitude of the source's line of sight velocity can reach up to this value. In the parameter space we study, this velocity is maximized over eccentricity when $e_o = 0.9$. At this eccentricity, the maximum velocity over semimajor axes in our parameter space occurs when $p \approx 12$ with $\beta_{max} \approx 0.37$. Then, the largest increase in GW frequency due to the Doppler shift is roughly 50%.

Making the approximation that $f_{obs} \approx f_{src}$ can produce some inaccuracies in the distance-accumulated phase terms in Eq. (5.53); however, because the Fisher matrix formalism includes integration of the product of the waveform and its complex conjugate, the value of the accumulated phase does not have any effect on the results. Furthermore, the sensitivity curves in Fig. 5.2 vary slowly in frequency, so therefore, our approximation that the source frame and observer frame GW frequencies are roughly equal does not significantly affect our Fisher matrix calculations and resulting parameter uncertainties.

Future work may implement more rigorous treatment of the waveform in the frequency domain, including corrections suggested in [72], for example. However, we

expect that the information provided by examining the shifts in observed GW frequencies, which track the BBH orbital velocity, is essentially already provided by the Doppler phase, which tracks the BBH orbital position. As such, we anticipate little improvement in parameter measurability by including this additional effect.

5.7 Appendix: Description of Measurement Accuracy

In Fig. 5.7, we note two power laws for the measurement accuracy of M_3 . We say that the pericenter precession gives $(a_o/M_3)^{3/2}$, while de Sitter precession scales like $a_o^{5/2}/M_3^{3/2}$. Below, we give scaling arguments to understand this plot. As described in Sec. 5.4, we measure $a_o \times \sin \iota_J$ and Ω_o very well via the Doppler shift

$$\Phi_D = 2\pi f \hat{N} \cdot \vec{r} = 2\pi f r \sin \iota_J \sin \phi, \quad (5.57)$$

however we need an additional effect to break the degeneracy between a_o and $\sin \iota_J$. In this appendix, we will show how the effect of precession can be understood as separating the radial and azimuthal periods $P_r \approx P_\phi - \# \frac{M}{a}$, and breaks the degeneracy. We will also explain how the Thomas phase and polarization phase terms allow us to also break the degeneracy.

Let us study a simple analytic toy model for precession where the radial period is shortened by a 1PN term. We will consider only a waveform with Doppler phase here to extract the physical reason that pericenter precession helps us measure the SMBH's orbit. We set

$$\tilde{h}(f) = \exp\left[i(\Phi_D + 2\pi f t_c)\right], \quad (5.58)$$

and provide the following simple dynamics to the outer orbit:

$$\Phi_D(t) = 2\pi f \sin \iota_J \frac{a_o(1 - e_o)^2}{1 + e_o \cos \xi_r} \sin(\xi_\varphi), \quad (5.59)$$

$$\xi_r = \xi_{r,0} + \Omega_o \left(1 - \epsilon \frac{3M_3}{a_o(1 - e_o^2)}\right) t, \quad (5.60)$$

$$\xi_\varphi = \xi_{\varphi,0} + \xi_{\varphi,0} + \Omega_o t, \quad (5.61)$$

where the variable ϵ is a counting parameter for precession, and set to 0 or 1 at the end of the calculation. This system gives a rough approximation for a low eccentricity orbit that includes relativistic pericenter precession, assuming $1/\Omega_o \ll t_{obs}$ so that many orbits are completed during t_{obs} and thus the angular velocities for the orbital and precessional motion average out to their secular values. The quantities $\xi_{r,0}$ and $\xi_{\varphi,0}$ are analogous to ϕ_0 and γ_o , respectively.

Since this is such a simple model, we can compute the Fisher matrix analytically under certain assumptions. We first compute the Fisher matrix with elements $\{M_3, \Omega_o, \sin \iota_J\}$. After computing the derivatives of \tilde{h} , we expand in $e_o \ll 1$ and consider only the secular effect of the trigonometric functions in ξ_r and ξ_φ , as the contributions from oscillating terms will be minimal after integration over f . We substitute $t \propto M^{-5/3} f^{-8/3}$ (cf. Eq. (5.18)) and after integrating over f with a flat PSD, we find that the resulting matrix is invertible only if we have some pericenter precession $\epsilon \neq 0$. The fractional error in mass then scales like

$$\frac{\Delta M_3}{M_3} \propto \frac{1}{\epsilon} \left(\frac{a_o}{M_3} \right)^{3/2}. \quad (5.62)$$

This result shows that pericenter precession will produce contours of constant $\Delta M_3/M_3$ which scale with $(a_o/M_3)^{3/2}$, which is in good agreement with the lines in Fig. 5.3, for example. These lines do not appear when $e_o = 0$, however, because the difference in the radial and azimuthal frequencies does not produce any change in the BBH's actual orbit when that orbit is circular.

We also expanded the Fisher matrix dimensions to include $\{M_3, \Omega_o, \sin \iota_J, \xi_{r,0}, \xi_{\varphi,0}, t_c\}$ and found identical scaling in $\Delta M_3/M_3$.

In contrast, let us examine the behavior of dS precession. We will now show how mass and orbital frequency can be independently measured by the the Thomas phase Φ_T and the polarization phase Φ_P . As discussed in [21], the Thomas phase for a circular orbit is approximately ⁴

$$\Phi_T \sim 2\pi(1 + \cos \lambda_L)\Omega_{\text{dS}}t, \quad (5.63)$$

where $\Omega_{\text{dS}} = \frac{3}{2} \frac{M_3 \Omega_o}{a_o} \approx \frac{3}{2} M_3^{2/3} \Omega_o^{5/3}$.

The Thomas phase breaks the degeneracy between M_3 , Ω_o , and $\sin \iota_J$. If we consider a waveform with perfectly measured Ω_o , with a simple waveform $h \propto e^{i\Phi_T}$ one can show the measurement scales as

$$\begin{aligned} \frac{\Delta M_3}{M_3} &\approx \sqrt{\frac{1}{\Gamma_{\log M_3 \log M_3}}} \propto \frac{1}{\partial_{\log M_3} \Omega_{\text{dS}}} \\ &= \frac{1}{M_3^{2/3} \Omega_o^2} \propto \frac{a_o^{5/2}}{M_3^{3/2}}. \end{aligned} \quad (5.64)$$

⁴This comes from Eq. (65) of [21]. There are multiple expressions for the average rate depending on the sign and dot products of (\hat{L}, \hat{N}) , which only differ by factors of order unity.

For contour plots such as Fig. 5.3, this result matches the power law for lines of constant $\Delta M_3/M_3$ found in the region where de Sitter precession is most rapid.

The polarization phase breaks the degeneracy between M_3 and Ω_o in the same manner as the Thomas phase. The power law can be seen by considering a waveform $h \propto e^{i\Phi_P}$. The polarization phase is defined as

$$\Phi_P(t) = -\arctan \left[\frac{A_{\times}(t)F_{\times}(t)}{A_{+}(t)F_{+}(t)} \right]. \quad (5.65)$$

In the context of the Fisher matrix, it is useful to compute the derivative of this phase,

$$\partial_{\theta} \Phi_P = -\frac{1}{(1 + \tan^2 \Phi_P)} \partial_{\theta} \left(\frac{A_{\times}(t)F_{\times}(t)}{A_{+}(t)F_{+}(t)} \right). \quad (5.66)$$

The fraction of amplitude factors and antenna patterns depends on the angles $\theta_S, \phi_S, \theta_J, \phi_J, \lambda_L$, and α_0 , as well as the integrated de Sitter precession rate, all of which appear exclusively in trigonometric functions (cf. Eqs. (5.8), (5.19), (5.20), (5.21), (5.22), and (5.23)). We assume the instantaneous de Sitter precession rate does not vary significantly, assigning the rate to its secular value $\Omega_{dS} \approx \frac{3}{2} \frac{M_3 \Omega_o}{a_o}$.

Taking $\theta = \log M_3$, then, the only dependence on M_3 in this fraction is through Ω_{dS} . Since Ω_{dS} appears only in the argument of sines and cosines, we expect that after applying the chain rule $\partial_{\log M_3} \rightarrow (\partial \Omega_{dS} / \partial \log M_3) \partial_{\Omega_{dS}}$, the magnitude of $\partial_{\log M_3} \Phi_P$ is primarily influenced by $\partial \Omega_{dS} / \partial \log M_3$. This expression evaluates to (cf. Eq. (5.64))

$$\frac{\partial \Omega_{dS}}{\partial \log M_3} = \frac{M_3^{3/2}}{a_o^{5/2}}. \quad (5.67)$$

Thus, assuming Ω_o is known, the Fisher matrix will scale like

$$\Gamma_{\log M_3 \log M_3} = \int df (\partial_{\log M_3} \Phi_P(f))^2 \propto (\partial_{\log M_3} \Omega_{dS})^2. \quad (5.68)$$

Therefore, considering both Φ_T and Φ_P , de Sitter precession produces an uncertainty in $\log M_3$ that scales roughly as $a_o^{5/2} / M_3^{3/2}$, following lines of constant Ω_{dS} .

It may seem counter-intuitive that two processes with identically-scaling rates (i.e., pericenter precession and de Sitter precession) produce different power laws in the shape of the contour lines. However, even though the rate of pericenter precession $\Omega_{\text{peri prec}} \propto M_3^{2/3} \Omega_o^{5/3}$ occurs at the same PN order as de Sitter precession $\Omega_{dS} \sim M_3^{2/3} \Omega_o^{5/3}$, there is an additional factor of a_o in the pericenter precession contribution due to the Doppler shift term being proportional to r . This causes the power law

dependence for the measurement accuracy of M_3 to scale differently by a factor of a_o .

References

- [1] B. P. Abbott et al. “GWTC-1: A Gravitational-Wave Transient Catalog of Compact Binary Mergers Observed by LIGO and Virgo during the First and Second Observing Runs.” In: *Phys. Rev. X* 9.3 (2019), p. 031040. DOI: [10.1103/PhysRevX.9.031040](https://doi.org/10.1103/PhysRevX.9.031040). arXiv: [1811.12907](https://arxiv.org/abs/1811.12907) [[astro-ph.HE](#)].
- [2] R. Abbott et al. “GWTC-2: Compact Binary Coalescences Observed by LIGO and Virgo During the First Half of the Third Observing Run.” In: *Phys. Rev. X* 11 (2021), p. 021053. DOI: [10.1103/PhysRevX.11.021053](https://doi.org/10.1103/PhysRevX.11.021053). arXiv: [2010.14527](https://arxiv.org/abs/2010.14527) [[gr-qc](#)].
- [3] R. Abbott et al. “GWTC-3: Compact Binary Coalescences Observed by LIGO and Virgo During the Second Part of the Third Observing Run.” In: (Nov. 2021). arXiv: [2111.03606](https://arxiv.org/abs/2111.03606) [[gr-qc](#)].
- [4] R. Abbott et al. “GW190521: A Binary Black Hole Merger with a Total Mass of $150M_\odot$.” In: *Phys. Rev. Lett.* 125.10 (2020), p. 101102. DOI: [10.1103/PhysRevLett.125.101102](https://doi.org/10.1103/PhysRevLett.125.101102). arXiv: [2009.01075](https://arxiv.org/abs/2009.01075) [[gr-qc](#)].
- [5] S. E. Woosley. “Pulsational Pair-Instability Supernovae.” In: *Astrophys. J.* 836.2 (2017), p. 244. DOI: [10.3847/1538-4357/836/2/244](https://doi.org/10.3847/1538-4357/836/2/244). arXiv: [1608.08939](https://arxiv.org/abs/1608.08939) [[astro-ph.HE](#)].
- [6] K. Belczynski et al. “The Effect of Pair-Instability Mass Loss on Black Hole Mergers.” In: *Astron. Astrophys.* 594 (2016), A97. DOI: [10.1051/0004-6361/201628980](https://doi.org/10.1051/0004-6361/201628980). arXiv: [1607.03116](https://arxiv.org/abs/1607.03116) [[astro-ph.HE](#)].
- [7] M. Spera and M. Mapelli. “Very massive stars, pair-instability supernovae and intermediate-mass black holes with the SEVN code.” In: *Mon. Not. Roy. Astron. Soc.* 470.4 (2017), pp. 4739–4749. DOI: [10.1093/mnras/stx1576](https://doi.org/10.1093/mnras/stx1576). arXiv: [1706.06109](https://arxiv.org/abs/1706.06109) [[astro-ph.SR](#)].
- [8] R. Abbott et al. “Properties and Astrophysical Implications of the $150 M_\odot$ Binary Black Hole Merger GW190521.” In: *Astrophys. J. Lett.* 900.1 (2020), p. L13. DOI: [10.3847/2041-8213/aba493](https://doi.org/10.3847/2041-8213/aba493). arXiv: [2009.01190](https://arxiv.org/abs/2009.01190) [[astro-ph.HE](#)].
- [9] D. Gerosa and M. Fishbach. “Hierarchical mergers of stellar-mass black holes and their gravitational-wave signatures.” In: *Nature Astron.* 5.8 (2021), pp. 749–760. DOI: [10.1038/s41550-021-01398-w](https://doi.org/10.1038/s41550-021-01398-w). arXiv: [2105.03439](https://arxiv.org/abs/2105.03439) [[astro-ph.HE](#)].
- [10] F. Antonini, M. Gieles, and A. Gualandris. “Black hole growth through hierarchical black hole mergers in dense star clusters: implications for gravitational wave detections.” In: *Mon. Not. Roy. Astron. Soc.* 486.4 (2019),

- pp. 5008–5021. DOI: [10.1093/mnras/stz1149](https://doi.org/10.1093/mnras/stz1149). arXiv: [1811.03640](https://arxiv.org/abs/1811.03640) [astro-ph.HE].
- [11] M. A. S. Martinez, G. Fragione, K. Kremer, et al. “Black Hole Mergers from Hierarchical Triples in Dense Star Clusters.” In: *ApJ* 903.1, 67 (Nov. 2020), p. 67. DOI: [10.3847/1538-4357/abba25](https://doi.org/10.3847/1538-4357/abba25). arXiv: [2009.08468](https://arxiv.org/abs/2009.08468) [astro-ph.GA].
- [12] Y. Yang, I. Bartos, V. Gayathri, et al. “Hierarchical Black Hole Mergers in Active Galactic Nuclei.” In: *Phys. Rev. Lett.* 123 (18 Nov. 2019), p. 181101. DOI: [10.1103/PhysRevLett.123.181101](https://doi.org/10.1103/PhysRevLett.123.181101). URL: <https://link.aps.org/doi/10.1103/PhysRevLett.123.181101>.
- [13] Y. Yang, I. Bartos, Z. Haiman, et al. “Cosmic Evolution of Stellar-mass Black Hole Merger Rate in Active Galactic Nuclei.” In: *Astrophys. J.* 896.2 (2020), p. 138. DOI: [10.3847/1538-4357/ab91b4](https://doi.org/10.3847/1538-4357/ab91b4). arXiv: [2003.08564](https://arxiv.org/abs/2003.08564) [astro-ph.HE].
- [14] I. Bartos, B. Kocsis, Z. Haiman, et al. “Rapid and Bright Stellar-mass Binary Black Hole Mergers in Active Galactic Nuclei.” In: *Astrophys. J.* 835.2 (2017), p. 165. DOI: [10.3847/1538-4357/835/2/165](https://doi.org/10.3847/1538-4357/835/2/165). arXiv: [1602.03831](https://arxiv.org/abs/1602.03831) [astro-ph.HE].
- [15] R. M. O’Leary, B. Kocsis, and A. Loeb. “Gravitational waves from scattering of stellar-mass black holes in galactic nuclei.” In: *Mon. Not. Roy. Astron. Soc.* 395.4 (2009), pp. 2127–2146. DOI: [10.1111/j.1365-2966.2009.14653.x](https://doi.org/10.1111/j.1365-2966.2009.14653.x). arXiv: [0807.2638](https://arxiv.org/abs/0807.2638) [astro-ph].
- [16] R. Abbott et al. “Population of Merging Compact Binaries Inferred Using Gravitational Waves through GWTC-3.” In: *Phys. Rev. X* 13.1 (2023), p. 011048. DOI: [10.1103/PhysRevX.13.011048](https://doi.org/10.1103/PhysRevX.13.011048). arXiv: [2111.03634](https://arxiv.org/abs/2111.03634) [astro-ph.HE].
- [17] L. Randall and Z.-Z. Xianyu. “A Direct Probe of Mass Density Near Inspiral Binary Black Holes.” In: *Astrophys. J.* 878.2 (2019), p. 75. DOI: [10.3847/1538-4357/ab20c6](https://doi.org/10.3847/1538-4357/ab20c6). arXiv: [1805.05335](https://arxiv.org/abs/1805.05335) [gr-qc].
- [18] K. Inayoshi, N. Tamanini, C. Caprini, et al. “Probing stellar binary black hole formation in galactic nuclei via the imprint of their center of mass acceleration on their gravitational wave signal.” In: *Phys. Rev. D* 96.6 (2017), p. 063014. DOI: [10.1103/PhysRevD.96.063014](https://doi.org/10.1103/PhysRevD.96.063014). arXiv: [1702.06529](https://arxiv.org/abs/1702.06529) [astro-ph.HE].
- [19] V. Cardoso, F. Duque, and G. Khanna. “Gravitational tuning forks and hierarchical triple systems.” In: *Phys. Rev. D* 103.8 (2021), p. L081501. DOI: [10.1103/PhysRevD.103.L081501](https://doi.org/10.1103/PhysRevD.103.L081501). arXiv: [2101.01186](https://arxiv.org/abs/2101.01186) [gr-qc].
- [20] H. Lim and C. L. Rodriguez. “Relativistic three-body effects in hierarchical triples.” In: *Phys. Rev. D* 102.6 (2020), p. 064033. DOI: [10.1103/PhysRevD.102.064033](https://doi.org/10.1103/PhysRevD.102.064033). arXiv: [2001.03654](https://arxiv.org/abs/2001.03654) [astro-ph.HE].

- [21] T. A. Apostolatos, C. Cutler, G. J. Sussman, et al. “Spin induced orbital precession and its modulation of the gravitational wave forms from merging binaries.” In: *Phys. Rev. D* 49 (1994), pp. 6274–6297. DOI: [10.1103/PhysRevD.49.6274](https://doi.org/10.1103/PhysRevD.49.6274).
- [22] B. Liu, D. Lai, and Y.-H. Wang. “Binary Mergers near a Supermassive Black Hole: Relativistic Effects in Triples.” In: *Astrophys. J. Lett.* 883.1 (2019), p. L7. DOI: [10.3847/2041-8213/ab40c0](https://doi.org/10.3847/2041-8213/ab40c0). arXiv: [1906.07726](https://arxiv.org/abs/1906.07726) [[astro-ph.HE](https://arxiv.org/archive/hep)].
- [23] B. Liu and D. Lai. “Probing the Spins of Supermassive Black Holes with Gravitational Waves from Surrounding Compact Binaries.” In: *Astrophys. J.* 924.2 (2022), p. 127. DOI: [10.3847/1538-4357/ac3aef](https://doi.org/10.3847/1538-4357/ac3aef). arXiv: [2105.02230](https://arxiv.org/abs/2105.02230) [[astro-ph.HE](https://arxiv.org/archive/hep)].
- [24] H. Yu and Y. Chen. “Direct determination of supermassive black hole properties with gravitational-wave radiation from surrounding stellar-mass black hole binaries.” In: *Phys. Rev. Lett.* 126.2 (2021), p. 021101. DOI: [10.1103/PhysRevLett.126.021101](https://doi.org/10.1103/PhysRevLett.126.021101). arXiv: [2009.02579](https://arxiv.org/abs/2009.02579) [[gr-qc](https://arxiv.org/archive/gr)].
- [25] I. M. Romero-Shaw, N. Loutrel, and M. Zevin. “Inferring interference: Identifying a perturbing tertiary with eccentric gravitational wave burst timing.” In: *Phys. Rev. D* 107.12 (2023), p. 122001. DOI: [10.1103/PhysRevD.107.122001](https://doi.org/10.1103/PhysRevD.107.122001). arXiv: [2211.07278](https://arxiv.org/abs/2211.07278) [[gr-qc](https://arxiv.org/archive/gr)].
- [26] Y. Meiron, B. Kocsis, and A. Loeb. “Detecting triple systems with gravitational wave observations.” In: *Astrophys. J.* 834.2 (2017), p. 200. DOI: [10.3847/1538-4357/834/2/200](https://doi.org/10.3847/1538-4357/834/2/200). arXiv: [1604.02148](https://arxiv.org/abs/1604.02148) [[astro-ph.HE](https://arxiv.org/archive/hep)].
- [27] E. D. Hall et al. “Gravitational-wave physics with Cosmic Explorer: Limits to low-frequency sensitivity.” In: *Phys. Rev. D* 103.12 (2021), p. 122004. DOI: [10.1103/PhysRevD.103.122004](https://doi.org/10.1103/PhysRevD.103.122004). arXiv: [2012.03608](https://arxiv.org/abs/2012.03608) [[gr-qc](https://arxiv.org/archive/gr)].
- [28] J. Harms, B. J. J. Slagmolen, R. X. Adhikari, et al. “Low-Frequency Terrestrial Gravitational-Wave Detectors.” In: *Phys. Rev. D* 88.12 (2013), p. 122003. DOI: [10.1103/PhysRevD.88.122003](https://doi.org/10.1103/PhysRevD.88.122003). arXiv: [1308.2074](https://arxiv.org/abs/1308.2074) [[gr-qc](https://arxiv.org/archive/gr)].
- [29] P. Amaro-Seoane et al. “Laser Interferometer Space Antenna.” In: (Feb. 2017). arXiv: [1702.00786](https://arxiv.org/abs/1702.00786) [[astro-ph.IM](https://arxiv.org/archive/hep)].
- [30] J. Luo et al. “TianQin: a space-borne gravitational wave detector.” In: *Class. Quant. Grav.* 33.3 (2016), p. 035010. DOI: [10.1088/0264-9381/33/3/035010](https://doi.org/10.1088/0264-9381/33/3/035010). arXiv: [1512.02076](https://arxiv.org/abs/1512.02076) [[astro-ph.IM](https://arxiv.org/archive/hep)].
- [31] W.-R. Hu and Y.-L. Wu. “The Taiji Program in Space for gravitational wave physics and the nature of gravity.” In: *Natl. Sci. Rev.* 4.5 (2017), pp. 685–686. DOI: [10.1093/nsr/nwx116](https://doi.org/10.1093/nsr/nwx116).
- [32] W.-H. Ruan, Z.-K. Guo, R.-G. Cai, et al. “Taiji program: Gravitational-wave sources.” In: *Int. J. Mod. Phys. A* 35.17 (2020), p. 2050075. DOI: [10.1142/S0217751X2050075X](https://doi.org/10.1142/S0217751X2050075X). arXiv: [1807.09495](https://arxiv.org/abs/1807.09495) [[gr-qc](https://arxiv.org/archive/gr)].

- [33] S. Kawamura et al. “Current status of space gravitational wave antenna DECIGO and BDECIGO.” In: (June 2020). arXiv: [2006.13545 \[gr-qc\]](#).
- [34] S. Sato et al. “The status of DECIGO.” In: *J. Phys. Conf. Ser.* 840.1 (2017). Ed. by D. Giardini and P. Jetzer, p. 012010. doi: [10.1088/1742-6596/840/1/012010](#).
- [35] K. A. Kuns. “Future Networks of Gravitational Wave Detectors: Quantum Noise and Space Detectors.” PhD thesis. University of California, Santa Barbara, Mar. 2019.
- [36] K. A. Kuns, H. Yu, Y. Chen, et al. “Astrophysics and cosmology with a decihertz gravitational-wave detector: TianGO.” In: *Phys. Rev. D* 102.4 (2020), p. 043001. doi: [10.1103/PhysRevD.102.043001](#). arXiv: [1908.06004 \[gr-qc\]](#).
- [37] M. Maggiore. “Gravitational Waves. Vol. 1: Theory and Experiments.” Oxford Master Series in Physics. Oxford University Press, 2007. ISBN: 978-0-19-857074-5, 978-0-19-852074-0.
- [38] B.M. Peterson. “Measuring the Masses of Supermassive Black Holes.” In: *Space Sci. Rev.* 183.253 (2014).
- [39] A. J. Barth, M. Sarzi, H.-W. Rix, et al. “Evidence for a Supermassive Black Hole in the S0 Galaxy NGC 3245.” In: *ApJ* 555.2 (July 2001), pp. 685–708. doi: [10.1086/321523](#). arXiv: [astro-ph/0012213 \[astro-ph\]](#).
- [40] C. A. Onken, M. Valluri, J. S. Brown, et al. “The Black Hole Mass of NGC 4151. II. Stellar Dynamical Measurement from Near-infrared Integral Field Spectroscopy.” In: *ApJ* 791.1, 37 (Aug. 2014), p. 37. doi: [10.1088/0004-637X/791/1/37](#). arXiv: [1406.6735 \[astro-ph.GA\]](#).
- [41] M. C. Bentz, P. R. Williams, R. Street, et al. “A Detailed View of the Broad-line Region in NGC 3783 from Velocity-resolved Reverberation Mapping.” In: *ApJ* 920.2, 112 (Oct. 2021), p. 112. doi: [10.3847/1538-4357/ac19af](#). arXiv: [2108.00482 \[astro-ph.GA\]](#).
- [42] M. C. Bentz, P. R. Williams, and T. Treu. “The Broad Line Region and Black Hole Mass of NGC 4151.” In: *ApJ* 934.2, 168 (Aug. 2022), p. 168. doi: [10.3847/1538-4357/ac7c0a](#). arXiv: [2206.03513 \[astro-ph.GA\]](#).
- [43] K. Akiyama et al. “First M87 Event Horizon Telescope Results. VI. The Shadow and Mass of the Central Black Hole.” In: *Astrophys. J. Lett.* 875.1 (2019), p. L6. doi: [10.3847/2041-8213/ab1141](#). arXiv: [1906.11243 \[astro-ph.GA\]](#).
- [44] H. Yu, Y. Wang, B. Seymour, et al. “Detecting gravitational lensing in hierarchical triples in galactic nuclei with space-borne gravitational-wave observatories.” In: (July 2021). arXiv: [2107.14318 \[gr-qc\]](#).

- [45] L. Sberna et al. “Observing GW190521-like binary black holes and their environment with LISA.” In: *Phys. Rev. D* 106.6 (2022), p. 064056. DOI: [10.1103/PhysRevD.106.064056](https://doi.org/10.1103/PhysRevD.106.064056). arXiv: [2205.08550](https://arxiv.org/abs/2205.08550) [gr-qc].
- [46] A. Kuntz and K. Leyde. “Transverse Doppler effect and parameter estimation of LISA three-body systems.” In: *Phys. Rev. D* 108.2 (2023), p. 024002. DOI: [10.1103/PhysRevD.108.024002](https://doi.org/10.1103/PhysRevD.108.024002). arXiv: [2212.09753](https://arxiv.org/abs/2212.09753) [gr-qc].
- [47] J. Stegmann, L. Zwick, S. M. Vermeulen, et al. “Observing supermassive black holes with deci-Hz gravitational-wave detectors.” In: (Nov. 2023). arXiv: [2311.06335](https://arxiv.org/abs/2311.06335) [astro-ph.HE].
- [48] D. C. Heggie. “Binary evolution in stellar dynamics.” In: *Mon. Not. Roy. Astron. Soc.* 173 (1975), pp. 729–787.
- [49] M. Vallisneri. “Use and abuse of the Fisher information matrix in the assessment of gravitational-wave parameter-estimation prospects.” In: *Phys. Rev. D* 77 (2008), p. 042001. DOI: [10.1103/PhysRevD.77.042001](https://doi.org/10.1103/PhysRevD.77.042001). arXiv: [gr-qc/0703086](https://arxiv.org/abs/gr-qc/0703086).
- [50] W. Martens and E. Joffre. “Trajectory Design for the ESA LISA Mission.” In: (Jan. 2021). DOI: [10.1007/s40295-021-00263-2](https://doi.org/10.1007/s40295-021-00263-2). arXiv: [2101.03040](https://arxiv.org/abs/2101.03040) [gr-qc].
- [51] C. Cutler, D. Kennefick, and E. Poisson. “Gravitational radiation reaction for bound motion around a schwarzschild black hole.” In: *Physical Review D* 50.6 (1994), pp. 3816–3835. DOI: [10.1103/physrevd.50.3816](https://doi.org/10.1103/physrevd.50.3816).
- [52] E. Poisson and C. M. Will. “Gravity: Newtonian, Post-Newtonian, Relativistic.” Cambridge Univ. Press, 2014.
- [53] Y. Hagihara. “Theory of the Relativistic Trajectories in a Gravitational Field of Schwarzschild.” In: *Japanese Journal of Astronomy and Geophysics* 8 (Jan. 1930), p. 67.
- [54] C. Darwin. “The Gravity Field of a Particle.” In: *Proceedings of the Royal Society of London Series A* 249.1257 (Jan. 1959), pp. 180–194. DOI: [10.1098/rspa.1959.0015](https://doi.org/10.1098/rspa.1959.0015).
- [55] C. Darwin. “The Gravity Field of a Particle. II.” In: *Proceedings of the Royal Society of London Series A* 263.1312 (Aug. 1961), pp. 39–50. DOI: [10.1098/rspa.1961.0142](https://doi.org/10.1098/rspa.1961.0142).
- [56] S. Chandrasekhar. “The mathematical theory of black holes.” 1985. ISBN: 978-0-19-850370-5.
- [57] C. M. Will. “New General Relativistic Contribution to Mercury’s Perihelion Advance.” In: *Phys. Rev. Lett.* 120.19 (2018), p. 191101. DOI: [10.1103/PhysRevLett.120.191101](https://doi.org/10.1103/PhysRevLett.120.191101). arXiv: [1802.05304](https://arxiv.org/abs/1802.05304) [gr-qc].

- [58] C. Cutler and E. E. Flanagan. “Gravitational waves from merging compact binaries: How accurately can one extract the binary’s parameters from the inspiral wave form?.” In: *Phys. Rev. D* 49 (1994), pp. 2658–2697. DOI: [10.1103/PhysRevD.49.2658](https://doi.org/10.1103/PhysRevD.49.2658). arXiv: [gr-qc/9402014](https://arxiv.org/abs/gr-qc/9402014).
- [59] C. Cutler. “Angular resolution of the LISA gravitational wave detector.” In: *Phys. Rev. D* 57 (1998), pp. 7089–7102. DOI: [10.1103/PhysRevD.57.7089](https://doi.org/10.1103/PhysRevD.57.7089). arXiv: [gr-qc/9703068](https://arxiv.org/abs/gr-qc/9703068).
- [60] S. Droz, D. J. Knapp, E. Poisson, et al. “Gravitational waves from inspiraling compact binaries: Validity of the stationary phase approximation to the Fourier transform.” In: *Phys. Rev. D* 59 (1999), p. 124016. DOI: [10.1103/PhysRevD.59.124016](https://doi.org/10.1103/PhysRevD.59.124016). arXiv: [gr-qc/9901076](https://arxiv.org/abs/gr-qc/9901076).
- [61] P. Christian, S. Vitale, and A. Loeb. “Detecting Stellar Lensing of Gravitational Waves with Ground-Based Observatories.” In: *Phys. Rev. D* 98.10 (2018), p. 103022. DOI: [10.1103/PhysRevD.98.103022](https://doi.org/10.1103/PhysRevD.98.103022). arXiv: [1802.02586](https://arxiv.org/abs/1802.02586) [[astro-ph.HE](https://arxiv.org/abs/1802.02586)].
- [62] H. Tagawa, Z. Haiman, I. Bartos, et al. “Spin Evolution of Stellar-mass Black Hole Binaries in Active Galactic Nuclei.” In: *Astrophys. J.* 899.1 (2020), p. 26. DOI: [10.3847/1538-4357/aba2cc](https://doi.org/10.3847/1538-4357/aba2cc). arXiv: [2004.11914](https://arxiv.org/abs/2004.11914) [[astro-ph.HE](https://arxiv.org/abs/2004.11914)].
- [63] H. Suzuki, P. Gupta, H. Okawa, et al. “Post-Newtonian Kozai–Lidov mechanism and its effect on cumulative shift of periastron time of binary pulsar.” In: *Mon. Not. Roy. Astron. Soc.* 500.2 (2020), pp. 1645–1665. DOI: [10.1093/mnras/staa3081](https://doi.org/10.1093/mnras/staa3081). arXiv: [2006.11545](https://arxiv.org/abs/2006.11545) [[gr-qc](https://arxiv.org/abs/2006.11545)].
- [64] A. Knee, J. McIver, S. Naoz, et al. “Characterizing LISA-band gravitational-wave signals from eccentric compact binaries orbiting a supermassive black hole.” In: *APS April Meeting Abstracts*. Vol. 2023. APS Meeting Abstracts. Jan. 2023, D14.003, p. D14.003.
- [65] A. Knee et al. “in prep..” In: (2023).
- [66] S. Naoz. “The Eccentric Kozai-Lidov Effect and Its Applications.” In: *Annual Review of Astronomy and Astrophysics* 54.1 (Sept. 2016), pp. 441–489. DOI: [10.1146/annurev-astro-081915-023315](https://doi.org/10.1146/annurev-astro-081915-023315). URL: <https://doi.org/10.1146/annurev-astro-081915-023315>.
- [67] A. Torres-Orjuela, X. Chen, and P. Amaro-Seoane. “Phase shift of gravitational waves induced by aberration.” In: *Phys. Rev. D* 101 (2020), p. 083028. DOI: [10.1103/PhysRevD.101.083028](https://doi.org/10.1103/PhysRevD.101.083028). arXiv: [2001.00721](https://arxiv.org/abs/2001.00721) [[astro-ph.HE](https://arxiv.org/abs/2001.00721)].
- [68] A. Torres-Orjuela and X. Chen. “Moving gravitational wave sources at cosmological distances: Impact on the measurement of the Hubble constant.” In: *Phys. Rev. D* 107.4 (2023), p. 043027. DOI: [10.1103/PhysRevD.107.043027](https://doi.org/10.1103/PhysRevD.107.043027). arXiv: [2210.09737](https://arxiv.org/abs/2210.09737) [[astro-ph.CO](https://arxiv.org/abs/2210.09737)].

- [69] C. M. Bender and S. A. Orszag. “Advanced Mathematical Methods for Scientists and Engineers I.” Springer New York, 1999. DOI: [10.1007/978-1-4757-3069-2](https://doi.org/10.1007/978-1-4757-3069-2). URL: <https://doi.org/10.1007/978-1-4757-3069-2>.
- [70] S. A. Hughes, N. Warburton, G. Khanna, et al. “Adiabatic waveforms for extreme mass-ratio inspirals via multivoice decomposition in time and frequency.” In: *Phys. Rev. D* 103.10 (2021). [Erratum: *Phys.Rev.D* 107, 089901 (2023)], p. 104014. DOI: [10.1103/PhysRevD.103.104014](https://doi.org/10.1103/PhysRevD.103.104014). arXiv: [2102.02713](https://arxiv.org/abs/2102.02713) [gr-qc].
- [71] A. Klein, N. Cornish, and N. Yunes. “Fast Frequency-domain Waveforms for Spin-Precessing Binary Inspirals.” In: *Phys. Rev. D* 90 (2014), p. 124029. DOI: [10.1103/PhysRevD.90.124029](https://doi.org/10.1103/PhysRevD.90.124029). arXiv: [1408.5158](https://arxiv.org/abs/1408.5158) [gr-qc].
- [72] K. Chamberlain, C. J. Moore, D. Gerosa, et al. “Frequency-domain waveform approximants capturing Doppler shifts.” In: *Phys. Rev. D* 99.2 (2019), p. 024025. DOI: [10.1103/PhysRevD.99.024025](https://doi.org/10.1103/PhysRevD.99.024025). arXiv: [1809.04799](https://arxiv.org/abs/1809.04799) [gr-qc].

Part III

Testing General Relativity with Gravitational Waves

GRAVITATIONAL-WAVE SIGNATURES OF NON-VIOLENT NON-LOCALITY

- [1] B. C. Seymour and Y. Chen. “Gravitational-wave signatures of non-violent non-locality.” Submitted to Physical Review Letters. Nov. 2024. arXiv: [2411.13714 \[gr-qc\]](#).

6.1 Introduction

The evaporation of black holes (BHs) via Hawking radiation [1] reveals an inconsistency between quantum mechanics and general relativity (GR) [2]: the semiclassical result that Hawking radiation carries no information contradicts the *unitarity* of quantum theory. Several resolutions to the *information paradox* have been proposed: the BH could never fully decay but remain as a massive remnant [3]. The interior geometry of the BH could be modified as a fuzzball [4] or gravastar [5]. Alternatively, the firewall scenario [6] suggests the region near the horizon could experience a breakdown of semiclassical gravity which destroys infalling observers. Finally, the information paradox may be resolved by accounting for non-perturbative contributions in semiclassical gravity through the replica wormhole trick, which restores unitarity without modifying GR [7, 8, 9, 10, 11].

Giddings proposed that the information which fell into the BH can escape it via *non-violent non-locality* (NVNL) [12, 13, 14, 15, 16], a non-local interaction between the inside and the outside of the BH, with associated non-violent space-time fluctuations from this information transfer. In the “strong” version of NVNL, space-time metric fluctuate stochastically at a level of $\mathcal{O}(1)$ [14] near BHs, while the “weak” version [15] has fluctuations of $\mathcal{O}(e^{-S_{\text{bh}}/2})$ [17]. Giddings and collaborators elaborated the phenomenology of NVNL [18, 19, 20] to observations of the Event Horizon Telescope (EHT) [21]. They recently considered scatterings of gravitational waves by BHs [22].

The detection of gravitational waves (GWs) allows us to probe directly the behavior of strong gravity around black holes (BHs) and neutron stars (NSs) [23, 24, 25, 26, 27, 28]. Deviations from GR can be extracted by adopting either the parameterized post-Einsteinian (PPE) framework [29] or the parameterized post-Newtonian (PN)

deformation framework [30, 31, 32], which measure deviations in the GW phase during the binary inspiral stage. Results of parametrized tests have been featured in LIGO-Virgo-KAGRA (LVK) results [33, 25, 26, 27, 28], which also treated the phase deviation parameters as hyperparameters and bounded their mean values as well as uncertainties [34, 35]. In this letter, we model the effect of NVNL on the inspiral of a binary black hole (BBH) and show that it can be constrained by the parametrized tests mentioned above, in particular via the uncertainties of the phase-deviation hyperparameters [34].

We begin with the effective-one-body (EOB) framework [36, 37, 38] which approximates a two-body relativistic problem as a one-body problem in a deformed Schwarzschild spacetime, the *effective* spacetime. Originally, this was developed for nonspinning quasicircular [36, 37, 38, 39, 40, 41] but subsequently was generalized to aligned spin [42, 43, 44, 45], precessing spin [46, 47, 48, 49, 50, 51], calibrated to NR [52, 53, 54], tides [55, 56, 57, 58], and eccentricity [59, 60] where the newest model is SEOBNRv5PHM [61, 62, 63, 64]. In particular, we modify a simple nonspinning EOBNRv2 spacetime [39], and we add stochastic metric perturbations characterized by a Gaussian spatial profile and a frequency spectrum related to the BH’s temperature, as proposed by Ref. [20] for an isolated BH. The resulting trajectories lead to gravitational waveforms that deviate from GR stochastically, primarily in the late-inspiral and plunge phases. Using a principal component analysis [65, 66, 67], we show that the frequency-domain phase deviations of these waveforms can be well approximated by a single dominant eigenmode multiplied by a normally distributed random amplitude. Finally, we estimate how well NVNL can be constrained by stacking together gravitational-wave events and computing the Savage-Dickey ratio [68]. These calculations give theoretical support to search for random phase deviations as proposed in the hierarchical tests of GR [34, 28, 69, 70, 71, 72].

6.2 Setup

For a Schwarzschild BH, Ref. [20] generically decomposes the NVNL-induced metric perturbations $g_{\mu\nu} = g_{\mu\nu}^s + n_{\mu\nu}$ into the even and odd perturbations [73]. In this work, we will consider the dominant NVNL correction which arises from $n_{\nu\nu}$ in the in-going Eddington-Finkelstein coordinates, decomposed as

$$n_{\nu\nu} = \sum_{\ell m} f_{\ell m} Y_{\ell m}, \quad (6.1)$$

where

$$f_{\ell m} = A_{\ell m} \exp \left[-(r - r_S)^2 / (2r_G^2) \right] n(t), \quad (6.2)$$

with $A_{\ell m}$ the amplitude of the mode, r_S the Schwarzschild radius, and $r_G \sim r_S$ the localization length of the perturbations [20]. Here $n(t)$ is a colored Gaussian noise with a power spectrum

$$S_n(f) = 1/(2f_Q) \exp \left[-|f|/f_Q \right], \quad (6.3)$$

where $f_Q = 1/8\pi M$ is the quantum frequency scale. We have normalized the power spectrum so that $n(t)$ has a variance equal to unity $\langle n^2(t) \rangle \equiv \int df S_n(f) = 1$. This spectrum is motivated by the Boltzman distribution for a BH of temperature $T_{\text{BH}} = 1/8\pi M$. Note that the standard deviation of $f_{\ell m}$ at the horizon is $\sim A_{\ell m}$, while the coherence time is around $\tau \sim 4M$.

If this were an EMRI, we could expand the metric like

$$g_{\mu\nu} = g_{\mu\nu}^S + \epsilon h_{\mu\nu}^{(0,1)} + \eta n_{\mu\nu} + \eta \epsilon h_{\mu\nu}^{(1,1)} \quad (6.4)$$

where ϵ is the GW counting parameter, η is the NVNL counting parameter. Assuming that we have a source $T_{\mu\nu}(x)$, then the Einstein equations are

$$\epsilon G_{\mu\nu}^{(0,1)}(h_{\mu\nu}) = \epsilon T_{\mu\nu}^{(0,1)}(x) \quad (6.5)$$

$$\eta G_{\mu\nu}^{(1,0)}(n_{\mu\nu}) = \eta T_{\mu\nu}^{(1,0)\text{nvnl}} \quad (6.6)$$

$$\epsilon \eta G_{\mu\nu}^{(0,1)}(h_{\mu\nu}^{(1,1)}) = -\epsilon \eta G_{\mu\nu}^{(1,1)}(h_{\mu\nu}^{(0,1)}, n_{\mu\nu}^{(1,0)}) + \epsilon \eta T_{\mu\nu}^{(1,1)}(x) \quad (6.7)$$

where the former term is the modification to the modifications to the radiation reaction while the latter contains deviations to the GR geodesics and note that $h^{(a,b)}$ means a order in NVNL and b order in GW (c.f. modified Teukolsky formalism [74, 75, 76]). This approach has already assumed that there is an EMRI. The radiation reaction is modified from wave optics because the outwardly traveling GW radiation does not follow geodesics on Schwarzschild anymore but on the perturbed Schwarzschild $g_{\mu\nu}^S + n_{\mu\nu}$. Since we are interested in (comparable mass) LIGO-like systems, we will focus on conservative terms corresponding to geodesic modifications from $h_{\mu\nu}^{(1,1)}$ and leave the other effects to future work.

Let us now review the EOB framework [36, 37, 77, 78, 39]. We define total mass $M = m_1 + m_2$, symmetric mass ratio $\eta = m_1 m_2 / M^2$, and mass ratio $q = m_1 / m_2$. The effective metric is given by

$$ds_{\text{eff}}^2 = -A(r) dt^2 + \frac{D(r)}{A(r)} dr^2 + r^2 d\Omega^2, \quad (6.8)$$

where $A(r) = 1 - \frac{2M}{r} + \mathcal{O}(\eta)$ and $D(r) = 1 + \mathcal{O}(\eta)$ are terms that describe the effective metric which is deformed by the symmetric mass ratio η away from Schwarzschild. (See the Supplemental Materials for further details.) If we parameterize our metric with coordinates $\vec{q} = (r, \phi)$ and their conjugate momenta $\vec{p} = (p_r, p_\phi)$, the effective Hamiltonian is found with the mass shell condition $p_\mu p_\nu g_S^{\mu\nu} = -1$

$$\hat{H}_{\text{eff}}^S = \sqrt{A(r) \left(1 + \frac{p_\phi^2}{r^2} + \frac{A}{D} p_r^2 \right)}. \quad (6.9)$$

The physical Hamiltonian for the system is related to the effective Hamiltonian via

$$\hat{H}_{\text{real}}^S = \eta^{-1} \sqrt{1 + 2\eta (\hat{H}_{\text{eff}}^S - 1)}, \quad (6.10)$$

where the hat denotes the Hamiltonian is in dimensionless units. Hamilton's equations are then

$$\frac{dq_i}{dt} = \frac{\partial \hat{H}_{\text{real}}}{\partial p_i}, \quad \frac{dp_i}{dt} = -\frac{\partial \hat{H}_{\text{real}}}{\partial q_i} + \mathcal{F}_i^{\text{rad}}, \quad (6.11)$$

where the generalized force $\mathcal{F}_i^{\text{rad}}$ is added to incorporate radiation reaction.

Let us now add NVNL into EOB by modifying the geometry of the effective spacetime, leading to a modified mass-shell relation $p_\mu p_\nu (g_S^{\mu\nu} + n^{\mu\nu}) = -1$ and yields a modified Hamiltonian

$$\hat{H}_{\text{real}} = \hat{H}_{\text{real}}^S + n_{\nu\nu}^{\ell m} \Delta \hat{H}_{\ell m}^{\text{real}}. \quad (6.12)$$

The reason that we can add NVNL directly to the EOB spacetime is that this is the leading order term, and all other terms will be smaller by a factor of the symmetric mass ratio $\eta \leq 1/4$ (so our calculations are accurate to $\mathcal{O}(A \cdot \eta)$). Thus for more asymmetric systems this approximation improves. In principle, the gravitational wave luminosity \dot{E} , hence $\mathcal{F}_i^{\text{rad}}$ is also modified by NVNL, but we will be focusing on the conservative modifications to the waveform while such effects are analyzed in other works [22]. We obtain the NVNL trajectory $(q_i(t), p_i(t))$ using Hamiltonian (6.12) and Eqs. (6.11). We then obtain the leading quadrupole wave h_{22} in the same way as Ref. [39], attaching a simple GR ringdown where the strain peaks via smoothness (in a similar manner to [61]). (See Supplemental Materials for details.)

6.3 NVNL Waveforms

In Fig. 6.1, we plot several realizations of an NVNL waveform $\text{Re}[h_{22}]$ (normalized by M/D with D the source distance) in the time domain, as functions of t/M , for a binary with $q = 1$, and compare this to a GR waveform. The random deviations are

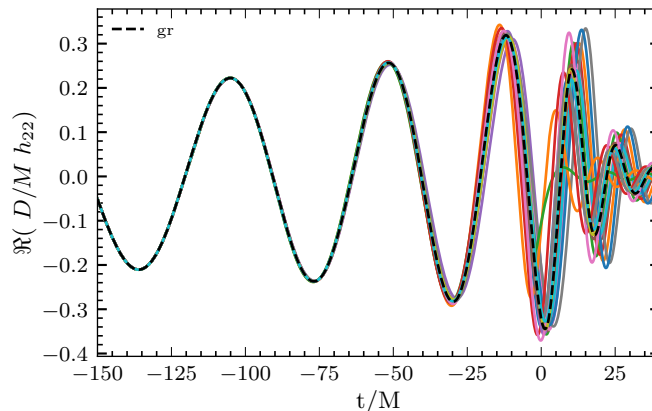


Figure 6.1: The real part of the dimensionless $h_{22}(t)$ strain for $A_{22} = 5 \times 10^{-2}$. This is the *full waveform* before the principal component analysis is done, so it contains all perturbations. These signals are aligned at very early times so that their signals overlap at low frequencies but they stochastically diverge as they reach the plunge. The apparent ringdown difference is primarily due to the phenomenological ringdown attachment, but we only do the testing GR analyses with the inspiral piece.

smooth in time due to the cutoff f_Q in Eq. (6.3) as well as the filtering effect due to the inertia of the binary.

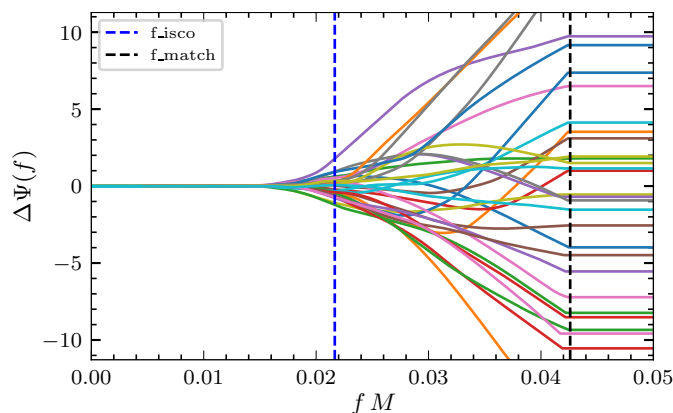


Figure 6.2: Frequency domain phase deviation realizations for $A_{22} = 1$. Using time domain waveform realizations shown in Fig. 6.1, we plot the amount of dephasing from GR that they will have. We also plot the frequency at which the binary crosses the inner most stable circular orbit (dashed blue) and the frequency at which the inspiral portion of the waveform is matched to the ringdown (dashed black). Note that $A_{22} = 1$ is not a small deviation from GR, so we calculated this at $A_{22} \ll 1$ and scaled it appropriately. One can see that the secular effect of NVNL is nearly zero while the theory predicts random dephasing from GR.

Going to the frequency domain, the NVNL waveform at linear order in $A_{\ell m}$ can be approximated by

$$h(f; \theta, A_{\ell m}) = h_{\text{gr}}(\theta) e^{i \sum_{\ell m} \Delta \Psi_{\ell m}(f; \theta)}, \quad (6.13)$$

with $\Delta \Psi_{\ell m}(f) \propto A_{\ell m}$ a stochastic phase deviation from GR. $\Delta \Psi_{\ell m}(f)$ is found by simulating a NVNL waveform with metric fluctuations $n_i(t)$ in the time domain and taking the Fourier transform for a particular noise realization.

Since our metric deviations are Gaussian, the deviation in the frequency domain is just the metric deviations multiplied by a transfer function. In Fig. 6.2, one can see the frequency domain phase deviations for various noise realizations. Notice that the frequency domain phase is primarily a stochastic deviation rather than having a secular effect that is common to all these noise realizations. Let us define the quantity $\mu_{\ell m} \equiv \langle \Delta \Psi_{\ell m}(f) \rangle$ and $\Sigma_{\ell m}(f, f') = \langle (\Delta \Psi_{\ell m}(f) - \mu_{\ell m}(f)) (\Delta \Psi_{\ell m}(f') - \mu_{\ell m}(f')) \rangle$. For this problem, the mean deviation is very small compared to the variance so detection hinges on finding the presence of $\Sigma_{\ell m}$.

We can make the waveform template in Eq. (6.13) more tractable by performing a principal component analysis (PCA). This corresponds to diagonalizing the covariance matrix

$$\Sigma_{\ell m}(f, f') = \sum_k \left(\sigma_{\ell m}^k \right)^2 z_{\ell m}^k(f) z_{\ell m}^k(f'), \quad (6.14)$$

where $(\sigma_{\ell m}^k)^2$ is the k th largest eigenvalue and $z_{\ell m}^k(f)$ its corresponding eigenvector. The PCA is performed for $f_{\text{start}} < f < f_{\text{match}}$ where $f_{\text{start}} = 0.004$ and $f_{\text{match}} = 0.042/M^1$. As it turns out, for a nearly equal mass ratio, using a single component is able to capture more than 97% of the total variance for the (2, 2) mode, and a similar amount for other (ℓ, m) modes. If we only include the largest principal component

$$h(f; \theta, A_{\ell m}) = h_{\text{gr}}(\theta) e^{i \sum_{\ell m} \zeta_{\ell m} z_{\ell m}(f)}, \quad (6.15)$$

where $\zeta_{\ell m} \sim \mathcal{N}(\mu_{\ell m}, \sigma_{\ell m})$ and we dropped the $k = 0$ index; we further scale the eigenvectors so that $\sigma_{\ell m} = A_{\ell m}$, and note that $\mu_{\ell m}/\sigma_{\ell m} \ll 1$. In Fig. 6.3, we plot $z_{\ell m}(f)$ for each mode up to $l = 2$. Since the profile of these curves looks very similar, we will only search for the $(\ell, m) = (2, 2)$ case and neglect the (ℓ, m) labeling henceforth. We stress that we apply PCA directly to the NVNL theory itself, rather than in the measurement space, which is the usual approach in the literature [65, 66, 67]. See Supplemental Materials for further details of the PCA.

¹Note that the output of the dominant PCA eigenvector is completely equivalent to finding $\min_z \sum_{ij} (\Sigma(f_i, f_j) - z(f_i)z(f_j))^2$ with constant norm.

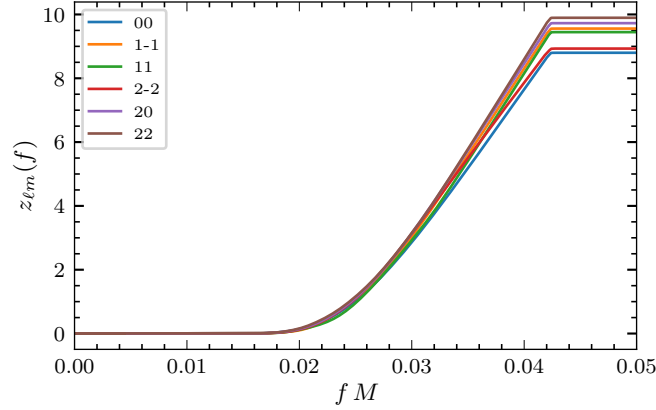


Figure 6.3: The largest principal component modes of the covariance matrix. All modes with odd $l+m$ are zero since we are confined to the orbital plane with $\theta = \pi/2$. The largest eigenvector accounts for $\sim 97\%$ of the phase variance for each of the modes. One can see that similar deviations happen for all (ℓ, m) modes.

6.4 Extraction of NVNL from data

Next, we describe how well hyperparameters (μ, σ) can be estimated from a collection of GW events. Each ζ realization is drawn from the true distribution $\mathcal{N}(\mu_t = 0, \sigma_t = A)$.

For events with high signal-to-noise ratio (SNR), parameter estimation accuracy can be quantified by the Fisher information matrix [79], defined as

$$\Gamma_{IJ} = (\partial_I h | \partial_J h)|_{\Theta=\Theta_t}. \quad (6.16)$$

We collect all our signal parameters into an uppercase-indexed vector $\Theta^I = (\theta^i, \zeta)$ where lower case index $i = 1, \dots, n_\Theta - 1$ run over the standard GR parameters θ^i and the extra entry ζ is the NVNL parameter. The capital letters range over $I = 1, \dots, n_\Theta$. The noise-weighted inner product is defined as

$$(g | h) = 4 \operatorname{Re} \int_0^\infty \frac{\tilde{g}^*(f) \tilde{h}(f)}{S(f)} df, \quad (6.17)$$

Given data d (which contains a high SNR signal) from a single event, under the Fisher approximation, the likelihood function is taken to be

$$p(d|\Theta) = \sqrt{\frac{\det \Gamma}{(2\pi)^{n_\Theta}}} \exp \left[-\frac{1}{2} (\Theta_I - \Theta_I^{\text{ML}}) \Gamma_{IJ} (\Theta_J - \Theta_J^{\text{ML}}) \right], \quad (6.18)$$

where we have used Θ_J^{ML} to denote the values of Θ_J where likelihood is maximized and n_Θ is the number of entries of Θ_I . In a frequentist approach, we can use Θ_I^{ML}

as the Maximum Likelihood Estimator (MLE) for signal parameters. Given a large number of trials with true parameters Θ_I^t , we can denote $\delta\Theta_I = \Theta_I^{\text{ML}} - \Theta_I^t$. For high SNR, $\delta\Theta_I$ is a Gaussian random vector with $\langle \delta\Theta_I \delta\Theta_J \rangle = (\Gamma^{-1})_{IJ}$. In particular, marginalizing over θ_i , the MLE estimator ζ^{ML} has an error of $\langle \delta\zeta^2 \rangle = (\Gamma^{-1})_{\zeta\zeta} \equiv \Delta\zeta^2$.

Let us take a quick aside and discuss how the generic PN deformation tests [29, 30, 31] would capture the effects of NVNL in the waveform. So far, we have been focused on searching for the PCA of NVNL directly (in Eq. (6.15) with the ζ parameters), but PN deformations can still be applied. This can still be done by standard techniques for biased waveform models [80, 81]. We fully derive this in [82], but here is an abbreviated version of the derivation. A n th order dephasing template has the form

$$\Delta\Psi_n = \frac{3}{128\eta} \varphi_n \delta\varphi_n (\pi M f)^{(n-5)/3}, \quad (6.19)$$

which is same convention as the LVK GWTC3 testing GR paper [28]. If we inject a ζ^t , and try to measure $\Theta^I = (\theta^i, \delta\varphi_n)$, we would find that the maximum likelihood estimator is

$$\Gamma_{IJ} \begin{pmatrix} \theta_i^{\text{ML}} - \theta_i^t \\ \delta\varphi_n^{\text{ML}} \end{pmatrix} = \begin{pmatrix} (\partial_{\theta^i} h | i \Delta\Psi_{\text{NVNL}} h_{\text{gr}}) \\ (\partial_{\delta\varphi_n} h | i \Delta\Psi_{\text{NVNL}} h_{\text{gr}}) \end{pmatrix} + \begin{pmatrix} (\partial_{\theta^i} h | n) \\ (\partial_{\delta\varphi_n} h | n) \end{pmatrix}, \quad (6.20)$$

where h is evaluated at $(\theta_i^t, \delta\varphi = 0)$ and the maximum likelihood values of θ_i^{ML} and $\delta\varphi_n^{\text{ML}}$ are implicitly defined in Eq. (6.20). We are expanding about small $\delta\varphi_n^{\text{ML}}$ and $\theta_i^{\text{ML}} - \theta_i^t$ and using Eq. (10) of [80]. This means that $\delta\varphi_n^{\text{ML}} = \Sigma_{\delta\varphi_n, J} (\partial_J h | i z(f) h_{\text{gr}}) \zeta^t$ with an uncertainty that comes from covariance matrix $\Sigma_{IJ} = (\Gamma^{-1})_{IJ}$. Thus for a small bias, the maximum likelihood point is shifted, but the statistical uncertainty is given by the Fisher matrix calculated with the parameterized test parameters $(\theta_i, \delta\varphi_n)$. In Ref. [82], we prove this fully and ascribe geometric meaning to how deviations are captured by parameterized PN templates.

Let us now construct a hierarchical analysis for the distribution of the ζ parameter for a collection of events, in a similar manner to how the LVK does [28]. We model ζ as $\zeta \sim \mathcal{N}(\mu, \sigma)$ and would like to estimate the posterior on the hyperparameters (μ, σ) . For event a , we write

$$\begin{aligned} p(d_a | \mu, \sigma) &= \int d\zeta p(d_a | \zeta) p(\zeta | \mu, \sigma), \\ &= \frac{1}{\sqrt{2\pi} \sqrt{\Delta\zeta_a^2 + \sigma^2}} \exp \left[-\frac{1}{2} \frac{(\zeta_a^{\text{ML}} - \mu)^2}{\Delta\zeta_a^2 + \sigma^2} \right], \end{aligned} \quad (6.21)$$

where ζ_a^{ML} and $\Delta\zeta_a$ are the MLE estimator and parameter uncertainty for ζ obtained from this event (and thus depend on d_a). Note that the maximum likelihood point for event a has the distribution

$$\zeta_a^{\text{ML}} \sim \mathcal{N}\left(0, \sqrt{\sigma_t^2 + \Delta\zeta_a^2}\right), \quad (6.22)$$

which follows from $\zeta_a^t \sim \mathcal{N}(0, \sigma_t)$ and $\zeta_a^{\text{ML}} \sim \mathcal{N}(\zeta_a^t, \Delta\zeta_a)$. If a generic PN test were performed instead, the maximum likelihood point is distributed like

$$\delta\varphi_{n,a}^{\text{ML}} \sim \mathcal{N}\left(0, \sqrt{\alpha_a^2 \sigma_t^2 + (\Delta\delta\varphi_{n,a})^2}\right), \quad (6.23)$$

since $\delta\varphi_{n,a}^{\text{ML}} \sim \mathcal{N}(\alpha_a \zeta_a^t, \Delta\delta\varphi_{n,a})$ where $\alpha_a \equiv \Sigma_{\delta\varphi_n, I}(\partial_I h|iz(f)h_{\text{gr}})$ is the coupling for event a given by Eq. (6.20) and $\Delta\delta\varphi_{n,a}$ is the statistical uncertainty on it. The entire collection of events leads to the joint likelihood

$$p(\{d_a\}|\mu, \sigma) = \prod_{a=1}^N p(d_a|\mu, \sigma), \quad (6.24)$$

where (μ, σ) are the hyper parameters for ζ , but the framework works analogously for PN deformation hyperparameters (μ_n, σ_n) . The number of events is N , and we do not include corrections for selection effects [83] or the probability of obtaining N events [84, 70]. To compute the consistency with GR, we use Bayes factors which compare the support for or against GR. Since we are comparing a nested model where GR is a single point $(0, 0)$ in the (μ, σ) plane, it becomes the well known Savage-Dickey ratio [68]. The Bayes factor \mathcal{B} is defined to be the ratio of the evidences

$$\log \mathcal{B}_{\text{GR}}^{\text{bGR}} = \log \left(\frac{p(d|\text{bGR})}{p(d|\text{GR})} \right) = \log \left(\frac{p(0, 0|d, \text{bGR})}{p(0, 0|\text{bGR})} \right), \quad (6.25)$$

where we are using the notation $p(x|d, M)$ to represent the posterior probability density x given data d under modeling assumptions M . One can see that the Savage-Dickey ratio compares how much the posterior has changed to the prior at the location of the GR limit. We use priors which are uniform in the range of $-1 \leq \mu \leq 1$ and $0 \leq \sigma \leq 1$.

Next, we investigate how detectible the effects of NVNL are if it were injected in the data. In Fig. 6.4 we show a contour plot of the Savage-Dickey ratio for a three detector network Livingston-Hanford-Virgo at O3 Livingston sensitivity. In particular, we calculate the Fisher information matrix for five years of events where we draw from the astrophysical rates. The merger rate density scales with the star formation rate

and the masses are drawn from the `POWER LAW+PEAK` (PP) model [85, 86] that is the best fit point from GWTC3 data [87]. We show the estimated measurement precision in the astrophysical parameters, marginalizing over the event-level parameters. We perform this analysis for the optimal principal component dephasing term. Additionally, we give the results for the traditional PN deformation coefficients based upon the biased framework [82]. We can see that NVNL can be constrained such that $A \lesssim 6 \times 10^{-3}$ after five years of observation at O3 sensitivities when using the PCA method ζ . The 3.5PN dephasing term, $\delta\varphi_7$, performed the best out of the parameterized tests and found the constraint $A \lesssim 7 \times 10^{-3}$. We note that for a single BBH event $A \lesssim 0.1$ which is comparable what [88] found using a different scheme (c.f. Table 1 [88]). The minimum detectable value doesn't strongly depend on which PN order you use, but the PCA method was optimal. This is consistent with previous work showing that deviations are detectable with most PN tests [89, 90].

We perform the same analysis for the case of third generation gravitational wave detectors. We consider three Cosmic Explorer detectors located at the locations of the current LIGO/Virgo network. With this improvement in sensitivity, we see that the five year constraint on A is $A \lesssim 4 \times 10^{-4}$ for the PCA method and $A \lesssim 5 \times 10^{-4}$ for the 3.5PN parameterized test, as shown in Fig. 6.5. For both of these cases, we produced the figure by resampling over many realizations of events and their associated noise realization so that very loud events do not show drastic shifts in the constraint. In the supplemental material, we show much the variance of the log Bayes factor versus observation time.

To perform our analysis on actual data, we need to take the further step making an NVNL-EOB model which includes spin effects and is properly calibrated to numerical relativity waveforms, for example with SEOBNRv5 [61].

6.5 Conclusion

In this work, we have modeled the effects of non-violent non-locality for a binary black hole merger and estimated how well this can be measured in current and third generation detectors. By incorporating NVNL fluctuations to an EOB model, we obtained modified trajectories for the binary, and the corresponding gravitational waveforms. These waveforms' phase deviation from GR in the frequency domain can be well approximated as a single mode function times a random coefficient with normal distribution with zero mean and standard deviation A , which in turn also characterizes the typical size of the metric perturbations close to the horizon.

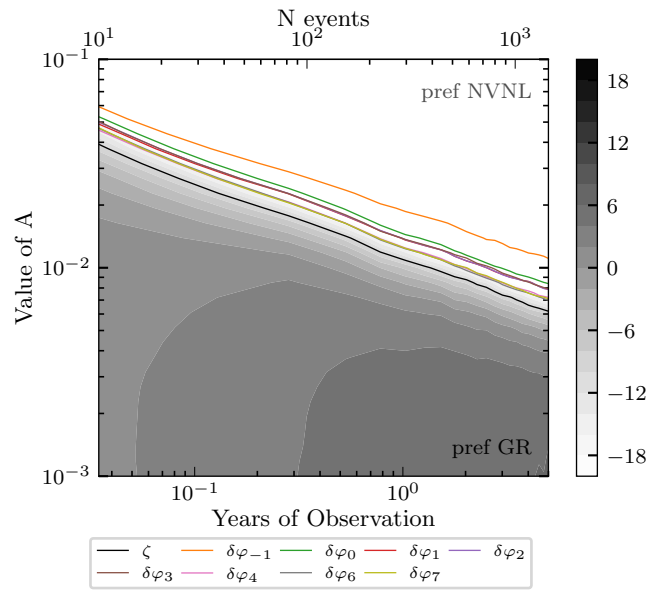


Figure 6.4: The log Bayes factor projected constraint for Hanford-Livingston-Virgo network operating at O3 Livingston sensitivity (positive favors GR). We plot this for various values of A and for increasing numbers of events. The line corresponding to $-10 \log$ Bayes factor is shown for the optimal PCA model (black) and PN coefficients (other colors) where GR is disfavored. Using an event list, we perform parameter estimation for five years of detectable events and then compute the Bayes factor for the hierarchical test of GR. Note that the PCA model is best able to constrain the effects of NVNL most stringently, but the PN coefficients are able to detect a violation of $A \neq 0$ nearly as well. We also see that the largest PN orders perform the best. For a five year observation, the bound for the PCA model is $A < 6.2 \times 10^{-3}$.

We estimated constraints that can be posed by LVK and third-generation detectors. We showed that the 'optimal' PCA templates constraints A tighter than the standard PN parameters by about 20%. To perform our analysis on actual data, we need to take the further step making an NVNL-EOB model which includes spin effects and is properly calibrated to numerical relativity waveforms, for example with SEOBNRv5 [61].

This work is primarily concerned with the finding a qualitative picture of waveforms in NVNL. Since we are particularly concerned with the behavior of comparable mass systems like LVK detects, we tuned our approach accordingly and used an EOB model. Thus, our work has been limited to conservative dynamics during the inspiral stage. To obtain a more complete picture of NVNL effects, one should: (i) combine our work with Ref. [22] to incorporate NVNL's modifications to radiation reaction during the inspiral stage, and (ii) model the effect of NVNL perturbations on wave

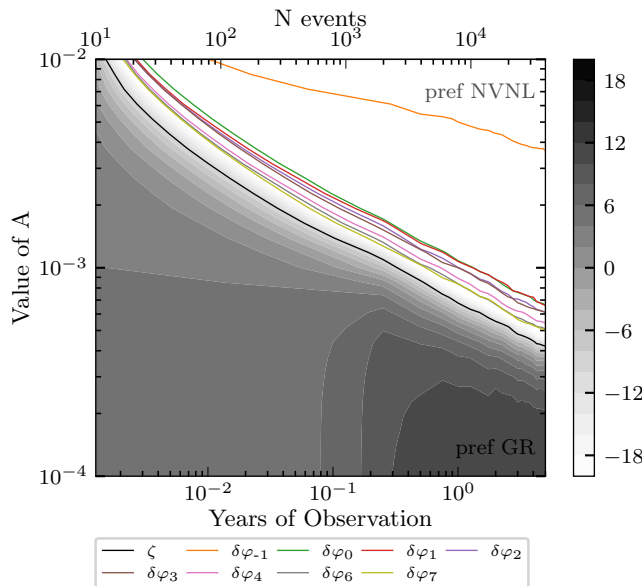


Figure 6.5: The log Bayes factor for the Hanford-Livingston-Virgo network operating at CE sensitivity (positive favors GR). This plot shows the same scaling as Fig. 6.4, but contains more events since CE detects more in a five year period. For a five year observation, the bound for the PCA model is $A < 4.2 \times 10^{-4}$.

propagation through the final BH's spacetime in order to capture how the ringdown waves will be modified. We stress that modeling the dissipative and ringdown effects is particularly difficult in the comparable mass case since these are not modeled with first principles for EOB. While there is no particular reason that the conservative effects are dominant, these results are a first order-of-magnitude picture for NVNL in ground based detectors.

ACKNOWLEDGMENTS

We thank Jacob Golomb, Ethan Payne, Sophie Hourihane, Max Isi, Bangalore Sathyaprakash, Matthew Giesler, Steve Giddings, Ian MacMillan, Hang Yu, and Katerina Chatziioannou for their insightful discussions. B.S. acknowledges support by the National Science Foundation Graduate Research Fellowship under Grant No. DGE-1745301. Y.C. and B.S. acknowledge support from the Brinson Foundation, the Simons Foundation (Award Number 568762), and by NSF Grants PHY-2309211 and PHY-2309231.

6.6 Appendix: Waveform Details

EOB Waveform

We made our EOB waveform by modifying the nonspinning EOBNRv2 waveform [39]. Given an effective metric, one can solve for the effective Hamiltonian by solving the mass-shell constraint $p_\mu p_\nu g^{\mu\nu} = -1 - Q(p^4)$

$$\hat{H}^{\text{eff}}(r, \phi, p_r, p_\phi) = \frac{g^{0i} p_i}{g^{00}} + \sqrt{\frac{1 + g^{ij} p^i p^j}{-g^{00}} + \left(\frac{g^{0ri} p_i}{g^{00}}\right)^2} + \frac{Q(p^4)}{-g^{00}}, \quad (6.26)$$

where the modification to the mass shell is $Q(p^4) = 2\eta(4 - 3\eta)p_r^4$ which we do not modify due to NVNL since it is a high PN order effect. By perturbing $g^{\mu\nu}$ in Eq. (6.26), we find the perturbation to the real Hamiltonian $\Delta\hat{H}^{\ell m}$

$$\hat{H}_{\text{real}} = \hat{H}_{\text{real}}^{\text{S}} + h_{\text{vv}}^{\ell m} \Delta\hat{H}_{\ell m}^{\text{real}}. \quad (6.27)$$

In this section, we will be using dimensionless units so $t = T/M$, $r = R/M$, $p_r = P_R/M$, and $p_\phi = P_\phi/(M\mu)$. The equations of motion for the EOB trajectory are found by solving Hamilton's equations with radiation reaction terms. If we explicitly write out the EOB trajectory evolution equations with the perturbations we have

$$\begin{aligned} \frac{\partial r}{\partial t} &= \frac{\partial \hat{H}_{\text{real}}^{\text{S}}}{\partial p_r} + \frac{\partial \Delta\hat{H}_{\ell m}^{\text{real}}}{\partial p_r} h_{\text{vv}}^{\ell m}, \\ \frac{\partial \phi}{\partial t} = \hat{\omega} &= \frac{\partial \hat{H}_{\text{real}}^{\text{S}}}{\partial p_\phi} + \frac{\partial \Delta\hat{H}_{\ell m}^{\text{real}}}{\partial p_\phi} h_{\text{vv}}^{\ell m}, \\ \frac{\partial p_r}{\partial t} &= -\frac{\partial \hat{H}_{\text{real}}^{\text{S}}}{\partial r} + \hat{\mathcal{F}}_\phi \frac{p_r}{p_\phi} - \frac{\partial (\Delta\hat{H}_{\ell m}^{\text{real}} h_{\text{vv}}^{\ell m})}{\partial r}, \\ \frac{\partial p_\phi}{\partial t} &= \hat{\mathcal{F}}_\phi - \frac{\partial (h_{\text{vv}}^{\ell m})}{\partial \phi} \Delta\hat{H}_{\ell m}^{\text{real}}, \end{aligned} \quad (6.28)$$

and the ϕ component of the radiation-reaction force is

$$\hat{\mathcal{F}}_\phi = -\frac{1}{\eta v_\omega^3} \frac{dE}{dt}, \quad (6.29)$$

where $v_\omega = \hat{\omega}^{1/3}$. The GW luminosity is generally

$$\frac{dE}{dt} = \frac{v_\omega^6}{8\pi} \sum_{\ell=2}^{\infty} \sum_{m=\ell-2}^{\ell} m^2 \left| \frac{D_L}{M} h_{\ell m} \right|^2, \quad (6.30)$$

however we make the approximation and only include the (2, 2) mode. To construct $h_{22}(t)$, we are using the Newtonian contribution as given in Eq. (16) of [39]. It is equal to

$$h_{22} = -\frac{32\pi}{5} \sqrt{\frac{2}{3}} \frac{M\eta}{D_L} v_\phi^2 Y^{2-2} \left(\frac{\pi}{2}, \phi \right), \quad (6.31)$$

where

$$v_\phi \equiv \hat{\omega} r_\omega \equiv \hat{\omega} r [\psi(r, p_\phi)]^{1/3}, \quad (6.32)$$

and

$$\psi(r, p_\phi) = \frac{2 \left\{ 1 + 2\eta \left[\sqrt{A(r) \left(1 + p_\phi^2 / r^2 \right)} - 1 \right] \right\}}{r^2 dA(r)/dr}. \quad (6.33)$$

Since our analysis is focusing on how the waveform differs by adding metric perturbations away from GR, we neglected to include various calibration terms that are included in EOBNRv2. In Ref. [39], they use the factorized resummed modes [91, 78, 53] which include corrections to the Newtonian modes motivated from numerical relativity. Specifically, we use $h_{\ell m}^F = h_{\ell m}^N$ in Eq. (14) of [39]. We also do not include the effects of the non-quasicircular orbit coefficients in Eq. (13) of [39].

We attach a phenomenological ringdown to our waveform. This is necessary so that the waveform can have a well defined Fourier transform / stationary phase approximation $h(f)$ which is well defined when a NVNL merges before the GR one. We stress that this is only used when extracting $\Delta\Psi(f)$, and the parameter estimation in the main work uses IMRPhenomD [92, 93] with extra beyond GR phase $\Delta\Psi(f)$. Since we did not include the GR calibration from the non-quasicircular orbit coefficients, we found that it was hard to get a good fit with the comb approach used in [39]. This is because the quasinormal modes are at a much higher frequency than the gravitational wave frequency at the merger-ringdown fit point. Without properly fitting to NR, we saw a preference for unphysical second peaks similar to what is shown in Fig. 3 of [39]. Instead, we choose the fit location $\partial_t |h_{22}| = 0$ and attach a ringdown. If we write the h_{22} waveform as

$$h_{22}(t) = A_{22}(t) e^{-i\phi_{22}(t)}, \quad (6.34)$$

where time is scaled so that merger happens $t = 0$. The phenomenological ringdown waveform is described by

$$\omega_{22,\text{RD}}^r(t) = \omega_{220}^r \left(1 - \sum_{i=1}^2 \alpha_i e^{-t/\tau_i} \right), \quad (6.35)$$

and the ringdown amplitude is

$$A_{22,\text{RD}}(t) = A_{22}|_{t=0} \exp \left[\omega_{220}^i t \left(1 + \sum_{i=1}^2 \beta_i e^{-t/\tau_i} \right) \right], \quad (6.36)$$

where $\omega_{220} = \omega_{220}^r + i \omega_{220}^i$. We set α_i and β_i by enforcing that the match between inspiral and ringdown is twice continuously differentiable $h'_{22,\text{IM}}(t) = h'_{22,\text{RD}}(t)$

and $h''_{22,\text{IM}}(t) = h''_{22,\text{RD}}(t)$. We note that the accuracy of the ringdown fit isn't that important because we are only searching for deviations from GR during the inspiral-merger and assume $\Delta\Psi(f)$ is constant after merger (as can be seen in Fig. 6.2 above $Mf \sim 0.4$). We stress that attaching a GR ringdown is a conservative choice, and suspect that proper modeling of the ringdown could improve constraints by a factor of ~ 2 . Our analysis of NVNL in the ringdown phase is part of an ongoing future work.

Analytical Description

In this section, we will describe how the coordinates are modified in the inspiral and explain the perturbative framework in more detail. Let us denote the EOB state space coordinate as $x^a(t) = (r, \phi, p_r, p_\phi)$ and consider deviations away from the trajectory that the GR waveform takes $x_{\text{GR}}^a(t)$. The deviations $\Delta x^a(t) = x_{\text{NVNL}}^a(t) - x_{\text{GR}}^a(t)$ follow a coupled system of differential equations

$$\frac{d\Delta x^a}{dt} = M^{ab}(t)\Delta x_b + F^a(t), \quad (6.37)$$

where $M^{ab}(t)$ represents perturbations away from the GR trajectory associated with perturbations of GR terms $\hat{H}_{\text{real}}^S/\hat{\mathcal{F}}_\phi$ in Eq. (6.28) while $F^a(t)$ is the original sourced deviation from terms containing $h_{\text{vv}}^{\ell m}$ in Eq. (6.28). Typically, $M^{ab}(t)$ is either constant—e.g. in a simple harmonic oscillator—or features damping when friction is present. In contrast, $M^{ab}(t)$ provides an anti-restoring feedback that causes perturbations to grow secularly. Consequently, although NVNL terms only initially source small deviations in the EOB equations of motion, the orbital dynamics secularly amplify these deviations over time. Physically, this can be understood as a slight eccentricity induced by the NVNL forces, which shortens/lengthens the inspiral and leads to an earlier coalescence (depending on sign of angular momentum kick).

Additionally, it is important to note how the frequency domain dephasing is related to the changes from NVNL waveform. If our waveforms are of the form $h_{\text{gr}}(t) = A_{\text{gr}}(t)e^{-2\phi_{\text{gr}}(t)}$, the frequency domain dephasing in the stationary phase approximation is equal to

$$\begin{aligned} \Delta\Psi(f) &= 2\pi f \Delta t(f) - 2 [\phi_{\text{nvnl}}(t_{\text{nvnl}}(f)) - \phi_{\text{gr}}(t_{\text{gr}}(f))] , \\ &= -2\Delta\phi(f), \end{aligned} \quad (6.38)$$

where $\Delta\phi(f) = \phi_{\text{nvnl}}(t_{\text{gr}}(f)) - \phi_{\text{gr}}(t_{\text{gr}}(f))$ is the time domain orbital phase deviation. Therefore, deviations to orbital phase in the inspiral are directly related to

the frequency domain phasing in the stationary phase approximation when appropriately using the time frequency relation (also true in ringdown).

Accuracy of PCA

Let us now discuss the accuracy of the PCA. We do this by comparing the variance in the phase deviation that is captured by our PCA model to the full phase deviation. We find the full dephasing by computing a FFT $\Delta\Psi_{\text{full}}(f)$ and the PCA dephasing is $\Delta\Psi_{\text{PCA}}(f) = \zeta z(f)$ where $z(f)$ is the most dominant principal mode and ζ is a parameter so that $|\Delta\Psi_{\text{full}}(f) - \Psi_{\text{PCA}}(f)|$ is minimized. The variance captured at each frequency f by the PCA is

$$\begin{aligned}\sigma_{\Delta\Psi}^{\text{est}}(f) &\equiv \frac{\langle \Delta\Psi_{\text{PCA}}(f) \Delta\Psi_{\text{full}}(f) \rangle}{\sqrt{\langle \Delta\Psi_{\text{PCA}}^2(f) \rangle}}, \\ &= \frac{\langle \zeta \Delta\Psi_{\text{full}}(f) \rangle}{\sqrt{\langle \zeta^2 \rangle}}.\end{aligned}\quad (6.39)$$

This needs to be compared to total amount of variance in the full waveform

$$\sigma_{\Delta\Psi}^{\text{tot}}(f) = \sqrt{\langle \Delta\Psi_{\text{full}}^2(f) \rangle}.\quad (6.40)$$

In Fig. 6.6, we compare these variance indicators and see the fit quality. One can see that the variance captured by the PCA estimator $\Psi_{\text{PCA}}(f)$ is less than the true variance in $\Delta\Psi_{\text{full}}(f)$, however it does a good job of estimating the variance at high frequencies when the dephasing is largest. Note that the reason that these do not perfectly match up is that the PCA is optimizing the quantity $|\Sigma(f, f') - \sigma^2 z(f)z(f')|$. The off diagonal elements of $\Sigma(f, f')$ where $f \neq f'$ are better fit by choosing $z(f)$.

Variance of Bayes Factor

As we noted in the discussion of Fig. 6.4 and Fig. 6.5, the Bayes factor measurement depends on randomness about the event order. In Fig. 6.7, we plot how the (log) Bayes Factor ratio scales for multiple injection sizes of A . In the center, we show the median Bayes factor for each injection size while the upper and lower bounds are $\pm 1\sigma$ percentile values for the Bayes factor after this many observations. This mostly occurs because the loudest events are the most informative, so the order of events can affect the rolling constraint. Furthermore, the statistical realization of the detector noise and hierarchical model draw add subdominant variations to the Bayes factor.

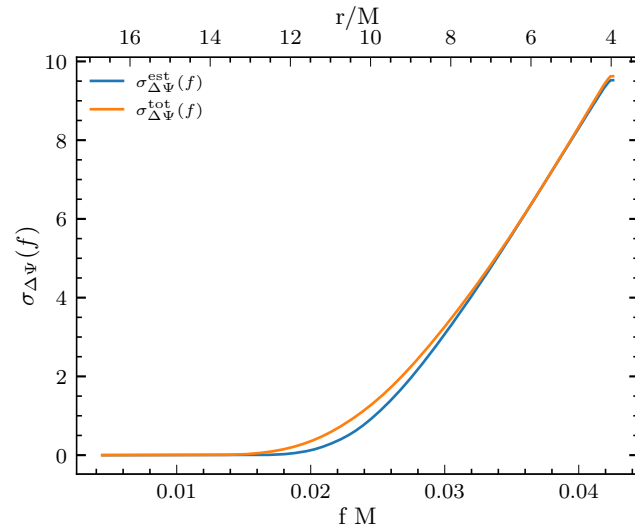


Figure 6.6: Comparison of how much variance is captured by the PCA estimator. We see that the full $\Delta\Psi$ is well described by this. While some of the variance is not captured at low frequencies, at high frequencies there is a nearly perfect match, especially at larger frequencies. The other PCA terms contain about 3% of the variance that is not accounted for in the primary one here as discussed in the main text.

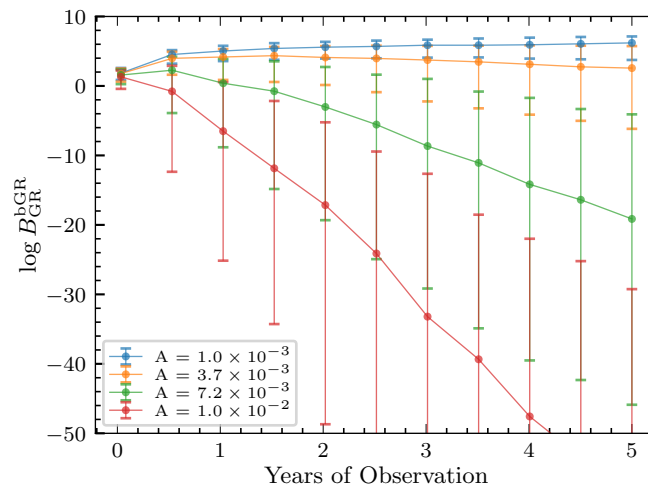


Figure 6.7: The log Bayes factor for the Hanford-Livingston-Virgo network at O3 Livingston sensitivity (positive favors GR). One can see that the red curve favors NVNL at large events, while blue favors GR. The whiskers correspond to the upper and lower bounds are $\pm 1\sigma$ percentile values due to randomness associated with the order of events. If one sees a loud clear event early, then it is easier to favor/disfavor GR.

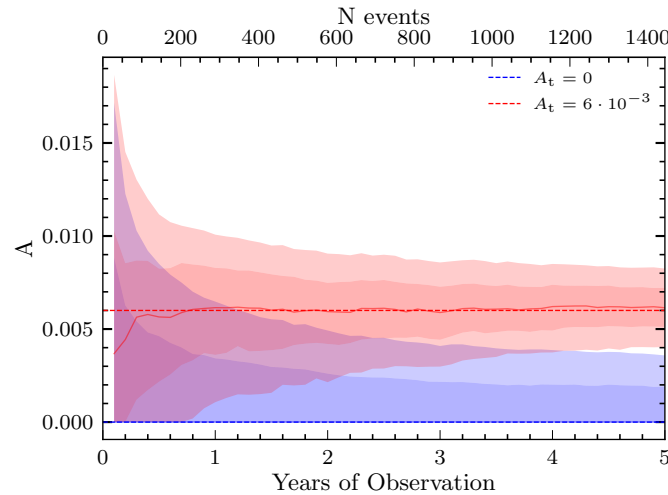


Figure 6.8: We show the running estimate of A for an O3 network. In blue, we show the 1σ and 2σ confidence region when we inject $A_t = 0$. We can see that the error shrinks as events are observed. In red, we inject $A_t = 6 \times 10^{-3}$, and one can see that as events are observed the probability density narrows and detects a violation.

Measuring A

While in the main text of this letter, we primarily focused on null tests of NVNL, one can directly measure the size of the deviations. In the same manner that we did before, we can compute the event posteriors for many events and then compute the posterior in the hierarchical model. The true value of NVNL parameter A is for the choice of $p(\mu, \sigma|d) = p(0, A|d)$. We can thus compute the confidence interval on A by finding the maximum posterior location and shade the interval which contains 1σ and 2σ of the posterior support. We do this for a LIGO-Virgo network at O3 Livingston sensitivity in Fig. 6.8, where in blue is an injection of $A_t = 0$, and $A_t = 6 \times 10^{-3}$ constraints are shown in red. We shade the $\pm 1\sigma$ and $\pm 2\sigma$ regions of the posterior as a function of the years of observation. One can see that the case of zero injection slowly asymptotes to a stronger constraint on A while injection a nonzero A the credible interval eventually detects it at 95% level after a little less than a year. In Fig. 6.9, we plot the same case for CE with $A_t = 0$ in blue and $A_t = 3 \times 10^{-4}$ in red. One can see similar features where the constraint narrows down to the true value as the network observes more events.

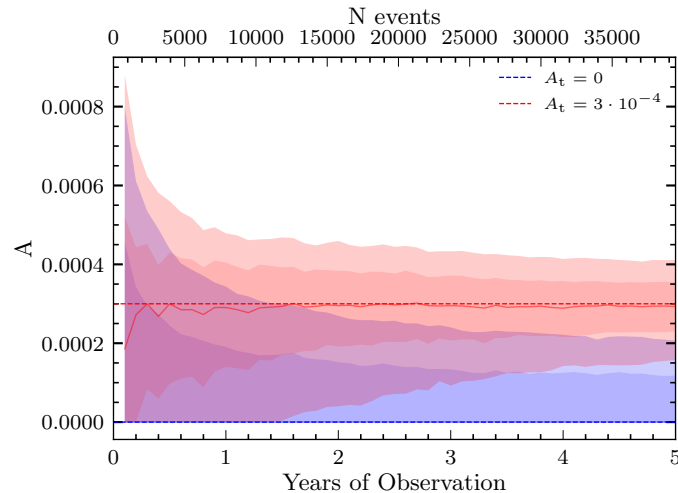


Figure 6.9: We show the running estimate of A for the CE network in an analogous manner of Fig. 6.8. In red, we inject $A_t = 0$, and in blue $A_t = 3 \times 10^{-4}$. One can see that as more observations are made, the confidence region begins to exclude $A = 0$.

References

- [1] S. W. Hawking. “Particle Creation by Black Holes.” In: *Commun. Math. Phys.* 43 (1975). Ed. by G. W. Gibbons and S. W. Hawking. [Erratum: *Commun.Math.Phys.* 46, 206 (1976)], pp. 199–220. DOI: [10.1007/BF02345020](https://doi.org/10.1007/BF02345020).
- [2] S. W. Hawking. “Breakdown of Predictability in Gravitational Collapse.” In: *Phys. Rev. D* 14 (1976), pp. 2460–2473. DOI: [10.1103/PhysRevD.14.2460](https://doi.org/10.1103/PhysRevD.14.2460).
- [3] S. B. Giddings. “Black holes and massive remnants.” In: *Phys. Rev. D* 46 (1992), pp. 1347–1352. DOI: [10.1103/PhysRevD.46.1347](https://doi.org/10.1103/PhysRevD.46.1347). arXiv: [hep-th/9203059](https://arxiv.org/abs/hep-th/9203059).
- [4] S. D. Mathur. “The Fuzzball proposal for black holes: An Elementary review.” In: *Fortsch. Phys.* 53 (2005). Ed. by E. Kiritsis, pp. 793–827. DOI: [10.1002/prop.200410203](https://doi.org/10.1002/prop.200410203). arXiv: [hep-th/0502050](https://arxiv.org/abs/hep-th/0502050).
- [5] P. O. Mazur and E. Mottola. “Gravitational vacuum condensate stars.” In: *Proc. Nat. Acad. Sci.* 101 (2004), pp. 9545–9550. DOI: [10.1073/pnas.0402717101](https://doi.org/10.1073/pnas.0402717101). arXiv: [gr-qc/0407075](https://arxiv.org/abs/gr-qc/0407075).
- [6] A. Almheiri, D. Marolf, J. Polchinski, et al. “Black Holes: Complementarity or Firewalls?.” In: *JHEP* 02 (2013), p. 062. DOI: [10.1007/JHEP02\(2013\)062](https://doi.org/10.1007/JHEP02(2013)062). arXiv: [1207.3123](https://arxiv.org/abs/1207.3123) [hep-th].
- [7] A. Almheiri, N. Engelhardt, D. Marolf, et al. “The entropy of bulk quantum fields and the entanglement wedge of an evaporating black hole.” In: *JHEP*

- 12 (2019), p. 063. DOI: [10.1007/JHEP12\(2019\)063](https://doi.org/10.1007/JHEP12(2019)063). arXiv: [1905.08762](https://arxiv.org/abs/1905.08762) [hep-th].
- [8] A. Almheiri, R. Mahajan, J. Maldacena, et al. “The Page curve of Hawking radiation from semiclassical geometry.” In: *JHEP* 03 (2020), p. 149. DOI: [10.1007/JHEP03\(2020\)149](https://doi.org/10.1007/JHEP03(2020)149). arXiv: [1908.10996](https://arxiv.org/abs/1908.10996) [hep-th].
- [9] G. Penington, S. H. Shenker, D. Stanford, et al. “Replica wormholes and the black hole interior.” In: *JHEP* 03 (2022), p. 205. DOI: [10.1007/JHEP03\(2022\)205](https://doi.org/10.1007/JHEP03(2022)205). arXiv: [1911.11977](https://arxiv.org/abs/1911.11977) [hep-th].
- [10] A. Almheiri, T. Hartman, J. Maldacena, et al. “Replica Wormholes and the Entropy of Hawking Radiation.” In: *JHEP* 05 (2020), p. 013. DOI: [10.1007/JHEP05\(2020\)013](https://doi.org/10.1007/JHEP05(2020)013). arXiv: [1911.12333](https://arxiv.org/abs/1911.12333) [hep-th].
- [11] A. Almheiri, T. Hartman, J. Maldacena, et al. “The entropy of Hawking radiation.” In: *Rev. Mod. Phys.* 93.3 (2021), p. 035002. DOI: [10.1103/RevModPhys.93.035002](https://doi.org/10.1103/RevModPhys.93.035002). arXiv: [2006.06872](https://arxiv.org/abs/2006.06872) [hep-th].
- [12] S. B. Giddings. “Models for unitary black hole disintegration.” In: *Phys. Rev. D* 85 (2012), p. 044038. DOI: [10.1103/PhysRevD.85.044038](https://doi.org/10.1103/PhysRevD.85.044038). arXiv: [1108.2015](https://arxiv.org/abs/1108.2015) [hep-th].
- [13] S. B. Giddings. “Nonviolent nonlocality.” In: *Phys. Rev. D* 88 (2013), p. 064023. DOI: [10.1103/PhysRevD.88.064023](https://doi.org/10.1103/PhysRevD.88.064023). arXiv: [1211.7070](https://arxiv.org/abs/1211.7070) [hep-th].
- [14] S. B. Giddings. “Modulated Hawking radiation and a nonviolent channel for information release.” In: *Phys. Lett. B* 738 (2014), pp. 92–96. DOI: [10.1016/j.physletb.2014.08.070](https://doi.org/10.1016/j.physletb.2014.08.070). arXiv: [1401.5804](https://arxiv.org/abs/1401.5804) [hep-th].
- [15] S. B. Giddings. “Nonviolent unitarization: basic postulates to soft quantum structure of black holes.” In: *JHEP* 12 (2017), p. 047. DOI: [10.1007/JHEP12\(2017\)047](https://doi.org/10.1007/JHEP12(2017)047). arXiv: [1701.08765](https://arxiv.org/abs/1701.08765) [hep-th].
- [16] S. B. Giddings. “The unitarity crisis, nonviolent unitarization, and implications for quantum spacetime.” Dec. 2024. arXiv: [2412.18650](https://arxiv.org/abs/2412.18650) [hep-th].
- [17] S. B. Giddings. “The deepest problem: some perspectives on quantum gravity.” Feb. 2022. arXiv: [2202.08292](https://arxiv.org/abs/2202.08292) [hep-th].
- [18] S. B. Giddings. “Possible observational windows for quantum effects from black holes.” In: *Phys. Rev. D* 90.12 (2014), p. 124033. DOI: [10.1103/PhysRevD.90.124033](https://doi.org/10.1103/PhysRevD.90.124033). arXiv: [1406.7001](https://arxiv.org/abs/1406.7001) [hep-th].
- [19] S. B. Giddings. “Gravitational wave tests of quantum modifications to black hole structure – with post-GW150914 update.” In: *Class. Quant. Grav.* 33.23 (2016), p. 235010. DOI: [10.1088/0264-9381/33/23/235010](https://doi.org/10.1088/0264-9381/33/23/235010). arXiv: [1602.03622](https://arxiv.org/abs/1602.03622) [gr-qc].

- [20] S. B. Giddings and D. Psaltis. “Event Horizon Telescope Observations as Probes for Quantum Structure of Astrophysical Black Holes.” In: *Phys. Rev. D* 97.8 (2018), p. 084035. DOI: [10.1103/PhysRevD.97.084035](https://doi.org/10.1103/PhysRevD.97.084035). arXiv: [1606.07814](https://arxiv.org/abs/1606.07814) [astro-ph.HE].
- [21] K. Akiyama et al. “First Sagittarius A* Event Horizon Telescope Results. I. The Shadow of the Supermassive Black Hole in the Center of the Milky Way.” In: *Astrophys. J. Lett.* 930.2 (2022), p. L12. DOI: [10.3847/2041-8213/ac6674](https://doi.org/10.3847/2041-8213/ac6674). arXiv: [2311.08680](https://arxiv.org/abs/2311.08680) [astro-ph.HE].
- [22] K. Fransen and S. B. Giddings. “Gravitational wave signatures of departures from classical black hole scattering.” In: *Phys. Rev. D* 110.6 (2024), p. 064029. DOI: [10.1103/PhysRevD.110.064029](https://doi.org/10.1103/PhysRevD.110.064029). arXiv: [2405.05970](https://arxiv.org/abs/2405.05970) [gr-qc].
- [23] B. P. Abbott et al. “Observation of Gravitational Waves from a Binary Black Hole Merger.” In: *Phys. Rev. Lett.* 116.6 (2016), p. 061102. DOI: [10.1103/PhysRevLett.116.061102](https://doi.org/10.1103/PhysRevLett.116.061102). arXiv: [1602.03837](https://arxiv.org/abs/1602.03837) [gr-qc].
- [24] B. P. Abbott et al. “GW170814: A Three-Detector Observation of Gravitational Waves from a Binary Black Hole Coalescence.” In: *Phys. Rev. Lett.* 119.14 (2017), p. 141101. DOI: [10.1103/PhysRevLett.119.141101](https://doi.org/10.1103/PhysRevLett.119.141101). arXiv: [1709.09660](https://arxiv.org/abs/1709.09660) [gr-qc].
- [25] B. P. Abbott et al. “Tests of General Relativity with GW170817.” In: *Phys. Rev. Lett.* 123.1 (2019), p. 011102. DOI: [10.1103/PhysRevLett.123.011102](https://doi.org/10.1103/PhysRevLett.123.011102). arXiv: [1811.00364](https://arxiv.org/abs/1811.00364) [gr-qc].
- [26] B. P. Abbott et al. “Tests of General Relativity with the Binary Black Hole Signals from the LIGO-Virgo Catalog GWTC-1.” In: *Phys. Rev. D* 100.10 (2019), p. 104036. DOI: [10.1103/PhysRevD.100.104036](https://doi.org/10.1103/PhysRevD.100.104036). arXiv: [1903.04467](https://arxiv.org/abs/1903.04467) [gr-qc].
- [27] R. Abbott et al. “Tests of general relativity with binary black holes from the second LIGO-Virgo gravitational-wave transient catalog.” In: *Phys. Rev. D* 103.12 (2021), p. 122002. DOI: [10.1103/PhysRevD.103.122002](https://doi.org/10.1103/PhysRevD.103.122002). arXiv: [2010.14529](https://arxiv.org/abs/2010.14529) [gr-qc].
- [28] R. Abbott et al. “Tests of General Relativity with GWTC-3.” Dec. 2021. arXiv: [2112.06861](https://arxiv.org/abs/2112.06861) [gr-qc].
- [29] N. Yunes and F. Pretorius. “Fundamental Theoretical Bias in Gravitational Wave Astrophysics and the Parameterized Post-Einsteinian Framework.” In: *Phys. Rev. D* 80 (2009), p. 122003. DOI: [10.1103/PhysRevD.80.122003](https://doi.org/10.1103/PhysRevD.80.122003). arXiv: [0909.3328](https://arxiv.org/abs/0909.3328) [gr-qc].
- [30] T. G. F. Li, W. Del Pozzo, S. Vitale, et al. “Towards a generic test of the strong field dynamics of general relativity using compact binary coalescence.” In: *Phys. Rev. D* 85 (2012), p. 082003. DOI: [10.1103/PhysRevD.85.082003](https://doi.org/10.1103/PhysRevD.85.082003). arXiv: [1110.0530](https://arxiv.org/abs/1110.0530) [gr-qc].

- [31] M. Agathos, W. Del Pozzo, T. G. F. Li, et al. “TIGER: A data analysis pipeline for testing the strong-field dynamics of general relativity with gravitational wave signals from coalescing compact binaries.” In: *Phys. Rev. D* 89.8 (2014), p. 082001. doi: [10.1103/PhysRevD.89.082001](https://doi.org/10.1103/PhysRevD.89.082001). arXiv: [1311.0420](https://arxiv.org/abs/1311.0420) [gr-qc].
- [32] A. K. Mehta, A. Buonanno, R. Cotesta, et al. “Tests of general relativity with gravitational-wave observations using a flexible theory-independent method.” In: *Phys. Rev. D* 107.4 (2023), p. 044020. doi: [10.1103/PhysRevD.107.044020](https://doi.org/10.1103/PhysRevD.107.044020). arXiv: [2203.13937](https://arxiv.org/abs/2203.13937) [gr-qc].
- [33] B. P. Abbott et al. “Tests of general relativity with GW150914.” In: *Phys. Rev. Lett.* 116.22 (2016). [Erratum: *Phys.Rev.Lett.* 121, 129902 (2018)], p. 221101. doi: [10.1103/PhysRevLett.116.221101](https://doi.org/10.1103/PhysRevLett.116.221101). arXiv: [1602.03841](https://arxiv.org/abs/1602.03841) [gr-qc].
- [34] M. Isi, K. Chatziioannou, and W. M. Farr. “Hierarchical test of general relativity with gravitational waves.” In: *Phys. Rev. Lett.* 123.12 (2019), p. 121101. doi: [10.1103/PhysRevLett.123.121101](https://doi.org/10.1103/PhysRevLett.123.121101). arXiv: [1904.08011](https://arxiv.org/abs/1904.08011) [gr-qc].
- [35] P. Saini, S. A. Bhat, M. Favata, et al. “Eccentricity-induced systematic error on parametrized tests of general relativity: Hierarchical Bayesian inference applied to a binary black hole population.” In: *Phys. Rev. D* 109.8 (2024), p. 084056. doi: [10.1103/PhysRevD.109.084056](https://doi.org/10.1103/PhysRevD.109.084056). arXiv: [2311.08033](https://arxiv.org/abs/2311.08033) [gr-qc].
- [36] A. Buonanno and T. Damour. “Effective one-body approach to general relativistic two-body dynamics.” In: *Phys. Rev. D* 59 (1999), p. 084006. doi: [10.1103/PhysRevD.59.084006](https://doi.org/10.1103/PhysRevD.59.084006). arXiv: [gr-qc/9811091](https://arxiv.org/abs/gr-qc/9811091).
- [37] A. Buonanno and T. Damour. “Transition from inspiral to plunge in binary black hole coalescences.” In: *Phys. Rev. D* 62 (2000), p. 064015. doi: [10.1103/PhysRevD.62.064015](https://doi.org/10.1103/PhysRevD.62.064015). arXiv: [gr-qc/0001013](https://arxiv.org/abs/gr-qc/0001013).
- [38] T. Damour. “Coalescence of two spinning black holes: an effective one-body approach.” In: *Phys. Rev. D* 64 (2001), p. 124013. doi: [10.1103/PhysRevD.64.124013](https://doi.org/10.1103/PhysRevD.64.124013). arXiv: [gr-qc/0103018](https://arxiv.org/abs/gr-qc/0103018).
- [39] Y. Pan, A. Buonanno, M. Boyle, et al. “Inspirals-mergers-ringdown multipolar waveforms of nonspinning black-hole binaries using the effective-one-body formalism.” In: *Phys. Rev. D* 84 (2011), p. 124052. doi: [10.1103/PhysRevD.84.124052](https://doi.org/10.1103/PhysRevD.84.124052). arXiv: [1106.1021](https://arxiv.org/abs/1106.1021) [gr-qc].
- [40] E. Barausse, A. Buonanno, and A. Le Tiec. “The complete non-spinning effective-one-body metric at linear order in the mass ratio.” In: *Phys. Rev. D* 85 (2012), p. 064010. doi: [10.1103/PhysRevD.85.064010](https://doi.org/10.1103/PhysRevD.85.064010). arXiv: [1111.5610](https://arxiv.org/abs/1111.5610) [gr-qc].
- [41] T. Damour and A. Nagar. “The Effective-One-Body Approach to the General Relativistic Two Body Problem.” In: *Lect. Notes Phys.* 905 (2016), pp. 273–312. doi: [10.1007/978-3-319-19416-5_7](https://doi.org/10.1007/978-3-319-19416-5_7).

- [42] Y. Pan, A. Buonanno, L. T. Buchman, et al. “Effective-one-body waveforms calibrated to numerical relativity simulations: coalescence of nonprecessing, spinning, equal-mass black holes.” In: *Phys. Rev. D* 81 (2010), p. 084041. DOI: [10.1103/PhysRevD.81.084041](https://doi.org/10.1103/PhysRevD.81.084041). arXiv: [0912.3466](https://arxiv.org/abs/0912.3466) [gr-qc].
- [43] A. Taracchini, Y. Pan, A. Buonanno, et al. “Prototype effective-one-body model for nonprecessing spinning inspiral-merger-ringdown waveforms.” In: *Phys. Rev. D* 86 (2012), p. 024011. DOI: [10.1103/PhysRevD.86.024011](https://doi.org/10.1103/PhysRevD.86.024011). arXiv: [1202.0790](https://arxiv.org/abs/1202.0790) [gr-qc].
- [44] A. Bohé et al. “Improved effective-one-body model of spinning, nonprecessing binary black holes for the era of gravitational-wave astrophysics with advanced detectors.” In: *Phys. Rev. D* 95.4 (2017), p. 044028. DOI: [10.1103/PhysRevD.95.044028](https://doi.org/10.1103/PhysRevD.95.044028). arXiv: [1611.03703](https://arxiv.org/abs/1611.03703) [gr-qc].
- [45] A. Nagar, G. Riemenschneider, G. Pratten, et al. “Multipolar effective one body waveform model for spin-aligned black hole binaries.” In: *Phys. Rev. D* 102.2 (2020), p. 024077. DOI: [10.1103/PhysRevD.102.024077](https://doi.org/10.1103/PhysRevD.102.024077). arXiv: [2001.09082](https://arxiv.org/abs/2001.09082) [gr-qc].
- [46] T. Damour, P. Jaranowski, and G. Schafer. “Effective one body approach to the dynamics of two spinning black holes with next-to-leading order spin-orbit coupling.” In: *Phys. Rev. D* 78 (2008), p. 024009. DOI: [10.1103/PhysRevD.78.024009](https://doi.org/10.1103/PhysRevD.78.024009). arXiv: [0803.0915](https://arxiv.org/abs/0803.0915) [gr-qc].
- [47] E. Barausse and A. Buonanno. “An Improved effective-one-body Hamiltonian for spinning black-hole binaries.” In: *Phys. Rev. D* 81 (2010), p. 084024. DOI: [10.1103/PhysRevD.81.084024](https://doi.org/10.1103/PhysRevD.81.084024). arXiv: [0912.3517](https://arxiv.org/abs/0912.3517) [gr-qc].
- [48] E. Barausse and A. Buonanno. “Extending the effective-one-body Hamiltonian of black-hole binaries to include next-to-next-to-leading spin-orbit couplings.” In: *Phys. Rev. D* 84 (2011), p. 104027. DOI: [10.1103/PhysRevD.84.104027](https://doi.org/10.1103/PhysRevD.84.104027). arXiv: [1107.2904](https://arxiv.org/abs/1107.2904) [gr-qc].
- [49] Y. Pan, A. Buonanno, A. Taracchini, et al. “Inspirals-merger-ringdown waveforms of spinning, precessing black-hole binaries in the effective-one-body formalism.” In: *Phys. Rev. D* 89.8 (2014), p. 084006. DOI: [10.1103/PhysRevD.89.084006](https://doi.org/10.1103/PhysRevD.89.084006). arXiv: [1307.6232](https://arxiv.org/abs/1307.6232) [gr-qc].
- [50] A. Taracchini et al. “Effective-one-body model for black-hole binaries with generic mass ratios and spins.” In: *Phys. Rev. D* 89.6 (2014), p. 061502. DOI: [10.1103/PhysRevD.89.061502](https://doi.org/10.1103/PhysRevD.89.061502). arXiv: [1311.2544](https://arxiv.org/abs/1311.2544) [gr-qc].
- [51] A. Nagar et al. “Time-domain effective-one-body gravitational waveforms for coalescing compact binaries with nonprecessing spins, tides and self-spin effects.” In: *Phys. Rev. D* 98.10 (2018), p. 104052. DOI: [10.1103/PhysRevD.98.104052](https://doi.org/10.1103/PhysRevD.98.104052). arXiv: [1806.01772](https://arxiv.org/abs/1806.01772) [gr-qc].

- [52] A. Buonanno, Y. Pan, J. G. Baker, et al. “Toward faithful templates for non-spinning binary black holes using the effective-one-body approach.” In: *Phys. Rev. D* 76 (2007), p. 104049. DOI: [10.1103/PhysRevD.76.104049](https://doi.org/10.1103/PhysRevD.76.104049). arXiv: [0706.3732](https://arxiv.org/abs/0706.3732) [gr-qc].
- [53] A. Buonanno, Y. Pan, H. P. Pfeiffer, et al. “Effective-one-body waveforms calibrated to numerical relativity simulations: Coalescence of non-spinning, equal-mass black holes.” In: *Phys. Rev. D* 79 (2009), p. 124028. DOI: [10.1103/PhysRevD.79.124028](https://doi.org/10.1103/PhysRevD.79.124028). arXiv: [0902.0790](https://arxiv.org/abs/0902.0790) [gr-qc].
- [54] S. Babak, A. Taracchini, and A. Buonanno. “Validating the effective-one-body model of spinning, precessing binary black holes against numerical relativity.” In: *Phys. Rev. D* 95.2 (2017), p. 024010. DOI: [10.1103/PhysRevD.95.024010](https://doi.org/10.1103/PhysRevD.95.024010). arXiv: [1607.05661](https://arxiv.org/abs/1607.05661) [gr-qc].
- [55] T. Damour and A. Nagar. “Effective One Body description of tidal effects in inspiralling compact binaries.” In: *Phys. Rev. D* 81 (2010), p. 084016. DOI: [10.1103/PhysRevD.81.084016](https://doi.org/10.1103/PhysRevD.81.084016). arXiv: [0911.5041](https://arxiv.org/abs/0911.5041) [gr-qc].
- [56] L. Baiotti, T. Damour, B. Giacomazzo, et al. “Accurate numerical simulations of inspiralling binary neutron stars and their comparison with effective-one-body analytical models.” In: *Phys. Rev. D* 84 (2011), p. 024017. DOI: [10.1103/PhysRevD.84.024017](https://doi.org/10.1103/PhysRevD.84.024017). arXiv: [1103.3874](https://arxiv.org/abs/1103.3874) [gr-qc].
- [57] J. Steinhoff, T. Hinderer, A. Buonanno, et al. “Dynamical Tides in General Relativity: Effective Action and Effective-One-Body Hamiltonian.” In: *Phys. Rev. D* 94.10 (2016), p. 104028. DOI: [10.1103/PhysRevD.94.104028](https://doi.org/10.1103/PhysRevD.94.104028). arXiv: [1608.01907](https://arxiv.org/abs/1608.01907) [gr-qc].
- [58] T. Hinderer et al. “Effects of neutron-star dynamic tides on gravitational waveforms within the effective-one-body approach.” In: *Phys. Rev. Lett.* 116.18 (2016), p. 181101. DOI: [10.1103/PhysRevLett.116.181101](https://doi.org/10.1103/PhysRevLett.116.181101). arXiv: [1602.00599](https://arxiv.org/abs/1602.00599) [gr-qc].
- [59] Z. Cao and W.-B. Han. “Waveform model for an eccentric binary black hole based on the effective-one-body-numerical-relativity formalism.” In: *Phys. Rev. D* 96.4 (2017), p. 044028. DOI: [10.1103/PhysRevD.96.044028](https://doi.org/10.1103/PhysRevD.96.044028). arXiv: [1708.00166](https://arxiv.org/abs/1708.00166) [gr-qc].
- [60] A. Ramos-Buades, A. Buonanno, M. Khalil, et al. “Effective-one-body multipolar waveforms for eccentric binary black holes with nonprecessing spins.” In: *Phys. Rev. D* 105.4 (2022), p. 044035. DOI: [10.1103/PhysRevD.105.044035](https://doi.org/10.1103/PhysRevD.105.044035). arXiv: [2112.06952](https://arxiv.org/abs/2112.06952) [gr-qc].
- [61] L. Pompili et al. “Laying the foundation of the effective-one-body waveform models SEOBNRv5: Improved accuracy and efficiency for spinning non-precessing binary black holes.” In: *Phys. Rev. D* 108.12 (2023), p. 124035. DOI: [10.1103/PhysRevD.108.124035](https://doi.org/10.1103/PhysRevD.108.124035). arXiv: [2303.18039](https://arxiv.org/abs/2303.18039) [gr-qc].

- [62] M. Khalil, A. Buonanno, H. Estelles, et al. “Theoretical groundwork supporting the precessing-spin two-body dynamics of the effective-one-body waveform models SEOBNRv5.” In: *Phys. Rev. D* 108.12 (2023), p. 124036. DOI: [10.1103/PhysRevD.108.124036](https://doi.org/10.1103/PhysRevD.108.124036). arXiv: [2303.18143](https://arxiv.org/abs/2303.18143) [gr-qc].
- [63] A. Ramos-Buades, A. Buonanno, H. Estellés, et al. “Next generation of accurate and efficient multipolar precessing-spin effective-one-body waveforms for binary black holes.” In: *Phys. Rev. D* 108.12 (2023), p. 124037. DOI: [10.1103/PhysRevD.108.124037](https://doi.org/10.1103/PhysRevD.108.124037). arXiv: [2303.18046](https://arxiv.org/abs/2303.18046) [gr-qc].
- [64] M. Haberland, A. Buonanno, and J. Steinhoff. “Modeling matter(s) in SEOBNRv5THM: Generating fast and accurate effective-one-body waveforms for spin-aligned binary neutron stars.” Mar. 2025. arXiv: [2503.18934](https://arxiv.org/abs/2503.18934) [gr-qc].
- [65] A. Pai and K. G. Arun. “Singular value decomposition in parametrised tests of post-Newtonian theory.” In: *Class. Quant. Grav.* 30 (2013), p. 025011. DOI: [10.1088/0264-9381/30/2/025011](https://doi.org/10.1088/0264-9381/30/2/025011). arXiv: [1207.1943](https://arxiv.org/abs/1207.1943) [gr-qc].
- [66] M. Saleem, S. Datta, K. G. Arun, et al. “Parametrized tests of post-Newtonian theory using principal component analysis.” In: *Phys. Rev. D* 105.8 (2022), p. 084062. DOI: [10.1103/PhysRevD.105.084062](https://doi.org/10.1103/PhysRevD.105.084062). arXiv: [2110.10147](https://arxiv.org/abs/2110.10147) [gr-qc].
- [67] S. Datta, M. Saleem, K. G. Arun, et al. “Multiparameter tests of general relativity using a principle component analysis with next-generation gravitational-wave detectors.” In: *Phys. Rev. D* 109.4 (2024), p. 044036. DOI: [10.1103/PhysRevD.109.044036](https://doi.org/10.1103/PhysRevD.109.044036). arXiv: [2208.07757](https://arxiv.org/abs/2208.07757) [gr-qc].
- [68] J. M. Dickey. “The Weighted Likelihood Ratio, Linear Hypotheses on Normal Location Parameters.” In: *The Annals of Mathematical Statistics* 42.1 (1971), pp. 204–223. DOI: [10.1214/aoms/1177693507](https://doi.org/10.1214/aoms/1177693507). URL: <https://doi.org/10.1214/aoms/1177693507>.
- [69] M. Isi, W. M. Farr, and K. Chatziioannou. “Comparing Bayes factors and hierarchical inference for testing general relativity with gravitational waves.” In: *Phys. Rev. D* 106.2 (2022), p. 024048. DOI: [10.1103/PhysRevD.106.024048](https://doi.org/10.1103/PhysRevD.106.024048). arXiv: [2204.10742](https://arxiv.org/abs/2204.10742) [gr-qc].
- [70] E. Payne, M. Isi, K. Chatziioannou, et al. “Fortifying gravitational-wave tests of general relativity against astrophysical assumptions.” In: *Phys. Rev. D* 108.12 (2023), p. 124060. DOI: [10.1103/PhysRevD.108.124060](https://doi.org/10.1103/PhysRevD.108.124060). arXiv: [2309.04528](https://arxiv.org/abs/2309.04528) [gr-qc].
- [71] E. Payne, M. Isi, K. Chatziioannou, et al. “The curvature dependence of gravitational-wave tests of General Relativity.” July 2024. arXiv: [2407.07043](https://arxiv.org/abs/2407.07043) [gr-qc].

- [72] H. Zhong, M. Isi, K. Chatziioannou, et al. “Multidimensional hierarchical tests of general relativity with gravitational waves.” In: *Phys. Rev. D* 110.4 (2024), p. 044053. DOI: [10.1103/PhysRevD.110.044053](https://doi.org/10.1103/PhysRevD.110.044053). arXiv: [2405.19556](https://arxiv.org/abs/2405.19556) [gr-qc].
- [73] T. Regge and J. A. Wheeler. “Stability of a Schwarzschild singularity.” In: *Phys. Rev.* 108 (1957), pp. 1063–1069. DOI: [10.1103/PhysRev.108.1063](https://doi.org/10.1103/PhysRev.108.1063).
- [74] D. Li, P. Wagle, Y. Chen, et al. “Perturbations of Spinning Black Holes beyond General Relativity: Modified Teukolsky Equation.” In: *Phys. Rev. X* 13.2 (2023), p. 021029. DOI: [10.1103/PhysRevX.13.021029](https://doi.org/10.1103/PhysRevX.13.021029). arXiv: [2206.10652](https://arxiv.org/abs/2206.10652) [gr-qc].
- [75] A. Hussain and A. Zimmerman. “Approach to computing spectral shifts for black holes beyond Kerr.” In: *Phys. Rev. D* 106.10 (2022), p. 104018. DOI: [10.1103/PhysRevD.106.104018](https://doi.org/10.1103/PhysRevD.106.104018). arXiv: [2206.10653](https://arxiv.org/abs/2206.10653) [gr-qc].
- [76] P. A. Cano, K. Fransen, T. Hertog, et al. “Universal Teukolsky equations and black hole perturbations in higher-derivative gravity.” In: *Phys. Rev. D* 108.2 (2023), p. 024040. DOI: [10.1103/PhysRevD.108.024040](https://doi.org/10.1103/PhysRevD.108.024040). arXiv: [2304.02663](https://arxiv.org/abs/2304.02663) [gr-qc].
- [77] T. Damour and A. Nagar. “Final spin of a coalescing black-hole binary: An Effective-one-body approach.” In: *Phys. Rev. D* 76 (2007), p. 044003. DOI: [10.1103/PhysRevD.76.044003](https://doi.org/10.1103/PhysRevD.76.044003). arXiv: [0704.3550](https://arxiv.org/abs/0704.3550) [gr-qc].
- [78] T. Damour and A. Nagar. “An Improved analytical description of inspiralling and coalescing black-hole binaries.” In: *Phys. Rev. D* 79 (2009), p. 081503. DOI: [10.1103/PhysRevD.79.081503](https://doi.org/10.1103/PhysRevD.79.081503). arXiv: [0902.0136](https://arxiv.org/abs/0902.0136) [gr-qc].
- [79] L. S. Finn. “Detection, measurement and gravitational radiation.” In: *Phys. Rev. D* 46 (1992), pp. 5236–5249. DOI: [10.1103/PhysRevD.46.5236](https://doi.org/10.1103/PhysRevD.46.5236). arXiv: [gr-qc/9209010](https://arxiv.org/abs/gr-qc/9209010).
- [80] C. Cutler and M. Vallisneri. “LISA detections of massive black hole inspirals: Parameter extraction errors due to inaccurate template waveforms.” In: *Phys. Rev. D* 76 (2007), p. 104018. DOI: [10.1103/PhysRevD.76.104018](https://doi.org/10.1103/PhysRevD.76.104018). arXiv: [0707.2982](https://arxiv.org/abs/0707.2982) [gr-qc].
- [81] Q. Hu and J. Veitch. “Accumulating Errors in Tests of General Relativity with Gravitational Waves: Overlapping Signals and Inaccurate Waveforms.” In: *Astrophys. J.* 945.2 (2023), p. 103. DOI: [10.3847/1538-4357/acbc18](https://doi.org/10.3847/1538-4357/acbc18). arXiv: [2210.04769](https://arxiv.org/abs/2210.04769) [gr-qc].
- [82] B. Seymour, J. Golomb, and Y. Chen. “Inspirational Tests of General Relativity and Waveform Geometry.” in progress. 2025.

- [83] R. Magee, M. Isi, E. Payne, et al. “Impact of selection biases on tests of general relativity with gravitational-wave inspirals.” In: *Phys. Rev. D* 109.2 (2024), p. 023014. DOI: [10.1103/PhysRevD.109.023014](https://doi.org/10.1103/PhysRevD.109.023014). arXiv: [2311.03656](https://arxiv.org/abs/2311.03656) [gr-qc].
- [84] E. Thrane and C. Talbot. “An introduction to Bayesian inference in gravitational-wave astronomy: parameter estimation, model selection, and hierarchical models.” In: *Publ. Astron. Soc. Austral.* 36 (2019). [Erratum: *Publ. Astron. Soc. Austral.* 37, e036 (2020)], e010. DOI: [10.1017/pasa.2019.2](https://doi.org/10.1017/pasa.2019.2). arXiv: [1809.02293](https://arxiv.org/abs/1809.02293) [astro-ph.IM].
- [85] M. Fishbach, D. E. Holz, and W. M. Farr. “Does the Black Hole Merger Rate Evolve with Redshift?.” In: *Astrophys. J. Lett.* 863.2 (2018), p. L41. DOI: [10.3847/2041-8213/aad800](https://doi.org/10.3847/2041-8213/aad800). arXiv: [1805.10270](https://arxiv.org/abs/1805.10270) [astro-ph.HE].
- [86] C. Talbot and E. Thrane. “Measuring the binary black hole mass spectrum with an astrophysically motivated parameterization.” In: *Astrophys. J.* 856.2 (2018), p. 173. DOI: [10.3847/1538-4357/aab34c](https://doi.org/10.3847/1538-4357/aab34c). arXiv: [1801.02699](https://arxiv.org/abs/1801.02699) [astro-ph.HE].
- [87] R. Abbott et al. “Population of Merging Compact Binaries Inferred Using Gravitational Waves through GWTC-3.” In: *Phys. Rev. X* 13.1 (2023), p. 011048. DOI: [10.1103/PhysRevX.13.011048](https://doi.org/10.1103/PhysRevX.13.011048). arXiv: [2111.03634](https://arxiv.org/abs/2111.03634) [astro-ph.HE].
- [88] S. L. Liebling, M. Kavic, and M. Lippert. “Probing Near-Horizon Fluctuations with Black Hole Binary Mergers.” In: *JHEP* 03 (2018), p. 176. DOI: [10.1007/JHEP03\(2018\)176](https://doi.org/10.1007/JHEP03(2018)176). arXiv: [1707.02299](https://arxiv.org/abs/1707.02299) [gr-qc].
- [89] L. Sampson, N. Cornish, and N. Yunes. “Gravitational Wave Tests of Strong Field General Relativity with Binary Inspirals: Realistic Injections and Optimal Model Selection.” In: *Phys. Rev. D* 87.10 (2013), p. 102001. DOI: [10.1103/PhysRevD.87.102001](https://doi.org/10.1103/PhysRevD.87.102001). arXiv: [1303.1185](https://arxiv.org/abs/1303.1185) [gr-qc].
- [90] J. Meidam et al. “Parametrized tests of the strong-field dynamics of general relativity using gravitational wave signals from coalescing binary black holes: Fast likelihood calculations and sensitivity of the method.” In: *Phys. Rev. D* 97.4 (2018), p. 044033. DOI: [10.1103/PhysRevD.97.044033](https://doi.org/10.1103/PhysRevD.97.044033). arXiv: [1712.08772](https://arxiv.org/abs/1712.08772) [gr-qc].
- [91] T. Damour, B. R. Iyer, and A. Nagar. “Improved resummation of post-Newtonian multipolar waveforms from circularized compact binaries.” In: *Phys. Rev. D* 79 (2009), p. 064004. DOI: [10.1103/PhysRevD.79.064004](https://doi.org/10.1103/PhysRevD.79.064004). arXiv: [0811.2069](https://arxiv.org/abs/0811.2069) [gr-qc].
- [92] S. Husa, S. Khan, M. Hannam, et al. “Frequency-domain gravitational waves from nonprecessing black-hole binaries. I. New numerical waveforms and anatomy of the signal.” In: *Phys. Rev. D* 93.4 (2016), p. 044006. DOI: [10.1103/PhysRevD.93.044006](https://doi.org/10.1103/PhysRevD.93.044006). arXiv: [1508.07250](https://arxiv.org/abs/1508.07250) [gr-qc].

- [93] S. Khan, S. Husa, M. Hannam, et al. “Frequency-domain gravitational waves from nonprecessing black-hole binaries. II. A phenomenological model for the advanced detector era.” In: *Phys. Rev. D* 93.4 (2016), p. 044007. doi: [10.1103/PhysRevD.93.044007](https://doi.org/10.1103/PhysRevD.93.044007). arXiv: [1508.07253](https://arxiv.org/abs/1508.07253) [gr-qc].

INSPIRAL TESTS OF GENERAL RELATIVITY AND WAVEFORM GEOMETRY

- [1] B. C. Seymour, J. Golomb, and Y. Chen. “Inspirational tests of general relativity and waveform geometry.” In preparation for submission.

7.1 Introduction

The detections of gravitational waves (GW) from compact binary coalescences [1, 2, 3, 4, 5] has provided new ways to directly test the behavior of strong gravity in general relativity (GR). Despite many searches in LVK data, no evidence for deviations have been found [6, 7, 8, 9, 10, 11, 12, 13]. The network currently consists of two LIGO interferometers [14], Virgo [15], KAGRA [16], and eventually LIGO India [17, 18]. To maximize the scientific reach of these current detectors, there are proposals for A# [19] and LIGO Voyager [20, 21]. Third-generation ground-based facilities—Cosmic Explorer [22, 23] and the Einstein Telescope [24, 25, 26]—are in the planning stages which are expected to improve the sensitivity compared to LIGO A+ by an order of magnitude. There are a number of space-based detectors planned of which LISA is expected to launch in 2035 [27, 28]. There are other concepts including TianQin [29], Taiji [30, 31], B-DECIGO/DECIGO [32, 33, 34], and TianGO [35, 36].

One of the most prominent techniques for searching for deviations to GR is the parameterized post-Einsteinian (ppE) framework [37, 38, 39]. This formalism searches for deviations to the phase of the waveform that appear at particular orders in velocity of the waveform. This framework was also extended in a number of ways throughout the years, to additional polarizations [40], precessing waveforms [41], higher-order modes [42, 43], approaches for parameterized searches in the plunge-merger phase [44, 45, 46], and a neural post-Einstein framework [47]. It is noted that such an expansion in v/c does not work for all types of perturbations, namely logarithmic or screened terms [48, 39]. It also needs the perturbations to the binding energy and GW fluxes to be able to be expressed as a factor of $(M/r)^\alpha$ which we have found is not possible for, e.g., nonviolent nonlocality that has an essential singularity [49].

These tests of GR are intimately connected to how well these beyond GR deviations are observable in data. Building upon approaches to understand how waveforms are biased due to unmodeled signals [50, 51], Vallisneri found that the GR parameters aim to mask the beyond GR signal deviation [52, 53] which is called *stealth bias* [53, 54]. Results have shown that it is only the perpendicular portion of the waveform that contributes to evidence in the Bayes factor supporting beyond GR deviation. This also brings up the possibility of a false positive test which disfavored GR due to waveform systematics. There is a number of works that examine the systematic effects of mismodeling the GR parameters and how this can bias the tests of GR [55, 56, 57, 58, 59].

In addition to this statistical hypothesis testing, eventually the community wants to find ways to better test GR than measuring a single parameter. If multiple ppE parameters are attempted to be measured for a particular waveform, the covariance between each of them mean that constraints are markedly reduced. The singular value decomposition (SVD) approach to searching for PN deviations in GR was originally devised by Pai and Arun [60, 61] which is an approach similar in spirit to surrogate modeling [62, 63]. This approach used features of PN deviations from GR to identify the features that are most common and most precisely measured [60, 61]. Additionally, if one attempts to measure multiple ppE parameters in data, a principal component analysis (PCA) can be performed to identify which directions that the covariance matrix is best measured [64, 65, 66, 67]. While the SVD and PCA differ due in origin from modeling with least parameters versus the statistical relationship of measuring multiple parameters, they are related to one another.

In this paper, we will build upon the existing literature and relate the tests of GR to the geometry of the signal manifold from the noise weighted inner product. We will begin by identifying how GR parameters are biased if a beyond GR signal [52] is introduced and show how the ppE formalism can capture generic deviations remarkably well due to the behavior of the geometrical picture. We will show how multiparameter tests of GR are difficult because the ppE deviations to GR have similar features when orthogonalized away from GR. Finally, we will build upon the work of Pai [60, 61] and introduce a new form of the SVD that identifies the common features of the ppE tests. Throughout, we will use geometric units where $c = G = 1$.

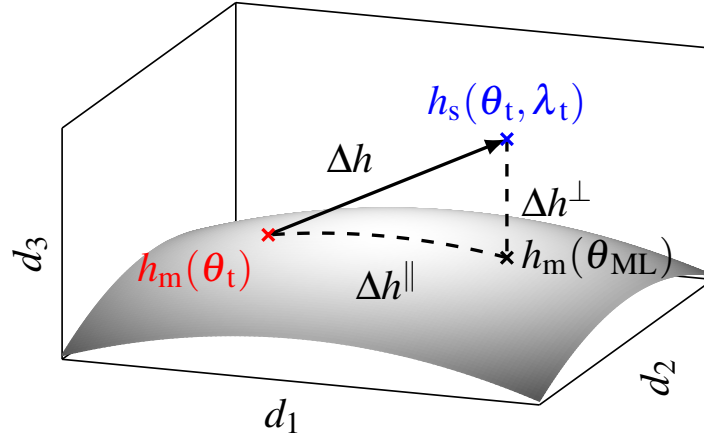


Figure 7.1: Illustration of degeneracy when testing GR. We show the injected signal (blue) which depends on the true GR parameters θ_t and the beyond GR parameters λ_t . The model signal at the true GR parameters θ_t (red) is shown and the best fit signal is at the maximum likelihood point θ_{ML} (black). The GR waveform is modified by Δh which causes biases to the GR waveform, thus residual signal to measure beyond GR deviations is given by the perpendicular signal Δh^\perp . Note that this is a high dimensional manifold where (d_1, d_2, d_3) are the values of the signal at particular frequency bins.

7.2 Background and Methods

This analysis is motivated by work done on calibration [50, 51] on calibration errors in a waveform. In Fig. 7.1, we show a visualization of how the true GR parameters θ_t are biased due a beyond GR signal $h_s(\theta_t, \lambda_t)$ (blue) where λ_t are the beyond GR parameters. The possible values of the model waveform $h_m(\theta_t)$ are shown in the grey manifold while the best fitting parameter is θ_{ML} . In this section, we will derive how the GR parameter are biased replicating [50, 51] and show how the Bayes factor depends strongly on the residual deviation from GR Δh^\perp as found in [52, 53].

Review of Biased Parameter Estimation

Suppose we have a true waveform that is $s_t \equiv h(\theta_t, \lambda_t)$ and we are attempting to recover it with a model $h_m(\theta)$. The likelihood in GR is just the true waveform plus gaussian noise

$$d = s_t + n, \quad (7.1)$$

while our template is $h_m(\theta)$. For stationary and Gaussian noise the likelihood for a waveform is equal to

$$\log L(\theta) \propto -\frac{1}{2} (d - h_m(\theta) | d - h_m(\theta)), \quad (7.2)$$

where the noise weighted inner product is defined as

$$(a, b) \equiv 4 \operatorname{Re} \int_0^\infty \frac{a^*(f)b(f)}{S_n(f)} df, \quad (7.3)$$

where $S_n(f)$ is the power spectral density (PSD) of the detector.

We wish to find the Fisher information about the point to characterize detectability. The maximum likelihood estimator is found where the derivative of the likelihood is zero

$$\partial_i \log L|_{\theta_{\text{ML}}} = (\partial_i h_m(\theta), d - h_m(\theta))|_{\theta_{\text{ML}}} = 0. \quad (7.4)$$

In general, this is a nonlinear equation to solve for θ_{ML} , but we make the standard assumption that it sharply peaked in θ so that $\theta_{\text{ML}} - \theta_t \ll 1$. Let us define Δh as

$$\Delta h = h(\theta_t, \lambda_t) - h_m(\theta_t). \quad (7.5)$$

We also assume that Δh is small. Therefore, we can use $d - h_m(\theta) = n + \Delta h + \Delta \theta^i \partial_i h_m$. The maximum likelihood estimate is thus equal to

$$\theta_{\text{ML}}^i = \theta_t^i + \Delta \theta_{\text{bias}}^i + \Delta \theta_{\text{stat}}^i, \quad (7.6)$$

where the bias and statistical errors are equal to

$$\Delta \theta_{\text{stat}}^i = \Sigma^{ij} (\partial_j h_m | n), \quad (7.7)$$

$$\Delta \theta_{\text{bias}}^i = \Sigma^{ij} (\partial_j h_m | \Delta h), \quad (7.8)$$

where Σ^{ij} is the matrix inverse of the Fisher matrix $\Gamma_{ij} \equiv (\partial_i h_m | \partial_j h_m)$. One can show that the expectation value of the $\Delta \theta_{\text{stat}}^i$ random variable is equal to the inverse of the Fisher matrix $E \left[\Delta \theta_{\text{stat}}^i \Delta \theta_{\text{stat}}^j \right] \equiv \Sigma^{ij} = (\Gamma^{-1})^{ij}$ [68]. We emphasize that the $\Delta \theta_{\text{bias}}$ comes from the mismodeling of the waveform and is independent of SNR.

Suppose that we are not in the nested case as described above, where our modeled waveform actually depends on some other parameters which are not in the signal. In this case, we model it as $h_m(\theta, \mu)$ where μ are some small parameters which we want to measure in the waveform. In this case, we can perform the same analysis as above. If we define $\Theta^I = (\theta, \mu)$ as the full parameter set, the maximum likelihood estimate is

$$\Theta_{\text{ML}}^I = \Theta_t^I + \Delta \Theta_{\text{stat}}^I + \Delta \Theta_{\text{bias}}^I, \quad (7.9)$$

where $\Theta_t^I = (\theta_t, \mathbf{0})$ so we are assuming the true value of $\mu_t \sim 0$. The statistical error is the same $\Delta \Theta^I = \Sigma^{IJ} (\partial_J h_m | n)$ while the bias is

$$\Delta \Theta_{\text{bias}}^I = \Sigma^{IJ} (\partial_J h_m | \Delta h). \quad (7.10)$$

We emphasize that at high SNR, our small model parameters will scale like

$$\boldsymbol{\mu}_{\text{ML}} = \Delta\boldsymbol{\mu}_{\text{bias}}(\boldsymbol{\theta}_t, \boldsymbol{\lambda}_t) + \Delta\boldsymbol{\mu}_{\text{stat}}, \quad (7.11)$$

where the bias term is linearly proportional to the $\boldsymbol{\lambda}_t$ parameter $\Delta\boldsymbol{\mu}_{\text{bias}} \propto \boldsymbol{\lambda}_t$. This key fact will be used to explain the *unreasonable effectiveness of PN templates for testing GR*. If you imagine that there is a generic phase deviation in the true waveform $\Delta\Psi_t$, this will be accessible if we measure any $\delta\phi_k$ since it is receptive to any modification to the waveform.

Geometric Interpretation of Bias Equation

In the previous section, we reviewed how an injection can bias the parameter estimation in a mismodeled waveform. Now, we will look at Eq. (7.10) and discover how it can be understood more deeply by thinking about the geometry of the waveform. We define the parallel and perpendicular components as

$$\begin{aligned} \Delta h_{\parallel} &= \Delta\Theta_{\text{bias}}^J \partial_J h_m, \\ \Delta h_{\perp} &= \Delta h - \Delta\Theta_{\text{bias}}^J \partial_J h_m. \end{aligned} \quad (7.12)$$

Using these identities, one can see that Eq. (7.10) becomes

$$\Delta\Theta_{\text{bias}}^J = \Sigma^{IJ} (\partial_J h_m | \Delta h_{\parallel}). \quad (7.13)$$

This demonstrates that *only deviations parallel to waveform manifold* bias the parameter estimation.

Let us now investigate the case that we have a waveform with a bias that is due to a small parameter $\boldsymbol{\lambda}$ and our model has a small parameter $\boldsymbol{\mu}$. For simplicity assume that $\boldsymbol{\lambda}$ and $\boldsymbol{\mu}$ are both one dimensional parameters. Then, one can show that the estimate for $\boldsymbol{\mu}$ is

$$\Delta\boldsymbol{\mu}_{\text{bias}} = \frac{\left((\partial_{\boldsymbol{\mu}} h_m)^{\perp\boldsymbol{\theta}} | (\Delta h)^{\perp\boldsymbol{\theta}} \right)}{\| (\partial_{\boldsymbol{\mu}} h_m)^{\perp\boldsymbol{\theta}} \|^2}, \quad (7.14)$$

where the $\perp\boldsymbol{\theta}$ denotes removing the part of the signal which is parallel to the main $\boldsymbol{\theta}$ parameters. Thus, we see evidence for $\boldsymbol{\mu}$ when both the waveform $h_m(\boldsymbol{\theta}, \boldsymbol{\mu})$ and the residual $\Delta h(\boldsymbol{\theta}_t, \boldsymbol{\lambda})$ cannot eliminate the effect by a redefinition of $\boldsymbol{\theta}$.

In Eq. (7.14), we performed this calculation for the simplest case that you are trying to measure a single parameter $\boldsymbol{\mu}$. If $\boldsymbol{\mu} = \mu^a$ is an array of beyond GR parameters, the equation above can be generalized using Schur decomposition which yields

$$\Delta\boldsymbol{\mu}_{\text{bias}}^a = \left(\Gamma_{\text{red}}^{-1} \right)_{ab} \left(\left(\partial_{\mu^b} h_m \right)^{\perp\boldsymbol{\theta}} | (\Delta h)^{\perp\boldsymbol{\theta}} \right), \quad (7.15)$$

where the reduced Fisher matrix is equal to

$$\Gamma_{ab}^{\text{red}} = \left((\partial_{\mu^a} h_m)^{\perp\theta} \mid (\partial_{\mu^b} h_m)^{\perp\theta} \right). \quad (7.16)$$

One can see in the single μ case the equation reduces to Eq. (7.14) since $\Gamma_{\mu\mu}^{\text{red}} = \| (\partial_{\mu} h_m)^{\perp\theta} \|^2$. In the App. 7.6, we perform derivation of Eq. (7.15) using the Schur decomposition identities of a matrix consisting of blocks.

Multidetector Geometry

The manifold language introduced in this chapter straightforwardly generalizes to the case of multiple detectors observing one GW event. The likelihood for parameters is

$$p(d|\boldsymbol{\theta}, \boldsymbol{\mu}) \propto \exp \left[-\frac{1}{2} \sum_A \|d_A - h_m^A(\boldsymbol{\theta}, \boldsymbol{\mu})\|^2 \right]. \quad (7.17)$$

It is useful to introduce the summed network inner product and use square brackets to represent this

$$[a|b] = \sum_A (a_A|b_A)_A, \quad (7.18)$$

then the maximum likelihood point is the solution to

$$\Gamma_{IJ} \Delta\Theta^J = [\partial_I h_m | \Delta h] + [\partial_I h_m | n], \quad (7.19)$$

where the network Fisher information matrix is $\Gamma_{IJ} \equiv [\partial_I h_m | \partial_J h_m]$. The equations for the statistical error and bias straightforwardly generalize from Eq. (7.7) and are equal to

$$\Delta\Theta_{\text{stat}}^I = \left(\Gamma^{-1} \right)^{IJ} [\partial_I h_m | n], \quad (7.20)$$

$$\Delta\Theta_{\text{bias}}^I = \left(\Gamma^{-1} \right)^{IJ} [\partial_I h_m | \Delta h]. \quad (7.21)$$

Henceforth, we will continue to do calculations as if they were a single detector and use the normal inner product (\cdot, \cdot) notation, but the geometric description of testing GR in multiple detectors follows the same paradigm.

Bayes Factors for Tests of GR

We wish to compare whether there is support for beyond GR (bGR) signals in the data. Vallisneri [52, 53] computed how the Bayes factor that gave evidence for the bGR signal and identified the geometric meaning. If we have two hypotheses (a) GR ($\boldsymbol{\theta}$) and (b) bGR ($\boldsymbol{\theta}, \boldsymbol{\lambda}$), the Bayes factor is equal to

$$\mathcal{B}_{\text{GR}}^{\text{bGR}} \equiv \frac{p(d|\text{bGR})}{p(d|\text{GR})}, \quad (7.22)$$

where the evidence of data d in model \mathcal{M} with parameters Θ is

$$p(d|\mathcal{M}) = \int d\Theta p(d|\Theta, \mathcal{M})p(\Theta), \quad (7.23)$$

where $p(\Theta)$ is the prior and $p(d|\Theta, \mathcal{M})$ is the likelihood. Vallisneri computed that the that the Bayes factor is

$$\mathcal{B}_{\text{GR}}^{\text{bGR}} \Big|_{s_{\text{bGR}}} = \frac{(2\pi)^{1/2} \Delta\lambda_{\text{stat}}}{\Delta\lambda_{\text{prior}}} e^{\rho_{\perp}^2/2 + x\rho_{\perp} + x^2/2}, \quad (7.24)$$

where $x \sim \mathcal{N}(0, 1)$ is a uniform random variable, $\Delta\lambda_{\text{stat}}$ is the statistical error on λ , and we assumed a flat prior with width $\Delta\lambda_{\text{prior}}$. The residual SNR is

$$\rho_{\perp} \equiv \|\Delta h_{\perp}\|^{1/2}, \quad (7.25)$$

and Δh_{\perp} is the *true* perpendicular signal to the GR waveform as defined in Eq. (7.5) and Eq. (7.12) due to λ_t . One can see that the residual SNR is what provides evidence for a GR violation. If the true signal is a GR signal, the Bayes factor is just

$$\mathcal{B}_{\text{GR}}^{\text{bGR}} \Big|_{s_{\text{GR}}} = \frac{p(\text{bGR})}{p(\text{GR})} \frac{(2\pi)^{1/2} \Delta\lambda_{\text{stat}}}{\Delta\lambda_{\text{prior}}} e^{x^2/2}, \quad (7.26)$$

which has a randomly distributed exponent $x^2/2$ and an *Occam factor* prefactor $\propto \Delta\lambda_{\text{stat}}/\Delta\lambda_{\text{prior}}$ that will cause the it to favor GR on average.

Suppose we searched for deviations from GR with post-Newtonian (PN) deviations from GR in the formalism of the parameterized post-Einsteinian/TIGER/FTI tests of GR [37, 69, 70, 71, 43] which mismodeled the bGR waveform. We will now generalize the Bayes factor formula in this case. We assume that the injected signal is $s_{\text{bGR}}^t = h(\theta_t, \lambda_t)$. We will compare between two hypotheses (a) GR (θ) and (b) ppE (θ, μ). Careful computation reveals that the Bayes factor is

$$\mathcal{B}_{\text{GR}}^{\text{ppE}} \Big|_{s_{\text{bGR}}} = \frac{(2\pi)^{1/2} \Delta\mu_{\text{stat}}}{\Delta\mu_{\text{prior}}} e^{(\rho_{\perp}^{\text{ppE}})^2/2 + x\rho_{\perp}^{\text{ppE}} + x^2/2}, \quad (7.27)$$

where the captured residual SNR $\rho_{\perp}^{\text{ppE}}$ is defined via

$$\rho_{\perp}^{\text{ppE}} = \mathcal{O}(\Delta h_{\text{ppE}}^{\perp}, \Delta h_{\text{bGR}}^{\perp}) \rho_{\perp}, \quad (7.28)$$

which depends on the overlap of the bGR and ppE waveform deviations. The overlap is equal to

$$\mathcal{O}(\Delta h_{\text{ppE}}^{\perp}, \Delta h_{\text{bGR}}^{\perp}) = \frac{(\Delta h_{\text{ppE}}^{\perp} | \Delta h_{\text{bGR}}^{\perp})}{\|\Delta h_{\text{ppE}}^{\perp}\| \|\Delta h_{\text{bGR}}^{\perp}\|}. \quad (7.29)$$

Note that this overlap is between 0 and 1, and tells you that the residual SNR loss is equal to $1 - \mathcal{O}$ from mismodeling the signal. In App. 7.7, we rederive the optimal Bayes factor in Eq. (7.24) using methods from [52] and generalize it to the parameterized test Bayes factor in Eq. (7.27).

In Fig. 7.2, we illustrate the geometric properties of this Bayes factor derivation. The GR waveform manifold is represented by the black line between the GR + ppE and GR + bGR manifolds (blue and red, respectively).

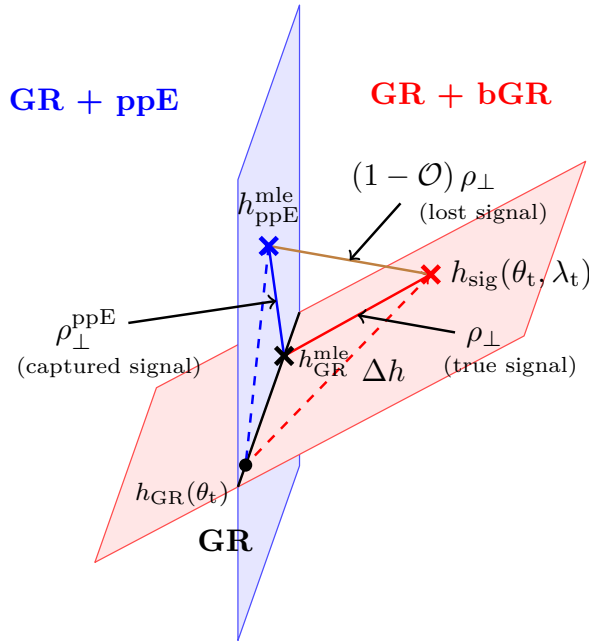


Figure 7.2: In this plot, we visually show how the ppE tests of GR can capture generic bGR deviations. The GR manifold (black) is a line that is at the intersection between the true bGR manifold (red) and the ppE manifold (blue). One can see that the perpendicular part of the signal from GR is $\rho_{\perp} = \|\Delta h_{\perp}\|$ which is the residual SNR after allowing the GR parameters to be biased $h_{\text{GR}}^{\text{ML}} = h_{\text{GR}}(\theta_t + \Delta\theta_{\text{bias}})$. One can see that the best fit ppE parameter is located at the blue mark and has residual SNR $\rho_{\perp}^{\text{ppE}} = \mathcal{O}\rho_{\perp}$ as given in Eq. (7.28). Finally, the brown line is the missed signal from our TGR model. With this picture in mind, we can explore how well tests of GR capture generic deviations.

The fitting factor is a number that characterizes how good of a fit the waveform is, and is related to the residual SNR. The fitting factor is defined as

$$\text{FF}_{\mathcal{M}} = \max_{\Delta\theta^i} \frac{(h_{\mathcal{M}} + \Delta h, h_{\mathcal{M}} + \Delta\theta^i \partial_i h)}{|h_{\mathcal{M}} + \Delta h| \cdot |h_{\mathcal{M}} + \Delta\theta^i \partial_i h|}, \quad (7.30)$$

where \mathcal{M} is the model. If $\mathcal{M} = \text{GR}$ and we want to see how similar a bGR signal is, it is [52]

$$1 - \text{FF}_{\text{GR}} = \frac{1}{2} \frac{\rho_{\perp}^2}{\|h_{\text{GR}}\|^2}. \quad (7.31)$$

For the case of a mismodeled bGR search with $\mathcal{M} = \text{ppE}$, the fitting factor is now

$$1 - \text{FF}_{\text{bGR}} = \frac{1}{2} \frac{(\rho_{\perp} - \rho_{\perp}^{\text{ppE}})^2}{\|h_{\text{GR}}\|^2}, \quad (7.32)$$

so the mismatch of mismodeling a bGR signal is small and depends directly proportionally to the overlap in Eq. (7.29).

7.3 PPE Parameters Capture Generic Phase Deviations

In the previous section, we showed that the perpendicular signal is what dominates the test of GR. So far, we have laid the groundwork where we stressed the relationship between the statistical nature of the problem and how it relates to the intrinsic behavior of the frequency domain waveforms. We will now show what the residual of the ppE tests of GR look like in the frequency domain.

I will use the ppE framework to add PN deviations to the GR waveform phase. I will use the normalizations that the LVK collaboration uses [10]. During the inspiral, the GR phase in the PN range is

$$\Psi_{\text{PN}}(f) = 2\pi f t_c - \varphi_c - \frac{\pi}{4} \quad (7.33)$$

$$+ \frac{3}{128\eta} (\pi \tilde{f})^{-5/3} \sum_{k=0}^7 [\varphi_k + \varphi_{kl} \log(\pi \tilde{f})] (\pi \tilde{f})^{k/3}, \quad (7.34)$$

where t_c, φ_c are the time and phase of coalescence at the geocenter, η is the symmetric mass ratio, and $\tilde{f} = M(1+z)f$ is the dimensionless GW frequency. M is the source frame mass while the detector frame total mass is $(1+z)M$ which accounts for how the detector frame mass changes with redshift z . The GR phasing coefficients are φ_k and φ_{kl} which depend on the GR parameters θ . In this work, I will focus on the non log terms and look for dephasing that occurs as

$$\Delta\Psi_k(f) = \frac{3}{128\eta} \delta\varphi_k \varphi_k (\pi \tilde{f})^{(k-5)/3}, \quad (7.35)$$

where $\delta\varphi_k$ is the k th order fractional deviation to the GR phase. The goal is to see how well this parameterized template can capture the effects of a generic bGR deviation that is parameterized like

$$\Delta\Psi_{\text{bGR}}(f) = \lambda\psi_{\lambda}(f). \quad (7.36)$$

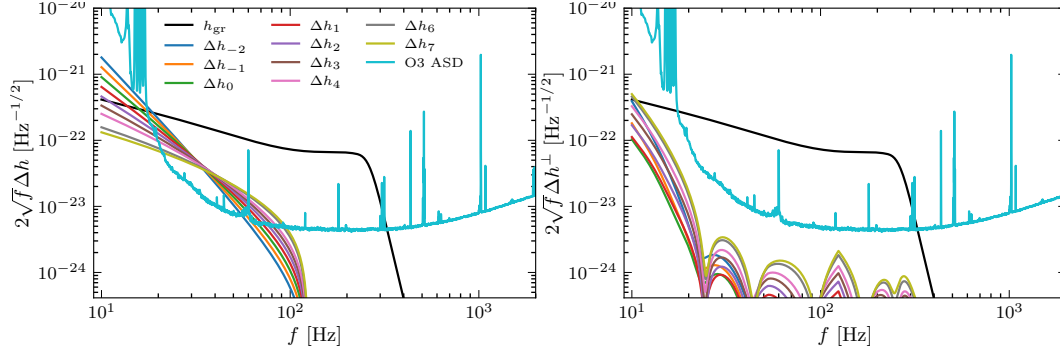


Figure 7.3: Residual amplitude for PN injected deviations from GR for a GW150914 like detection. On the left is the GR waveform (black) and O3 Livingston ASD (cyan). We show the waveform residuals that would be caused by injection what we show in Fig. 7.4 from parameterized tests. On the right, we show what the residual deviation is after the stealth biases in the GR parameters are accounted for. While the original total bias to the SNR is $\|\Delta h\| = 5$, the perpendicular waveforms have much less signal $\|\Delta h_{\perp}\| \sim 0.5$.

Both the parameterized test and true bGR waveform are assumed to be phase deviations in the frequency domain so the waveforms are

$$h(f) = h_{\text{GR}}(f)e^{i\Delta\Psi(f)}, \quad (7.37)$$

so the nominal waveform discrepancy is

$$\Delta h(f) \approx i\Delta\Psi(f)h_{\text{GR}}(f; \theta_{\text{t}}), \quad (7.38)$$

because the phase deviation to the waveform is small.

We can visualize how the parameterized test coefficients affect the waveform by plotting the nominal and residual deviations. On the left side of Fig. 7.3, we plot nominal Δh as shown from Eq. (7.38) using GR parameters given by GW150914. We normalize the value of $\delta\varphi_k$ so that the total original deviation has SNR of $\|\Delta h_k\| = 5$. As we have shown throughout this paper, it is the perpendicular component of the waveform that really influences observation. On the right side of the plot we show the residual component of Δh_{\perp}^k . One can see that the amount of signal is significantly reduced where each one has $\|\Delta h_{\perp}^k\| \sim 0.5$. One significant takeaway is that *there is a similarity between each perpendicular PN test*. This occurs because the GR parameters are biased – notably the masses (M, η) and spins ($\chi_{\text{eff}}, \chi_{\text{p}}$) compensate for this deviation.

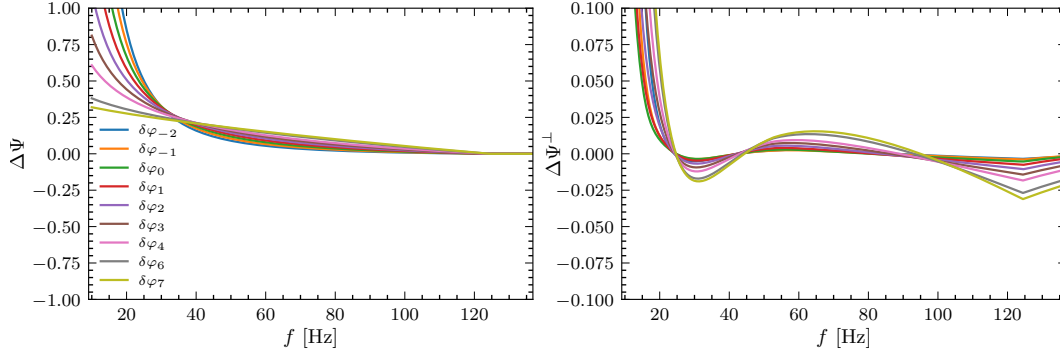


Figure 7.4: Visualization of how the frequency domain representations of the parameterized tests. On the left, we show the dephasing for a GW150914 like detection and scale the parameter normalizations such that $\|\Delta h\| = 5$. On the right, we show the residual (perpendicular) phase deviation in the injection after the GR deviations are marginalized over. One can see that the total dephasing of the perpendicular waveforms is noticeably smaller, and the function has multiple roots that correspond to what the residual deviation looks like after removing the GR uncertainties.

Figure 7.3 is difficult to interpret because we are used to seeing the phase plotted instead of the amplitude. If we instead look for the perpendicular phase, we can see how biased GR parameters change the effective power law behavior of the ppE tests. We can read off the phase in the following fashion

$$\Delta h_{\perp} = i\Delta\Psi_{\perp}(f)h_{\text{GR}}(f), \quad (7.39)$$

where $\Delta\Psi_{\perp}(f)$ is the phase deviation after removing the GR biases. Note that in general, there could be a second term $\mathcal{O}(\Delta A \cdot h_{\text{GR}}(f))$ if we were adding additional amplitude corrections. In practice since our perturbations from GR are purely phase deviations, this has a negligible effect. In Fig. 7.4, we show the nominal phase deviations $\Delta\Psi_k$ (left) and the perpendicular phase deviations $\Delta\Psi_k^{\perp}$ (right). One can see that the power law behavior of the $\Delta\Psi \propto f^{\alpha}$ does not exist in the residuals because GR parameters are biased so it has an alternating pattern on the right.

Overlap between Different PPE Orders

In Sec. 7.2, we studied how good a parameterized template is at capturing the bGR waveform deviation and its relation to the Bayes factor. One can compute the overlap between two different PPE tests as given in Eq. (7.29).

We compute the overlap between different PN tests of GR as a simple way to see how important mismodeling is for constraints on bGR theories. In Fig. 7.5, we

compute the overlap between $\Delta h_{k_{\text{inj}}}^\perp$ injected signal residual and the $\Delta h_{k_{\text{rec}}}^\perp$ which is the perpendicular template. We compute this plot using $\theta = (\theta_{\text{ext}}, \theta_{\text{int}}, \delta\varphi_k)$. θ_{ext} is the extrinsic parameters

$$\theta_{\text{ext}} = (d_L, \text{ra}, \text{dec}, \iota, \psi, t_c, \phi_c) , \quad (7.40)$$

which are the luminosity distance, right ascension, declination, inclination, polarization, time of coalescence, and phase of coalescence, respectively. The intrinsic parameters are

$$\theta_{\text{int}} = (\mathcal{M}_c, \eta, \chi_{\text{eff}}, \chi_p) , \quad (7.41)$$

which are chirp mass, symmetric mass ratio, effective inspiral spin parameter, and effective precession spin parameter, respectively. We used GW150914 event parameters but use Hanford, Livingston, and Virgo network operating at O3 Livingston sensitivity. We compute the residual waveform via Eq. (7.12) for both the injected and recovery models and then plot the overlap in Fig. 7.5. One can see that if $k_{\text{rec}} = k_{\text{inj}}$, the overlap is 1 so there is no bias since we are searching with the same model as we are recovering with. In contrast, if we had a true deviation at $k_{\text{inj}} = -2$ and tried to recover with $k_{\text{rec}} = 7$, we would miss out in about 50% of the residual SNR. Note that the values of this plot strongly depend on the values of θ_{int} . If we had picked a chirp mass which was in the BNS range $\mathcal{M}_c \sim 1.2M_\odot$, this would change significantly. This case is further discussed in the appendix where we show the overlap plots.

We also stress that the result of this overlap computation depends on what GR parameters are measured. If we take our intrinsic parameters to be just the masses

$$\theta_{\text{int}} = (\mathcal{M}_c, \eta) , \quad (7.42)$$

the the result of the overlap plot in Fig. 7.5 would be very different. In Fig. 7.6, we show the result of this computation. You can see that including less GR parameters means that the overlaps between mismodeled PN waveforms are much higher. This means that the amount of distinguishability between different PN models is fractionally more similar. However note that the residual SNR ρ^\perp is higher if you have less GR parameters total so this effect may wash out.

7.4 SVD Approach

As we have seen in the previous sections, the ppE waveform deviations look relatively similar after removing the effects of GR biases. One can see that the right

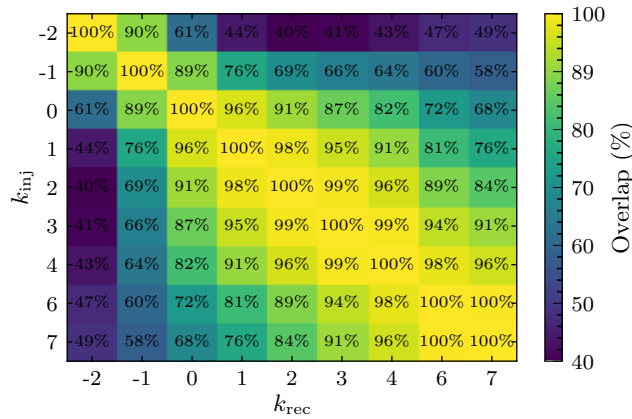


Figure 7.5: The overlap between deviations injected (y-axis) and the recovery model (x-axis). We use GW150914 event parameters with three detectors at O3 Livingston sensitivity, all extrinsic parameters measured and intrinsic parameters ($\mathcal{M}_c, q, \chi_{\text{eff}}, \chi_p$). One can see that injecting a deviation at $k/2$ -th PN order fractionally from GR is perfectly captured on the diagonal but has less overlap as the injection and recovery order grow. This means that if there is a true deviation, the significance drops slowly as you search for the wrong PN order $k_{\text{rec}} \neq k_{\text{inj}}$ because the intrinsic parameters will capture the difference. Note that we do not include $k = 5$ in either of these plots because it is nearly completely degenerate with phase of coalescence.

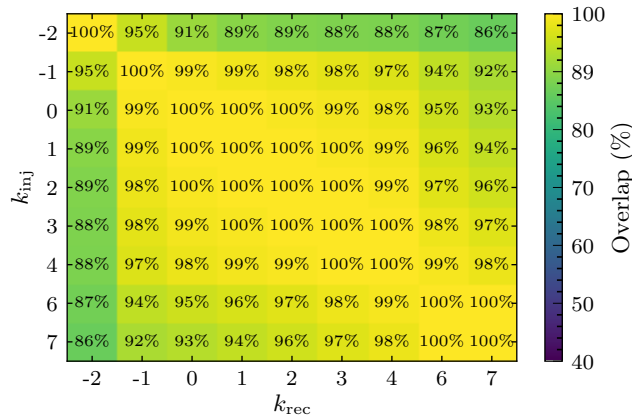


Figure 7.6: The overlap between deviations injected (y-axis) and the recovery model (x-axis). We use GW150914 event parameters with three detectors at O3 Livingston sensitivity, all extrinsic parameters measured and intrinsic parameters (\mathcal{M}_c, q). This can be directly compared to Fig. 7.5 which measures the parameters ($\chi_{\text{eff}}, \chi_p$) additionally. One can see that ignoring the parameter uncertainty of the spin parameters means that the overlap is higher for these waveforms since the spins cannot bias the waveforms.

side of Fig. 7.4 has some properties that look similar across each PN order. The consequence of this is that attempting to measure multiple $\delta\varphi_k$ at once would make the covariance blow up and thus it is difficult to perform multiparameter tests of GR. Due to the allure of measuring multiple PN parameters simultaneously, there has been a large amount of work in this area with the singular value decomposition (SVD) approach [60, 61] and with the similar but distinct principal component analysis approach [72, 65, 64, 66, 67, 49]. In this section, we will propose an improved SVD test of GR that build upon the groundwork of the original Pai results [60].

In this work, we want to find the common features of Δh_k^\perp where each k is a different PN order deviation from GR. The SVD finds the best projector [63] such that

$$C(v_\alpha) = \sum_k \|\Delta h_k^\perp - \mathcal{P}_\alpha \Delta h_k^\perp\|^2, \quad (7.43)$$

where we assume that \mathcal{P}_n is an orthogonal projector onto the SVD basis and $\|\cdot\|$ is a norm. The orthogonal projector is equal to

$$\mathcal{P}_n h_a = \sum_{\alpha=1}^n (v_\alpha | h_a) v_\alpha, \quad (7.44)$$

and v_α are the SVD basis elements. These elements are orthonormal for the inner product

$$(v_\alpha | v_\beta) = \delta_{\alpha\beta}, \quad (7.45)$$

In the appendix, we demonstrate that the SVD described by Pai et al [60] is equivalent to minimizing Eq. (7.43). Thus, *the SVD corresponds to finding an orthogonal basis that best projects all input waveforms.*

Let us lay the groundwork for the SVD by noting properties of the noise weighted inner product. Note that the noise weighted inner product is equal to

$$(a|b) = 4\Re \int_0^\infty df \frac{a^*(f)b(f)}{S(f)} \quad (7.46)$$

If we break it up into finite differences, the noise weighted inner product is

$$(a|b) = \Re \sum_{i=0}^{N_f-1} a^*(f_i)b(f_i)w^2(f_i), \quad (7.47)$$

where the weight is defined via

$$w(f_i) = \frac{2\sqrt{\Delta f_i}}{\sqrt{S(f_i)}}, \quad (7.48)$$

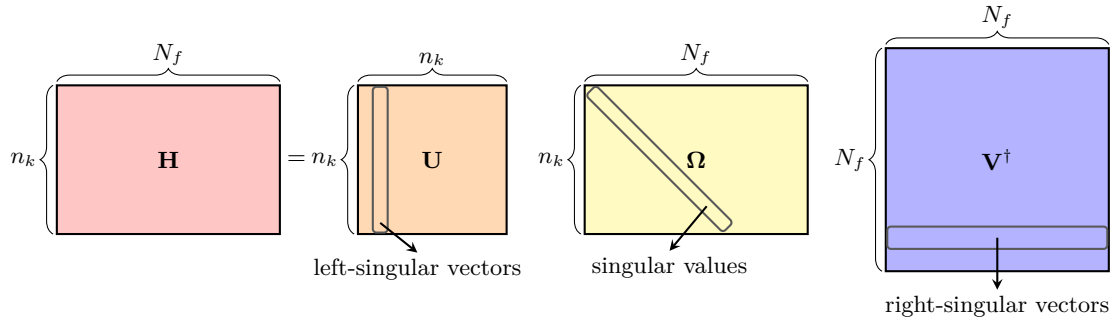


Figure 7.7: We show the visualization of the SVD operation. For our choice of the SVD, we use $H_{ik} = \Delta h_k^\perp(f_i)w(f_i)$ as given in Eq. (7.49). The matrix \mathbf{U} is a square matrix that represents linear redefinitions of $\delta\varphi_k$ while the matrix \mathbf{V} is linear combinations of $\Delta h_k^\perp(f_i)w(f_i)$ which diagonalize \mathbf{H} . Finally, the matrix $\mathbf{\Sigma}$ is ordered by singular value that ranks the importance of each principal mode.

which is the frequency spacing between $\Delta f_i = f_{i+1} - f_i$ and the value of the PSD at frequency bin i . One can see that you could define the matrix \mathbf{H} via

$$H_{ik} = \Delta h_k^\perp(f_i)w(f_i), \quad (7.49)$$

where i indexes frequency and k indexes PN order. Note that since we are working in the perpendicular basis, the covariance matrix is decoupled from the GR parameters. The Fisher matrix is thus equal to

$$\mathbf{\Gamma} = \mathbf{H}\mathbf{H}^\dagger. \quad (7.50)$$

Since we showed that we have a bunch of "snapshots" and we defined the snapshot matrix

$$\mathbf{H} = [\dots, \Delta h_k^\perp(f)w(f), \dots] \in \mathbb{C}^{n_k \times N_f}, \quad (7.51)$$

where n_k is the number of PN waveform deviations and N_f is the number of frequency bins. One can then define the SVD of \mathbf{H} [60, 63]

$$\mathbf{H} = \mathbf{U}\mathbf{\Omega}\mathbf{V}^\dagger \quad (7.52)$$

where \mathbf{U} and \mathbf{V}^\dagger are left and right unitary square matrices of n_k and N_f dimensions, respectively. $\mathbf{\Omega}$ is a diagonal matrix consisting of the singular values of \mathbf{H} in descending order. The SVD can be equivalently represented as

$$\mathbf{H} = \sum_{\alpha}^{n_k} \omega_{\alpha} \mathbf{u}_{\alpha} \mathbf{v}_{\alpha}^*, \quad (7.53)$$

since the rank of the matrix is the number of PN waveform deviations. The \mathbf{u}_α are the left-singular vectors and the \mathbf{v}_α^* are the right-singular vectors. This is shown in Fig. 7.7, which has the \mathbf{H} matrix in red, and the left-singular and right-singular vectors denoted.

We have introduced the SVD to identify the common features in the PN templates. \mathbf{U} is a unitary matrix that converts between the PN template parameters $\delta\varphi_k$ to the SVD basis $\delta\varphi_\alpha$. If one naively does the SVD as given in previous equations Eq. (7.52) we would find that the transformation is now complex $\mathbf{U} \in \mathbb{C}^{n_k \times n_k}$. Instead, we want to write the matrix in the following manner

$$\mathbf{H} = i\tilde{\mathbf{H}}\mathbf{D}, \quad (7.54)$$

where we have made explicit that

$$\tilde{H}_{ik} = \Delta\Psi_k^\perp(f_i)A_{\text{gr}}(f_i), \quad (7.55)$$

and

$$D_{ij} = \delta_{ij}e^{i\Psi_{\text{gr}}(f_i)}. \quad (7.56)$$

Now, if we do a SVD on $\tilde{\mathbf{H}}$, it will be well behaved and have a meaningful way to read off the phase deviation of the SVD modes. If we write

$$\mathbf{H} = i\tilde{\mathbf{U}}\tilde{\mathbf{\Omega}}\tilde{\mathbf{V}}^\dagger\mathbf{D}, \quad (7.57)$$

where the matrices with $\tilde{}$ on them are SVD of $\tilde{\mathbf{H}}$. In this way, the rows of $\tilde{\mathbf{V}}^\dagger$ are

$$\tilde{\mathbf{v}}_\alpha(f_i) = \Delta\Psi_\alpha(f_i)A(f_i)w(f_i), \quad (7.58)$$

which allows unique identification of the dominant parts of the SVD as $\Delta\Psi_\alpha(f_i)$.

We also comment that the SVD can be generalized to multiple detectors by just appending each detector to H_{ik} to the right for each block. This works because the sum of the inner products are

$$\sum_{\det A} (a|b)_A = \sum_{\det A} \sum_{i=0}^{N_f-1} a_A^*(f_i)b_A(f_i)w_A^2(f_i), \quad (7.59)$$

where you could just write this as a sum over $\tilde{i} = 0, \dots, n_{\det}N_f - 1$ where the weights $w_A(f_i)$ depend on the individual detector sensitivity. This also generalizes trivially to detectors of different bandwidths (e.g. LISA + LIGO) where the frequency bins are not the same in each detector.

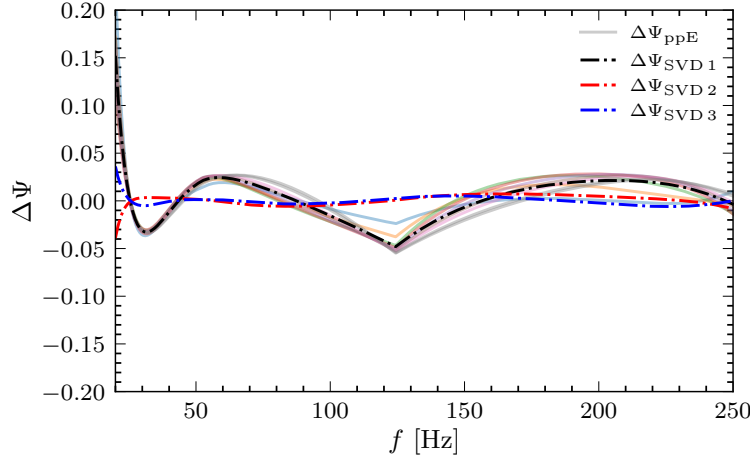


Figure 7.8: Demonstration of the SVD on different PN waveform deviations. In transparent solid, different $\Delta\Psi_k^\perp$ are shown and the dashed lines are the SVD modes for GW150914 like event. Note that we normalize each $\Delta\Psi_k^\perp$ so that $\|\Delta h_k^\perp\| = 1$ so each signal is equally weighted in the SVD. One can see that the dashed black line is the dominant SVD term that best fits each waveform. Additionally the red and blue curves represent subdominant SVD dephasing that are orthogonal to each other. One can see that each of these PN waveform deviations is captured by only a few SVD modes, which explains how degeneracies would form when using the original parameter space.

Let us now show what the SVD looks like for a particular signal. In Fig. 7.8, we took the example of GW150914 again and computed the SVD of Δh_k^\perp between $k = -2, -1, \dots, 4, 6, 7$. We normalized each of the perpendicular strain such that they are equally important ($\|\Delta h_k^\perp\| = 1$). Each of the Δh_k^\perp are plotted in the solid, semi-transparent lines in Fig. 7.8. We plot the dominant SVD lines with dot dashed (black, red, blue). You can see that black SVD tracks each line very well while the blue and red ones are orthogonal to it. This demonstrates that there is a main principal feature of the PN tests that exists in all of them. This figure directly demonstrates why we saw such high overlaps between each of the PN tests in Fig. 7.5.

7.5 Conclusion

In this work, we have shown that there is a relationship between searches for beyond GR morphologies and the geometric description of noise in parameter estimation. We showed that the ppE parameters are able to capture generic beyond GR deviations due to them being biased. We also showed that these parameterized tests should do a good job in real data analysis and there is not too big of a loss by having systematic issues in the beyond GR template. We demonstrated that the techniques

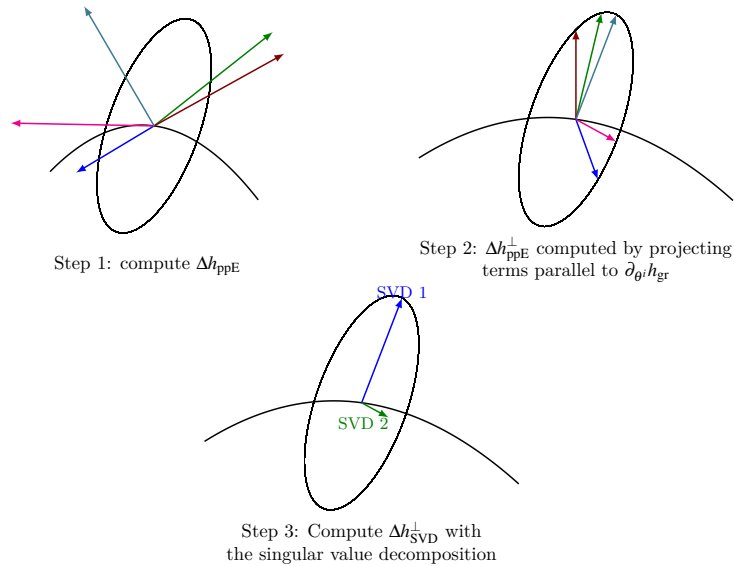


Figure 7.9: Construction of SVD multiparameter tests. We start by orthogonalizing the ppE deviations from GR. One can see that each of these three ppE waveforms had approximately the same but they have different perpendicular length of the GR manifold at the point. Next, we construct the SVD basis by choosing the directions that are best fit by looking at the perpendicular ppE components. One can see that the SVD 1 in the third step is perpendicular to SVD 2.

for multiparameter tests of GR suffer from degeneracies, so this means measuring multiple ones simultaneously is difficult. Finally, we proposed a new template for searching for deviations from GR using the SVD.

In this work, we have put an explanatory picture for why the parameterized tests are surprisingly good at capturing monotonic dephasing behavior from GR. It remains to be seen whether there are some dephasing terms that could not be captured by the ppE tests. Additionally, since detectors suffer from non-Gaussian glitches and also non-stationary behavior, this formalism could be used to help understand analytically when such behavior can mask as GR deviation.

ACKNOWLEDGEMENTS

We thank Michele Vallisneri, Ethan Payne, Max Isi, Bangalore Sathyaprakash, and Katerina Chatziioannou for their insightful discussions. B.S. acknowledges support by the National Science Foundation Graduate Research Fellowship under Grant No. DGE-1745301. Y.C. and B.S. acknowledge support from the Brinson Foundation, the Simons Foundation (Award Number 568762), and by NSF Grants PHY-2011961, PHY-2011968, PHY-1836809. J.G. would like to gratefully acknowledge

the support from the National Science Foundation through the Grant NSF PHY-2207758

7.6 Appendix: Bias Formula for Multiple μ^a Parameters

This can generically be proved in the following way. Assume $\mu = \mu^a$ and $\lambda = \lambda^A$. Then the estimate for μ^a is

$$\Gamma_{IJ} \mu_{\text{bias}}^J = (\partial_I h_m | \Delta h) . \quad (7.60)$$

Let us now write this equation as a matrix equation in block form

$$\begin{pmatrix} \Gamma_{ij} & \Gamma_{ib} \\ \Gamma_{ai} & \Gamma_{ab} \end{pmatrix} \begin{pmatrix} \Delta \theta_{\text{bias}}^i \\ \Delta \mu_{\text{bias}}^b \end{pmatrix} = \begin{pmatrix} (\partial_i h_m | \Delta h) \\ (\partial_a h_m | \Delta h) \end{pmatrix} . \quad (7.61)$$

Using properties of the Schur complement, we can solve for $\Delta \mu_{\text{bias}}^a$ where the degeneracy with θ is removed

$$\left[\Gamma_{ab} - \Gamma_{ai} (\Gamma_{ij})^{-1} \Gamma_{jb} \right] \Delta \mu_{\text{bias}}^a = (\partial_a h_m | \Delta h) - \Gamma_{ai} (\Gamma_{ij})^{-1} (\partial_j h_m | \Delta h) . \quad (7.62)$$

The part which is perpendicular to θ is $(\partial_a h_m)^{\perp \theta} = \partial_a h_m - \Gamma_{aj} (\Gamma_{ij})^{-1} \partial_j h_m$ (this can be proven by a simple calculation). We also note that the reduced Fisher matrix is defined to be

$$\Gamma_{ab}^{\text{red}} = \left[\Gamma_{ab} - \Gamma_{ai} (\Gamma_{ij})^{-1} \Gamma_{jb} \right] = \left((\partial_a h_m)^{\perp \theta} | (\partial_b h_m)^{\perp \theta} \right) . \quad (7.63)$$

Thus the reduced Fisher matrix is the inner product of the derivatives of μ^a which have been made orthogonal to θ . Therefore, the geometric value for the bias to μ is

$$\Delta \mu_{\text{bias}}^a = \Sigma_{\text{red}}^{ab} \left((\partial_b h_m)^{\perp \theta} | (\Delta h)^{\perp \theta} \right) . \quad (7.64)$$

This equation describes how biases can affect our measurement of small parameters. For example, a deviation from GR Δh can cause a measurement with a PN parameter to find deviation. Additionally, it explains how eccentricity and precession can be confused with one another.

7.7 Appendix: Derivation of Bayes Factor

In this appendix, we will compute the Bayes factor in two different cases. The first is if you a bGR theory, and you know it a priori and search with the correct waveform which was originally done in [52]. The second case, we will generalize this equation to the case where are searching for violation with an incorrect model (for example a parameterized test of GR). Generally, the Bayes factor is a ratio of the evidences

$$\mathcal{B}_{\mathcal{M}_1}^{\mathcal{M}_2} \equiv \frac{p(d | \mathcal{M}_2)}{p(d | \mathcal{M}_1)} , \quad (7.65)$$

where d is the data and \mathcal{M}_i are the models. The evidence is equal to the integral over all the parameters

$$p(d|\mathcal{M}) = \int d^n \theta p(\theta|\mathcal{M}) p(d|\theta, \mathcal{M}), \quad (7.66)$$

and n is the number of parameters in the model.

Bayes Factor for a Correctly Modeled Theory

We will first derive the Bayes factor for the case of a beyond-GR (bGR) injection where we have perfectly modeled the bGR morphology. If we inject $s_{\text{bGR}} = h_{\text{bGR}}(\theta_t, \lambda_t)$, in the Fisher matrix limit the likelihood is

$$p(s_{\text{bGR}} | \delta\theta^\mu) = \mathcal{N} e^{-|n|^2/2 + (G^{-1})^{\mu\nu} (n, h_\mu)(n, h_\nu)/2 - G_{\mu\nu} \delta\theta^\mu \delta\theta^\nu / 2}, \quad (7.67)$$

where $G_{\mu\nu} = (h_\mu|h_\nu)$ is the $(m+1)$ dimensional bGR Fisher matrix and greek letters (μ, ν) range over (θ^i, λ) parameters. The value of $\delta\theta^\mu$ is defined as

$$\delta\theta^\mu = (G^{-1})^{\mu\nu} (n|h_\nu). \quad (7.68)$$

If we assume flat priors, the evidence is

$$\begin{aligned} p(s_{\text{bGR}} | \text{bGR}) &= \int p(\theta^\mu | \text{bGR}) p(\delta\theta^\mu | s_{\text{bGR}}), \\ &= \frac{(2\pi)^{(m+1)/2} \sqrt{|G^{-1}|}}{\prod_\mu \Delta\theta_{\text{prior}}^\mu} \times \mathcal{N} e^{-|n|^2/2 + (G^{-1})^{\mu\nu} (n, h_\mu)(n, h_\nu)/2}. \end{aligned} \quad (7.69)$$

Next, we will compute the evidence for GR when we have beyond GR morphology

$$\begin{aligned} P(s_{\text{bGR}} | \text{GR}) &= \frac{(2\pi)^{m/2} \sqrt{|F^{-1}|}}{\prod_i \Delta\theta_{\text{prior}}^i} \\ &\times \mathcal{N} e^{-|n+\Delta h|^2/2 + (F^{-1})^{ij} (n+\Delta h, h_i)(n+\Delta h, h_j)/2}, \end{aligned} \quad (7.70)$$

where F_{ij} is the (m) dimensional GR Fisher matrix and (i, j) range of θ^i . After further simplification, the GR evidence can be compactly written as

$$\begin{aligned} p(s_{\text{bGR}} | \text{GR}) &= \frac{(2\pi)^{m/2} \sqrt{|F^{-1}|}}{\prod_i \Delta\theta_{\text{prior}}^i} \\ &\times \mathcal{N} e^{-|n|^2/2 - |\Delta h_{\perp \text{gr}}|^2/2 - x|\Delta h_{\perp \text{gr}}| + (F^{-1})^{ij} n_i n_j}, \end{aligned} \quad (7.71)$$

where $\Delta h = h_{\text{bGR}}(\boldsymbol{\theta}_t, \lambda_t) - h_{\text{GR}}(\boldsymbol{\theta}_t)$. Therefore the Bayes factor is equal to

$$\mathcal{B}_{\text{GR}}^{\text{bGR}} = \frac{(2\pi)^{1/2} \Delta \lambda_{\text{est}}}{\Delta \lambda_{\text{prior}}^{\text{bGR}}} e^{|\Delta h_{\perp \text{GR}}|^2/2 + x|\Delta h_{\perp \text{GR}}| + x^2/2}, \quad (7.72)$$

where $x = (\Delta h_{\perp}, n) / |\Delta h_{\perp}|$ is a normal random variable and the standard deviation on λ from the observation is equal to

$$\begin{aligned} \Delta \lambda_{\text{est}} &\equiv \sqrt{|F| / |G|}, \\ &= \frac{1}{\|(\partial_{\lambda} h_{\text{bGR}})^{\perp \text{GR}}\|}, \end{aligned} \quad (7.73)$$

where $(\partial_{\lambda} h_{\text{bGR}})^{\perp \text{GR}}$ is the component of the derivative that is perpendicular to GR. This equation matches the results of [52] in Eq. (11). One can see that the prefactor $\Delta \lambda_{\text{est}} / \Delta \lambda_{\text{prior}}^{\text{bGR}}$ outside Eq. (7.72) is an Occam factor that disfavors more complicated models while the evidence for beyond-GR morphology comes from the term $\Delta h_{\perp \text{GR}}$ in the exponential.

Bayes Factor for a Mismodeled Modeled Theory

Let us now turn to the case that we are using a ppE model to search for beyond GR morphology which has mismodeled it. The GR evidence is the same as in Eq. (7.70) while the evidence for ppE is equal to

$$\begin{aligned} p(s_{\text{GR}} | \text{ppE}) &= \frac{(2\pi)^{(m+1)/2} \sqrt{|H^{-1}|}}{\prod_{\alpha} \Delta \theta_{\text{prior}}^{\alpha}} \\ &\times \mathcal{N} e^{-|n|^2/2 - |\Delta h_{\perp \text{ppE}}|^2/2 - x|\Delta h_{\perp \text{ppE}}| + (H^{-1})^{\alpha\beta} n_{\alpha} n_{\beta}}, \end{aligned} \quad (7.74)$$

where $H^{\alpha\beta}$ is the $(m+1)$ dimensional the ppE Fisher matrix and (α, β) range over (θ^i, μ) . I am using notation $\Delta h_{\perp \text{ppE}}$ to mean perpendicular to both GR and $\partial_{\mu} h$. The odds ratio between ppE and GR for a bGR injection is thus

$$\begin{aligned} \mathcal{B}_{\text{GR}}^{\text{ppE}} &= \frac{(2\pi)^{1/2} \Delta \mu_{\text{est}}}{\Delta \mu_{\text{prior}}^{\text{ppE}}} \exp \left[-|\Delta h_{\perp \text{ppE}}|^2/2 - y|\Delta h_{\perp \text{ppE}}| + y^2/2 + |\Delta h_{\perp \text{gr}}|^2/2 + x|\Delta h_{\perp \text{gr}}| \right], \\ &= \frac{(2\pi)^{1/2} \Delta \mu_{\text{est}}}{\Delta \mu_{\text{prior}}^{\text{ppE}}} \exp \left[\frac{1}{2} \left(\rho_{\text{ppE}}^{\perp} \right)^2 - \rho_{\text{ppE}}^{\perp} y + \frac{1}{2} y^2 \right], \end{aligned} \quad (7.75)$$

where (x, y) are random unit variables

$$\begin{aligned} x &\equiv (\Delta h_{\perp \text{gr}}, n) / |\Delta h_{\perp \text{gr}}|, \\ y &\equiv (\Delta h_{\perp \text{ppE}}, n) / |\Delta h_{\perp \text{ppE}}|, \end{aligned}$$

and the *captured residual SNR* is

$$\rho_{\perp}^{\text{ppE}} = \mathcal{O}(\Delta h_{\text{ppE}}^{\perp}, \Delta h_{\text{bGR}}^{\perp}) \rho_{\perp}, \quad (7.76)$$

and the *overlap* between the bGR and ppE waveforms is defined via

$$\mathcal{O}_{\text{ppE}}^{\text{bGR}} \equiv \frac{(\Delta h^{\perp \text{gr}} | \partial_{\mu} h^{\perp \text{gr}})}{\|\Delta h^{\perp \text{gr}}\| \|\partial_{\mu} h^{\perp \text{gr}}\|}. \quad (7.77)$$

In this derivation we used the block matrices to show that the random unit variables are related via

$$x |\Delta h_{\perp \text{gr}}| = y |\Delta h_{\perp \text{ppE}}| + \mathcal{O}(\Delta h_{\text{ppE}}^{\perp}, \Delta h_{\text{bGR}}^{\perp}) (\partial_{\mu} h^{\perp \text{gr}} | n), \quad (7.78)$$

which allowed simplification of the equation above. Finally, note that the covariance on the ppE parameter is equal to

$$\begin{aligned} \Delta \mu_{\text{est}} &= \sqrt{\frac{|F|}{|H|}} \\ &= \frac{1}{\|(\partial_{\mu} h_{\text{ppE}})^{\perp \text{gr}}\|}. \end{aligned} \quad (7.79)$$

7.8 Appendix: Multidetector Geometry

Let us use terminology that is from the polarization part of the LVK GWTC-3 paper. A multidetector signal looks like

$$d^A(f) = F^{A\alpha} h_{\alpha}(f, \boldsymbol{\theta}_t) + n^A(f) \quad (7.80)$$

where A is the detector index and $\alpha = (+, \times)$ is the polarization index. The antenna responses are $F^{A\alpha} = D_A^{ij} \epsilon_{ij}^{\alpha}$ where D_A^{ij} is the A th detector tensor and ϵ_{ij}^{α} is the GW polarization tensor of the α polarization. If we introduce the square brackets to represent the sum over detectors

$$[a|b] = \sum_A (a_A | b_A)_A, \quad (7.81)$$

then the maximum likelihood point is the solution to

$$\Gamma_{IJ} \Delta \Theta^J = [\partial_I h_m | \Delta h] + [\partial_I h_m | n] \quad (7.82)$$

where the network Fisher information matrix is $\Gamma_{IJ} \equiv [\partial_I h_m | \partial_J h_m]$. The equations for the statistical error and bias straightforwardly generalize from Eq. (7.7) and are equal to

$$\Delta \Theta_{\text{stat}}^I = \Sigma^{IJ} [\partial_I h_m | n], \quad (7.83)$$

$$\Delta \Theta_{\text{bias}}^I = \Sigma^{IJ} [\partial_I h_m | \Delta h]. \quad (7.84)$$

Thus, the effect of searching for deviations $\Delta\mu^a$ in a waveform described by true parameters $(\theta_t^i, \lambda_t^A)$ is

$$\Delta\mu_{\text{bias}}^a = \Sigma_{\text{red}}^{ab} [(\partial_b h_m)^{\perp\theta} | (\Delta h)^{\perp\theta}] \quad (7.85)$$

where Σ_{red}^{ab} is the reduced network covariance matrix and the sum is understood.

We stress that the formalism in the section so far is only applicable to a detector A , and we will now generalize this to the complex strain. The complex strain is defined as

$$H(f) = h_+(f) - ih_\times(f), \quad (7.86)$$

where we choose the center of the earth as the location of where the signal is calculated. The complex strain is nice because it does not depend on any of the geometrical quantities associated with the detectors. If we define $\Delta H = H(\theta_t, \lambda_t) - H_m(\theta_t, \mu = 0)$ then the perpendicular component of the strain is

$$\Delta H_{\perp}(f) = \Delta H(f) - \Delta\Theta_{\text{bias}}^I \partial_I H_m. \quad (7.87)$$

If this signal is small, it quantifies how well a parameterized test μ captures any GR deviation λ_t .

References

- [1] B. P. Abbott et al. ‘‘Observation of Gravitational Waves from a Binary Black Hole Merger.’’ In: *Phys. Rev. Lett.* 116.6 (2016), p. 061102. DOI: [10.1103/PhysRevLett.116.061102](https://doi.org/10.1103/PhysRevLett.116.061102). arXiv: [1602.03837](https://arxiv.org/abs/1602.03837) [gr-qc].
- [2] B. P. Abbott et al. ‘‘GW170817: Observation of Gravitational Waves from a Binary Neutron Star Inspiral.’’ In: *Phys. Rev. Lett.* 119.16 (2017), p. 161101. DOI: [10.1103/PhysRevLett.119.161101](https://doi.org/10.1103/PhysRevLett.119.161101). arXiv: [1710.05832](https://arxiv.org/abs/1710.05832) [gr-qc].
- [3] B. P. Abbott et al. ‘‘GWTC-1: A Gravitational-Wave Transient Catalog of Compact Binary Mergers Observed by LIGO and Virgo during the First and Second Observing Runs.’’ In: *Phys. Rev. X* 9.3 (2019), p. 031040. DOI: [10.1103/PhysRevX.9.031040](https://doi.org/10.1103/PhysRevX.9.031040). arXiv: [1811.12907](https://arxiv.org/abs/1811.12907) [astro-ph.HE].
- [4] R. Abbott et al. ‘‘GWTC-2: Compact Binary Coalescences Observed by LIGO and Virgo During the First Half of the Third Observing Run.’’ In: *Phys. Rev. X* 11 (2021), p. 021053. DOI: [10.1103/PhysRevX.11.021053](https://doi.org/10.1103/PhysRevX.11.021053). arXiv: [2010.14527](https://arxiv.org/abs/2010.14527) [gr-qc].
- [5] R. Abbott et al. ‘‘GWTC-3: Compact Binary Coalescences Observed by LIGO and Virgo During the Second Part of the Third Observing Run.’’ In: (Nov. 2021). arXiv: [2111.03606](https://arxiv.org/abs/2111.03606) [gr-qc].

- [6] B. P. Abbott et al. “Tests of general relativity with GW150914.” In: *Phys. Rev. Lett.* 116.22 (2016). [Erratum: *Phys.Rev.Lett.* 121, 129902 (2018)], p. 221101. DOI: [10.1103/PhysRevLett.116.221101](https://doi.org/10.1103/PhysRevLett.116.221101). arXiv: [1602.03841](https://arxiv.org/abs/1602.03841) [gr-qc].
- [7] B. P. Abbott et al. “Tests of General Relativity with GW170817.” In: *Phys. Rev. Lett.* 123.1 (2019), p. 011102. DOI: [10.1103/PhysRevLett.123.011102](https://doi.org/10.1103/PhysRevLett.123.011102). arXiv: [1811.00364](https://arxiv.org/abs/1811.00364) [gr-qc].
- [8] B. P. Abbott et al. “Tests of General Relativity with the Binary Black Hole Signals from the LIGO-Virgo Catalog GWTC-1.” In: *Phys. Rev. D* 100.10 (2019), p. 104036. DOI: [10.1103/PhysRevD.100.104036](https://doi.org/10.1103/PhysRevD.100.104036). arXiv: [1903.04467](https://arxiv.org/abs/1903.04467) [gr-qc].
- [9] R. Abbott et al. “Tests of general relativity with binary black holes from the second LIGO-Virgo gravitational-wave transient catalog.” In: *Phys. Rev. D* 103.12 (2021), p. 122002. DOI: [10.1103/PhysRevD.103.122002](https://doi.org/10.1103/PhysRevD.103.122002). arXiv: [2010.14529](https://arxiv.org/abs/2010.14529) [gr-qc].
- [10] R. Abbott et al. “Tests of General Relativity with GWTC-3.” Dec. 2021. arXiv: [2112.06861](https://arxiv.org/abs/2112.06861) [gr-qc].
- [11] N. Yunes, K. Yagi, and F. Pretorius. “Theoretical Physics Implications of the Binary Black-Hole Mergers GW150914 and GW151226.” In: *Phys. Rev. D* 94.8 (2016), p. 084002. DOI: [10.1103/PhysRevD.94.084002](https://doi.org/10.1103/PhysRevD.94.084002). arXiv: [1603.08955](https://arxiv.org/abs/1603.08955) [gr-qc].
- [12] R. Nair, S. Perkins, H. O. Silva, et al. “Fundamental Physics Implications for Higher-Curvature Theories from Binary Black Hole Signals in the LIGO-Virgo Catalog GWTC-1.” In: *Phys. Rev. Lett.* 123.19 (2019), p. 191101. DOI: [10.1103/PhysRevLett.123.191101](https://doi.org/10.1103/PhysRevLett.123.191101). arXiv: [1905.00870](https://arxiv.org/abs/1905.00870) [gr-qc].
- [13] H. O. Silva, A. M. Holgado, A. Cárdenas-Avenidaño, et al. “Astrophysical and theoretical physics implications from multimessenger neutron star observations.” In: *Phys. Rev. Lett.* 126.18 (2021), p. 181101. DOI: [10.1103/PhysRevLett.126.181101](https://doi.org/10.1103/PhysRevLett.126.181101). arXiv: [2004.01253](https://arxiv.org/abs/2004.01253) [gr-qc].
- [14] J. Aasi et al. “Advanced LIGO.” In: *Class. Quant. Grav.* 32 (2015), p. 074001. DOI: [10.1088/0264-9381/32/7/074001](https://doi.org/10.1088/0264-9381/32/7/074001). arXiv: [1411.4547](https://arxiv.org/abs/1411.4547) [gr-qc].
- [15] F. Acernese et al. “Advanced Virgo: a second-generation interferometric gravitational wave detector.” In: *Class. Quant. Grav.* 32.2 (2015), p. 024001. DOI: [10.1088/0264-9381/32/2/024001](https://doi.org/10.1088/0264-9381/32/2/024001). arXiv: [1408.3978](https://arxiv.org/abs/1408.3978) [gr-qc].
- [16] T. Akutsu et al. “Overview of KAGRA: Detector design and construction history.” In: *PTEP* 2021.5 (2021), 05A101. DOI: [10.1093/ptep/ptaa125](https://doi.org/10.1093/ptep/ptaa125). arXiv: [2005.05574](https://arxiv.org/abs/2005.05574) [physics.ins-det].

- [17] B. Iyer, T. Souradeep, C. Unnikrishnan, et al. “LIGO-India: proposal of the consortium for Indian initiative in gravitational-wave observations (IndIGO).” Tech. rep. LIGO Tech. Rep. LIGO-M1100296-v2 <https://dcc.ligo.org/LIGO-M1100296-v2/public>, 2013.
- [18] M. Saleem et al. “The science case for LIGO-India.” In: *Class. Quant. Grav.* 39.2 (2022), p. 025004. DOI: [10.1088/1361-6382/ac3b99](https://doi.org/10.1088/1361-6382/ac3b99). arXiv: [2105.01716](https://arxiv.org/abs/2105.01716) [gr-qc].
- [19] P. Fritschel et al. “Report of the lsc post-o5 study group.” In: *LIGO Document: LIGO-T2200287* (2022).
- [20] R. X. Adhikari et al. “LIGO Voyager Upgrade Concept.” In: *LIGO Document: LIGO-T1400226* (2024). URL: <https://dcc.ligo.org/LIGO-T1400226>.
- [21] R. X. Adhikari et al. “A cryogenic silicon interferometer for gravitational-wave detection.” In: *Class. Quant. Grav.* 37.16 (2020), p. 165003. DOI: [10.1088/1361-6382/ab9143](https://doi.org/10.1088/1361-6382/ab9143). arXiv: [2001.11173](https://arxiv.org/abs/2001.11173) [astro-ph.IM].
- [22] D. Reitze et al. “Cosmic Explorer: The U.S. Contribution to Gravitational-Wave Astronomy beyond LIGO.” In: *Bull. Am. Astron. Soc.* 51.7 (2019), p. 035. arXiv: [1907.04833](https://arxiv.org/abs/1907.04833) [astro-ph.IM].
- [23] M. Evans et al. “A Horizon Study for Cosmic Explorer: Science, Observatories, and Community.” In: (Sept. 2021). arXiv: [2109.09882](https://arxiv.org/abs/2109.09882) [astro-ph.IM].
- [24] M. Punturo et al. “The Einstein Telescope: A third-generation gravitational wave observatory.” In: *Class. Quant. Grav.* 27 (2010). Ed. by F. Ricci, p. 194002. DOI: [10.1088/0264-9381/27/19/194002](https://doi.org/10.1088/0264-9381/27/19/194002).
- [25] M. Maggiore et al. “Science Case for the Einstein Telescope.” In: *JCAP* 03 (2020), p. 050. DOI: [10.1088/1475-7516/2020/03/050](https://doi.org/10.1088/1475-7516/2020/03/050). arXiv: [1912.02622](https://arxiv.org/abs/1912.02622) [astro-ph.CO].
- [26] M. Branchesi et al. “Science with the Einstein Telescope: a comparison of different designs.” In: *JCAP* 07 (2023), p. 068. DOI: [10.1088/1475-7516/2023/07/068](https://doi.org/10.1088/1475-7516/2023/07/068). arXiv: [2303.15923](https://arxiv.org/abs/2303.15923) [gr-qc].
- [27] P. Amaro-Seoane et al. “Laser Interferometer Space Antenna.” In: (Feb. 2017). arXiv: [1702.00786](https://arxiv.org/abs/1702.00786) [astro-ph.IM].
- [28] P. Auclair et al. “Cosmology with the Laser Interferometer Space Antenna.” In: (Apr. 2022). arXiv: [2204.05434](https://arxiv.org/abs/2204.05434) [astro-ph.CO].
- [29] J. Luo et al. “TianQin: a space-borne gravitational wave detector.” In: *Class. Quant. Grav.* 33.3 (2016), p. 035010. DOI: [10.1088/0264-9381/33/3/035010](https://doi.org/10.1088/0264-9381/33/3/035010). arXiv: [1512.02076](https://arxiv.org/abs/1512.02076) [astro-ph.IM].

- [30] W.-R. Hu and Y.-L. Wu. “The Taiji Program in Space for gravitational wave physics and the nature of gravity.” In: *Natl. Sci. Rev.* 4.5 (2017), pp. 685–686. DOI: [10.1093/nsr/nwx116](https://doi.org/10.1093/nsr/nwx116).
- [31] W.-H. Ruan, Z.-K. Guo, R.-G. Cai, et al. “Taiji program: Gravitational-wave sources.” In: *Int. J. Mod. Phys. A* 35.17 (2020), p. 2050075. DOI: [10.1142/S0217751X2050075X](https://doi.org/10.1142/S0217751X2050075X). arXiv: [1807.09495](https://arxiv.org/abs/1807.09495) [gr-qc].
- [32] N. Seto, S. Kawamura, and T. Nakamura. “Possibility of direct measurement of the acceleration of the universe using 0.1-Hz band laser interferometer gravitational wave antenna in space.” In: *Phys. Rev. Lett.* 87 (2001), p. 221103. DOI: [10.1103/PhysRevLett.87.221103](https://doi.org/10.1103/PhysRevLett.87.221103). arXiv: [astro-ph/0108011](https://arxiv.org/abs/astro-ph/0108011).
- [33] S. Sato et al. “The status of DECIGO.” In: *J. Phys. Conf. Ser.* 840.1 (2017). Ed. by D. Giardini and P. Jetzer, p. 012010. DOI: [10.1088/1742-6596/840/1/012010](https://doi.org/10.1088/1742-6596/840/1/012010).
- [34] S. Kawamura et al. “Current status of space gravitational wave antenna DECIGO and BDECIGO.” In: (June 2020). arXiv: [2006.13545](https://arxiv.org/abs/2006.13545) [gr-qc].
- [35] K. A. Kuns, H. Yu, Y. Chen, et al. “Astrophysics and cosmology with a decihertz gravitational-wave detector: TianGO.” In: *Phys. Rev. D* 102.4 (2020), p. 043001. DOI: [10.1103/PhysRevD.102.043001](https://doi.org/10.1103/PhysRevD.102.043001). arXiv: [1908.06004](https://arxiv.org/abs/1908.06004) [gr-qc].
- [36] K. A. Kuns. “Future Networks of Gravitational Wave Detectors: Quantum Noise and Space Detectors.” PhD thesis. University of California, Santa Barbara, Mar. 2019.
- [37] N. Yunes and F. Pretorius. “Fundamental Theoretical Bias in Gravitational Wave Astrophysics and the Parameterized Post-Einsteinian Framework.” In: *Phys. Rev. D* 80 (2009), p. 122003. DOI: [10.1103/PhysRevD.80.122003](https://doi.org/10.1103/PhysRevD.80.122003). arXiv: [0909.3328](https://arxiv.org/abs/0909.3328) [gr-qc].
- [38] N. Cornish, L. Sampson, N. Yunes, et al. “Gravitational Wave Tests of General Relativity with the Parameterized Post-Einsteinian Framework.” In: *Phys. Rev. D* 84 (2011), p. 062003. DOI: [10.1103/PhysRevD.84.062003](https://doi.org/10.1103/PhysRevD.84.062003). arXiv: [1105.2088](https://arxiv.org/abs/1105.2088) [gr-qc].
- [39] N. Yunes, X. Siemens, and K. Yagi. “Gravitational-wave tests of general relativity with ground-based detectors and pulsar-timing arrays.” In: *Living Rev. Rel.* 28.1 (2025), p. 3. DOI: [10.1007/s41114-024-00054-9](https://doi.org/10.1007/s41114-024-00054-9).
- [40] K. Chatziioannou, N. Yunes, and N. Cornish. “Model-Independent Test of General Relativity: An Extended post-Einsteinian Framework with Complete Polarization Content.” In: *Phys. Rev. D* 86 (2012). [Erratum: *Phys. Rev. D* 95, 129901 (2017)], p. 022004. DOI: [10.1103/PhysRevD.86.022004](https://doi.org/10.1103/PhysRevD.86.022004). arXiv: [1204.2585](https://arxiv.org/abs/1204.2585) [gr-qc].

- [41] N. Loutrel, P. Pani, and N. Yunes. “Parametrized post-Einsteinian framework for precessing binaries.” In: *Phys. Rev. D* 107.4 (2023), p. 044046. doi: [10.1103/PhysRevD.107.044046](https://doi.org/10.1103/PhysRevD.107.044046). arXiv: [2210.10571](https://arxiv.org/abs/2210.10571) [gr-qc].
- [42] S. Mezzasoma and N. Yunes. “Theory-agnostic framework for inspiral tests of general relativity with higher-harmonic gravitational waves.” In: *Phys. Rev. D* 106.2 (2022), p. 024026. doi: [10.1103/PhysRevD.106.024026](https://doi.org/10.1103/PhysRevD.106.024026). arXiv: [2203.15934](https://arxiv.org/abs/2203.15934) [gr-qc].
- [43] A. K. Mehta, A. Buonanno, R. Cotesta, et al. “Tests of general relativity with gravitational-wave observations using a flexible theory-independent method.” In: *Phys. Rev. D* 107.4 (2023), p. 044020. doi: [10.1103/PhysRevD.107.044020](https://doi.org/10.1103/PhysRevD.107.044020). arXiv: [2203.13937](https://arxiv.org/abs/2203.13937) [gr-qc].
- [44] G. S. Bonilla, P. Kumar, and S. A. Teukolsky. “Modeling compact binary merger waveforms beyond general relativity.” In: *Phys. Rev. D* 107.2 (2023), p. 024015. doi: [10.1103/PhysRevD.107.024015](https://doi.org/10.1103/PhysRevD.107.024015). arXiv: [2203.14026](https://arxiv.org/abs/2203.14026) [gr-qc].
- [45] E. Maggio, H. O. Silva, A. Buonanno, et al. “Tests of general relativity in the nonlinear regime: A parametrized plunge-merger-ringdown gravitational waveform model.” In: *Phys. Rev. D* 108.2 (2023), p. 024043. doi: [10.1103/PhysRevD.108.024043](https://doi.org/10.1103/PhysRevD.108.024043). arXiv: [2212.09655](https://arxiv.org/abs/2212.09655) [gr-qc].
- [46] D. Watarai, A. Nishizawa, and K. Cannon. “Physically consistent gravitational waveform for capturing beyond general relativity effects in the compact object merger phase.” In: *Phys. Rev. D* 109.8 (2024), p. 084058. doi: [10.1103/PhysRevD.109.084058](https://doi.org/10.1103/PhysRevD.109.084058). arXiv: [2309.14061](https://arxiv.org/abs/2309.14061) [gr-qc].
- [47] Y. Xie, D. Chatterjee, G. Narayan, et al. “Neural post-Einsteinian framework for efficient theory-agnostic tests of general relativity with gravitational waves.” In: *Phys. Rev. D* 110.2 (2024), p. 024036. doi: [10.1103/PhysRevD.110.024036](https://doi.org/10.1103/PhysRevD.110.024036). arXiv: [2403.18936](https://arxiv.org/abs/2403.18936) [gr-qc].
- [48] L. Sampson, N. Cornish, and N. Yunes. “Mismodeling in gravitational-wave astronomy: The trouble with templates.” In: *Phys. Rev. D* 89.6 (2014), p. 064037. doi: [10.1103/PhysRevD.89.064037](https://doi.org/10.1103/PhysRevD.89.064037). arXiv: [1311.4898](https://arxiv.org/abs/1311.4898) [gr-qc].
- [49] B. C. Seymour and Y. Chen. “Gravitational-wave signatures of non-violent non-locality.” Nov. 2024. arXiv: [2411.13714](https://arxiv.org/abs/2411.13714) [gr-qc].
- [50] C. Cutler and M. Vallisneri. “LISA detections of massive black hole inspirals: Parameter extraction errors due to inaccurate template waveforms.” In: *Phys. Rev. D* 76 (2007), p. 104018. doi: [10.1103/PhysRevD.76.104018](https://doi.org/10.1103/PhysRevD.76.104018). arXiv: [0707.2982](https://arxiv.org/abs/0707.2982) [gr-qc].
- [51] Q. Hu and J. Veitch. “Accumulating Errors in Tests of General Relativity with Gravitational Waves: Overlapping Signals and Inaccurate Waveforms.” In: *Astrophys. J.* 945.2 (2023), p. 103. doi: [10.3847/1538-4357/acbc18](https://doi.org/10.3847/1538-4357/acbc18). arXiv: [2210.04769](https://arxiv.org/abs/2210.04769) [gr-qc].

- [52] M. Vallisneri. “Testing general relativity with gravitational waves: a reality check.” In: *Phys. Rev. D* 86 (2012), p. 082001. DOI: [10.1103/PhysRevD.86.082001](https://doi.org/10.1103/PhysRevD.86.082001). arXiv: [1207.4759](https://arxiv.org/abs/1207.4759) [gr-qc].
- [53] M. Vallisneri and N. Yunes. “Stealth Bias in Gravitational-Wave Parameter Estimation.” In: *Phys. Rev. D* 87.10 (2013), p. 102002. DOI: [10.1103/PhysRevD.87.102002](https://doi.org/10.1103/PhysRevD.87.102002). arXiv: [1301.2627](https://arxiv.org/abs/1301.2627) [gr-qc].
- [54] S. Vitale and W. Del Pozzo. “How serious can the stealth bias be in gravitational wave parameter estimation?.” In: *Phys. Rev. D* 89.2 (2014), p. 022002. DOI: [10.1103/PhysRevD.89.022002](https://doi.org/10.1103/PhysRevD.89.022002). arXiv: [1311.2057](https://arxiv.org/abs/1311.2057) [gr-qc].
- [55] C. J. Moore, E. Finch, R. Busicchio, et al. “Testing general relativity with gravitational-wave catalogs: The insidious nature of waveform systematics.” In: *iScience* 24 (2021), p. 102577. DOI: [10.1016/j.isci.2021.102577](https://doi.org/10.1016/j.isci.2021.102577). arXiv: [2103.16486](https://arxiv.org/abs/2103.16486) [gr-qc].
- [56] S. Perkins and N. Yunes. “Are parametrized tests of general relativity with gravitational waves robust to unknown higher post-Newtonian order effects?.” In: *Phys. Rev. D* 105.12 (2022), p. 124047. DOI: [10.1103/PhysRevD.105.124047](https://doi.org/10.1103/PhysRevD.105.124047). arXiv: [2201.02542](https://arxiv.org/abs/2201.02542) [gr-qc].
- [57] S. Kejriwal, L. Speri, and A. J. K. Chua. “Impact of correlations on the modeling and inference of beyond vacuum–general relativistic effects in extreme-mass-ratio inspirals.” In: *Phys. Rev. D* 110.8 (2024), p. 084060. DOI: [10.1103/PhysRevD.110.084060](https://doi.org/10.1103/PhysRevD.110.084060). arXiv: [2312.13028](https://arxiv.org/abs/2312.13028) [gr-qc].
- [58] R. S. Chandramouli, K. Prokup, E. Berti, et al. “Systematic biases in parametrized tests of general relativity due to waveform mismodeling: the impact of neglecting spin precession and higher modes.” Oct. 2024. arXiv: [2410.06254](https://arxiv.org/abs/2410.06254) [gr-qc].
- [59] A. Gupta et al. “Possible causes of false general relativity violations in gravitational wave observations.” In: *SciPost Phys. Comm. Rep.* (May 2024). DOI: [10.21468/SciPostPhysCommRep.5](https://doi.org/10.21468/SciPostPhysCommRep.5). arXiv: [2405.02197](https://arxiv.org/abs/2405.02197) [gr-qc].
- [60] A. Pai and K. G. Arun. “Singular value decomposition in parametrised tests of post-Newtonian theory.” In: *Class. Quant. Grav.* 30 (2013), p. 025011. DOI: [10.1088/0264-9381/30/2/025011](https://doi.org/10.1088/0264-9381/30/2/025011). arXiv: [1207.1943](https://arxiv.org/abs/1207.1943) [gr-qc].
- [61] K. G. Arun and A. Pai. “Tests of General Relativity and Alternative theories of gravity using Gravitational Wave observations.” In: *Int. J. Mod. Phys. D* 22 (2013), p. 1341012. DOI: [10.1142/S0218271813410125](https://doi.org/10.1142/S0218271813410125). arXiv: [1302.2198](https://arxiv.org/abs/1302.2198) [gr-qc].
- [62] D. Keppel. “Use of Singular-Value Decomposition in Gravitational-Wave Data Analysis.” In: *Int. J. Mod. Phys. Conf. Ser.* 23 (2013). Ed. by Z. Cao, X. Chen, R. Ruffini, et al., p. 01113. DOI: [10.1142/S2010194513011136](https://doi.org/10.1142/S2010194513011136). arXiv: [1201.1739](https://arxiv.org/abs/1201.1739) [physics.data-an].

- [63] M. Tiglio and A. Villanueva. “Reduced order and surrogate models for gravitational waves.” In: *Living Rev. Rel.* 25.1 (2022), p. 2. DOI: [10.1007/s41114-022-00035-w](https://doi.org/10.1007/s41114-022-00035-w). arXiv: [2101.11608](https://arxiv.org/abs/2101.11608) [gr-qc].
- [64] S. Datta, M. Saleem, K. G. Arun, et al. “Multiparameter tests of general relativity using a principle component analysis with next-generation gravitational-wave detectors.” In: *Phys. Rev. D* 109.4 (2024), p. 044036. DOI: [10.1103/PhysRevD.109.044036](https://doi.org/10.1103/PhysRevD.109.044036). arXiv: [2208.07757](https://arxiv.org/abs/2208.07757) [gr-qc].
- [65] M. Saleem, S. Datta, K. G. Arun, et al. “Parametrized tests of post-Newtonian theory using principal component analysis.” In: *Phys. Rev. D* 105.8 (2022), p. 084062. DOI: [10.1103/PhysRevD.105.084062](https://doi.org/10.1103/PhysRevD.105.084062). arXiv: [2110.10147](https://arxiv.org/abs/2110.10147) [gr-qc].
- [66] S. Datta. “Enhancing the performance of multiparameter tests of general relativity with LISA using Principal Component Analysis.” Mar. 2023. arXiv: [2303.04399](https://arxiv.org/abs/2303.04399) [gr-qc].
- [67] Z.-C. Ma, R. Niu, and W. Zhao. “The Multi-parameter Test of Gravitational Wave Dispersion with Principal Component Analysis.” In: *Res. Astron. Astrophys.* 24.5 (2024), p. 055012. DOI: [10.1088/1674-4527/ad3c70](https://doi.org/10.1088/1674-4527/ad3c70). arXiv: [2401.17666](https://arxiv.org/abs/2401.17666) [gr-qc].
- [68] L. S. Finn. “Detection, measurement and gravitational radiation.” In: *Phys. Rev. D* 46 (1992), pp. 5236–5249. DOI: [10.1103/PhysRevD.46.5236](https://doi.org/10.1103/PhysRevD.46.5236). arXiv: [gr-qc/9209010](https://arxiv.org/abs/gr-qc/9209010).
- [69] T. G. F. Li, W. Del Pozzo, S. Vitale, et al. “Towards a generic test of the strong field dynamics of general relativity using compact binary coalescence.” In: *Phys. Rev. D* 85 (2012), p. 082003. DOI: [10.1103/PhysRevD.85.082003](https://doi.org/10.1103/PhysRevD.85.082003). arXiv: [1110.0530](https://arxiv.org/abs/1110.0530) [gr-qc].
- [70] M. Agathos, W. Del Pozzo, T. G. F. Li, et al. “TIGER: A data analysis pipeline for testing the strong-field dynamics of general relativity with gravitational wave signals from coalescing compact binaries.” In: *Phys. Rev. D* 89.8 (2014), p. 082001. DOI: [10.1103/PhysRevD.89.082001](https://doi.org/10.1103/PhysRevD.89.082001). arXiv: [1311.0420](https://arxiv.org/abs/1311.0420) [gr-qc].
- [71] J. Meidam et al. “Parametrized tests of the strong-field dynamics of general relativity using gravitational wave signals from coalescing binary black holes: Fast likelihood calculations and sensitivity of the method.” In: *Phys. Rev. D* 97.4 (2018), p. 044033. DOI: [10.1103/PhysRevD.97.044033](https://doi.org/10.1103/PhysRevD.97.044033). arXiv: [1712.08772](https://arxiv.org/abs/1712.08772) [gr-qc].
- [72] F. Ohme, A. B. Nielsen, D. Keppel, et al. “Statistical and systematic errors for gravitational-wave inspiral signals: A principal component analysis.” In: *Phys. Rev. D* 88.4 (2013), p. 042002. DOI: [10.1103/PhysRevD.88.042002](https://doi.org/10.1103/PhysRevD.88.042002). arXiv: [1304.7017](https://arxiv.org/abs/1304.7017) [gr-qc].

Part IV

High-Frequency Gravitational Wave Detection

PROSPECTS FOR HIGH-FREQUENCY GRAVITATIONAL-WAVE DETECTION WITH GEO600

- [1] C. M. Jungkind, B. C. Seymour, L. Laeuger, et al. “Prospects for High-Frequency Gravitational-Wave Detection with GEO600.” In preparation for submission.

8.1 Introduction

The era of gravitational-wave (GW) astronomy began in 2015 with the first detection of a binary black-hole (BBH) merger by the LIGO observatories and has flourished since then with more than 100 observed compact merger events [1, 2, 3, 4, 5]. Despite these achievements, current GW detectors are only sensitive between a few tens of Hz and several kilohertz (kHz). The high frequency sensitivity is set primarily by quantum shot noise. While shot noise is frequency independent (white noise), the response of the interferometer to GWs weakens with increasing frequency in the low kHz regime, resulting in poorer sensitivity [6, 7, 8]. Thus, the pathway to detecting high frequency GWs lies in either building new detectors or modifying the response of existing detectors.

Recent years have yielded a diverse set of proposals to improve the high frequency sensitivity of GW detectors. The LIGO and Virgo interferometers have developed both frequency-independent and frequency-dependent squeezing technologies, though in the O3, O4a and O4b observing runs, Virgo has only employed frequency-independent squeezing while LIGO has operated with frequency-dependent squeezing [9, 10, 11]. LIGO A+, Voyager, and A# are design concepts that aim to retrofit the existing LIGO observatory facilities by implementing upgraded technology [12, 13, 14]. Third generation ground interferometers [15, 16] will expand the sensitivity range of such experiments. At higher frequencies, resonant spheres [17, 18] could detect GWs up to 10 kHz, optically-levitated sensors [19, 20] will search for GWs at tens to hundreds of kHz, and resonant electromagnetic detectors [21, 22, 23, 24, 25], bulk acoustic wave devices [26, 27, 28], and tabletop-scale interferometers [29, 30, 31] will probe frequencies at MHz and above. Additionally, space-based interferometers [32, 33, 34], atom interferometry experiments [35, 36, 37], and pulsar timing

arrays [38, 39] will target frequencies below 1 Hz. While these technologies are very promising, they will require decades of development to become operational.

Detecting GWs at frequencies in the tens of kHz holds the potential to unveil signatures of new physics such as very light compact object binaries or ultralight boson clouds [40, 41]. Sub-solar mass (SSM) compact objects could be astrophysical objects like BHs created through an unconventional formation channel [42, 43, 44], a primordial BH [45, 46, 47], or some other exotic compact object [48, 49, 50, 51]. If multiple SSM objects form a binary, it will be detectable by searching for its effects with a high-frequency GW detector [52, 53]. Additionally, isolated spinning black holes can form boson clouds via the superradiance effect if there is some unknown ultralight boson cloud [54, 55]. Detection of the GWs emitted by the boson clouds could be evidence of new physics. The quantum chromodynamics (QCD) axion [56, 57, 58, 59] and the dark photon [60, 61, 62] are two prominent ultralight bosons that could have astrophysical effects in GWs [63, 64, 65]. The LVK collaboration has actively searched for GWs from SSM binaries [66, 67, 68, 69, 70] and superradiant boson clouds in their data [71, 72, 73]. It is likely that SSM binaries and superradiant boson clouds could have characteristic frequencies that are higher than current generation GW detectors [74]. In addition to superradiance, ultralight bosons could be bound to the gravitational potential of a NS [75, 76] or BH which would allow indirect detection via fifth-force in GW signals [77, 78, 79] or in binary pulsar observations [80, 81, 82, 83]. Outside of GW observations, ultralight bosons and sub-solar mass compact objects have been searched for with both direct and indirect experiments; however, no evidence has been found [84, 85, 86, 87, 88, 89, 90, 91].

As a more near term solution to detecting these high-frequency sources, we consider modifications to existing GW detectors that could enhance their sensitivity in the $\sim 5 - 100$ kHz range. When the GW period approaches the photon round-trip time in optical cavities within an interferometer, the sideband fields produced by a GW can be resonantly amplified inside optical cavities within the experiment [92]. This sideband amplification offers special frequencies at which the sensitivity of the detector could be greatly improved. In this work, we investigate whether GEO600 [93], a dual-recycled, folded-arm, Michelson interferometer (MI) [94, 95, 96], can be made sensitive to sources in the tens of kHz frequency range by utilizing these special frequencies.

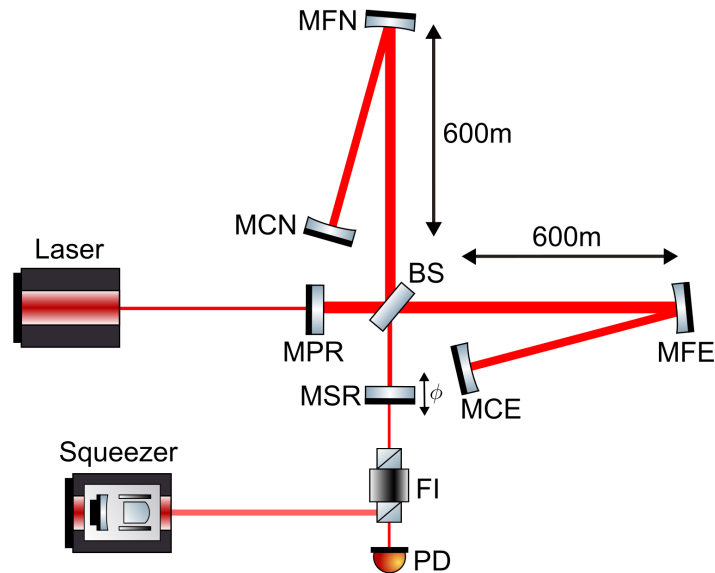


Figure 8.1: GEO600 optical layout used in Finesse model. FI: Faraday isolator, MPR: power-recycling mirror, MSR: signal-recycling mirror, BS: beam splitter, PD: photodiode for DC readout. MFE and MCE are the far east mirror and central east mirror. ϕ is the detuning angle of the MSR in degrees of a wavelength. The notation for the north arm is analogous.

The rest of this paper is organized as follows. In Sec. 8.2, we discuss the underlying detector physics that motivated the investigation of GEO600 as a high-frequency GW detector. We describe our methods for simulating the sky-averaged strain sensitivities of GEO600. We discuss the resulting sensitivities of different interferometer configurations and compare them to other ground-based interferometric detectors. In Sec. 8.3, we introduce the high-frequency astrophysical sources and describe their GW waveforms and properties. We discuss how the SNR is calculated and the resulting ability of each interferometer to detect the sources. In Sec. 8.4, we conclude our work and discuss future research. Python code and Jupyter notebooks for generating the results shown in this document can be downloaded from GitHub [97].

8.2 Detector Sensitivity

Underlying Physics

To improve the sensitivity of a GW detector, one can either weaken the background noise sources or amplify the magnitude of the detector's response to an incident GW. GEO600's potential as a high-frequency GW detector originates in the latter option, namely through the resonant enhancement of GW-induced sideband fields

within the interferometer [98]. Resonant amplification of the sideband fields in turn amplifies the signal power at the detection port, boosting the overall response. GEO600 features two mirrors which reflect laser light departing the Michelson arms back into the MI, thus forming effective cavities with the north and east Michelson arm mirrors (shown in Fig. 8.1). The power-recycling cavity (PRC), created by the power-recycling mirror (MPR) and MI, increases the sensitivity of the interferometer by building up the cavity light's intensity and distance traveled [99]. The signal-recycling cavity (SRC), created by the MSR and MI, allows the signal sidebands to resonate at specific Fourier frequencies, denoted resonant frequencies [100, 101, 102].

The resonant frequencies in the SRC are those which experience a net phase shift of $2\pi n$ during a round trip in this effective cavity. When the MSR is detuned by angle ϕ , the SRC resonates for sideband frequencies f which satisfy

$$2 \times (2\pi(\nu + f)L_{\text{SRC}}/c + \phi) = 2\pi n, \quad (8.1)$$

where ν is the laser frequency, and n is an integer. For GEO600, $L_{\text{SRC}} = L_{\text{MI}} + L_{\text{SR}}$ is the optical distance light travels from the MI's end mirror to the MSR (when the detuning is zero). For this folded configuration, $L_{\text{MI}} = 2 \times 600 = 1200\text{m}$. The definition of L_{SRC} ensures that $2\nu L_{\text{SRC}}/c$ is an integer already; since GWs create sidebands at $\pm f_{\text{GW}}$, the condition simplifies to one for the (positive) GW frequencies which produce sidebands that are resonant in the SRC,

$$f_{\text{res}} = \frac{c}{2L_{\text{SRC}}} \left| n - \frac{\phi}{\pi} \right|. \quad (8.2)$$

For this work, we primarily target the frequency which appears for $n = 0$ ¹. The detuning angle ϕ is related to the MSR displacement δl by $\phi = k\delta l$, where $k = 2\pi c/\nu$. Therefore, by finely tuning the MSR location, we can scan the SRC resonant frequencies, and thus the resonant peaks in the GEO600 detector response, over a broad frequency range [103]. Detuning the MSR allows for lowest-order resonant peaks in the detector response function to occur as high as 62.5 kHz.

Unlike GEO600, the LIGO detector response displays two distinct resonant features, but we will see that they are not well suited for broadband high-frequency detection. The first occurs at multiples of the FSR of the Fabry-Perot arms (37.5 kHz), but it is unaffected by the detuning of the MSR, and thus cannot be scanned with this

¹The resonant frequencies for $|n| > 0$ are less advantageous for detection because the GW-induced phase delay in the MI is diminished for frequencies greater than $f_{\text{fsr}} = c/2L_{\text{src}}$ (see App. 8.5).

procedure. One might envision detuning the Fabry-Perot mirrors themselves, but this would drastically reduce the DC power circulating in the arms (that is, intentionally moving the cavities away from their locked position), heavily attenuating the available power for sideband generation.

The other feature can be scanned by detuning the SRC; however, the presence of Fabry-Perot arm cavities increases the effective SRC length by a factor of $\sim 2\mathcal{F}$, where \mathcal{F} is the cavity finesse. As a result, the lowest-order SRC resonant frequency in LIGO can only occur as high as ~ 125 Hz with current mirror transmissivity. Furthermore, the high finesse of the Fabry-Perot arms causes them to dominate the cavity storage time. Therefore, not only is the resulting amplified peak in the detector response less pronounced relative to the tuned configuration than in the case of GEO600, but all the higher-order SRC resonances are washed out completely. Thus, a GEO600-like detector geometry — namely, one featuring shorter arms (and thus a higher FSR) and a lack of Fabry-Perot cavities — is more favorable for broadband high-frequency detection via the procedure we have described.

All the features of the detector response functions we have described can be seen in Figs. 8.2 and 8.3, the generation of which is outlined in the following section. In particular, when the MSR is detuned, the sensitivity improves in exchange for it becoming increasingly narrowband.

Methods

To construct the strain sensitivity function for a given configuration of GEO600, we include the following dominant noise sources n_i : laser quantum noise, classical laser amplitude and frequency noise, seismic noise, and thermal noise in the suspensions, substrates, and coatings of the optics. The expressions for the amplitude spectral densities for each noise source $A_{n_i}(f)$ (with units $[n_i]/\sqrt{\text{Hz}}$) are presented in App. 8.6.

The total sky-averaged strain noise power spectral density (PSD) is given by

$$\langle S_h(f) \rangle = \left\langle \frac{\partial P}{\partial h} \right\rangle^{-2} \sum_{n_i} S_{n_i}(f) \left(\frac{\partial P}{\partial n_i} \right)^2, \quad (8.3)$$

where the summation occurs over all the noise sources n_i , $S_{n_i} \equiv A_{n_i}^2$ is the PSD of the noise source n_i , and $\partial P/\partial n_i$ is the transfer function from noise source n_i to the detection observable P . In this paper, we designate the observable as the power at the dark port of the interferometer — see the optical layout depicted in Fig. 8.1. Lastly, $\langle \partial P/\partial h \rangle$ is the transfer function from an incident GW to the observable (i.e., the

detector response function). We use the notation $\langle \cdot \rangle$ to represent the sky-averaged response. To summarize, the transfer function $\partial P / \partial n_i$ projects a given noise source onto the readout, and $\partial P / \partial h$ projects the GW strain onto the same readout; thus, Eq. (8.3) projects each noise source into some equivalent sky-averaged strain noise.

To compute $S_h(f)$, we employ the Finesse 3.0 package [104, 105], which we use to extract the frequency-domain transfer functions $\partial P / \partial n_i$ ² and $\partial P / \partial h$ from a model of GEO600. Notably, the transfer functions from a GW to an observable are computed in Finesse under the assumption that the GW is incident from directly above the interferometer. Denoting the transfer function to the dark port power calculated by Finesse as $\left. \frac{\partial P}{\partial h} \right|_{\text{Finesse}}$, the sky-averaged detector response function is therefore equal to

$$\left\langle \frac{\partial P}{\partial h} \right\rangle = \left. \frac{\partial P}{\partial h} \right|_{\text{Finesse}} \times \frac{\mathcal{R}(f)}{|F_+^{\text{fold}}(f, \hat{n} = \hat{z})|}, \quad (8.4)$$

where $\mathcal{R}(f)$ is the sky-averaged detector antenna pattern and $|F_+^{\text{fold}}(f, \hat{n} = \hat{z})|$ is the antenna pattern function evaluated for a GW incident from overhead. In the low-frequency limit $\mathcal{R}(f) = 2/5$, but for frequencies comparable to the inverse light travel time in the Michelson arms, high frequency effects become important. In App. 8.5, we derive the antenna pattern of a folded Michelson interferometer as done in Ref. [106] and clarify how the folded geometry modifies the high-frequency response.

Table 8.1 displays the parameters of the important mirrors in GEO600 needed to model the experiment accurately. We model the detection readout method using a DC readout [113] and maintain the arms at a phase difference equivalent to a 50-picometer offset from the dark fringe [95]. Recently, a new laser amplifier providing 70 Watts of available power, with 50-60 Watts being detected on average at the MPR, was installed in GEO600 [110]. Thus, we use 50 Watts of laser power for our model of GEO600 as a confident lower bound of the amount of power able to enter the interferometer's dual-recycled cavity through the MPR.

We note here that the sky-averaged design sensitivity for Advanced LIGO was computed directly using GWINC [112].

An important noise source under active research investigation at high frequencies is the parametric instability of the resonant eigenmodes in the substrate of the test

²Finesse features a method to compute the quantum noise at any optical port, so for quantum noise in particular, we directly extract the noise at the detection port.

Mirror	Transmission	Loss	Mass
Beam splitter (BS)	0.513872	130 ppm	9.3 kg
Central East mirror (MCE)	13 ppm	130 ppm	5.6 kg
Central North mirror (MCN)	13 ppm	130 ppm	5.6 kg
Far East mirror (MFE)	8.3 ppm	130 ppm	5.6 kg
Far North mirror (MFN)	8.3 ppm	130 ppm	5.6 kg
Power-recycling mirror (MPR)	900 ppm	130 ppm	2.92 kg
Signal-recycling mirror (MSR)	0.09995	50 ppm	2.92 kg

Table 8.1: Mirror parameters used in the GEO600 Finesse model [107, 108, 109, 110]. Ppm: parts per million, kg: kilogram.

masses in the tens of kHz [114, 115]. The temperature dependence of the test mass eigenmode frequencies renders the parametric instability a difficult noise source to attenuate [116]. We did not model this effect in our simulation of LIGO’s GW response, using the aLIGO design sensitivity only. In addition, the current configuration of LIGO cannot search for GWs over 10 kHz due to the DC electronic and anti-aliasing (AA) filters suppressing the signal data. Therefore, the sensitivity function we implement for aLIGO represents an optimistic estimate for the future capabilities of this detector design. The resonant eigenmodes of the test masses’ substrates have not been observed during observation at GEO600; without high-finesse Fabry-Perot cavities, the circulating laser power in the dual-recycled cavity is not amplified sufficiently to excite these instabilities [117], and thus we leave the inclusion of this noise source for future work. Therefore, we did not simulate parametric instability or include it in our noise budget for the interferometer.

Sensitivities

In Fig. 8.2, we show the resulting sensitivity curves for GEO600 with various detuning angles of the MSR, along with a ‘‘scanned’’ mode where the mirror is swept through the full range of detuning angles and the optimal sensitivity is selected at each value of the detuning. Conversely, the inability of the aLIGO design to scan the

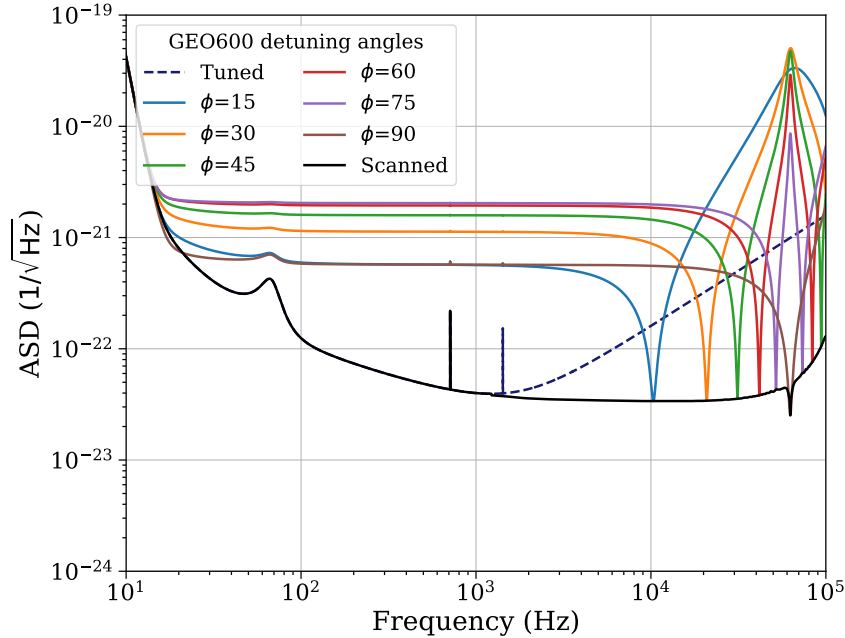


Figure 8.2: Strain sensitivity $A_h(f)$ of GEO600 at different detuning angles of the MSR, as well as a scanned sensitivity curve (black), which is a summation of all possible MSR detuning angles. All sensitivities assume normal incidence of the GWs. As the detuning angle of the MSR is increased from $\phi = 0^\circ$ (tuned configuration for GEO600), the detection region becomes increasingly narrow-band, in that the frequency bandwidth stays constant while the SRC resonant frequency increases. The scanned sensitivity curve is plotted to show the possible values that can be achieved across the kHz frequency range by shifting the MSR.

interferometer's fundamental resonance peak over a large frequency range is shown in Fig. 8.3. The sky-averaged strain sensitivity for the tuned, anti-tuned, and scanned detuning angles of GEO600 is shown in Fig. 8.4, along with other design sensitivity curves for advanced interferometers. GEO600 gains advantageous sensitivity over the aLIGO design starting at ~ 6.7 kHz by using various detuning angles to have superior narrow band detection. For our prospective detection calculations, we use individual detuning angles of the MSR with a detection time of one week. The scanned sensitivity curve is only plotted to illustrate the possible values that can be achieved across the kHz frequency range by shifting the MSR.

Fig. 8.3 portrays how aLIGO experiences resonant amplification in sensitivity at 37.5 and 75 kHz. At these specific frequencies, which are integer multiples of the Fabry-Perot cavity's FSR, the sideband fields are amplified in power as they resonate in each arm's Fabry-Perot cavity. Detuning the MSR does not affect these resonant

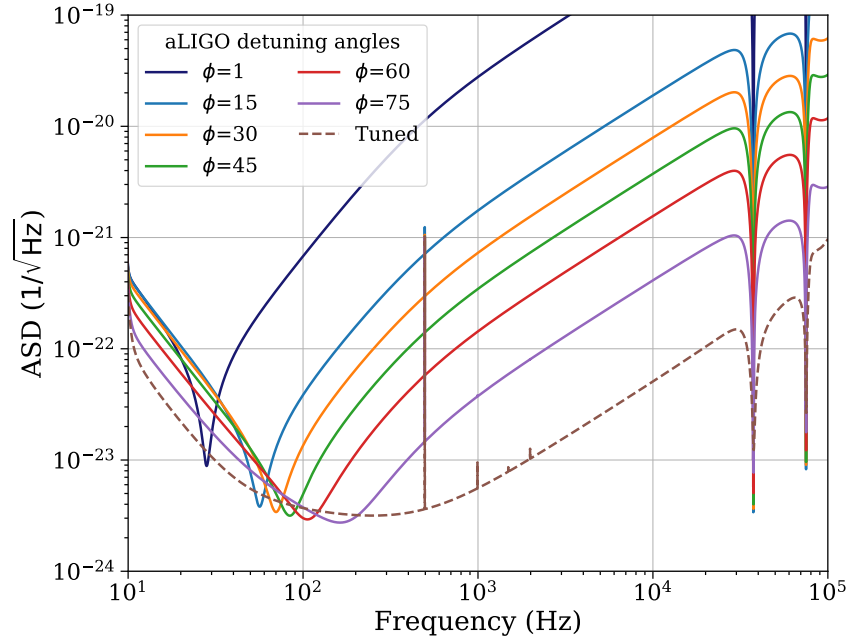


Figure 8.3: Strain sensitivity $A_h(f)$ of the aLIGO design at different detuning angles of the MSR, assuming normal incidence of the GWs. When the angle of the MSR is decreased from $\phi = 90^\circ$ (tuned configuration for aLIGO that corresponds to ‘signal extraction’ [111, 103]), the frequency of peak sensitivity gradually decreases in the neighborhood of $f \sim \mathcal{O}(100 \text{ Hz})$, while its bandwidth simultaneously narrows. Note that we use $\phi = 1^\circ$ to represent the ‘signal recycling’ limit, as setting $\phi = 0$ exactly corresponds to a configuration completely dominated by classical noise. There is no enhancement in sensitivity at frequencies in the kHz from aLIGO detuning the MSR. The peaks in sensitivity occurring at integer multiples of 37.5 kHz (FSR) are created by the Fabry-Perot cavities and are independent of the MSR detuning angle.

frequencies, rendering the sharp features in the aLIGO sensitivity curves at 37.5 and 75 kHz independent of the MSR detuning angle.

To assess the potential advantages of using GEO600 as a detection instrument for each source, we compared the signal-to-noise ratio (SNR) of the aLIGO design, GEO600, and GEO600 detuned to various frequencies. The sky-averaged strain sensitivities of these interferometer configurations, as well as that of Cosmic Explorer’s [16] for further comparison, are shown in Fig. 8.4. GEO600’s scanned sensitivity curve shows the possible frequencies in the kHz range where it would have an advantageous narrow band detection to that of Cosmic Explorer and aLIGO.

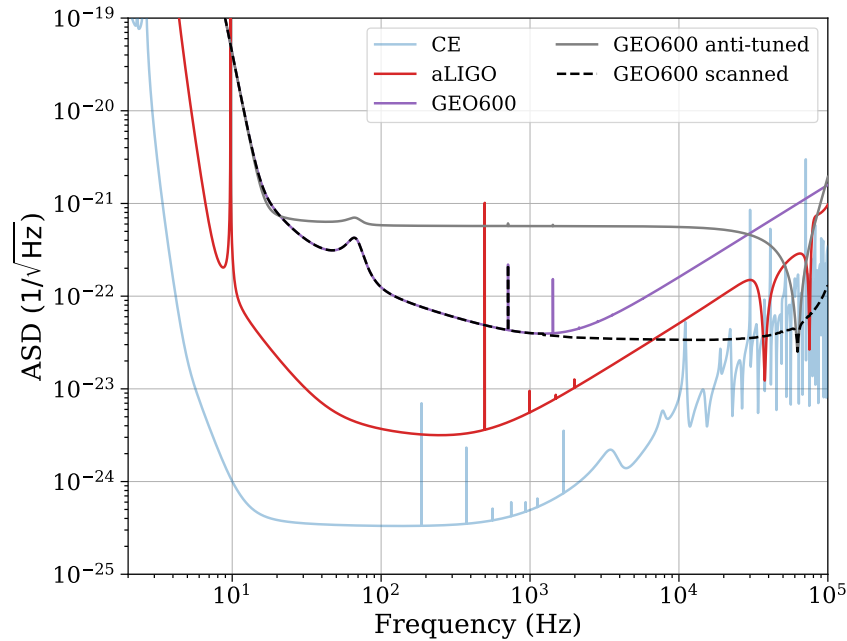


Figure 8.4: Strain sensitivity $A_h(f)$ of GEO600 tuned (purple), anti-tuned (gray), and scanned (dashed), which is a summation of all possible MSR detuning angles. The aLIGO design sensitivity (red) [112] and Cosmic Explorer’s design sensitivity (light blue) [112] are also shown. All sensitivities assume normal incidence of the GWs. GEO600’s scanned sensitivity curve shows the possible frequencies in the kHz range where it would have an advantageous narrow band detection to that of Cosmic Explorer and aLIGO.

8.3 High Frequency Sources

In this section, we investigate two classes of hypothesized high-frequency GW sources and compute benchmarks for how well they could be detected with a detuned GEO600 setup.

Ultralight Boson Clouds

GW Strain Model

A number of proposals to the Standard Model contain ultralight scalar and vector bosons that could have observable astrophysical effects. For example, the scalar axion, derived as a solution to the Strong Charge-Parity problem in QCD [56, 57, 58, 59], or the vector dark photon, derived from compactifications of string theory [60, 61, 62]. If the Compton wavelength of the bosons is comparable to the BH mass, the phenomenon of superradiance predicts scenarios with exponential growth of the bosons occurs around spinning BHs, resulting in a macroscopic boson cloud. As the

cloud forms, the BH loses angular momentum, causing the emission of continuous GWs at a frequency proportional to the mass of the ultralight bosons [118].

The gravitational potential of a BH allows for particle bound states that can be approximated by hydrogenic wave functions with radial, orbital, and azimuthal quantum numbers (n, l, m) [119]. Thus, the resulting boson cloud formed by superradiance can be described as a hydrogenic wave function, with all of the bosons occupying the same state. For our simulation, we only consider the fundamental radial quantum number $n = 0$ and the dominant unstable mode $j = l + s = m = 1$ —where l , s , and m are the orbital angular momentum, spin angular momentum, and magnetic quantum numbers, respectively. This unstable mode is chosen because it has the fastest superradiant growth rate in a given system [118, 120], making it the most dominant energy mode. Notably, this also requires that we assume that the BHs which source these scalar axion clouds are *not* primordial in origin, as previous works considering primordial BHs have found that only states with quantum numbers $n \geq 5$ can still exist and radiate GWs in the present day [40]. We furthermore constrain our BHs to have initial dimensionless spin parameter of $\chi_i = 0.7$.

The amplification process can only occur when the angular velocity of the black hole at the event horizon is higher than the angular frequency of the bosons divided by the magnetic quantum number [118]:

$$\omega_\mu/m < \Omega_{\text{BH}}(\chi_i), \quad (8.5)$$

where $\omega_\mu = \mu/\hbar$, $m = 1$, and $\Omega_{\text{BH}}(0.7) = 1.38 \times 10^5 \left(\frac{0.3M_\odot}{M}\right) \text{ s}^{-1}$. Rearranging this superradiance condition constrains the rest energy of bosons surrounding a BH of mass M to be $\mu < 9.10 \times 10^{-11} \left(\frac{0.3M_\odot}{M}\right) \text{ eV}$. For boson clouds with boson rest energies in the target range of 10^{-12} to 10^{-10} eV, the GW emission frequency is given by [118] as

$$f_{\text{GW}} \approx 48750 \text{ Hz} \times \frac{\mu}{10^{-10} \text{ eV}}. \quad (8.6)$$

Since there is an upper bound on μ based on the corresponding mass of the BH it is orbiting, there is also an upper bound on the GW emission frequencies that are possible for every BH mass. The GW strain for vector bosons is given as

$$h_0^v \approx 1.28 \times 10^{-22} \left(\frac{M}{0.3M_\odot}\right) \left(\frac{\alpha}{0.2}\right)^5 \left(\frac{0.03 \text{ Mpc}}{r}\right) \left(\frac{0.7 - \chi_f}{0.1}\right), \quad (8.7)$$

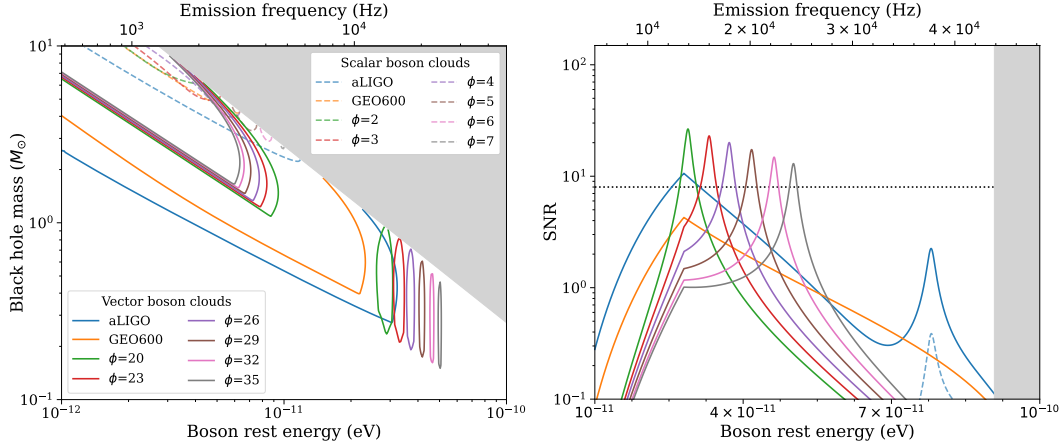


Figure 8.5: Left: contour lines corresponding to a SNR of eight for GWs sourced from both vector (solid) and scalar (dashed) boson clouds. The contour lines correspond to the strain sensitivities of aLIGO (blue), tuned GEO600 (orange), and GEO600 with different MSR detuning angles. The shaded gray region corresponds to the parameter space where the superradiance condition fails. Right: SNR of GWs sourced from both vector (solid) and scalar (dashed) boson clouds across a range of boson rest energies for a $0.3 M_{\odot}$ BH. The SNR curves are calculated with the same strain sensitivities as the left plot and have the same corresponding colors. The dotted black line represents where the SNR is eight. All GWs are sourced from within the galaxy, being simulated from a distance of 30 kPc.

where α is the ratio of the characteristic lengths of the boson cloud and the BH, and χ_f is the BH spin after superradiance occurs. α and χ_f are given as

$$\alpha = \frac{\mu GM}{\hbar c^3}, \quad \chi_f = \frac{4\alpha_f}{4\alpha_f^2 + 1}. \quad (8.8)$$

Here, $\alpha_f = \frac{\mu GM_f}{\hbar c^3}$, and $M_f = 0.9M$ is the mass of the BH after the boson cloud has extracted its energy during the superradiant growth [118]. The GW signal duration for vector bosons is given as

$$\tau_{\text{GW}}^v \approx 1.81 \text{ s} \left(\frac{M}{0.3M_{\odot}} \right) \left(\frac{0.2}{\alpha} \right)^{11}. \quad (8.9)$$

For scalar bosons, the GW strain and signal duration are both given as

$$h_0^s \approx 10^{-25} \left(\frac{M}{0.3M_{\odot}} \right) \left(\frac{\alpha}{0.2} \right)^7 \left(\frac{0.03 \text{ Mpc}}{r} \right) \left(\frac{0.7 - \chi_f}{0.1} \right), \quad (8.10)$$

$$\tau_{\text{GW}}^s \approx 31 \text{ days} \left(\frac{M}{0.3M_{\odot}} \right) \left(\frac{0.2}{\alpha} \right)^{15}. \quad (8.11)$$

Detection Prospects

Our figure of merit to compare the detection capabilities of our detuned GEO600 configurations against LIGO is the sky-averaged SNR produced by a characteristic high-frequency source in each detector. Since the boson clouds produce a monochromatic signal, the sky-averaged SNR is given by [6] as

$$\langle \rho^2 \rangle = \frac{|h_0^b|^2 T}{\langle S_h(f_0) \rangle}, \quad (8.12)$$

where $b = s, v$ for either scalar or vector boson strain and h_0 is averaged over source inclination angles. Here, $T \equiv \min\{1 \text{ week}, \tau_{GW}\}$ is the observation time. Note that $\langle S_h(f_0) \rangle = \langle A_h(f_0)^2 \rangle = \left(\frac{A_h(f_0)}{\mathcal{R}(f_0)} \right)^2$.

In Fig. 8.5, we show contours of SNR equal to 8 for vector and scalar boson clouds for different interferometer configurations, representing regions of this parameter space which are detectable by each system. The plot shows the feasibility of certain configurations of GEO600 detecting GWs for different combinations of boson rest energies and BH mass. We also present a horizontal cross-section of the contour plot, taken for a black hole mass of $0.3M_\odot$. The cross-section plot shows the SNR of the interferometer at different boson rest energies for a given BH mass $m_{\text{BH}} = 0.3M_\odot$.

Both tuned GEO600 and aLIGO have a large parameter area where the interferometers would be able to detect vector boson clouds, though aLIGO generally tends to outperform GEO600 due to its superior broadband sensitivity. However, if GEO600 shifts the MSR to different detuning angles, the narrow band sensitivity produced by the detuning, which can exceed the broadband sensitivity of aLIGO at those same high frequencies, affords GEO600 a competitive advantage for boson rest energies whose corresponding GW frequencies fall in that narrow band. GEO600 gains the advantage over aLIGO at 15.1 kHz, with aLIGO not being able to detect GWs sourced at higher frequencies. That is, for all frequencies above 15.1 kHz, there exists some detuning angle which produces a narrow band (~ 2 kHz) around the chosen frequency within which GEO600 outperforms aLIGO. By detuning the MSR and observing at that frequency range for a week, GEO600 can search for GWs sourced from boson clouds from 500 Hz to 31.3 kHz, with the latter frequency being obtained with a detuning angle of $\phi = 45^\circ$ (not plotted). Note that the pattern of high-frequency narrow bands in the left plot of Fig. 8.5 is only shown up to $\phi = 35^\circ$, which results in a detection bandwidth centered at 24.5 kHz. Thus, GEO600 would

be able to detect GWs from a larger frequency range, increasing the likelihood the interferometer observes the phenomena. It would be advantageous to use GEO600 as a high-frequency GW interferometer targeting GWs sourced from boson clouds within the galaxy in comparison to using aLIGO. Expanding the region of the BH-axion cloud system parameter space which sources detectable GWs increases the likelihood of detecting the superradiance phenomenon. Note that the current operational LIGO design would not be able to detect GWs over 10 kHz due to the DC electronic and anti-aliasing (AA) filters suppressing the signal data past this cutoff frequency.

Conversely, Fig. 8.5 shows that both interferometers have a very small area of parameters that result in the possible detection of scalar boson clouds, and the area does not extend into the high-frequency emission range like the vector boson parameter area does. The primary cause for the inability to detect high-frequency GWs from scalar boson clouds is that the strain is a factor of $\sim 10^3$ weaker than that of vector boson clouds.

Sub-Solar Mass Compact Object Mergers

GW Strain Model

Sub-solar mass compact objects represent a compelling category of potential GW sources in the high-frequency regime accessible to current and future detectors. While conventional astrophysical compact objects such as neutron stars and black holes are typically formed with masses above one solar mass, various theoretical models predict the existence of sub-solar mass compact objects through unconventional formation channels or as entirely new types of exotic matter configurations [41]. Outside the conventional BH-formation theory of stellar evolution, PBHs may have formed from the gravitational collapse of density perturbations in the early Universe [47, 45, 46], and BHs formed from the gravitational collapse of dark matter halos [44] have been proposed as sub-solar mass compact objects. Additionally, there exist theories of exotic compact objects, such as gravitino stars [50], boson stars [48], moduli stars [51], and gravastars [49], that are sub-solar mass. If a sub-solar mass binary were found, classification between BBH and BNS is possible since tidal deformabilities strongly affect the waveform for light NS [121].

We simulate GWs from sub-solar mass compact binary mergers within the mass range of $10^{-6} M_{\odot}$ to $1 M_{\odot}$. Note that the detection of GWs sourced from compact objects within this mass range would not provide the sufficient parameters to

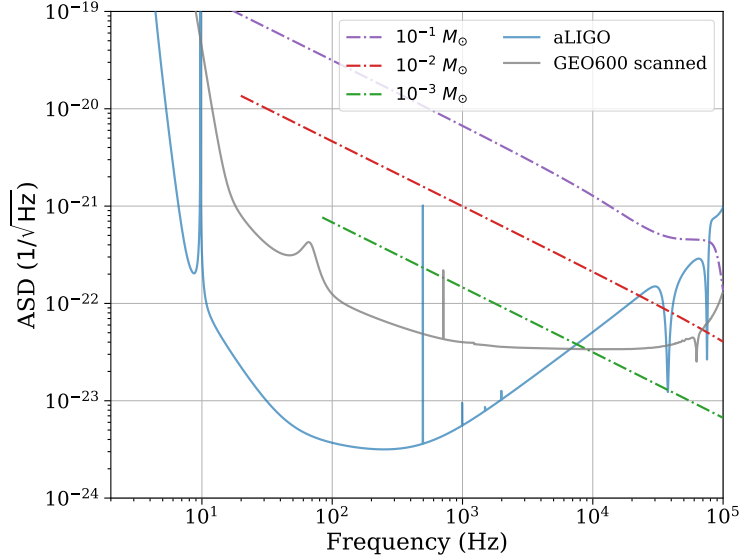


Figure 8.6: Strain sensitivity $A_h(f)$ of the aLIGO design (light blue) and scanned GEO600 (light gray), assuming normal incidence of the GWs. Three different GW waveforms are plotted as $2|\tilde{h}_+(f)|\sqrt{f}$. The GW amplitudes are from compact binary mergers of three different sub-solar masses, observed from a distance of 30 kPc.

distinguish that the object is a PBH specifically. In addition, if the source were a PBH, a detection within this mass range could only provide evidence that PBHs constitute some fraction of dark matter [74]. We compute the characteristic strain from the binary merger of sub-solar mass compact objects using the inspiral, merger, and ringdown waveforms available in PyCBC’s IMRPhenomD package [122]. For simplicity, we assume an inclination angle of 0° , making $\tilde{h}_+(f) = \tilde{h}_\times(f)$ and $\tilde{h}(f) = \mathcal{R}(f)\tilde{h}_0(f)$ (see App. 8.5). We calculated the sky-averaged SNR using the chirp formula given by [6] as

$$\langle \rho^2 \rangle = 4 \int_{f_{\min}}^{\infty} \frac{|\tilde{h}(f)|^2}{\langle S_h(f) \rangle} df, \quad (8.13)$$

where f_{\min} is the GW frequency emitted exactly one week before the compact objects merge [6]:

$$f_{\min}(\tau) \simeq 4.72 \text{ Hz} \left(\frac{0.087 M_\odot}{M_c} \right)^{5/8} \left(\frac{1 \text{ wk}}{\tau} \right)^{3/8}, \quad (8.14)$$

where the chirp mass M_c for two $0.1 M_\odot$ BHs is equal to $0.087 M_\odot$, and in general is given by [6] as

$$M_c = \frac{(m_1 m_2)^{3/5}}{(m_1 + m_2)^{1/5}}. \quad (8.15)$$

In our calculations, we set the time to coalescence τ equal to one week.

Detection Prospects

Our figure of merit to compare the detection capabilities of our detuned GEO600 configurations against LIGO is the sky-averaged SNR produced by a characteristic high-frequency SSM compact binary merger in each detector. In Fig. 8.6, we show the GW strain of compact mergers with individual BH masses of 10^{-1} , 10^{-2} , and $10^{-3} M_{\odot}$, located a distance of 30 kPc from the detector. As the chirp mass decreases, f_{\min} increases while the GW strain is reduced. The frequency-domain signal is calculated with an observation time of one week, and the SNR is related to the area in the plot between the strain and noise spectral functions. We find that there are not sub-solar mass binaries which can be detected easier with a detuned GEO600 detector. Over the frequency range where the detuning-scanned GEO600 has a better sensitivity than aLIGO, the strain from the merger is weak, and thus the accumulated SNR is so little that it does not sway the total SNR in favor of GEO600. While the time domain signal is stronger at high frequencies, the early inspiral dominates the SNR because it has more cycles in band. If there were a sub-solar mass binary that were very slowly evolving in frequency at a timescale of \sim months, then detuning GEO to the exact frequency could improve the sensitivity compared with LIGO. For nearly monochromatic sub-solar mass signals, one would see a similar improvement as to what we saw in Sec. 8.3. Thus, GEO600 is not an optimal ground-based interferometer for the detection of most sub-solar mass compact binary mergers.

8.4 Conclusion

In this work, we investigated how the high-frequency sensitivity of GEO600 can be scanned by detuning the location of the signal recycling mirror. We estimated the SNR in the experiment for characteristic high-frequency GW sources located within the Milky Way. This setup of detuning GEO600 does not result in an improvement in searches for sub-solar mass binaries due to their long inspiral in low frequencies, and the bandwidth being ~ 2 kHz. However, GEO600 could outperform the aLIGO design sensitivity for the detection of GWs sourced from nearly monochromatic sources like boson clouds within the galaxy. The interferometer would be able to detect GWs sourced from vector boson clouds at frequencies between 500 Hz to 31.3 kHz, gaining the advantage over the aLIGO design sensitivity at 15.1 kHz and over O4 LIGO at 10 kHz.

In the future, it would be interesting to extend our analysis on GEO600 to include time domain simulations as there are lots of complications associated with maintaining the resonance condition of the MSR while it is detuned for high-frequency GW detection. Neural-network-based sensing and auxiliary sub-carrier field injections are innovative control system methods to maintain the detuned MSR in the resonant state during high-frequency detection [123, 124]. In addition, a new FPGA-based fast data acquisition system has been installed that samples data up to 100 MHz, extending data collection availability into the hundreds of kHz [106]. Throughout this work, we used frequency-independent squeezing where we optimized the squeezing angle to maximize the sensitivity at the resonant frequencies. Normally for a Michelson interferometer, a filter cavity is designed to rotate the light in a frequency-dependent way which results in higher bandwidth for the detuned detector. This is a very interesting followup work to investigate possible ways to achieve frequency-dependent squeezing that is also tunable [125, 126, 127, 128]. We leave these studies to future work.

ACKNOWLEDGMENTS

C.J. acknowledges the support of the National Science Foundation Research Experience for Undergraduates program (NSF REU), the LIGO Laboratory Summer Undergraduate Research Fellowship program (LIGO SURF), and the California Institute of Technology Student-Faculty Programs (Caltech SFP). A.L. is supported by the John and Fannie Hertz Foundation. B.S. acknowledges support by the National Science Foundation Graduate Research Fellowship under Grant No. DGE-1745301. Y.C.'s research is supported by the Simons Foundation (Award No. 568762), the Brinson Foundation, and the National Science Foundation (via Grants No. PHY-2309211 and PHY-2309231). We wish to acknowledge Aaron Goodwin-Jones, Su Direkci, and James Gardner for their useful discussion and comments on the manuscript, and Dr. James Lough for his useful information about GEO600's parameters.

8.5 Appendix: Antenna Response Patterns

In this appendix, we provide a derivation for the sky-averaged antenna response pattern at high frequencies for two interferometer geometries.

Unfolded Michelson Interferometer

When studying high-frequency ($f \sim c/L_{\text{arm}}$) interferometric detection, an important piece of physics which typically can be neglected in low-frequency calculations is the evolution of the GW strain as a photon travels out and back along an arm of the interferometer. For certain frequencies and angles of incidence, the phase accumulated by a photon during a full round-trip in the interferometer can deviate significantly from $2hk_{\text{photon}}L$ — at some frequencies even being identically zero. Thus, to properly model the response of GEO600 and LIGO to high-frequency GWs, we must compute the generalized response function for a folded and unfolded Michelson interferometer which includes the GW and photon propagation effects. This is done originally in Ref. [7] and Ref. [8].

We will now replicate the derivation of the high-frequency response of a Michelson interferometer as outlined in [8]. The time-domain form of a plane wave GW is given by

$$h_{ij}(t, \vec{x}) = h_+(t, \vec{x})e_{ij}^+(\hat{n}) + h_\times(t, \vec{x})e_{ij}^\times(\hat{n}), \quad (8.16)$$

where \hat{n} points toward the GW source. The polarization tensors are defined via

$$\hat{e}_{ij}^+ = \ell_i \ell_j - m_i m_j, \quad (8.17a)$$

$$e_{ij}^\times = \ell_i m_j + \ell_j m_i, \quad (8.17b)$$

where the unit vectors $\hat{\ell}, \hat{m}, \hat{n}$ form a right-handed orthonormal basis. In this discussion, we suppress the relative rotation that is due to the polarization angle. In the long-wavelength approximation, the Michelson interferometer response is given by

$$h(t) = \frac{1}{2} (a^i a^j - b^i b^j) h_{ij}(t, \vec{0}). \quad (8.18)$$

One can then write this as

$$h(t) = F_+(\hat{n})h_+(t) + F_\times(\hat{n})h_\times(t). \quad (8.19)$$

If we take unit vectors a^i and b^i to represent the two arms of the detector, the antenna patterns are given by

$$F_A(\hat{n}) = \frac{1}{2} (a_i a_j - b_i b_j) e_A^{ij}(\hat{n}), \quad (8.20)$$

where we use $A = +, \times$ to denote polarization. In this long-wavelength regime, the antenna patterns do not depend on the frequency.

Let us now generalize the results of Eq. (8.20) to high-frequency regime. As discussed in Eqs.(15-17) of Ref. [8], the response of the GW detector is related to the time delay accumulated in the round trip

$$h(t) = \frac{1}{2T} \left[\delta T_{\text{r.t.},\hat{a}}^{\text{mich}}(t) - \delta T_{\text{r.t.},\hat{b}}^{\text{mich}} \right] \quad (8.21)$$

where $\delta T_{\text{r.t.},\hat{a}}^{\text{mich}}$ is the round trip time delay incurred from the presence of the GW along the \hat{a} direction and $T = L/c$. The round trip time delay along direction \hat{a} is the sum of the delay from the out and back journey³

$$\delta T_{\text{r.t.},\hat{a}}^{\text{mich}}(t) = \delta T_{\hat{a}}(t - T) + \delta T'_{\hat{a}}(t), \quad (8.22)$$

where

$$\delta T_{\hat{a}}(t) = \frac{1}{2c} a^i a^j \int_0^L h_{ij} \left(t - T + \frac{\xi}{c} + \frac{\hat{n} \cdot \hat{a}}{c} \xi \right) d\xi, \quad (8.23a)$$

$$\delta T'_{\hat{a}}(t) = \frac{1}{2c} a^i a^j \int_0^L h_{ij} \left(t - \frac{\xi}{c} + \frac{\hat{n} \cdot \hat{a}}{c} \xi \right) d\xi. \quad (8.23b)$$

We note that the time translation property of the GW is used $h_{ij}(t, \vec{x}) = h_{ij}(t + \vec{x} \cdot \hat{n}/c)$, which is why these expressions only are a function of one number.

Using the expressions for the round trip time delay, we can write the frequency-dependent antenna patterns in the frequency domain. In the Fourier domain, the time delay is

$$\frac{\delta \tilde{T}_{\text{r.t.},\hat{a}}^{\text{mich}}(f)}{T} = a_i a_j D(\hat{a}, f) e_A^{ij}(\hat{n}) \tilde{h}_A(f), \quad (8.24)$$

where we define the transfer function $D(\hat{a}, f)$ as

$$D(\hat{a}, f) = \frac{e^{-i2\pi f T}}{2} \left[e^{i\pi f T_+} \text{sinc}(\pi f T_-) + e^{-i\pi f T_-} \text{sinc}(\pi f T_+) \right], \quad (8.25)$$

and define $T_{\pm} = T(1 \pm \hat{a} \cdot \hat{n})$. In the end, the frequency-domain GW signal is

$$\tilde{h}(f) = F_+(\hat{n}, f) \tilde{h}_+(f) + F_{\times}(\hat{n}, f) \tilde{h}_{\times}(f), \quad (8.26)$$

where the frequency-dependent antenna patterns are defined via [8] as

$$F_A(\hat{n}, f) = \frac{1}{2} \left[a_i a_j D(\hat{a}, f) - b_i b_j D(\hat{b}, f) \right] e_A^{ij}(\hat{n}). \quad (8.27)$$

³Note that the normalization $1/2T$ comes from enforcing that $\max_{\hat{n}} F_A(\hat{n}, f) = 1$ when $f = 0$.

Folded Michelson Interferometer

GEO600 has folded interferometer arms, making the antenna patterns deviate at high frequencies from that of a MI with unfolded arms [106]. To ensure that the SNR of GEO600 is accurate in the high-frequency range of a few kHz to tens of kHz, we will now replicate the derivation of Ref. [106] and derive the folded-arm MI antenna response pattern. In this derivation, we will ignore the effects caused by the folding angle of GEO600's interferometer arms. Since $\alpha_{\text{fold}} = 0.42$ mrad [129], the effects of the triangular shape of the fold occur when the GW wavelength approaches $\lambda_{\text{gw}} \sim \alpha_{\text{fold}}L \approx 0.25$ m, which corresponds to a GW frequency of $f \gtrsim 1$ GHz.

One can now do the analysis of the time delay that the light accumulates along the trip of a folded detector in arm \hat{a} . This can be written as

$$\delta T_{\text{r.t.},\hat{a}}^{\text{fold}}(t) = \delta T_{\hat{a}}(t - 3T) + \delta T'_{\hat{a}}(t - 2T) + \delta T_{\hat{a}}(t - T) + \delta T'_{\hat{a}}(t), \quad (8.28)$$

where we use the same definitions as the previous section. It is useful to relate the round trip of a folded Michelson to a unfolded Michelson trip delay:

$$\delta T_{\text{r.t.},\hat{a}}^{\text{fold}}(t) = \delta T_{\text{r.t.},\hat{a}}^{\text{mich}}(t - 2T) + \delta T_{\text{r.t.},\hat{a}}^{\text{mich}}(t). \quad (8.29)$$

If we take the Fourier transform of this, we find that the folded Michelson time delay is equal to

$$\delta \tilde{T}_{\text{r.t.},\hat{a}}^{\text{fold}}(f) = \left(1 + e^{4\pi i f T}\right) \delta \tilde{T}_{\text{r.t.},\hat{a}}^{\text{mich}}(f). \quad (8.30)$$

Since the round trip time delay is changed by a non-directionally-dependent factor, the antenna pattern of a folded Michelson interferometer is directly proportional to an unfolded Michelson interferometer via

$$F_A^{\text{fold}}(\hat{n}, f) = \frac{1 + e^{4\pi i f T}}{2} F_A^{\text{mich}}(\hat{n}, f), \quad (8.31)$$

where the extra factor of 2 comes from the DC antenna pattern normalization. In this equation, we stress that $F_A^{\text{mich}}(\hat{n}, f)$ is a Michelson interferometer of length 600m while $F_A^{\text{fold}}(\hat{n}, f)$ is a folded Michelson interferometer of length 600m+600m. So while it is understood that GEO600 has an effective arm length of 1200m because of the folding, the high-frequency antenna patterns of GEO600 behave more like a 600m detector times a factor. One notable feature of the folded detector is that there is zero response for every angle at frequency values of

$$f = \frac{c}{4L} (1 + 2n), \quad n \in \mathbb{N}_0. \quad (8.32)$$

In the next section, we will see that there are complete dips in the angle averaged sensitivity for a folded detector.

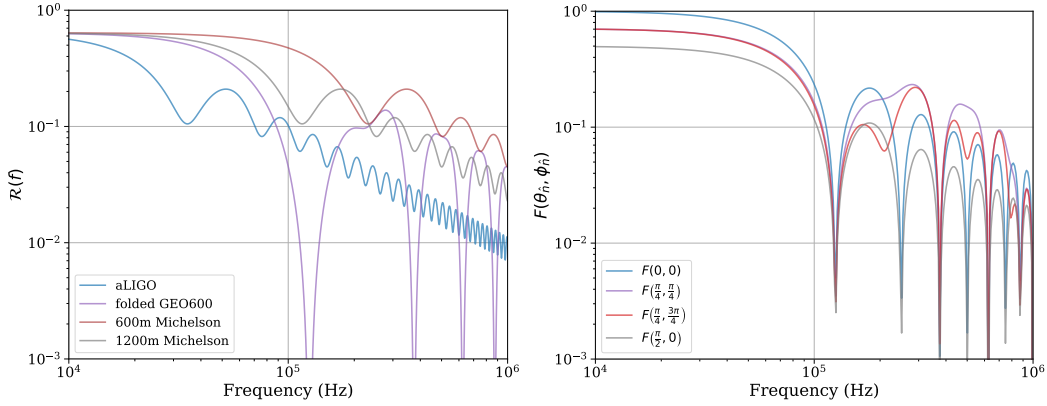


Figure 8.7: Left: sky-averaged antenna patterns $\mathcal{R}(f)$ for aLIGO (light blue), folded GEO600 (purple), a 600m Michelson interferometer (brown), and a 1200m Michelson interferometer (gray). The folding factor given in Eq. (8.31) relates the angular response of an unfolded Michelson interferometer (brown) to its folded counterpart (purple); one can see that the folding factor sharply reduces the angular response at frequencies where it was previously strong. Right: antenna patterns $F(\theta_{\hat{n}}, \phi_{\hat{n}})$ of folded GEO600 for the following incident-angled GWs: overhead (light blue), completely along one detector arm (gray), and two in-between angles (purple and brown). Here, $F(\theta_{\hat{n}}, \phi_{\hat{n}}) = \sqrt{|F_+(f; \phi_{\hat{n}}, \theta_{\hat{n}})|^2 + |F_\times(f; \phi_{\hat{n}}, \theta_{\hat{n}})|^2}$ since we assume an inclination angle of zero. One can see that the angular behavior of antenna patterns is very frequency dependent at high frequencies.

Sky Averaging

Let us now calculate the response of the detector to a signal where we average over all possible directions and inclinations. If we define $\tilde{h}_+(f) = A_+ \tilde{h}_0(f)$ and $\tilde{h}_\times(f) = A_\times e^{i\pi/2} \tilde{h}_0(f)$, the signal measured in the detector would be defined as

$$\tilde{h}(f) = Q(f; \phi_{\hat{n}}, \theta_{\hat{n}}, \iota, \psi) \tilde{h}_0(f), \quad (8.33)$$

where the angle effects are contained in

$$Q(f; \phi_{\hat{n}}, \theta_{\hat{n}}, \iota, \psi) = F_+(f; \phi_{\hat{n}}, \theta_{\hat{n}}; \psi) A_+(\iota) + i F_\times(f; \phi_{\hat{n}}, \theta_{\hat{n}}; \psi) A_\times(\iota), \quad (8.34)$$

where $A_+ = \frac{1+\cos^2 \iota}{2}$ and $A_\times = \cos \iota$. We care about the absolute value of this squared. We first note that the average of the square of Q over ψ is

$$\langle |Q|^2 \rangle_\psi = \frac{1}{2} \left(A_+^2 + A_\times^2 \right) \left(|F_+|^2 + |F_\times|^2 \right), \quad (8.35)$$

where $F_+ = F_+(\phi_{\hat{n}}, \theta_{\hat{n}})$ only at $\psi = 0$. If we average over the direction that the GW arrives, we can write this as

$$\langle |Q|^2 \rangle_{\hat{n}} = \frac{g(\iota)}{2} \mathcal{R}^2(f), \quad (8.36)$$

where $g(\iota) = A_+^2 + A_\times^2$. Now note that

$$\langle A_+^2 + A_\times^2 \rangle_\iota = \langle g(\iota) \rangle_\iota, \quad (8.37)$$

$$= \frac{1}{4\pi} \int d\Omega_L \left(A_+^2(\iota) + A_\times^2(\iota) \right), \quad (8.38)$$

$$= \frac{4}{5}, \quad (8.39)$$

where $d\Omega_L = \sin \iota d\iota d\phi_L$. Now the response function is defined via

$$\langle |F_+|^2 + |F_\times|^2 \rangle_{\phi_{\hat{n}}, \theta_{\hat{n}}} = \mathcal{R}^2(f), \quad (8.40)$$

where the DC limit would be given as $\mathcal{R}^2(f) = \frac{2}{5} + \mathcal{O}(\frac{fL}{c})$. This is the sky-averaged antenna response patterns for the plus and cross polarization. Taking the square root of Eq. (8.40) obtains the sky-averaged antenna patterns used in our SNR calculations:

$$\mathcal{R}(f) = \sqrt{\langle |F_+|^2 + |F_\times|^2 \rangle_{\phi_{\hat{n}}, \theta_{\hat{n}}}}. \quad (8.41)$$

In Fig. 8.7, $\mathcal{R}(f)$ is plotted for aLIGO and GEO600. We also compare the response to a Michelson detector of length 600m and 1200m to help clarify how folded detectors differ from normal Michelson detectors. $\mathcal{R}(f)$ is the same shape for aLIGO and the Michelson interferometers, but it is shifted in frequency according to the detector arm length. The folded GEO600 antenna pattern shows the accurate troughs of minimized sensitivity to GWs at odd integer multiples of the FSR, as derived in Eq. (8.32). One can see that the angle-averaged response of folded detectors differs significantly from that of Michelson ones.

8.6 Appendix: Noise Spectral Densities

In this appendix, we provide the analytical expressions for the various noise spectral densities that source important contributions to the GEO600 sensitivity function.

Quantum Noise

Quantum noise is the combination of quantum shot noise and radiation-pressure noise. Radiation pressure is the optomechanical momentum that high-energy photons give to test masses when they hit them. It is strongest at low frequencies and decreases with frequency at the rate of $\frac{1}{f^2}$ [130]. Quantum shot noise is derived from the fundamental law that light is discretely quantized, meaning the power is detected from the number of photons N that hit the detector per unit time. Since N is a discrete value, it is calculated using a Poisson distribution, and for large N ,

it becomes a Gaussian with a standard deviation $\sqrt{\langle N \rangle}$. The inherent standard deviation creates a random fluctuation in the number of photons that hit the detector per unit time, creating a fluctuation in the amount of power that is detected [6]. The small fluctuation in the detected power is called the quantum shot noise, and it is frequency-independent. Our computation of the quantum noise in GEO600 is done directly in Finesse, which has the capability to compute the total quantum noise at some optical readout originating from both photon shot noise and quantum radiation pressure [105].

The injection of a squeezed state at the dark port of an interferometer can decrease the noise in one quadrature at the expense of the orthogonal quadrature, which can improve detection sensitivities especially at higher frequencies [131, 130]. We use the squeezer component built into Finesse to model this procedure; while each distinct model of GEO600 implements frequency-independent squeezing, for each detuning angle of the MSR, we choose the squeezing angle that minimizes the noise at the dark port at the resonant frequency of the SRC.

Dark Noise

Dark noise is created by the readout electronics even when no light is hitting the detector. The noise originates from temperature fluctuations inside the ohmic resistance R of the photodiode detection circuit, otherwise known as Johnson noise [130]. The ASD of the raw noise is given in dimensions of $W/\sqrt{\text{Hz}}$ by [132] as

$$A_n^{\text{DN}} = \sqrt{\frac{4k_B T}{R}}, \quad (8.42)$$

where T is the temperature of the resistor. Since dark noise is frequency independent and a factor of 30 below GEO600's shot noise [132], we did not include it in our high-frequency noise budget.

Laser Amplitude Noise

Laser amplitude noise is power fluctuations created in the laser light during the main laser creation process. We used the relative intensity noise (RIN) ASD, which is given by [133] as

$$A_{\text{RIN}}(f) = 1.5 \cdot 10^{-7} \left(\frac{1\text{Hz}}{f} \right) \frac{1}{\sqrt{\text{Hz}}}. \quad (8.43)$$

Using Eq. (8.3) to multiply $A_{\text{RIN}}(f)$ by the necessary transfer functions in Finesse, we obtain the final sky-averaged strain sensitivity for laser amplitude noise.

Laser Frequency Noise

Laser frequency noise is created by frequency fluctuations of the main laser light while traveling through the interferometer. The ASD for the raw frequency noise is given in dimensions of Hz/ $\sqrt{\text{Hz}}$ by [134] as

$$A_f(f) = \pi f \cdot \sqrt{\frac{2hc}{P\lambda}}, \quad (8.44)$$

where P is the laser power hitting the MPR and λ is the laser wavelength. Using Eq. (8.3) to multiply $A_f(f)$ by the necessary transfer functions in Finesse, we obtain the final sky-averaged strain sensitivity for laser frequency noise.

Seismic Noise

Seismic noise is created from external shock waves moving through the ground, causing the mirrors to move. The displacement ASD of the seismic noise in one of GEO600's mirrors without any attenuation is given by [135] as

$$A_x^{\text{SN}}(f) = 10^{-7} \left(\frac{1\text{Hz}}{f^2} \right) \frac{\text{m}}{\sqrt{\text{Hz}}}. \quad (8.45)$$

However, when $f_{gw} \gg f_0$, and there are 3 stages of the pendulum, the displacement of the mirror is attenuated by a factor of $(\frac{f_0^2}{f^2})^3$ [6]. Since GEO600's main mirrors have a fundamental pendulum resonant frequency of 0.5 Hz [108], the displacement ASD for the seismic noise in each mirror becomes

$$A_x^{\text{SN}}(f) = 10^{-7} \left(\frac{1\text{Hz}}{f^2} \right) \left(\frac{0.5^2}{f^2} \right)^3 \frac{\text{m}}{\sqrt{\text{Hz}}}. \quad (8.46)$$

Using Eq. (8.3) to multiply $A_x^{\text{SN}}(f)$ by the necessary transfer functions in Finesse, we obtain the sky-averaged strain sensitivity of seismic noise for each test mass in GEO600. Adding the seismic strain noise from the BS, MCE, MCN, MFE, and MFN together in quadrature obtains the total sky-averaged strain sensitivity of seismic noise.

Thermal Noise

Thermal noise is the most impactful noise source in the middle frequency range $\sim \mathcal{O}(10^2 \text{ Hz})$. It affects the central mirrors, far mirrors, and the beam splitter (BS). Thermal noise is calculated separately for the three main parts of each mirror: the substrate, coating, and pendulum suspension. The cause of thermal noise in each of the three parts of the mirrors is due to three different noise sources: Brownian motion, thermo-elastic, and thermo-refractive. For the substrate and coating of the test

masses, we calculated the Brownian motion and thermo-elastic noise; the thermo-refractive noise was a factor of 3 below the thermo-elastic, making it negligible to the phase fluctuation created by the signal $\tilde{h}(f)$. For the pendulum suspension noise, we only included the fundamental longitudinal eigenmode, exempting any cross-coupling with other pendulum eigenmodes. All pendulum eigenmodes are at negligibly low frequencies relative to our targeted astrophysical sources. For the BS, only the Brownian motion and thermo-refractive noises were calculated - they are the only relevant noise sources created by the BS.

Test Mass Suspension Thermal Noise

The suspension thermal noise is the Brownian motion of the molecules moving in the triple pendulum suspending the mirrors. Since the test mass is suspended by a pendulum, the Brownian motion of the suspension has pendulum and violin resonant frequencies where the noise peaks. The displacement ASD for the violin mode noise is given in dimensions of $m/\sqrt{\text{Hz}}$ by [108] as

$$A_x^{\text{VM}}(\omega) = \sqrt{\frac{8k_B T \omega_0^2 \phi_{\text{fiber } n}}{m\omega[(\omega_n^2 - \omega^2)^2 + \omega_n^4 \phi_n^2]}}, \quad (8.47)$$

where $\omega = 2\pi f$, and $\phi_{\text{fiber } n}$ is the loss in the n th violin mode:

$$\phi_{\text{fiber } n} = D_n^{-1} \cdot \left(1 + \frac{8d_s}{R}\right) (\phi_{\text{bulk}} + \phi_{\text{nonlin}}). \quad (8.48)$$

D_n^{-1} is the dilution factor given by [108] as

$$D_n^{-1} = \frac{2}{k_+ L} \left[1 + \left(4 + \frac{(n\pi)^2}{2}\right) \left(\frac{1}{k_+ L}\right)\right], \quad (8.49)$$

where k_+ is

$$k_+ = \sqrt{\frac{\sqrt{P^2 + 4AEI\rho_L\omega^2 + P}}{2EI}}. \quad (8.50)$$

$P = mg$ is the tension per wire, $\rho_L = \rho\pi R^2$ is the linear mass density of the pendulum fiber, E is Young's modulus of the fiber, and $I = \frac{\pi}{4}R^4$ is the bending moment of inertia of the fiber. ω_n from Eq. (8.47) is the frequency of the n th violin-mode oscillation, given by [108] as

$$\omega_n = \frac{n\pi}{L} \sqrt{\frac{P}{\rho L}} \left[1 + \frac{2}{L} \sqrt{\frac{EI}{P}} + \left(4 + \frac{(n\pi)^2}{2}\right) \frac{2EI}{L^2 P}\right]. \quad (8.51)$$

Using the parameters from [108], we obtained the sky-averaged strain sensitivity of the violin mode noise in each mirror by using Eq. (8.3). We calculated the total sky-averaged strain sensitivity of the violin mode noise for GEO600 by adding the noise from every test mass together in quadrature.

The displacement ASD for the pendulum mode noise is given in dimensions of $m/\sqrt{\text{Hz}}$ by [108] as

$$A_x^{\text{PM}}(\omega) = \sqrt{\frac{4k_B T \omega_0^2 \phi}{m\omega[(\omega_0^2 - \omega^2)^2 + \omega_0^4 \phi^2]}}. \quad (8.52)$$

Using the parameters from [108], we obtained the sky-averaged strain sensitivity of the pendulum mode noise in each mirror by using Eq. (8.3). Finally, adding the noise from each mirror together in quadrature, we obtained the total sky-averaged strain sensitivity.

Test Mass Substrate Thermal Noise

We simulated the Brownian motion and thermo-elastic noise within the substrate of the test mass mirrors. The displacement ASD for the Brownian motion substrate noise is given in dimensions of $m/\sqrt{\text{Hz}}$ by [129] as

$$A_x^{\text{TMBM}}(\omega) = \sqrt{\frac{8k_B T \mathbb{E} \phi}{\omega F_0^2}}, \quad (8.53)$$

where \mathbb{E} is the mean elastic energy stored in the test mass. For the substrate, the mean elastic energy is given by [129] as

$$\mathbb{E}_{\text{Substrate}} = \frac{1 - \sigma^2}{2\sqrt{2\pi} Y r_0} \cdot F_0^2. \quad (8.54)$$

Using the parameters from [129], we obtained the sky-averaged strain sensitivity of the Brownian motion substrate noise in each mirror by using Eq. (8.3). We added the noise from each individual mirror together in quadrature to obtain the total sky-averaged strain sensitivity for the Brownian motion in the substrate of GEO600's mirrors.

For the thermo-elastic noise, the displacement ASD is given in dimensions of $m/\sqrt{\text{Hz}}$ by [129] as

$$A_x^{\text{TMTE}}(\omega) = \sqrt{\left[1 + \frac{k_s r_0}{\sqrt{2\pi}}\right] \times \left[\frac{8\kappa\alpha^2 (1 + \sigma)^2 k_B T_0^2}{\sqrt{2\pi}\rho^2 C_p^2 r_0^3 \omega^2}\right]}. \quad (8.55)$$

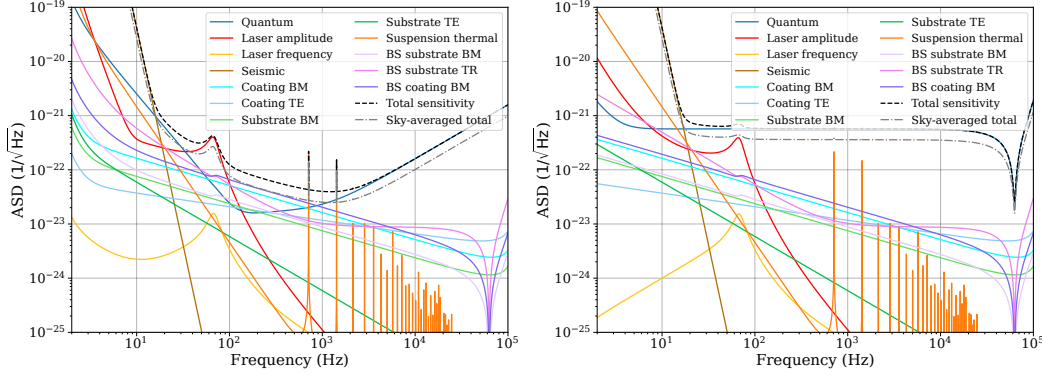


Figure 8.8: Strain sensitivity $A_h(f)$ of GEO600 with a tuned MSR (left) and an anti-tuned MSR (right), including all modeled noise sources and the total sensitivity, both with and without sky-averaging (though individual sources are only shown for normal incidence). BM: Brownian motion, TE: thermo-elastic, TR: thermo-refractive.

Using the parameters from [129], we obtained the sky-averaged strain sensitivity of the thermo-elastic noise in the substrate of each mirror by using Eq. (8.3). We added the noise from each individual mirror together in quadrature to obtain the total sky-averaged strain sensitivity for the thermo-elastic noise in the substrate of GEO600's mirrors.

Test Mass Coating Thermal Noise

The coating thermal noise we simulated was the Brownian motion in each reflective coating layer and the thermo-elastic noise created by temperature fluctuations within the mirror coatings. The noise caused by the Brownian motion in the mirror coatings is given in dimensions of $\text{m}/\sqrt{\text{Hz}}$ by [129] as

$$A_x^{\text{TMBM}}(\omega) = \sqrt{\frac{8k_B T \mathbb{E}\phi}{\omega F_0^2}}, \quad (8.56)$$

where the mean elastic energy \mathbb{E} for the coating is calculated as

$$\mathbb{E}_{\text{Coating}} = \frac{HF_0^2}{4\pi r_0^2} \left[\frac{(1 + \sigma_c)(1 - 2\sigma_c)}{Y_c(1 - \sigma_c)} + \frac{Y_c(1 + \sigma)^2(1 - 2\sigma)^2}{Y^2(1 - \sigma_c^2)} \right]. \quad (8.57)$$

Using the parameters from [129], we obtained the sky-averaged strain sensitivity of the Brownian motion in the coating of each of GEO600's mirrors by using Eq. (8.3). We added the noise from each individual mirror together in quadrature to obtain the total sky-averaged strain sensitivity for the test-mass coating Brownian motion noise.

The displacement ASD of the thermo-elastic coating noise is given in dimensions of $\text{m}/\sqrt{\text{Hz}}$ by [129] as

$$A_x^{\text{TMTE}}(\omega) = \sqrt{\frac{3\sqrt{2}\alpha^2 Y_c^2 M^2 k_B T_0^2 H^2}{2\pi\sqrt{\kappa\rho} C_p r_0^2 \sqrt{\omega}}}. \quad (8.58)$$

Using the parameters from [129], we obtained the sky-averaged strain sensitivity of the coating thermo-elastic noise in each mirror by using Eq. (8.3). We added the noise from each individual mirror together in quadrature to obtain the total sky-averaged strain sensitivity for the thermo-elastic noise in GEO600's test mass coatings.

Beam Splitter Thermal Noise

The absence of Fabry-Perot cavities in GEO600 allows kilowatts of power to pass through the BS as light propagates in the PRC, creating the most dominant noise sources in the hundreds of Hz. The high levels of power create pockets of fluctuating temperature within the BS's substrate, changing the index of refraction and adding extra phase to the light [136]. In addition to the substrate thermo-refractive noise, we calculated the coating Brownian motion and substrate Brownian motion noises within the BS [137]. The displacement ASD of the thermo-refractive noise in the BS's substrate is given in dimensions of $\text{m}/\sqrt{\text{Hz}}$ by [136] as

$$A_x^{\text{BSTR}}(\omega) = \sqrt{\left[\frac{4k_B \kappa T^2 \beta^2 a' (\eta + \eta^{-1})}{\pi (C_p r_0^2 \omega)^2 2\eta^2} \right] \left[1 + \frac{2k^2 r_0^2 \eta}{(\eta + \eta^{-1}) (1 + (2kl_{th}(\omega))^4)} \right]}. \quad (8.59)$$

Using the parameter values that represent GEO600 from [136], we obtained the sky-averaged strain sensitivity of the thermo-refractive noise in the BS's substrate by using Eq. (8.3).

The displacement ASD of the Brownian motion in the BS is given in dimensions of $\text{m}/\sqrt{\text{Hz}}$ by [137] as

$$A_x^{\text{BSBM}}(\omega) = \sqrt{\frac{8k_B T \mathbb{E}\phi}{\omega F_0^2}}. \quad (8.60)$$

For the substrate, the mean elastic energy is given by [137] as

$$\mathbb{E}_{\text{Substrate}} = (1.97 \cdot 10^{-9}) \cdot F_0^2. \quad (8.61)$$

Plugging both \mathbb{E} and the parameter values from [137] into $A_x^{\text{BSBM}}(\omega)$ —and then using Eq. (8.3)—we obtained the sky-averaged strain sensitivity for the Brownian motion noise within the BS’s substrate.

For the BS coating, we found the mean elastic energy by solving for \mathbb{E} given the stated outcome of the PSD at 100 Hz given by [137]:

$$\mathbb{E}_{\text{Coating}} = \left(4.91 \cdot 10^{-13}\right) \cdot F_0^2. \quad (8.62)$$

Plugging both \mathbb{E} and the parameter values from [137] into $A_x^{\text{BSBM}}(\omega)$ —and then using Eq. (8.3)—we obtained the sky-averaged strain sensitivity for the Brownian motion noise within the coating of the BS. The sky-averaged strain sensitivity $\langle A_h(f) \rangle$ of every noise sources we modeled, as well as the total sky-averaged strain sensitivity of the interferometer, are shown in an ASD plot in Fig. 8.8.

References

- [1] J. Aasi et al. “Advanced LIGO.” In: *Class. Quant. Grav.* 32 (2015), p. 074001. DOI: [10.1088/0264-9381/32/7/074001](https://doi.org/10.1088/0264-9381/32/7/074001). arXiv: [1411.4547 \[gr-qc\]](https://arxiv.org/abs/1411.4547).
- [2] B. P. Abbott et al. “Observation of Gravitational Waves from a Binary Black Hole Merger.” In: *Phys. Rev. Lett.* 116.6 (2016), p. 061102. DOI: [10.1103/PhysRevLett.116.061102](https://doi.org/10.1103/PhysRevLett.116.061102). arXiv: [1602.03837 \[gr-qc\]](https://arxiv.org/abs/1602.03837).
- [3] F. Acernese et al. “Advanced Virgo: a second-generation interferometric gravitational wave detector.” In: *Class. Quant. Grav.* 32.2 (2015), p. 024001. DOI: [10.1088/0264-9381/32/2/024001](https://doi.org/10.1088/0264-9381/32/2/024001). arXiv: [1408.3978 \[gr-qc\]](https://arxiv.org/abs/1408.3978).
- [4] B. P. Abbott et al. “GW170817: Observation of Gravitational Waves from a Binary Neutron Star Inspiral.” In: *Phys. Rev. Lett.* 119.16 (2017), p. 161101. DOI: [10.1103/PhysRevLett.119.161101](https://doi.org/10.1103/PhysRevLett.119.161101). arXiv: [1710.05832 \[gr-qc\]](https://arxiv.org/abs/1710.05832).
- [5] R. Abbott et al. “GWTC-3: Compact Binary Coalescences Observed by LIGO and Virgo during the Second Part of the Third Observing Run.” In: *Phys. Rev. X* 13.4 (2023), p. 041039. DOI: [10.1103/PhysRevX.13.041039](https://doi.org/10.1103/PhysRevX.13.041039). arXiv: [2111.03606 \[gr-qc\]](https://arxiv.org/abs/2111.03606).
- [6] M. Maggiore. “Gravitational Waves. Vol. 1: Theory and Experiments.” Oxford University Press, 2008. ISBN: 978-0-19-171766-6, 978-0-19-852074-0. DOI: [10.1093/acprof:oso/9780198570745.001.0001](https://doi.org/10.1093/acprof:oso/9780198570745.001.0001).
- [7] R. Essick, S. Vitale, and M. Evans. “Frequency-dependent responses in third generation gravitational-wave detectors.” In: *Phys. Rev. D* 96.8 (2017), p. 084004. DOI: [10.1103/PhysRevD.96.084004](https://doi.org/10.1103/PhysRevD.96.084004). arXiv: [1708.06843 \[gr-qc\]](https://arxiv.org/abs/1708.06843).

- [8] M. Rakhmanov, J. D. Romano, and J. T. Whelan. “High-frequency corrections to the detector response and their effect on searches for gravitational waves.” In: *Classical and Quantum Gravity* 25.18 (Sept. 2008), p. 184017. ISSN: 1361-6382. DOI: [10.1088/0264-9381/25/18/184017](https://doi.org/10.1088/0264-9381/25/18/184017). URL: <http://dx.doi.org/10.1088/0264-9381/25/18/184017>.
- [9] M. Tse et al. “Quantum-Enhanced Advanced LIGO Detectors in the Era of Gravitational-Wave Astronomy.” In: *Phys. Rev. Lett.* 123.23 (2019), p. 231107. DOI: [10.1103/PhysRevLett.123.231107](https://doi.org/10.1103/PhysRevLett.123.231107).
- [10] D. Ganapathy et al. “Broadband Quantum Enhancement of the LIGO Detectors with Frequency-Dependent Squeezing.” In: *Phys. Rev. X* 13.4 (2023), p. 041021. DOI: [10.1103/PhysRevX.13.041021](https://doi.org/10.1103/PhysRevX.13.041021).
- [11] F. Acernese et al. “Frequency-Dependent Squeezed Vacuum Source for the Advanced Virgo Gravitational-Wave Detector.” In: *Phys. Rev. Lett.* 131.4 (2023), p. 041403. DOI: [10.1103/PhysRevLett.131.041403](https://doi.org/10.1103/PhysRevLett.131.041403).
- [12] L. Barsotti, L. McCuller, M. Evans, et al. “The A+ Design Curve.” Technical Report T1800042. LIGO, 2018. URL: <https://dcc.ligo.org/public/0149/T1800042/004/T1800042-v4.pdf>.
- [13] R. X. Adhikari et al. “A cryogenic silicon interferometer for gravitational-wave detection.” In: *Classical and Quantum Gravity* 37.16 (July 2020), p. 165003. ISSN: 1361-6382. DOI: [10.1088/1361-6382/ab9143](https://doi.org/10.1088/1361-6382/ab9143). URL: <http://dx.doi.org/10.1088/1361-6382/ab9143>.
- [14] B. P. Abbott et al. “Prospects for observing and localizing gravitational-wave transients with Advanced LIGO, Advanced Virgo and KAGRA.” In: *Living Rev. Rel.* 19 (2016), p. 1. DOI: [10.1007/s41114-020-00026-9](https://doi.org/10.1007/s41114-020-00026-9). arXiv: [1304.0670](https://arxiv.org/abs/1304.0670) [gr-qc].
- [15] M. Punturo et al. “The Einstein Telescope: A third-generation gravitational wave observatory.” In: *Class. Quant. Grav.* 27 (2010). Ed. by F. Ricci, p. 194002. DOI: [10.1088/0264-9381/27/19/194002](https://doi.org/10.1088/0264-9381/27/19/194002).
- [16] D. Reitze et al. “Cosmic Explorer: The U.S. Contribution to Gravitational-Wave Astronomy beyond LIGO.” In: *Bull. Am. Astron. Soc.* 51.7 (2019), p. 035. arXiv: [1907.04833](https://arxiv.org/abs/1907.04833) [astro-ph.IM].
- [17] C. Z. Zhou and P. F. Michelson. “Spherical resonant mass gravitational wave detectors.” In: *Phys. Rev. D* 51 (1995), pp. 2517–2545. DOI: [10.1103/PhysRevD.51.2517](https://doi.org/10.1103/PhysRevD.51.2517).
- [18] G. M. Harry, T. R. Stevenson, and H. J. Paik. “Detectability of gravitational wave events by spherical resonant mass antennas.” In: *Phys. Rev. D* 54 (1996), pp. 2409–2420. DOI: [10.1103/PhysRevD.54.2409](https://doi.org/10.1103/PhysRevD.54.2409). arXiv: [gr-qc/9602018](https://arxiv.org/abs/gr-qc/9602018).

- [19] N. Aggarwal, G. P. Winstone, M. Teo, et al. “Searching for New Physics with a Levitated-Sensor-Based Gravitational-Wave Detector.” In: *Phys. Rev. Lett.* 128.11 (2022), p. 111101. DOI: [10.1103/PhysRevLett.128.111101](https://doi.org/10.1103/PhysRevLett.128.111101). arXiv: [2010.13157](https://arxiv.org/abs/2010.13157) [gr-qc].
- [20] A. Arvanitaki and A. A. Geraci. “Detecting high-frequency gravitational waves with optically-levitated sensors.” In: *Phys. Rev. Lett.* 110.7 (2013), p. 071105. DOI: [10.1103/PhysRevLett.110.071105](https://doi.org/10.1103/PhysRevLett.110.071105). arXiv: [1207.5320](https://arxiv.org/abs/1207.5320) [gr-qc].
- [21] N. Herman, A. Fúzfa, L. Lehoucq, et al. “Detecting planetary-mass primordial black holes with resonant electromagnetic gravitational-wave detectors.” In: *Physical Review D* 104.2 (July 2021). ISSN: 2470-0029. DOI: [10.1103/physrevd.104.023524](https://doi.org/10.1103/physrevd.104.023524). URL: <http://dx.doi.org/10.1103/PhysRevD.104.023524>.
- [22] N. Herman, L. Lehoucq, and A. Fúzfa. “Electromagnetic antennas for the resonant detection of the stochastic gravitational wave background.” In: *Physical Review D* 108.12 (Dec. 2023). ISSN: 2470-0029. DOI: [10.1103/physrevd.108.124009](https://doi.org/10.1103/physrevd.108.124009). URL: <http://dx.doi.org/10.1103/PhysRevD.108.124009>.
- [23] V. Domcke, C. Garcia-Cely, and N. L. Rodd. “Novel Search for High-Frequency Gravitational Waves with Low-Mass Axion Haloscopes.” In: *Physical Review Letters* 129.4 (July 2022). ISSN: 1079-7114. DOI: [10.1103/physrevlett.129.041101](https://doi.org/10.1103/physrevlett.129.041101). URL: <http://dx.doi.org/10.1103/PhysRevLett.129.041101>.
- [24] A. Berlin, D. Blas, R. T. D’Agnolo, et al. “Detecting high-frequency gravitational waves with microwave cavities.” In: *Physical Review D* 105.11 (June 2022). ISSN: 2470-0029. DOI: [10.1103/physrevd.105.116011](https://doi.org/10.1103/physrevd.105.116011). URL: <http://dx.doi.org/10.1103/PhysRevD.105.116011>.
- [25] A. Berlin et al. “Searches for New Particles, Dark Matter, and Gravitational Waves with SRF Cavities.” Mar. 2022. arXiv: [2203.12714](https://arxiv.org/abs/2203.12714) [hep-ph].
- [26] M. Goryachev and M. E. Tobar. “Gravitational wave detection with high frequency phonon trapping acoustic cavities.” In: *Physical Review D* 90.10 (Nov. 2014). ISSN: 1550-2368. DOI: [10.1103/physrevd.90.102005](https://doi.org/10.1103/physrevd.90.102005). URL: <http://dx.doi.org/10.1103/PhysRevD.90.102005>.
- [27] M. Goryachev, W. M. Campbell, I. S. Heng, et al. “Rare Events Detected with a Bulk Acoustic Wave High Frequency Gravitational Wave Antenna.” In: *Physical Review Letters* 127.7 (Aug. 2021). ISSN: 1079-7114. DOI: [10.1103/physrevlett.127.071102](https://doi.org/10.1103/physrevlett.127.071102). URL: <http://dx.doi.org/10.1103/PhysRevLett.127.071102>.
- [28] M. A. Page, M. Goryachev, H. Miao, et al. “Gravitational wave detectors with broadband high frequency sensitivity.” In: *Communications Physics*

- 4.1 (Feb. 2021). ISSN: 2399-3650. DOI: [10.1038/s42005-021-00526-2](https://doi.org/10.1038/s42005-021-00526-2). URL: <http://dx.doi.org/10.1038/s42005-021-00526-2>.
- [29] T. Akutsu, S. Kawamura, A. Nishizawa, et al. “Search for a Stochastic Background of 100-MHz Gravitational Waves with Laser Interferometers.” In: *Physical Review Letters* 101.10 (Sept. 2008). ISSN: 1079-7114. DOI: [10.1103/PhysRevLett.101.101101](https://doi.org/10.1103/PhysRevLett.101.101101). URL: <http://dx.doi.org/10.1103/PhysRevLett.101.101101>.
- [30] A. Patra et al. “Broadband limits on stochastic length fluctuations from a pair of table-top interferometers.” Oct. 2024. arXiv: [2410.09175](https://arxiv.org/abs/2410.09175) [gr-qc].
- [31] A. S. Chou et al. “MHz Gravitational Wave Constraints with Decameter Michelson Interferometers.” In: *Phys. Rev. D* 95.6 (2017), p. 063002. DOI: [10.1103/PhysRevD.95.063002](https://doi.org/10.1103/PhysRevD.95.063002). arXiv: [1611.05560](https://arxiv.org/abs/1611.05560) [astro-ph.IM].
- [32] P. Amaro-Seoane et al. “Laser Interferometer Space Antenna.” In: (Feb. 2017). arXiv: [1702.00786](https://arxiv.org/abs/1702.00786) [astro-ph.IM].
- [33] K. A. Kuns, H. Yu, Y. Chen, et al. “Astrophysics and cosmology with a decihertz gravitational-wave detector: TianGO.” In: *Phys. Rev. D* 102.4 (2020), p. 043001. DOI: [10.1103/PhysRevD.102.043001](https://doi.org/10.1103/PhysRevD.102.043001). arXiv: [1908.06004](https://arxiv.org/abs/1908.06004) [gr-qc].
- [34] S. Kawamura et al. “Current status of space gravitational wave antenna DECIGO and B-DECIGO.” In: *PTEP* 2021.5 (2021), 05A105. DOI: [10.1093/ptep/ptab019](https://doi.org/10.1093/ptep/ptab019). arXiv: [2006.13545](https://arxiv.org/abs/2006.13545) [gr-qc].
- [35] M. Abe et al. “Matter-wave Atomic Gradiometer Interferometric Sensor (MAGIS-100).” In: *Quantum Sci. Technol.* 6.4 (2021), p. 044003. DOI: [10.1088/2058-9565/abf719](https://doi.org/10.1088/2058-9565/abf719). arXiv: [2104.02835](https://arxiv.org/abs/2104.02835) [physics.atom-ph].
- [36] S. Dimopoulos, P. W. Graham, J. M. Hogan, et al. “An Atomic Gravitational Wave Interferometric Sensor (AGIS).” In: *Phys. Rev. D* 78 (2008), p. 122002. DOI: [10.1103/PhysRevD.78.122002](https://doi.org/10.1103/PhysRevD.78.122002). arXiv: [0806.2125](https://arxiv.org/abs/0806.2125) [gr-qc].
- [37] S. Dimopoulos, P. W. Graham, J. M. Hogan, et al. “Gravitational Wave Detection with Atom Interferometry.” In: *Phys. Lett. B* 678 (2009), pp. 37–40. DOI: [10.1016/j.physletb.2009.06.011](https://doi.org/10.1016/j.physletb.2009.06.011). arXiv: [0712.1250](https://arxiv.org/abs/0712.1250) [gr-qc].
- [38] F. Jenet et al. “The North American Nanohertz Observatory for Gravitational Waves.” Sept. 2009. arXiv: [0909.1058](https://arxiv.org/abs/0909.1058) [astro-ph.IM].
- [39] J. P. W. Verbiest et al. “The International Pulsar Timing Array: First Data Release.” In: *Mon. Not. Roy. Astron. Soc.* 458.2 (2016), pp. 1267–1288. DOI: [10.1093/mnras/stw347](https://doi.org/10.1093/mnras/stw347). arXiv: [1602.03640](https://arxiv.org/abs/1602.03640) [astro-ph.IM].

- [40] J. R. Sprague, S. L. Larson, Z. Wang, et al. “Simulating the Galactic population of axion clouds around stellar-origin black holes: Gravitational wave signals in the 10–100 kHz band.” In: *Phys. Rev. D* 110.12 (2024), p. 123025. DOI: [10.1103/PhysRevD.110.123025](https://doi.org/10.1103/PhysRevD.110.123025). arXiv: [2409.03714](https://arxiv.org/abs/2409.03714) [[astro-ph.HE](#)].
- [41] N. Aggarwal et al. “Challenges and opportunities of gravitational-wave searches at MHz to GHz frequencies.” In: *Living Rev. Rel.* 24.1 (2021), p. 4. DOI: [10.1007/s41114-021-00032-5](https://doi.org/10.1007/s41114-021-00032-5). arXiv: [2011.12414](https://arxiv.org/abs/2011.12414) [[gr-qc](#)].
- [42] C. Kouvaris, P. Tinyakov, and M. H. G. Tytgat. “NonPrimordial Solar Mass Black Holes.” In: *Phys. Rev. Lett.* 121.22 (2018), p. 221102. DOI: [10.1103/PhysRevLett.121.221102](https://doi.org/10.1103/PhysRevLett.121.221102). arXiv: [1804.06740](https://arxiv.org/abs/1804.06740) [[astro-ph.HE](#)].
- [43] T. Nakamura, M. Sasaki, T. Tanaka, et al. “Gravitational waves from coalescing black hole MACHO binaries.” In: *Astrophys. J. Lett.* 487 (1997), pp. L139–L142. DOI: [10.1086/310886](https://doi.org/10.1086/310886). arXiv: [astro-ph/9708060](https://arxiv.org/abs/astro-ph/9708060).
- [44] S. Shandera, D. Jeong, and H. S. G. Gebhardt. “Gravitational Waves from Binary Mergers of Subsolar Mass Dark Black Holes.” In: *Phys. Rev. Lett.* 120.24 (2018), p. 241102. DOI: [10.1103/PhysRevLett.120.241102](https://doi.org/10.1103/PhysRevLett.120.241102). arXiv: [1802.08206](https://arxiv.org/abs/1802.08206) [[astro-ph.CO](#)].
- [45] Y. B. Zel’dovich and I. D. Novikov. “The Hypothesis of Cores Retarded during Expansion and the Hot Cosmological Model.” In: *Sov. Astron.* 10 (1967), p. 602.
- [46] S. Hawking. “Gravitationally collapsed objects of very low mass.” In: *Mon. Not. Roy. Astron. Soc.* 152 (1971), p. 75. DOI: [10.1093/mnras/152.1.75](https://doi.org/10.1093/mnras/152.1.75).
- [47] B. J. Carr and S. W. Hawking. “Black holes in the early Universe.” In: *MNRAS* 168 (Aug. 1974), pp. 399–416. DOI: [10.1093/mnras/168.2.399](https://doi.org/10.1093/mnras/168.2.399).
- [48] C. Palenzuela, P. Pani, M. Bezares, et al. “Gravitational Wave Signatures of Highly Compact Boson Star Binaries.” In: *Phys. Rev. D* 96.10 (2017), p. 104058. DOI: [10.1103/PhysRevD.96.104058](https://doi.org/10.1103/PhysRevD.96.104058). arXiv: [1710.09432](https://arxiv.org/abs/1710.09432) [[gr-qc](#)].
- [49] P. O. Mazur and E. Mottola. “Gravitational vacuum condensate stars.” In: *Proc. Nat. Acad. Sci.* 101 (2004), pp. 9545–9550. DOI: [10.1073/pnas.0402717101](https://doi.org/10.1073/pnas.0402717101). arXiv: [gr-qc/0407075](https://arxiv.org/abs/gr-qc/0407075).
- [50] G. Narain, J. Schaffner-Bielich, and I. N. Mishustin. “Compact stars made of fermionic dark matter.” In: *Phys. Rev. D* 74 (2006), p. 063003. DOI: [10.1103/PhysRevD.74.063003](https://doi.org/10.1103/PhysRevD.74.063003). arXiv: [astro-ph/0605724](https://arxiv.org/abs/astro-ph/0605724).
- [51] S. Krippendorf, F. Muia, and F. Quevedo. “Moduli Stars.” In: *JHEP* 08 (2018), p. 070. DOI: [10.1007/JHEP08\(2018\)070](https://doi.org/10.1007/JHEP08(2018)070). arXiv: [1806.04690](https://arxiv.org/abs/1806.04690) [[hep-th](#)].

- [52] S. Shandera, D. Jeong, and H. S. G. Gebhardt. “Gravitational Waves from Binary Mergers of Subsolar Mass Dark Black Holes.” In: *Phys. Rev. Lett.* 120.24 (2018), p. 241102. doi: [10.1103/PhysRevLett.120.241102](https://doi.org/10.1103/PhysRevLett.120.241102). arXiv: [1802.08206](https://arxiv.org/abs/1802.08206) [astro-ph.CO].
- [53] A. L. Miller. “Gravitational waves from sub-solar mass primordial black holes.” Apr. 2024. arXiv: [2404.11601](https://arxiv.org/abs/2404.11601) [gr-qc].
- [54] A. Arvanitaki, M. Baryakhtar, and X. Huang. “Discovering the QCD Axion with Black Holes and Gravitational Waves.” In: *Phys. Rev. D* 91.8 (2015), p. 084011. doi: [10.1103/PhysRevD.91.084011](https://doi.org/10.1103/PhysRevD.91.084011). arXiv: [1411.2263](https://arxiv.org/abs/1411.2263) [hep-ph].
- [55] R. Brito, S. Ghosh, E. Barausse, et al. “Gravitational wave searches for ultra-light bosons with LIGO and LISA.” In: *Phys. Rev. D* 96.6 (2017), p. 064050. doi: [10.1103/PhysRevD.96.064050](https://doi.org/10.1103/PhysRevD.96.064050). arXiv: [1706.06311](https://arxiv.org/abs/1706.06311) [gr-qc].
- [56] R. D. Peccei and H. R. Quinn. “CP Conservation in the Presence of Instantons.” In: *Phys. Rev. Lett.* 38 (1977), pp. 1440–1443. doi: [10.1103/PhysRevLett.38.1440](https://doi.org/10.1103/PhysRevLett.38.1440).
- [57] R. D. Peccei and H. R. Quinn. “Constraints Imposed by CP Conservation in the Presence of Instantons.” In: *Phys. Rev. D* 16 (1977), pp. 1791–1797. doi: [10.1103/PhysRevD.16.1791](https://doi.org/10.1103/PhysRevD.16.1791).
- [58] F. Wilczek. “Problem of Strong P and T Invariance in the Presence of Instantons.” In: *Phys. Rev. Lett.* 40 (1978), pp. 279–282. doi: [10.1103/PhysRevLett.40.279](https://doi.org/10.1103/PhysRevLett.40.279).
- [59] S. Weinberg. “A New Light Boson?.” In: *Phys. Rev. Lett.* 40 (1978), pp. 223–226. doi: [10.1103/PhysRevLett.40.223](https://doi.org/10.1103/PhysRevLett.40.223).
- [60] M. Goodsell, J. Jaeckel, J. Redondo, et al. “Naturally Light Hidden Photons in LARGE Volume String Compactifications.” In: *JHEP* 11 (2009), p. 027. doi: [10.1088/1126-6708/2009/11/027](https://doi.org/10.1088/1126-6708/2009/11/027). arXiv: [0909.0515](https://arxiv.org/abs/0909.0515) [hep-ph].
- [61] K. Petraki and R. R. Volkas. “Review of asymmetric dark matter.” In: *Int. J. Mod. Phys. A* 28 (2013), p. 1330028. doi: [10.1142/S0217751X13300287](https://doi.org/10.1142/S0217751X13300287). arXiv: [1305.4939](https://arxiv.org/abs/1305.4939) [hep-ph].
- [62] M. Fabbrichesi, E. Gabrielli, and G. Lanfranchi. “The Dark Photon.” May 2020. doi: [10.1007/978-3-030-62519-1](https://doi.org/10.1007/978-3-030-62519-1). arXiv: [2005.01515](https://arxiv.org/abs/2005.01515) [hep-ph].
- [63] L. Hui, J. P. Ostriker, S. Tremaine, et al. “Ultralight scalars as cosmological dark matter.” In: *Phys. Rev. D* 95.4 (2017), p. 043541. doi: [10.1103/PhysRevD.95.043541](https://doi.org/10.1103/PhysRevD.95.043541). arXiv: [1610.08297](https://arxiv.org/abs/1610.08297) [astro-ph.CO].
- [64] P. Arias, D. Cadamuro, M. Goodsell, et al. “WISPy Cold Dark Matter.” In: *JCAP* 06 (2012), p. 013. doi: [10.1088/1475-7516/2012/06/013](https://doi.org/10.1088/1475-7516/2012/06/013). arXiv: [1201.5902](https://arxiv.org/abs/1201.5902) [hep-ph].

- [65] G. Bertone and D. Hooper. “History of dark matter.” In: *Rev. Mod. Phys.* 90.4 (2018), p. 045002. doi: [10.1103/RevModPhys.90.045002](https://doi.org/10.1103/RevModPhys.90.045002). arXiv: [1605.04909](https://arxiv.org/abs/1605.04909) [[astro-ph.CO](#)].
- [66] B. P. Abbott et al. “Search for Substellar-Mass Ultracompact Binaries in Advanced LIGO’s First Observing Run.” In: *Phys. Rev. Lett.* 121.23 (2018), p. 231103. doi: [10.1103/PhysRevLett.121.231103](https://doi.org/10.1103/PhysRevLett.121.231103). arXiv: [1808.04771](https://arxiv.org/abs/1808.04771) [[astro-ph.CO](#)].
- [67] B. P. Abbott et al. “Search for Substellar Mass Ultracompact Binaries in Advanced LIGO’s Second Observing Run.” In: *Phys. Rev. Lett.* 123.16 (2019), p. 161102. doi: [10.1103/PhysRevLett.123.161102](https://doi.org/10.1103/PhysRevLett.123.161102). arXiv: [1904.08976](https://arxiv.org/abs/1904.08976) [[astro-ph.CO](#)].
- [68] R. Abbott et al. “Search for Substellar-Mass Binaries in the First Half of Advanced LIGO’s and Advanced Virgo’s Third Observing Run.” In: *Phys. Rev. Lett.* 129.6 (2022), p. 061104. doi: [10.1103/PhysRevLett.129.061104](https://doi.org/10.1103/PhysRevLett.129.061104). arXiv: [2109.12197](https://arxiv.org/abs/2109.12197) [[astro-ph.CO](#)].
- [69] A. H. Nitz and Y.-F. Wang. “Search for Gravitational Waves from the Coalescence of Substellar-Mass Binaries in the First Half of Advanced LIGO and Virgo’s Third Observing Run.” In: *Phys. Rev. Lett.* 127.15 (2021), p. 151101. doi: [10.1103/PhysRevLett.127.151101](https://doi.org/10.1103/PhysRevLett.127.151101). arXiv: [2106.08979](https://arxiv.org/abs/2106.08979) [[astro-ph.HE](#)].
- [70] A. L. Miller, N. Aggarwal, S. Clesse, et al. “Gravitational Wave Constraints on Planetary-Mass Primordial Black Holes Using LIGO O3a Data.” In: *Phys. Rev. Lett.* 133.11 (2024), p. 111401. doi: [10.1103/PhysRevLett.133.111401](https://doi.org/10.1103/PhysRevLett.133.111401). arXiv: [2402.19468](https://arxiv.org/abs/2402.19468) [[gr-qc](#)].
- [71] R. Abbott et al. “All-sky search for gravitational wave emission from scalar boson clouds around spinning black holes in LIGO O3 data.” In: *Phys. Rev. D* 105.10 (2022), p. 102001. doi: [10.1103/PhysRevD.105.102001](https://doi.org/10.1103/PhysRevD.105.102001). arXiv: [2111.15507](https://arxiv.org/abs/2111.15507) [[astro-ph.HE](#)].
- [72] L. Sun, R. Brito, and M. Isi. “Search for ultralight bosons in Cygnus X-1 with Advanced LIGO.” In: *Phys. Rev. D* 101.6 (2020). [Erratum: *Phys. Rev. D* 102, 089902 (2020)], p. 063020. doi: [10.1103/PhysRevD.101.063020](https://doi.org/10.1103/PhysRevD.101.063020). arXiv: [1909.11267](https://arxiv.org/abs/1909.11267) [[gr-qc](#)].
- [73] H.-K. Guo, K. Riles, F.-W. Yang, et al. “Searching for Dark Photon Dark Matter in LIGO O1 Data.” In: *Commun. Phys.* 2 (2019), p. 155. doi: [10.1038/s42005-019-0255-0](https://doi.org/10.1038/s42005-019-0255-0). arXiv: [1905.04316](https://arxiv.org/abs/1905.04316) [[hep-ph](#)].
- [74] G. Franciolini, A. Maharana, and F. Muia. “Hunt for light primordial black hole dark matter with ultrahigh-frequency gravitational waves.” In: *Phys. Rev. D* 106.10 (2022), p. 103520. doi: [10.1103/PhysRevD.106.103520](https://doi.org/10.1103/PhysRevD.106.103520). arXiv: [2205.02153](https://arxiv.org/abs/2205.02153) [[astro-ph.CO](#)].

- [75] I. Goldman and S. Nussinov. “Weakly Interacting Massive Particles and Neutron Stars.” In: *Phys. Rev. D* 40 (1989), pp. 3221–3230. DOI: [10.1103/PhysRevD.40.3221](https://doi.org/10.1103/PhysRevD.40.3221).
- [76] C. Kouvaris and P. Tinyakov. “Can Neutron stars constrain Dark Matter?.” In: *Phys. Rev. D* 82 (2010), p. 063531. DOI: [10.1103/PhysRevD.82.063531](https://doi.org/10.1103/PhysRevD.82.063531). arXiv: [1004.0586](https://arxiv.org/abs/1004.0586) [[astro-ph.GA](#)].
- [77] A. Hook and J. Huang. “Probing axions with neutron star inspirals and other stellar processes.” In: *JHEP* 06 (2018), p. 036. DOI: [10.1007/JHEP06\(2018\)036](https://doi.org/10.1007/JHEP06(2018)036). arXiv: [1708.08464](https://arxiv.org/abs/1708.08464) [[hep-ph](#)].
- [78] J. Huang, M. C. Johnson, L. Sagunski, et al. “Prospects for axion searches with Advanced LIGO through binary mergers.” In: *Phys. Rev. D* 99.6 (2019), p. 063013. DOI: [10.1103/PhysRevD.99.063013](https://doi.org/10.1103/PhysRevD.99.063013). arXiv: [1807.02133](https://arxiv.org/abs/1807.02133) [[hep-ph](#)].
- [79] S. Alexander, E. McDonough, R. Sims, et al. “Hidden-Sector Modifications to Gravitational Waves From Binary Inspirals.” In: *Class. Quant. Grav.* 35.23 (2018), p. 235012. DOI: [10.1088/1361-6382/aaeb5c](https://doi.org/10.1088/1361-6382/aaeb5c). arXiv: [1808.05286](https://arxiv.org/abs/1808.05286) [[gr-qc](#)].
- [80] I. H. Stairs. “Testing general relativity with pulsar timing.” In: *Living Rev. Rel.* 6 (2003), p. 5. DOI: [10.12942/lrr-2003-5](https://doi.org/10.12942/lrr-2003-5). arXiv: [astro-ph/0307536](https://arxiv.org/abs/astro-ph/0307536).
- [81] N. Wex. “Testing Relativistic Gravity with Radio Pulsars.” In: (Feb. 2014). arXiv: [1402.5594](https://arxiv.org/abs/1402.5594) [[gr-qc](#)].
- [82] B. C. Seymour and K. Yagi. “Probing Massive Scalar Fields from a Pulsar in a Stellar Triple System.” In: *Class. Quant. Grav.* 37.14 (2020), p. 145008. DOI: [10.1088/1361-6382/ab9933](https://doi.org/10.1088/1361-6382/ab9933). arXiv: [1908.03353](https://arxiv.org/abs/1908.03353) [[gr-qc](#)].
- [83] B. C. Seymour and K. Yagi. “Probing massive scalar and vector fields with binary pulsars.” In: *Phys. Rev. D* 102.10 (2020), p. 104003. DOI: [10.1103/PhysRevD.102.104003](https://doi.org/10.1103/PhysRevD.102.104003). arXiv: [2007.14881](https://arxiv.org/abs/2007.14881) [[gr-qc](#)].
- [84] S. J. Asztalos et al. “A SQUID-based microwave cavity search for dark-matter axions.” In: *Phys. Rev. Lett.* 104 (2010), p. 041301. DOI: [10.1103/PhysRevLett.104.041301](https://doi.org/10.1103/PhysRevLett.104.041301). arXiv: [0910.5914](https://arxiv.org/abs/0910.5914) [[astro-ph.CO](#)].
- [85] R. Agnese et al. “Silicon Detector Dark Matter Results from the Final Exposure of CDMS II.” In: *Phys. Rev. Lett.* 111.25 (2013), p. 251301. DOI: [10.1103/PhysRevLett.111.251301](https://doi.org/10.1103/PhysRevLett.111.251301). arXiv: [1304.4279](https://arxiv.org/abs/1304.4279) [[hep-ex](#)].
- [86] E. Armengaud et al. “Final results of the EDELWEISS-II WIMP search using a 4-kg array of cryogenic germanium detectors with interleaved electrodes.” In: *Phys. Lett. B* 702 (2011), pp. 329–335. DOI: [10.1016/j.physletb.2011.07.034](https://doi.org/10.1016/j.physletb.2011.07.034). arXiv: [1103.4070](https://arxiv.org/abs/1103.4070) [[astro-ph.CO](#)].

- [87] A. A. Abdo et al. “Constraints on Cosmological Dark Matter Annihilation from the Fermi-LAT Isotropic Diffuse Gamma-Ray Measurement.” In: *JCAP* 04 (2010), p. 014. DOI: [10.1088/1475-7516/2010/04/014](https://doi.org/10.1088/1475-7516/2010/04/014). arXiv: [1002.4415](https://arxiv.org/abs/1002.4415) [astro-ph.CO].
- [88] W. B. Atwood et al. “The Large Area Telescope on the Fermi Gamma-Ray Space Telescope Mission.” In: *ApJ* 697.2 (June 2009), pp. 1071–1102. DOI: [10.1088/0004-637X/697/2/1071](https://doi.org/10.1088/0004-637X/697/2/1071). arXiv: [0902.1089](https://arxiv.org/abs/0902.1089) [astro-ph.IM].
- [89] T. F. L. collaboration. “Limits on dark matter annihilation signals from the Fermi LAT 4-year measurement of the isotropic gamma-ray background.” In: *Journal of Cosmology and Astroparticle Physics* 2015.09 (Sept. 2015), pp. 008–008. ISSN: 1475-7516. DOI: [10.1088/1475-7516/2015/09/008](https://doi.org/10.1088/1475-7516/2015/09/008). URL: <http://dx.doi.org/10.1088/1475-7516/2015/09/008>.
- [90] P. Tisserand et al. “Limits on the Macho Content of the Galactic Halo from the EROS-2 Survey of the Magellanic Clouds.” In: *Astron. Astrophys.* 469 (2007), pp. 387–404. DOI: [10.1051/0004-6361:20066017](https://doi.org/10.1051/0004-6361:20066017). arXiv: [astro-ph/0607207](https://arxiv.org/abs/astro-ph/0607207).
- [91] T. Lasserre. “Not enough stellar mass machos in the galactic halo.” In: *Astron. Astrophys.* 355 (2000), pp. L39–L42. arXiv: [astro-ph/0002253](https://arxiv.org/abs/astro-ph/0002253).
- [92] N. Aggarwal et al. “Challenges and Opportunities of Gravitational Wave Searches above 10 kHz.” Jan. 2025. arXiv: [2501.11723](https://arxiv.org/abs/2501.11723) [gr-qc].
- [93] K. L. Dooley et al. “GEO 600 and the GEO-HF upgrade program: successes and challenges.” In: *Class. Quant. Grav.* 33 (2016), p. 075009. DOI: [10.1088/0264-9381/33/7/075009](https://doi.org/10.1088/0264-9381/33/7/075009). arXiv: [1510.00317](https://arxiv.org/abs/1510.00317) [physics.ins-det].
- [94] B. Willke et al. “The GEO 600 gravitational wave detector.” In: *Class. Quant. Grav.* 19 (2002). Ed. by D. G. Blair, pp. 1377–1387. DOI: [10.1088/0264-9381/19/7/321](https://doi.org/10.1088/0264-9381/19/7/321).
- [95] S. Hild. “Beyond the First Generation: Extending the Science Range of the Gravitational Wave Detector GEO600..” PhD thesis. Gottfried Wilhelm Leibniz Universität Hannover, Hannover, 2007.
- [96] A. Freise. “The next generation of interferometry: Multi frequency modelling, control concepts and implementation.” PhD thesis. Hannover U., 2003.
- [97] C. M. Jungkind, B. C. Seymour, and A. Laeuger. *GEO600 High-Frequency Modeling*. Version 2.39.3. Dec. 2024. URL: <https://github.com/Chris19j/GEO600-High-Frequency-Modeling>.
- [98] H. Grote, A. Freise, M. Malec, et al. “Dual recycling for GEO 600.” In: *Class. Quant. Grav.* 21 (2004). Ed. by C. Bradaschia, S473–S480. DOI: [10.1088/0264-9381/21/5/013](https://doi.org/10.1088/0264-9381/21/5/013).

- [99] M. Rakhmanov, R. Savage, D. Reitze, et al. “Dynamic resonance of light in Fabry–Perot cavities.” In: *Physics Letters A* 305.5 (Dec. 2002), pp. 239–244. ISSN: 0375-9601. DOI: [10.1016/S0375-9601\(02\)01469-X](https://doi.org/10.1016/S0375-9601(02)01469-X). URL: [http://dx.doi.org/10.1016/S0375-9601\(02\)01469-X](http://dx.doi.org/10.1016/S0375-9601(02)01469-X).
- [100] B. J. Meers. “Recycling in Laser Interferometric Gravitational Wave Detectors.” In: *Phys. Rev. D* 38 (1988), pp. 2317–2326. DOI: [10.1103/PhysRevD.38.2317](https://doi.org/10.1103/PhysRevD.38.2317).
- [101] J. Mizuno, K. Strain, P. Nelson, et al. “Resonant sideband extraction: a new configuration for interferometric gravitational wave detectors.” In: *Physics Letters A* 175.5 (1993), pp. 273–276. ISSN: 0375-9601. DOI: [https://doi.org/10.1016/0375-9601\(93\)90620-F](https://doi.org/10.1016/0375-9601(93)90620-F). URL: <https://www.sciencedirect.com/science/article/pii/037596019390620F>.
- [102] G. Heinzl, J. Mizuno, R. Schilling, et al. “An experimental demonstration of resonant sideband extraction for laser-interferometric gravitational wave detectors.” In: *Physics Letters A* 217.6 (1996), pp. 305–314. ISSN: 0375-9601. DOI: [https://doi.org/10.1016/0375-9601\(96\)00361-1](https://doi.org/10.1016/0375-9601(96)00361-1). URL: <https://www.sciencedirect.com/science/article/pii/0375960196003611>.
- [103] G. Heinzl. “Advanced optical techniques for laser-interferometric gravitational-wave detectors.” Other thesis. Feb. 1999.
- [104] A. Freise, G. Heinzl, H. Luck, et al. “Frequency domain interferometer simulation with higher order spatial modes.” In: *Class. Quant. Grav.* 21 (2004). Ed. by C. Bradaschia, S1067–S1074. DOI: [10.1088/0264-9381/21/5/102](https://doi.org/10.1088/0264-9381/21/5/102). arXiv: [gr-qc/0309012](https://arxiv.org/abs/gr-qc/0309012).
- [105] C. Bond, D. Brown, A. Freise, et al. “Interferometer Techniques for Gravitational-Wave Detection.” In: *Living Rev. Rel.* 19 (2017), p. 217. DOI: <https://doi.org/10.1007/s41114-016-0002-8>.
- [106] J. Lough. “Calibrating a folded interferometer for short gravitational waves.” Tech. rep. P2400382. LIGO, 2024. URL: <https://dcc.ligo.org/LIGO-P2400382>.
- [107] H. Wittel. “Compensation of the thermal lens in the GEO600 beam splitter.” PhD thesis. Hannover, Max Planck Inst. Grav., 2009.
- [108] S. Gossler. “The suspension systems of the interferometric gravitational-wave detector GEO600.” PhD thesis. Hannover U., 2004.
- [109] C. Affeldt et al. “Advanced techniques in GEO 600.” In: *Class. Quant. Grav.* 31.22 (2014), p. 224002. DOI: [10.1088/0264-9381/31/22/224002](https://doi.org/10.1088/0264-9381/31/22/224002).
- [110] J. Lough. “Private Communication (2024).”

- [111] A. Buonanno and Y.-b. Chen. “Quantum noise in second generation, signal recycled laser interferometric gravitational wave detectors.” In: *Phys. Rev. D* 64 (2001), p. 042006. DOI: [10.1103/PhysRevD.64.042006](https://doi.org/10.1103/PhysRevD.64.042006). arXiv: [gr-qc/0102012](https://arxiv.org/abs/gr-qc/0102012).
- [112] J. G. Rollins, E. Hall, C. Wipf, et al. *pygwinc: Gravitational Wave Interferometer Noise Calculator*. Astrophysics Source Code Library, record ascl:2007.020. July 2020.
- [113] C. Affeldt. “Laser power increase for GEO 600: commissioning aspects towards an operation of GEO 600 at high laser power.” PhD thesis. Leibniz U., Hannover, 2014. DOI: [10.15488/8213](https://doi.org/10.15488/8213).
- [114] V. B. Braginsky, S. E. Strigin, and S. P. Vyatchanin. “Parametric oscillatory instability in Fabry-Perot (FP) interferometer.” In: *Phys. Lett. A* 287 (2001), pp. 331–338. DOI: [10.1016/S0375-9601\(01\)00510-2](https://doi.org/10.1016/S0375-9601(01)00510-2). arXiv: [gr-qc/0107079](https://arxiv.org/abs/gr-qc/0107079).
- [115] M. Evans et al. “Observation of Parametric Instability in Advanced LIGO.” In: *Phys. Rev. Lett.* 114.16 (2015), p. 161102. DOI: [10.1103/PhysRevLett.114.161102](https://doi.org/10.1103/PhysRevLett.114.161102). arXiv: [1502.06058](https://arxiv.org/abs/1502.06058) [[astro-ph.IM](https://arxiv.org/abs/1502.06058)].
- [116] C. D. Blair, Y. Levin, and E. Thrane. “Constraining temperature distribution inside LIGO test masses from frequencies of their vibrational modes.” In: *Phys. Rev. D* 103.2 (2021), p. 022003. DOI: [10.1103/PhysRevD.103.022003](https://doi.org/10.1103/PhysRevD.103.022003). arXiv: [2011.00957](https://arxiv.org/abs/2011.00957) [[astro-ph.IM](https://arxiv.org/abs/2011.00957)].
- [117] A. Gurkovsky and S. Vyatchanin. “Parametric instability in GEO 600 interferometer.” In: *Physics Letters A* 370.3 (2007), pp. 177–183. ISSN: 0375-9601. DOI: <https://doi.org/10.1016/j.physleta.2007.05.063>. URL: <https://www.sciencedirect.com/science/article/pii/S0375960107008006>.
- [118] M. Isi, L. Sun, R. Brito, et al. “Directed searches for gravitational waves from ultralight bosons.” In: *Phys. Rev. D* 99.8 (2019). [Erratum: *Phys.Rev.D* 102, 049901 (2020)], p. 084042. DOI: [10.1103/PhysRevD.99.084042](https://doi.org/10.1103/PhysRevD.99.084042). arXiv: [1810.03812](https://arxiv.org/abs/1810.03812) [[gr-qc](https://arxiv.org/abs/1810.03812)].
- [119] S. J. Zhu, M. Baryakhtar, M. A. Papa, et al. “Characterizing the continuous gravitational-wave signal from boson clouds around Galactic isolated black holes.” In: *Phys. Rev. D* 102.6 (2020), p. 063020. DOI: [10.1103/PhysRevD.102.063020](https://doi.org/10.1103/PhysRevD.102.063020). arXiv: [2003.03359](https://arxiv.org/abs/2003.03359) [[gr-qc](https://arxiv.org/abs/2003.03359)].
- [120] W. E. East. “Superradiant instability of massive vector fields around spinning black holes in the relativistic regime.” In: *Phys. Rev. D* 96.2 (2017), p. 024004. DOI: [10.1103/PhysRevD.96.024004](https://doi.org/10.1103/PhysRevD.96.024004). arXiv: [1705.01544](https://arxiv.org/abs/1705.01544) [[gr-qc](https://arxiv.org/abs/1705.01544)].

- [121] J. Golomb, I. Legred, K. Chatziioannou, et al. “Using equation of state constraints to classify low-mass compact binary mergers.” In: *Phys. Rev. D* 110.6 (2024), p. 063014. DOI: [10.1103/PhysRevD.110.063014](https://doi.org/10.1103/PhysRevD.110.063014). arXiv: [2403.07697](https://arxiv.org/abs/2403.07697) [astro-ph.HE].
- [122] C. M. Biwer, C. D. Capano, S. De, et al. “PyCBC Inference: A Python-based Parameter Estimation Toolkit for Compact Binary Coalescence Signals.” In: *Publications of the Astronomical Society of the Pacific* 131.996 (Jan. 2019), p. 024503. ISSN: 1538-3873. DOI: [10.1088/1538-3873/aaef0b](https://doi.org/10.1088/1538-3873/aaef0b). URL: <http://dx.doi.org/10.1088/1538-3873/aaef0b>.
- [123] N. Mukund et al. “Neural sensing and control in a kilometer-scale gravitational-wave observatory.” In: *Phys. Rev. Applied* 20.6 (2023), p. 064041. DOI: [10.1103/PhysRevApplied.20.064041](https://doi.org/10.1103/PhysRevApplied.20.064041). arXiv: [2301.06221](https://arxiv.org/abs/2301.06221) [physics.ins-det].
- [124] F. Bergamin. “Development of a squeezing-compatible signal recycling cavity control at GEO600.” PhD thesis. Leibniz U., Hannover, 2024. DOI: [10.15488/17442](https://doi.org/10.15488/17442).
- [125] F. Khalili and E. S. Polzik. “Overcoming the SQL in gravitational wave detectors using spin systems with negative effective mass.” In: *Phys. Rev. Lett.* 121 (2018), p. 031101. DOI: [10.1103/PhysRevLett.121.031101](https://doi.org/10.1103/PhysRevLett.121.031101). arXiv: [1710.10405](https://arxiv.org/abs/1710.10405) [quant-ph].
- [126] E. Zeuthen, E. S. Polzik, and F. Y. Khalili. “Gravitational wave detection beyond the standard quantum limit using a negative-mass spin system and virtual rigidity.” In: *Phys. Rev. D* 100.6 (2019), p. 062004. DOI: [10.1103/PhysRevD.100.062004](https://doi.org/10.1103/PhysRevD.100.062004). arXiv: [1908.03416](https://arxiv.org/abs/1908.03416) [gr-qc].
- [127] Y. Nishino, S. Danilishin, Y. Enomoto, et al. “Frequency-dependent squeezing for gravitational-wave detection through quantum teleportation.” In: *Phys. Rev. A* 110.2 (2024), p. 022601. DOI: [10.1103/PhysRevA.110.022601](https://doi.org/10.1103/PhysRevA.110.022601). arXiv: [2401.04295](https://arxiv.org/abs/2401.04295) [quant-ph].
- [128] M. J. Yap, P. Altin, T. G. McRae, et al. “Generation and control of frequency-dependent squeezing via Einstein–Podolsky–Rosen entanglement.” In: *Nature Photonics* 14.4 (Apr. 2020), pp. 223–226. DOI: [10.1038/s41566-019-0582-4](https://doi.org/10.1038/s41566-019-0582-4).
- [129] D. Heinert, K. Craig, H. Grote, et al. “Thermal noise of folding mirrors.” In: *Phys. Rev. D* 90.4 (2014), p. 042001. DOI: [10.1103/PhysRevD.90.042001](https://doi.org/10.1103/PhysRevD.90.042001).
- [130] E. Schreiber. “Gravitational-wave detection beyond the quantum shot-noise limit: the integration of squeezed light in GEO 600.” PhD thesis. Leibniz U., Hannover, 2018. DOI: [10.15488/3773](https://doi.org/10.15488/3773).
- [131] C. M. Caves. “Quantum Mechanical Noise in an Interferometer.” In: *Phys. Rev. D* 23 (1981), pp. 1693–1708. DOI: [10.1103/PhysRevD.23.1693](https://doi.org/10.1103/PhysRevD.23.1693).

- [132] H. Grote, M. Weinert, R. X. Adhikari, et al. “High power and ultra-low-noise photodetector for squeezed-light enhanced gravitational wave detectors.” In: *Opt. Express* 24.18 (Sept. 2016), pp. 20107–20118. doi: [10.1364/OE.24.020107](https://doi.org/10.1364/OE.24.020107). URL: <https://opg.optica.org/oe/abstract.cfm?URI=oe-24-18-20107>.
- [133] V. Quetschke. “Korrelationen von Rauschquellen bei Nd:YAG Lasersystemen.” PhD thesis. Hannover U., 2003.
- [134] P. Kwee. “Laser Characterization and Stabilization for Precision Interferometry.” PhD thesis. Hannover U, 2010. doi: [10.15488/7443](https://doi.org/10.15488/7443).
- [135] T. S. Adams. “Detector characterisation and searches for gravitational waves using GEO 600.” PhD thesis. Cardiff U., 2014.
- [136] B. Benthem and Y. Levin. “Thermo-refractive and thermo-chemical noise in the beamsplitter of GEO600 gravitational-wave interferometer.” In: *Phys. Rev. D* 80 (2009), p. 062004. doi: [10.1103/PhysRevD.80.062004](https://doi.org/10.1103/PhysRevD.80.062004). arXiv: [0907.1015](https://arxiv.org/abs/0907.1015) [gr-qc].
- [137] J. Dickmann, S. Kroker, Y. Levin, et al. “Thermal noise of beam splitters in laser gravitational wave detectors.” In: *Phys. Rev. D* 98.8 (2018), p. 082002. doi: [10.1103/PhysRevD.98.082002](https://doi.org/10.1103/PhysRevD.98.082002). arXiv: [1809.10994](https://arxiv.org/abs/1809.10994) [astro-ph.IM].

